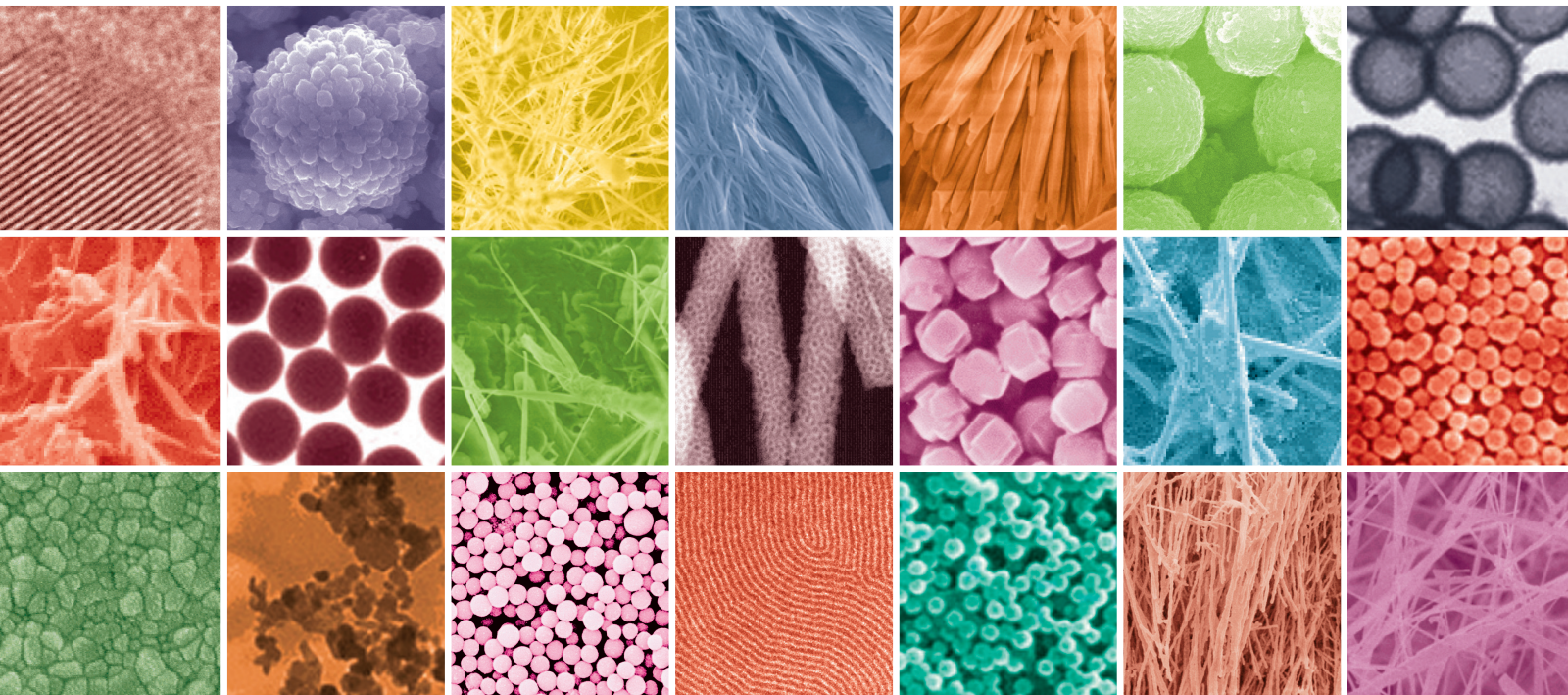


Nanomaterial Properties: Size and Shape Dependencies

Guest Editors: Grégory Guisbiers, Sergio Mejía-Rosales,
Francis Leonard Deepak, and Chang Q. Sun





Nanomaterial Properties: Size and Shape Dependencies

Nanomaterial Properties: Size and Shape Dependencies

Guest Editors: Grégory Guisbiers, Sergio Mejía-Rosales, Francis Leonard Deepak, and Chang Q. Sun



Copyright © 2012 Hindawi Publishing Corporation. All rights reserved.

This is a special issue published in "Journal of Nanomaterials." All articles are open access articles distributed under the Creative Commons Attribution License, which permits unrestricted use, distribution, and reproduction in any medium, provided the original work is properly cited.

Editorial Board

- Katerina Aifantis, Greece
Nageh K. Allam, USA
Margarida Amaral, Portugal
Xuedong Bai, China
L. Balan, France
Enrico Bergamaschi, Italy
Theodorian Borca-Tasciuc, USA
C. Jeffrey Brinker, USA
Christian Brosseau, France
Xuebo Cao, China
Shafiul Chowdhury, USA
Kwang-Leong Choy, UK
Cui ChunXiang, China
Miguel A. Correa-Duarte, Spain
Shadi A. Dayeh, USA
Claude Estournes, France
Alan Fuchs, USA
Lian Gao, China
Russell E. Gorga, USA
Hongchen Chen Gu, China
Mustafa O. Guler, Turkey
John Zhanhu Guo, USA
Smrati Gupta, Germany
Michael Harris, USA
Zhongkui Hong, USA
Michael Z. Hu, USA
David Hui, USA
Y.-K. Jeong, Republic of Korea
Sheng-Rui Jian, Taiwan
Wanqin Jin, China
Rakesh K. Joshi, India
Zhenhui Kang, China
Fathallah Karimzadeh, Iran
Alireza Khataee, Iran
- Do Kyung Kim, Korea
Kin Tak Lau, Australia
Burtrand Lee, USA
Benxia Li, China
Jun Li, Singapore
Shijun Liao, China
Gong Ru Lin, Taiwan
J.-Y. Liu, USA
Jun Liu, USA
Tianxi Liu, China
Songwei Lu, USA
Daniel Lu, China
Jue Lu, USA
Ed Ma, USA
Gaurav Mago, USA
Santanu K. Maiti, Israel
Sanjay R. Mathur, Germany
A. McCormick, USA
Vikas Mittal, UAE
Weihai Ni, Germany
Sherine Obare, USA
Abdelwahab Omri, Canada
Edward Andrew Payzant, USA
Kui-Qing Peng, China
Anukorn Phuruangrat, Thailand
Ugur Serincan, Turkey
Huaiyu Shao, Japan
Donglu Shi, USA
Suprakas Sinha Ray, South Africa
Vladimir Sivakov, Germany
Marinella Striccoli, Italy
Bohua Sun, South Africa
Saikat Talapatra, USA
Nairong Tao, China
- Titipun Thongtem, Thailand
Somchai Thongtem, Thailand
Alexander Tolmachev, Ukraine
Valeri P. Tolstoy, Russia
Tsung-Yen Tsai, Taiwan
Takuya Tsuzuki, Australia
Raquel Verdejo, Spain
Mat U. Wahit, Malaysia
Shiren Wang, USA
Yong Wang, USA
Ruibing Wang, Canada
Cheng Wang, China
Zhenbo Wang, China
Jinquan Wei, China
Ching Ping Wong, USA
Xingcai Wu, China
Guodong Xia, Hong Kong
Zhi Li Xiao, USA
Ping Xiao, UK
Shuangxi Xing, China
Yangchuan Xing, USA
N. Xu, China
Doron Yadlovker, Israel
Ying-Kui Yang, China
Khaled Youssef, USA
William W. Yu, USA
Kui Yu, Canada
Haibo Zeng, China
Tianyou Zhai, Japan
Renyun Zhang, Sweden
Yanbao Zhao, China
Lianxi Zheng, Singapore
Chunyi Zhi, Japan

Contents

Nanomaterial Properties: Size and Shape Dependencies, Grégory Guisbiers, Sergio Mejía-Rosales, and Francis Leonard Deepak
Volume 2012, Article ID 180976, 2 pages

Phototriggered Production of Reactive Oxygen Species by TiO_2 Nanospheres and Rods, Bianca Geiseler, Marko Miljevic, Philipp Müller, and Ljiljana Fruk
Volume 2012, Article ID 708519, 9 pages

Functionalization of Silica Nanoparticles for Polypropylene Nanocomposite Applications, Diego Bracho, Vivianne N. Dougnac, Humberto Palza, and Raúl Quijada
Volume 2012, Article ID 263915, 8 pages

Glassy Carbon Electrode-Supported Au Nanoparticles for the Glucose Electrooxidation: On the Role of Crystallographic Orientation, M. Guerra-Balcázar, J. Torres-González, I. Terol-Villalobos, J. Morales-Hernández, and F. Castañeda
Volume 2012, Article ID 387581, 8 pages

Effect of Tetramethylammonium Hydroxide on Nucleation, Surface Modification and Growth of Magnetic Nanoparticles, Ângela L. Andrade, José D. Fabris, José D. Ardisson, Manuel A. Valente, and José M. F. Ferreira
Volume 2012, Article ID 454759, 10 pages

Spark Plasma Sintering of Metals and Metal Matrix Nanocomposites: A Review, Nouari Saheb, Zafar Iqbal, Abdullah Khalil, Abbas Saeed Hakeem, Nasser Al Aqeeli, Tahar Laoui, Amro Al-Qutub, and René Kirchner
Volume 2012, Article ID 983470, 13 pages

Hybrid Scaffolds for Tissue Regeneration: Chemotaxis and Physical Confinement as Sources of Biomimesis, Simone Sprio, Monica Sandri, Silvia Panseri, Carla Cunha, and Anna Tampieri
Volume 2012, Article ID 418281, 10 pages

Polycation-Capped CdS Quantum Dots Synthesized in Reverse Microemulsions, Karina Lemke and Joachim Koetz
Volume 2012, Article ID 478153, 10 pages

Optical and Structural Properties of Silicon Nanocrystals Embedded in SiO_x Matrix Obtained by HWCVD, A. Coyopol, G. García-Salgado, T. Díaz-Becerril, H. Juárez, E. Rosendo, R. López, M. Pacio, J. A. Luna-López, and J. Carrillo-López
Volume 2012, Article ID 368268, 7 pages

Nanomechanics of Nonideal Single- and Double-Walled Carbon Nanotubes, C. H. Wong and V. Vijayaraghavan
Volume 2012, Article ID 490872, 9 pages

Size-Dependent Dynamic Behavior of a Microcantilever Plate, Xiaoming Wang and Fei Wang
Volume 2012, Article ID 891347, 5 pages

SnO_2 Nanoparticle-Based Passive Capacitive Sensor for Ethylene Detection, Mangilal Agarwal, Mercyma D. Balachandran, Sudhir Shrestha, and Kody Varahramyan
Volume 2012, Article ID 145406, 5 pages

Structural Properties of Zn-ZnO Core-Shell Microspheres Grown by Hot-Filament CVD Technique,
R. López, T. Díaz, G. García, R. Galeazzi, E. Rosendo, A. Coyopol, M. Pacio, H. Juárez, and A. I. Oliva
Volume 2012, Article ID 865321, 7 pages

Solubility of Carbon in Nanocrystalline α -Iron, Alexander Kirchner and Bernd Kieback
Volume 2012, Article ID 953828, 4 pages

Elastic Analysis for Nanocontact Problem with Surface Stress Effects under Shear Load, D. X. Lei,
L. Y. Wang, and Z. Y. Ou
Volume 2012, Article ID 505034, 7 pages

One-Step Method for Preparation of Magnetic Nanoparticles Coated with Chitosan,
Karla M. Gregorio-Jauregui, Ma. Guadalupe Pineda, Jorge E. Rivera-Salinas, Gil Hurtado, Hened Saade,
José L. Martínez, Anna Ilyina, and Raúl G. López
Volume 2012, Article ID 813958, 8 pages

A First-Principle Study of B- and P-Doped Silicon Quantum Dots, Jieqiong Zeng and Hong Yu
Volume 2012, Article ID 147169, 7 pages

Particle Size Effect on TL Emission of ZnS Nanoparticles and Determination of Its Kinetic Parameters,
L. Robindro Singh and S. Dorendrajit Singh
Volume 2012, Article ID 239182, 8 pages

Catalysis of Methanol-Air Mixture Using Platinum Nanoparticles for Microscale Combustion,
James R. Applegate, Howard Pearlman, and Smitesh D. Bakrania
Volume 2012, Article ID 460790, 8 pages

**Effect of Size, Shape, and Surface Modification on Cytotoxicity of Gold Nanoparticles to Human HEP-2
and Canine MDCK Cells,** Yinan Zhang, Dan Xu, Wenqin Li, Jun Yu, and Yu Chen
Volume 2012, Article ID 375496, 7 pages

Magnetic Properties of FePt Nanoparticles Prepared by Sonoelectrodeposition, Nguyen Hoang Nam,
Nguyen Thi Thanh Van, Nguyen Dang Phu, Tran Thi Hong, Nguyen Hoang Hai, and Nguyen Hoang Luong
Volume 2012, Article ID 801240, 4 pages

Study on Vibration Behavior of Doubly Clamped Silicon Nanowires by Molecular Dynamics, H. Yu,
W. W. Zhang, S. Y. Lei, L. B. Lu, C. Sun, and Q. A. Huang
Volume 2012, Article ID 342329, 5 pages

Size and Shape Dependence on Melting Temperature of Gallium Nitride Nanoparticles,
Paneerselvam Antoniammal and Dakshanamoorthy Arivuoli
Volume 2012, Article ID 415797, 11 pages

Top-Down Processing of NaNbO_3 Nanopowder, Jurij Koruza, Barbara Malič, Oleksandr Noshchenko,
and Marija Kosec
Volume 2012, Article ID 469143, 7 pages

The Size and Shape Dependence of Ferromagnetism in Nanomagnets, Ying Li, Yongfeng Li,
and Tianxing Wang
Volume 2012, Article ID 897203, 6 pages

Layer-by-Layer Self-Assembled Metal-Ion- (Ag-, Co-, Ni-, and Pd-) Doped TiO₂ Nanoparticles: Synthesis, Characterisation, and Visible Light Degradation of Rhodamine B, Mphilisi M. Mahlambi, Ajay K. Mishra, Shivani B. Mishra, Ashok M. Raichur, Bhekie B. Mamba, and Rui W. Krause
Volume 2012, Article ID 302046, 12 pages

Cubic-to-Tetragonal Phase Transitions in AgCu Nanorods, Francesco Delogu and Michele Mascia
Volume 2012, Article ID 453062, 8 pages

Editorial

Nanomaterial Properties: Size and Shape Dependencies

Grégory Guisbiers,¹ Sergio Mejía-Rosales,² and Francis Leonard Deepak³

¹ *Research Institute for Materials Science and Engineering, University of Mons, Place du Parc No. 23, 7000 Mons, Belgium*

² *Facultad de Ciencias Físico-Matemáticas, Universidad Autónoma de Nuevo León, San Nicolás de los Garza, NL 66450, Mexico*

³ *The International Iberian Nanotechnology Laboratory (INL), Av. Mestre José Veiga s/n, Braga 4715-330, Portugal*

Correspondence should be addressed to Grégory Guisbiers, gregory.guisbiers@physics.org

Received 6 December 2012; Accepted 6 December 2012

Copyright © 2012 Grégory Guisbiers et al. This is an open access article distributed under the Creative Commons Attribution License, which permits unrestricted use, distribution, and reproduction in any medium, provided the original work is properly cited.

Nanoscience and nanotechnology are among the most widely used terms in the modern scientific and technological literature. The idea of nanotechnology appeared for the first time in the famous talk “*There is plenty of room at the bottom*” given by the physicist Richard Feynman at the American Physical Society meeting at Caltech on December 29, 1959. Feynman described a process by which the ability to manipulate individual atoms and molecules might be developed, using one set of precise tools to build and operate another proportionally smaller set and so on down to the needed scale. In the course of this, he noted, scaling issues would arise from the changing magnitude of various physical phenomena: gravity would become less important whereas surface effects would become increasingly more significant. The term *nanotechnology* was originally defined by Norio Taniguchi in 1974 as follows: “Nano-technology mainly consists of the processing of separation, consolidation and deformation of materials by one atom or by one molecule.” Nanotechnology and nanoscience got started in the early 1980s with two major developments: the advances in computing power and material modeling coupled with significant advances in characterization such as the scanning tunneling microscope (STM) and the atomic force microscope (AFM).

The field of nanoscience and nanotechnology is now growing very rapidly. According to the UK Royal Society, nanoscience is defined as the study of phenomena and manipulation of materials at atomic, molecular, and macromolecular scales, where properties differ significantly from those at a larger scale. Nanotechnologies are the design, characterization, production, and application of structures, devices, and systems by controlling shape and size at the

nanoscale. Nanomaterials cross the boundary between nanoscience and nanotechnologies and link these both areas together. Generally, nanomaterials deal with sizes of 100 nanometers or smaller in at least one dimension. The material properties of nanostructures are different from the bulk due to the high surface area over volume ratio and possible appearance of quantum effects at the nanoscale. The study of size and shape effects on material properties has attracted enormous attention due to their scientific and industrial importance.

It is therefore a great pleasure to edit this special issue. In this rapidly progressing area of nanoscience and nanotechnology, it is always important to highlight the most recent and active areas that are being pursued and highlight them to the scientific community. Thus, this special issue brings to fore several such closely related yet diverse areas that encompass this field and are actively being investigated. The papers that appear in this special issue have been grouped according to their themes: size effect on mechanical properties, size effect on catalytic properties, and so forth.

The effect of size in the structural and electronic properties of quantum dots, using DFT calculations, is the topic of study of the paper “*A first-principle study of B- and P-doped silicon quantum dots*,” by J. Zeng and H. Yu; they found that the structural distortions on the quantum dots depend both on the kind of dopant and on the size of the dots. The paper entitled “*Cubic-to-tetragonal phase transitions in Ag–Cu nanorods*” by F. Delogu and M. Moscia describes molecular dynamics simulation results concerning the structural phase transition of the Ag–Cu nanoalloy. W. W. Zhang et al., also using a computational approach, investigate the size dependence of the resonant frequencies in

silicon nanowires, and their molecular dynamics simulations show that, at small sizes, surface reconstruction affects greatly the vibrational properties of the nanowires; you can find these results in the paper “*Study on vibration behavior of doubly clamped silicon nanowires by molecular dynamics.*” The paper by C. H. Wong and V. Vijayaraghavan showcases the nanomechanics of single- and double-walled carbon nanotubes using molecular dynamics simulations. Also investigating elastic properties, D. X. Lei take a more analytical approach to study the properties of nanocontacts in the paper “*Elastic analysis for nanocontact problem with surface stress effects under shear load.*” The mechanical behavior of a microcantilever has been investigated by X. Wang and F. Wang in the paper “*Size-dependent dynamic behavior of a microcantilever plate.*” D. Bracho et al. investigate the use of silica nanoparticles in the preparation of nanocomposites in the paper “*Functionalization of silica nanoparticles for polypropylene nanocomposite applications,*” where they report interesting dependencies of the mechanical properties of nanocomposites on the size of silica particles. The size and shape dependencies on the melting temperature of gallium nitride has been discussed by D. Arivuoli and P. Antoniammal while the size and shape dependence of ferromagnetism in nanomagnets has been discussed by Y. Li et al. The paper entitled “*Magnetic properties of FePt nanoparticles prepared by sonoelectrodeposition*” by N. H. Nam et al. describes the method of sonoelectrodeposition as a facile method to successfully synthesize large quantities of ferromagnetic Fe₄₅Pt₅₅ nanoparticles. The synthesis and colloidal stability of Fe₃O₄ magnetic nanoparticles which can have potential applications for hyperthermia are highlighted in the paper “*Effect of tetramethylammonium hydroxide on nucleation, surface modification and growth of magnetic nanoparticles*” by A. L. Andeade et al. In the paper “*One-step method for preparation of magnetic nanoparticles coated with chitosan,*” K. M. Gregorio-Jáuregui et al. propose another simple method for the production of magnetic nanoparticles.

The effect of size in the catalytic properties of gold nanoparticles supported on glassy carbon is investigated in the paper “*Glassy carbon electrode-supported Au nanoparticles for the glucose electrooxidation: on the role of crystallographic orientation,*” by M. Guerra-Balcázar et al. The effect of size and shape on the toxicity of gold nanoparticles has been investigated by Y. Zhang et al. The catalytic properties of platinum nanoparticles have been studied by J. R. Applegate et al. in the paper entitled “*Catalysis of methanol-air mixture using platinum nanoparticles for microscale combustion.*” The study done by M. M. Mahlambi et al. shows that m-TiO₂ nanocatalyst has the potential to be used in water treatment processes for the degradation of pollutants using solar energy as the source of irradiation energy.

The review paper “*Spark plasma sintering of metals and metal matrix nanocomposites*” by N. Saheb et al. describes the spark-plasma-sintering process as an effective method to generate successfully a wide variety of metals, alloys, and metal matrix nanocomposites. The work of J. Koruza et al. on the paper “*Top-down processing of NaNbO₃ nanopowder*” focuses in the establishment of a straightforward method to produce nanopowders with a fair control on the size of the

particles. The synthesis of quantum dots has been discussed in the paper “*Polycation-capped CdS quantum dots synthesized in reverse microemulsions*” by K. Lemke and J. Koetz. The synthesis of Zn-ZnO core-shell particles was described and characterized by López et al. The optical properties of silicon nanoparticles embedded in a matrix have been investigated by A. Coyopol et al. The thermoluminescence properties of different diameter ZnS Nanoparticles are described in the paper entitled “*Particle size effect on TL emission of ZnS nanoparticles and determination of its kinetic parameters*” by L. R. Singh and S. D. Singh. The production of reactive oxygen species under the light irradiation of two different types of TiO₂ nanocrystals has been studied by L. Fruk et al. The paper on biomineralization processes by S. Sprio et al. describes the synthesis of hybrid hydroxyapatite/collagen scaffolds for bone and osteochondral regeneration. Finally, let us present an application using nanoparticles; a passive capacitor sensor using SnO₂ nanoparticles is presented by M. Agarwal et al. for the detection of ethylene gas.

As the reader may realize, the papers that conform this issue are connected not only by the nature of the systems that are being investigated, and by the techniques used for synthesis and measurement, but also for the emphasis on size effects on the properties of their subjects of study. We believe that we are living in an exciting age where these size dependencies offer both challenges and opportunities, and that, if we take the appropriate approach, this will give us more room for discoveries and applications, even more than the *plenty of room* that Feynman was thinking on.

Grégory Guisbiers
Sergio Mejía-Rosales
Francis Leonard Deepak

Research Article

Phototriggered Production of Reactive Oxygen Species by TiO₂ Nanospheres and Rods

Bianca Geiseler,¹ Marko Miljevic,¹ Philipp Müller,² and Ljiljana Fruk¹

¹DFG-Centre for Functional Nanostructures, Karlsruhe Institute of Technology (KIT), Wolfgang-Gaede-Straße 1a, 76131 Karlsruhe, Germany

²Laboratorium für Elektronmikroskopie, Karlsruhe Institute of Technology (KIT), Engessestrasse, 76131 Karlsruhe, Germany

Correspondence should be addressed to Ljiljana Fruk, ljiljana.fruk@kit.edu

Received 5 March 2012; Revised 20 September 2012; Accepted 25 September 2012

Academic Editor: Grégory Guisbiers

Copyright © 2012 Bianca Geiseler et al. This is an open access article distributed under the Creative Commons Attribution License, which permits unrestricted use, distribution, and reproduction in any medium, provided the original work is properly cited.

We present the study of reactive oxygen species production under the light irradiation of two different types of TiO₂ nanocrystals. Both TiO₂ spheric NPs and anisotropic nanorods were investigated using activation of the horseradish peroxidase enzyme and subsequent substrate oxidation into a fluorescent product. The influence of the surface ligand dopamine was also explored to shed more light on the effect of catechol binders on the photoactivity of TiO₂ species.

1. Introduction

In recent years, anisotropic nanostructures such as nanorods, nanodiscs, cubes, or prisms [1] have started to attract more attention not only of researchers working in the field of materials science and synthetic chemistry but also biochemistry and cancer research [1–3]. Anisotropic structures have a range of properties such as large surface plasmons, which can often be tuned by changing the shape and size during the growth process [4]. Therefore, they are interesting candidates for design of different sensors, photovoltaic devices, or bioactive elements (Au rods in cancer treatment) [5, 6]. The plasmonic bands of Au nanorods, for example, can be tuned by the length of the rods, which can enable design of powerful SERS sensors or plasmonic solar cells [7–10]. Recently, they were also used as biocompatible, optically active absorbers and scatterers for targeted photodiagnosics and as contrast agents for biological imaging [11, 12]. In addition, anisotropic nanomaterials can possess different chemical affinities and therefore enable assembly of larger structures through an end-to-end binding under certain conditions [13, 14]. Furthermore, their high surface-to-volume ratio results in a high density of active surface reagents enabling further modification and improved catalytic action [15].

Titanium dioxide (TiO₂) has found numerous applications in photovoltaics [16], sensor [17] and new material

design [18] and catalysis [19]. Nanoscaled semiconducting TiO₂ has also been shown to induce the production of reactive oxygen species (ROS) such as hydroxyl (OH) and peroxy (HO₂) radicals, superoxide anions (O₂⁻), and hydrogen peroxide (H₂O₂) [20], upon the light irradiation in aqueous solutions, the amount depending largely on the size [21] and the morphology of the nanostructures [22]. Recently, Sayer and coworkers have shown that anatase form of TiO₂ produced more ROS species than the rutile after being exposed to the UV irradiation therefore rendering it more cytotoxic [23, 24]. Several *in vitro* studies have demonstrated that ROS produced by light triggered activation of TiO₂ nanospheres can induce oxidative damage of DNA strands [25–27]. Due to these properties, TiO₂ nanomaterials can be used for application in photodynamic cancer therapy (PDT), where the tumor cells containing TiO₂ species can be destroyed by ROS produced upon light activation [28, 29]. However, most of the ROS studies performed until now have been done using commercial Degussa P-25 and, to our knowledge, no systematic studies of the ROS production of anisotropic TiO₂ nanostructures have been reported. Furthermore, the effect of the catechol based surface binding molecules has not been explored. Herewith, we present the study and the comparison of ROS production between spherical and anisotropic rod TiO₂ as well as the influence of the bound catechol moieties onto the amount of phototriggered reactive species.

2. Experimental Section

2.1. Materials and Instrumentation. All chemicals were purchased from Sigma Aldrich and used without further purification. Horseradish peroxidase (HRP) type VI-A was used for ROS experiments. The UV/Vis absorption spectra were recorded using a CARY50 UV/Vis spectrophotometer (Agilent Technology, Germany). The TEM images were obtained on a Philips CM200 FEG/ST electron microscope. Malvern Zetasizer Nano instrument (Malvern, UK) was used to perform dynamic light scattering (DLS) and zeta potential measurements. FT-IR measurements were performed using a Bruker IFS88 FTIR-spectrometer (Bruker Corporation, Germany).

2.2. Synthesis of TiO₂ Nanoparticles

2.2.1. Diethylene Glycol TiO₂ Nanoparticles (TiO₂ NPdeg). TiO₂ nanoparticles were prepared using a protocol by Wang et al. with slight modification [30]. Briefly, 0.2 mL titanium(IV) chloride was added to 6 mL of DEG under vigorous stirring and inert atmosphere at 60°C. The suspension was heated at 75°C until the solution became clear. Then, 0.1 mL ddH₂O was injected into the solution and further refluxed at 160°C for 3 h. After cooling to the room temperature, 15 mL acetone was added to aid the NP precipitation. The NP solution was centrifuged and washed several times with acetone to remove residual surfactants. The average size of obtained nanoparticles, determined by TEM, was 3 nm.

2.2.2. Synthesis of Oleic Acid/Oleylamine TiO₂ Nanoparticles (TiO₂ NPole). TiO₂ nanoparticles were prepared using a protocol by Seo et al. [31] resulting in the dispersion of, in average, 3 nm TiO₂ in toluene.

2.3. Synthesis of TiO₂ Nanorods. TiO₂ nanorods (TiO₂ NR) were prepared using a protocol by Seo et al., but under different reaction times [31]. In a typical synthesis, 0.55 mL titanium(IV) chloride was added at 250°C to a solution of 3.21 mL oleic acid and 24.8 mL oleylamine. The reaction mixture was heated to 270°C under water cooling. After 2.5, 4, 6, and 8 hours, the reaction was quenched by the addition of cold toluene (6 mL) and then the reaction mixture was allowed to cool to room temperature. White or brownish TiO₂ nanorods were obtained by the addition of an excess of acetone. After centrifugation (10 min at 5000 rpm), the white powder was redissolved in 3 mL toluene and precipitated with 7 mL ethanol. These washing steps were performed three times. The nanorods were characterized by TEM.

2.4. Surface Modification of the TiO₂ NR. TiO₂ NRs (1.00 mg) were suspended in 2 mL toluene, followed by addition of 3.00 mg dopamine hydrochloride (DA) in 2 mL water. After five seconds, a color change from colorless to brown was observed indicating the formation of the charge transfer complex. The reaction mixture was further stirred overnight at 22°C. After purification by centrifugation (3x), the residue was dispersed in ddH₂O (TiO₂ NR + DA).

2.5. Radical Oxygen Species Determination. For ROS measurements, we have used an assay previously described by

Fruk et al. [32] for CdS quantum dot nanoparticles, based on the activation of horse radish peroxidase (HRP) in presence of fluorogenic substrate 10-Acetyl-3,7-dihydroxyphenoxazine (Ampliflu Red). Ampliflu Red solution was prepared according to the manufacturer's instructions as a 10 mM stock in DMSO. Standard 96-well plates were used to load them with desired amounts of various TiO₂ NC. The samples were always prepared as 1 mg/mL stock solutions in KPi buffer (50 mM KH₂PO₄, 50 mM K₂HPO₄, pH = 7.0). Four different volumes were investigated (0, 1, 50, and 100 μL). When the samples were in the wells (150 μL), the plate was placed below the 4-W UV handheld lamp and irradiated for 30 minutes at 366 and 254 nm. The distance between the plate and the light source was 3 cm. Immediately after irradiation, HRP was added (37.6 μL, 1.33 μM) followed by addition of Ampliflu Red (10 μL, 0.9 mM). The plate was mixed in a Synergy H1 Hybrid Multi-Mode Microplate Reader for additional five minutes prior to the fluorescence measurements ($\lambda_{\text{ex}} = 540 \text{ nm}$, $\lambda_{\text{em}} = 585 \text{ nm}$).

2.6. Infrared Spectroscopy. FT-IR spectra of TiO₂ powders before and after ligand exchange procedures were measured.

2.7. Transmission Electron Microscopy (TEM). The TEM samples were prepared by ultrasonic dispersion of the particle solution in toluene on a carbon support film (3 nm, TED Pella Inc., California). TEM experiments were performed using a Philips CM200FEG/ST microscope. Debye diffraction patterns were analyzed using the method described in the literature [33]. The diffraction pattern of anatase and rutile were simulated using the JEMS software package.

3. Results

3.1. Synthesis and Characterization of the TiO₂ Nanorods. The nanorods were prepared using a high temperature, oleylamine-oleic acid protocol by Seo et al. [34] but introducing longer reactions time. We were interested in exploring if the prolonged reaction time has an effect of the size and the shape of the nanostructures obtained. Titanium (IV) chloride (TiCl₄) precursor was added to oleic acid and oleylamine, refluxed at 270°C and the morphology of prepared nanostructures was checked in regular intervals. 3 nm spherical TiO₂ NPs were obtained after 30 minutes (data not shown), but after additional reflux, only TiO₂ nanorods were present in the suspension. Samples taken after 2.5, 4, 6, and 8 hours of reflux have been imaged by TEM and it was observed that uniformly shaped NRs were obtained (Figure 1).

Mean length and widths were determined by manually measuring the dimensions of 100 rods in each sample and the data are summarized in Table 1. It can be clearly seen that 17 nm NRs are already formed after 2.5 hours and there was no significant change in length or width after the increased growth time or after the further addition of the TiCl₄ precursor.

These results are in slight contradiction with previously reported work by Ge et al. [35] where prolonged refluxing favored the formation of larger needle-like TiO₂ particles.

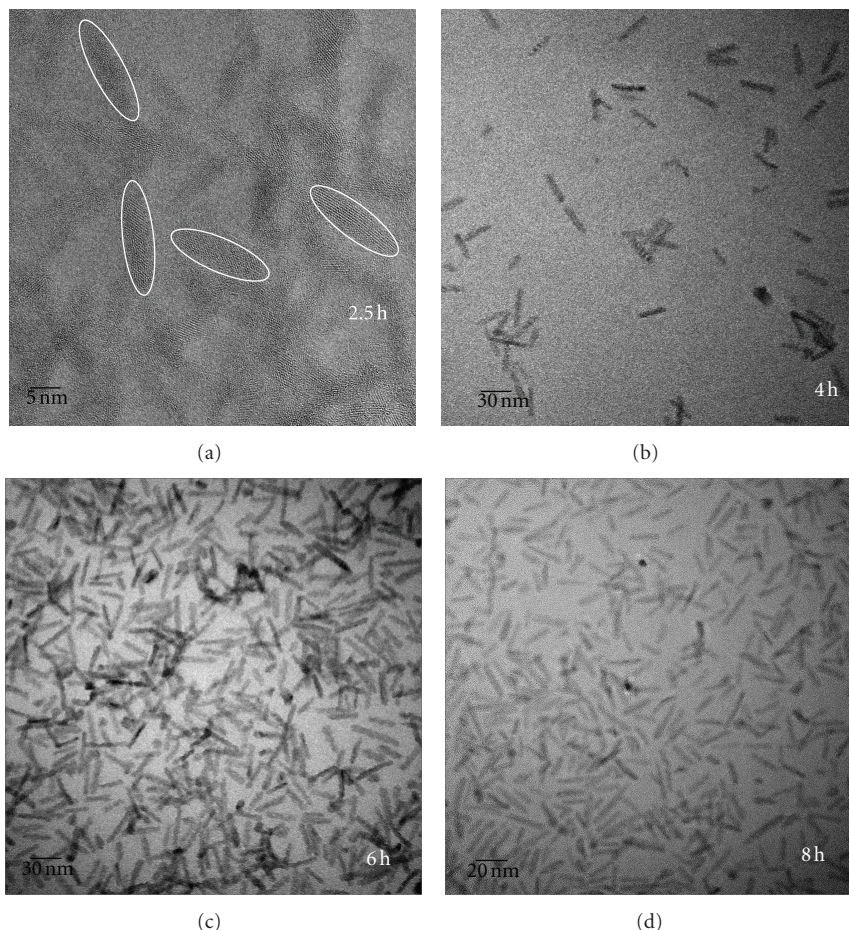


FIGURE 1: TEM images of TiO_2 NR obtained by oleic acid-oleylamine high-temperature method after (a) 2.5, (b) 4, (c) 6, and (d) 8 hours of reflux.

TABLE 1: Dimensions of produced TiO_2 nanorods using oleylamine-oleic acid protocol.

Heating period (hours)	Mean length (nm)	Mean width (nm)
2.5	17.0 ± 5.0	3.20 ± 1.2
4.0	17.0 ± 4.0	3.60 ± 0.6
6.0	17.0 ± 4.0	3.60 ± 0.6
8.0	16.0 ± 4.0	3.60 ± 0.6

However, it should be noted that we have used different solvents (oleic acid oleylamine versus water) as well as different titanium precursor (TiCl_4 versus TiSO_4), which resulted in different kinetics of the crystal growth. The crystallinity of the prepared NRs was confirmed by Debye diffraction pattern and the obtained curves were in a good agreement with the anatase form (SI, See Figure S1 in supplementary material available online at doi:10.1155/2012/708519). Prepared NRs were further characterized by UV-VIS, which showed a broad peak centered around 270 nm (Figure 2(a)).

Previous studies reported that oleic acid is able to anchor onto the surface of TiO_2 [36], but it can be easily replaced by the addition of strongly binding enediol ligands like catechols [37]. Recently, we have described the synthesis of

different bifunctional dopamine (DA) based linkers, which, on one side, bind strongly onto the TiO_2 NP surface and, on the other, contain additional functional groups that enable further modification [38] and preparation of bio-friendly, aqueous suspensions of nanoparticles. For the same reasons, dopamine was used to modify the surface of the nanorods and the successful binding was determined by UV-Vis spectrometry and FT-IR spectroscopy. Catechol moieties form a strong surface charge complex with TiO_2 which results in the immediate change of color upon the addition of dopamine to TiO_2 NRs. The broad absorption peak centered around 370 nm results in excitation of an electron from the valence to the conduction band [39].

FT-IR spectra shown in Figure 3 also confirm the successful modification of TiO_2 NR surface with dopamine ligand. Above 2000 cm^{-1} , TiO_2 NR alone (Figure 3(b)) as well as TiO_2 NR + DA (Figure 3(c)) exhibit the intense antisymmetric and symmetric C-H stretching vibrations (at 2920 and 2850 cm^{-1} , resp.) of the $-\text{CH}_2-$ groups in the hydrocarbon moiety [36]. The vibrational band of the primary amine positioned around 3300 cm^{-1} is visible in the spectrum of pure dopamine (Figure 3(a)) and also for the dopamine modified NR at 3250 cm^{-1} (TiO_2 NR + DA), which indicates that dopamine is bound to the NR surface [40]. At around

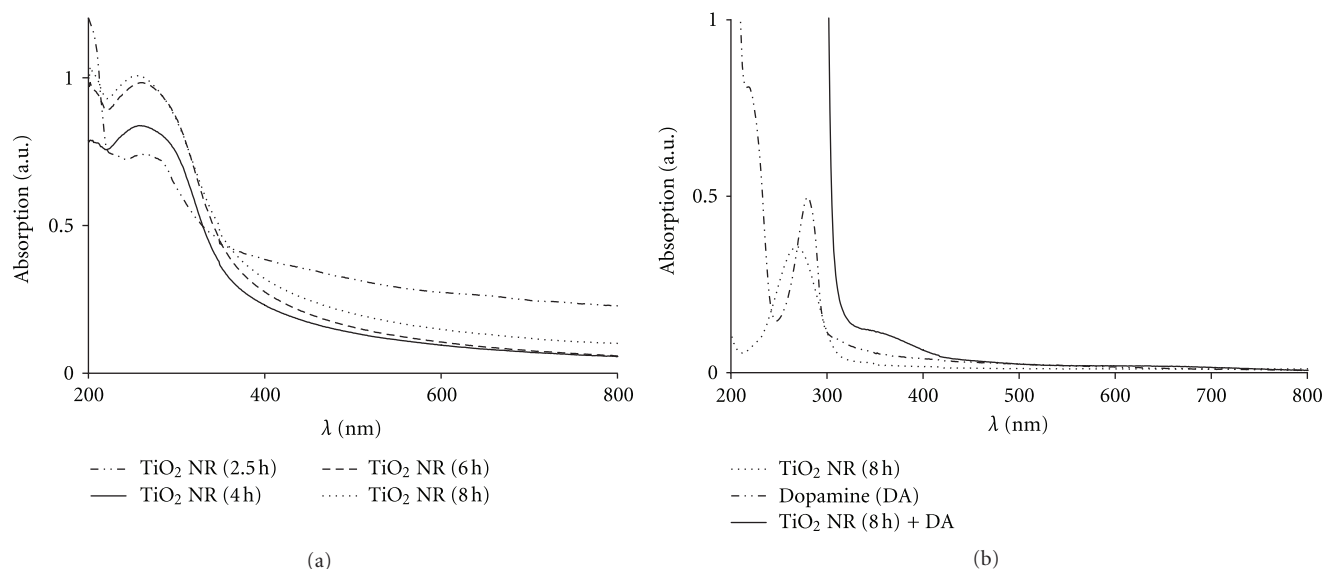


FIGURE 2: UV-Vis spectra of (a) TiO₂ NR synthesized by varying the reaction times and (b) after the addition of DA to TiO₂ NR (8 h).

TABLE 2: ζ potentials of the bare TiO₂ NRs and dopamine-modified NRs.

Heating period (hours)	Zeta average (mV) without dopamine	Zeta average (mV) modified with dopamine
2.5	13.1 ± 0.6	53.5 ± 0.8
4.0	-6.50 ± 0.1	47.7 ± 0.3
6.0	-22.5 ± 0.8	44.0 ± 1.0
8.0	-39.4 ± 0.5	38.7 ± 0.4

1012 cm^{-1} , the deformation of C=CH can be observed in pure DA and also for TiO₂ NR + DA. Below 2000 cm^{-1} , the COO⁻ antisymmetric and symmetric stretching vibrations (characteristic band centered at 1454 cm^{-1}) of carboxylate anions [41] complexed with surface Ti centers dominate in the spectra of the oleylamine and oleic acid capped TiO₂ nanocrystals.

We have additionally characterized both unmodified and modified TiO₂ NR by measuring their ξ -potential both in prior and following dopamine (DA) functionalization and the results are summarized in Table 2.

The data show that there is a change of ξ -potential of the nanorods upon the modification. More positive zeta potential confirms that the dopamine is bound through catechol groups leaving positive amino group exposed on the surface. Interestingly, the ξ -potential of different unmodified NR becomes more negative with the time of reflux, which indicates that the amount of negative charges increases. This is probably due to the recombination of the TiO₂ species and corresponding Ti(IV) and O(II) centers on the crystal surface during the crystal growth and ripening, resulting in the change of the atom coordination [42]. The crystallinity of anatase crystals increases with the reflux time [35] resulting

in the formation of basic pentacoordinated surface titanium atom and more negative surface charges.

3.2. Radical Oxygen Species Production. When a semiconductor absorbs photons with an energy greater than its band gap, electrons can be excited to the conduction band, thus creating electron-hole pairs [43]. Those excited electrons can be then recombined with the species close to the surface and it has been shown that a number of radical species can be produced in aqueous environment (Figure 4). It has been shown previously that irradiation of CdS quantum dots [32, 44] leads to the production of superoxide and hydroxyl radicals, which can recombine into H₂O₂ in aqueous solutions. Numerous enzymes are involved in H₂O₂ metabolic cycle both as a H₂O₂ generating or scavenging agents and peroxide is an important molecular fuel for triggering a range of oxidative reactions. In particular, heme containing enzymes such as peroxidases or P450 utilize H₂O₂ as an activating species to enable oxidation of a range of reactions. Not only they have important metabolic function but also have an increased application in chemical catalysis [45]. As some of the peroxidases have found applications in biosensing and catalysis, there is a number of fluorogenic substrates that can be used as peroxidase substrates and the oxidation of which results in fluorescent products in presence of H₂O₂ and the active enzyme [46].

It has been recently shown by Zhang et al. that there is a relationship between the photocatalytic activity and the surface phase [47]. The band gap of rutile was determined to be around 3.06 eV and that of anatase 3.23 eV [48] which means that UV light can be used to induce the charge separation and electron (e⁻)-hole (h⁺) pair generation in nanosized structures [49]. Both can recombine with the species in the proximity of the nanomaterials surface and, in aqueous solution, lead to the production of superoxide (O₂^{-•}) and hydroxyl (OH[•]) ROS (Figure 4). These radical species can act

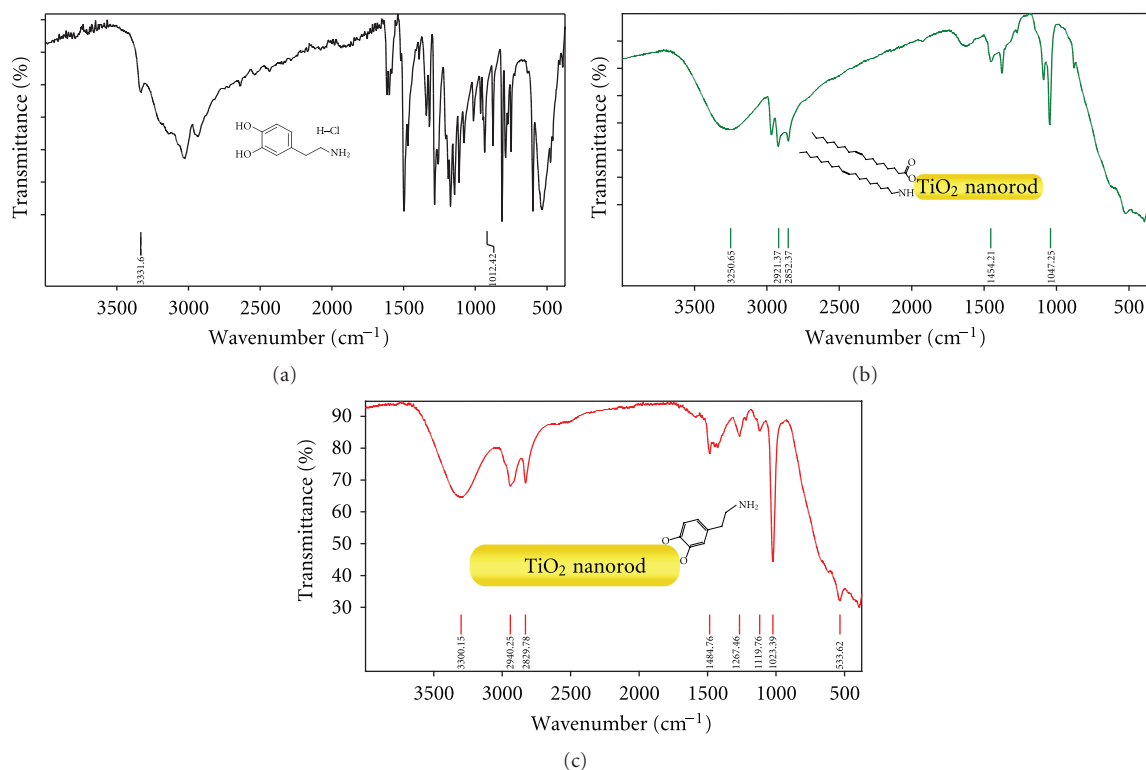


FIGURE 3: IR (ATR) spectra of (a) pure dopamine, (b) unmodified TiO₂ NR, and (c) TiO₂ NR + DA.

alone as heme enzyme activators [44] or could recombine into H₂O₂, which can be coordinated to the heme center and induce the cascade of reactions. The nature or the ROS species itself will be reported elsewhere as in this investigation we were interested in demonstrating that heme enzyme can be activated upon TiO₂ irradiation and the amount of activating species quantified using enzymatic assay.

To achieve this, the nonfluorescent Ampliflu Red substrate was used [50], which is oxidized by activated HRP into fluorescent resorufin. Commonly, H₂O₂ needs to be added to the enzyme solution to activate the heme center and enable the substrate oxidation. However, this can be circumvented by the addition of the semiconducting NPs, which act as light triggered generators of the activating species.

3.2.1. Activation of HRP through Irradiation of TiO₂ NPs. Oxidation of Ampliflu Red in presence of irradiated TiO₂ NPs and HRP is shown in Figure 5. To avoid any damage of Ampliflu Red and HRP that might be induced upon prolonged UV irradiation, TiO₂ NPs alone were first irradiated with 366 nm for 30 minutes and both the enzyme and the substrate subsequently added. It can be seen in Figure 5 that only in case of the commercial TiO₂ NP (TiO₂ NP_{comm}), significant fluorescence from the oxidized product can be observed. Both TiO₂ NP_{deg} and TiO₂ NP_{ole} showed small or no change. The reason for this lies in the size of the NPs—both are, on average, smaller than 5 nm. Thus, the band gap is larger [51] and requires more energy to produce electron-hole pairs, which recombine with the surrounding

O₂ and H₂O molecules to generate radical species (UV-Vis SI, Figure S3). For much bigger commercial TiO₂ NPs with average diameter of 20 nm, 366 nm light is energetic enough to ensure the production of ROS species which can activate the HRP and lead to the oxidation of the substrate. More substrate is oxidized as more TiO₂ NPs is irradiated, indicating the increase of the activating species (Figure 5).

Control samples, where no NPs were added, showed no significant fluorescence. When more energetic 254 nm light source was used, increased fluorescence was observed for all three types of NPs (SI, Figure S2a). However, interestingly, in the case of TiO₂ NP_{deg}, which are coated with diethylene glycol, the fluorescence decreased with the increase of the TiO₂ NP concentration, indicating that there are some other effects, which play an important role in this case. We hypothesize that this is due to the degradation of ethylene glycol species upon UV irradiation with degradation products acting as radical scavengers therefore limiting the enzyme activation [52]. This effect is currently under investigation although for *in situ*, temporal control of the enzyme activation, the use of 254 nm irradiation is not desirable as it can lead to a fast degradation processes and possible deactivation of the biological molecules.

Next, dopamine coated NPs (NP + DA) were investigated to probe the influence of the surface ligands onto the ROS production. Dopamine is known to be an efficient antioxidant and it has been shown that it protects neurocytes from oxidative stress by scavenging free radicals [53]. The ROS production of dopamine depends on the concentration,

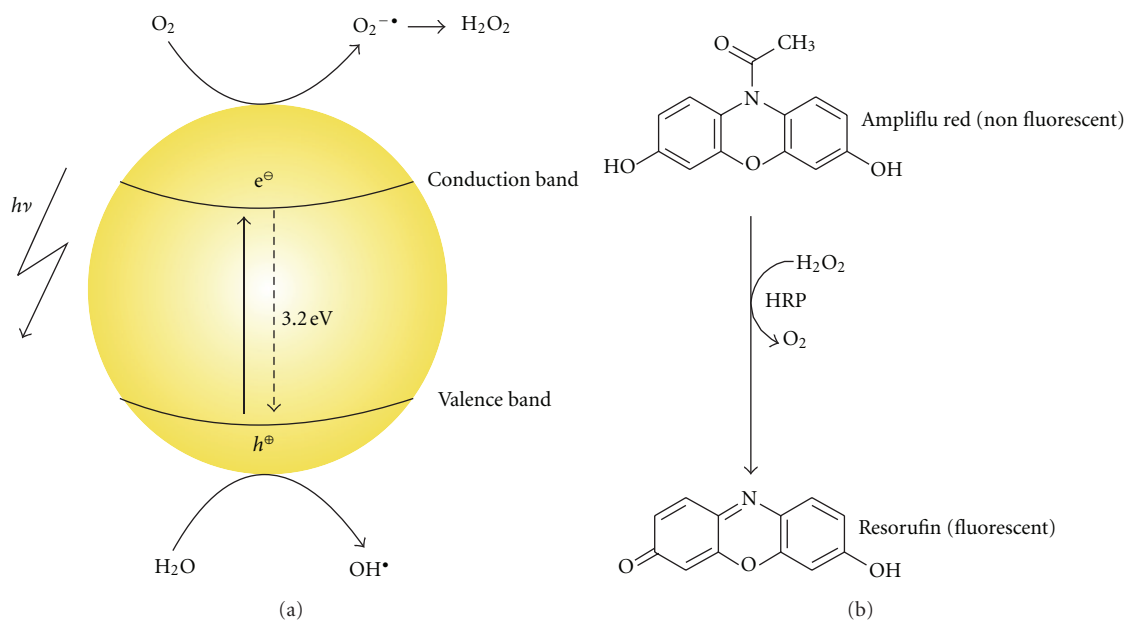


FIGURE 4: Generation of ROS under irradiation of semiconducting TiO_2 NP in aqueous solution and the Ampliflu activity test for HRP peroxidase.

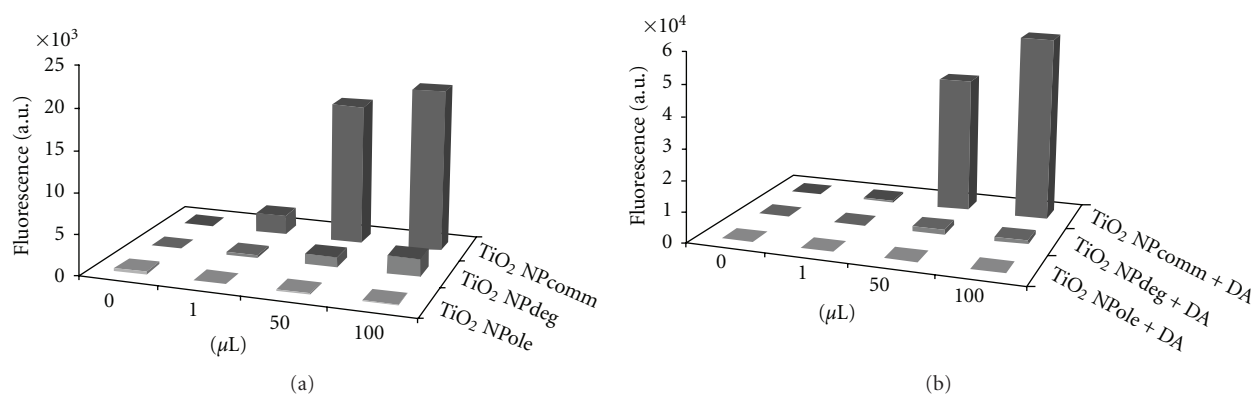


FIGURE 5: ROS production of three types of TiO_2 NPs: (a) TiO_2 NPcomm, and TiO_2 NPdeg, TiO_2 NPole using 366 nm light source; (b) TiO_2 NPcomm + DA, TiO_2 NPdeg + DA, and TiO_2 NPole + DA. Samples are background corrected; fluorescence of the sample kept in dark is subtracted from the fluorescence of the irradiated sample.

it can act as an antioxidant at physiologically relevant concentrations and as prooxidant at high concentrations [54]. It has been demonstrated that the generation of superoxide (O_2^-) and H_2O_2 can be increased when high concentrations of dopamine are used [55] and that the catechol and amine groups are the main structural features responsible for the antioxidant effect [56, 57]. Figure 5(b) shows that fluorescence intensity further increases for TiO_2 NPcomm despite the dopamine quenching ability, and there is no fluorescence in case of smaller, less active TiO_2 . This result indicates that there is an apparent synergistic effect of the dopamine on the surface and NPs itself for highly active NPs probably due to the effect of the size, the ligand nature, and the charge transfer complex. The same effect was observed in case of the 254 nm light irradiation (SI, Figure S2b).

We have then explored the photo-activation of TiO_2 NRs. The activation of the HRP was successful in all of the

cases although the efficiency and the fluorescence intensity increased as the TiO_2 NRs with longer reflux times were used (Figure 6(a)).

The reason for this lies in the increased crystallinity of the NRs with the reflux time. Prolonged time of crystal ripening increases the crystallinity of the rods [42] and results in less defects and higher ability to produce the ROS. The concentration dependence was also observed as the amount of the activated enzyme and the oxidized substrate increased with the increase of TiO_2 NRs concentration. We have also functionalized TiO_2 NRs with DA and compared its ROS production to the bare NRs (Figure 6(b)).

In contrast to the bare NRs, DA functionalization has a significant effect on the ROS production (Figure 6(b)). As mentioned earlier, DA is an excellent radical quencher with ability to scavenge ROS depending on the concentration. The size of the nanoobjects investigated needs to be taken into

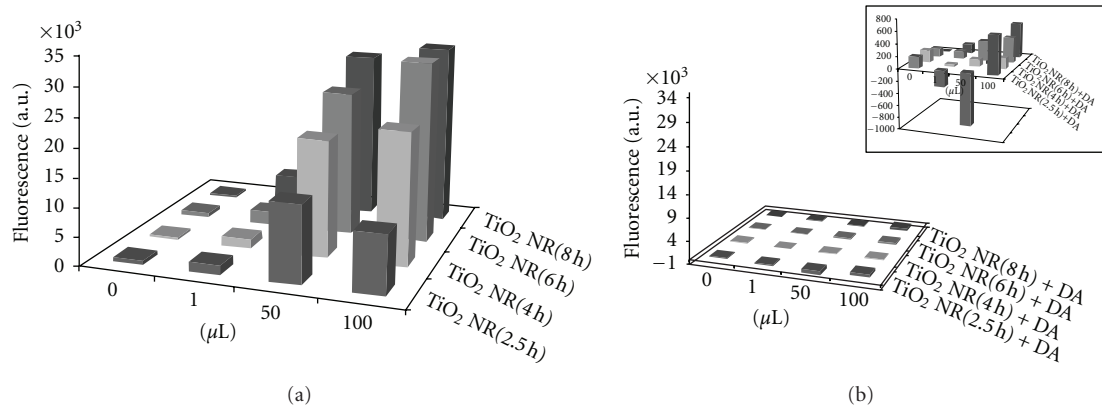


FIGURE 6: ROS production of four types of TiO_2 NRs: (a) bare (b) DA functionalized NRs (inset shows scale enlargement to show that there is a small activity that can be observed). Samples are background corrected; fluorescence of the sample kept in dark is subtracted from the fluorescence of the irradiated sample.

account—NRs have a larger surface available for dopamine binding. Surface area is approximately 4 times larger than that of investigated spheric NPs, which means that there is 4 times more DA that can act as an efficient dopamine scavenger. We are currently exploring other classes of catechol ligands and investigate this phenomenon.

3.2.2. Light-Induced Triggering of Peroxidase Activity Using TiO_2 NRs. As the light activation allows temporal and spatial control over the protein activity, we were interested to see if the HRP activity be switched on and off with the light irradiation to allow us to have controlled turn on activity. TiO_2 NR (8 h) were mixed with HRP and Ampliflu Red in the fluorescence quartz cuvette and the fluorescence of the resorufin measured *in situ* upon the light irradiation. The results in Figure 7 show that the activity of HRP can indeed be switched on and off with light in presence of TiO_2 NRs throughout 20 minutes. Controls in which only TiO_2 NR or HRP were used showed no such effect. This indeed indicated that such hybrid systems can be used for temporal (and spatia, i.e., in TiO_2 films) control of enzymatic activity, which could have potential applications in catalysis and biosensing.

At the beginning of the experiment, the increase of fluorescence was observed when the light was switched on. After the initial 5 minutes, the light was switched off and the mixture kept in dark for 5 minutes during which there was no further increase of fluorescence. Fluorescence increase was restored again upon the subsequent irradiation proving that the temporal control over the enzyme activity can be achieved by addition of photoactive species.

4. Conclusion

Production of enzyme activating ROS species by irradiation of different TiO_2 nanospecies was investigated. Commercially available and prepared TiO_2 spheric nanoparticles were compared to the crystalline TiO_2 nanorods. As there is a growing interest to use TiO_2 in photodynamic therapy, it is crucial to understand the influence of the surface ligands onto the ROS production. Therefore, dopamine modified

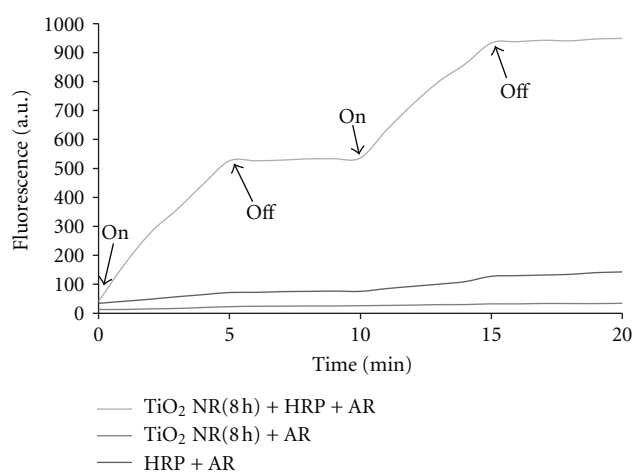


FIGURE 7: Light-induced triggering of peroxidase activity using TiO_2 NRs. The instances at which the light is turned on and off are labeled.

TiO_2 was studied showing that there are a significant difference between nanoparticles, which showed increased activity and nanorods, where dopamine acts as a ROS scavenger. This is an important finding, which renders dopamine undesirable in functionalization of anatase nanorods of similar dimensions, which are intended for use in ROS-related reactions. Our ongoing work is directed towards synthesis of other catechol based linkers and their effect on the phototriggered production of ROS species to aid the future design of powerful elements for photodynamic therapy.

Conflict of Interests

The authors declare they have no conflict of interests.

Acknowledgments

This work was supported by KIT Excellence Initiative 2006–2011, Grant DFG-CFN A5.7. The authors would like to thank

Dr. Vidyakshmi Rajendran for the helpful discussions on ROS producing nanoparticles.

References

- [1] E. Hao, G. C. Schatz, and J. T. Hupp, "Synthesis and optical properties of anisotropic metal nanoparticles," *Journal of Fluorescence*, vol. 14, no. 4, pp. 331–341, 2004.
- [2] X. Peng, L. Manna, W. Yang et al., "Shape control of CdSe nanocrystals," *Nature*, vol. 404, pp. 59–61, 2000.
- [3] Y. H. Kim, Y. W. Jun, B. H. Jun, S. M. Lee, and J. Cheon, "Sterically induced shape and crystalline phase control of GaP nanocrystals," *Journal of the American Chemical Society*, vol. 124, no. 46, pp. 13656–13657, 2002.
- [4] Y. Xia, Y. Sun, Y. Wu et al., "One-dimensional nanostructures: synthesis, characterization, and applications," *Advanced Materials*, vol. 15, no. 5, pp. 353–389, 2003.
- [5] Z. Wang, S. Zong, J. Yang, C. Song, J. Li, and Y. Cui, "One-step functionalized gold nanorods as intracellular probe with improved SERS performance and reduced cytotoxicity," *Biosensors and Bioelectronics*, vol. 26, no. 1, pp. 241–247, 2010.
- [6] A. R. A. Lojudice, L. De Marco, M. R. Belviso, G. Caputo, P. D. Cozzoli, and G. Gigli, "Organic photovoltaic devices with colloidal TiO₂ nanorods as key functional components," *Physical Chemistry Chemical Physics*, vol. 14, pp. 3987–3995.
- [7] S. E. Dobrovolskaia, "Immunological properties of engineered nanomaterials," *Nature Nanotechnology*, vol. 2, pp. 469–478, 2007.
- [8] H. K. Y. Zhu, L. Xu, W. Ma et al., "Gold nanorod assembly based approach to toxin detection by SERS," *Journal of Materials Chemistry*, vol. 22, pp. 2387–2391, 2012.
- [9] S. J. J. Stone and D. Wright, "Wiley interdisciplinary reviews: nanomedicine and nanobiotechnology," *Nanobiotechnology*, vol. 3, no. 1, pp. 100–109, 2011.
- [10] M. P. R. Wang, L. Fruk, D. Hu, and D. M. Schaadt, "Nanoparticles and efficiency enhancement in plasmonic solar cells," *Journal of Nanoelectronics and Optoelectronics*, vol. 7, pp. 322–327.
- [11] X. Huang, I. H. El-Sayed, W. Qian, and M. A. El-Sayed, "Cancer cell imaging and photothermal therapy in the near-infrared region by using gold nanorods," *Journal of the American Chemical Society*, vol. 128, no. 6, pp. 2115–2120, 2006.
- [12] Q. W. L. Tong, A. Wei, and J. X. Cheng, "Gold nanorods as contrast agents for biological imaging: optical properties, surface conjugation and photothermal effects," *Photochemistry and Photobiology*, vol. 85, no. 1, pp. 21–32.
- [13] C. J. Murphy, A. M. Gole, S. E. Hunyadi et al., "Chemical sensing and imaging with metallic nanorods," *Chemical Communications*, no. 5, pp. 544–557.
- [14] N. M. Dimitrijevic, Z. V. Saponjic, B. M. Rabatic, and T. Rajh, "Assembly and charge transfer in hybrid TiO₂ architectures using biotin–avidin as a connector," *Journal of the American Chemical Society*, vol. 127, no. 5, pp. 1344–1345, 2005.
- [15] P. D. Cozzoli, A. Kornowski, and H. Weller, "Low-temperature synthesis of soluble and processable organic-capped anatase TiO₂ Nanorods," *Journal of the American Chemical Society*, vol. 125, no. 47, pp. 14539–14548, 2003.
- [16] M. Adachi, Y. Murata, J. Takao, J. Jiu, M. Sakamoto, and F. Wang, "Highly efficient dye-sensitized solar cells with a titania thin-film electrode composed of a network structure of single-crystal-like TiO₂ nanowires made by the "oriented attachment" mechanism," *Journal of the American Chemical Society*, vol. 126, no. 45, pp. 14943–14949, 2004.
- [17] Y. Zhu, J. Shi, Z. Zhang, C. Zhang, and X. Zhang, "Development of a gas sensor utilizing chemiluminescence on nano-sized titanium dioxide," *Analytical Chemistry*, vol. 74, no. 1, pp. 120–124, 2002.
- [18] B. L. Bischoff and M. A. Anderson, "Peptization process in the sol-gel preparation of porous anatase (TiO₂)," *Chemistry of Materials*, vol. 7, no. 10, pp. 1772–1778, 1995.
- [19] H. Y. Zhu, Y. Lan, X. P. Gao et al., "Phase transition between nanostructures of titanate and titanium dioxides via simple wet-chemical reactions," *Journal of the American Chemical Society*, vol. 127, no. 18, pp. 6730–6736, 2005.
- [20] P. F. Schwarz, N. J. Turro, S. H. Bossmann, A. M. Braun, A. M. A. Abdel Wahab, and H. Dürr, "A new method to determine the generation of hydroxyl radicals in illuminated TiO₂ suspensions," *Journal of Physical Chemistry B*, vol. 101, no. 36, pp. 7127–7134, 1997.
- [21] M. K. K. Matsui, M. Segawa, S. Y. Hwang, T. Tanaka, C. Ogino, and A. Kondo, "Biofunctional TiO₂ nanoparticle-mediated photokilling of cancer cells using UV irradiation," *MedChemComm*, vol. 1, no. 3, pp. 209–211, 2011.
- [22] Y. Luo, Y. Tian, and Q. Rui, "Electrochemical assay of superoxide based on biomimetic enzyme at highly conductive TiO₂ nanoneedles: from principle to applications in living cells," *Chemical Communications*, no. 21, pp. 3014–3016, 2009.
- [23] K. Y. K. Kakinoki, R. Teraoka, M. Otsuka, and Y. Matsuda, "Effect of relative humidity on the photocatalytic Titanium dioxide and photostability of famotidine," *Journal of Pharmaceutical Sciences*, vol. 93, no. 3, pp. 582–589, 2004.
- [24] R. W. C. M. Sayes, P. A. Kurian, Y. Liu et al., "Correlating nanoscale titania structure with toxicity: a cytotoxicity and inflammatory response study with human dermal fibroblasts and human lung epithelial cells," *The Journal of Toxicological Sciences*, vol. 92, no. 1, pp. 174–185, 2006.
- [25] J. R. Gurr, A. S. Wang, C. H. Chen, and K. Y. Jan, "Ultrafine titanium dioxide particles in the absence of photoactivation can induce oxidative damage to human bronchial epithelial cells," *Toxicology*, vol. 213, no. 1–2, pp. 66–73, 2005.
- [26] H. Turkez and F. Geyikoglu, "An in vitro blood culture for evaluating the genotoxicity of titanium dioxide: the responses of antioxidant enzymes," *Toxicology and Industrial Health*, vol. 23, no. 1, pp. 19–23, 2007.
- [27] J. J. Wang, B. J. Sanderson, and H. Wang, "Cyto- and genotoxicity of ultrafine TiO₂ particles in cultured human lymphoblastoid cells," *Mutation Research*, vol. 628, no. 2, pp. 99–106, 2007.
- [28] T. J. Dougherty, C. J. Gomer, B. W. Henderson et al., "Photodynamic therapy," *Journal of the National Cancer Institute*, vol. 90, no. 12, pp. 889–905, 1998.
- [29] Z. W. Chen and J. Zhang, "Using nanoparticles to enable simultaneous radiation and photodynamic therapies for cancer treatment," *Journal of Nanoscience and Nanotechnology*, vol. 6, no. 4, pp. 1159–1166, 2006.
- [30] P. Wang, D. Wang, H. Li, T. Xie, H. Wang, and Z. Du, "A facile solution-phase synthesis of high quality water-soluble anatase TiO₂ nanocrystals," *Journal of Colloid and Interface Science*, vol. 314, no. 1, pp. 337–340, 2007.
- [31] J. W. Seo, H. Chung, M. Y. Kim, J. Lee, I. H. Choi, and J. Cheon, "Development of water-soluble single-crystalline TiO₂ nanoparticles for photocatalytic cancer-cell treatment," *Small*, vol. 3, no. 5, pp. 850–853, 2007.
- [32] L. Fruk, V. Rajendran, M. Spengler, and C. M. Niemeyer, "Light-induced triggering of peroxidase activity using quantum dots," *ChemBioChem*, vol. 8, no. 18, pp. 2195–2198, 2007.

- [33] C. M. C. Gammer, C. Rentenberger, and H. P. Karthaler, "Quantitative local profile analysis of nanomaterials by electron diffraction," *Scripta Materialia*, vol. 63, no. 3, pp. 312–315, 2010.
- [34] J. W. Seo, Y. W. Jun, S. J. Ko, and J. Cheon, "In situ one-pot synthesis of 1-dimensional transition metal oxide nanocrystals," *Journal of Physical Chemistry B*, vol. 109, no. 12, pp. 5389–5391, 2005.
- [35] M. X. L. Ge, M. Sun, and H. Fang, "Low-temperature synthesis of photocatalytic TiO₂ thin film from aqueous anatase precursor sols," *Journal of Sol-Gel Science and Technology*, vol. 38, no. 1, pp. 47–53, 2006.
- [36] P. J. Thistlethwaite and M. S. Hook, "Diffuse reflectance Fourier transform infrared study of the adsorption of oleate/oleic acid onto titania," *Langmuir*, vol. 16, no. 11, pp. 4993–4998, 2000.
- [37] B. Malisova, S. Tosatti, M. Textor, K. Gademann, and S. Zürcher, "Poly(ethylene glycol) adlayers immobilized to metal oxide substrates through catechol derivatives: influence of assembly conditions on formation and stability," *Langmuir*, vol. 26, no. 6, pp. 4018–4026, 2010.
- [38] B. Geiseler and L. Fruk, "Bifunctional catechol based linkers for modification of TiO₂ surfaces," *Journal of Materials Chemistry*, vol. 22, no. 2, pp. 735–741, 2012.
- [39] N. M. Dimitrijevic, E. Rozhkova, and T. Rajh, "Dynamics of localized charges in dopamine-modified TiO and their effect on the formation of reactive oxygen species," *Journal of the American Chemical Society*, vol. 131, no. 8, pp. 2893–2899, 2009.
- [40] M. Hesse, H. Meier, and B. Zeeh, *Spektroskopischen Methoden in der Organischen Chemie*, Stuttgart, New York, NY, USA, 1991.
- [41] M. Nara, H. Torri, and M. Tasumi, "Correlation between the vibrational frequencies of the carboxylate group and the types of its coordination to a metal ion: an ab initio Molecular Orbital Study," *Journal of Physical Chemistry*, vol. 100, no. 51, pp. 19812–19817, 1999.
- [42] Y. Liu, "Study of interfacial charge-transfer complex on TiO₂ particles in aqueous suspension by second-harmonic generation," *The Journal of Physical Chemistry B*, vol. 103, pp. 2480–2486, 1999.
- [43] A. Fujishima and K. Honda, "Electrochemical photolysis of water at a semiconductor electrode," *Nature*, vol. 238, no. 5358, pp. 37–38, 1972.
- [44] B. I. Ipe and C. M. Niemeyer, "Nanohybrids composed of quantum dots and cytochrome P450 as photocatalysts," *Angewandte Chemie International Edition*, vol. 45, no. 3, pp. 504–507, 2006.
- [45] S. J. Sigg, F. Seidi, K. Renggli, T. B. Silva, G. Kali, and N. Bruns, "Horseradish peroxidase as a catalyst for atom transfer radical polymerization," *Macromolecular Rapid Communications*, vol. 32, no. 21, pp. 1710–1715, 2011.
- [46] M. Tarpey, D. Wink, and M. Grisham, "Methods for detection of reactive metabolites of oxygen and nitrogen: in vitro and in vivo considerations," *American Journal of Physiology*, vol. 286, no. 3, pp. R431–R444, 2004.
- [47] Q. X. J. Zhang, Z. Feng, M. Li, and C. Li, "Importance of the relationship between surface phases and photocatalytic activity of TiO₂," *Angewandte Chemie International Edition*, vol. 47, no. 9, pp. 1766–1769.
- [48] A. Welte, C. W. A. Waldauf, C. Brabec, and P. J. Wellmann, "Application of optical absorbance for the investigation of electronic and structural properties of sol-gel processed TiO₂ films," *Thin Solid Films*, vol. 516, no. 20, pp. 7256–7259, 2008.
- [49] Z. V. S. N. M. Dimitrijevic, B. M. Rabatic, O. G. Poluektov, and T. Rajh, "Effect of size and shape of nanocrystalline TiO₂ on photogenerated charges. An EPR study," *The Journal of Physical Chemistry C*, vol. 111, no. 40, pp. 14597–14601, 2007.
- [50] K. J. Reszka, B. A. Wagner, C. P. Burns, and B. E. Britigan, "Effects of peroxidase substrates on the Amplex red/peroxidase assay: antioxidant properties of anthracyclines," *Analytical Biochemistry*, vol. 342, no. 2, pp. 327–337, 2005.
- [51] N. Serpone, D. Lawless, and R. Khairutdinov, "Size effects on the photophysical properties of colloidal anatase TiO₂ particles: size quantization or direct transitions in this indirect semiconductor?" *Journal of Physical Chemistry*, vol. 99, no. 45, pp. 16646–16654, 1995.
- [52] M. Suthanthiran, S. D. Solomon, and P. S. Williams, "Hydroxyl radical scavengers inhibit human natural killer cell activity," *Nature*, vol. 307, no. 5948, pp. 276–278, 1984.
- [53] C. Luga, J. R. Alvarez-Idaboy, and A. Vivier-Bunge, "ROS initiated oxidation of dopamine under oxidative stress conditions in aqueous and lipidic environments," *The Journal of Physical Chemistry B*, vol. 115, no. 42, pp. 12234–12246, 2011.
- [54] Z. Yang, L. D. Asico, P. Yu et al., "D5 dopamine receptor regulation of reactive oxygen species production, NADPH oxidase, and blood pressure," *American Journal of Physiology*, vol. 290, no. 1, pp. R96–R104, 2006.
- [55] J. Chen, C. Wersinger, and A. Sidhu, "Chronic stimulation of D1 dopamine receptors in human SK-N-MC neuroblastoma cells induces nitric-oxide synthase activation and cytotoxicity," *Journal of Biological Chemistry*, vol. 278, no. 30, pp. 28089–28100, 2003.
- [56] C. L. H and G.C. Yen, "Antioxidant effects of dopamine and related compounds," *Bioscience, Biotechnology, and Biochemistry*, vol. 61, no. 10, pp. 1646–1649, 1997.
- [57] C. Luga, J. R. Alvarez-Idaboy, and A. Vivier-Bunge, "ROS initiated oxidation of dopamine under oxidative stress conditions in aqueous and lipidic environments," *The Journal of Physical Chemistry B*, vol. 115, no. 42, pp. 12234–12246, 2011.

Research Article

Functionalization of Silica Nanoparticles for Polypropylene Nanocomposite Applications

Diego Bracho, Vivianne N. Dougnac, Humberto Palza, and Raúl Quijada

Departamento de Ingeniería Química y Biotecnología, FCFM, Universidad de Chile, 850 Beauchef, 8370448 Santiago, Chile

Correspondence should be addressed to Raúl Quijada, raquijad@ing.uchile.cl

Received 14 May 2012; Accepted 8 August 2012

Academic Editor: Sergio J. Mejía-Rosales

Copyright © 2012 Diego Bracho et al. This is an open access article distributed under the Creative Commons Attribution License, which permits unrestricted use, distribution, and reproduction in any medium, provided the original work is properly cited.

Synthetic silica nanospheres of 20 and 100 nm diameter were produced via the sol-gel method to be used as filler in polypropylene (PP) composites. Modification of the silica surface was further performed by reaction with organic chlorosilanes in order to improve the particles interaction with the hydrophobic polyolefin matrix. These nanoparticles were characterized using transmission electronic microscopy (TEM), elemental analysis, thermogravimetric analysis (TGA), and solid-state nuclear magnetic resonance (NMR) spectroscopy. For unmodified silica, it was found that the 20 nm particles have a greater effect on both mechanical and barrier properties of the polymeric composite. In particular, at 30 wt%, Young's modulus increases by 70%, whereas water vapor permeability (WVP) increases by a factor of 6. Surface modification of the 100 nm particles doubles the value of the composite breaking strain compared to unmodified particles without affecting Young's modulus, while 20 nm modified particles presented a slight increase on both Young's modulus and breaking strain. Modified 100 nm particles showed a higher WVP compared to the unmodified particles, probably due to interparticle condensation during the modification step. Our results show that the addition of nanoparticles on the composite properties depends on both particle size and surface modifications.

1. Introduction

Polyolefin materials have grown to a crucial role in modern society, from daily life to high-performance engineering applications. The low cost of production, facile and inexpensive processability, and good properties of these materials have allowed them to replace some of the traditional more expensive and less adaptable materials. Moreover, the addition of organic and inorganic fillers has opened a wide field of research for new possible applications for these materials.

Over the last 20 years, there has been a strong interest in the study and development of polymer nanocomposites, where at least one dimension of the filler has nanometric dimensions. The high interest for these materials is the high effective surface of the nanosized filler making it possible to tailor and handle the properties of the material with very small proportions of the filler. Low loadings of silica nanoparticles (<10 wt%) in polymeric matrices can considerably improve the performance of these materials, such as mechanical, thermic, and barrier properties [1–3].

Traditionally, these nanocomposites have been widely studied by using natural aluminosilicate clays, mainly because of the high availability and low cost, with good results. Recent studies have shown that modified clays can reduce by 90% the permeability coefficient of different gases at 20 vol% of clay [2]. Nevertheless, synthetic particles have grown interest over the past decade, especially for food packaging and medicine applications, due to the absence of heavy metals and toxins in the particles. The sol-gel method is a good alternative for silica nanoparticle synthesis, being able to tailor the particles geometry and size [3–6]. The mechanism of the sol-gel method, using organic silanes as precursors, starts with hydrolysis of the functional groups, followed by condensation of the silanol groups. The mechanism is, of course, much more complicated and includes a number of parallel reactions such as the condensation of organic groups from the precursor. In basic conditions, hydroxyl groups acts as a catalysts. By controlling the pH of the reaction, it is possible to control particle size due to the relative rate at which both hydrolysis and condensation occur. At a high pH,

condensation occurs much more rapidly than hydrolysis, so fewer nuclei will be formed and the reaction will occur by monomer addition leading to larger particles [6].

Different studies have demonstrated the importance of the nanoparticles geometry and aspect ratio in the final properties of the nanocomposite material [1, 2]. However, aspect ratio is only one of the many different variables that must be taken into account in the study of these materials. Both size and effective surface of the nanofiller play a crucial role in the mechanical, thermal, and barrier properties of the material [3]. The level of filler dispersion within the polymer matrix and the level of adhesion and physical or chemical interactions between the filler and the polymer also plays an important role in the material final properties [7]. As discussed by Takahashi and Paul [8, 9], when untreated silica particles were incorporated in a poly(ether imide) matrix the permeability was increased due to the presence of voids in the particle-polymer interface, while surface-treated silica reduced the material permeability coefficient.

Different approaches have been developed in order to modify silica surface functionality, such as incorporation of compatibilizing agents such as maleic anhydride (PPgMA) [7], in situ polymerization of the polymer matrix in the presence of the inorganic filler [10], grafting of coupling agents in both silica and PP [11, 12], or by grafting reactions of the silanol groups on the surface of the silica particle with different compounds, such as organic silanes [13–15]. This produces a better interaction and dispersion of the silica particles in the polymeric matrix, and as a consequence an improvement in the composite properties [13, 14].

The main goal of this work is to synthesize silica nanospheres with different diameters and modify its surface by grafting reactions with chlorosilanes with various organic chain lengths, which will be used as filler in polyolefin matrices in order to study the materials mechanical and barrier properties.

2. Experimental

2.1. Materials. Tetraethoxysilane ($\geq 98\%$, TEOS), trimethylchlorosilane (97%, TMCS) and dimethyloctylchlorosilane (97%, DMOCS) were acquired from Sigma-Aldrich and used as received. Ammonia (25%) and heptane (99%, anhydrous) were acquired from Equilab. Polypropylene with a melt flow index (MFI) of 7.5 g/10 min (PP-H401) was obtained from Braskem and used as received. The antioxidant agent used in nanocomposite preparation was a mixture (2 : 1) of Irganox 1010 and Irganox 168.

2.2. Synthesis of Spherical Silica Nanoparticles via Sol-Gel Method. Silica nanospheres of different sizes were prepared using the sol-gel method, with TEOS as the precursor. The molar ratio of $\text{H}_2\text{O}/\text{TEOS}/\text{EtOH}$ was held constant at 4/1/8, while the amount of ammonia was changed for particle size control, using a molar ratio NH_3/TEOS from 0.03 to 0.35. A solution containing TEOS and 90% of the absolute ethanol was poured into a 2000 mL flat-bottom vessel equipped with a heating bath and a magnetic stirrer, while a second solution containing water, ammonia and the remaining ethanol was

added dropwise to it. The mixture was sealed and stirred for 5 h at $50 \pm 2^\circ\text{C}$ to obtain a silica sol. The solvent was then evaporated at 70°C , obtaining a fine white powder which was homogenized using an analytical mill at 10°C . Finally, the powder was calcined at 400°C for 8 hours.

2.3. Surface Modification of Silica Nanospheres. TMCS and DMOCS were used as grafting reactants, while heptane was used as reaction medium. Silica nanospheres were calcinated at 400°C under vacuum for 5 h in a sealed round bottom flask in order to remove the adsorbed water on the silica surface and isomerize the silanol groups into the more reactive isolated silanol groups.

Heptane was poured into the flask and sonicated for 20 min in order to disperse the silica nanospheres in the heptane. After sonication, the corresponding chlorosilane was added into the flask, while maintaining a nitrogen atmosphere inside the flask. The TMCS modification occurred at 50°C for 24 h under constant stirring, while the DMOCS modification was performed under reflux for 24 h. The mixture was subsequently centrifuged to separate the powder from the solvent and rinsed with clean heptane in order to remove the unreacted chlorosilanes. The powder was finally dried at 150°C under vacuum for 5 h to remove the remaining solvent.

2.4. Characterization of the Modified and Unmodified Silica Nanospheres. The resulting silica nanospheres were characterized by TEM (JEOL 1011 operated at 100 kV) and BET surface analysis (Micromeritics ASAP 2010 Physisorption Analyzer, pretreatment at 200°C) in order to establish the particle diameter and specific surface. Elemental analysis (Leeman Labs Inc. CE440 elemental analyzer and Control Equipment Corporation 440), TGA (SDT (TGA-DSC) Q600, $20^\circ\text{C}/\text{min}$ under N_2), and ^{29}Si CP MAS NMR spectroscopy (Bruker AVANCE 300, 4 mm double resonance broadband probe using a MAS rate of 10 KHz) were carried in order to verify and quantify the effect of the surface modification.

2.5. Nanocomposite Blending. The PP/SiO₂ nanocomposites were produced by melt mixing in a Brabender Plasti-Corder at 190°C and 110 RPM for 10 min. Approximately 35 g per mixing was produced, containing PP, SiO₂ nanoparticles, and a small spoonful of Irganox 1010: Irganox 168 (2 : 1) as antioxidant. Mixture was then flattened in a cold hydraulic press to solidify and was then cut into smaller pieces of ca. 5 mm.

2.6. Mechanical Properties of Nanocomposites. Samples were prepared by melt pressing of the material at 190°C and 50 bar in a heated hydraulic press for 5 min. Samples were then cooled using a water cooling system, solidifying the sample and releasing the pressure. Test samples were cut from these sheets using a stainless steel die in a hydraulic press, obtaining a 12 cm \times 1 cm and 1 mm thickness testing samples, according to the ATSM D638. Mechanical properties were measured using an HP D500 dynamometer with a strain rate of 50 mm/min at room temperature. Young's modulus was

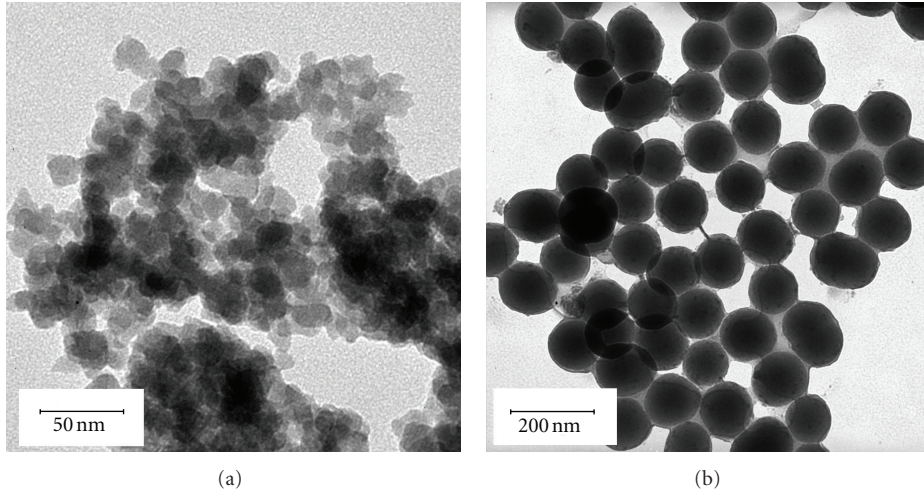


FIGURE 1: TEM images of SiO_2 nanospheres synthesized via sol-gel method. (a) NS20. (b) NS100.

TABLE 1: Silica nanospheres diameter and specific surface.

Sample	Molar ratio NH_3/TEOS	TEM diameter (nm)	BET surface (m^2/g)
NS20	0.03	22 ± 4.3	287 ± 0.7
NS100	0.35	113 ± 13.5	41.7 ± 0.2

calculated as the slope of the linear elastic zone on the stress-strain curve. Breaking strain is defined as the last point of the curve before the stress abruptly falls to a value of zero.

2.7. Water Vapor Permeability. Samples for barrier properties were prepared by melt pressing the material at 190°C and 50 bar in a heated hydraulic press for 5 min using a 0.2 mm stainless steel mold. The system was then cooled using a water cooling system to solidify the samples. Circular test samples of diameter 3.5 cm were cut off from the film.

The water vapor permeability (WVP) was measured using the dry cup method [16]. Aluminum sample cups, equipped with rubber o-rings, were filled with 2 g of phosphorous pentoxide and covered with a 3 cm diameter film of the polymer sample and top secured above. The total mass of the cups was measured and then placed in a sealed chamber with a 90% relative humidity and 20°C . The mass of the cups was measured every 24 h for a minimum of 15 days. The daily weight uptake of each cup corresponds to the water vapor that has permeated through the polymeric film, thus the slope of the graph “weight versus time” corresponds to the water vapor transmission rate. Water vapor permeability was calculated using the formula (1) expressed below:

$$\text{WVP} = \frac{e * 100}{A * P_{\text{sat}} * \text{RH}\% * \text{PM}_w} \left(\frac{dm}{dt} \right), \quad (1)$$

where e corresponds to the film thickness, A is the effective area of the polymer film, P_{sat} is the saturation pressure of water at the given temperature, $\text{RH}\%$ if the relative humidity at the sealed chamber, PM_w is the molecular water, and dm/dt is the slope of the weight/time curve after system has reached

the steady state condition (linear region). WVP is expressed in $\text{mol}/\text{m}^2 \cdot \text{s} \cdot \text{Pa}$.

3. Results and Discussion

3.1. Sol-Gel Synthesis. Two sets of silica nanospheres were successfully synthesized via sol-gel method and characterized by various techniques. TEM images of the spherical silica particles synthesized are shown in Figure 1. By changing the molar ratio NH_3/TEOS and, therefore the pH of the reaction medium, the final size of the synthesized silica nanospheres was controlled (Table 1), resulting particles of approximately 20 and 100 nm, named as NS20 and NS100, respectively (NS stands for nanosilica, while number stands for particle average diameter). A higher pH in the reaction medium results in a higher yield due to the basic catalysis, and larger particles due to the ionization of the condensed species causing growth to occur by monomer addition rather than particle aggregation [6].

3.2. Silica Surface Modification. Modification of silica nanoparticles was performed in order to improve the particle-polymer interaction when used as fillers in polyolefin nanocomposites, such as polypropylene. These modified particles were characterized in order to establish the effective addition of carbon chains into the silica surface. Reaction occurs in the silica surface between the silanol groups and the alkylchlorosilane, grafting the alkylsilane to the surface of the silica via Si–O–Si bonding releasing HCl in gas form (Figure 2).

The solid state ^{29}Si CP MAS NMR spectra of the modified and unmodified silica particles are presented in

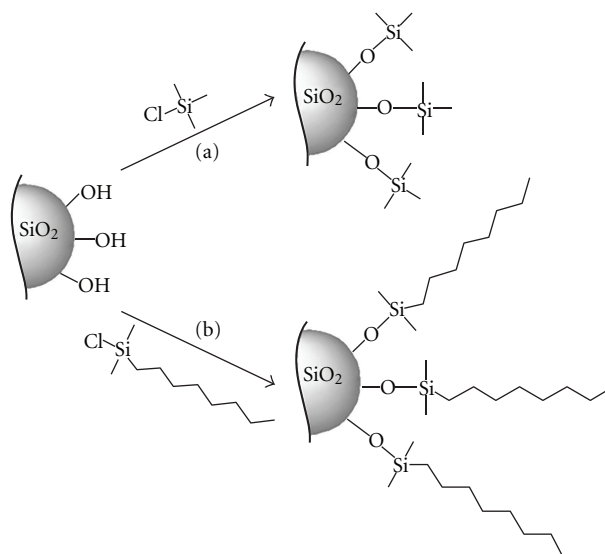


FIGURE 2: Modification of the silica surface via grafting reaction with (a) TMCS and (b) DMOCS.

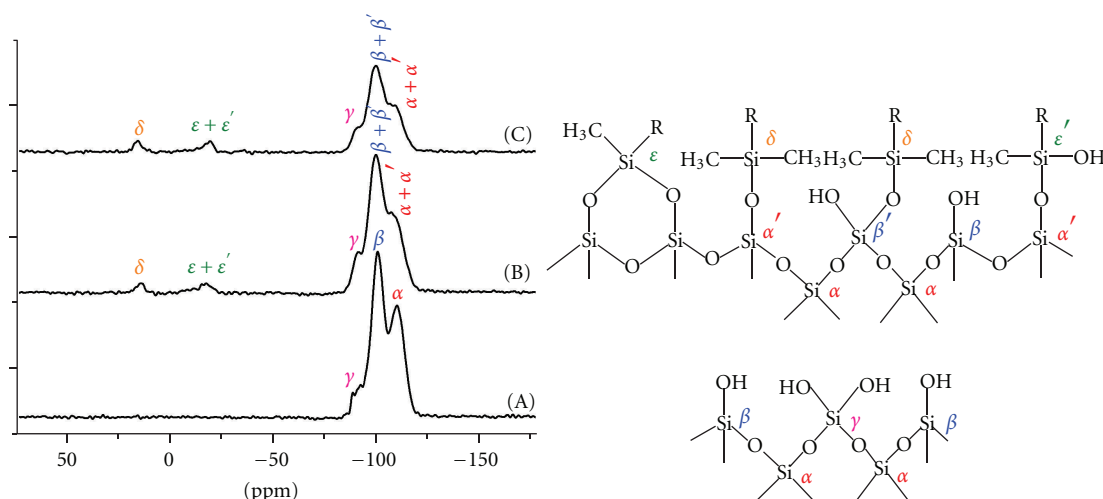


FIGURE 3: Solid state ^{29}Si CP MAS NMR spectra for the unmodified (A) and modified 20 nm particles with TMCS (B) and DMOCS (C). The notation “R” at δ , ϵ and ϵ' corresponds to methyl (TMCS) or octyl (DMOCS) groups.

Figure 3. Unmodified silica (Figure 3(A)) presents 3 characteristic peaks: -110 ppm (α), corresponding to silicon from $\text{Si}(\text{OSi})_4$, -100 (β), and -90 ppm (γ), corresponding to free and germinal silanol groups, respectively. After modification with both TMCS and DMOCS, the number of silanol groups was diminished, as the line intensities β and γ were decreased [13, 14]. Smaller peaks appear on both modifications at $+15$ (δ) and -16 ppm (ϵ and ϵ'). The first (δ) corresponds to the silicon from the chlorosilanes reactants, now grafted to the surface of the particle via $\text{Si}-\text{O}-\text{Si}$ bonding, with 3 organic groups attached to it (three methyl for the TMCS and two methyl and one octyl group for the DMOCS) as presented in Figure 2. The second chemical shift at -16 ppm ($\epsilon + \epsilon'$) corresponds to silicon from the chlorosilanes reactants that have lost one of their organic groups, leaving a free OH group, or attaching itself to adjacent silicon via $\text{Si}-\text{O}-\text{Si}$

bonding. The loss of one of these groups may occur after a heating treatment at high temperatures, such as the drying of the particles at 150°C after the modification was performed [14]. These results confirm the success of the surface modification of the silica surface by grafting of the organic silanes. The absence of peaks near $+30$ ppm shows that all of the unreacted chlorosilane was successfully removed in the washing stage after modification.

Table 2 shows the results of elemental analysis of the unmodified and modified silica particles. The low carbon content on unmodified silica particles comes from unreacted TEOS and ethoxy groups that were not fully oxidized by calcination of the particles (400°C). The carbon content of modified silica is higher because of the grafting of chlorosilanes on the surface of the particles containing organic groups. For the DMOCS modified silica, the carbon

TABLE 2: Carbon content from elemental analysis of silica nanospheres.

Particle size	Modification	Carbon content (%)
20 nm	—	0.91%
	TMCS	3.04%
	DMOCS	4.74%
100 nm	—	0.44%
	TMCS	0.63%
	DMOCS	2.92%

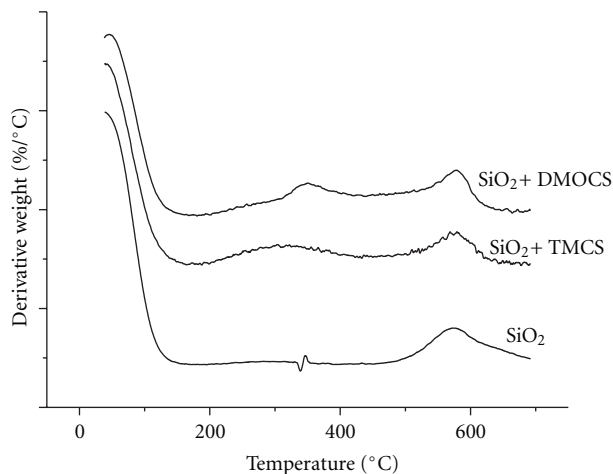


FIGURE 4: Derivative of thermogravimetric analysis (TGA) of NS100 samples. Tests run 20°C/min under N₂. From bottom to top: unmodified, TMCS modified, and DMOCS modified silica.

content is higher because of the large carbon chain of the octyl group.

The incorporation of organic groups in the silica is further confirmed by TGA of NS100 samples in Figure 4. Results showed that unmodified silica particles lose up to 4.3% of their total mass at 200°C, which corresponds mainly to adsorbed water at the hygroscopic surface, while the TMCS and DMOCS modified silica only lose up to 2.9 and 2.7% of their mass at the same temperature. Because of the presence of organic hydrophobic groups in the modified silica surface, water cannot be as easily adsorbed as it is on the unmodified silica. In the 200 to 450°C, unmodified silica particles show a small linear loss, corresponding mainly to vicinal hydroxyls condensation on the silica surface [17–19], while modified silica also start losing the organic groups grafted to the surface, showing a peak in the differential weight loss curve [18, 19]. This analysis confirms that DMOCS has a higher carbon content than TMCS modified silica. Finally, above 450°C silica loses the rest of the silanol groups, especially free silanol groups. The NS20 samples showed similar results.

3.3. Nanocomposite Blending and Mechanical Properties. Unmodified silica of 20 and 100 nm were used to prepare 10, 20, and 30 wt% nanocomposites with polypropylene, whereas TMCS and DMOCS modified silica of 100 nm and

TMCS modified silica of 20 nm was used to prepare 10 wt% nanocomposites.

Results from mechanical testing are shown in Figure 5. For both 20 and 100 nm particles, Young's modulus is increased (Figure 5(a)) and breaking strain is highly decreased with the addition of unmodified silica (Figure 5(c)). The increase in the Young's modulus and decrease in the breaking strain are more significant for the 20 nm particles due to the higher specific surface of these, with an increase in Young's modulus up to 70% at 30 wt%.

For 100 nm particles, surface modification of the silica did not affect Young's modulus considerably (Figure 5(b)); nevertheless, with both TMCS and DMOCS modification, the breaking strain increased to almost twice the value of the unmodified silica nanocomposite (Figure 5(d)). This effect is caused due to the presence of organic groups in the silica surface acting as coupling agents in the particle-polymer interface giving greater mobility to polymer molecules around the SiO₂ nanoparticles in the composite under tensile stress conditions. The TMCS modified 20 nm silica composites presented a lower increment in breaking strain than larger particles, but also resulted in an increment in Young's modulus. This increase in Young's modulus could be caused by a better adhesion level between of the modified silica surface and the PP matrix. Similar results were obtained by Panaitescu et al. [20] for PP/SiO₂ nanocomposites using styrene-(ethylene-co-butylene)-styrene triblock copolymer as compatibilizer between the silica nanoparticles and the PP matrix.

3.4. Water Vapor Permeability. For the water vapor permeability test, it was found that unmodified silica increases the WVP, mainly due to the hygroscopic nature of the silica surface, which increases the solubility factor of the vapor in the polymer, thus increasing the permeability (Figure 6(a)) [3]. This effect is greater for the smaller 20 nm particles due to the larger specific surface, increasing the WVP up to a factor of 6 at 30 wt% compared to the neat PP matrix.

Modification of the silica surface with alkylsilanes should decrease the silica affinity toward water by making the silica surface more hydrophobic, therefore decreasing the solubility factor and the permeability. Modified 100 nm silica composites were studied (Figure 6(b)), presenting greater permeability coefficients compared to the unmodified particles, increasing WVP to twice its value compared to unmodified silica composite. This effect may be caused due to interparticle condensation during the modification step, forming agglomerates and increasing the polymer free volume and creating void channels, thus increasing the permeability for water vapor [8, 9].

4. Conclusions

Silica nanospheres of 20 and 100 nm diameter were synthesized via the sol-gel method, using TEOS as the precursor. By changing the reaction medium pH, it was possible to control the final size of the nanoparticles. Modification of the silica surface was successfully performed by grafting reactions with organic chlorosilanes. Solid-state ²⁹Si CP MAS

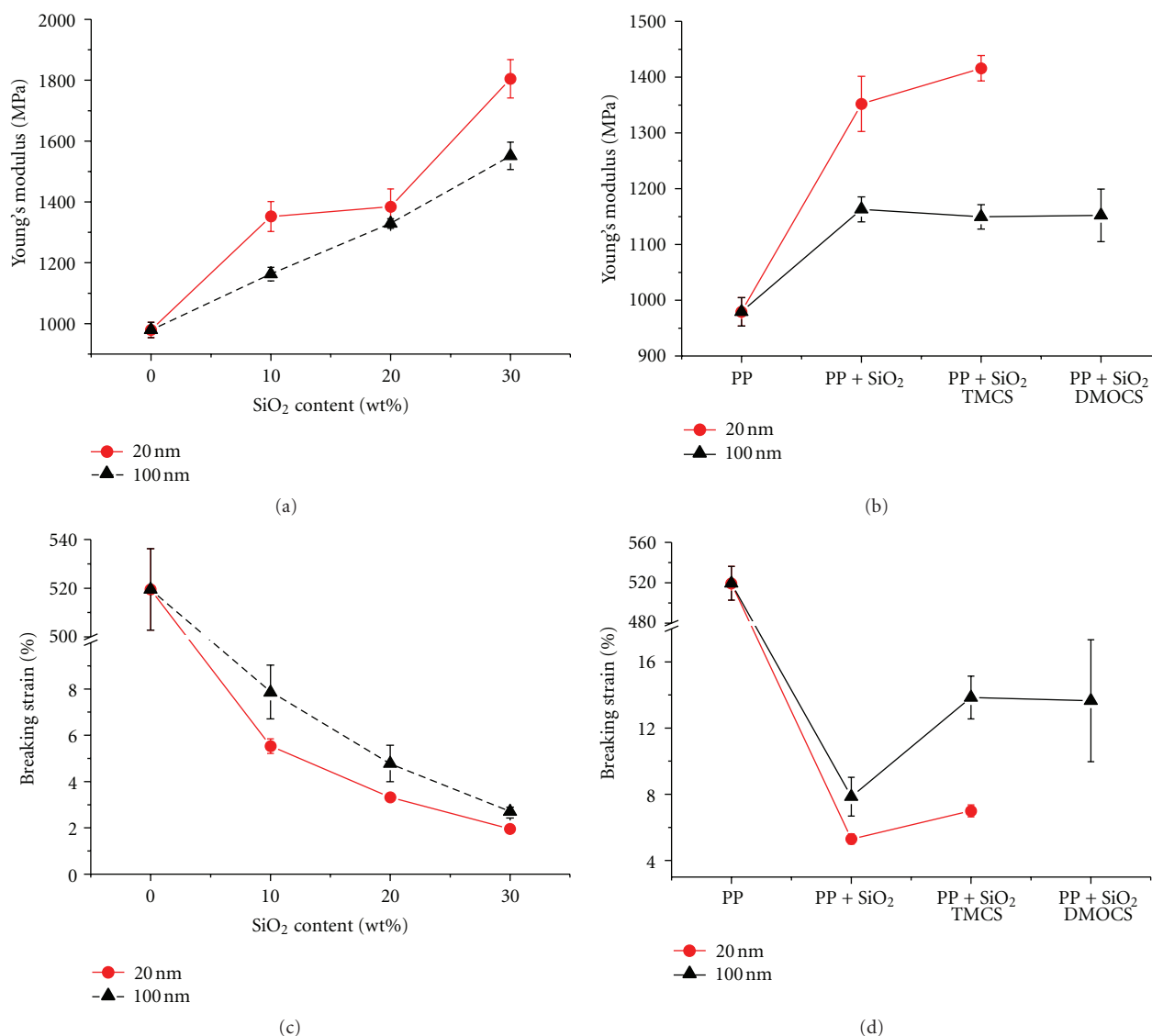


FIGURE 5: Mechanical properties of modified and unmodified SiO₂/PP nanocomposites. (a, c) Young's modulus and breaking strain of unmodified SiO₂ nanocomposites; (b, d) Young's modulus and breaking strain of modified SiO₂ nanocomposites (10 wt%).

NMR spectroscopy, elemental analysis, and TGA confirmed the effective modification of the silica surface with both TMCS and DMOCS.

PP nanocomposites were prepared using unmodified and modified silica particles. The addition of these particles increases the Young's modulus of the original PP matrix, but it highly decreases the breaking strain of the material. The smaller 20 nm particles had a greater effect both on the increase of the Young's modulus and on the decrease of the breaking strain, mainly due to the higher specific surface. Surface modification for the 100 nm particles did not affect Young's modulus, but considerably increased the breaking strain of the composite due to the presence of organic groups in the silica surface. TMCS modified 20 nm particles showing a small increase in the composite breaking strain and Young's modulus due to a better adhesion level between the modified particle's surface and the polymer matrix. In

barrier properties, it was found that the addition of silica increases the WVP of the material, due to the hygroscopic nature of the silica surface. However, modification of the 100 nm silica particles did not reduce the WVP but increased it probably due to interparticle condensation during the modification step increasing the polymer free volume.

These results show that the addition of nanoparticles on the final properties of the polymeric composite depends on both particle size and surface modifications.

Acknowledgments

The authors would like to thank project FONDECYT N° 1100058 for financial support. Also, the authors would like to thank Professor Griselda Barrera (Universidade Federal do Rio Grande do Sul, Brazil) for TGA; Professor René Rojas for

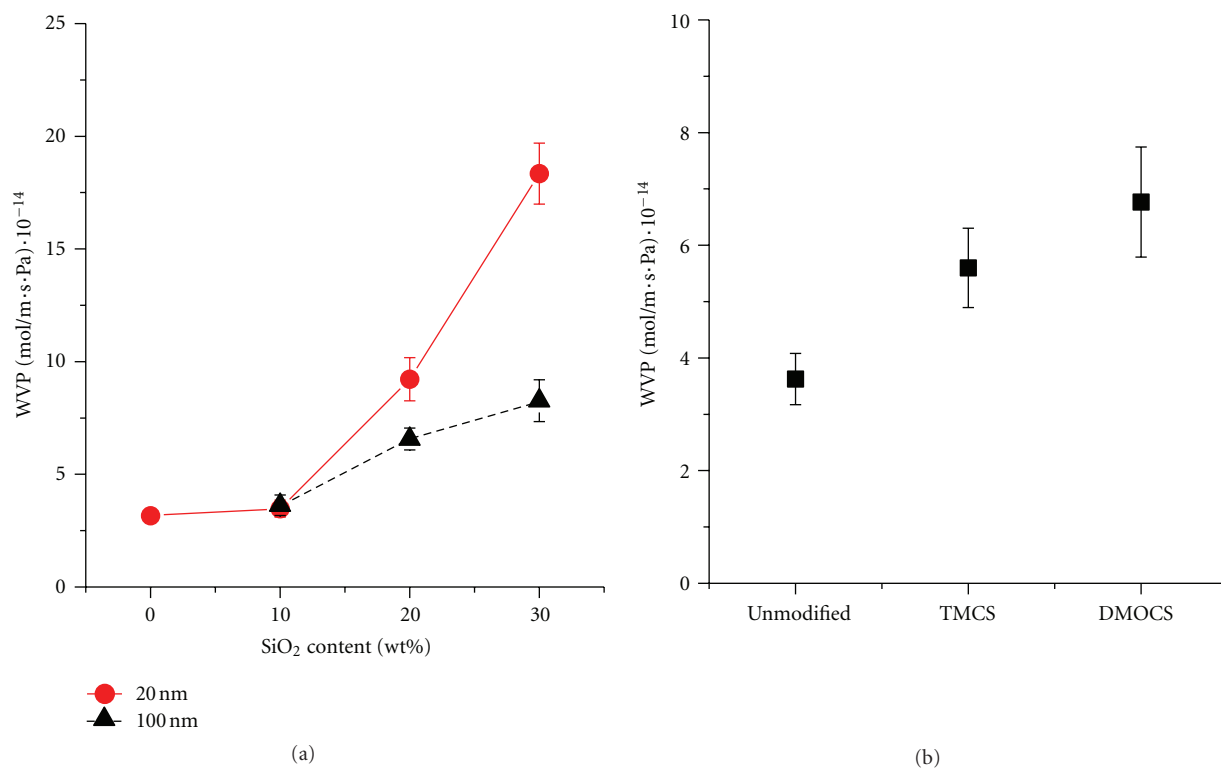


FIGURE 6: Water vapor permeability of the prepared nanocomposites: (a) unmodified silica of 20 and 100 nm; (b) modified and unmodified silica of 100 nm at 10 wt%.

Elemental Analysis (Facultad de Química, Pontificia Universidad Católica de Chile, Chile); Dr. Jason M. Spruell (MRL, University of California Santa Barbara, USA) for solid-state CP MAS ²⁹Si NMR analysis.

References

- [1] H. Zou, S. Wu, and J. Shen, "Polymer/silica nanocomposites: preparation, characterization, properties, and applications," *Chemical Reviews*, vol. 108, no. 9, pp. 3893–3957, 2008.
- [2] G. Choudalakis and A. D. Gotsis, "Permeability of polymer/clay nanocomposites: a review," *European Polymer Journal*, vol. 45, no. 4, pp. 967–984, 2009.
- [3] V. N. Dognac, R. Alamillo, B. C. Peoples, and R. Quijada, "Effect of particle diameter on the permeability of polypropylene/SiO₂ nanocomposites," *Polymer*, vol. 51, no. 13, pp. 2918–2926, 2010.
- [4] L. L. Hench and J. K. West, "The Sol-Gel process," *Chemical Reviews*, vol. 90, no. 1, pp. 33–72, 1990.
- [5] Y. Chen, S. Zhou, G. Chen, and L. Wu, "Preparation and characterization of polyester/silica nanocomposite resins," *Progress in Organic Coatings*, vol. 54, no. 2, pp. 120–126, 2005.
- [6] C. J. Brinker and G. W. Scherer, *Sol-Gel Science: The Physics and Chemistry of Sol-Gel Processing*, Academic Press, San Diego, Calif, USA, 1990.
- [7] D. García-López, O. Picazo, J. C. Merino, and J. M. Pastor, "Polypropylene-clay nanocomposites: effect of compatibilizing agents on clay dispersion," *European Polymer Journal*, vol. 39, no. 5, pp. 945–950, 2003.
- [8] S. Takahashi and D. R. Paul, "Gas permeation in poly(ether imide) nanocomposite membranes based on surface-treated silica. Part 1: without chemical coupling to matrix," *Polymer*, vol. 47, no. 21, pp. 7519–7534, 2006.
- [9] S. Takahashi and D. R. Paul, "Gas permeation in poly(ether imide) nanocomposite membranes based on surface-treated silica. Part 2: with chemical coupling to matrix," *Polymer*, vol. 47, no. 21, pp. 7535–7547, 2006.
- [10] R. Quijada and P. Zapata, "Polypropylene nanocomposites obtained by in situ polymerization using metallocene catalyst. Influence of the nanoparticles on the final polymer morphology," *Journal of Nanomaterials*, vol. 2012, Article ID 194543, 6 pages, 2012.
- [11] H. J. Zhou, M. Z. Rong, M. Q. Zhang, and K. Friedrich, "Effects of reactive compatibilization on the performance of nano-silica filled polypropylene composites," *Journal of Materials Science*, vol. 41, no. 17, pp. 5767–5770, 2006.
- [12] K. Suzuki, S. Siddiqui, C. Chappell, J. A. Siddiqui, and R. M. Ottenbrite, "Modification of porous silica particles with poly(acrylic acid)," *Polymers for Advanced Technologies*, vol. 11, no. 2, pp. 92–97, 2000.
- [13] E. Barna, B. Bommer, J. Kürsteiner et al., "Innovative, scratch proof nanocomposites for clear coatings," *Composites Part A*, vol. 36, no. 4, pp. 473–480, 2005.
- [14] H. Ishii, K. Itabashi, T. Okubo, and A. Shimojima, "Synthesis of silicalite-1 using a disiloxane-based structure-directing agent," *Microporous and Mesoporous Materials*, vol. 139, no. 1–3, pp. 158–163, 2011.
- [15] R. Brambilla, G. P. Pires, J. H. Z. dos Santos, M. S. L. Miranda, and B. Chornik, "Octadecylsilane-modified silicas prepared by

- grafting and sol-gel methods,” *Journal of Electron Spectroscopy and Related Phenomena*, vol. 156–158, pp. 413–420, 2007.
- [16] R. Saito and T. Hosoya, “Water vapor barrier property of organic-silica nanocomposite derived from perhydropolysilazane on polyvinyl alcohol substrate,” *Polymer*, vol. 49, no. 21, pp. 4546–4551, 2008.
- [17] E. F. Vansant, P. Van der Voort, and K. C. Vrancken, “Characterization and chemical modification of the silica surface,” in *Studies in Surface Science and Catalysis*, vol. 93, Elsevier Science B.V., Amsterdam, The Netherlands, 1995.
- [18] S. A. Kulkarni, S. B. Ogale, and K. P. Vijayamohan, “Tuning the hydrophobic properties of silica particles by surface silanization using mixed self-assembled monolayers,” *Journal of Colloid and Interface Science*, vol. 318, no. 2, pp. 372–379, 2008.
- [19] S. A. Kulkarni, S. A. Mirji, A. B. Mandale, and K. P. Vijayamohan, “Thermal stability of self-assembled octadecyltrichlorosilane monolayers on planar and curved silica surfaces,” *Thin Solid Films*, vol. 496, no. 2, pp. 420–425, 2006.
- [20] D. M. Panaitescu, Z. Vuluga, C. Radovici et al., “Morphological investigation of PP/nanosilica composites containing SEBS,” *Polymer Testing*, vol. 31, no. 2, pp. 355–365, 2012.

Research Article

Glassy Carbon Electrode-Supported Au Nanoparticles for the Glucose Electrooxidation: On the Role of Crystallographic Orientation

M. Guerra-Balcázar,^{1,2} J. Torres-González,¹ I. Terol-Villalobos,¹
J. Morales-Hernández,¹ and F. Castañeda¹

¹ Centro de Investigación y Desarrollo Tecnológico en electroquímica (CIDETEQ), Parque Tecnológico Querétaro-Sanfandila, 76703 Pedro Escobedo, QRO, Mexico

² División de Investigación y Posgrado, Facultad de Ingeniería, Universidad Autónoma de Querétaro, 76010 Cerro de las Campanas, QRO, Mexico

Correspondence should be addressed to F. Castañeda, fcastaneda@cideteq.mx

Received 23 February 2012; Accepted 14 June 2012

Academic Editor: Sergio J. Mejía-Rosales

Copyright © 2012 M. Guerra-Balcázar et al. This is an open access article distributed under the Creative Commons Attribution License, which permits unrestricted use, distribution, and reproduction in any medium, provided the original work is properly cited.

Glucose electrooxidation in alkaline solution was examined using glassy carbon electrodes modified with Au nanoparticles. Au nanoparticles were prepared following the two-phase protocol and characterized by transmission electron microscopy (TEM), UV-Vis spectroscopy, X-ray diffraction spectroscopy (XRD), and cyclic voltammetry (CV). It was found that, under the study conditions, it is possible to obtain nanoparticles between 1 and 5 nm; also it was found that the crystallographic orientation is strongly influenced by the ratio metal/thiol and to a lesser extent by the synthesis temperature. The voltammetric response for the electrocatalytic oxidation of glucose at carbon Au nanoparticle-modified electrode shows an increasing activity with nanoparticles size. Electroactivity and possibly selectivity are found to be nanoparticles' crystallographic orientation dependent. Classical electrochemical analysis shows that glucose electrooxidation is a diffusion-controlled process followed by a homogenous reaction.

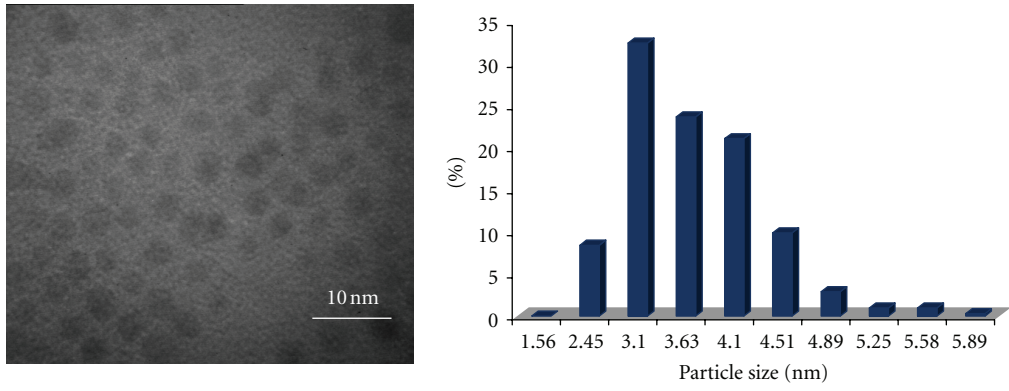
1. Introduction

Glucose electrooxidation has been extensively studied for glucose fuel cells, glucose sensor for medical applications, and food industry [1–11]. A variety of metals as Cu, Ni, Fe, Pt, and Au have been investigated for glucose electrocatalytic activity, and different results have been found: formic acid is the main product for glucose electrooxidation on Cu, Ni, and Fe [12–17], while glycolic acid is obtained when Pt electrodes are employed [4]. In the case of Au electrodes the products are, depending on media pH, gluconolactone, gluconic acid, or gluconate [8–10]. Au single-crystal electrode modified with Ag under potential deposition (Ag-UPD) has been tested and showed good results for glucose electrooxidation [6, 7]. Coming to the nanoparticles, Au shows high catalytic activities at nanoscale level [18–20]. It has been shown that

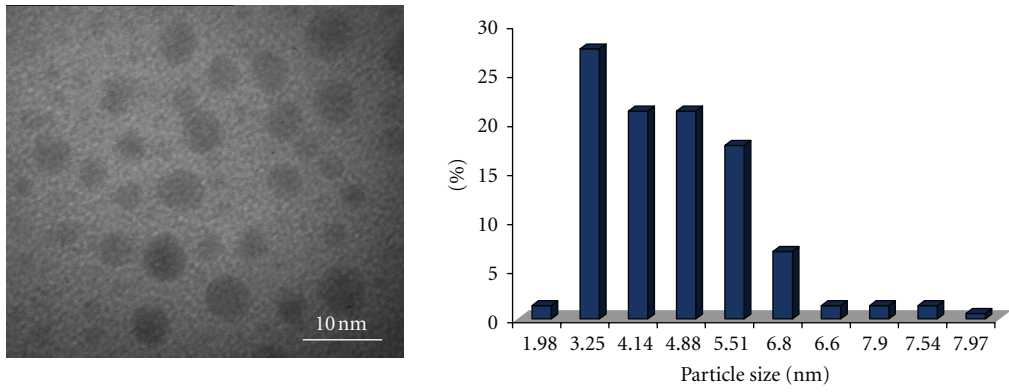
the catalytic activity was improved using carbon electrodes modified with Au nanoparticles [8, 9]. Furthermore carbon electrode bearing bimetallic Au-Ag nanoparticles containing not less than 73% Au is composed of atomically mixed Au and Ag atoms which give improvements on electrocatalytic activity for glucose oxidation [21]. Similar behavior has been found for Au-Cu nanoparticles [22]. This paper reports preliminary experimental findings suggesting that nanoparticle size and crystallographic orientation are important in achieving high electroactivity and selectivity for the electrocatalytic oxidation of glucose.

2. Experimental Section

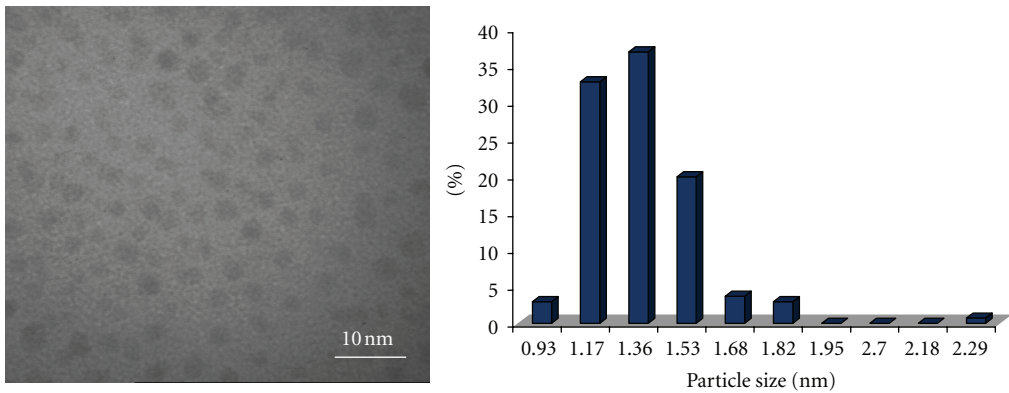
2.1. Preparation of Gold Nanoparticles. Gold nanoparticles were prepared according to a previously published procedure



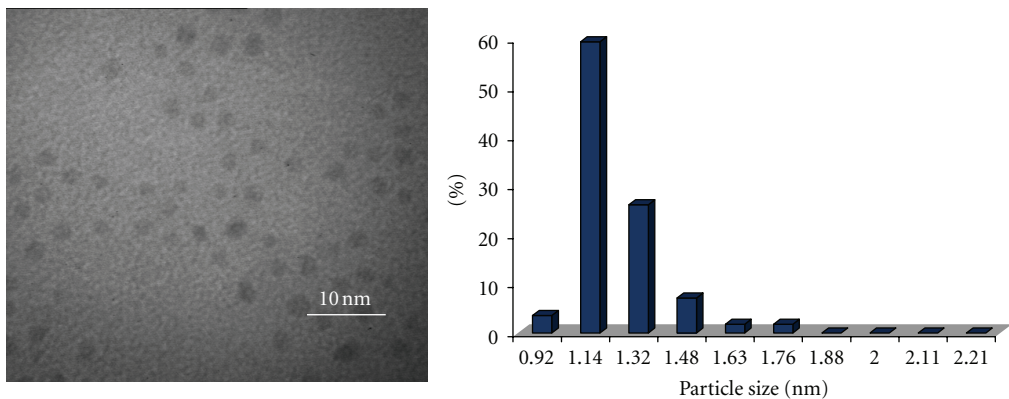
(a)



(b)



(c)



(d)

FIGURE 1: Continued.

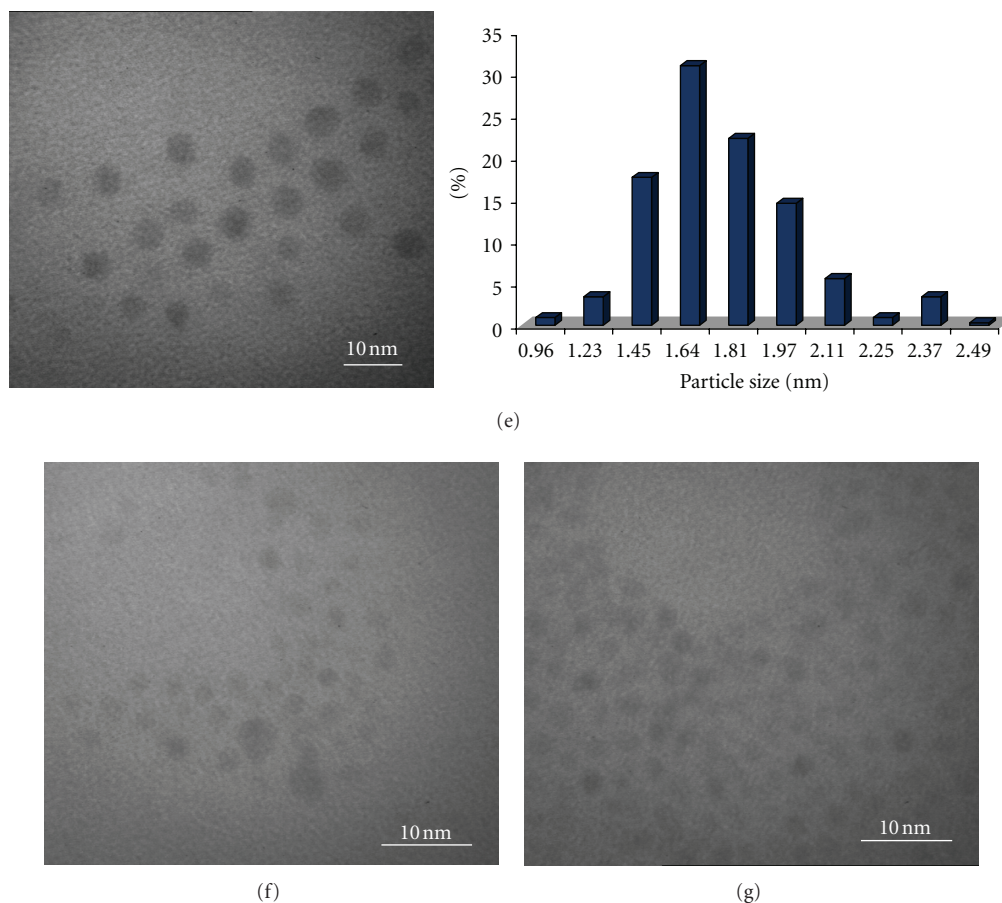


FIGURE 1: (a) TEM micrograph and distribution size of M1. (b) TEM micrograph and distribution size of M2. (c) TEM micrograph and distribution size of M3. (d) TEM micrograph and distribution size of M4. (e) TEM micrograph and distribution size of M5. (f) TEM micrograph of M7. (g) TEM micrograph of M8.

[23]. 0.184 mM $\text{HAuCl}_4 \cdot 3\text{H}_2\text{O}$ (J. T. Baker) aqueous solution, which was added to 10 mL of toluene (Aldrich) containing 0.34 mM tetraoctylammonium bromide (TOAB 98%, Fluka) as a phase-transfer agent. Dodecanethiol (Aldrich) was incorporated to this solution as a stabilizing agent; two Au/thiol ratios were used, 3:1 and 1:1/16 followed by the addition of an excess of NaBH_4 as an aqueous reducing agent. NaBH_4 was added to the solution at two different addition times, 10 and 60 sec. The reaction was allowed to proceed under constant stirring at different controlled temperatures for 3 h. Finally, a colored dispersion was obtained and purified several times with ethanol (J. T. Baker). The resulting gold nanoparticles were characterized by transmission electron microscopy (TEM), UV-Visible spectroscopy (UV-Vis), X-ray diffraction spectroscopy (XRD), and cyclic voltammetry (CV).

2.2. Preparation of Carbon Electrodes Modified with Nanoparticles. Au nanoparticle-modified electrodes were prepared as follows: 1 μL aliquot of thiol-Au nanoparticles in hexane was mixed with Vulcan XC-72 and Nafion 5% ELECTROCHEM (1:10 ratio) and cast onto a carbon disk (CD) followed by natural evaporation at room temperature. To remove

the thiol stabilizing agent layer from nanoparticles, CD-modified electrodes were heated at 300°C for 2 h under air atmosphere, the temperature was controlled to within $\pm 2^\circ\text{C}$.

2.3. Characterization of Nanoparticles. Synthesized Au nanoparticles were characterized using TEM, UV-Vis, XRD, and CV. TEM characterizations were performed on a Philips CM-200 microscope. Images and statistical treatment were performed using the SIMM software developed by one of us. Nanoparticle samples dissolved in hexane were cast onto a carbon-coated copper grid sample holder followed by natural evaporation at room temperature.

UV-Vis measurements were carried out on a HP spectrophotometer model 8453.

XRD measurements were obtained using a Bruker model D8 Advance diffractometer. Spectra were collected from 10 to 50° at a speed of $0.0025^\circ\text{seg}^{-1}$.

Cyclic voltammetric measurements were performed using a BAS Epsilon potentiostat/galvanostat (Bioanalytical Systems), with a conventional three electrode cell. An Hg/HgO was used as reference electrode and a Pt wire as the

TABLE 1: Summary of sizes and plane orientation ratio as a function of synthesis conditions.

Addition time of reducing agent (sec)	10				60			
Synthesis temperature ($^{\circ}\text{C}$)	10		50		10		50	
Au : thiol ratio	3 : 1	1 : 1/16	3 : 1	1 : 1/16	3 : 1	1 : 1/16	3 : 1	1 : 1/16
Size (nm)	3.6	1.4	4.6	1.2	1.7	1.4		1
(111) : (200) ratio	1	2.25	1.87	2.12	1.4	1.59		1.2
Sample	M1	M3	M2	M4	M5	M7		M8

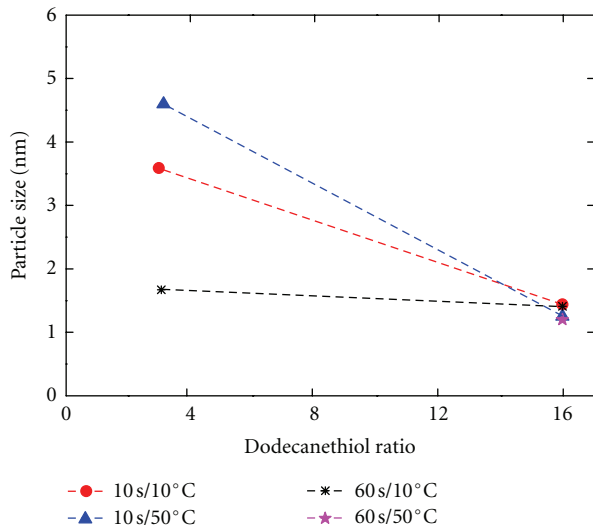


FIGURE 2: Nanoparticle size versus Au : thiol ratio, reducing agent addition rate, and synthesis temperature.

counter electrode. All potentials were referred to this electrode. The electrolyte solution was purged for twenty minutes with high-purity nitrogen before taking measurements. Glucose was used at various concentrations ranging from 0.00625 to 0.1 M in 0.1 M NaOH.

3. Results and Discussion

3.1. Characterization of Au Nanoparticles

3.1.1. TEM Characterization. Figures 1(a)–1(g) show TEM micrographs of the synthesized Au nanoparticles (labeled as M1 to M8), their population core size, and their average size. The synthesis conditions are summarized in Table 1. Synthesis of Au nanoparticles can be easily controlled to obtain nanoparticles with a suitable size and low dispersion.

3.1.2. Influence of Reducing Agent Addition Rate and Temperature. It is known that the addition rate of reducing agent affects the nanoparticles size [24]. We have synthesized the Au nanoparticles using two different addition times.

For the 10-second reducing agent addition, it was found that the greater the Au/thiol ratio, the smallest core size is obtained regardless of synthesis temperature; at least temperature seems to have less influence than Au/thiol ratio on nanoparticles size. Increasing temperature tends to reduce

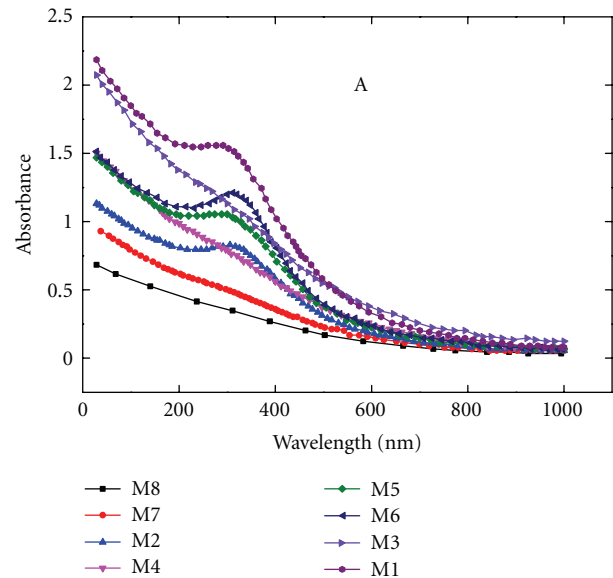


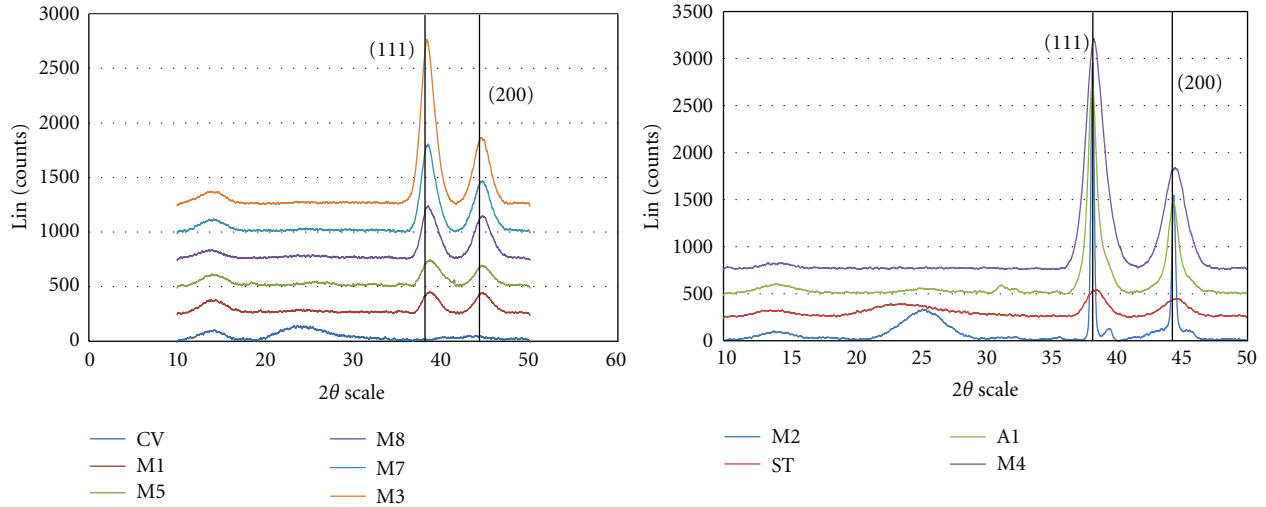
FIGURE 3: UV-Visible spectra for Au nanoparticles.

nanoparticles size. Core size for the highest Au/thiol ratio is about three times smaller than the lowest Au/thiol ratio (Table 1 and Figure 2).

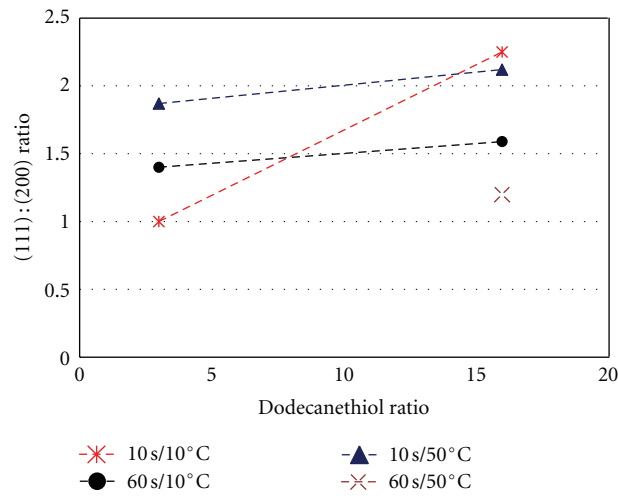
Taking into account the measurements uncertainty, there is no significant size variation at the 60 seconds reducing agent addition time (Table 1 and Figure 2).

3.1.3. UV-Visible. It is well known that Au nanoparticles have surface plasmon (SP) resonance absorption bands in the visible region. SP resonance bands are strongly dependent on the size, shape, composition, and dielectric properties of nanoparticles and their local environment. Figure 3 shows UV-Visible spectra from Au nanoparticles in hexane. Results are in agreement with the literature [23]; only nanoparticles having a size greater than 1.5 nm present the Plasmon band.

3.1.4. XRD Characterization. Figure 4 shows the diffractograms for the different Au nanoparticles synthesized. One can see the presence of two signals corresponding to (111) and (200) crystallographic plane orientation. The intensity of signals means the proportion of each orientation present in that particular nanoparticle. As for nanoparticles size, the main factor influencing the orientation plane is the Au : thiol ratio (Table 1, Figure 4(b)). We can see that the higher the Au-to-thiol ratio, the more intense the (111) signal

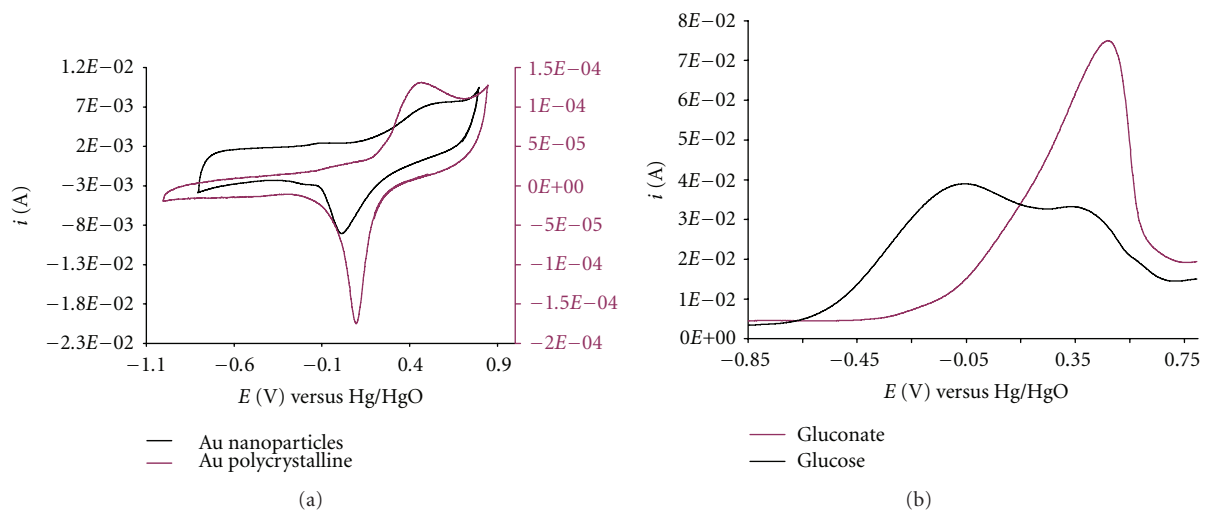


(a)



(b)

FIGURE 4: (a) XRD spectra for the Au nanoparticles. (b) (111) : (200) ratio versus Au : thiol ratio.



(a)

(b)

FIGURE 5: (a) Cyclic voltammetry of Au and carbon-modified electrodes with Au nanoparticles in 0.1 M NaOH, 50 mVs⁻¹. (b) Cyclic voltammetry of carbon modified electrode with Au nanoparticles in 0.1 M NaOH in presence of glucose and gluconate.

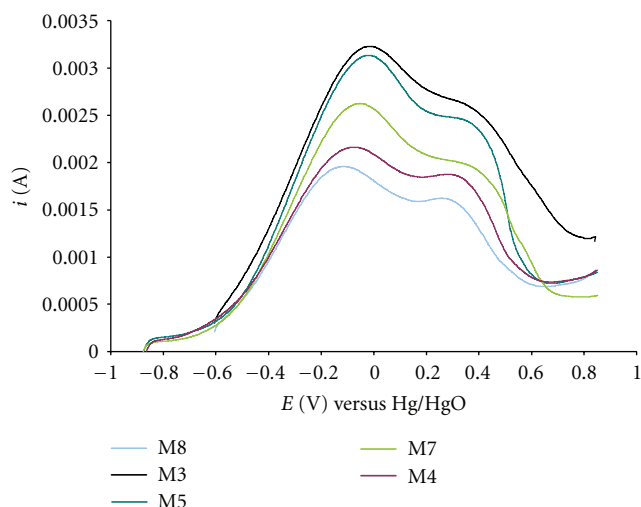


FIGURE 6: Cyclic voltammetry of carbon modified electrodes with different size Au nanoparticles in 0.1 M NaOH 50 mVs^{-1} in presence of glucose.

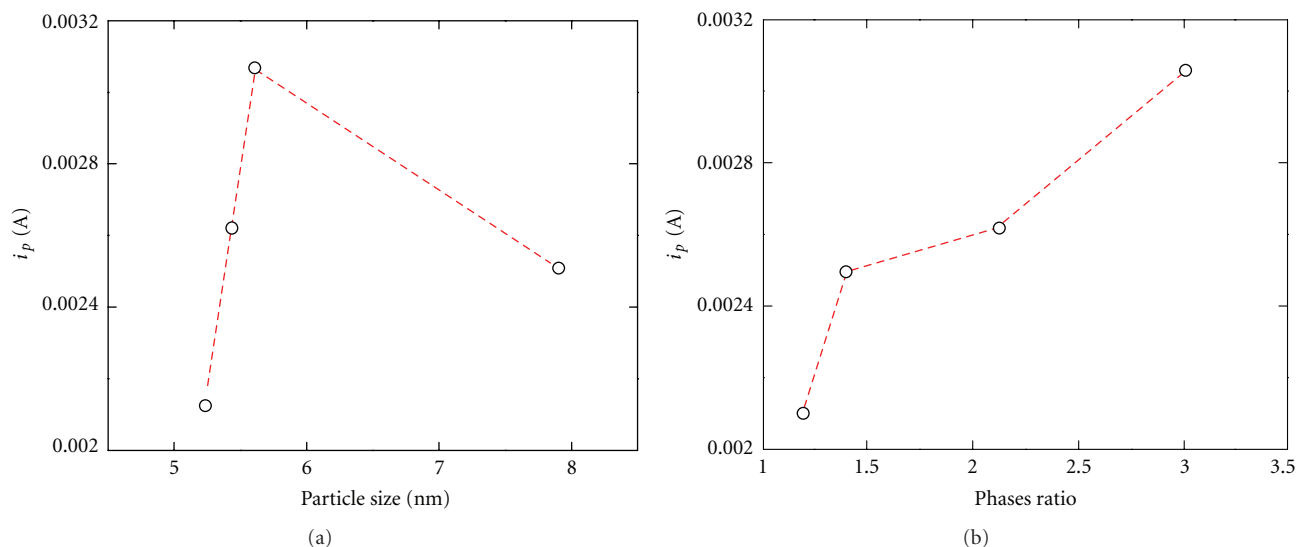


FIGURE 7: (a) Peak current versus particle size. (b) Peak current versus (111):(200) ratio.

is (Figures 4(a) and 4(b)). Results suggest that we can, by controlling the synthesis conditions, obtain the desired size and suitable crystallographic plane orientation in the Au nanoparticles.

3.1.5. Electrochemical Characterization. We have used cyclic voltammetry for the Au nanoparticles electrochemical characterization. Figure 5(a) shows the response of both electrodes Au polycrystalline and a carbon electrode modified with Au nanoparticle in 0.1 M NaOH. We can see the typical Au response with the formation and reduction of Au oxides. Figure 5(b) shows the electrocatalytic activity of a carbon-modified electrode with Au nanoparticles in presence of glucose and gluconate in 0.1 M NaOH.

Figure 6 shows the typical Au nanoparticle responses in the presence of glucose in 0.1 M NaOH. All the nanoparticles

capped onto carbon electrodes gave similar electrocatalytic activity. Nevertheless some differences arise from Figures 6 and 7. As can be seen, the current peak is a function of Au nanoparticle size with an apparent maxima around 6-7 nm. Moreover, peak current is also a function of crystallographic orientation meaning at least that the electrocatalytic activity of carbon modified with Au nanoparticles depend on the plane orientation of Au nanoparticles (Figures 6 and 7). Results suggest that selectivity could also be plane orientation dependent.

Figure 8(a) shows a classical electrochemical analysis (voltammograms not shown). The peak current versus glucose concentration plot gives a linear correlation with the highest slope for carbon-modified electrode with nanoparticles suggesting a lower poisoning of electrode surface than massive Au electrodes. In Figures 8(b) and 8(c), the analysis

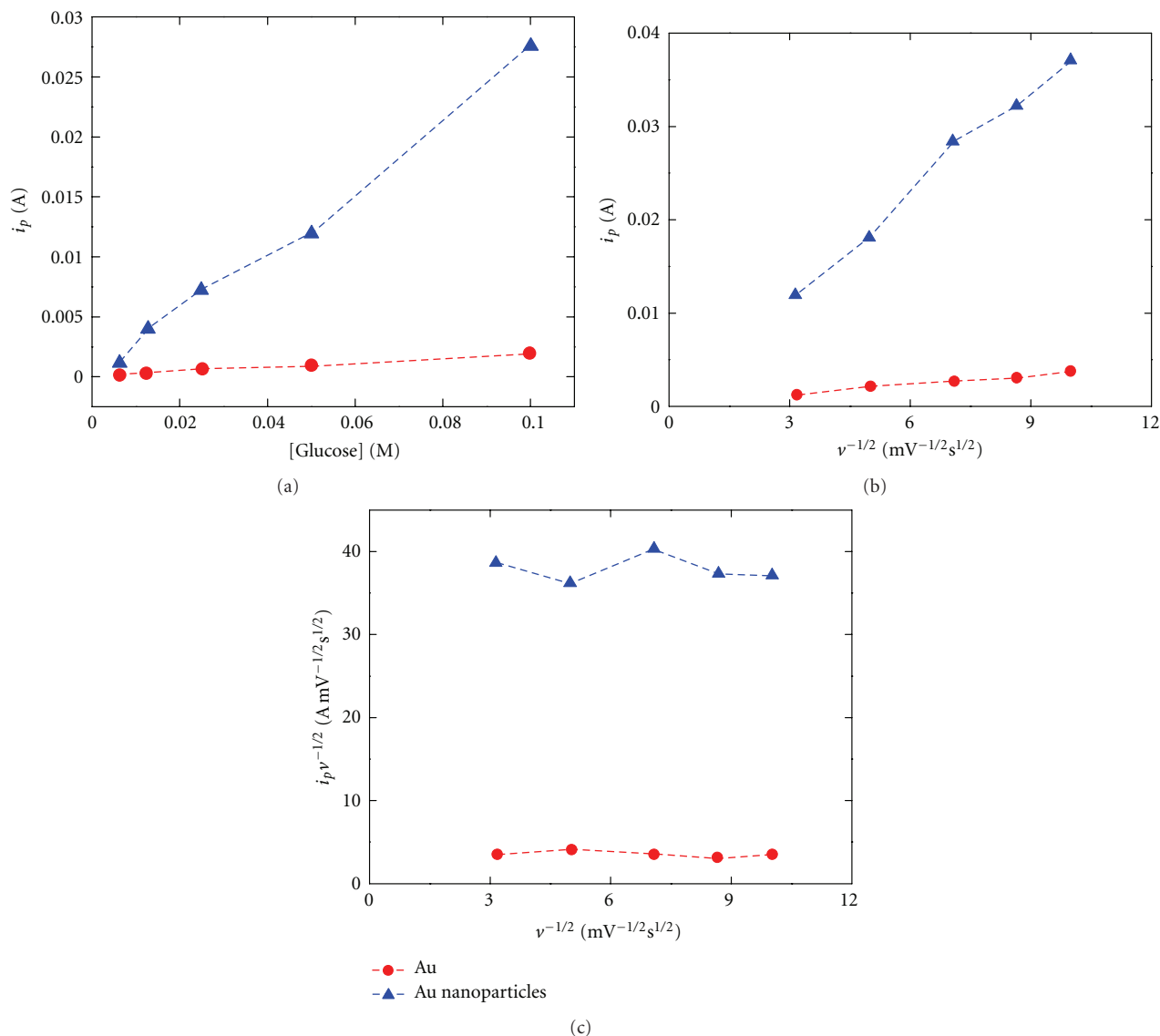


FIGURE 8: Plots of (a) i_p versus glucose concentration, (b) i_p versus $v^{-1/2}$, (c) $i_p v^{1/2}$ versus $v^{-1/2}$.

shows an irreversible process and the possibility of coupled chemical reactions.

4. Conclusions

It was found that Au nanoparticles supported on glassy carbon presented a catalytic activity and selectivity towards glucose oxidation, depending on the particle size and on the crystallographic orientation.

Results also suggest that oxidation process in these conditions is taking place with lower poisoning of the surface in the case of the Au nanoparticles than for massive gold, and that this process is irreversible, with perhaps some chemical reactions involved in the overall oxidation process.

Acknowledgments

Nafion is a trade mark, and the authors do not have any financial relation. The SIMM software was developed by Dr. Ivan Terol-Villalobos in behalf of CIDETEQ (Centro de Investigación y Desarrollo Tecnológico en Electroquímica S. C.), owner of the registered mark. The authors thank the Mexican Council for Science and Technology (CONACYT) for financial support through Fomix-Guanajuato, Grant GTO-2006-C01-23776. M. Guerra-Balcázar thanks the Mexican Council for Science and Technology (CONACYT) for graduate fellowship.

References

- [1] Y. B. Vassilyev, O. A. Khazova, and N. N. Nikolaeva, "Kinetics and mechanism of glucose electrooxidation on different

- electrode-catalysts. Part II. Effect of the nature of the electrode and the electrooxidation mechanism," *Journal of Electroanalytical Chemistry*, vol. 196, no. 1, pp. 127–144, 1985.
- [2] L. A. Larew and D. C. Johnson, "Concentration dependence of the mechanism of glucose oxidation at gold electrodes in alkaline media," *Journal of Electroanalytical Chemistry*, vol. 262, no. 1-2, pp. 167–182, 1989.
- [3] R. R. Adzic, M. W. Hsiao, and E. B. Yeager, "Electrochemical oxidation of glucose on single crystal gold surfaces," *Journal of Electroanalytical Chemistry*, vol. 260, no. 2, pp. 475–485, 1989.
- [4] K. B. Kokoh, J. M. Léger, B. Beden, H. Huser, and C. Lamy, "'On line' chromatographic analysis of the products resulting from the electrocatalytic oxidation of d-glucose on pure and adatoms modified Pt and Au electrodes-Part II. Alkaline medium," *Electrochimica Acta*, vol. 37, no. 11, pp. 1909–1918, 1992.
- [5] M. W. Hsiao, R. R. Adzic, and E. B. Yeager, "Electrochemical oxidation of glucose on single crystal and polycrystalline gold surfaces in phosphate buffer," *Journal of The Electrochemical Society*, vol. 143, no. 3, pp. 759–767, 1996.
- [6] S. B. Aoun, Z. Dursun, T. Koga, G. S. Bang, T. Sotomura, and I. Taniguchi, "Effect of metal ad-layers on Au(1 1 1) electrodes on electrocatalytic oxidation of glucose in an alkaline solution," *Journal of Electroanalytical Chemistry*, vol. 567, no. 2, pp. 175–183, 2004.
- [7] S. Ben Aoun, G. S. Bang, T. Koga, Y. Nonaka, T. Sotomura, and I. Taniguchi, "Electrocatalytic oxidation of sugars on silver-UPD single crystal gold electrodes in alkaline solutions," *Electrochemistry Communications*, vol. 5, no. 4, pp. 317–320, 2003.
- [8] M. Tominaga, T. Shimazoe, M. Nagashima, and I. Taniguchi, "Electrocatalytic oxidation of glucose at gold nanoparticle-modified carbon electrodes in alkaline and neutral solutions," *Electrochemistry Communications*, vol. 7, no. 2, pp. 189–193, 2005.
- [9] M. Tominaga, T. Shimazoe, M. Nagashima et al., "Electrocatalytic oxidation of glucose at gold-silver alloy, silver and gold nanoparticles in an alkaline solution," *Journal of Electroanalytical Chemistry*, vol. 590, no. 1, pp. 37–46, 2006.
- [10] M. Tominaga, M. Nagashima, K. Nishiyama, and I. Taniguchi, "Surface poisoning during electrocatalytic monosaccharide oxidation reactions at gold electrodes in alkaline medium," *Electrochemistry Communications*, vol. 9, no. 8, pp. 1892–1898, 2007.
- [11] M. Tominaga, T. Shimazoe, M. Nagashima, and I. Taniguchi, "Electrocatalytic oxidation of glucose at carbon electrodes modified with gold and gold-platinum alloy nanoparticles in an alkaline solution," *Chemistry Letters*, vol. 31, no. 2, pp. 202–203, 2005.
- [12] P. Parpot, N. Nunes, and A. P. Bettencourt, "Electrocatalytic oxidation of monosaccharides on gold electrode in alkaline medium: structure-reactivity relationship," *Journal of Electroanalytical Chemistry*, vol. 596, no. 1, pp. 65–73, 2006.
- [13] M. Z. Luo and R. P. Baldwin, "Characterization of carbohydrate oxidation at copper electrodes," *Journal of Electroanalytical Chemistry*, vol. 387, no. 1-2, pp. 87–94, 1995.
- [14] N. Torto, T. Ruzgas, and L. Gorton, "Electrochemical oxidation of mono- and disaccharides at fresh as well as oxidized copper electrodes in alkaline media," *Journal of Electroanalytical Chemistry*, vol. 464, no. 2, pp. 252–258, 1999.
- [15] K. B. Male, S. Hrapovic, Y. Liu, D. Wang, and J. H. T. Luong, "Electrochemical detection of carbohydrates using copper nanoparticles and carbon nanotubes," *Analytica Chimica Acta*, vol. 516, no. 1-2, pp. 35–41, 2004.
- [16] R. Ojani, J. B. Raoof, and P. Salmany-Afagh, "Electrocatalytic oxidation of some carbohydrates by poly(1-naphthylamine)/nickel modified carbon paste electrode," *Journal of Electroanalytical Chemistry*, vol. 571, no. 1, pp. 1–8, 2004.
- [17] A. Salimi and M. Roushani, "Non-enzymatic glucose detection free of ascorbic acid interference using nickel powder and nafion sol-gel dispersed renewable carbon ceramic electrode," *Electrochemistry Communications*, vol. 7, no. 9, pp. 879–887, 2005.
- [18] M. Haruta, H. Kageyama, N. Kajimo, T. Kobayashi, and F. Delannay, "Fine structure of novel gold catalysts prepared by coprecipitation," *Studies in Surface Science and Catalysis*, vol. 44, pp. 33–42, 1989.
- [19] J. M. Gottfried, K. J. Schmidt, S. L. M. Schroeder, and K. Christmann, "Adsorption of carbon monoxide on Au(1 1 0)-(1 × 2)," *Surface Science*, vol. 536, no. 1–3, pp. 206–224, 2003.
- [20] M. S. El-Deab, T. Sotomura, and T. Oshaka, "Oxygen reduction at electrochemically deposited crystallographically oriented Au(1 0 0)-like gold nanoparticles," *Electrochemistry Communications*, vol. 7, no. 1, pp. 29–34, 2005.
- [21] M. Tominaga, T. Shimazoe, M. Nagashima, and I. Taniguchi, "Composition-activity relationships of carbon electrode-supported bimetallic gold-silver nanoparticles in electrocatalytic oxidation of glucose," *Journal of Electroanalytical Chemistry*, vol. 615, no. 1, pp. 51–61, 2008.
- [22] M. Tominaga, Y. Taema, and I. Taniguchi, "Electrocatalytic glucose oxidation at bimetallic gold-copper nanoparticle-modified carbon electrodes in alkaline solution," *Journal of Electroanalytical Chemistry*, vol. 624, no. 1-2, pp. 1–8, 2008.
- [23] M. Guerra-Balcázar, D. Morales-Acosta, F. Castaneda, J. Ledesma-García, and L. G. Arriaga, "Synthesis of Au/C and Au/Pani for anode electrodes in glucose microfluidic fuel cell," *Electrochemistry Communications*, vol. 12, no. 6, pp. 864–867, 2010.
- [24] M. J. Hostetler, J. E. Wingate, C. J. Zhong et al., "Alkanethiolate gold cluster molecules with core diameters from 1.5 to 5.2 nm: core and monolayer properties as a function of core size," *Langmuir*, vol. 14, no. 1, pp. 17–30, 1998.

Research Article

Effect of Tetramethylammonium Hydroxide on Nucleation, Surface Modification and Growth of Magnetic Nanoparticles

Ângela L. Andrade,^{1,2} José D. Fabris,³ José D. Ardisson,⁴ Manuel A. Valente,⁵
and José M. F. Ferreira¹

¹ Department of Ceramics and Glass Engineering, CICECO, University of Aveiro, 3810193 Aveiro, Portugal

² Department of Chemistry, ICEB, Federal University of Ouro Preto, 35400-000 Ouro Preto, MG, Brazil

³ Federal University of Jequitinhonha and Mucuri Valleys (UFVJM), 39100-000 Diamantina, MG, Brazil

⁴ Applied Physics Laboratory, Nuclear Technology Development Center, (CDTN)/CNEN, 31270-901 Belo Horizonte, MG, Brazil

⁵ Department of Physics, University of Aveiro, I3N, 3810193 Aveiro, Portugal

Correspondence should be addressed to José M. F. Ferreira, jmf@ua.pt

Received 26 March 2012; Accepted 11 June 2012

Academic Editor: Leonard Deepak Francis

Copyright © 2012 Ângela L. Andrade et al. This is an open access article distributed under the Creative Commons Attribution License, which permits unrestricted use, distribution, and reproduction in any medium, provided the original work is properly cited.

Nanoparticles of magnetite (Fe_3O_4) were obtained by reacting ferric chloride with sodium sulphite, through the reduction-precipitation method. The effects of adding tetramethylammonium hydroxide (TMAOH) during or after the precipitation of the iron oxide were studied in an attempt to obtain well-dispersed magnetite nanoparticles. Accordingly, the following experimental conditions were tested: (i) precipitation in absence of TMAOH (sample Mt), (ii) the same as (i) after peptizing with TMAOH (Mt1), (iii) TMAOH added to the reaction mixture during the precipitation of magnetite (Mt2). Analyses with transmission electron microscopy (TEM), X-ray diffraction, Mössbauer spectroscopy, attenuated total reflectance Fourier transform infrared spectroscopy (ATR-FTIR), zeta potential, and magnetization measurements up to 2.5 T revealed that magnetite was normally formed also in the medium containing TMAOH. The degree of particles agglomeration was monitored with laser diffraction and technique and inspection of TEM images. The relative contributions of Néel and Brownian relaxations on the magnetic heat dissipation were studied by investigating the ability of suspensions of these magnetite nanoparticles to release heat in aqueous and in hydrogel media. Based on ATR-FTIR and zeta potential data, it is suggested that the surfaces of the synthesized magnetite particles treated with TMAOH become coated with $(\text{CH}_3)_4\text{N}^+$ cations.

1. Introduction

Studying fundamental properties of synthetic analogous magnetite (Fe_3O_4) nanoparticles keeps drawing much scientific attention and technological interest mainly due to their actual and many potential uses on data storage [1, 2], biolabeling, and on the separation of biomolecules [3, 4]. Most of those applications require chemically stable and uniformly sized nanoparticles that will be well dispersed in liquid media. Usually, a protection layer on the particle surface is necessary to ensure their chemical stability and improve their dispersion ability, in order to increase the surface area to volume ratios. Fe_3O_4 nanoparticles are inherently unstable and tend to spontaneously aggregate to minimize their high surface energies.

Stable concentrated suspensions of magnetic nanoparticles in either organic or inorganic solvents are known as magnetic fluids or ferrofluids [5]. Magnetic fluids were firstly synthesized in 1964, by Papell [6]. They behave as a functional fluid and have increasingly found technological applications in a variety of fields, such as electronic packing, mechanical engineering, aerospace, and bioengineering [7]. Over the recent years, new ferrofluids and their derivatives have been developed for medical diagnosis and therapeutic practices in oncology, specifically, in these cases, for materials with magnetic ferrofluid hyperthermia (MFH) [8, 9], and for many other biomedical technologies [10–13].

Hyperthermia is a physical phenomenon that fundamentals a medical practice in cancer therapy. The practice consists in selectively heating the malignant tumor, by

placing the magnetocaloric material closely to or in direct contact with the affected internal organ of human body. Those organs tend to have fewer blood vessels and are less oxygenated than health ones. Consequently, they are more sensible and die when the local temperature goes above 43°C.

The heat dissipation from magnetic particles is caused by the delay of the relaxation of the magnetic moment through either the rotation within the particle (Néel) or the rotation of the particle itself (Brownian), when they are exposed to an AC-magnetic field with magnetic field reversal times shorter than the magnetic relaxation times of the particles [14]. In 2009, Suto et al. [14] showed that the relative contribution between Néel and Brownian relaxations varies depending upon the particle size. Differently from the Brownian relaxation, the heat dissipated through Néel relaxation is not influenced by viscosity of the medium. For example, if the viscosity of the medium is high or if the rotational degree of freedom of the particle restricted, the heat dissipated may either diminish or even completely seize. It is always necessary to determine the relative simultaneous contribution of heat from Néel and Brownian relaxations, to estimate the possible minimum and maximum heat that could be generated with *in vivo* experiments.

Berger et al. [15] have successfully prepared a ferrofluid of Fe₃O₄ by reacting iron (II) and iron (III) ions in an aqueous ammonia solution with the addition of tetramethylammonium hydroxide (TMAOH), in order to chemically stabilize the magnetic nanoparticles in a colloidal suspension. Cheng et al. [16] have synthesized ferrofluids of magnetite by coprecipitating iron (II) and iron (III) ions in an aqueous solution alkalized with TMAOH. According to Jolivet et al. [17], TMAOH acts as a surfactant to nanoparticles by absorbing the cationic species at the surface OH groups thus creating an electrostatic repulsion layer surrounding the particles keeping them apart. On the other hand, a number of earlier studies by Yang et al. [18–23] on hydrothermal synthesis of TiO₂ [18–22] and α -Al₂O₃ nanoparticles [23] confirmed that TMAOH plays a very active peptizing role, enhancing the state of dispersion and the crystallinity of the synthesized materials.

In the present work, Fe₃O₄ nanoparticles were synthesized *via* precipitation of partially reduced ferric chloride with sodium sulfide, in an alkaline solution. The effects of adding TMAOH either during the precipitation or after the synthesis of magnetite on the characteristics of the nanoparticles and on the colloidal stability of the suspensions will be discussed in this report.

2. Experimental Procedure

2.1. Reagents. All chemicals used, such as iron (III) chloride hexahydrate, FeCl₃·6H₂O (Riedel-de Haen, France); sodium sulfite, Na₂SO₃ (Sigma-Aldrich, Japan); ammonium hydroxide, NH₄OH (Fluka, Germany); 25% aqueous tetramethylammonium hydroxide solution, C₄H₁₃NO·5H₂O (TMAOH) (Aldrich, Germany, Japan) and hydrochloric acid, HCl (Sigma-Aldrich) were of analytical grade and used as received.

2.2. Synthesis of Iron Oxide Nanoparticles. Samples of Fe₃O₄ nanoparticles were obtained *via* the reduction-precipitation method, following the procedure described in details elsewhere [24]. In one of them, the iron ions solution was alkalized with ammonium hydroxide and the particles were peptized with TMAOH. In the other, the iron ions solution was directly alkalized with the peptizing agent (TMAOH), as described below.

2.2.1. Alkalinizing with Ammonia. 30 mL of a FeCl₃·6H₂O stock solution containing 0.5 mol L⁻¹ (dissolved in 0.5 mol L⁻¹ HCl), 20 mL of a Na₂SO₃ stock solution with 1 mol L⁻¹, and 50.8 mL of a NH₄OH solution diluted to a total volume of 800 mL were used. Just after mixing Fe³⁺ and SO₃⁻², the color of the solution changed from yellow to red and, after few minutes, the yellow color reappeared. A diluted ammonia solution was then quickly poured into the mixture under vigorous stirring; a black precipitate was then formed. Stirring continued for an additional 30 min. The pH of the solution was monitored to be maintained at 10.0 ± 0.1. The suspension containing the precipitated powder was centrifuged at 2,000 rpm for 3 min; the supernatant was discarded. This procedure was repeated for five times by redispersing the resultant cakes in distilled water, each time. The as-obtained precipitate sample was labeled Mt. The Mt nanoparticles were peptized with TMAOH. Typically, 1 mL of 25 mass% TMAOH solution was added to each centrifuge tube containing an amount of wet cake corresponding to about 1 g of dry powder and re-dispersed by stirring with a thin glass rod until obtaining homogeneous suspensions. These suspensions were then dried to obtain the powders for the different measurements. This sample peptized with TMAOH was labeled Mt1.

2.2.2. Alkalinizing with TMAOH. In this case, magnetite nanoparticles were synthesized in the same way as described above, but alkalizing was made by quickly pouring 25 mass% TMAOH solution until a pH of about 10.0 ± 0.1 was obtained. A precipitate was formed. The mixture was stirred for further 30 min. The obtained suspension was centrifuged at 2,000 rpm for 3 min, and the supernatant was discarded. This procedure was repeated five times by redispersing the resultant cakes in distilled water. The centrifuged cakes were dried to obtain the powders to be used for further characterization. The obtained solid sample, precipitated in medium containing TMAOH, was labeled Mt2.

2.3. Characterization Techniques. For transmission electron microscopy analysis (TEM), a drop of the suspension of the magnetite sample was placed onto a copper mesh coated with an amorphous carbon film and then dried in an evacuated desiccator. TEM micrographs were recorded on a transmission electron microscope (Hitachi, 9000 NA, Japan) and the particle size was measured with the software Image J. The crystalline phases were determined by X-ray powder diffraction (XRD) analysis (Rigaku Geigerflex D/Max, C Series; CuK α radiation; 2 θ angle range 20°–70°; step 0.02 s⁻¹) after evaporation of the liquid carrier. Phases were

identified by comparing the experimental X-ray patterns with standard files compiled by the International Centre for Diffraction Data. The Rietveld structural refinement was performed with FULLPROF 2010 program. Mössbauer spectra were collected in constant acceleration transmission mode with a ~ 50 mCi $^{57}\text{Co}/\text{Rh}$ gamma-ray source. Spectra at 298 K and 100 K were obtained with a spectrometer equipped with a transducer (CMTE model MA250) controlled by a linear function driving unit (CMTE model MR351). Values of Mössbauer isomer shifts are quoted relatively to $\alpha\text{-Fe}$. The experimental reflections were fitted to Lorentzian functions by least-square fitting with software NORMOS-90 (this NORMOS package was developed by R. A. Brand, Laboratorium für Angewandte Physik, Universität Duisburg, D-47048, Duisburg-Germany). The ATR-FTIR data were collected with a FT-IR model Mattson Galaxy S-7000, 32 scans, and resolution of 4 cm^{-1} .

The determination of zeta potential (ξ) was performed on a COULTER DELSA 440SX, by using a stock suspension of the ground material in deionized water, prepared and homogenized by ultrasonication for 15 min. Drops of this stock suspension were then added to an aqueous solution of $\text{KCl } 10^{-3}\text{ mol L}^{-1}$ for the zeta potential measurements. The pH of the measuring solution was varied and adjusted to several values, in the pH range of 3.5 to 10.5, by using $10^{-3}\text{ mol L}^{-1}$ aqueous solutions of KOH and HNO_3 .

The agglomerate grain sizes in suspension were determined by dynamic light scattering (DSL) using a Zetasizer Nano ZS instrument (Malvern Instruments Ltd., UK) that allows specific measurements of the z -average diameter (defined as the intensity-weighted average hydrodynamic diameter of the particles being measured). An aliquot of a stock suspension of the ground material in deionized water was prepared and homogenized by ultrasonication for 5 min. The used water was purified by passing through a $0.22\text{ }\mu\text{m}$ Millipore filter. The z -average diameter was calculated as the average of six measurements.

The DC magnetic measurements were performed on powder samples (100–150 mg) using a vibrating sample magnetometer (VSM) with a cryogen-free magnet (cryogenic-cryofree), at the University of Aveiro, Portugal. Typical hysteresis curves were obtained at $300 \pm 0.1\text{ K}$ with a magnetic field varying between -2.5 and 2.5 T . The magnetic parameters such as saturation magnetization (M_s), coercivity (H_c), and retentivity (M_r) were obtained from the VSM results.

Heat dissipation experiments were carried out by transferring the suspensions with dispersed magnetite in both water and hydrogel into a test tube. This tube was placed at the center of a three-loop coil of the VSM equipment, consisting of a power supply (Nova Star 5 kW RF Power Supply, Ameritherm, Inc, Scottsville, NY, USA) and a heating station (Induction atmospheres). The sample concentration was approximately 2 mg mL^{-1} in water and 2 mg g^{-1} in polyvinyl alcohol hydrogel. In the hydrogel dispersed samples, rotation of particles was restricted and the magnetic moment relaxed only through Néel relaxation. The temperature of the magnetic suspension was measured with an optical fiber thermometer. Results were taken as the mean of triplicate measurements.

The polyvinyl alcohol hydrogel was based on the method earlier proposed by Hyon et al. [25], with minor modifications. A homogeneous polyvinyl alcohol (PVA) solution with a PVA concentration of 15 wt% was obtained by heating the mixture of PVA and a mixed water/dimethyl sulfoxide (DMSO) solvent at 140°C for 2 hrs. The mixing ratio of water to DMSO was kept to 20/80 by weight. Then the casted PVA was placed in a freezer at -20°C for 24 h.

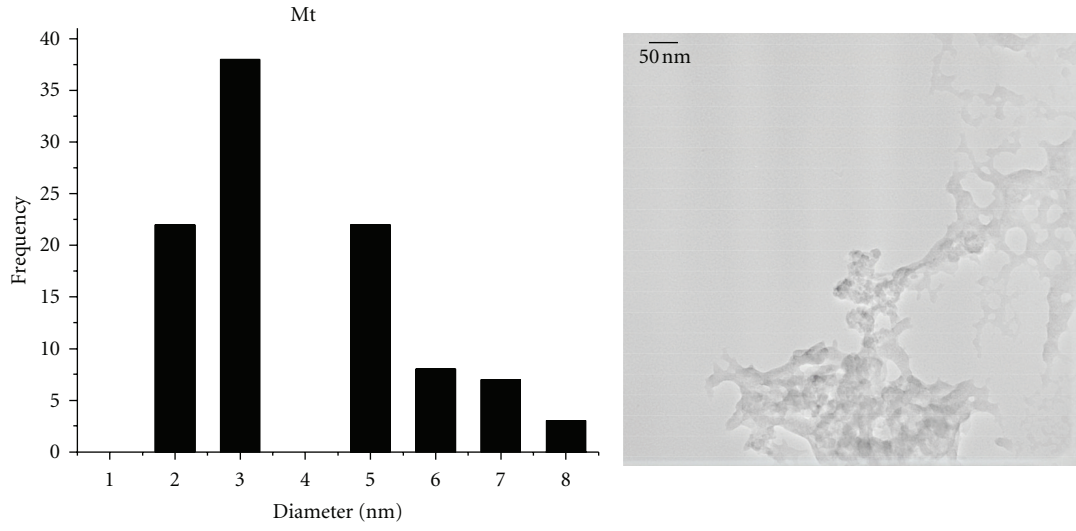
3. Results and Discussion

Centrifuging the just formed precipitate, still in aqueous suspension, in order to finally obtain the Mt2 sample, at 2,000 rpm for 3 min was found to be enough condition to separate the solid particles from the liquid phase, whereas for the corresponding Mt1 sample, centrifugation even at 12,000 rpm for 6 min was insufficient to separate the two phases. This suggests that Mt2 particles are coarser and/or strongly agglomerated than Mt1.

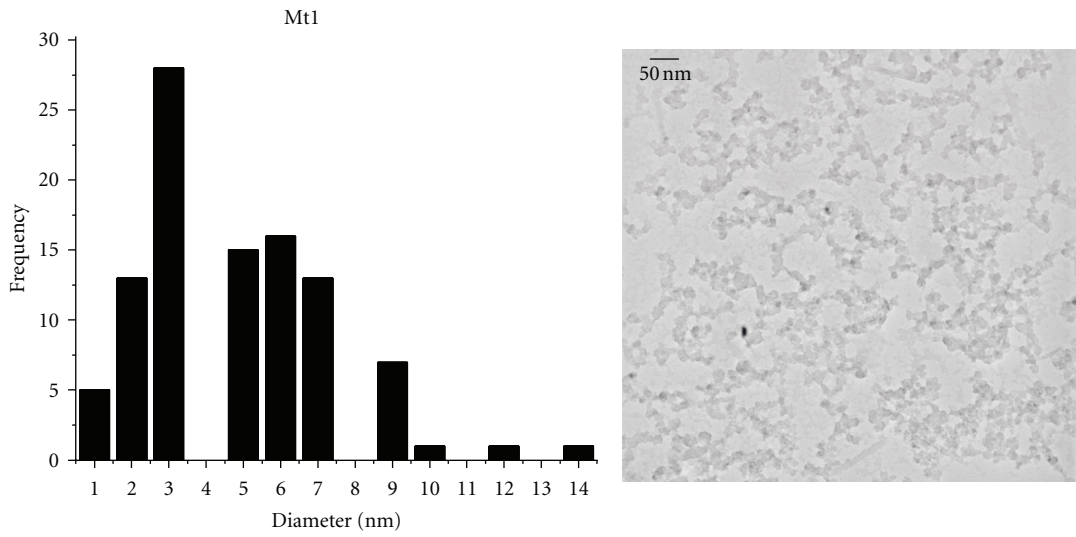
The obtained Mt, Mt1, and Mt2 samples were black in color and exhibited magnetic behavior, as it could be observed from their response to the magnetic field of a small hand magnet. The Mt1 suspension kept their colloidal characteristics for up to 5 months with negligible sedimentation in this ferrofluid. Contrarily, the Mt2 sample was completely sedimented when the ferrofluid flask was in rest for 1 h, evidencing again the coarser and/or aggregated nature of its particles.

The z -average diameter of the Mt, Mt1, and Mt2 samples in water was as follows: 243.7 ± 18.59 , 85.86 ± 2.736 , and $1,906 \pm 495.8\text{ nm}$, respectively. The large individual or aggregated grains, as observed for sample Mt2, explains the reason by which it sedimented even faster than the Mt1 sample. The Mt1 ferrofluid is also much better dispersed than Mt and Mt2.

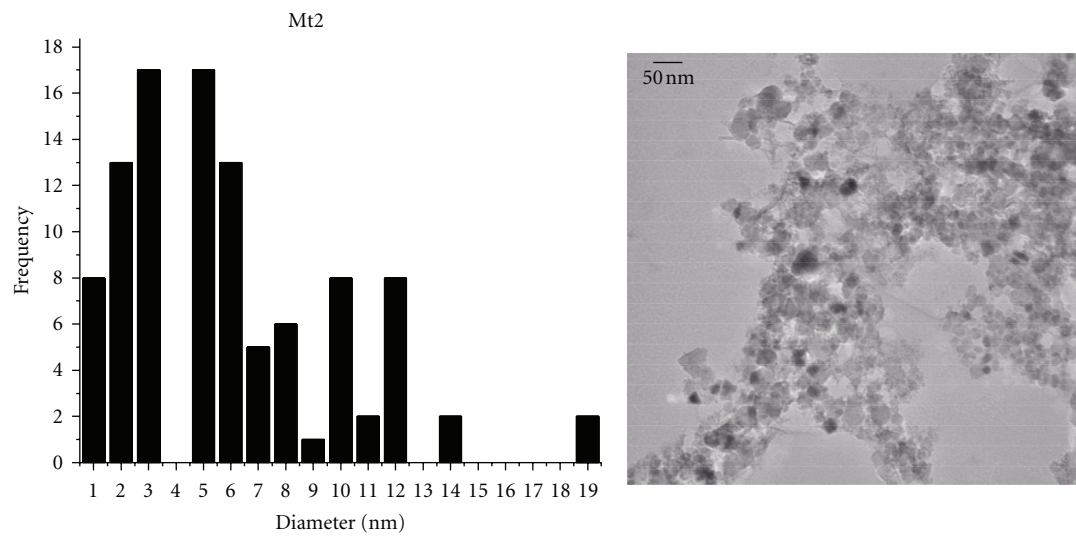
Figure 1 shows TEM images of Mt, Mt1, and Mt2 nanoparticles. The mean particle size diameters for the samples Mt, Mt1, and Mt2 were found to be about $5.7 \pm 2.9\text{ nm}$, $5.8 \pm 2.7\text{ nm}$, and $9.7 \pm 6.4\text{ nm}$, respectively. The mean size of the particles/aggregates is larger in the case of Mt2 sample. The higher tendency of particles in sample Mt2 to be aggregated can be explained by the bigger particle sizes but also by their higher crystallinity (Figure 2), well favored by the addition of the peptizing agent (TMAOH). Larger particles of well-crystallized magnetite in which the bulk properties supersede surface properties, and they are expected to magnetically attract more strongly each other. Hosono et al. [26] suggested that the bigger particles could be a consequence of higher concentration of charged ions in the solution since agglomeration between particles occurs by shrinkage of electric double layer. Moreover, the role of the ionic strength on the particle size also is largely dependent on the nature of the electrolyte. The smallest cations being the best screening ions, their influence on the surface charge is highest. The surface of iron oxides is negatively charged at $\text{pH} > \text{PZC}$ (point of zero charge). These characteristics explain the strong influence of NH_4^+ on reducing particle sizes, as compared to the $[\text{N}(\text{CH}_3)_4]^+$ cations, and also on



(a)



(b)



(c)

FIGURE 1: TEM micrograph of samples: Mt, Mt1, and Mt2.

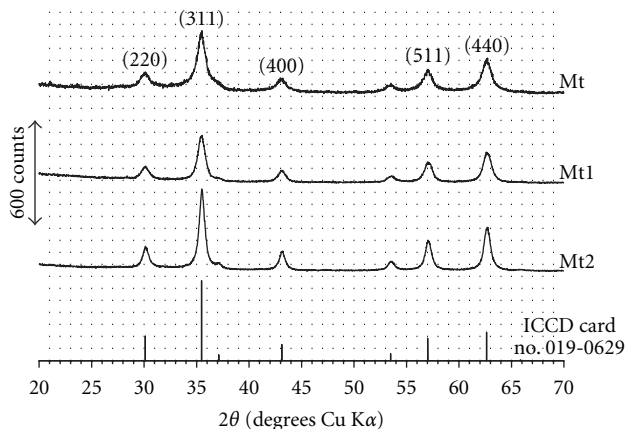


FIGURE 2: X-ray diffraction patterns of samples: Mt, Mt1, Mt2, and magnetite (ICDD file no. 019-0629).

preventing particles aggregation. This interpretation is in line with that of Bacri et al. [27, 28], who proposed a decreasing stability of the iron oxide nanoparticles as a consequence of a decrease of the electrical double layer thickness around the particles, driven by the increased ionic strength of the media upon adding TMAOH.

The crystalline structure of the synthesized iron oxide species analyzed by powder XRD (Figure 2) shows that Fe_3O_4 was identified in these Mt, Mt1, and Mt2 samples. The most intense reflections for this phase were registered at $2\theta = 30.095^\circ$, 35.423° , 43.053° , 57.22° and 62.76° , corresponding to the planes of (220), (311), (400), (511), and (440), respectively, of the iron oxide spinel. The peaks in the diffractograms match well with the PDF data for magnetite from the powder diffraction file (PDF) from International Centre for Diffraction Data (ICDD) card number 019-0629. The average particle sizes for Mt, Mt1, and Mt2 magnetites, from breadths of reflection 311, estimated with Scherrer equation were 11, 10, and 13 nm, respectively [29]. From routine powder XRD data only, it may be difficult to differentiate the coexisting maghemite ($\gamma\text{Fe}_2\text{O}_3$) and magnetite (Fe_3O_4) in a same sample since structure is cubic with relatively close unit cell dimension. The diffraction patterns for both phases are quite similar. Therefore, one might presume that magnetite and maghemite are components of the obtained ferromagnetic phases, as oxidation processes could not be totally avoided during chemical synthesis and solid powder washings and handling in air. Results in Figure 2 confirm that the sample Mt that has not been in contact with the peptizing agent exhibits the lowest degree of crystallinity as it can be drawn from the noisy background and from the broader diffraction peaks. Contrarily, the Mt2 sample that has been synthesized from the very beginning in presence of TMAOH presents the sharpest XRD diffraction peaks, which is in good consistence with its coarser morphology (Figure 1). When the peptizing agent was added to the precipitated Mt sample, it promoted a better dispersion of the partially amorphous nanoparticles and enhanced the degree of spatial arrangement of the matter, thus increasing the crystallinity. This effect was reportedly proposed for other systems [18–23]. These results suggest that, in the case

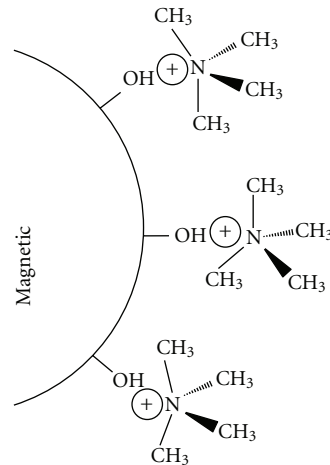


FIGURE 3: Peptization exerted by tetramethyl ammonium cations adsorbed onto the surface of magnetic nanoparticles thus, creating repulsive forces and enabling the particle growing species to be added to the surface in an organized manner.

of Mt2, the $[(\text{CH}_3)_4\text{N}]^+$ cations are prone to readily adsorb specifically onto the surface of the early nuclei being formed, as schematized in Figure 3, hindering some of them to achieve the critical size for growing. Under this perspective, a smaller number of effective nuclei would be formed, explaining the greater size of the resulting nanoparticles in the case of Mt2 sample.

Mössbauer spectra obtained at variable temperatures (Figure 4) reveal that these nanosized particles do contain ferric iron oxides in small particle sizes, more clearly for samples Mt and Mt2.

These magnetic nanoparticles in a liquid medium experience reorientations of the magnetization vector, in single anisotropic magnetic domains (Néel relaxation time, τ_N) but also due to viscous rotation of the particle (Brownian relaxation time, τ_B) [30, 31].

The global magnetic relaxation times (τ) of colloids are the sum of the Néel and Brownian relaxation rates, which is given by [31, 32]

$$\frac{1}{\tau} = \frac{1}{\tau_B} + \frac{1}{\tau_N}. \quad (1)$$

These relaxations explain the obtained Mössbauer spectra with a relatively intense central Fe^{3+} doublet along with a magnetic sextet, as it was more clearly observed for samples Mt and Mt2. However, lowering the sample temperature tends to progressively block the relaxations effect and promote the magnetic ordering. The coexistence of these two major spectral contributions, that is, superparamagnetic and magnetically ordered patterns, in different proportions, means that particle sizes distributions are different in each case. From Mössbauer data only, the sample Mt does contain higher proportion of smaller particles than in Mt2, but sample Mt1 contains the highest proportion of bigger particles of all three. The corresponding hyperfine field distributions clearly reflect these trends. The 80 K probability profile for sample Mt1 is considerably narrower

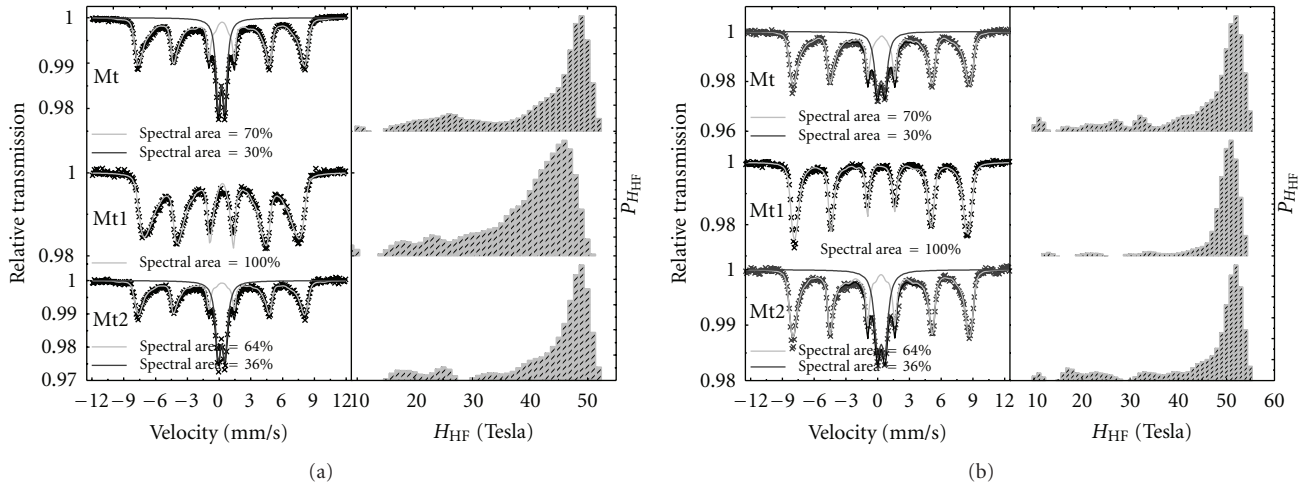


FIGURE 4: Mössbauer spectra of Mt, Mt1, and Mt2 at (a) RT, and (b) 80 K.

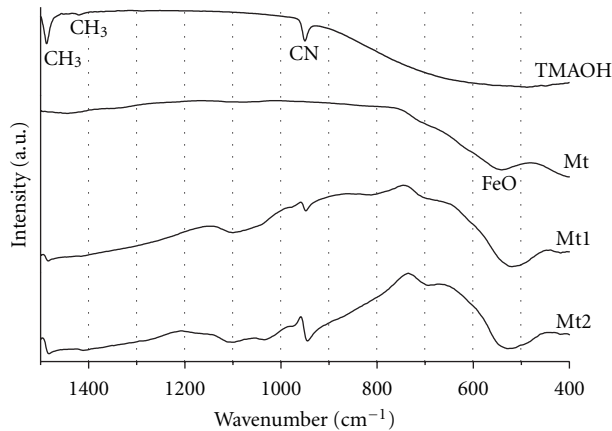


FIGURE 5: ATR-FTIR spectra of TMAOH, Mt, Mt1, and Mt2.

than for the other two samples. Values of hyperfine magnetic fields at maximum probability for all these magnetic samples steadily increase on going from 297 K to 80 K, following values well around those expected for maghemite ($\gamma\text{-Fe}_2\text{O}_3$).

The apparent contradiction with evidences from hyperthermic measurements that point to sample Mt2 as the sample containing bigger particles than Mt and Mt1 is explained by assuming that the Brownian relaxation rate in sample Mt2, with more strongly aggregated nanoparticles, is much slower so to produce a more significant hyperthermic effect. However, Mössbauer spectra are necessarily collected with the solid sample. In this condition, the global relaxation time is only influenced by the Néel relaxation, for which magnitude, particularly for samples Mt and Mt2, would be comparable or below the time-scale window for Mössbauer spectroscopy, or $\sim 10^{-7}$ s.

A Mössbauer spectrum results from the hyperfine coupling arising from extranuclear electric and magnetic fields that influence the energy levels of the probe nucleus. The fast fluctuation of the magnetization vector between easy

directions in the monodomain nanosystem, relatively to the lifetime decay of the ^{57}Fe 14.4 keV Mössbauer level, would lead to an electric quadrupole coupling, resulting in a spectral superparamagnetic doublet. Particles aggregation that is promoted by coating their surface with surfactant or polymerizing organic materials may be enough to change the hyperthermic behavior of the material but not necessarily the hyperfine structure of the solid material. Aggregates of fine particles may present typical hyperthermic behavior as of bigger particles, essentially due to the increasing Brownian reorientation energy in the colloidal medium, but their hyperfine structure still accounts for local interactions at the atomic nuclear level in the superparamagnetic state of the solid material.

Figure 5 compares the ATR-FTIR spectra of the TMAOH and of the Mt, Mt1, and Mt2 samples. The ATR-FTIR spectrum of the TMAOH shows a strong band at 1490 cm^{-1} , assigned to the asymmetric methyl deformation mode, $\delta_{\text{asym}}(\text{CH}_3)$. A smaller one assigned to the symmetrical methyl deformation mode $\delta_{\text{sym}}(\text{CH}_3)$ appears near 1430 cm^{-1} . A single band appeared at 950 cm^{-1} is attributed to the $\nu_{\text{asym}}(\text{C-N})$ mode which is generally observed in the domain $900\text{--}1000\text{ cm}^{-1}$ [33]. The Mt sample shows a band at 550 cm^{-1} . Since magnetite has an inverse spinel-type structure, it shows bands indicating the vibrations $\text{M}_\text{T}\text{-O-M}_\text{O}$ ($\nu_1 \approx 600\text{--}550\text{ cm}^{-1}$), where M_T and M_O correspond to the metal occupying tetrahedral and octahedral positions, respectively [34–36]. The ATR-FTIR spectra of the Mt1 and Mt2 samples also show the band at 550 cm^{-1} characteristic of magnetite and the characteristic vibration of Fe-O in maghemite ($\gamma\text{-Fe}_2\text{O}_3$) at 690 cm^{-1} [37–39], as well as the transmittance bands typical of TMAOH, proving that the peptizing agent has been strongly adsorbed at the surface of the nanoparticles.

Zeta potential data are a powerful tool being extensively used to evaluate the effects of the presence of surface-active agents in different systems. In the present work, this technique was also used to help evaluating the influence of

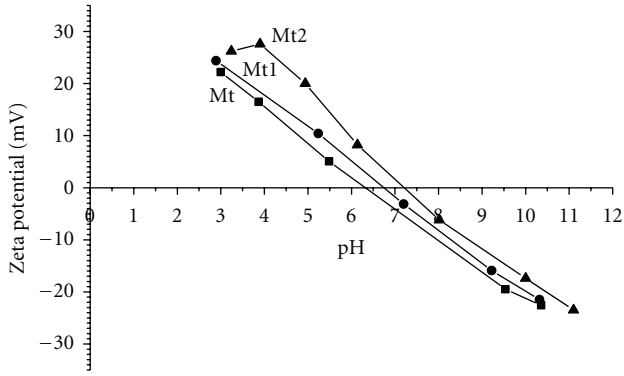


FIGURE 6: Variation of zeta potential of samples: Mt, Mt1, and Mt2.

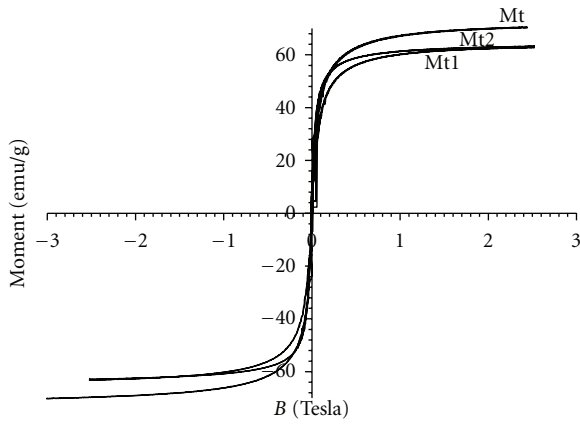


FIGURE 7: Magnetization curves of samples: Mt, Mt1, and Mt2.

added TMAOH on the solid/liquid interface properties of magnetite nanoparticles. Results presented in Figure 6 show that the pH values corresponding to the isoelectric points (pH_{IEP}) of the Mt and Mt1 samples were found to be about 6.4 and 6.8, respectively. This is in good agreement with the reported data in the scientific literature for magnetite [40, 41]. In the Mt2 sample, the pH_{IEP} was about 7.3. The increase in pH_{IEP} of the Mt1 and Mt2 samples, with respect to that determined for Mt sample, indicates that $[(\text{CH}_3)_4\text{N}]^+$ cations were specifically adsorbed onto the surface of the synthesized iron oxide species [42]. This specific adsorption is partially driven by the negative charge exhibited by magnetite above its pH_{IEP} (6.4) and has been apparently more extensive when the peptizing agent was added during the precipitation. Thus, the adsorbed $[(\text{CH}_3)_4\text{N}]^+$ ions tend to decrease the negative charge of the iron oxide powder at alkaline pH range.

Magnetization curves obtained for Mt, Mt1, and Mt2 samples at 300 K are presented in Figure 7. The curves indicate a superparamagnetic behavior, for all these samples, as evidenced by zero coercivity and remanence on the magnetization loop. The saturation magnetization (M_S) was obtained from moment versus magnetic field (B) curves. For the Mt sample, the saturation magnetization value is 70.7 emu g^{-1} , being higher than values reported in the literature (46.3 emu g^{-1}) for samples prepared by the

TABLE 1: The ΔT_{max} values of the magnetite samples dispersed in water and hydrogel under 220 Oe AC magnetic field.

Sample	ΔT_{max}	
	Water	Hydrogel
Mt	23	12
Mt1	11	6
Mt2	19	8

same method [43], whereas for peptized samples Mt1 and Mt2 with TMAOH the corresponding values are 62.8 and 63.2 emu g^{-1} . The magnetic saturation values of magnetite nanoparticles are experimentally determined to be in the range of $30\text{--}50 \text{ emu g}^{-1}$, which is lower than the bulk value, 90 emu g^{-1} [44]. Similar values have been obtained for Mt sample. It was expected that the saturation magnetization was higher for samples Mt1 and Mt2, as they have a higher degree of crystallinity and, in the case of Mt2, a larger particle size. The differences between the saturation magnetization between the samples with and without TMAOH can be ascribed to the previous presumption that magnetite and maghemite are both present in these peptized powders with TMAOH.

The magneto caloric behavior, influencing the heating ability of magnetite samples Mt, Mt-1, and Mt-2, is shown in Figure 8. For each experiment, the temperature rising was measured for every 1 min up to an accumulated time of 20 min and then every 5 min up to 1 h. Superparamagnetic particles generate heat by conversion of magnetic energy into thermal energy caused by the delay in magnetic relaxation. According to the Néel model, the magnetic moment originally locked along the crystal easy axis rotates away from that axis, tending to align with the external field. The Néel mechanism is analogous to the hysteresis loss in multidomain magnetic particles whereby there is an internal friction due to the movement of the magnetic moment in an external field that results in heat generation. In the Brownian mode, the whole particle rotates in the direction of the field with the moment locked along the crystal axis. The heat generated through Néel or Brownian relaxation in an applied AC magnetic field depends on the size of the nanoparticles. Smaller nanoparticles generate heat preferentially by the Néel model.

The amount of heat generated by pure water and hydrogel in 220 Oe AC magnetic fields was measured to obtain any contribution of water and hydrogel in the increase of temperature by the dispersed nanoparticles. The whole contribution of both pure water and gel was discounted from the final temperature value for each ferrofluid.

The results of heat dissipation experiments of the samples Mt, Mt1, and Mt2 dispersed in water and hydrogel are shown in Figure 8. The ΔT_{max} values for magnetite nanoparticles dispersed in water and hydrogel were determined from the gradients of temperature-time curves obtained by exposing the samples to an AC magnetic field strength of 220 Oe at frequency of 198 kHz. Results are summarized in Table 1.

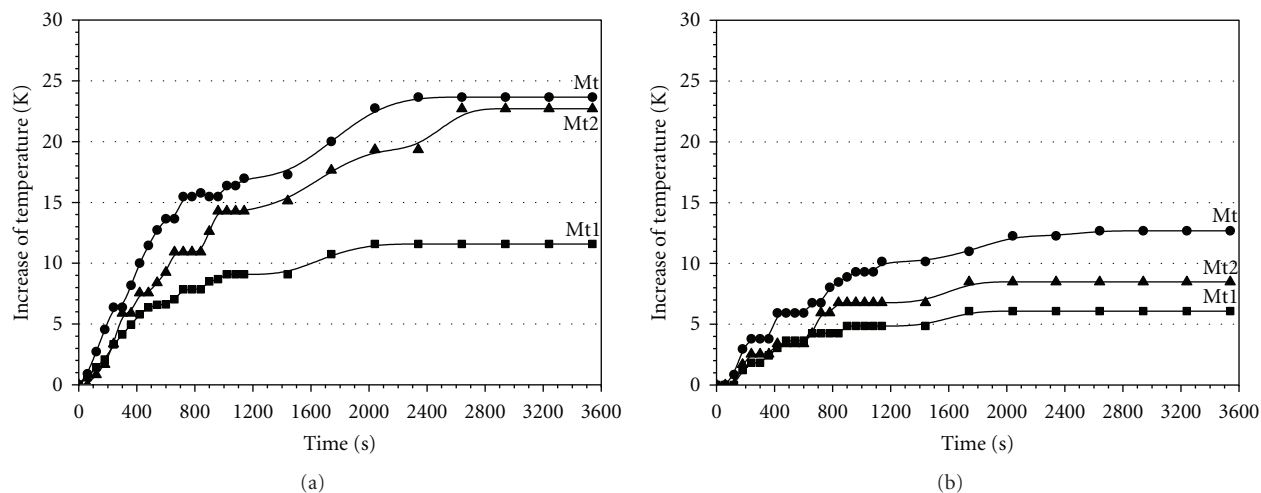


FIGURE 8: Temperature-time curves of the samples Mt, Mt1, and Mt2 dispersed in (a) water and (b) PVA hydrogel.

The ΔT_{\max} values for dispersed samples Mt, Mt1, and Mt2 in hydrogel were roughly 52, 54, and 42% less than that of the sole sample dispersed in water. The reduction in heat dissipation was attributed to the inhibition of particle rotation. In other words, particles should have an average Brownian magnetic relaxation time (TB) less than room temperature (RT) and narrow particle size distribution. This suggested that the fraction of the particles that generated heat through Brownian rotation was comparatively large. The sample with an average diameter below 13 nm had large fraction of particles dissipating heat through Néel relaxation losses. On the other hand, the sample with average diameter larger than 13 nm had large fraction of particles dissipating heat through Brownian relaxation [14]. Furthermore, these results suggested that it is important to analyze the relative contributions of Néel and Brownian relaxations losses to formulate the appropriate strategy for effective *in vivo* treatments. And also, it could be concluded that the samples with blocking temperature below RT are more suitable for a reliable *in vivo* MFH treatment. Thus, to derive at the appropriate sample for *in vivo* experiments, similar study on size-classified particles with TB less than RT and narrow size distribution should be pursued.

Hyperthermia is a cancer therapy that consists in heating selectively tumour in focusing organ zones. Those zones have fewer blood vessels and are less oxygenated than health ones. Consequently, they are more sensible and can die if the local temperature increases above 43°C. Thus, a temperature variation of $\Delta T_{\max} = 11^\circ\text{C}$ would be sufficient to produce therapeutical effects.

4. Conclusions

Tetramethylammonium hydroxide (TMAOH) was revealed to be an effective peptizing agent for magnetite nanoparticles in ferrofluid systems based on. The $[(\text{CH}_3)_4\text{N}]^+$ cations specifically adsorbed onto the surface of the synthesized iron oxide species give rise to repulsive stabilization forces that enable the particle growing species to be added to the

surface in a more organized manner. Accordingly, when TMAOH is added during precipitation as in the case of Mt2 samples it promotes the formation of larger particles having a higher degree of crystallinity, including magnetite and maghemite. The addition of TMAOH after the magnetite has been synthesized promotes the colloidal stability of the nanoparticles and enhances the transformation of the amorphous material into more ordered crystalline phases.

Acknowledgments

This work was supported by CNPq (Brazil including Grants nos. 202212/2007-6 and 302479/2010-4), FAPEMIG (including Grant no. PPM 00419-10 and no. APQ-00651-11) (Brazil) and by CICECO, (University of Aveiro, Portugal). CAPES (Brazil) grants the Visiting Professor PVNS fellowship to JDF at UFVJM.

References

- [1] S. Sun, C. B. Murray, D. Weller, L. Folks, and A. Moser, "Monodisperse FePt nanoparticles and ferromagnetic FePt nanocrystal superlattices," *Science*, vol. 287, no. 5460, pp. 1989–1992, 2000.
- [2] V. Skumryev, S. Stoyanov, Y. Zhang, G. Hadjipanayis, D. Givord, and J. Nogués, "Beating the superparamagnetic limit with exchange bias," *Nature*, vol. 423, no. 6942, pp. 850–853, 2003.
- [3] M. Zhao, L. Josephson, Y. Tang, and R. Weissleder, "Magnetic sensors for protease assays," *Angewandte Chemie*, vol. 42, no. 12, pp. 1375–1378, 2003.
- [4] P. S. Doyle, J. Bibette, A. Bancaud, and J. L. Viovy, "Self-assembled magnetic matrices for DNA separation chips," *Science*, vol. 295, no. 5563, p. 2237, 2002.
- [5] R. E. Rosensweig, "Magnetic fluids," in *Ferrohydrodynamics*, Cambridge University Press, Cambridge, UK, 1985.
- [6] S. S. Papell, US Patent No: 3 215 572, 1965.
- [7] Q. Li, Y. Xuan, and J. Wang, "Experimental investigations on transport properties of magnetic fluids," *Experimental Thermal and Fluid Science*, vol. 30, no. 2, pp. 109–116, 2005.

- [8] A. Jordan, R. Scholz, P. Wust et al., "Endocytosis of dextran and silan-coated magnetite nanoparticles and the effect of intracellular hyperthermia on human mammary carcinoma cells *in vitro*," *Journal of Magnetism and Magnetic Materials*, vol. 194, no. 1, pp. 185–196, 1999.
- [9] D. C. F. Chan, D. B. Kirpotin, and J. P. A. Bunn, "Synthesis and evaluation of colloidal magnetic iron oxides for the site-specific radiofrequency-induced hyperthermia of cancer," *Journal of Magnetism and Magnetic Materials*, vol. 122, no. 1–3, pp. 374–378, 1993.
- [10] C. Grob, K. Buscher, E. Romanus, C. A. Helm, and W. Weitschies, "Characterization of a ferrofluid by atomic force microscopy and photon correlation spectroscopy after magnetic fractionation," *European Cells and Materials*, vol. 3, supplement 2, pp. 163–166, 2002.
- [11] L. M. Lacava, Z. G. M. Lacava, M. F. Da Silva et al., "Magnetic resonance of a dextran-coated magnetic fluid intravenously administered in mice," *Biophysical Journal*, vol. 80, no. 5, pp. 2483–2486, 2001.
- [12] Z. G. M. Lacava, R. B. Azevedo, L. M. Lacava et al., "Toxic effects of ionic magnetic fluids in mice," *Journal of Magnetism and Magnetic Materials*, vol. 194, no. 1, pp. 90–95, 1999.
- [13] M. Răcuciu, D. E. Creangă, V. Bădescu, and N. Sulitanu, "Microstructural investigation of some biocompatible ferrofluids," *Journal of Magnetism and Magnetic Materials*, vol. 316, no. 2, pp. e772–e775, 2007.
- [14] M. Suto, Y. Hirota, H. Mamiya et al., "Heat dissipation mechanism of magnetite nanoparticles in magnetic fluid hyperthermia," *Journal of Magnetism and Magnetic Materials*, vol. 321, no. 10, pp. 1493–1496, 2009.
- [15] P. Berger, N. B. Adelman, K. J. Beckman, D. J. Campbell, A. B. Ellis, and G. C. Lisensky, "Preparation and properties of an aqueous ferrofluid," *Journal of Chemical Education*, vol. 76, no. 7, pp. 943–948, 1999.
- [16] F. Y. Cheng, C. H. Su, Y. S. Yang et al., "Characterization of aqueous dispersions of Fe₃O₄ nanoparticles and their biomedical applications," *Biomaterials*, vol. 26, no. 7, pp. 729–738, 2005.
- [17] J. P. Jolivet, R. Massart, and J. M. Fruchart, "Synthesis and physicochemical study of non-surfactant magnetic colloids in an aqueous-medium," *Nouveau Journal De Chimie-New Journal of Chemistry*, vol. 7, no. 5, pp. 325–331, 1983.
- [18] J. Yang, S. Mei, and J. M. F. Ferreira, "Hydrothermal synthesis of nanosized titania powders: influence of peptization and peptizing agents on the crystalline phases and phase transitions," *Journal of the American Ceramic Society*, vol. 83, no. 6, pp. 1361–1368, 2000.
- [19] J. Yang, S. Mei, and J. M. F. Ferreira, "Hydrothermal synthesis of nanosized titania powders: influence of tetraalkyl ammonium hydroxides on particle characteristics," *Journal of the American Ceramic Society*, vol. 84, no. 8, pp. 1696–1702, 2001.
- [20] J. Yang, S. Mei, and J. M. F. Ferreira, "Hydrothermal synthesis of TiO₂ nanopowders from tetraalkylammonium hydroxide peptized sols," *Materials Science and Engineering C*, vol. 15, no. 1-2, pp. 183–185, 2001.
- [21] J. Yang, S. Mei, and J. M. F. Ferreira, "In situ preparation of weakly flocculated aqueous anatase suspensions by a hydrothermal technique," *Journal of Colloid and Interface Science*, vol. 260, no. 1, pp. 82–88, 2003.
- [22] J. Yang, S. Mei, and J. M. F. Ferreira, "Hydrothermal processing of nanocrystalline anatase films from tetraethylammonium hydroxide peptized titania sols," *Journal of the European Ceramic Society*, vol. 24, no. 2, pp. 335–339, 2004.
- [23] J. Yang, S. Mei, and J. M. F. Ferreira, "Hydrothermal synthesis of submicrometer α -alumina from seeded tetraethylammonium hydroxide-peptized aluminum hydroxide," *Journal of the American Ceramic Society*, vol. 86, no. 12, pp. 2055–2058, 2003.
- [24] Á. L. Andrade, D. M. Souza, M. C. Pereira, J. D. Fabris, and R. Z. Domingues, "pH effect on the synthesis of magnetite nanoparticles by the chemical reduction-precipitation method," *Quimica Nova*, vol. 33, no. 3, pp. 524–527, 2010.
- [25] S. H. Hyon, W. I. Cha, and Y. Ikada, "Preparation of transparent poly(vinyl alcohol) hydrogel," *Polymer Bulletin*, vol. 22, no. 2, pp. 119–122, 1989.
- [26] T. Hosono, H. Takahashi, A. Fujita, R. J. Joseyphus, K. Tohji, and B. Jeyadevan, "Synthesis of magnetite nanoparticles for AC magnetic heating," *Journal of Magnetism and Magnetic Materials*, vol. 321, no. 19, pp. 3019–3023, 2009.
- [27] J. C. Bacri, R. Perzynski, V. Cabuil, and R. Massart, "Phase diagram of an ionic magnetic colloid: experimental study of the effect of ionic strength," *Journal of Colloid And Interface Science*, vol. 132, no. 1, pp. 43–53, 1989.
- [28] E. Hasmonay, A. Bee, J. C. Bacri, and R. Perzynski, "pH effect on an ionic ferrofluid: evidence of a thixotropic magnetic phase," *Journal of Physical Chemistry B*, vol. 103, no. 31, pp. 6421–6428, 1999.
- [29] A. L. Patterson, "The scherrer formula for X-ray particle size determination," *Physical Review*, vol. 56, no. 10, pp. 978–982, 1939.
- [30] S. Laurent, S. Dutz, U. O. Häfeli, and M. Mahmoudi, "Magnetic fluid hyperthermia: focus on superparamagnetic iron oxide nanoparticles," *Advances in Colloid and Interface Science*, vol. 166, no. 1-2, pp. 8–23, 2011.
- [31] S. Laurent, D. Forge, M. Port et al., "Magnetic iron oxide nanoparticles: synthesis, stabilization, vectorization, physicochemical characterizations and biological applications," *Chemical Reviews*, vol. 108, no. 6, pp. 2064–2110, 2008.
- [32] R. E. Rosensweig, *Ferrohydrodynamics*, Cambridge University Press, New York, NY, USA, 1985.
- [33] A. Ouasri, A. Rhandour, M. C. Dhamelincourt, P. Dhamelincourt, and A. Mazzah, "Vibrational study of (CH₃)₄NsBCl₆ and [(CH₃)₄N]₂SiF₆," *Spectrochimica Acta*, vol. 58, no. 12, pp. 2779–2788, 2002.
- [34] E. Barrado, F. Prieto, J. Medina, and F. A. López, "Characterisation of solid residues obtained on removal of Cr from waste water," *Journal of Alloys and Compounds*, vol. 335, no. 1-2, pp. 203–209, 2002.
- [35] J. L. Martín De Vidales, A. López-Delgado, E. Vila, and F. A. López, "Effect of the starting solution on the physico-chemical properties of zinc ferrite synthesized at low temperature," *Journal of Alloys and Compounds*, vol. 287, no. 1-2, pp. 276–283, 1999.
- [36] M. Ma, Y. Zhang, W. Yu, H. Y. Shen, H. Q. Zhang, and N. Gu, "Preparation and characterization of magnetite nanoparticles coated by amino silane," *Colloids and Surfaces A*, vol. 212, no. 2-3, pp. 219–226, 2003.
- [37] S. N. Inamdar and S. K. Haram, "Synthesis and characterization of uncapped γ -Fe₂O₃ nanoparticles prepared by flame pyrolysis of ferrocene in ethanol," *Journal of Nanoscience and Nanotechnology*, vol. 6, no. 7, pp. 2155–2158, 2006.
- [38] M. P. Morales, S. Veintemillas-Verdaguer, M. I. Montero et al., "Surface and internal spin canting in γ -Fe₂O₃ nanoparticles," *Chemistry of Materials*, vol. 11, no. 11, pp. 3058–3064, 1999.
- [39] Z. Jing, "Preparation and magnetic properties of fibrous gamma iron oxide nanoparticles via a nonaqueous medium," *Materials Letters*, vol. 60, no. 17-18, pp. 2217–2221, 2006.

- [40] E. Baumgartner, M. A. Blesa, and A. J. G. Maroto, "Kinetics of the dissolution of magnetite in thioglycolic acid solutions," *Journal of the Chemical Society, Dalton Transactions*, no. 9, pp. 1649–1654, 1982.
- [41] S. C. Pang, S. F. Chin, and M. A. Anderson, "Redox equilibria of iron oxides in aqueous-based magnetite dispersions: effect of pH and redox potential," *Journal of Colloid and Interface Science*, vol. 311, no. 1, pp. 94–101, 2007.
- [42] M. P. Albano and L. B. Garrido, "Dispersion of concentrated aqueous Si_3N_4 - Y_2O_3 - Al_2O_3 slips with tetramethylammonium hydroxide," *Ceramics International*, vol. 25, no. 1, pp. 13–18, 1999.
- [43] T. Sato, T. Iijima, M. Seki, and N. Inagaki, "Magnetic properties of ultrafine ferrite particles," *Journal of Magnetism and Magnetic Materials*, vol. 65, no. 2-3, pp. 252–256, 1987.
- [44] A. H. Lu, E. L. Salabas, and F. Schüth, "Magnetic nanoparticles: synthesis, protection, functionalization, and application," *Angewandte Chemie*, vol. 46, no. 8, pp. 1222–1244, 2007.

Review Article

Spark Plasma Sintering of Metals and Metal Matrix Nanocomposites: A Review

Nouari Saheb,^{1,2} Zafar Iqbal,¹ Abdullah Khalil,¹ Abbas Saeed Hakeem,² Nasser Al Aqeeli,^{1,2} Tahar Laoui,^{1,2} Amro Al-Qutub,¹ and René Kirchner³

¹Department of Mechanical Engineering, King Fahd University of Petroleum & Minerals, Dhahran 31261, Saudi Arabia

²Center of Excellence in Nanotechnology, King Fahd University of Petroleum & Minerals, Dhahran 31261, Saudi Arabia

³FCT Systeme GmbH, 96528 Rauenstein, Germany

Correspondence should be addressed to Nouari Saheb, nouari@kfupm.edu.sa

Received 23 March 2012; Revised 4 June 2012; Accepted 4 June 2012

Academic Editor: Leonard Deepak Francis

Copyright © 2012 Nouari Saheb et al. This is an open access article distributed under the Creative Commons Attribution License, which permits unrestricted use, distribution, and reproduction in any medium, provided the original work is properly cited.

Metal matrix nanocomposites (MMNCs) are those metal matrix composites where the reinforcement is of nanometer dimensions, typically less than 100 nm in size. Also, it is possible to have both the matrix and reinforcement phases of nanometer dimensions. The improvement in mechanical properties of MMNCs is attributed to the size and strength of the reinforcement as well as to the fine grain size of the matrix. Spark plasma sintering has been used extensively over the past years to consolidate wide range of materials including nanocomposites and was shown to be effective noneconventional sintering method for obtaining fully dense materials with preserved nanostructure features. The objective of this work is to briefly present the spark plasma sintering process and review published work on spark-plasma-sintered metals and metal matrix nanocomposites.

1. Introduction

Metal matrix composites (MMCs) refer to materials in which rigid ceramic reinforcements are embedded in ductile metal or alloy matrix. MMCs combine metallic properties (ductility and toughness) with ceramic characteristics (high strength and modulus). Attractive physical and mechanical properties such as high specific modulus, strength-to-weight ratio, fatigue strength, temperature stability, and wear resistance can be obtained with MMCs [1, 2]. Metal matrix Nanocomposites (MMNCs) are those metal matrix composites where the reinforcement is of nanometer dimensions, typically less than 100 nm in size [3]. Also, it is possible to have both the matrix and reinforcement phases of nanometer dimensions. Recently, MMNCs received much attraction because of their better properties compared with MMCs. The improvement in mechanical properties is due to the size and strength of the nanosize reinforcement. Also, the fine grain size of the matrix contributes to the improvement of the properties. However, achieving a uniform distribution/dispersion of the nanosize reinforcement phase is not easy using liquid-processing methods because of the difference

in densities between the two components of the composite besides the nonwetting between the molten metal and the reinforcement which makes mixing very difficult leading to a heterogeneous structure that affects the properties of the composite. On the other hand, grain growth during sintering of powder metallurgy consolidated products remains a major problem to obtain MMNCs with desired properties [4]. The use of solid-state processing methods such as mechanical alloying [5–8] permitted the development of nanocomposite materials having large volume fraction of nanosize reinforcement phase homogeneously dispersed in a nanostructured matrix. However, the use of conventional sintering methods such as hot pressing, high-temperature extrusion, and hot isostatic pressing to consolidate these materials often results in grain growth which affects the properties of the end product. Preventing or at least minimizing grain growth to maintain the nanostructure features of the matrix is possible through careful control of consolidation parameters, particularly heating rate, sintering temperature, and time. In this regard, spark plasma sintering (SPS), also known as field assisted sintering (FAST), has been shown to be effective noneconventional sintering method for obtaining fully dense

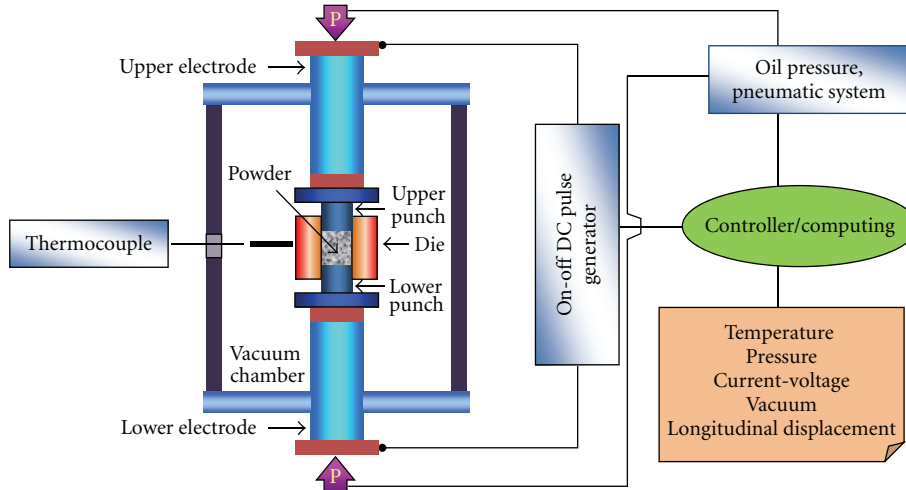


FIGURE 1: Schematic of SPS process.

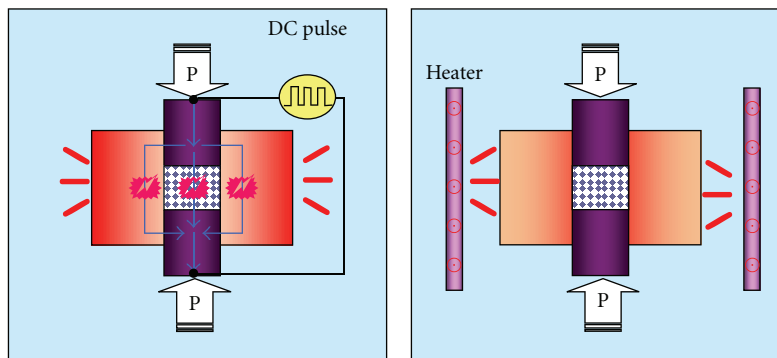


FIGURE 2: Comparison between SPS and conventional sintering.

materials [9, 10]. The objective of this work is to briefly present the spark plasma sintering process and review published data on spark-plasma-sintered metals and metal matrix nanocomposites.

2. The Spark Plasma Sintering Process

Figure 1 shows schematic of the SPS process. The sintering machine is assisted by a uniaxial press, punch electrodes, vacuum chamber, controlled atmosphere, DC pulse generator and position, temperature, and pressure measuring units [11].

Control of sintering temperature is possible through setting the holding time, ramp rate, pulse duration, and pulse current and voltage. The DC pulse discharge could generate spark plasma, spark impact pressure, Joule heating, and an electrical field diffusion effect. In SPS, sintering is assisted by the on-off DC pulse voltage compared to conventional hot pressing as shown in Figure 2. The application of pressure helps plastic flow of the material. Figure 3 illustrates the flow of DC pulse current through the particles.

Usually, SPS is carried out in four main stages as shown in Figure 4. The first stage is performed to remove gases and

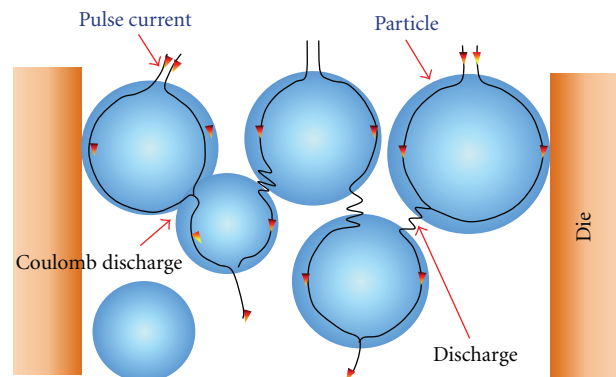


FIGURE 3: DC pulse current flow through the particles.

create vacuum. Then pressure is applied in the second stage followed by resistance heating in the third stage and finally cooling in the fourth stage. When a spark discharge appears in a gap or at the contact point between the particles of a material, a local high-temperature state of several to ten thousands of degrees centigrade is generated momentarily. This causes evaporation and melting on the surface of

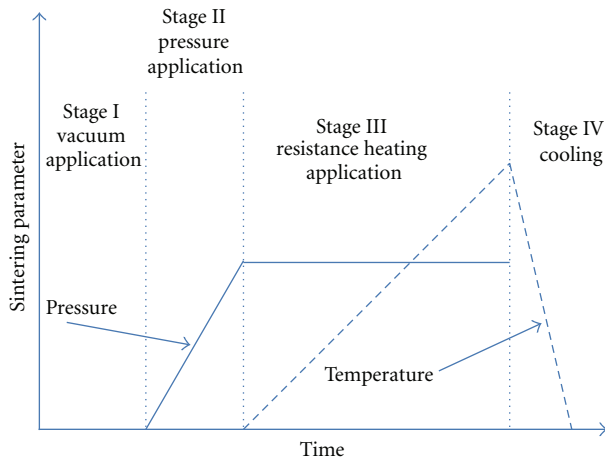


FIGURE 4: Spark plasma sintering stages.

powder particles in the SPS process, and necks are formed around the area of contact between particles. The application of pressure and current, in addition to the high-localized temperatures generated through resistance pulse heating, improves heating rates and reduces sintering time and temperature leading to the consolidation of nanopowders without excessive grain growth. On the other hand, the SPS is not only a binderless process, but also does not require a precompaction step. The powder is directly filled into a graphite die through which current is passed and pressure is applied leading to a fully dense material with superior mechanical properties.

Munir and coworkers [9] have critically examined the important features of SPS method and their individual roles in the observed enhancement of the consolidation process and the properties of the resulting materials. A comprehensive review on the electric current-activated/assisted sintering (ECAS) apparatuses and methods was performed by Grasso and coworkers [10], where the progress of ECAS technology was traced from 1906 to 2008 and 642 ECAS patents published over more than a century were surveyed. An updated and comprehensive description of the development of the electric current-activated/assisted sintering technique for the obtainment of dense materials including nanostructured ones was provided by Orrù et al. [12]. Recently, Hulbert and coworkers [13] opened a discussion on the presence of momentary plasma generated between particles in spark plasma sintering. Using a variety of powders and SPS conditions, they investigated the existence of plasma using *in situ* atomic emission spectroscopy, direct visual observations, and ultrafast *in situ* voltage measurements. The authors concluded that there was no plasma, sparking or arcing present during the SPS process, either during the initial or in the final stages of sintering. However, they emphasized the effectiveness of the SPS process to rapidly and efficiently consolidate a wide variety of materials with novel microstructures. More recently, Kieback [14] outlined the fundamentals of spark plasma sintering and critically reviewed past research on the topic. He questioned

the importance of alleged electrical effects such as sparks, plasma, heat diffusion, electromigration, or electron wind because of lack of experimental evidence of what really happens inside samples during SPS. He concluded that spark plasma sintering appears not to be fundamentally different from traditional hot pressing, except that the current leads to a much faster heating rate. However, he reiterated the advantages of the very high heating rates, short sintering cycles, and low sintering temperatures that are achieved by SPS. Very recently, some researchers [15] demonstrated that the so-called Brantly effect can occur in the early stages of the SPS treatment of preoxidized metallic material due to inductive effects generated by the applied pulsed current and leads to the formation of melting zones between contact areas of copper grains which can enhance material densification.

3. Spark-Plasma-Sintered Pure Metals

Diouf and Molinari [16] investigated densification mechanisms in spark plasma sintering using commercial copper powder with three particle size ranges (<25, 25–45, and 45–90 μm). They found that under low initial pressure, densification was due to particle rearrangement, localized deformation, bulk deformation, and neck growth. With the increase of pressure, sintering temperature did not significantly influence the sintered density but tensile ductility increased with pressure applied either during or after the bulk densification. In another study, Diouf and coworkers [17] investigated the effect of particle size on the densification mechanism in the temperature range 600–700°C and pressure range 20–30 MPa. They found that deformation and neck formation were enhanced by an increase in the particle size. Also, they reported that the extremely high and localized temperature on the contact points between particles leads to melting, giving rise to neck formation. Zhang and coworkers [18, 19] showed that high-quality bulk compact can be obtained through spark plasma sintering of fine copper powder in four stages: activation and refining of the powder, formation and growth of the sintering neck, rapid densification, and plastic deformation densification. In another investigation, Zhang and coworkers [20] reported that large-size ultrafine-grained copper with improved mechanical properties having average grain size less than 2.2 μm and a relative density greater than 96% could be prepared by SPS process with initial pressure of 1 MPa, holding pressure of 50 MPa, sintering temperature of 750°C, holding time of 6 min, and heating rate of 80°C/min. Srivatsan et al. [21] consolidated bulk fine-grained copper powder using plasma pressure compaction at two different temperatures under conditions of electrical pulse and noelectrical pulse. They found that pulsing of the powders prior to consolidation led to higher microhardness. They reported increased nanohardness and microhardness with the increase of the temperature of consolidation.

A nanosized copper powder with an average size of 50 nm was prepared by Zhang and coworkers [22] through a chemical reduction method and consolidated using SPS. In their investigation, they found that the sintering temperature has a significant effect on the relative density and the yield

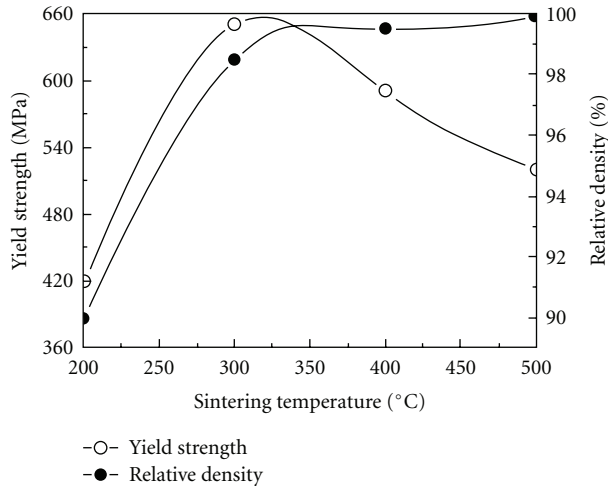
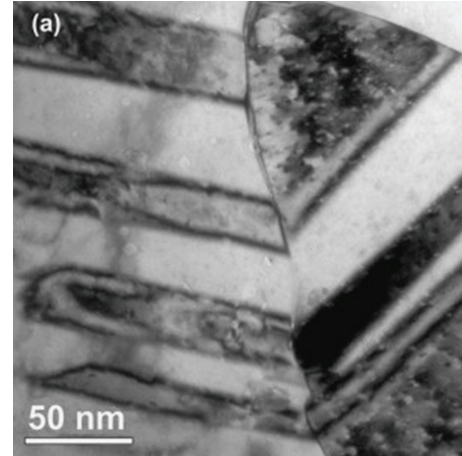


FIGURE 5: Curves of sintering temperature versus relative density and yield strength [22].

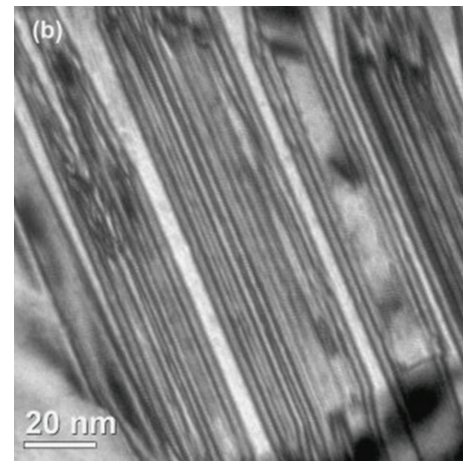
strength of the nanocrystalline (NC) bulk copper as it is shown in Figure 5 [22]. They reported that when the sintering temperature is less than 300°C, the relative density of the NC bulk copper is less than 98.5%. Thus, the relative density is the main factor to decide the yield strength, and the yield strength increases with raising the relative density. When the sintering temperature reaches 350°C, the relative density of the NC bulk copper exceeds 99%. Hence, the grain size becomes the main factor to decide the yield strength, and the yield strength decreases with increasing the grain size.

Figure 6 [22] shows a typical TEM micrograph of NC bulk copper sintered at a temperature of 300°C; both nanoscale twins with wide twins spacing of about 60 nm and narrow twins spacing of less than 2 nm were present. The authors concluded that NC bulk copper with average grain size of 120 nm, relative density greater than 99%, and yield strength of nearly 650 MPa could be fabricated by SPS with holding pressure of 600 MPa, sintering temperature of 350°C, holding time of 5 min, and heating rate of 100°C/min.

The deformation behavior of spark-plasma-sintered Ni powders with unimodal and bimodal grain size distributions was investigated by Holland et al. [23]. They showed that it is possible to densify nanometric grain size Ni using fast heating rates and somewhat high uniaxial sintering pressures at low homologous temperatures and retain the low starting grain sizes with little to no grain growth. In another investigation, Holland and coworkers [24] used scanning tunneling microscopy inside the TEM to apply an electric current directly to agglomerated nanometric nickel particles. Figure 7 [24] shows TEM micrographs with SAD patterns for the same agglomerate of four to six particles before and during the annealing experiment. The authors noticed a transformation from the initial soft agglomerate to a stage of early neck formation with relative particle rotation during the first sintering stage which implies mass transfer. Annealing for approximately 145 s at 10 V caused rapid consolidation of the particle agglomerate.



(a)



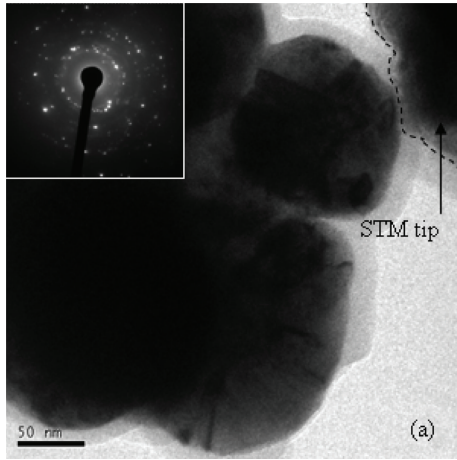
(b)

FIGURE 6: TEM micrographs of NC bulk copper (a) wide twins spacing and (b) narrow twins spacing [22].

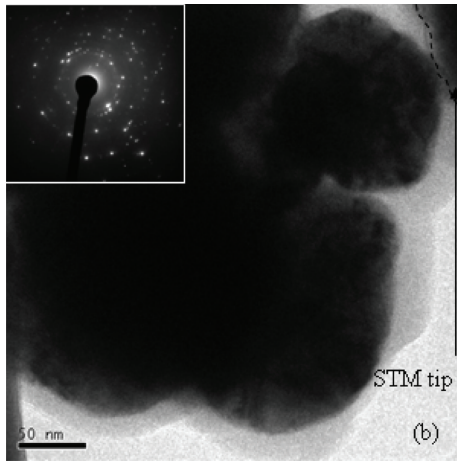
A high-angle annular dark field image of the resulting dense and oval-shaped agglomerate with dimensions ranging between 300 and 600 nm and some small pores retained in its interior is shown in Figure 8 [24]. Image analysis revealed polycrystallinity with grain boundaries and no apparent interconnected porosity. The authors concluded that consolidation occurs in the absence of an external heat source. Neck formation between adjacent particles and attendant increase in local Joule heating causes rapid densification.

Kodash and coworkers [25] investigated the influence of heating rate (90 to 1100°C/min) on densification and final grain structure of spark-plasma-sintered Ni nanopowders. They found that a moderate heating rate was beneficial for the densification, whereas a high heating rate was conducive to a lower final density. Very high heating rates resulted in nonuniform densification of the samples and formation of cracks during sintering.

The sintering and mechanical behavior of spark-plasma-sintered high purity nickel nanopowder was investigated by



(a)



(b)

FIGURE 7: Bright-field images and SAD patterns of Ni agglomerate before (a) and after annealing (b) for 1 min at -10 V [24].

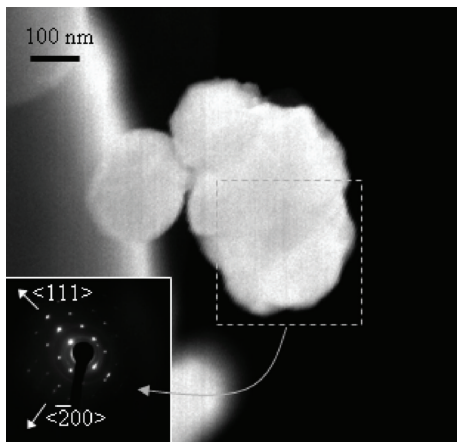


FIGURE 8: *Ex situ* high-angle annular dark-field image of the agglomerate after rapid consolidation [24].

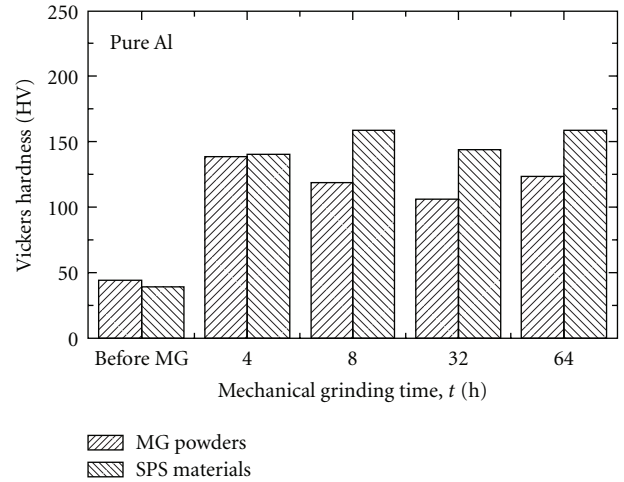


FIGURE 9: Comparison of hardness between various MG powders and SPS materials [28].

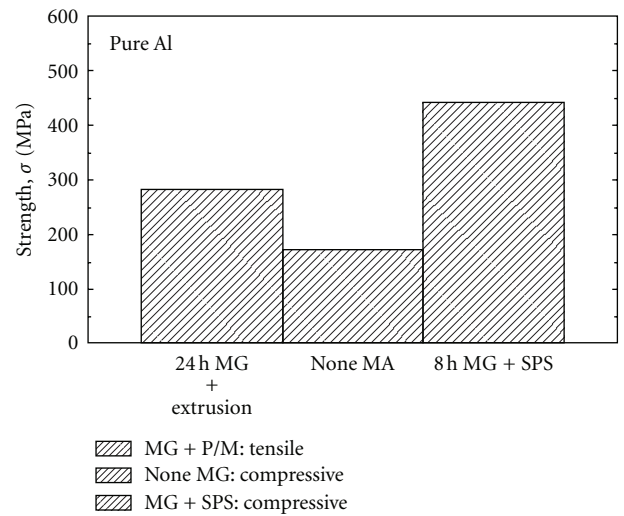


FIGURE 10: Compressive proof strength at room temperature of MG 0 h and MG 8 h SPS materials compared with tensile strength of as-extruded MG 24 h P/M [28].

Dirras et al. [26]. Wiedemann et al. [27] studied the effect of sintering parameters on SPS of molybdenum powders and found that specimen sintered at 1400°C and 67 MPa exhibited lower hardness as compared to the specimen sintered at same temperature but at 57 MPa. However, for much higher temperatures, opposite trend was observed.

Kubota [28] reported great improvement in the hardness and compressive proof stress of mechanically ground pure aluminum sintered by SPS as seen in Figures 9 and 10 [28], respectively. Hardness values of the SPS materials produced from 8, 32, and 64 h MG powders were higher than that of the MG powders. Also, compressive proof stress of the 8 h MG SPS material (440 MPa) was approximately 2.5 times higher than that of no-MG SPS material (173 MPa). Furthermore, the values were only 20% lower than that of conventional high-strength 7075-T6 alloy (505 MPa). Also,

it their characterisations of the solid-state reactions between the MG powder and process control agent (PCA) after heating at temperatures from 573 to 873 K for 24 h, the authors reported that no solid-state reaction was observed after heating up to 573 K for 24 h. Formation of γ -Al₂O₃ occurred in the 4 h MG powder after heating at 773 K for 24 h, whereas the mixture of γ -Al₂O₃ and Al₄C₃ was observed in the 8 h MG powder after heating at 773 K for 24 h. The full density of the SPS material was obtained with the condition of applied pressure at 49 MPa at 873 K for 1 h.

Spark plasma sintering behavior of pure coarse aluminium powder was reported by Zadra and coworkers [29]. They showed that the presence of the current flow and applying the sintering pressure with a certain delay in respect to the beginning of the cycle promoted better sintering and mechanical properties. With a heating rate of 100 K/min, a sintering temperature of 525°C, dwell time of 1 min, and pressure of 60 MPa, the mechanical properties and the fracture morphology were very similar to those of pure annealed wrought aluminium. Fully dense pure iron with high hardness was obtained through spark plasma sintering Fe nanopowder [30].

4. Spark Plasma Sintered Alloys

Skiba et al. [31] studied the effect of varying sintering temperatures and heating rate in spark plasma sintering FeAl intermetallics. They concluded that sintering temperature of 1100°C and heating rates up to 400°C/min were the best conditions. Matsugi and coworkers [32] investigated the microstructural properties of SPS titanium aluminide (Ti-53 mol%Al) at four temperatures that is 1573, 1623, 1648, and 1673 K after pulsed electrical discharge and found that the microstructure changed with sintering temperature and the grain growth was prevented. They reported that Vickers microhardness values for each phase in the sintered specimens were almost the same as those in specimens produced by other manufacturing methods. Feng and coworkers [33] investigated the effects of sintering temperature on densification of TiB/Ti-4.0Fe-7.3Mo composites synthesized through mechanical alloying of Ti, Fe65Mo and B powders, and SPS. They obtained a dense composite after sintering at 1000°C for 5 min. Specimens with good shape memory effect and density were prepared from Ti₅₀Ni₅₀ nanopowder through SPS at a temperature of 800°C [34]. Below this temperature, specimens had high porosity but with apparent shape memory effect, while specimens sintered at higher temperatures had bulk density and experienced extensive oxidation which led to the loss of the shape memory effect. A high Nb containing TiAl alloy from prealloyed powder of Ti-45Al-8.5Nb-0.2B-0.2W-0.1Y was processed by SPS [35]. The authors reported that specimens sintered at 1100°C were characterized by fine duplex microstructure which led to superior room temperature mechanical properties with a tensile strength of 1024 MPa and an elongation of 1.16%; specimens sintered at 1200°C had fully lamellar microstructure with a tensile strength of 964 MPa and an elongation of 0.88%. Couret et al. [36] used SPS technique to

densify prealloyed Ti₄₉Al₄₇Cr₂Nb₂ and Ti₅₁Al₄₄Cr₂Nb₂B₁ powders at temperatures ranging between 1100°C and 1250°C. They achieved full compaction in a short period of time which did not exceed 30 min and reported promising tensile properties at room temperature and a limited creep resistance at 700°C. A fine-grained Ti-47%Al alloy was prepared by double mechanical milling (DMM) and SPS [37]. The main phase TiAl and Ti₃Al and Ti₂Al phases were observed. Samples sintered at 1000°C had compressive strength of 2013 MPa, compression ratio of 4.6%, and bending strength of 896 MPa. Samples sintered at 1100°C, had compressive strength of 1990 MPa, compression ratio of 6.0%, and bending strength of 705 MPa. The microhardness of samples sintered at 1000°C was higher than that of the samples sintered at 1100°C.

Amorphous NiTi alloy obtained by mechanical alloying was sintered by SPS [38] and densified samples with Ni₃Ti, NiTi, and NiTi₂ phases were produced. Grain sizes were retained to within 500 nm and 1 μm for sintering temperatures of 900°C and 1100°C, respectively. Figure 11 [38] shows TEM images of two compacts [38]. The grains are equiaxed with a size range from 50 to 500 nm in the sample compacted at 900°C. From the SAD pattern, the authors found that the grains with stripe-like structure are of the Ni₃Ti phase, and the one devoid of any internal structure, with grain size around 200 nm is NiTi₂. The phase with grain size less than 100 nm is NiTi phase according to XRD analysis. For the sample sintered at 1100°C, areas with the stripe structure also correspond to Ni₃Ti phase, the phase with round structure which has been observed in SEM is NiTi₂ and the grain with dotted-spot is B2-NiTi phase.

Nb-Al, Nb-Al-W, Nb-Al-Mo, and Nb-Al-N powders prepared by mechanical alloying [39] were sintered by SPS. The authors obtained fully dense Nb-Al compacts at sintering temperature higher than 1773 K. However, the microstructure of Nb-Al-W and Nb-Al-Mo compacts was not homogeneous; this was attributed to probably insufficient sintering time. Murakami and coworkers [40] investigated the microstructure, mechanical properties, and oxidation behavior of SPS powder compacts in the Nb-Si-B system. They found that the oxidation resistance of Nb₅Si₃B₂ compacts was better than that of Nb₅Si₃ compacts, but extremely poorer than that of NbSi₂ compacts. Also, they reported that compacts with compositions around the line of Nb₅Si₃-Nb₅Si₃B₂-NbB₂ exhibited high hardness at room temperature and high compressive strength at high temperatures in comparison to those with compositions away from the line. The strength of compacts containing NbSi₂ was found to decrease with the increase of the volume fraction of NbSi₂ phase. Good quality amorphous alloy billets having very few micropores or crystalline phase particles were obtained through SPS of Cu-based bulk amorphous alloy at a sintering temperature of 480°C under a pressure of 80 MPa [41]. A compressive strength of 1.8 GPa was reported which was about 6% lower than that of the cast amorphous alloy. Shi et al. [42] studied the effect of varying SPS temperature on the properties of W-Cu alloy. They found that the specimen sintered at 1200°C displayed best mechanical properties.

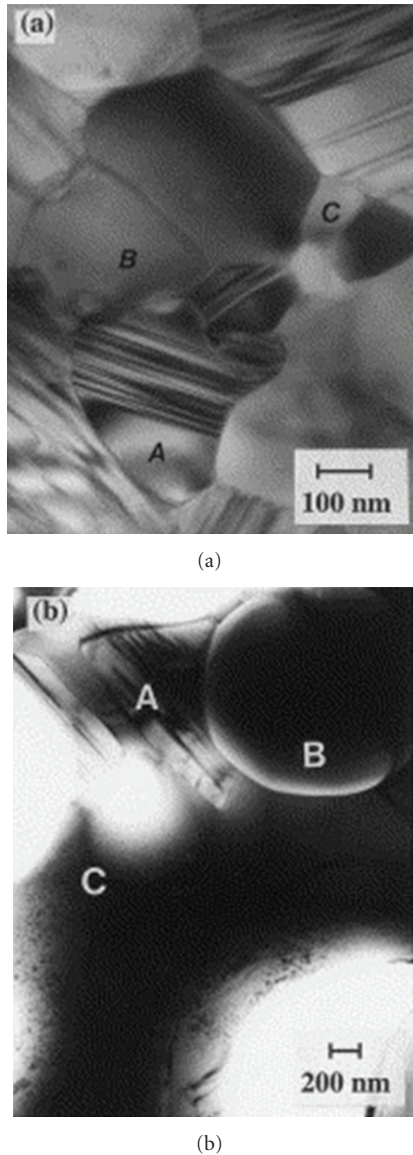


FIGURE 11: TEM micrographs of as-milled amorphous NiTi powders SPS at (a) 900°C/50 MPa/10 min and (b) 1100°C/50 MPa/10 min. (A) Ni₃Ti; (B) NiTi₂; (C) NiTi [38].

Researchers [43] who investigated Al-Mn-Ce system showed that high density, high hardness, and high wear resistance can be achieved in samples processed through SPS. The effect on compressive behavior of spark-plasma-sintered Al-5 at.% Fe alloy has also been studied [44] where substantial increase in compressive strength was reported. Improvement in mechanical properties as a consequence of SPS was also reported by Sasaki and coworkers [45] in Al-Fe alloy. Bin and coworkers [46] observed the precipitation of two types of MgZn₂ particles in spark-plasma-sintered Al-Zn-Mg-Cu alloy. Improvement in mechanical characteristics after spark plasma sintering and after heat treatments was reported in Al-Mg-Si alloy powders [47].

Fully dense Al6061 and Al2124 alloys were obtained through spark plasma sintering [48]. The optimization of

process parameters in spark-plasma-sintered Al6061 and Al2124 alloys [49] showed that 450°C is the optimum sintering temperature for achieving full densification and highest hardness. Further increase in temperature had no significant advantage in terms of densification and hardness improvement. Pressure was found to have a negligible effect on the sinterability of specimens. The lowest pressure of 35 MPa at a temperature of 450°C produced fully dense and hard specimens. The increase in pressure beyond 35 MPa resulted in grain growth which decreased the hardness.

Akinrinlola and coworkers [50] produced dense bimodal-grained aluminum magnesium alloys by spark plasma sintering of cryomilled powders. They found that the use of a two-stage sintering cycle did not induce grain growth or influence the hardness and flexural strength, but doubled the fracture strength distribution statistic (Weibull modulus) from 13 to 25. The increased duration of the second hold (from 5 to 20 min) marginally increased the Weibull Modulus, from 23 to 25. Cryomilled nanostructured Al 5083 alloy powder was consolidated by SPS [51]. The authors observed both bimodal microstructure and banded structure and attributed them to the starting powder and the process conditions, which are associated with the thermal, electrical, and pressure fields present during SPS. Also, they used a finite element method to investigate distributions in temperature, current, and stress between metallic powder particles.

5. Spark-Plasma-Sintered Metal Matrix Nanocomposites

5.1. Al Nanocomposites. Nanocrystalline Al-alloy/SiC nanocomposite powders were synthesized using high-energy ball milling and spark plasma sintering at a temperature of 500°C with a heating rate of 300°C/min and a total sintering cycle of 8 min. [52]. A substantial increase of mechanical properties was reported as a result of sintering through SPS. Al-20 wt.% TiB₂ nanocomposite was prepared by mechanical alloying of elemental Ti, B, and Al powder mixture [53–55] and consolidated using spark plasma sintering followed by hot extrusion. The authors used a double-step process to prevent the formation of undesirable phases like Al₃Ti intermetallic compound. The prepared nanocomposite had good thermal stability against grain growth and particle coarsening. Extruded samples showed a hardness value of 180 VHN and yield and tensile strength of 480 and 540 MPa, respectively [54]. A typical stress–strain curve obtained from the extruded sample is shown in Figure 12 [54]. The Al-TiB₂ nanocomposite showed a brittle behavior in tensile testing with a total elongation of 1.4%.

Bulk Al5356-B₄C nanocomposites with large microhardness and flexural strengths of 244 HV and 707 MPa, respectively, were fabricated through cryomilling and spark plasma sintering [56]. Srinivasarao and coworkers [57] developed Al-Zr nanocomposite using mechanical alloying and spark plasma sintering. The milled powder was found to consist of either a solid solution of Zr in Al or a mixture of Al-solid solution and Al₃Zr phases. The nanocomposite

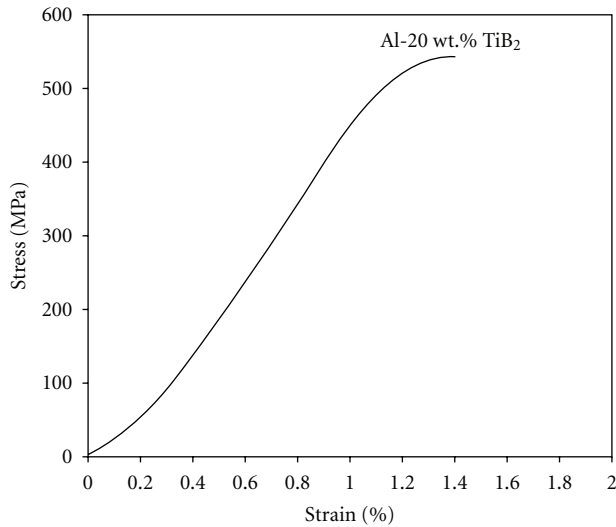


FIGURE 12: A typical stress-strain curve obtained from the extruded Al-20 wt% TiB₂ composite [54].

alloys exhibited a high compressive strength of 1 GPa with 10% plasticity. The authors attributed the high strength to the retention of nanometer-sized grains and also the fine dispersion of the Al₃Zr phase. The plasticity was explained to be due to excellent bonding between the powder particles and the presence of coarse Al grains in the matrix. Highly densified carbon nanotube-reinforced aluminum nanocomposites were consolidated through spark plasma sintering and subsequent hot extrusion [58]. The composites had tensile strength three folds higher than pure aluminum. Bhatt and coworkers [59] used high-energy ball milling and spark plasma sintering to produce Al-Mg (0.5, 1, 2.5, and 5 by wt.%) reinforced with 5 wt.% SiO₂ nanocomposites. The authors found that as a result of milling the Mg was completely dissolved into the Al matrix, the crystallite size was decreased, and the lattice strain was increased. However, they reported the formation of MgAl₂O₄ spinel structure along with Al₂O₃ in spark-plasma-sintered samples. The nanocomposites had Vickers hardness twice as high as that of the microcomposites.

Saheb and coworkers [62] successfully produced carbon nanotube-reinforced Al6061 and Al2124 nanocomposites using ball milling and spark plasma sintering. They reported that CNTs were better dispersed, less agglomerated, and had good adhesion to the matrix in composites containing 1 wt.% CNTs. The increase of CNT content to 2 wt.% led to the formation of CNT clusters which resulted in less uniform and homogenous composite powders. Almost full densification of Al6061 reinforced with CNTs was achieved at 500°C. Also, CNTs reinforced Al2124 nanocomposites reached very high densities at 500°C. Composites reinforced with 1 wt.% CNTs displayed better densification compared to composites containing 2 wt.% CNTs. The increase of CNTs content from 0.5 to 1 wt.% increased the hardness of the Al6061 and Al2124 alloys to maximum values. Further increase of CNTs content to 2 wt.% decreased the hardness

to values lower than that of the monolithic alloys. In another investigation, Al-Qutub and coworkers [63] investigated the friction and wear behavior of Al6061 monolithic alloy and 1 wt.% CNTs reinforced Al6061 nanocomposite prepared through ball milling and spark plasma sintering. They found that, under mild wear conditions, the composite displayed lower wear rate and friction coefficient compared to the monolithic alloy. However, for severe wear conditions, the composite displayed higher wear rate and friction coefficient compared to the monolithic alloy. Also, they clarified that the friction and wear behavior of Al-CNT composites is largely influenced by the applied load and there exists a critical load beyond which CNTs could have a negative impact on the wear resistance of aluminum alloy.

5.2. Cu Nanocomposites. Dash and coworkers [60] reinforced copper matrix with 5, 10, and 15 vol.% alumina particles (average size 5.71 μm) to prepare microcomposites and conventionally sintered them under N₂, H₂, and Ar atmospheres. Also, they reinforced the same matrix with 1, 5, 7 vol.% alumina (average size < 50 nm) to prepare nanocomposites and consolidated them through spark plasma sintering. The authors reported maximum Vickers hardness of 60, 75, and 80 for Cu-15 vol.% Al₂O₃ conventionally sintered in N₂, Ar, and H₂ atmosphere, respectively, and maximum hardness value of 125 for the Cu-5 vol.% Al₂O₃ nanocomposite prepared by spark plasma sintering. Also, they observed that Cu-Al₂O₃ composite showed poor mechanical properties when it was conventionally sintered in N₂ or Ar atmosphere compared to H₂ atmosphere. Hardness for Cu-Al₂O₃ microcomposites and nanocomposites fabricated using conventional and spark plasma sintering is shown in Figures 13(a) and 13(b), respectively [60]. Microcomposites sintered in hydrogen showed higher hardness than those sintered in nitrogen. The latter had hardness close to that of microcomposites sintered in argon. The hardness of the nanocomposites showed an increase up to 5 vol.% alumina and then a decrease of the hardness for 7 vol.% alumina. The authors believed that 7 vol.% alumina may facilitate higher degree of agglomeration of alumina nanoparticles but till 5 vol.% alumina the agglomeration seems to be insignificant. Also, 5 vol.% of alumina may resulted in effective dispersion strengthening associated with small-scale pinning in the nanocomposite, which prevents grain growth leading to higher hardness.

Copper and nanodiamond with 20 at.% C powders were mechanically alloyed and consolidated via hot extrusion or spark plasma sintering to produce Cu-diamond nanocomposites [64]. A novel fabrication technique consisting of molecular level mixing and controlled oxidation process was proposed by Lim et al. [65] for the production of CNT/Cu nanocomposite powders. The fabricated CNT/Cu₂O nanocomposites were reduced to CNT/Cu nanocomposite powders with H₂ gas and then consolidated through SPS. The authors reported that hot compression enhanced the ductility, strength, and electrical conductivity of the CNT/Cu nanocomposites. *In situ* synthesis of TiB₂-Cu composites [66] starting from powder mixtures

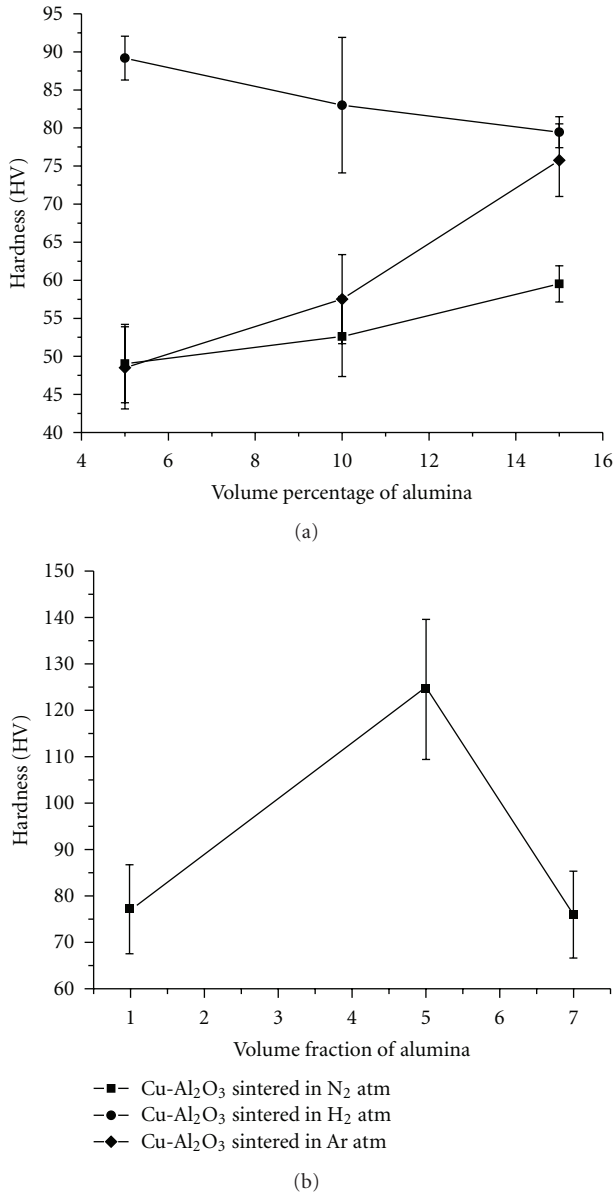


FIGURE 13: Comparison of hardness for Cu-Al₂O₃ microcomposites (a) and Cu-Al₂O₃ nanocomposites (b) fabricated using conventional and spark plasma sintering, respectively [60].

with full conversion into TiB₂ phase was reported. The authors used SPS to obtain a highly conductive 4.5 vol.% TiB₂-Cu nanocomposite with 82–87% IACS (International Annealed Copper Standard) conductivity. Synthesis of TiB₂-Cu nanocomposites was reported in other studies [67–70]. Authors reported that the increase of TiB₂ content from 2.5 up to 7.5 wt.% resulted in a 1.5-fold increase in yield strength, tensile strength, and hardness and 5-fold increase in wear resistance with only 10% decrease in conductivity [67]. Also, SPS at 650°C for 30 min under 50 MPa was reported to decrease the electrical conductivity from 75 to 54% IACS with increasing TiB₂ content from 2.5 to 10 wt.%. Hardness increased from 56 to 97 H_RB and tensile strength increased

with increasing TiB₂ content [68]. Hanada and coworkers synthesized homogeneous Cu nanocomposites containing 0–30 at % diamond nanoparticles through mechanical milling and spark plasma sintering followed by hot extrusion [71]. Kim et al. [72] prepared Cu matrix nanocomposites by spark plasma sintering, high-energy ball-milled nanosized Cu powders, and MWCNTs followed by cold rolling. The CNT/Cu nanocomposites showed a tensile strength of 281 MPa, which is approximately 1.6 times higher than that of monolithic Cu. In another study [73], carbon-nanotube-(CNT-) reinforced Cu matrix (CNT/Cu) nanocomposites were fabricated by a novel fabrication process, named as molecular level process, which involves suspending CNTs in solvent by surface functionalization, mixing Cu ions with CNT suspension, drying, calcination, and reduction. The nanocomposites were consolidated by SPS. The authors reported the enhancement of hardness and sliding wear resistance by two and three times, respectively, of the SPS consolidated nanocomposite compared to those of Cu matrix.

5.3. Fe Nanocomposites. Fe-Al₂O₃ nanocomposite was synthesized by reactive milling of Fe-Al₂O₃-Al-Fe powder mixture in toluene medium and consolidated by SPS. The nanocomposite showed heterogeneous grain structure of Fe consisting of nano-, submicron-, and micron-size grains together with nanometer Fe-Al₂O₃ particles. The nanocomposites consolidated at 800°C had a hardness of 795 MPa [74]. Fe/Cr-Al₂O₃ nanocomposite powders were prepared by H₂ selective reduction of oxide solid solutions and consolidated by SPS [75]. The composites showed a lower microhardness and higher fracture strength than unreinforced alumina. The friction coefficient against an alumina ball was lower, because of the presence of the intergranular metal particles; however, FeAl₂O₄ grains formed during SPS were beneficial for higher cycle numbers. Li and coworkers [76] synthesized nanocomposite Nd₂Fe₁₄B/α-Fe magnets using Fe nanoparticles prepared by sonochemical treatment of carbonyl iron which were applied to coat micrometer-sized Nd₂Fe₁₄B permanent magnetic powder. The bulk nanocomposite was consolidated using SPS. The authors obtained magnets with B_r of 0.86 T, H_{ci} of 683.8 kA/m and $(BH)_{max}$ of 95.92 kJ/m³. They also reported that a high ball-milling pretreatment was helpful for obtaining magnets with fine grains and even microstructure with an increase of the B_r and $(BH)_{max}$ to 0.94 T and 113.6 kJ/m³, respectively.

Libardi and coworkers [61] produced iron-based nanocomposite reinforced with nanometric silica and used thermal analysis to calculate the activation energy of the grain growth process and extrapolate the temperature at which the powder could be consolidated by SPS without losing nanostructure. They found that without the addition of SiO₂, the hardness was constant up to 400°C, whereas the dispersion of SiO₂ kept a constant hardness value up to 600°C. Also, the powders lost the nanostructure after annealing at 600°C for the material without SiO₂ and above 750°C with SiO₂ addition. Microhardness results as a function of annealing temperature are presented in Figure 14

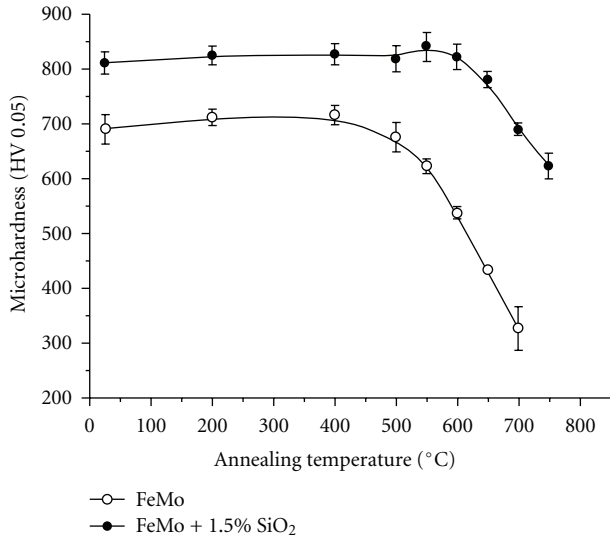


FIGURE 14: Microhardness as a function of annealing temperature [61].

[61]. The “FeMo + SiO₂ 20 h” nanocomposite had a thermal stability remarkably higher than the “FeMo 20 h” nanocomposite. Without addition of silica, the powder kept constant the initial hardness up to 400°C, but above 500°C it softened. With the addition of silica nanoparticles, the material was not affected by thermal treatments up to 600°C and softened only above 650°C, and even after annealing at 750°C for 1 h, it remained considerably hard.

Highly dense iron-based amorphous alloy and its tungsten particulate-reinforced composites were consolidated by SPS [77]. The authors reported the partial devitrification of amorphous matrix into nanocrystalline Fe₂₃(C, B)₆ during sintering which led to the formation of *in situ* amorphous matrix composites. Also, they successfully fabricated *ex situ* amorphous matrix composites reinforced with micron-size tungsten particles.

5.4. Other Nanocomposites. Udhayabanu and coworkers [78] developed Ni-30 vol.% Al₂O₃ *in situ* nanocomposite through reaction milling of NiO-Al-Ni powder mixture followed by SPS. The nanocomposite had hardness and yield strength approximately two times higher than that of pure Ni of similar grain size. A nickel-matrix composite with MWNT [79] was prepared by slurry mixing process using ethanol as a solvent. The SPS-sintered relative densities of the composites containing up to 5 vol% of MWNT were above 99%. The thermal conductivity was found to increase by 10% for the composition with 3 vol% MWNT. Al₂O₃/Ni nanocomposite was also prepared through pulse electric current sintering [80]. Umeda and coworkers [81] prepared magnesium reinforced with CNTs and Mg₂Si/MgO compounds. They used amorphous and porous silica particles originated from rice husks, which were coated with CNTs and contained nanotubes in the pores. The *in situ* synthesis of Mg₂Si and MgO via deoxidization and oxidation reaction occurred from the elemental mixture of pure magnesium and CNT-SiO₂

composite particles through SPS. They reported a low and stable friction coefficient and a decreased wear rate with increased CNTs and Mg₂Si content.

6. Conclusion

In this work, the spark plasma sintering process was presented and recently published work on spark-plasma-sintered metals and metal matrix nanocomposites was reviewed. The spark plasma sintering process has been shown to be an effective technique for consolidating metallic materials including nanocomposites. The advantages of spark plasma sintering such as high heating rates, short sintering cycles, and low sintering temperatures that allow sintering nanostructured materials were emphasized by all researchers. However, more experimental work is needed to better understand the SPS process and prove the existence or absence of some phenomenon such as plasma, sparks, electromigration, and Brany effect.

Acknowledgment

The authors would like to acknowledge the financial support from King Abdul Aziz City for Science and Technology (KACST) through Project no. ARP-28-122.

References

- [1] L. Ceschini, G. Minak, and A. Morri, “Tensile and fatigue properties of the AA6061/20 vol% Al₂O_{3p} and AA7005/10 vol% Al₂O_{3p} composites,” *Composites Science and Technology*, vol. 66, no. 2, pp. 333–342, 2006.
- [2] I. J. Shon and H. S. Kang, “Properties and fast low-temperature consolidation of nanocrystalline Ni–ZrO₂ composites by high-frequency induction heated sintering,” *Journal of Alloys and Compounds*, vol. 509, pp. 2964–2969, 2011.
- [3] C. Suryanarayana, “Synthesis of nanocomposites by mechanical alloying,” *Journal of Alloys and Compounds*, vol. 509, supplement 1, pp. S229–S234, 2011.
- [4] V. Viswanathan, T. Laha, K. Balani, A. Agarwal, and S. Seal, “Challenges and advances in nanocomposite processing techniques,” *Materials Science and Engineering R*, vol. 54, no. 5-6, pp. 121–285, 2006.
- [5] C. Suryanarayana, “Mechanical alloying and milling,” *Progress in Materials Science*, vol. 46, no. 1-2, pp. 1–184, 2001.
- [6] S. Kamrani, R. Riedel, S. M. S. Reihani, and H. J. Kleebe, “Effect of reinforcement volume fraction on the mechanical properties of Al–SiC nanocomposites produced by mechanical alloying and consolidation,” *Journal of Composite Materials*, vol. 44, no. 3, pp. 313–326, 2010.
- [7] S. H. Hwang, D. S. Bang, K. H. Yoon, Y. B. Park, D. Y. Lee, and S. S. Jeong, “Fabrication and characterization of aluminum-carbon nanotube powder and polycarbonate/aluminum-carbon nanotube composites,” *Journal of Composite Materials*, vol. 44, no. 23, pp. 2711–2722, 2010.
- [8] M. K. Habibi, K. S. Tun, and M. Gupta, “An investigation into the effect of ball milling of reinforcement on the enhanced mechanical response of magnesium,” *Journal of Composite Materials*, vol. 45, no. 24, pp. 2483–2493, 2011.
- [9] Z. A. Munir, U. A. Tamburini, and M. Ohyanagi, “The effect of electric field and pressure on the synthesis and consolidation

- of materials: a review of the spark plasma sintering method," *Journal of Materials Science*, vol. 41, no. 3, pp. 763–777, 2006.
- [10] S. Grasso, Y. Sakka, and G. Maizza, "Electric current activated/assisted sintering (ECAS): a review of patents 1906–2008," *Science and Technology of Advanced Materials*, vol. 10, no. 5, Article ID 053001, 2009.
- [11] H. U. Kessel, J. Hennicke, R. Kirchner, and T. Kessel, "Rapid sintering of novel materials by FAST/SPS—further development to the point of an industrial production process with high cost efficiency," FCT Systeme GmbH, Rauenstein, Germany, 2010.
- [12] R. Orrù, R. Licheri, A. M. Locci, A. Cincotti, and G. Cao, "Consolidation/synthesis of materials by electric current activated/assisted sintering," *Materials Science and Engineering R*, vol. 63, no. 4–6, pp. 127–287, 2009.
- [13] D. M. Hulbert, A. Anders, J. Andersson, E. J. Lavernia, and A. K. Mukherjee, "A discussion on the absence of plasma in spark plasma sintering," *Scripta Materialia*, vol. 60, no. 10, pp. 835–838, 2009.
- [14] B. Kieback, "A review of spark plasma sintering," in *Proceedings of the Hagen Symposium*, Hagen, Germany, November 2011.
- [15] P. Guyot, V. Rat, J. F. Coudert, F. Jay, A. Maitre, and N. Pradeilles, "Does the Branly effect occur in spark plasma sintering?" *Journal of Physics D*, vol. 45, no. 9, Article ID 092001, 2012.
- [16] S. Diouf and A. Molinari, "Densification mechanisms in spark plasma sintering: effect of particle size and pressure," *Powder Technology*, vol. 221, pp. 220–227, 2012.
- [17] S. Diouf, C. Menapace, and A. Molinari, "Study of effect of particle size on densification of copper during spark plasma sintering," *Powder Metallurgy*. In press.
- [18] Z. Zhaohui, W. Fuchi, W. Lin, L. Shukui, and S. Osamu, "Sintering mechanism of large-scale ultrafine-grained copper prepared by SPS method," *Materials Letters*, vol. 62, no. 24, pp. 3987–3990, 2008.
- [19] Z. H. Zhang, F. C. Wang, L. Wang, S. K. Li, M. W. Shen, and S. Osamu, "Microstructural characteristics of large-scale ultrafine-grained copper," *Materials Characterization*, vol. 59, no. 3, pp. 329–333, 2008.
- [20] Z. H. Zhang, F. C. Wang, L. Wang, and S. K. Li, "Ultrafine-grained copper prepared by spark plasma sintering process," *Materials Science and Engineering A*, vol. 476, no. 1–2, pp. 201–205, 2008.
- [21] T. S. Srivatsan, B. G. Ravi, A. S. Naruka, L. Riestler, S. Yoo, and T. S. Sudarshan, "Microstructure and hardness of copper powders consolidated by plasma pressure compaction," *Journal of Materials Engineering and Performance*, vol. 10, no. 4, pp. 449–455, 2001.
- [22] Z. H. Zhang, F. C. Wang, S. K. Lee, Y. Liu, J. W. Cheng, and Y. Liang, "Microstructure characteristic, mechanical properties and sintering mechanism of nanocrystalline copper obtained by SPS process," *Materials Science and Engineering A*, vol. 523, no. 1–2, pp. 134–138, 2009.
- [23] T. B. Holland, I. A. Ovid'ko, H. Wang, and A. K. Mukherjee, "Elevated temperature deformation behavior of spark plasma sintered nanometric nickel with varied grain size distributions," *Materials Science and Engineering A*, vol. 528, no. 2, pp. 663–671, 2010.
- [24] T. B. Holland, A. M. Thron, C. S. Bonifacio, A. K. Mukherjee, and K. Van Benthem, "Field assisted sintering of nickel nanoparticles during in situ transmission electron microscopy," *Applied Physics Letters*, vol. 96, no. 24, Article ID 243106, 2010.
- [25] V. Y. Kodash, J. R. Groza, K. C. Cho, B. R. Klotz, and R. J. Dowding, "Field-assisted sintering of Ni nanopowders," *Materials Science and Engineering A*, vol. 385, no. 1–2, pp. 367–371, 2004.
- [26] G. Dirras, S. Bouvier, J. Gubicza, B. Hasni, and T. Szilágyi, "Mechanical characteristics under monotonic and cyclic simple shear of spark plasma sintered ultrafine-grained nickel," *Materials Science and Engineering A*, vol. 526, no. 1–2, pp. 201–210, 2009.
- [27] R. O. Wiedemann, U. Martin, H. J. Seifert, and A. Müller, "Densification behaviour of pure molybdenum powder by spark plasma sintering," *International Journal of Refractory Metals and Hard Materials*, vol. 28, no. 4, pp. 550–557, 2010.
- [28] M. Kubota, "Properties of nano-structured pure Al produced by mechanical grinding and spark plasma sintering," *Journal of Alloys and Compounds*, vol. 434–435, pp. 294–297, 2007.
- [29] M. Zadra, F. Casari, L. Girardini, and A. Molinari, "Spark plasma sintering of pure aluminium powder: mechanical properties and fracture analysis," *Powder Metallurgy*, vol. 50, no. 1, pp. 40–45, 2007.
- [30] D. Fabrègue, J. Piallat, E. Maire, Y. Jorand, V. M. Jourdan, and G. Bonnefont, "Spark plasma sintering of pure iron nanopowders by simple route," *Powder Metallurgy*, vol. 55, no. 1, pp. 76–79, 2012.
- [31] T. Skiba, P. Haušild, M. Karlík, K. Vanmeensel, and J. Vleugels, "Mechanical properties of spark plasma sintered FeAl intermetallics," *Intermetallics*, vol. 18, no. 7, pp. 1410–1414, 2010.
- [32] K. Matsugi, N. Ishibashi, T. Hatayama, and O. Yanagisawa, "Microstructure of spark sintered titanium-aluminide compacts," *Intermetallics*, vol. 4, no. 6, pp. 457–467, 1996.
- [33] H. Feng, Y. Zhou, D. Jia, and Q. Meng, "Rapid synthesis of Ti alloy with B addition by spark plasma sintering," *Materials Science and Engineering A*, vol. 390, no. 1–2, pp. 344–349, 2005.
- [34] C. Shearwood, Y. Q. Fu, L. Yu, and K. A. Khor, "Spark plasma sintering of TiNi nano-powder," *Scripta Materialia*, vol. 52, no. 6, pp. 455–460, 2005.
- [35] X. Lu, X. B. He, B. Zhang, L. Zhang, X. H. Qu, and Z. X. Guo, "Microstructure and mechanical properties of a spark plasma sintered Ti-45Al-8.5Nb-0.2W-0.2B-0.1Y alloy," *Intermetallics*, vol. 17, no. 10, pp. 840–846, 2009.
- [36] A. Couret, G. Molénat, J. Galy, and M. Thomas, "Microstructures and mechanical properties of TiAl alloys consolidated by spark plasma sintering," *Intermetallics*, vol. 16, no. 9, pp. 1134–1141, 2008.
- [37] X. S. Long, T. Jing, X. L. Juan, C. Y. Yong, Y. H. Bao, and H. J. Cai, "Microstructures and mechanical properties of TiAl alloy prepared by spark plasma sintering," *Transactions of Nonferrous Metals Society of China*, vol. 19, no. 6, pp. 1423–1427, 2009.
- [38] L. L. Ye, Z. G. Liu, K. Raviprasad, M. X. Quan, M. Umamoto, and Z. Q. Hu, "Consolidation of MA amorphous NiTi powders by spark plasma sintering," *Materials Science and Engineering A*, vol. 241, no. 1–2, pp. 290–293, 1998.
- [39] T. Murakami, A. Kitahara, Y. Koga, M. Kawahara, H. Inui, and M. Yamaguchi, "Microstructure of Nb-Al powders consolidated by spark plasma sintering process," *Materials Science and Engineering A*, vol. 239–240, no. 1–2, pp. 672–679, 1997.
- [40] T. Murakami, C. N. Xu, A. Kitahara et al., "Microstructure, mechanical properties and oxidation behavior of powder compacts of the Nb-Si-B system prepared by spark plasma sintering," *Intermetallics*, vol. 7, no. 9, pp. 1043–1048, 1999.
- [41] C. K. Kim, H. S. Lee, S. Y. Shin, J. C. Lee, D. H. Kim, and S. Lee, "Microstructure and mechanical properties of Cu-based bulk

- amorphous alloy billets fabricated by spark plasma sintering,” *Materials Science and Engineering A*, vol. 406, no. 1-2, pp. 293–299, 2005.
- [42] X. Shi, H. Yang, and S. Wang, “Spark plasma sintering of W-15Cu alloy from ultrafine composite powder prepared by spray drying and calcining-continuous reduction technology,” *Materials Characterization*, vol. 60, no. 2, pp. 133–137, 2009.
- [43] C. Y. Xü, S. S. Jia, and Z. Y. Cao, “Synthesis of Al-Mn-Ce alloy by the spark plasma sintering,” *Materials Characterization*, vol. 54, no. 4-5, pp. 394–398, 2005.
- [44] T. T. Sasaki, T. Mukai, and K. Hono, “A high-strength bulk nanocrystalline Al-Fe alloy processed by mechanical alloying and spark plasma sintering,” *Scripta Materialia*, vol. 57, no. 3, pp. 189–192, 2007.
- [45] T. T. Sasaki, T. Ohkubo, and K. Hono, “Microstructure and mechanical properties of bulk nanocrystalline Al-Fe alloy processed by mechanical alloying and spark plasma sintering,” *Acta Materialia*, vol. 57, no. 12, pp. 3529–3538, 2009.
- [46] C. H. Bin, T. Kai, Y. Bin, and Z. J. Shan, “Nanostructured Al-Zn-Mg-Cu alloy synthesized by cryomilling and spark plasma sintering,” *Transactions of Nonferrous Metals Society of China*, vol. 19, no. 5, pp. 1110–1115, 2009.
- [47] J. K. Rana, D. Sivaprahasam, K. S. Raju, and V. S. Sarma, “Microstructure and mechanical properties of nanocrystalline high strength Al-Mg-Si (AA6061) alloy by high energy ball milling and spark plasma sintering,” *Materials Science and Engineering A*, vol. 527, no. 1-2, pp. 292–296, 2009.
- [48] N. Saheb, “Spark plasma sintering of Al6061 and Al2124 alloys,” *Advanced Materials Research*, vol. 284–286, pp. 1656–1660, 2011.
- [49] A. Khalil, A. S. Hakeem, and N. Saheb, “Optimization of process parameters in spark plasma sintering Al6061 and Al2124 aluminum alloys,” *Advanced Materials Research*, vol. 328–330, pp. 1517–1522, 2011.
- [50] B. Akinrinlola, R. Gauvin, and M. Brochu, “Improving the mechanical reliability of cryomilled Al-Mg alloy using a two-stage spark plasma sintering cycle,” *Scripta Materialia*, vol. 66, no. 7, pp. 455–458, 2012.
- [51] Y. Xiong, D. Liu, Y. Li et al., “Spark plasma sintering of cryomilled nanocrystalline Al alloy—part I: microstructure evolution,” *Metallurgical and Materials Transactions A*, vol. 43, no. 1, pp. 327–339, 2012.
- [52] S. Bathula, R. C. Anandani, A. Dhar, and A. K. Srivastava, “Synthesis and characterization of Al-alloy/SiCp nanocomposites employing high energy ball milling and spark plasma sintering,” *Advanced Materials Research*, vol. 410, pp. 224–227, 2012.
- [53] Z. Sadeghian, M. H. Enayati, B. Lotfi, and P. Beiss, “Development of AL-TiB₂ nanocomposite,” in *Proceedings of the Annual Meeting and Exhibition (TMS '11)*, vol. 2, pp. 129–136, March 2011.
- [54] Z. Sadeghian, B. Lotfi, M. H. Enayati, and P. Beiss, “Microstructural and mechanical evaluation of Al-TiB₂ nanostructured composite fabricated by mechanical alloying,” *Journal of Alloys and Compounds*, vol. 509, no. 29, pp. 7758–7763, 2011.
- [55] Z. Sadeghian, B. Lotfi, M. H. Enayati, and P. Beiss, “Fabrication of bulk Al-TiB₂ nanocomposite by spark plasma sintering of mechanically alloyed powder,” in *Technical Proceedings of the NSTI Nanotechnology Conference and Expo, NSTI-Nanotech (Nanotech '10)*, pp. 107–110, June 2010.
- [56] R. Vintila, A. Charest, R. A. L. Drew, and M. Brochu, “Synthesis and consolidation via spark plasma sintering of nanostructured Al-5356/B₄C composite,” *Materials Science and Engineering A*, vol. 528, no. 13-14, pp. 4395–4407, 2011.
- [57] B. Srinivasarao, C. Suryanarayana, K. Oh-ishi, and K. Hono, “Microstructure and mechanical properties of Al-Zr nanocomposite materials,” *Materials Science and Engineering A*, vol. 518, no. 1-2, pp. 100–107, 2009.
- [58] H. Kwon, M. Estili, K. Takagi, T. Miyazaki, and A. Kawasaki, “Combination of hot extrusion and spark plasma sintering for producing carbon nanotube reinforced aluminum matrix composites,” *Carbon*, vol. 47, no. 3, pp. 570–577, 2009.
- [59] J. Bhatt, N. Balachander, S. Shekher, R. Karthikeyan, D. R. Peshwe, and B. S. Murty, “Synthesis of nanostructured Al-Mg-SiO₂ metal matrix composites using high-energy ball milling and spark plasma sintering,” *Journal of Alloys and Compounds*. In press.
- [60] K. Dash, B. C. Ray, and D. Chandra, “Synthesis and characterization of copper-alumina metal matrix composite by conventional and spark plasma sintering,” *Journal of Alloys and Compounds*, vol. 516, pp. 78–84, 2012.
- [61] S. Libardi, M. Leoni, L. Facchini, M. D’Incau, P. Scardi, and A. Molinari, “Effect of the dispersion of nanometric silica particles on the thermal stability of a nanostructured iron based powder,” *Materials Science and Engineering A*, vol. 445–446, pp. 244–250, 2007.
- [62] N. Saheb, A. Khalil, A. S. Hakeem, N. Al-Aqeeli, T. Laoui, and A. K. Qutub, “Spark plasma sintering of CNT reinforced Al6061 and Al2124 nanocomposites,” submitted to *Journal of Composite Materials*.
- [63] A. M. Al-Qutub, A. Khalil, N. Saheb, and A. S. Hakeem, “Wear and friction behavior of Al6061 alloy reinforced with carbonnanotubes,” submitted to *Wear*.
- [64] D. Nunes, V. Livramento, J. B. Correia et al., “Consolidation of Cu-nDiamond nanocomposites: hot extrusion vs spark plasma sintering,” *Materials Science Forum*, vol. 636–637, pp. 682–687, 2010.
- [65] B. K. Lim, C. B. Mo, D. H. Nam, and S. H. Hong, “Mechanical and electrical properties of carbon nanotube/Cu nanocomposites by molecular-level mixing and controlled oxidation process,” *Journal of Nanoscience and Nanotechnology*, vol. 10, no. 1, pp. 78–84, 2010.
- [66] J. S. Kim, D. V. Dudina, J. C. Kim, Y. S. Kwon, J. J. Park, and C. K. Rhee, “Properties of Cu-based nanocomposites produced by mechanically-activated self-propagating high-temperature synthesis and spark-plasma sintering,” *Journal of Nanoscience and Nanotechnology*, vol. 10, no. 1, pp. 252–257, 2010.
- [67] D. H. Kwon, T. D. Nguyen, D. Dudina, J. S. Kim, Y. J. Yum, and Y. S. Kwon, “Properties of dispersion strengthened Cu-TiB₂ nanocomposites prepared by spark plasma sintering,” *Diffusion and Defect Data B*, vol. 119, pp. 63–66, 2007.
- [68] D. H. Kwon, K. X. Huynh, T. D. Nguyen et al., “Mechanical behavior of TiB₂ nanoparticles reinforced Cu matrix composites synthesized by in-situ processing,” *Materials Science Forum*, vol. 510–511, pp. 346–349, 2006.
- [69] D. H. Kwon, T. D. Nguyen, D. Dudina et al., “Thermal stability and properties of Cu-TiB₂ nanocomposites prepared by combustion synthesis and spark-plasma sintering,” *Materials Science Forum*, vol. 534–536, no. 2, pp. 1517–1520, 2007.
- [70] D. H. Kwon, D. N. Thuy, X. H. Khoa et al., “Mechanical, electrical and wear properties of Cu-TiB₂ nanocomposites fabricated by MA-SHS and SPS,” *Journal of Ceramic Processing Research*, vol. 7, no. 3, pp. 275–279, 2006.
- [71] K. Hanada, K. Yamamoto, T. Taguchi et al., “Further studies on copper nanocomposite with dispersed single-digit-nanodiamond particles,” *Diamond and Related Materials*, vol. 16, no. 12, pp. 2054–2057, 2007.

- [72] K. T. Kim, S. I. Cha, and S. H. Hong, "Microstructures and tensile behavior of carbon nanotube reinforced Cu matrix nanocomposites," *Materials Science and Engineering A*, vol. 430, no. 1-2, pp. 27-33, 2006.
- [73] K. T. Kim, S. I. Cha, and S. H. Hong, "Hardness and wear resistance of carbon nanotube reinforced Cu matrix nanocomposites," *Materials Science and Engineering A*, vol. 448-451, pp. 46-50, 2007.
- [74] K. R. Ravi, A. Murugesan, V. Udhayabanu, R. Subramanian, and B. S. Murty, "Microstructure and mechanical property of Fe-Al₂O₃ nanocomposites synthesized by reactive milling followed by spark plasma sintering," *Materials Science Forum*, vol. 710, pp. 291-296, 2012.
- [75] J. G. Santanach, C. Estourns, A. Weibel, A. Peigney, G. Chevalier, and C. Laurent, "Mechanical and tribological properties of Fe/Cr-FeAl₂O₄-Al₂O₃ nano/micro hybrid composites prepared by spark plasma sintering," *Scripta Materialia*, vol. 64, no. 8, pp. 777-780, 2011.
- [76] B. Li, Y. Li, M. Yue, and J. Zhang, "Preparation and properties of Nd₂Fe₁₄B/ α -Fe nanocomposite permanent magnets," *Chinese Journal of Materials Research*, vol. 21, no. 3, pp. 319-323, 2007.
- [77] A. Singh and S. P. Harimkar, "Spark plasma sintering of in situ and ex situ iron-based amorphous matrix composites," *Journal of Alloys and Compounds*, vol. 497, no. 1-2, pp. 121-126, 2010.
- [78] V. Udhayabanu, K. R. Ravi, K. Murugan, D. Sivaprahasam, and B. S. Murty, "Development of Ni-Al₂O₃ in-situ nanocomposite by reactive milling and spark plasma sintering," *Metallurgical and Materials Transactions A*, vol. 42, no. 7, pp. 2085-2093, 2011.
- [79] S. Yamanaka, R. Gonda, A. Kawasaki et al., "Fabrication and thermal properties of carbon nanotube/nickel composite by spark plasma sintering method," *Materials Transactions*, vol. 48, no. 9, pp. 2506-2512, 2007.
- [80] B. S. Kim, T. Sekino, T. Nakayama, M. Wada, J. S. Lee, and K. Niihara, "Pulse electric current sintering of alumina/nickel nanocomposites," *Materials Research Innovations*, vol. 7, no. 2, pp. 57-61, 2003.
- [81] J. Umeda, K. Kondoh, and H. Imai, "Friction and wear behavior of sintered magnesium composite reinforced with CNT-Mg₂Si/MgO," *Materials Science and Engineering A*, vol. 504, no. 1-2, pp. 157-162, 2009.

Research Article

Hybrid Scaffolds for Tissue Regeneration: Chemotaxis and Physical Confinement as Sources of Biomimesis

Simone Sprio,¹ Monica Sandri,¹ Silvia Panseri,^{1,2} Carla Cunha,^{1,2} and Anna Tampieri¹

¹Laboratory of Bioceramics and Bio-Hybrid Composites, Institute of Science and Technology for Ceramics, National Research Council, 48018 Faenza, Italy

²Laboratory of Biomechanics and Technology Innovation, Rizzoli Orthopaedic Institute, 40136 Bologna, Italy

Correspondence should be addressed to Anna Tampieri, anna.tampieri@istec.cnr.it

Received 7 April 2012; Accepted 21 June 2012

Academic Editor: Leonard Deepak Francis

Copyright © 2012 Simone Sprio et al. This is an open access article distributed under the Creative Commons Attribution License, which permits unrestricted use, distribution, and reproduction in any medium, provided the original work is properly cited.

Biom mineralization is a complex *ensemble* of concomitant phenomena, driving the development of vertebrate and invertebrate organisms, particularly the formation of human bone tissue. In such a process collagen molecules assemble and organize in a complex 3-D structure and simultaneously mineralize with nearly amorphous apatite nanoparticles, whose heterogeneous nucleation, growth, and specific orientation are mediated by various chemical, physical, morphological, and structural control mechanisms, activated by the organic matrix at different size levels. The present work investigates on in-lab biom mineralization processes, performed to synthesize hybrid hydroxyapatite/collagen scaffolds for bone and osteochondral regeneration. The synthesis processes are carried out by soft-chemistry procedures, with the purpose to activate all the different control mechanisms at the basis of new bone formation *in vivo*, so as to achieve scaffolds with high biomimesis, that is, physical, chemical, morphological, and ultrastructural properties very close to the newly formed human bone. Deep analysis of cell behaviour in contact with such hybrid scaffolds confirms their strong affinity with human bone, which in turn determines high regenerative properties *in vivo*.

1. Introduction

Advances in technology demand an ever-increasing degree of control over material structure, properties, and function, and the synthesis of materials with well-defined morphology, structure, and properties is one of the big challenges in materials synthesis today. In this respect, significant steps forward have recently been made in the generation of inorganic/organic hybrid composite following the discovery that many crystals grow via the assembly of macromolecular units and can therefore be used to generate composites with hierarchical and complex structures [1].

In seeking ways to achieve this, nature provides a unique inspiration for the design and synthesis of new materials [2–4]. Indeed, the structure of most animal organisms is characterised by the coexistence of three-dimensional organic matrices and nanostructured, well-ordered inorganic phases, nucleated, and grown on the matrices during a process known as “biom mineralization” [5, 6], strictly guided

by chemical, physical, morphological, and structural controlling mechanisms. Through such processes, natural organisms form highly organized structures with characteristic texture and anisotropy [7–10], devoted to their sustenance and/or physical protection (i.e., the skeleton in mammals, exoskeleton in insects, and shells in molluscs) characterised by high resistance, lightness, and the capacity to continuously adapt to ever-variable external stimuli, and remodel and self-repair following traumas of moderate entity.

Several control mechanisms regulate the formation and organization of the mineral phase in such organisms: (i) *chemical factors*, consisting in the precipitation of ions naturally present in the environment, mediated by complex macromolecular organic structures, which act as sites of heterogeneous nucleation and control specific chemical interactions, (ii) *spatial factors*, consisting in the confinement of the nuclei growth, as well as constraint in their shape and contact with the organic substrate, (iii) *structural factors*, inducing peculiar crystallographic features driven by the

interaction between mineral phase and the organic template and (iv) finally, *morphologic factors* (morphogenesis), where the mineral phase takes a complex architecture on a macroscopic scale, strictly dependent on the combination of the various phenomena above described, which hierarchically occur on different dimensional scales in correspondence with the sites of heterogeneous nucleation. All these control mechanisms concur to the realization of three-dimensional hybrid (organic-inorganic) composites showing superior physicochemical and texturing properties, as well as marked biomimicry and bioactivity. In this respect, the formation of hard tissues in mammals takes place through the assembling of collagen nanofibrils in the extracellular space and the nucleation of the mineral phase, driven by noncollagenous acidic macromolecules [11]. The mineral phase is made of a nearly amorphous calcium phosphate with the structure of hydroxyapatite (HA), containing several ions substituting calcium and phosphate (e.g., Mg^{2+} , CO_3^{2-} , K^+ , Na^+ , SiO_4^{4-}), each of them carrying out specific functions active in the formation of new bone [12–31]. The nucleation of mineral nanocrystals initiates in specific loci corresponding to the gap between the collagen molecules that act as an organic template transferring information to the mineral phase [13, 15, 16, 32, 33]. Recently biologically inspired biomineralization processes were carried out in laboratory, thus achieving hybrid HA/collagen osteochondral scaffolds that when implanted in osteochondral defects resulted able to recruit progenitor cells from the bloodstream and direct their differentiation to the proper phenotype (i.e., bone or cartilage) thus yielding reconstruction of different anatomical regions [34–36]. The present work aims to explore the physicochemical and ultrastructural features inherent to such in-lab performed biomineralization which, as the natural biological processes, drive the formation of bone-like hybrid constructs with enhanced bioactivity. Particularly, it will be evaluated how the control of pH during synthesis and the introduction of multiple ions relevant for the activation of the biologic processes can regulate the kinetics of collagen assembling and organization as well as the HA nucleation and crystallization, thus affecting crystal growth and the exposure (i.e., bioavailability) of the mineral phase.

2. Materials and Methods

The organic matrix mediating the mineralization process was developed starting from type I collagen (Coll) extracted from equine tendon, telopeptides-free and supplied as an aqueous acetic buffer solution stabilized at pH = 3.5 and containing 1 wt% of pure collagen. The Coll suspension was dispersed in a diluted phosphoric acid solution and dropped into a calcium hydroxide aqueous suspension also containing additional doping ions. Various compositions were defined in order to achieve crystallization of apatite nanocrystals with different stoichiometry, in turn resulting in hybrid composites with stoichiometric apatite (HA) and apatite with biomimetic content of doping ions (bHA).

Synthesis of hybrid composites with stoichiometric apatite (HA/Coll): 244 mL of H_3PO_4 (0.040 M) solution,

added with 70 g of 1 wt% collagen gel, was dropped in a basic suspension containing 1.203 g of $Ca(OH)_2$ in 184 mL of distilled water to yield a composite HA/Coll material in the ratio 70/30 wt%.

Synthesis of composite with biomimetic apatite (bHA/Coll): the same mineralization process was performed to nucleate Mg^{2+} , SiO_4^{4-} -doped HA on the collagen fibers. In particular, 244 mL of H_3PO_4 (0.040 M) solution, mixed with 70 g of 1 wt% collagen gel, was dropped in a basic suspension containing 1.27 g of $Ca(OH)_2$ (95% pure), 0.58 g of $MgCl_2 \cdot 6H_2O$ (99.5% pure) [Mg/Ca molar ratio = 0.15], and 0.138 g of $Si(CH_3COO)_4$ (TEOS: 98% pure) in 200 mL of distilled water [Si/P molar ratio = 0.05]. All reactants are provided by Sigma-Aldrich (S. Louis, MO, USA). The amounts of $MgCl_2 \cdot 6H_2O$ and TEOS were calculated in order to obtain the molar ratio (Mg/Ca) = 5% and (Si/PO_4) = 0.4% in the mineral phase.

The dropwise addition procedure was performed under stirring and assuring a slow decrease of pH up to neutrality (total dropping time for the considered volumes ~30 min). The final scaffolds were obtained by controlled freeze drying where freezing and heating ramps were performed from 25°C to -25°C and from -25°C to 25°C in 36 hours under vacuum conditions ($P = 0.20$ mbar).

2.1. Chemicophysical Morphological Characterization. X-ray diffraction patterns (XRDs) were recorded by a Bruker AXS D8 Advance instrument in reflection mode (Cu-K α radiation). The samples were ground through a cryomilling apparatus to obtain relatively uniform particle size powder. Infrared spectroscopy (FTIR) was performed by using a Nicolet 4700 Spectroscopy on pellets (13 mm \varnothing) which were prepared by mixing 2 mg of ground sample with 100 mg of KBr in a mortar and pressing. The composites were also examined by scanning electron microscopy (SEM; Stereoscan 360, Leica, Cambridge, UK). ICP-OES quantitative analysis, by using an inductively coupled plasma-atomic emission spectrometry (ICP-AES: Liberty 200, Varian, Clayton South, Australia), was applied to determine the content of Ca^{2+} , PO_4^{3-} , Mg^{2+} , and Si^{4+} ions in the mineral phase. The samples were previously dissolved in nitric acid (65 wt%). Thermogravimetric analysis (Netzsch Gerätebau, STA449, Selb, Germany) was carried out to explore the thermal behavior of the composites and to assess the amount of mineral phase. This analysis was performed on specimens of about 20 mg and using a heating rate of 10°C min⁻¹ up to 1000°C in air flow. Observations of composite materials by transmission electron microscopy (TEM) were performed with a JEOL EX4000 instrument with acceleration potential of 400 kV. Samples were dispersed on lacy carbon Cu grids by contact with the grids and subsequent gentle shaking. Time-resolved microscopic analysis of the biomineralization process was carried out by Cryo-TEM (CM12, FEI, Eindhoven, The Netherlands). For this analysis the synthesis of hybrid composites was performed on the TEM grid, covered with holey carbon thin film; 5 μ L of $Ca(OH)_2$ suspension and 5 μ L of acid collagen solution were deposited on the grid, at defined Ca/P molar ratios. After a blotting step to remove the

excess of liquid, the synthesis was stopped at predetermined moments by freezing the intermediate product by an ethane bath, and then the resulting specimen was transferred to a cryo-holder and observed.

2.2. Cell Culture and Scaffold Seeding. MG-63 Human Osteoblast-like cells purchased by Lonza (Italy) were cultured in Dulbecco Modified Eagle's Medium (DMEM, PAA, Austria), containing penicillin/streptomycin (100 U/100 $\mu\text{g}/\text{mL}$), supplemented with 10% fetal bovine serum, and kept at 37°C in an atmosphere of 5% CO_2 . Cells were detached from culture flasks by trypsinization and centrifuged; cell number and viability were assessed with trypan-blue dye exclusion test.

Scaffolds were 5.00 mm diameter and 6.00 mm high, sterilized by 25 kGy γ -ray radiation prior to use. Scaffolds were placed one per well in a 24-multiwell plate well and presoaked in culture medium. Each scaffold was seeded by carefully dropping 20 μL of cell suspension (5×10^4 cells) onto the scaffold upper surface, and allowing cell attachment for 20 min, before addition into each well of 1 mL of cell culture medium supplemented with 10 $\mu\text{g}/\text{mL}$ ascorbic acid and 5 mM β -glycerophosphate for osteoblast activation. After a 6 h incubation step, each scaffold was carefully placed in a new 24 multiwell plate to eliminate any contribution of remnant cells from the cell suspension that might grow into the scaffold from its bottom surface. The medium was changed every 2 days. All cell-handling procedures were performed in a sterile laminar flow hood. All cell culture incubation steps were performed at 37°C with 5% CO_2 . The medium was changed every 2 days for the duration of the experiment. Samples ($n = 9$) were analyzed at day 7 and equally distributed between the following tests.

2.3. Cell Viability Assay. Live/dead Viability/Cytotoxicity assay kit for mammalian cells (Invitrogen) was performed according to manufacturer's instructions. Briefly, scaffolds were washed with 1x PBS for 5 min and incubated with Calcein acetoxymethyl (Calcein AM) 2 μM plus Ethidium homodimer-1 (EthD-1) 4 μM for 15 min at 37°C in the dark. Samples were rinsed in 1x PBS, finely cut with a scalpel in order to examine also the internal surface and images acquired by an inverted Nikon Ti-E fluorescence microscope (Nikon).

2.4. Cell Morphology Analysis. Actin immunofluorescence: samples were washed with 1x PBS for 5 min, fixed with 4% (w/v) paraformaldehyde for 15 min, and washed with 1x PBS for 5 min. Permeabilization was performed with 1x PBS with 0.1% (v/v) Triton X-100 for 15 min. FITC-conjugated Phalloidin antibody (Invitrogen) 1 : 500 in 1x PBS was added for 30 min at 37°C in the dark. Samples were washed with 1x PBS for 5 min and incubated with 300 nM DAPI solution (Invitrogen) for 5 min. Samples were washed with 1x PBS for 5 min and then finely cut with a scalpel in order to examine also the internal morphology. Analysis and imaging were performed by an Inverted Nikon Ti-E fluorescence microscope (Nikon).

SEM characterization: cell-seeded scaffolds were imaged and characterized using a SEM Stereoscan 360 Scanning Electron Microscope (Cambridge Instruments, UK). Samples were washed with 0.1 M sodium cacodylate buffer pH 7.4 and fixed in 2.5% glutaraldehyde in 0.1 M sodium cacodylate buffer pH 7.4 for 2 h at 4°C, washed in 0.1 M sodium cacodylate buffer pH 7.4, and freeze dried. Samples were finely cut with a scalpel in order to examine also the internal morphology and then sputter coated with gold using a Polaron Range sputter coater (DentonVaccum, USA) and mounted on a copper grid to be examined at SEM.

3. Results

3.1. Physicochemical, Morphological, and Ultrastructural Features. The XRD spectra of the mineralized construct (Figure 1) put in evidence the formation of a low crystalline mineral phase with the structure of hydroxyapatite (HA) (ICDD card no. 09-0432), superimposed to a broad spectrum belonging to the collagen matrix. The broadening of the XRD pattern belonging to HA is due to the very small crystal size, estimated as 10–15 nm. No secondary phases were detected besides hydroxyapatite, even in case of biomineralization with biomimetic HA where a nearly amorphous phase was detected (Figure 1(b)), thus confirming that ions were incorporated in the apatite structure.

FTIR analysis highlights that the mineral phase is heterogeneously nucleated on the collagen matrix, in correspondence to the carboxyl group. In fact in FTIR spectrum of the hybrid composite (Figure 2) a shift from 1340 to 1337 cm^{-1} in the absorption band corresponding to $-\text{COO}^-$ stretching is evident, due to the chemical interaction with Ca^{2+} surface site of the apatite lattice [32].

FTIR spectra also put in evidence the low crystal order of the mineral phase, particularly in case of heterogeneous nucleation of bHA, also confirming the results obtained by XRD analysis. Indeed, the absorption bands related to phosphate, which are located at about 630, 600, and 550 cm^{-1} [37] are poorly defined and merge into a single broad band. Moreover, the broad band at about 550–600 cm^{-1} , assigned to HPO_4^{2-} , becomes more intense in case of biomimetic mineral phase. These features are typical of young and immature bone where the low crystallinity of the mineral phase results in high biological activity [37–39]. FTIR spectrum also evidences carbonation of the apatite phase, specifically in B position (i.e., phosphate site), due to the presence of the related absorption band at 870 cm^{-1} [37]; moreover no evidence of absorption at 880 cm^{-1} is evident, thus highlighting that carbonation in A position (i.e., hydroxyl site) resulted in being prevented, probably due to steric hindrance by the collagenous matrix that hampered access to the OH^- sites of the mineral phase. Chemical analysis (Table 1) further confirms the occurred carbonation, since an increase of carbon was always accompanied by a reduction in phosphorus.

The estimated carbonation is consistent with the weight loss detected in our hybrid composites upon heating at 1000°C (see Figure 3). The analysis of weight loss also

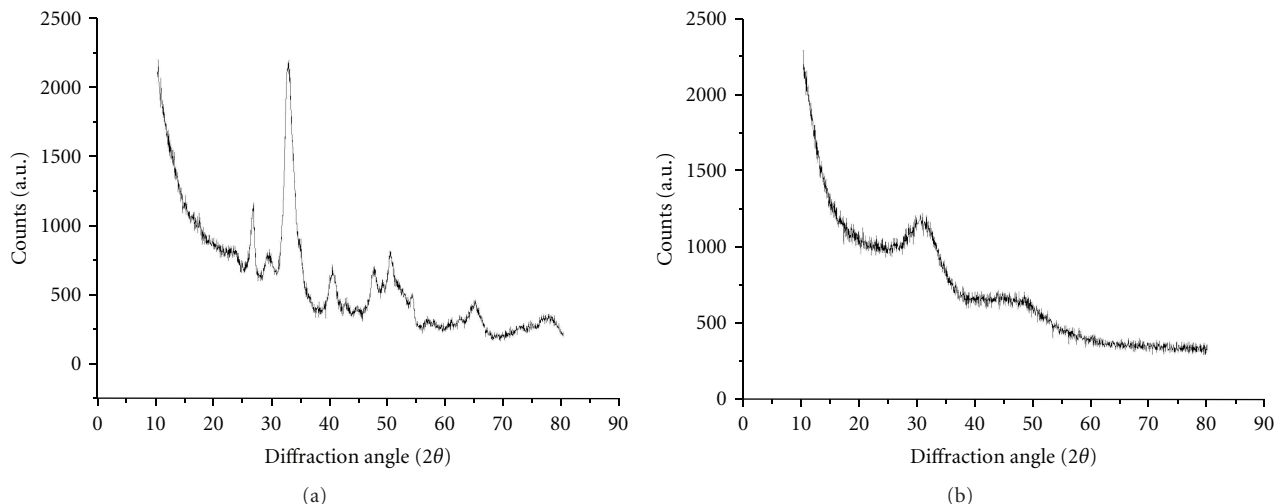


FIGURE 1: XRD spectra of hybrid biomineralized constructs. (a) Stoichiometric HA phase; (b) biomimetic HA phase.

TABLE 1: Composition of the mineral phase in HA/Coll and bHA/Coll scaffolds in comparison with human bone.

	Typical composition of human bone (wt%)	Introduced ions (wt%)	Actual HA/Coll (wt%)	Actual bHA/Coll (wt%)
Ca ²⁺	24.36	27.98	26.06	25.54
PO ₄ ³⁻	32.62	39.79	36.04	31.78
Si ⁴⁺	0.29–0.58	0.63	—	0.41
Mg ²⁺	0.35–0.91	2.96	—	0.53
CO ₃ ²⁻	2.1–5.6	—	>2	>2

shows that in nucleated bHA higher amounts of water are coordinated to the mineral phase by physical or chemical bonds, compared to stoichiometric mineral phase, thus evidencing a higher density of active sites as well as increased affinity with water molecules.

The multiple ionic substitutions in the apatite heterogeneously nucleated on the collagen matrix are assessed by chemical analysis, which put in evidence that when biomineralization is carried out in presence of magnesium and silicate ions, the resulting mineral phase exhibits a bone-like composition (Table 1), even in case of introduction of higher amount of Mg²⁺ and SiO₄⁴⁻ ions in the reaction flask. This feature is also confirmed by thermogravimetric analysis carried out on hybrid composites mineralized with both stoichiometric and biomimetic HA to determine the maximum amount of mineral phase which could be heterogeneously nucleated on the collagen matrix. The samples selected for this analysis were obtained by biomineralization with high amounts of Ca²⁺ and PO₄³⁻ so as to overcome the upper limit for the mineral phase that can be heterogeneously nucleated and to obtain precipitation of excess mineral phase. On the basis of the detected weight loss (Figure 3) it is determined that the maximum amount of mineral phase that can be heterogeneously nucleated by biologically inspired mineralization is about 70 wt%, that is, a typical bone-like composition. Microscopic observations carried out by TEM further confirm the formation of the mineral phase by heterogeneous nucleation; TEM micrographs show nano-sized nuclei formed inside the collagen fibres and growing

parallel to fibres (Figure 4). This feature is accompanied by a preferential orientation of HA crystals, detected by flat film XRD analysis carried out on calcified fibres (Figure 5); in particular the (002) reflection of HA, detected at 0.34 nm, preferentially orients parallel to the direction of orientation of the typical collagen molecular axial spacing at 0.29 nm. When analysing hybrid composites biomineralized with stoichiometric HA, it can be observed that the growth of HA nuclei proceeds towards development of acicular nanosized grains (Figure 4(a)). Conversely, when the mineral phase has a bone-like composition, HA nuclei exhibit a globular-like shape and very short-range crystal order (Figure 4(b)), as evidenced by Fourier-transform analysis of HRTEM images, thus exhibiting features of a nearly amorphous calcium phosphate (see also XRD analysis in Figure 1).

Deeper investigation on the biomineralization process, carried out by time-resolved cryo-TEM observations in function of pH variation, evidences that at low pH the organization of fibres is still at a preliminary stage (Figure 6(a)); then, by increasing pH during the biomineralization process the fibres assume the typical banding pattern of organized collagen showing local disorder in correspondence of the mineral nuclei (Figure 6(b)), which result located at the gaps between collagen molecules.

Further evidence of inner mineralization of assembled collagen fibres comes from SEM observation of hybrid composites thermally treated at 1000°C during thermogravimetric analysis. In particular Figure 7 shows that HA particles occupied the whole volume of the construct; more

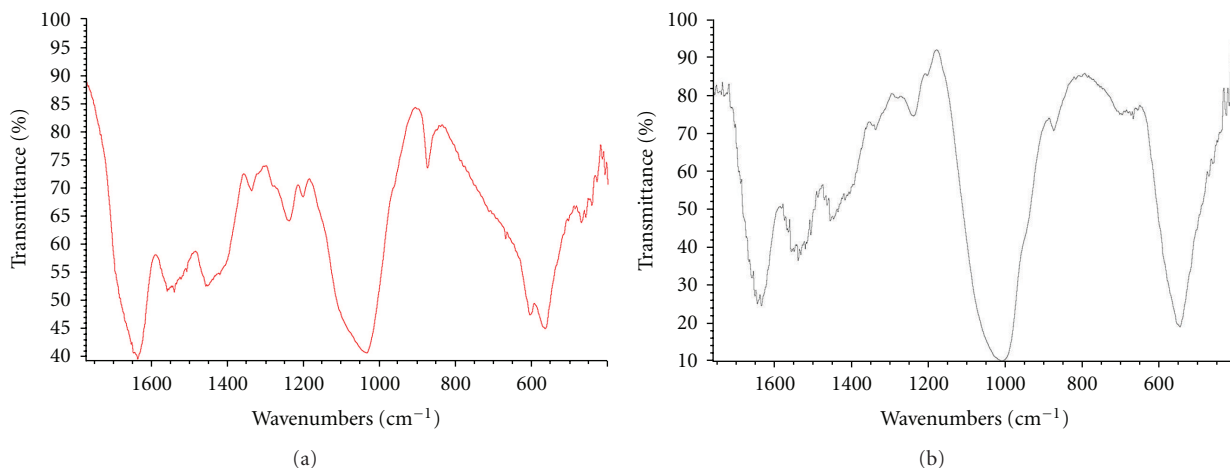


FIGURE 2: FTIR spectra of hybrid composite mineralized with (a) stoichiometric HA; (b) bHA.

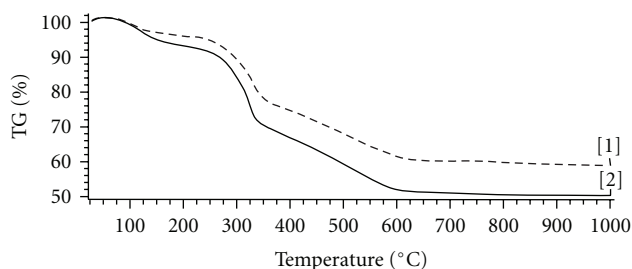


FIGURE 3: TG analysis of hybrid composites reporting weight loss of stoichiometric HA (dashed line) and bHA (continuous line).

in detail, it is noticeable that the HA particles assume a prismatic shape in case of stoichiometric composition (Figure 7(a)), whereas they become nearly globular in case of mineralization with multisubstituted HA (Figure 7(b)).

3.2. Analysis of Cell Behaviour. MG-63 human osteoblast-like cells were cultured within the hybrid HA/Coll composites for 7 days. The live/dead assay showed a very high ratio of viable cells on scaffold surface. Cells cover nearly the entire upper scaffold surface, and they grew into the porous scaffold structure and infiltrated the scaffolds as shown in Figure 8(a). The analysis of cell morphology showed a very tight relationship between osteoblast cells and the mineralized collagen fibres (Figures 8(b) and 9). Attached cells exhibited their characteristic intricate morphology analysed by phalloidin staining on day 7 (Figure 8(b)). Moreover SEM images showed human osteoblast-like cells completely embedded within the nanostructure of the hybrid collagen-HA construct (Figure 9). It was observed the cells capability of adhering and spreading over single-collagen fibres, which impose directionality, as if cells were dangling on collagen (Figures 9(a) and 9(b)). Cells and biomaterials seemed to coalesce thus illustrating the high biocompatibility and osteoconductivity performances of the hybrid construct (Figure 9(c)).

4. Discussion

The synthesis process adopted for in-lab biomineralization is based on dropwise addition of acidic collagen suspensions containing phosphate ions into a basic suspension under continuous stirring. This resulted in a locally occurring neutralization process whereas the overall pH in the reaction flask was maintained nearly constant at pH \sim 12 due to the Ca(OH)₂ suspension. The average pH in the small volume where neutralization took place resulted steeply in increasing from \sim 2.5 to 10.

Within this range, particularly from 4.5 to 6.5 the dispersed nanosized collagen fibrils start their assembling, thus giving rise to formation of progressively thicker and more organized fibres; on the other hand, at higher pH values (i.e., pH \geq 5.5) the formation of hydroxyapatite crystals, supported by Ca²⁺ and PO₄³⁻ ions dispersed in the solution, was thermodynamically favoured against other calcium phosphates. When collagen comes in contact with Ca²⁺ ions, they soon link to COO⁻ groups exposed by C-terminal regions of tropocollagen fibrils, so that the formation of apatite crystals is initiated by phenomena of heterogeneous nucleation. This process involves the same functional groups responsible for the assembling of collagen fibrils; thus, the free sites for heterogeneous nucleation of the mineral phase result in being those located in the periodically spaced gaps which form along the staggered collagen fibrils during their assembling and organization [5, 32, 40, 41].

The fast local increase of pH from acidic to slightly basic values allows to achieve the formation of HA nuclei onto the newly formed collagen matrix; in particular, since the two pH ranges where fibres assembling and HA nucleation, respectively, occur are not completely distinct, amorphous HA nuclei form onto the fibrils before their complete assembling into more organized fibres. Upon further increase of pH two processes enter in competition, that is, (i) the organization of collagen fibers into a three-dimensional network and (ii) the proceeding HA crystallization, involving the same binding chemical groups on the fibres surface. Cryo-TEM observations well describe this scenario, where the organization of

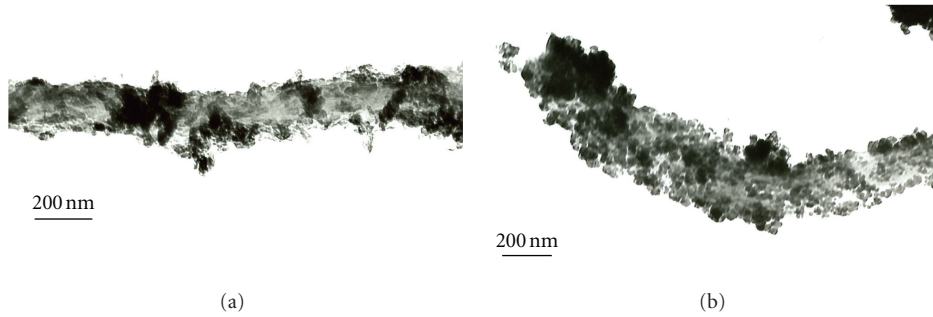


FIGURE 4: TEM micrographs of collagen fibres. (a) Mineralized with stoichiometric HA; (b) mineralized with biomimetic HA.

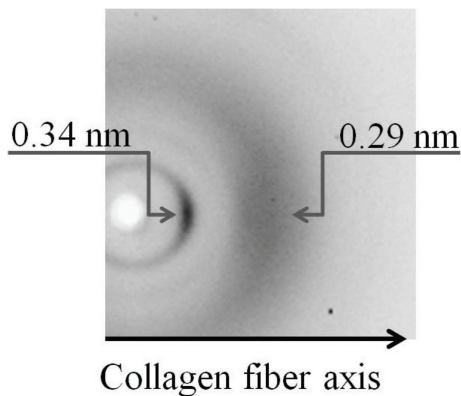


FIGURE 5: Flat film XRD pattern of a thin bundle of parallel calcified fibers, evidencing the orientation of HA (002) reflection along the axial collagen fibers direction.

collagen fibres appears in progress whereas at pH above 5.5 the formation of mineral nuclei initiates and provokes a local distortion in correspondence to the band gaps. Even if such a biomineralization process is carried out in stoichiometric conditions (i.e., amount of reactants calculated to obtain HA phase with $\text{Ca}_{10}(\text{PO}_4)_6(\text{OH})_2$ composition), the crystallization of the mineral phase is prevented owing to the contact with the collagen surface. Indeed, the interaction with the collagenous matrix at the nanoscale is mediated by ultrastructural, chemotactic, and physical constraints affecting crystal growth and organization of the mineral phase. In particular, the crystal structure of the mineral phase results in being characterized by amorphous or very short-range order; in addition, the topotactic information provided by the collagenous matrix at the sites of heterogeneous nucleation induces preferential crystal growth of the HA-hexagonal crystals with c axis elongated along the long axis of collagen. As a consequence the crystallographic ab plane of the newly formed HA phase results in being exposed perpendicularly to the long axis of the collagen fibers; this feature is supposed to promote specific adsorption of proteins specifically involved in new bone formation [5]. Besides the structural control, a chemical control mechanism is also active in our biomineralization process; in fact CO_3^{2-} ions partially replace PO_4^{3-} ions (B-site carbonation) in the lattice of the nucleated apatite phase; the chemical

substitution in B position is commonly detected in young and immature bone and is known to promote the establishment of chemotactic and polarity features at the surface level which favor osteoblast adhesion. The carbonation in B position results in being selectively imposed by the physical constraints inherent to the polymeric matrix, thus preventing the incorporation of CO_3^{2-} ions in OH^- sites (A-site carbonation), which is known to confer stability to the mineral phase and is commonly found predominantly in mature bone.

In presence of additional foreign ions (Mg^{2+} and SiO_4^{4-}) introduced in the reaction flask during in-lab biomineralization, the crystal disorder of the heterogeneously nucleated HA particles favours their incorporation and substitution of Ca^{2+} and PO_4^{3-} , respectively, in the apatite structure thus forming a biomimetic HA strongly mimicking in composition the inorganic part of human bone. Such ions are present in the mineral phase of young and immature bone and have relevant function in the formation of new bone. In this respect Mg^{2+} ions have a specific role in guiding the processes of new bone formation; in particular, it is well known that ionic substitution with Mg^{2+} ions promotes nucleation phenomena while preventing grain growth, so that the mineral phase results in being organized in a very high number of nanonuclei so as to provide increased bioavailability [18]. Indeed surface Mg^{2+} sites exhibit different polarity, structure and stereochemistry that also result in stronger coordination with H_2O molecules, compared to Ca^{2+} [23], which in turn affects the ability of favouring protein adhesion. Moreover, in our observation the introduction of Mg^{2+} ions favoured the chemical link of the mineral phase with collagen in correspondence to the band gaps, which is likely due to the increase of nucleation kinetics. In this respect previous works have shown that the presence of polyelectrolytes during in-lab biomineralization can mimic the function of noncollagenic acidic macromolecules in the guidance of mineral phase nucleation in the band gap [42]; in consequence we can suppose that Mg^{2+} ions present in newly formed human bone can have a further relevant role in biological processes and can act in the same way as polyelectrolytes during in-lab biomineralization.

Besides, the incorporation of silicon in the phosphate site further increased biomimesis and affinity with the newly formed bone since silicon is associated with the formation

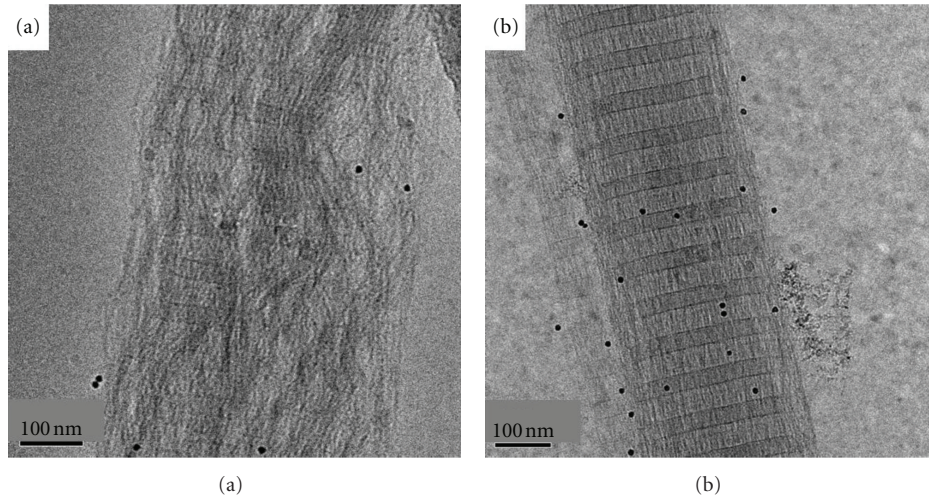


FIGURE 6: Cryo-TEM images of a collagen fiber during biomineralization. (a) At a first stage of the reaction; (b) at an advanced stage.

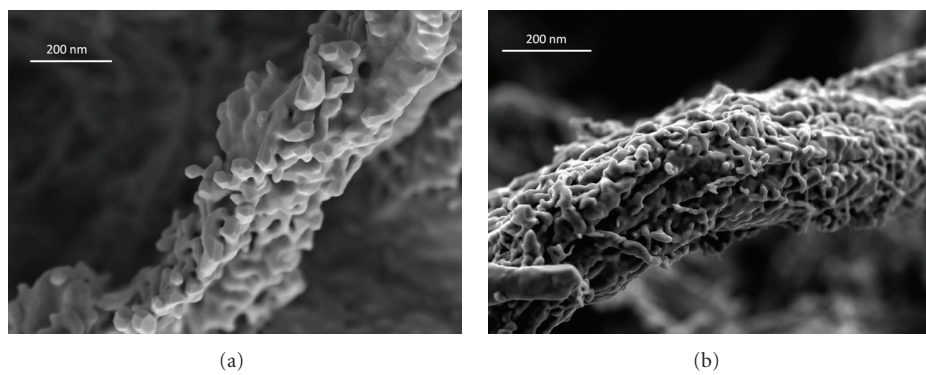


FIGURE 7: SEM micrographs of mineralized collagen fibers after heating at 1000°C.

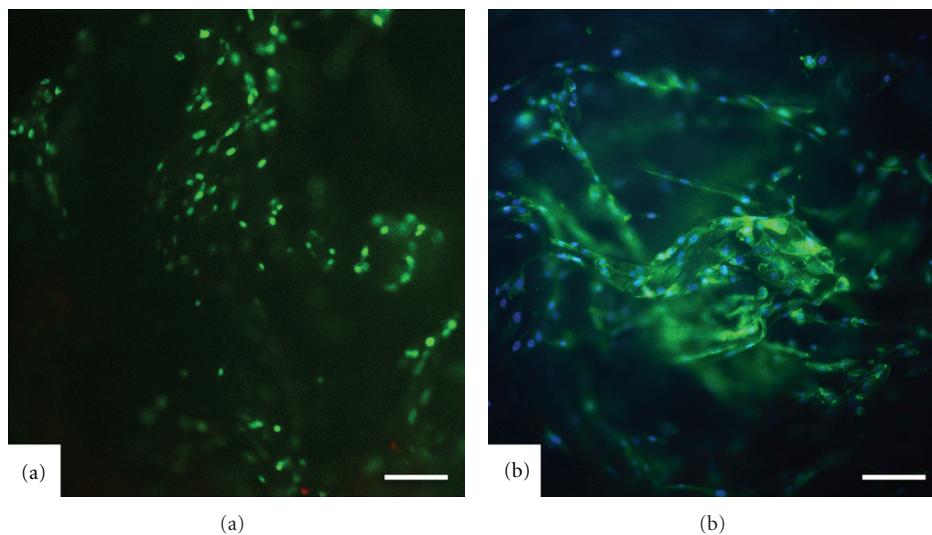


FIGURE 8: Analysis of cell viability and morphology. (a) Cell viability was analysed by the live/dead assay (calcein acetoxymethyl stains live cells in green ethidium homodimer-1 stains dead cells in red). (b) Cell morphology was analysed by actin staining (actin is shown in green, DAPI in blue). Scale bars: 100 μm.

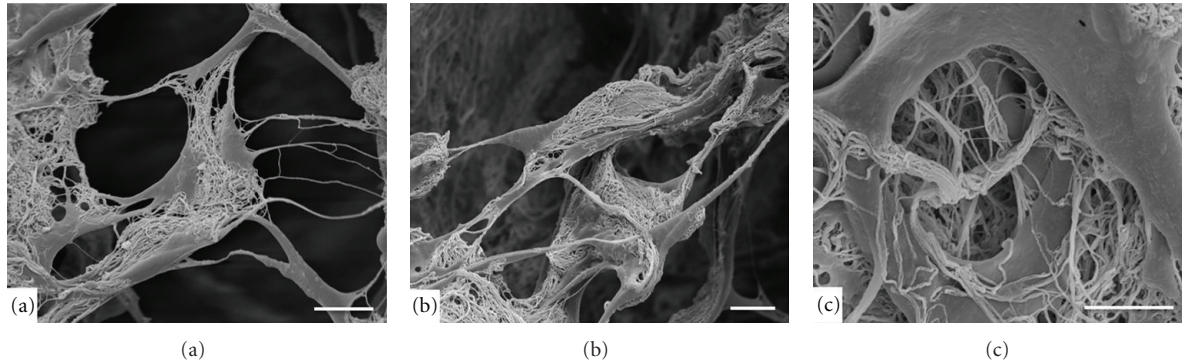


FIGURE 9: SEM analysis. Detailed analysis of morphology of biohybrid scaffold. (a and b) Intricate mesh of cells and HA/collagen fibers. (c) Higher magnification picture showing completely embedded cells within the nanostructure of a bioinspired collagen-HA scaffold. Scale bars: (a and b) 20 μm ; (c) 10 μm .

of cross-links between collagen and proteoglycans [21] in the early stages of bone formation, in turn leading to bone matrix stabilization against enzymatic resorption.

With these multiple substitutions, the composition of mineral phase in our in-lab biomineralized composites results in being very close to the one of natural bone, that is,



The expression of ultrastructural mimesis with bone in our hybrid composites was found to depend on the presence of biomimetic ions. In fact, the introduction of substituting ions during the process of heterogeneous nucleation not only affected composition but also crystal growth. In particular the interaction with collagen and the presence of magnesium activate topotactic control mechanisms which drive specific preferential orientation and growth of the mineral phase.

All the above-described features, expressing chemico-physical, morphological, and ultrastructural mimesis with the newly formed human bone, were achieved due to the different control mechanisms inherent to the polymeric matrix that were activated during the in-lab performed biomineralization.

Such process confers to the mineral phase features that cannot be achieved by conventional methods of powder synthesis. In fact, even though low-crystalline HA nanoparticles with biomimetic composition can be obtained by wet methods at room temperature, in such particles a crystal-like order is always detected [30]; moreover the peculiar shape and size of the mineral phase driving specific cell behaviour can be only achieved by mediation of the information provided at the nanosize by the collagenous template. In this respect, when in biomimetic conditions, the collagenous matrix self-assemble and organize, thus providing an *ensemble* of control mechanisms that unambiguously determine the characteristics of the mineral phase, in turn driving new bone formation.

A further evidence that our in-lab biomineralization is consistent with biological processes of bone formation is in the intrinsic stability of the 3-D hybrid construct versus mineral/polymer ratio. Indeed, our hybrid system, intended

as bHA nanoparticles heterogeneously nucleated on a self-assembled collagen matrix, resulted in being stable only when mineral/polymer ratio was consistent with the composition of natural mineralized tissues. In fact, the amount of the mineral phase in the composite can be controlled by adjusting the composition of the starting solutions in terms of Ca^{2+} and PO_4^{3-} ions, in turn determining the final amount of apatite phase; in this respect, it was observed that precipitation of the mineral phase during synthesis in biomimetic conditions occurred when in concentrations above ≈ 70 wt%, that is, a bone-like composition. This means that, in our 3-D biomineralized constructs, the amount of mineral phase that can nucleate and grow, driven by information provided by the collagen matrix, is intrinsically defined and limited to bone-like composition.

Cell-surface interaction includes specific chemico-physical linkages between cells and material, where cell adhesion and spreading pave the way to cell proliferation, finally providing a surface well covered by cells. Cell-material surface interaction and cell adhesion are complex processes involving the reorganization of cytoskeleton proteins further stimulated in this case by the ordered alignment of needle-like HA crystals along their *c* axis on collagen fibers. The SEM images in Figures 9(a) and 9(b) are emblematic of how much the cells like such a biomimetic substrate so that they actually “go on swing” with its biomineralized collagen fibers.

The possibility to vary the mineralization degree over a wide range up to bone-like composition offers a significant tool to develop graded constructs able to mimic different anatomical regions in hard connective tissues such as bones or teeth. In particular, the different compartment of articular regions, namely, subchondral bone, mineralized cartilage, and hyaline cartilage, can be accurately mimicked to achieve biomimetic scaffolds for osteochondral regeneration [34]. Moreover, the possibility to vary the degree of fibrillation and assembling of collagen fibers makes possible to develop chemically and morphologically graded scaffolds mimicking the different components of dentin (i.e., pulp, predentin, mineralized dentin) and of periodontal bone (i.e., cementum, alveolar bone, and periodontal ligament).

In contact with such graded scaffolds, mesenchymal stem cells receive information which guides their selective

differentiation into osteoblasts or chondrocytes. In particular, when implanted in vivo the high porosity of the hybrid constructs allows cell recruitment from the bloodstream and subsequent colonization and proliferation, whereas the chemical and ultrastructural features of the mineral phase, strongly mimicking bone tissue, act as osteogenic signals [35]. In this respect, the absence of mineral phase in the cartilage-like layer promotes cell differentiation into chondrocytes, thus leading to in vivo regeneration of the cartilaginous part.

5. Conclusions

The achievement of scaffolds exhibiting strong mimicry with natural tissues is a key feature for hard tissue regeneration. However, conventional manufacturing processes suffer from strong limitations to achieve materials with high complexity and organization at the nanoscale. In this respect we have shown that, by soft chemistry procedures, it is possible to activate all the control mechanisms inherent to natural self-assembling polymers such as collagen and to direct biological-like mineralization processes towards formation of hybrid constructs with very high chemico-physical, morphological, and ultrastructural mimesis with the natural bone tissue. The high regenerative potential of such devices is due to the synergistic combination of the organic matrix and the mineral phase, whose osteogenic properties are conferred by specific chemical and topotactic features as well as by the physical confinement imposed by the organic matrix itself. The hybrid constructs can be flexibly addressed to specific designed functions, so that they can be designed to regenerate different anatomical districts.

Acknowledgments

The research leading to these results has received funding from the European Union's Seventh Framework Programme ([FP7/2007–2013]) under Grant agreement no. 246373, OPHIS. The authors gratefully acknowledge as well Prof. N. A. J. M. Sommerdijk and Dr. F. Nudelman, Technical University of Eindhoven, for valuable discussion and Cryo-TEM images.

References

- [1] J. Aizenberg, J. C. Weaver, M. S. Thanawala, V. C. Sundar, D. E. Morse, and P. Fratzl, "Materials science: skeleton of euplectella sp.: structural hierarchy from the nanoscale to the macroscale," *Science*, vol. 309, no. 5732, pp. 275–278, 2005.
- [2] Z. Y. Tang, N. A. Kotov, S. Magonov, and B. Ozturk, "Nanostructured artificial nacre," *Nature Materials*, vol. 2, no. 6, pp. 413–418, 2003.
- [3] S. Deville, E. Saiz, R. K. Nalla, and A. P. Tomsia, "Freezing as a path to build complex composites," *Science*, vol. 311, no. 5760, pp. 515–518, 2006.
- [4] E. Munch, M. E. Launey, D. H. Alsem, E. Saiz, A. P. Tomsia, and R. O. Ritchie, "Tough, bio-inspired hybrid materials," *Science*, vol. 322, no. 5907, pp. 1516–1520, 2008.
- [5] S. Mann, *Biomaterialization Principles and Concepts in Bioinorganic Materials Chemistry*, Oxford University Press, Oxford, UK, 2001.
- [6] A. Tampieri, S. Sprio, M. Sandri, and F. Valentini, "Mimicking natural bio-mineralization processes: a new tool for osteochondral scaffold development," *Trends in Biotechnology*, 2011.
- [7] H. A. Lowenstam and S. Weiner, *On Biomaterialization*, Oxford University Press, New York, NY, USA, 1989.
- [8] A. Berman, J. Hanson, L. Leiserowitz, T. F. Koetzle, S. Weiner, and L. Addadi, "Biological control of crystal texture: a widespread strategy for adapting crystal properties to function," *Science*, vol. 259, no. 5096, pp. 776–779, 1993.
- [9] R. A. Metzler, G. A. Tribello, M. Parrinello, and P. U. P. A. Gilbert, "Asprich peptides are occluded in calcite and permanently disorder biomineral crystals," *Journal of the American Chemical Society*, vol. 132, no. 33, pp. 11585–11591, 2010.
- [10] J. J. De Yoreo and P. G. Vekilov, "Principles of crystal nucleation and growth," in *Biomaterialization*, P. M. Dove, J. J. DeYoreo, and S. Weiner, Eds., vol. 54, pp. 57–93, Mineralogical Society of America, Washington, DC, USA, 2003.
- [11] E. M. Pouget, P. H. H. Bomans, J. A. C. M. Goos, P. M. Frederik, G. De With, and N. A. J. M. Sommerdijk, "The initial stages of template-controlled CaCO₃ formation revealed by Cryo-TEM," *Science*, vol. 323, no. 5920, pp. 1455–1458, 2009.
- [12] M. J. Olszta, X. Cheng, S. S. Jee et al., "Bone structure and formation: a new perspective," *Materials Science and Engineering R*, vol. 58, no. 3–5, pp. 77–116, 2007.
- [13] S. V. Dorozhkin and M. Epple, "Biological and medical significance of calcium phosphates," *Angewandte Chemie*, vol. 41, no. 17, pp. 3130–3146, 2002.
- [14] R. Z. LeGeros, "Calcium phosphates in oral biology and medicine," *Monographs in oral science*, vol. 15, pp. 1–201, 1991.
- [15] Q. Zhang, J. Chen, J. Feng, Y. Cao, C. Deng, and X. Zhang, "Dissolution and mineralization behaviors of HA coatings," *Biomaterials*, vol. 24, no. 26, pp. 4741–4748, 2003.
- [16] C. T. Laurencin, Ed., *Bone Graft Substitutes*, ASTM International, West Conshohocken, Pa, USA, 2003.
- [17] A. L. Boskey, "Mineralization, structure and function of bone," in *Dynamics of Bone and Cartilage Metabolism*, M. J. Seibel, S. P. Robins, and J. P. Bilezikian, Eds., p. 201, Academic Press, New York, NY, USA, 2006.
- [18] A. Bigi, E. Foresti, R. Gregorini, A. Ripamonti, N. Roveri, and J. S. Shah, "The role of magnesium on the structure of biological apatites," *Calcified Tissue International*, vol. 50, no. 5, pp. 439–444, 1992.
- [19] N. B. Matsko, N. Žnidaršič, I. Letofsky-Papst et al., "Silicon: the key element in early stages of biocalcification," *Journal of Structural Biology*, vol. 174, no. 1, pp. 180–186, 2011.
- [20] A. M. Pietak, J. W. Reid, M. J. Stott, and M. Sayer, "Silicon substitution in the calcium phosphate bioceramics," *Biomaterials*, vol. 28, no. 28, pp. 4023–4032, 2007.
- [21] K. Schwarz, "A bound form of silicon in glycosaminoglycans and polyuronides," *Proceedings of the National Academy of Sciences of the United States of America*, vol. 70, no. 5, pp. 1608–1612, 1973.
- [22] Y. Sakhno, L. Bertinetti, M. Iafisco, A. Tampieri, N. Roveri, and G. Martra, "Surface hydration and cationic sites of nanohydroxyapatites with amorphous or crystalline surfaces: a comparative study," *Journal of Physical Chemistry C*, vol. 114, no. 39, pp. 16640–16648, 2010.
- [23] L. Bertinetti, C. Drouet, C. Combes et al., "Surface characteristics of nanocrystalline apatites: effect of Mg surface

- enrichment on morphology, surface hydration species, and cationic environments,” *Langmuir*, vol. 25, no. 10, pp. 5647–5654, 2009.
- [24] L. Bertinetti, A. Tampieri, E. Landi et al., “Surface structure, hydration, and cationic sites of nanohydroxyapatite: UHR-TEM, IR, and microgravimetric studies,” *Journal of Physical Chemistry C*, vol. 111, no. 10, pp. 4027–4035, 2007.
- [25] L. Bertinetti, A. Tampieri, E. Landi, G. Martra, and S. Coluccia, “Punctual investigation of surface sites of HA and magnesium-HA,” *Journal of the European Ceramic Society*, vol. 26, no. 6, pp. 987–991, 2006.
- [26] G. Celotti, A. Tampieri, S. Sprio et al., “Crystallinity in apatites: how can a truly disordered fraction be distinguished from nanosize crystalline domains?” *Journal of Materials Science*, vol. 17, no. 11, pp. 1079–1087, 2006.
- [27] E. Landi, A. Tampieri, M. Mattioli-Belmonte et al., “Biomimetic Mg- and Mg,CO₃-substituted hydroxyapatites: synthesis characterization and in vitro behaviour,” *Journal of the European Ceramic Society*, vol. 26, no. 13, pp. 2593–2601, 2006.
- [28] E. Landi, A. Tampieri, G. Celotti, R. Langenati, M. Sandri, and S. Sprio, “Nucleation of biomimetic apatite in synthetic body fluids: dense and porous scaffold development,” *Biomaterials*, vol. 26, no. 16, pp. 2835–2845, 2005.
- [29] E. Landi, A. Tampieri, G. Celotti, L. Vichi, and M. Sandri, “Influence of synthesis and sintering parameters on the characteristics of carbonate apatite,” *Biomaterials*, vol. 25, no. 10, pp. 1763–1770, 2004.
- [30] S. Sprio, A. Tampieri, E. Landi et al., “Physico-chemical properties and solubility behaviour of multi-substituted hydroxyapatite powders containing silicon,” *Materials Science and Engineering C*, vol. 28, no. 1, pp. 179–187, 2008.
- [31] E. Landi, S. Sprio, M. Sandri, G. Celotti, and A. Tampieri, “Development of Sr and CO₃ co-substituted hydroxyapatites for biomedical applications,” *Acta Biomaterialia*, vol. 4, no. 3, pp. 656–663, 2008.
- [32] A. Tampieri, G. Celotti, E. Landi, M. Sandri, N. Roveri, and G. Falini, “Biologically inspired synthesis of bone-like composite: self-assembled collagen fibers/hydroxyapatite nanocrystals,” *Journal of Biomedical Materials Research A*, vol. 67, no. 2, pp. 618–625, 2003.
- [33] A. Tampieri, G. Celotti, and E. Landi, “From biomimetic apatites to biologically inspired composites,” *Analytical and Bioanalytical Chemistry*, vol. 381, no. 3, pp. 568–576, 2005.
- [34] A. Tampieri, M. Sandri, E. Landi et al., “Design of graded biomimetic osteochondral composite scaffolds,” *Biomaterials*, vol. 29, no. 26, pp. 3539–3546, 2008.
- [35] E. Kon, M. Delcogliano, G. Filardo et al., “Orderly osteochondral regeneration in a sheep model using a novel nanocomposite multilayered biomaterial,” *Journal of Orthopaedic Research*, vol. 28, no. 1, pp. 116–124, 2010.
- [36] S. Scaglione, P. Giannoni, P. Bianchini et al., “Order versus disorder: in vivo bone formation within osteoconductive scaffolds,” *Scientific Reports*, vol. 2, p. 274, 2012.
- [37] C. Rey, M. Shimizu, B. Collins, and M. J. Glimcher, “Resolution-enhanced Fourier transform infrared spectroscopy study of the environment of phosphate ions in the early deposits of a solid phase of calcium-phosphate in bone and enamel, and their evolution with age. I: investigations in the ν_4 PO₄ domain,” *Calcified Tissue International*, vol. 46, no. 6, pp. 384–394, 1990.
- [38] B. O. Fowler, E. C. Moreno, and W. E. Brown, “Infrared spectra of hydroxyapatite, octacalcium phosphate and pyrolysed octacalcium phosphate,” *Archives of Oral Biology*, vol. 11, no. 5, pp. 477–492, 1966.
- [39] L. M. Miller, V. Vairavamurthy, M. R. Chance et al., “In situ analysis of mineral content and crystallinity in bone using infrared micro-spectroscopy of the ν_4 PO₄⁻³ vibration,” *Biochimica et Biophysica Acta*, vol. 1527, no. 1-2, pp. 11–19, 2001.
- [40] M. Gelinsky, P. B. Welzel, P. Simon, A. Bernhardt, and U. König, “Porous three-dimensional scaffolds made of mineralised collagen: preparation and properties of a biomimetic nanocomposite material for tissue engineering of bone,” *Chemical Engineering Journal*, vol. 137, no. 1, pp. 84–96, 2008.
- [41] J. H. Bradt, M. Mertig, A. Teresiak, and W. Pompe, “Biomimetic mineralization of collagen by combined fibril assembly and calcium phosphate formation,” *Chemistry of Materials*, vol. 11, no. 10, pp. 2694–2701, 1999.
- [42] F. Nudelman, K. Pieterse, A. George et al., “The role of collagen in bone apatite formation in the presence of hydroxyapatite nucleation inhibitors,” *Nature Materials*, vol. 9, no. 12, pp. 1004–1009, 2010.

Research Article

Polycation-Capped CdS Quantum Dots Synthesized in Reverse Microemulsions

Karina Lemke and Joachim Koetz

Institut für Chemie, Universität Potsdam, Karl-Liebknecht-Straße 24-25, Haus 25 Golm, 14476 Potsdam, Germany

Correspondence should be addressed to Joachim Koetz, koetz@rz.uni-potsdam.de

Received 21 February 2012; Accepted 21 June 2012

Academic Editor: Grégory Guisbiers

Copyright © 2012 K. Lemke and J. Koetz. This is an open access article distributed under the Creative Commons Attribution License, which permits unrestricted use, distribution, and reproduction in any medium, provided the original work is properly cited.

This paper is focused on the formation and recovery of cadmium sulfide (CdS) nanoparticles in two different types of polycation-modified reverse microemulsions using low molecular weight poly(diallyldimethylammonium chloride) (PDADMAC) and poly(ethyleneimine) (PEI). Both polymers were incorporated in a quaternary w/o microemulsion consisting of water, toluene-pentanol (1 : 1), and sodium dodecyl sulfate (SDS), as well as in a ternary w/o microemulsion consisting of water, heptanol, and 3-(N,N-dimethyl-dodecylammonio)-propanesulfonate (SB). UV-vis and fluorescence measurements in the microemulsion illustrate the capping effect of the polycations on the formation of the CdS quantum dots. The nanoparticles are redispersed in water and characterized by using UV-vis and fluorescence spectroscopy, in combination with dynamic light scattering. From the quaternary microemulsion, only nanoparticle aggregates of about 100 nm can be redispersed, but, from the ternary microemulsion, well-stabilized polycation-capped CdS quantum dots can be obtained. The results show that the electrostatic interactions between the polycation and the surfactant are of high relevance especially in the solvent evaporation and redispersion process. That means only that in the case of moderate polycation-surfactant interactions a redispersion of the polymer-capped CdS quantum dots without problems of aggregation is possible.

1. Introduction

The importance of small, monodisperse semiconductor particles has greatly increased in the recent years, due to the growing interest in technological applications of the resulting materials in electronic devices like solar cells or LEDs [1–4], medical diagnostics [5–7], and photo catalysis [8–10]. The optical, optoelectronic, and magnetic properties of such materials are strongly depending on the size according to the well-investigated size quantization effect [11–14]. Nanoscale semiconductors like cadmium sulfide show a size-dependent onset of light absorption, and a blue shift of the fluorescence band with decreasing particle size. Therefore, the formation of monodisperse cadmium sulfide (CdS), CdSe, or ZnS nanocrystals, so-called quantum dots, is of importance. For the preparation of such materials, different methods can be used, for example, sol-gel [15, 16] or solvothermal [17, 18] and irradiation processes [19, 20]. An important way to synthesize monodisperse nanoparticles of very small

dimensions is to use a template phase. The nanoparticles can be formed in block copolymer micelles or polymer microgels [21–24] in dendrimers or microemulsions [25–31]. Especially microemulsion template phases are widely used as “nano-reactors” to make ultrafine particles [32, 33]. For this process, two w/o microemulsions are mixed together containing reactant A and reactant B, respectively. Hereby, the size of the droplets, and the bending elasticity as well as the rigidity of the droplet film is of importance, due to the fact that droplet diffusion and fusion is the rate-determining step in the microemulsion and not the reaction between the components A and B [31]. Two different mechanisms for the droplet exchange process are discussed in the literature, that is, the water channel mechanism and the droplet coalescence mechanism [34].

By adding polymers one can influence the droplet size [35–37], the droplet-droplet interactions [38–40], and the stability [41] and rigidity [42–44] of the surfactant film in w/o microemulsion due to polymer-surfactant interactions.

Our own experiments have shown that polyelectrolytes can be incorporated into water-in-oil microemulsions, too [45–47]. Molecular dynamic simulations of inverse micelles in presence of a cationic polyelectrolyte have shown that the polymer is located nearby the surfactant film [48]. The polyelectrolyte-modified water-in-oil microemulsions can be used as a template phase for the formation of different types of very small nanoparticles, for example, BaSO₄, ZnS, gold, and magnetite [49–52].

It has to be mentioned here that it is possible to produce ultrafine CdS nanoparticles inside the microemulsion droplets with a narrow size distribution in absence of an additive [26, 32, 53], but an efficient recovery of the nanoparticles from microemulsion is still an open problem [54]. There are different approaches, for example, water or temperature-induced separation [55, 56], precipitation by antisolvents [57] or surfactants [58], or a so-called cloud point extraction [59], but due to their high surface energy the ultrafine particles tend to coagulate irreversibly during the separation process. Therefore, it is necessary to protect the nanoparticles during the separation and recovery process. To overcome this problem organic molecules can be added to stabilize the particles during the recovery process. Agostiano et al. have used, for example, thiophenol as a capping agent to redisperse CdS nanoparticles in pyridine [26], and Tamborra et al. immobilized octylamine-capped CdS nanocrystals in polymers, that is, poly(methylmethacrylate) or polystyrene [60].

To stabilize nanoparticles in water, polyelectrolytes are of special relevance due to their electrosterical stabilization effect [61, 62]. Therefore, polyelectrolyte-modified microemulsions are of special interest, because of the fact that the polyelectrolytes are already present during the process of particle formation, solvent evaporation as well as during the process of redispersion in water.

This paper describes the influence of two polycations incorporated into microemulsions on the CdS nanoparticle formation process and the possibility to recover the nanoparticles after solvent evaporation and redispersion in water.

The aim of this paper is to learn more about the role of electrostatic interactions in the nanoparticle recovery process.

Therefore, two microemulsions were used: one containing the strong anionic SDS and the other the amphoteric SB.

The formation of CdS in both types of microemulsion is possible by mixing microemulsions containing the corresponding salts, that is, CdCl₂ and (NH₄)₂S [63]. The nanoparticle formation was investigated by means of UV-vis and fluorescence spectroscopy, and the redispersed particles were also characterized by UV-vis and fluorescence measurement, as well as dynamic light scattering (DLS).

2. Experimental Part

2.1. Materials. The poly(diallyldimethylammonium chloride), with a molecular weight of Mw = 21.000 g/mol, was synthesized by radical polymerization. DADMAC (N,N'-Diallyl-N,N'-dimethylammonium-chloride) (65 wt. % in

water) was purchased from Sigma-Aldrich and used as received. The branched Poly(ethyleneimine) with a molecular weight of Mw = 25.000 g/mol was obtained from the BASF. Toluene (>99%; Fluka), pentanol (>99%, Fluka), and heptanol (>99%, Merck) were used without further purification. Sodium dodecylsulfate (SDS) (>99% Fluka), cadmium chloride (CdCl₂) (>99%, Fluka), and a 20 wt% aqueous solution of (NH₄)₂S are used as obtained. 3-(N,N-dimethyl-dodecylammonio)-propanesulfonate (SB) (>97%) was obtained from Raschig company. Water is purified with the Milli-Q Reference A+ water purification system (Millipore).

2.2. Phase Diagram. The determination of the isotropic phase range of all systems mentioned above has been carried out by titration of the pseudobinary oil-cosurfactant/surfactant, or oil/surfactant mixture with a 1 wt. % aqueous polymer solution. The mixture was shaken or treated by ultrasonification and optically tested in order to survey a transparent phase region of reverse microemulsions (L₂-phase).

2.3. Preparation of CdS Nanoparticles. CdS nanoparticles are prepared by mixing two microemulsions: one containing 40 mmol/L CdCl₂ and 2 wt% polymer and the other 40 mmol/L (NH₄)₂S. The spontaneous induced formation of the nanoparticles in the w/o microemulsion droplets occurs after shaking the received microemulsion mixture of the corresponding precursor salts. Afterwards the mixture was dried under vacuum at 40°C for one week to remove the solvents (water, toluene, pentanol, and heptanol). The received powder was redispersed in water by ultrasonification for further characterization.

2.4. Characterization of CdS Nanoparticles

2.4.1. UV-Vis Spectroscopy. Absorption spectra are obtained by using a Cary 5000 UV-vis NIR spectrophotometer (Varian) in a wave length range between 200 and 800 nm. For this, the microemulsion samples, as well as the redispersed samples, were placed in a quartz cuvette with a path length of 1 cm.

2.4.2. Fluorescence Spectroscopy. Fluorescence measurements are carried out by using a FluoroMax-3 spectrometer (Horiba) in the wave length region between 370 and 700 nm at the excitation wavelength between 340 and 370 nm.

2.4.3. Dynamic Light Scattering and Electrophoretic Light Scattering. The determination of the particle size and the particle size distribution by dynamic light scattering measurements is carried out at a fixed angle of 173° (backscattering) at 25°C using the Zetasizer Nano ZS (Malvern), equipped with a He-Ne laser and a digital autocorrelator. The averaged particle diameters were obtained from five separate measurements by using a peak analysis by number, volume, or intensity.

The zeta potential that means the electrokinetic potential at the effective shear plane between the moveable and

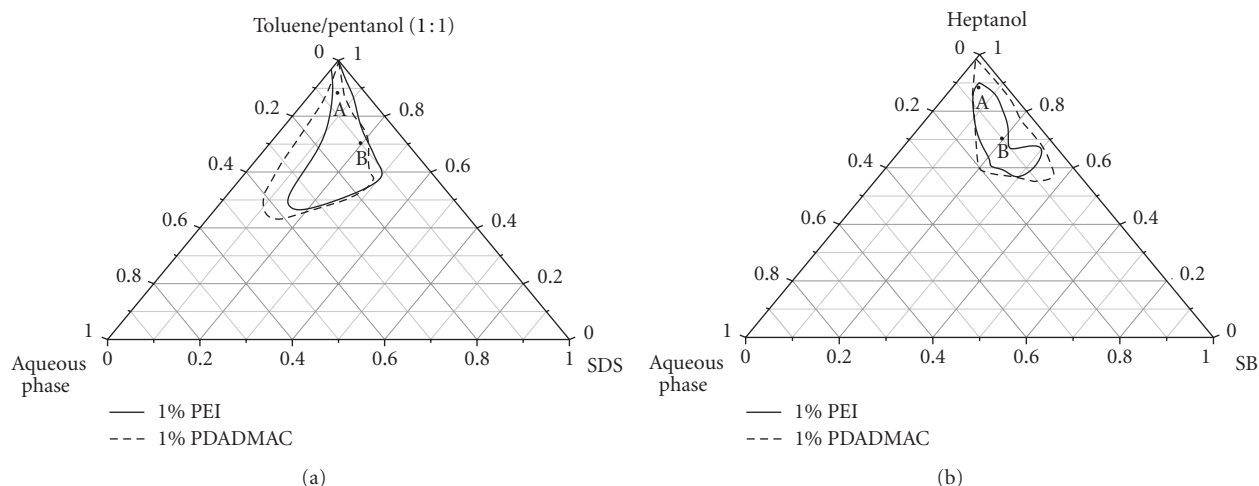


FIGURE 1: Partial phase diagram of the L_2 -phase of the modified quasi ternary system toluene-pentanol (1:1)/SDS/water (a) and of the modified ternary system heptanol/SB/water (b).

nonmovable part of the double layer, was measured by means of the Zetasizer Nano ZS (Malvern) based on the principle of electrophoretic light scattering.

3. Results

3.1. Phase Behaviour. The partial phase diagrams with PEI and PDADMAC, determined at room temperature, show a transparent phase region of reverse microemulsions (L_2 -phase) in the “oil” corner in all systems (Figures 1(a) and 1(b)). For the quasiternary system toluene-pentanol (1:1)/SDS/water, the L_2 -phase is extended towards the water corner when PDADMAC is incorporated in comparison to the PEI-modified system. The phase range of the L_2 -phase of the ternary system heptanol/SB/water is decreased by replacing PDADMAC with PEI. In both cases the reduction of the L_2 -phase in presence of PEI is accompanied by lower interactions between the branched polymer and the surfactant film.

Furthermore, an extension of the phase range of the L_2 -phase for both polymers in direction to the water corner can be observed in the quasiternary SDS-modified system. This effect can be explained by an enhancement of the bending elasticity of the surfactant film caused by interactions between the anionic surfactants and the polycations.

3.2. Nanoparticle Formation

3.2.1. Toluene-Pentanol (1:1)/SDS/Water Template Phase. The formation of CdS nanoparticles has been carried out at Point A with a composition oil/surfactant/water = 88/6/6, that means at a water to surfactant ratio, $R = 1.0$. For checking the influence of the droplet size on the results, additional investigations were made at point B (composition oil/surfactant/water = 70/20/10), at $R = 0.5$. After elimination of the reference spectra, the absorption spectra are given in Figure 2(a) in absence and in presence of low molecular weight PEI and PDADMAC, respectively.

For poly(ethyleneimine) two pronounced absorption maxima, the first one at 324 nm and the second one at 348 nm, could be observed. Note, that the presence of two absorption maxima could be a hint for the existence of two different particle fractions. However, the fluorescence spectrum for the PEI modified system shows only one well defined band with a maximum at 508 nm (Figure 2(b)), which should be more asymmetric, if there are different particle fractions. Due to that, one can conclude that a surface modification or cluster formation with PEI influence the absorption behaviour of the particles in that characteristic way. Similar absorption and emission spectra were obtained by us with PEI of significant lower and higher molar masses [63].

In comparison a modification with poly(diallyldimethylammonium chloride) leads to a broad shoulder between 390 and 440 nm, similar to the unmodified water system, in good agreement to the results given in references [63, 64]. Fluorescence measurements (Figure 2(b)) show an expanded emission peak between 450 and 800 nm for PDADMAC with a maximum at 690 nm. In both systems the spectra indicate the formation of nanometer-sized CdS nanoparticles, taken into account that the position and the height of the absorption band are well related to the size of the semiconductor particles [26]. For that reason, one can assume a mean particle size range between 2 and 10 nm for the CdS nanoparticles formed in presence of PEI or PDADMAC. Nevertheless, the blue shift of the two absorption bands in the UV-vis spectrum indicates the formation of PEI-capped small CdS nanoparticles with a narrow size distribution, in good agreement with the shift of the emission peak towards the blue region.

Note that similar results were obtained at point B (compare Figure 8 in the Supplementary part), indicating that the droplet size is of minor relevance.

The blue emission colour of the PEI-modified and the orange colour of the PDADMAC-modified systems excited

TABLE 1: Experimental values of the band gap (E_g) corresponding to the calculated diameter of the CdS nanoparticles.

System		Wavelength (nm)		E_g (eV)		d (nm) calculated [65]	
Microemulsion SDS based	PEI	324	348	3.83	3.57	2.2	2.5
	PDADMAC	420		2.96		3.6	
Microemulsion SB based	PEI	330	360	3.76	3.45	2.3	2.6
	PDADMAC	380		3.27		2.9	
Redispersion system SB based	PEI	320	350	3.88	3.55	2.2	2.5
	PDADMAC	415		2.99		3.5	

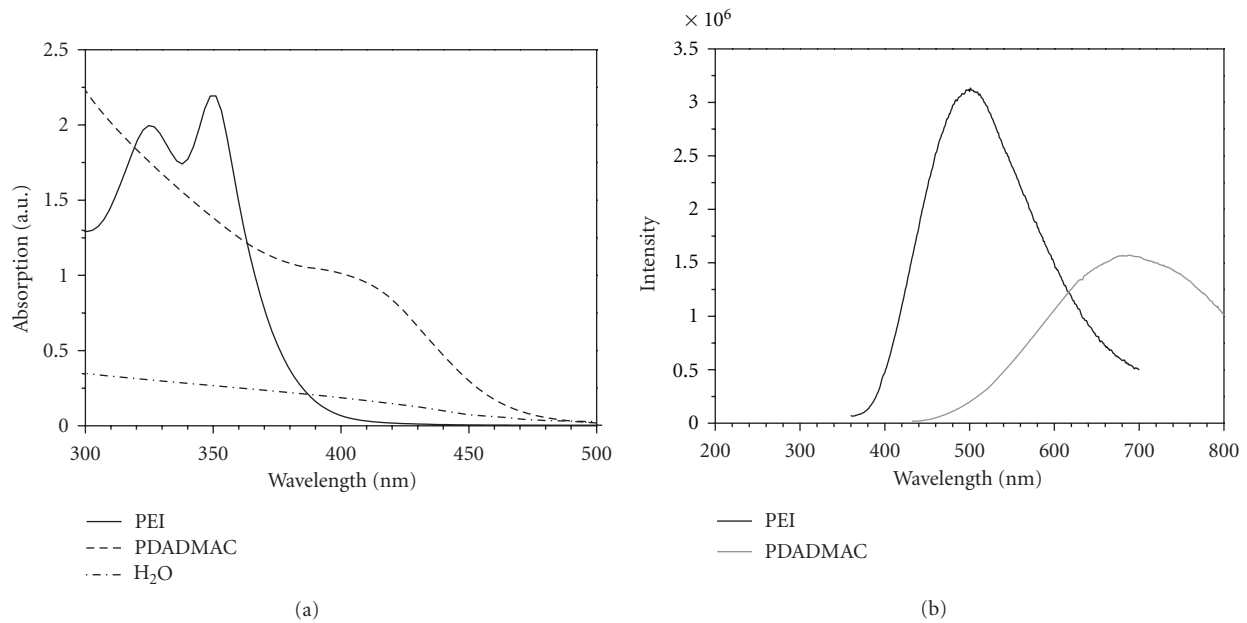


FIGURE 2: Absorption (a) and fluorescence spectra (b) of the microemulsion system toluene-pentanol (1:1), SDS, water after CdS nanoparticle formation in presence of PEI or PDADMAC at point A.

with a near-UV lamp (shown in Figure 9 in the Supplementary Material available online at doi:10.1155/2012/478153) underline the statements given before.

Summarizing the results, one can conclude that the PEI-modified nanoparticles are of about 2 nm, and the PDADMAC-modified ones of about 4 nm in size. This is in full agreement with calculated diameter based on the band gap according to reference [65] summarized in Table 1.

3.2.2. Heptanol/SB/Water Template Phase. To compare the characteristics of the CdS nanoparticles synthesized in the ternary system with the nanoparticles synthesized in the quaternary system, the formation of the particles has been carried out in all cases at point A and point B, respectively. In Figure 3(a) the absorption spectra (after elimination of the reference spectra) are given for CdS nanoparticles in presence of PEI and PDADMAC in comparison to the spectrum in absence of a polymer.

The absorption spectra for PEI show two absorption maxima, the first one, weakly distinctive, at 330 nm and the second one at 360 nm. In comparison to the results in the quaternary microemulsion a marginal bathochromic shift of both maxima can be observed. The shoulder,

obtained for CdS nanoparticles modified with PDADMAC, between 350 and 420 nm is shifted to lower wavelengths. The hypsochromic shift indicates the formation of smaller particles in case of the ternary microemulsion system. This can be explained by lower interactions between the amphoteric surfactant and PDADMAC located more in the inner core of the droplets. Due to this the particle growing process inside of the droplets is more restricted. PEI is not going to be affected by this effect, because of the branched structure of the polymer located more in the inner part of the droplet and significant weaker electrostatic interactions. Fluorescence measurements illustrated in Figure 3(b) show a broad emission peak with a maximum at 520 nm. The emission peaks are nearly in the same range already obtained in the quaternary microemulsion. According to these results one can conclude that PEI-capped CdS nanoparticles are formed in the same size range for both systems. This will be confirmed by the blue emission colour of the PEI-modified particles, which is quite similar in both microemulsions (Figures 9 and 10 in the supplementary part).

Fluorescence measurements for PDADMAC modified particles show a broad emission peak between 400 and 700 nm, with an emission maximum shifted to lower wavelengths at 590 nm. Our results show that in comparison

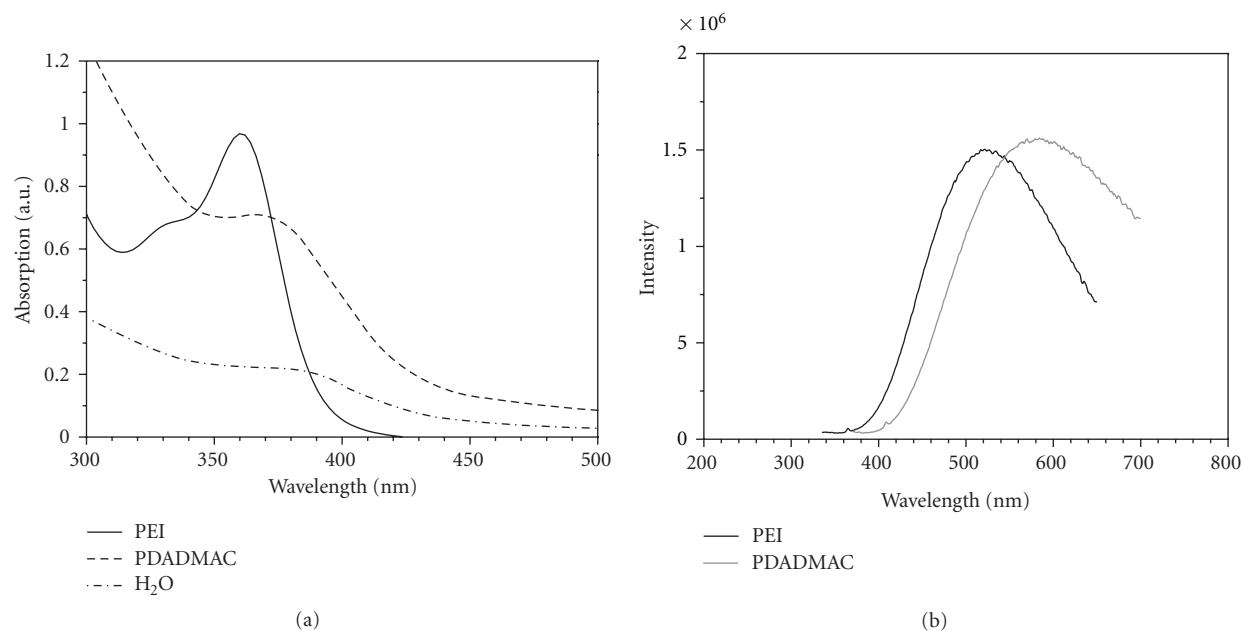


FIGURE 3: Absorption (a) and fluorescence spectra (b) of the microemulsion system heptanol, SB, water after CdS nanoparticle formation in presence of PEI or PDADMAC at point A.

to the PEI-modified system these particles are of course larger, but smaller in comparison to the quaternary SDS-based system. This corresponds with the yellow emission colour (Figure 10 in the supplementary part). Taking into account the emission colour and the fluorescence spectra one can conclude that PDADMAC-capped CdS nanoparticles of about 3 nm have been produced.

At point B similar results were obtained for the PEI-modified system, in contrast to a significant smaller absorption maximum in presence of PDADMAC, disappearing in absence of a polymer. These results underline the additional templating effect of the PEI in the SB-based microemulsion.

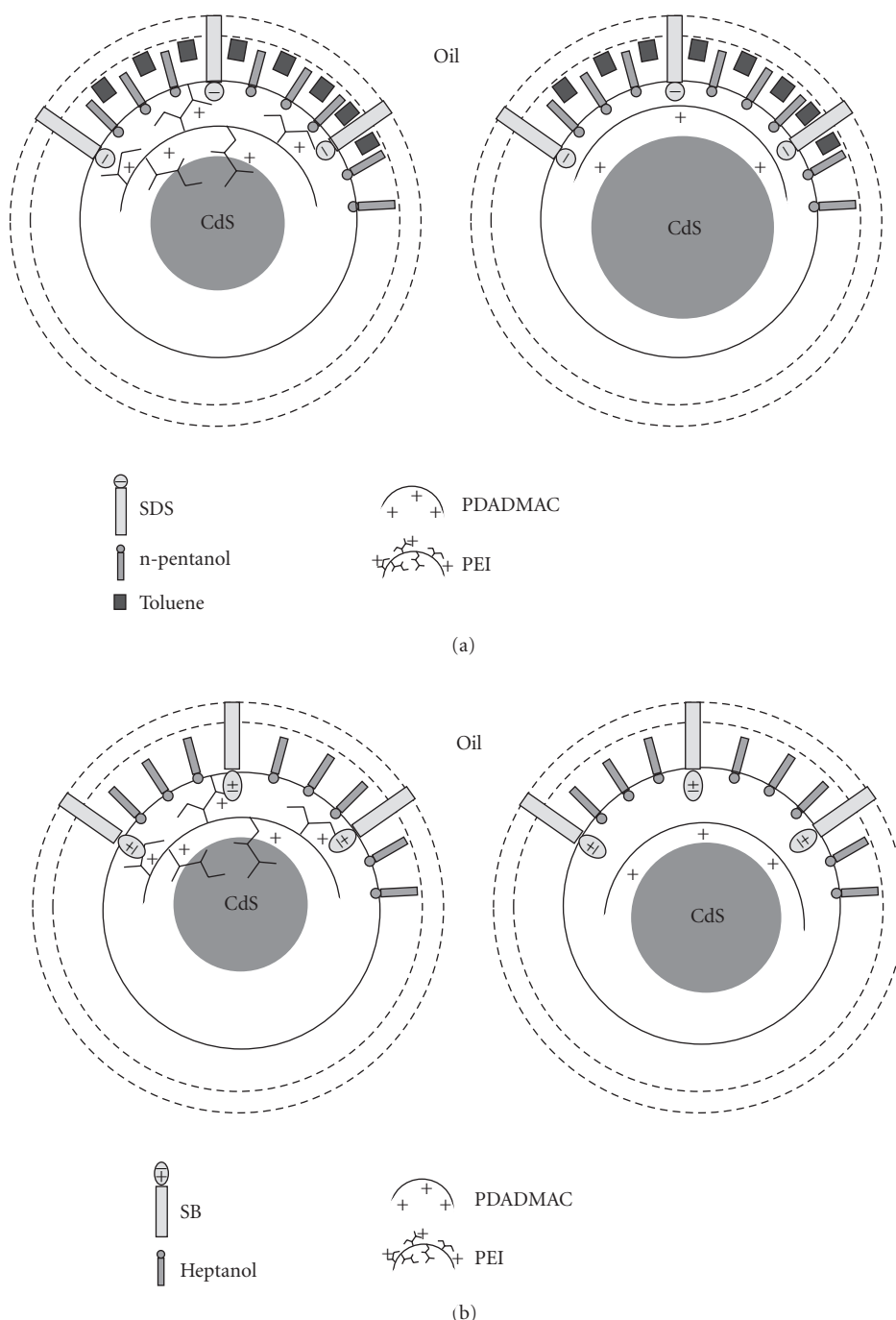
It is noteworthy that the different absorption and fluorescence behaviour cannot only trace back to different particle sizes. We also have to take into account that two different polycations, on the one hand branched PEI and on the other hand linear PDADMAC, in two different types of microemulsion, are used. Capping exchange at the nanoparticle surface can also influence the optical properties of the system, as already shown by Tamborra et al. [60]. In general one can conclude stronger electrostatic interactions (illustrated in Scheme 1) of the polycations with SDS, especially for the linear PDADMAC. Therefore, PDADMAC is located at the interphase and stabilize the surfactant film. In contrast, branched PEI, located more in the inner part of the droplet, influences the particle-growing process much more (additional templating effect).

3.3. Characterization of the Redispersed Nanoparticles

3.3.1. Nanoparticles Redispersed from the Toluene-Pentanol (1:1)/SDS/Water Template Phase. After a complete solvent evaporation, the received powder was redispersed in water by ultrasonification. The obtained turbid solution was

filtrated to separate aggregates and bad stabilized individual nanoparticles. To get more information on the size and surface charge of the redispersed particles dynamic and zeta potential measurements were conducted. The results of dynamic light scattering shown in Figure 4 demonstrate that the diameters of the redispersed CdS nanoparticles are significant larger than the particle dimensions estimated in the microemulsion. Two main particle fractions with diameters of about 440 nm (± 120 nm) and 120 nm (± 20 nm) can be found for PEI, and of about 270 nm (± 140 nm) and 65 nm (± 20 nm) for PDADMAC, respectively. According to the results of UV-vis and fluorescence measurements in the microemulsion, one can conclude that individual-polymer capped CdS nanoparticles formed in the microemulsion droplets can be not redispersed after solvent evaporation without particle aggregation. Furthermore, zeta potential measurements show for both polymers a negative value of about -50 ± 2 mV. Taking into account that SDS (a strong anionic surfactant) is in excess, one can assume that the interactions between the surfactant and the polycations are strong enough to form polycation-surfactant complexes combined by a destabilization of the individual nanoparticles by stripping the polycation from the surface of the CdS particles.

3.3.2. Nanoparticles Redispersed from the Heptanol/SB/Water Template Phase. After solvent evaporation, the received powder can be completely redispersed in water by ultrasonification without problems of phase separation. Dynamic light-scattering experiments demonstrate that in the transparent solution only one fraction of nanoparticles can be obtained, with a mean diameter of 10 nm (± 3 nm) in presence of PEI and 13 nm (± 4 nm) in presence of PDADMAC, respectively (Figure 5).



SCHEME 1: Schematic representation of the location and interactions of the polycations PEI and PDADMAC within the w/o microemulsion droplets of a SDS-based system (a) and a SB-based system (b).

The particles show a positive zeta potential of $+8 \pm 3$ mV. From this data, one can conclude a polymer adsorption onto the surface of the CdS nanoparticles.

For further characterization UV-vis and fluorescence measurements were conducted. For PEI two absorption maxima could be observed in Figure 6(a), the first one at 320 nm and the second one at 350 nm. A broad shoulder between 390 and 450 nm can be observed in presence of PDADMAC, a hint for larger nanoparticle diameter.

A direct comparison, between the absorption peaks obtained in the microemulsion and the redispersed aqueous

system, shows no significant differences in the PEI system, but a marginal bathochromic shift of the absorption band for the PDADMAC modified system. According to this one can conclude that CdS nanoparticles could be redispersed without a significant change in the particle dimension much better in presence of PEI.

The fluorescence spectrum of the redispersed CdS nanoparticles in presence of PEI is shown in Figure 6(b); for PDADMAC the emission peak is very small and correspondingly not significant. One can see that the emission peak for PEI-capped CdS nanoparticles is shifted to lower

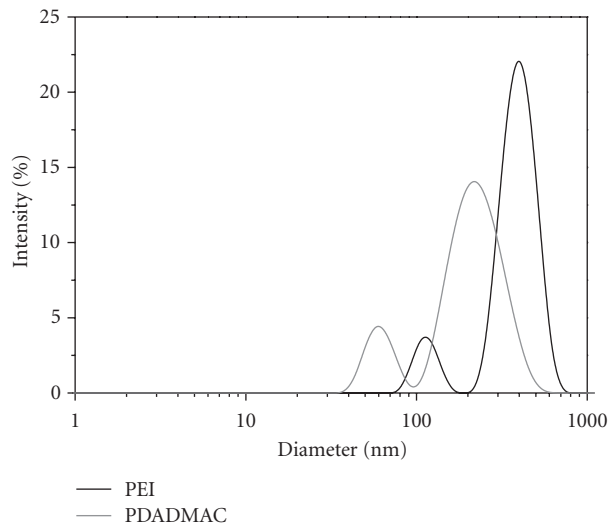


FIGURE 4: Size distribution of redispersed CdS nanoparticles produced in the microemulsion system toluene-pentanol (1:1), SDS, water (PEI) or (PDADMAC) at point A.

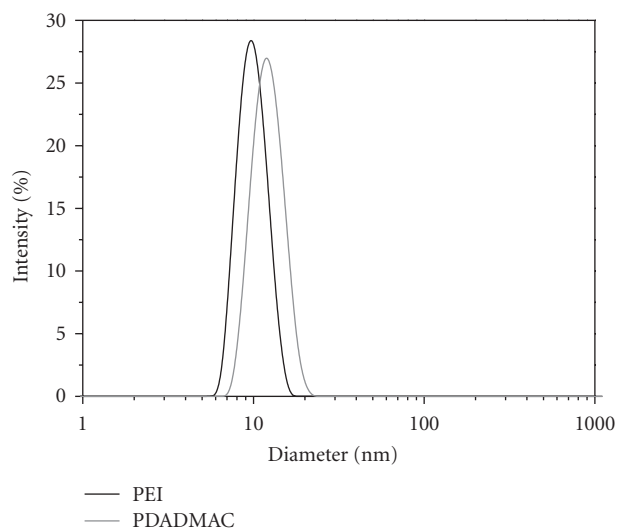
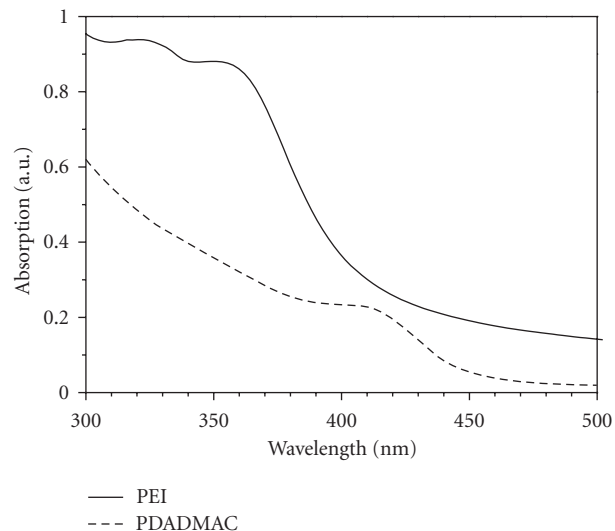


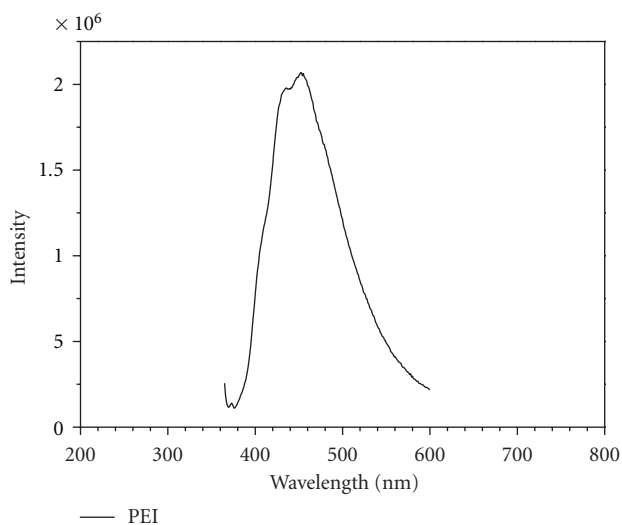
FIGURE 5: Size distribution of redispersed CdS nanoparticles produced in the microemulsion system heptanol SB, water (PEI), or (PDADMAC) at point A.

wave length and becomes more narrow in comparison to the microemulsion. The blue emission colour for PEI supports our finding that PEI-capped CdS quantum dots are redispersed without a change in the particle dimension. According to our assumption that redispersed PDADMAC-capped nanoparticles are larger than in the microemulsion, the emission colour is turned to orange for the redispersed particles, illustrated in Figure 11 in the supplementary part.

Based on the UV-vis spectroscopically obtained band gap the particle size of quantum dots can be determined according to Patidar et al. [65]. The calculated particle size is in the same range as expected according to UV-vis and fluorescence spectroscopy, as well as the observed emission colour (compare Table 1).



(a)



(b)

FIGURE 6: Absorption (a) and fluorescence spectra (b) of redispersed CdS nanoparticles produced in the microemulsion system heptanol, SB, water (PEI), and for the system with PDADMAC at point A.

In order to assure the size and the shape of the particles and explain the discrepancy between DLS and UV-vis data a supporting technique, like transmission electron microscopy (TEM), should be helpful as already shown by Pons et al. [66]. Unfortunately, it is not possible to get some micrographs of these systems with a TEM due to the excess of surfactants. Noteworthy, that CdS nanoparticles produced in a SB-based hexane-pentanol microemulsion could be successfully analyzed only by high-resolution transmission electron microscopy (HRTEM). The particle dimensions of 2-3 nm (shown in Figure 12 in the supplementary part) are also in that case in disagreement with the diameter of 9 ± 2 nm observed in DLS. Inspired by these results we have synthesized in addition CdS nanoparticles in absence of surfactants, that means in a diluted aqueous PEI-solution. By this procedure we were able to produce PEI stabilized

CdS nanoparticles with quite similar properties. However, in that case, that means in absence of surfactants, TEM can be successfully applied. The TEM micrographs (Figures 7(a) and 7(b)) in the supplementary part clearly show that in addition to the individual nanoparticles of about 3 nm (Figure 7(a)) particle aggregates of about 10 nm (Figure 7(b)) exist.

In the heptanol-based microemulsion system investigated here, individual CdS nanoparticles of about 3 nm are redispersed, which aggregated to clusters containing 3–4 nanoparticles. Therefore, one can conclude that in the intensity plot of the DLS experiments predominantly the QD clusters are detected. The existence of two absorption peaks in the UV-vis spectrum can be related to QD's varying in the surrounding medium in dependence on the state of aggregation.

To underline the effect of the polyelectrolytes in the microemulsion template phase as well as in the recovery process we made two additional experiments.

In a “reference” experiment we produced CdS particles in the SB microemulsion in absence of a polyelectrolyte, followed by the solvent evaporation and redispersion in analogy to the procedure described above. In a second experiment we added the polyelectrolyte PEI during the redispersion procedure. The absorption and fluorescence spectra (given in Figure 13 in the supplementary part) clearly demonstrate that in absence of the polyelectrolyte quantum dots cannot be recovered. When the PEI is added during the redispersion procedure, only a marginal part of the nanoparticles can be stabilized.

4. Conclusion

Our results show that the quaternary template phase consisting of water, toluene-pentanol (1:1), and the anionic surfactant SDS in presence of PEI or PDADMAC can be successfully used for the synthesis of polymer-capped CdS nanoparticles. Unfortunately a recovery of the quantum dots without a particle aggregation is not possible due to the strong surfactant polycation interactions.

When the ternary template phase with the amphoteric SB surfactant is used, the polymer-capped nanoparticles produced in the microemulsion template phase can be recovered. That means the individual polymer-capped quantum dots and QD clusters are stable during the process of solvent evaporation and can be redispersed.

The results show on the one hand that the recovery process is only successful when the electrostatic interactions between the polycation and the surfactant headgroups are moderate. On the other hand one can see that the polyelectrolytes should be incorporated already into the microemulsion, because of the additional templating effect of the polymer during the particle formation process, and the protecting effect during the recovery process.

Conflict of Interests

The authors declare no conflict of interests with Rashing company.

Acknowledgements

The authors would like to thank the UP Transfer GmbH for the financial support. The Raschig company is gratefully acknowledged for the supply of the SB surfactant, and the BASF for providing the PEI sample.

References

- [1] L. Han, D. Qin, X. Jiang et al., “Synthesis of high quality zinc-blende CdSe nanocrystals and their application in hybrid solar cells,” *Nanotechnology*, vol. 17, no. 18, pp. 4736–4742, 2006.
- [2] W. U. Huynh, J. J. Dittmer, and A. P. Alivisatos, “Hybrid nanorod-polymer solar cells,” *Science*, vol. 295, no. 5564, pp. 2425–2427, 2002.
- [3] C. Wei, D. Grouquist, and J. Roark, “Voltage tunable electroluminescence of CdTe nanoparticle light emitting diodes,” *Journal of Nanoscience and Nanotechnology*, vol. 2, no. 1, pp. 47–53, 2002.
- [4] I. Matsui, “Nanoparticles for electronic device applications: a brief review,” *Journal of Chemical Engineering of Japan*, vol. 38, no. 8, pp. 535–546, 2005.
- [5] S. Nie, Y. Xing, G. J. Kim, and J. W. Simons, “Nanotechnology applications in cancer,” *Annual Review of Biomedical Engineering*, vol. 9, pp. 257–288, 2007.
- [6] M. N. Rhyner, A. M. Smith, X. Gao, H. Mao, L. Yang, and S. Nie, “Quantum dots and multifunctional nanoparticles: new contrast agents for tumor imaging,” *Nanomedicine*, vol. 1, no. 2, pp. 209–217, 2006.
- [7] S. Santra, J. Xu, K. Wang, and W. Tan, “Luminescent nanoparticle probes for bioimaging,” *Journal of Nanoscience and Nanotechnology*, vol. 4, no. 6, pp. 590–599, 2004.
- [8] N. Serpone and R. Khairutdinov, “Application of nanoparticles in the photocatalytic degradation of water pollutants,” *Studies in Surface Science and Catalysis*, vol. 103, pp. 417–444, 1997.
- [9] J. J. Zou, C. Chen, C. J. Liu, Y. P. Zhang, Y. Han, and L. Cui, “Pt nanoparticles on TiO₂ with novel metal-semiconductor interface as highly efficient photocatalyst,” *Materials Letters*, vol. 59, no. 27, pp. 3437–3440, 2005.
- [10] W. Zhang, Y. Zhong, J. Fan et al., “Preparation, morphology, size quantization effect and photocatalytic properties of CdS Q-nanocrystals,” *Science China Chemistry B*, vol. 46, no. 2, pp. 196–206, 2003.
- [11] L. E. Brus, “A simple model for the ionization potential, electron affinity, and aqueous redox potentials of small semiconductor crystallites,” *The Journal of Chemical Physics*, vol. 79, no. 11, pp. 5566–5572, 1983.
- [12] L. E. Brus, “Electron-electron and electron-hole interactions in small semiconductor crystallites: the size dependence of the lowest excited electronic state,” *The Journal of Chemical Physics*, vol. 80, no. 9, pp. 4403–4409, 1984.
- [13] A. Henglein, “Small-particle research: physicochemical properties of extremely small colloidal metal and semiconductor particles,” *Chemical Reviews*, vol. 89, no. 8, pp. 1861–1873, 1989.
- [14] H. Weller, “Colloidal semiconductor Q-particles: chemistry in the transition region between solid state and molecules,” *Angewandte Chemie*, vol. 32, no. 1, pp. 41–53, 1993.
- [15] E. Lifshitz, I. Dag, I. Litvin et al., “Optical properties of CdSe nanoparticle films prepared by chemical deposition and sol-gel methods,” *Chemical Physics Letters*, vol. 288, no. 2–4, pp. 188–196, 1998.

- [16] B. Bhattacharjee, D. Ganguli, S. Chaudhuri, and A. K. Pal, "Synthesis and optical characterization of sol-gel derived zinc sulphide nanoparticles confined in amorphous silica thin films," *Materials Chemistry and Physics*, vol. 78, no. 2, pp. 372–379, 2003.
- [17] Y. Li, F. Huang, Q. Zhang, and Z. Gu, "Solvothermal synthesis of nanocrystalline cadmium sulfide," *Journal of Materials Science*, vol. 35, no. 23, pp. 5933–5937, 2000.
- [18] Q. Lu, F. Gao, and D. Zhao, "The assembly of semiconductor sulfide nanocrystallites with organic reagents as templates," *Nanotechnology*, vol. 13, no. 6, pp. 741–745, 2002.
- [19] Y. Yin, X. Xu, X. Ge, Y. Lu, and Z. Zhang, "Synthesis and characterization of ZnS colloidal particles via γ -radiation," *Radiation Physics and Chemistry*, vol. 55, no. 3, pp. 353–356, 1999.
- [20] M. Shao, Q. Li, B. Xie, J. Wu, and Y. Qian, "The synthesis of CdS/ZnO and CdS/Pb₃O₄ composite materials via microwave irradiation," *Materials Chemistry and Physics*, vol. 78, no. 1, pp. 288–291, 2003.
- [21] I. W. Hamley, "Nanostructure fabrication using block copolymers," *Nanotechnology*, vol. 14, no. 10, pp. R39–R54, 2003.
- [22] M. Moffitt, H. Vali, and A. Eisenberg, "Spherical assemblies of semiconductor nanoparticles in water-soluble block copolymer aggregates," *Chemistry of Materials*, vol. 10, no. 4, pp. 1021–1028, 1998.
- [23] J. Zhang, S. Xu, and E. Kumacheva, "Polymer microgels: reactors for semiconductor, metal, and magnetic nanoparticles," *Journal of the American Chemical Society*, vol. 126, no. 25, pp. 7908–7914, 2004.
- [24] D. Mandal and U. Chatterjee, "Synthesis and spectroscopy of CdS nanoparticles in amphiphilic diblock copolymer micelles," *Journal of Chemical Physics*, vol. 126, no. 13, Article ID 134507, 8 pages, 2007.
- [25] T. F. Towey, A. Khan-Lodhi, and B. H. Robinson, "Kinetics and mechanism of formation of quantum-sized cadmium sulphide particles in water-Aerosol-OT-oil microemulsions," *Journal of the Chemical Society, Faraday Transactions*, vol. 86, no. 22, pp. 3757–3762, 1990.
- [26] A. Agostiano, M. Catalano, M. L. Curri, M. Della Monica, L. Manna, and L. Vasaneli, "Synthesis and structural characterisation of CdS nanoparticles prepared in a four-components "water-in-oil" microemulsion," *Micron*, vol. 31, no. 3, pp. 253–258, 2000.
- [27] E. Caponetti, L. Pedone, D. Chillura Martino, V. Pantò, and V. Turco Liveri, "Synthesis, size control, and passivation of CdS nanoparticles in water/AOT/n-heptane microemulsions," *Materials Science and Engineering C*, vol. 23, no. 4, pp. 531–539, 2003.
- [28] P. S. Khiew, S. Radiman, N. M. Huang, and M. S. Ahmad, "Studies on the growth and characterization of CdS and PbS nanoparticles using sugar-ester nonionic water-in-oil microemulsion," *Journal of Crystal Growth*, vol. 254, no. 1–2, pp. 235–243, 2003.
- [29] P. S. Khiew, N. M. Huang, S. Radiman, and M. S. Ahmad, "Synthesis and characterization of conducting polyaniline-coated cadmium sulphide nanocomposites in reverse microemulsion," *Materials Letters*, vol. 58, no. 3–4, pp. 516–521, 2004.
- [30] I. Capek, "Preparation of metal nanoparticles in water-in-oil (w/o) microemulsions," *Advances in Colloid and Interface Science*, vol. 110, no. 1–2, pp. 49–74, 2004.
- [31] J. Eastoe, M. J. Hollamby, and L. Hudson, "Recent advances in nanoparticle synthesis with reversed micelles," *Advances in Colloid and Interface Science*, vol. 128–130, pp. 5–15, 2006.
- [32] C. Petit, T. K. Jain, F. Billouet, and M. P. Pileni, "Oil in water micellar solution used to synthesize CdS particles: structural study and photoelectron transfer reaction," *Langmuir*, vol. 10, no. 12, pp. 4446–4450, 1994.
- [33] M. A. López-Quintela, "Synthesis of nanomaterials in microemulsions: formation mechanisms and growth control," *Current Opinion in Colloid & Interface Science*, vol. 8, no. 2, pp. 137–144, 2003.
- [34] P. D. I. Fletcher, A. M. Howe, and B. H. Robinson, "The kinetics of solubilisation exchange between water droplets of a water-in-oil microemulsion," *Journal of the Chemical Society, Faraday Transactions 1*, vol. 83, no. 4, pp. 985–1006, 1987.
- [35] M. J. Suarez, H. Lévy, and J. Lang, "Effect of addition of polymer to water-in-oil microemulsions on droplet size and exchange of material between droplets," *Journal of Physical Chemistry*, vol. 97, no. 38, pp. 9808–9816, 1993.
- [36] D. Papoutsis, P. Lianos, and W. Brown, "Interaction of polyethylene glycol with water-in-oil microemulsions. 3. Effect of polymer size and polymer concentration," *Langmuir*, vol. 10, no. 10, pp. 3402–3405, 1994.
- [37] P. Lianos, S. Modes, G. Staikos, and W. Brown, "Interaction of poly(oxyethylene glycol) with cyclohexane-pentanol-sodium dodecyl sulfate water-in-oil microemulsions," *Langmuir*, vol. 8, no. 4, pp. 1054–1059, 1992.
- [38] A. Kabalnov, U. Olsson, K. Thuresson, and H. Wennerström, "Polymer effects on the phase equilibrium of a balanced microemulsion: adsorbing versus nonadsorbing polymers," *Langmuir*, vol. 10, no. 13, pp. 4509–4513, 1994.
- [39] C. González-Blanco, L. J. Rodríguez, and M. M. Velázquez, "Effect of the addition of water-soluble polymers on the structure of aerosol OT water-in-oil microemulsions: a fourier transform infrared spectroscopy study," *Langmuir*, vol. 13, no. 7, pp. 1938–1945, 1997.
- [40] M. J. Suarez and J. Lang, "Effect of addition of water-soluble polymers in water-in-oil microemulsions made with anionic and cationic surfactants," *Journal of Physical Chemistry*, vol. 99, no. 13, pp. 4626–4631, 1995.
- [41] W. Meier, "Poly(oxyethylene) adsorption in water/oil microemulsions: a conductivity study," *Langmuir*, vol. 12, no. 5, pp. 1188–1192, 1996.
- [42] J. Appell, C. Ligoure, and G. Porte, "Bending elasticity of a curved amphiphilic film decorated with anchored copolymers: a small angle neutron scattering study," *Journal of Statistical Mechanics*, vol. 2004, Article ID P08002, 2004.
- [43] K. C. Tam and E. Wyn-Jones, "Insights on polymer surfactant complex structures during the binding of surfactants to polymers as measured by equilibrium and structural techniques," *Chemical Society Reviews*, vol. 35, no. 8, pp. 693–709, 2006.
- [44] A. Shioi, M. Harada, M. Obika, and M. Adachi, "Structure and properties of fluids composed of polyelectrolyte and ionic surfactant in organic phase: poly(acrylic acid) and didodecyldimethylammonium bromide," *Langmuir*, vol. 14, no. 17, pp. 4737–4743, 1998.
- [45] M. Fechner, M. Kramer, E. Kleinpeter, and J. Koetz, "Polyampholyte-modified ionic microemulsions," *Colloid and Polymer Science*, vol. 287, no. 10, pp. 1145–1153, 2009.
- [46] M. Fechner and J. Koetz, "Polyampholyte-surfactant film tuning in reverse microemulsions," *Langmuir*, vol. 27, no. 9, pp. 5316–5323, 2011.
- [47] C. Note, S. Kosmella, and J. Koetz, "Structural changes in poly(ethyleneimine) modified microemulsion," *Journal of Colloid and Interface Science*, vol. 302, no. 2, pp. 662–668, 2006.
- [48] A. H. Poghosyan, L. H. Arsenyan, H. H. Gharabekyan, S. Falkenhagen, J. Koetz, and A. A. Shahinyan, "Molecular

- dynamics simulations of inverse sodium dodecyl sulfate (SDS) micelles in a mixed toluene/pentanol solvent in the absence and presence of poly(diallyldimethylammonium chloride) (PDADMAC)," *Journal of Colloid and Interface Science*, vol. 358, no. 1, pp. 175–181, 2011.
- [49] J. Koetz, J. Bahnemann, G. Lucas, B. Tiersch, and S. Kosmella, "Polyelectrolyte-modified microemulsions as new templates for the formation of nanoparticles," *Colloids and Surfaces A*, vol. 250, no. 1–3, pp. 423–430, 2004.
- [50] J. Koetz, J. Baier, and S. Kosmella, "Formation of zinc sulfide and hydroxylapatite nanoparticles in polyelectrolyte-modified microemulsions," *Colloid and Polymer Science*, vol. 285, no. 15, pp. 1719–1726, 2007.
- [51] J. Baier, J. Koetz, S. Kosmella, B. Tiersch, and H. Rehage, "Polyelectrolyte-modified inverse microemulsions and their use as templates for the formation of magnetite nanoparticles," *Journal of Physical Chemistry B*, vol. 111, no. 29, pp. 8612–8618, 2007.
- [52] C. Note, J. Koetz, L. Wattebled, and A. Laschewsky, "Effect of a new hydrophobically modified polyampholyte on the formation of inverse microemulsions and the preparation of gold nanoparticles," *Journal of Colloid and Interface Science*, vol. 308, no. 1, pp. 162–169, 2007.
- [53] J. Zhang, L. Sun, C. Liao, and C. Yan, "Size control and photoluminescence enhancement of CdS nanoparticles prepared via reverse micelle method," *Solid State Communications*, vol. 124, no. 1–2, pp. 45–48, 2002.
- [54] M. F. Nazar, O. Myakonkaya, S. S. Shah, and J. Eastoe, "Separating nanoparticles from microemulsions," *Journal of Colloid and Interface Science*, vol. 354, no. 2, pp. 624–629, 2011.
- [55] M. J. Hollamby, J. Eastoe, A. Chemelli et al., "Separation and purification of nanoparticles in a single step," *Langmuir*, vol. 26, no. 10, pp. 6989–6994, 2010.
- [56] B. Abécassis, F. Testard, and T. Zemb, "Gold nanoparticle synthesis in worm-like catanionic micelles: microstructure conservation and temperature induced recovery," *Soft Matter*, vol. 5, no. 5, pp. 974–978, 2009.
- [57] R. Zhang, J. Liu, J. He et al., "Organic reactions and nanoparticle preparation in Co²⁺-induced water/P104/p-xylene microemulsions," *Chemistry*, vol. 9, no. 10, pp. 2167–2172, 2003.
- [58] A. Salabat, J. Eastoe, A. Vesperinas, R. F. Tabor, and K. J. Muteh, "Photorecovery of nanoparticles from an organic solvent," *Langmuir*, vol. 24, no. 5, pp. 1829–1832, 2008.
- [59] J. F. Liu, R. Liu, Y. G. Yin, and G. B. Jiang, "Triton X-114 based cloud point extraction: a thermoreversible approach for separation/concentration and dispersion of nanomaterials in the aqueous phase," *Chemical Communications*, no. 12, pp. 1514–1516, 2009.
- [60] M. Tamborra, M. Striccoli, R. Comparelli, M. L. Curri, A. Petrella, and A. Agostiano, "Optical properties of hybrid composites based on highly luminescent CdS nanocrystals in polymer," *Nanotechnology*, vol. 15, no. 4, pp. S240–S244, 2004.
- [61] I. R. Collins, "Surface electrical properties of barium sulfate modified by adsorption of poly α , β aspartic acid," *Journal of Colloid and Interface Science*, vol. 212, no. 2, pp. 535–544, 1999.
- [62] D. H. Chen and Y. Y. Chen, "Synthesis of barium ferrite ultrafine particles by coprecipitation in the presence of polyacrylic acid," *Journal of Colloid and Interface Science*, vol. 235, no. 1, pp. 9–14, 2001.
- [63] J. Koetz, K. Gawlitza, and S. Kosmella, "Formation of organically and inorganically passivated CdS nanoparticles in reverse microemulsions," *Colloid and Polymer Science*, vol. 288, no. 3, pp. 257–263, 2010.
- [64] M. L. Curri, A. Agostiano, L. Manna et al., "Synthesis and characterization of CdS nanoclusters in a quaternary microemulsion the role of the cosurfactant," *Journal of Physical Chemistry B*, vol. 104, no. 35, pp. 8391–8397, 2000.
- [65] D. Patidar, K. Rathore, N. Saxena, K. Sharma, and T. Sharma, "Energy band gap studies of CdS nanomaterials," *Journal of Nano Research*, vol. 3, pp. 97–102, 2008.
- [66] T. Pons, H. T. Uyeda, I. L. Medintz, and H. Mattoussi, "Hydrodynamic dimensions, electrophoretic mobility, and stability of hydrophilic quantum dots," *Journal of Physical Chemistry B*, vol. 110, no. 35, pp. 20308–20316, 2006.

Research Article

Optical and Structural Properties of Silicon Nanocrystals Embedded in SiO_x Matrix Obtained by HWCVD

A. Coyopol, G. García-Salgado, T. Díaz-Becerril, H. Juárez, E. Rosendo, R. López, M. Pacio, J. A. Luna-López, and J. Carrillo-López

CIDS-ICUAP, Benemérita Universidad Autónoma de Puebla, 14 sur y Avenida San Claudio, Edif. 137, 72570 Puebla, PUE, Mexico

Correspondence should be addressed to A. Coyopol, acoyopol@gmail.com

Received 24 February 2012; Accepted 22 May 2012

Academic Editor: Grégory Guisbiers

Copyright © 2012 A. Coyopol et al. This is an open access article distributed under the Creative Commons Attribution License, which permits unrestricted use, distribution, and reproduction in any medium, provided the original work is properly cited.

The interest in developing optoelectronic devices integrated in the same silicon chip has motivated the study of Silicon nanocrystals (Si-ncs) embedded in SiO_x (nonstoichiometric silicon oxides) films. In this work, Si-ncs in SiO_x films were obtained by Hot Wire Chemical Vapor Deposition (HWCVD) at 800, 900, and 1000°C. The vibration modes of SiO_x films were determined by FTIR measurements. Additionally, FTIR and EDAX were related to get the proper composition of the films. Micro-Raman studies in the microstructure of SiO_x films reveal a transition from amorphous-to-nanocrystalline phase when the growth temperature increases; thus, Si-ncs are detected. Photoluminescence (PL) measurement shows a broad emission from 400 to 1100 nm. This emission was related with both Si-ncs and interfacial defects present in SiO_x films. The existence of Si-ncs between 3 and 6 nm was confirmed by HRTEM.

1. Introduction

It is known that bulk silicon is the dominant semiconductor material in microelectronics industry; however, limited to the development of optoelectronic devices due to be an indirect band-gap semiconductor.

Since the observation of intense photoluminescence from porous silicon (PS) at room temperature [1], properties of low dimensional silicon quantum structures have been a subject of extensive investigations [2, 3]. Silicon-based nanostructures have been published so far with the majority devoted to the optical properties of nanocrystalline silicon embedded in SiO_x films. Although the phenomenon of emission produced in the SiO_x films has not yet been satisfactorily explained, there are different theories about the origin of the PL, such as quantum confinement [4], siloxanes (Si₆O₃H₆) [5], surface defects by bonds (SiH₂)_x [6], and interfacial defects in networks Si/SiO_x [7–9]. The widely accepted theory is the Quantum confinement; this theory says that Si-ncs produce a change in the bands structure by increasing the width of the band-gap crystalline silicon and making the direct transitions possible.

SiO_x films are obtained by different growth techniques such as: Sputtering [10], ion-implantation [11], catalytic-CVD (Cat-CVD) [12], Plasma Enhanced Chemical Vapor Deposition (PECVD) [13], and HWCVD [14]. The SiO_x films grown by different techniques have interesting characteristics due to presence of large number of Si–Si bonds, which are subsequently ordered and, therefore, they can be considered as Si clusters embedded in SiO_x matrix. In most cases the Si clusters can be crystallized only under high temperature annealing [15, 16] to form Si-ncs. However, it is known that thermal annealing increases the technological cost because it requires both high temperatures and long annealing times on inert atmospheres.

In this paper, optical and structural properties of SiO_x films are reported, we demonstrated the presence of Si-ncs in SiO_x films grown by HWCVD technique without using subsequent thermal process. The SiO_x films were characterized by FTIR (Fourier Transform Infrared), EDAX (Energy-Dispersive X-Ray Spectroscopy), Micro-Raman, PL, and HRTEM (High Resolution Transmission Electron Microscopy) techniques.

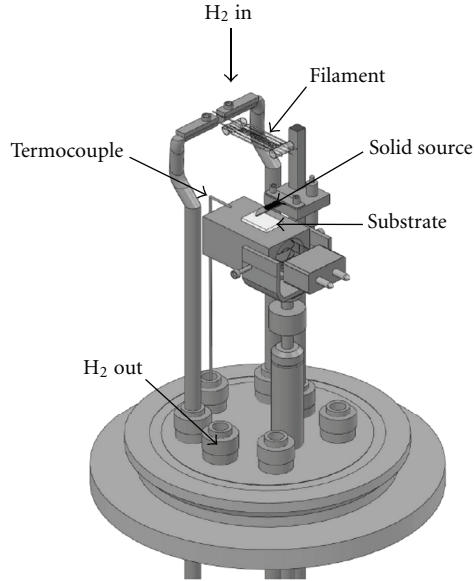


FIGURE 1: Detailed diagram of the HWCVD system.

2. Experimental Details

SiO_x films were synthesized in an HWCVD reactor at temperatures of 800, 900, and 1000°C, using a solid source of PS and atomic hydrogen.

The HWCVD technique involves the dissociation of molecular hydrogen using a hot filament at about 2000°C. To reach this temperature, measurements of applied voltage versus resistivity of tungsten filament are performed to obtain the voltage necessary (84.6 V) and keep a temperature of 2000°C during the process. The growth of SiO_x films by HWCVD is as follows: molecular hydrogen is introduced through the chamber with a constant flow of 20 sccm. A tungsten filament heated to 2000°C produces atomic hydrogen which reacts with a solid source of porous silicon. Gas precursors of Silane (SiH_4) and silicon monoxide (SiO) are generated and transported to the substrate forming SiO_x films.

The HWCVD technique used in this work, differs from conventional Cat-CVD; which consist in the thermal decomposition of reactant gases at the surface of a hot-filament heated at temperatures in the range of 1500–2000°C [12]. HWCVD produces its gaseous precursors from the interaction of atomic hydrogen and a solid source of PS or quartz. This peculiarity of the HWCVD technique makes it a potential alternative for the growth of SiO_x films.

The filament-source distance was kept constant at 3 mm, while the filament-substrate distance was 10 mm, 11.5 mm and 13.2 mm, to obtain a deposition temperature of 1000, 900, and 800°C, respectively. The growth time was 10 minutes for each sample. A detailed diagram of the HWCVD system is shown in Figure 1.

For the different optical and structural characterizations, SiO_x films were deposited on two types of substrates. Quartz was used for characterization of PL, HRTEM, Micro-Raman,

TABLE 1: Main bonds of the SiO_x films grown at different temperatures.

Vibration type	Vibration of SiO_x obtained in this work (cm^{-1})			Reference
	1000°C	900°C	800°C	
Si–O–Si rocking	450	452	448	[17]
Si–O–Si bending	800	801	798	[17]
Si–O–Si stretching	1080	1077	1066	[18]
SiH bending	878	880	881	[19]
SiH wagging	660	670	674	[20]

and silicon (n-type (100)) for FTIR and EDAX measurements. The substrates of silicon were carefully cleaned with an MOS standard cleaning process and the native oxide was removed with an HF buffer solution before being introduced into the reactor. PS layers used as solid sources were prepared by anodic etching a p-type Si (100) wafer, resistivity $\sim 0.04 \Omega\text{-cm}$, in a 40% HF and ethanol electrolyte (1:2).

FTIR absorbance measurements were performed on a Bruker Vector 22 spectrometer in the range 400 to 4000 cm^{-1} . The composition of the films was determined by EDAX and FTIR by using the relation $\text{SiO}_x \rightarrow a\text{Si} + b\text{SiO}_x$, where a , b are called the silicon separation coefficient and silicon oxide matrix coefficient, respectively.

Micro-Raman measurements were performed at room temperature by using a He-Ne laser (632.8 nm). A laser with a wavelength of 405 nm and 40 mW of power was used to excite the sample in PL measurements; the range detected by monochromator was from 400 to 1100 nm. Finally, a HRTEM FEI Tecnai F30 STWIN G2 was used to observe the presence of Si-ncs in SiO_x films.

3. Results and Discussions

Infrared absorption spectra of SiO_x films grown at 800, 900, and 1000°C on silicon substrates are shown in Figure 2(a). Characteristics bands of SiO_2 have been reported around 460, 800, and 1080 cm^{-1} . The main absorption peak around of 1080 cm^{-1} is associated with the Si–O–Si stretching mode, while those at 800 and 460 cm^{-1} correspond to bending and rocking modes, respectively. Results of infrared spectroscopy of films grown at different temperatures are shown in Table 1, where absorption peaks, their identifications, and references are recorded.

We observe that as the substrate temperature decreases (Table 1), the wavenumber of the main peak shifts from 1080 cm^{-1} (SiO_x , $x = 2$) to 1066 cm^{-1} (SiO_x , $x < 2$). According to the FTIR analysis of SiO_x films produced by PECVD [17], the silicon atoms have a higher probability of having one or more silicon atom neighbors, when $x < 2$.

In this way, it is likely that two phases coexist in the films; the silicon oxide (SiO_x) phase and another due to silicon bonds [21]. The shift observed in the stretching peak indicates phase separation in the films according to

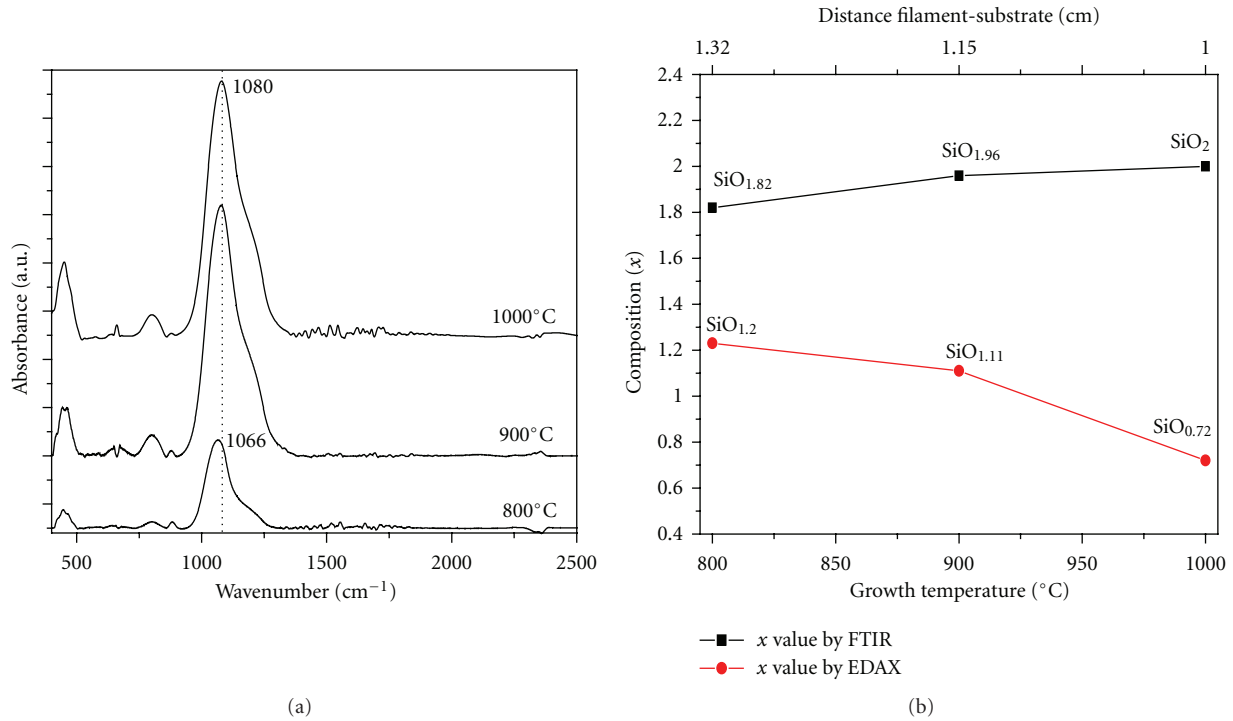


FIGURE 2: (a) Spectra FTIR of SiO_x films grown at different temperatures, (b) graphics composition of the silicon oxide phase obtained by FTIR and of the whole film found by EDAX.

TABLE 2: Composition data of the silicon oxide phase by FTIR and composition data of the whole film found by EDAX.

Growth temperature (°C)	Composition by EDAX	Composition of SiO _x phase by FTIR	Coefficient	
	<i>x</i>	<i>x</i>	<i>a</i>	<i>b</i>
800	1.2	1.82	0.34	0.65
900	1.11	1.96	0.43	0.56
1000	0.72	2	0.64	0.36

the variation in the x value. By FTIR spectroscopy the x value of the silicon oxide phase could be calculated by $x = (\nu - 918)/81$ [17], where ν is the shift Si–O–Si stretching frequency. From this result, we find the x value of the silicon oxide phase; $x = 2, 1.96,$ and 1.82 for the samples grown at 1000, 900, and 800°C respectively, these data are shown in Table 2. In general, we observe that the x value obtained by FTIR is close to silicon dioxide (SiO₂) stoichiometry value.

In order to determine the composition of the whole film, qualitative studies in the SiO_x films were done by EDAX. It was found a composition ratio ($x = O/Si$) of 1.23, 1.17, and 0.72 for samples grown at 800, 900, and 1000°C respectively (Table 2). It is important to mention that the EDAX results are for the whole film and the FTIR outcomes gives the composition of the silicon oxide phase only. The actual Si clusters and Si and oxygen of silicon oxide matrix were detected by EDAX measurement.

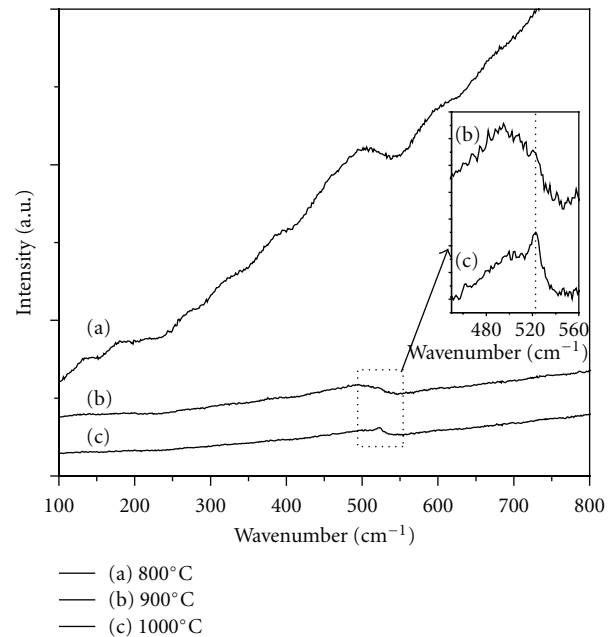


FIGURE 3: Micro-Raman of the films growth at 800, 900, and 1000°C.

EDAX studies reveal a high concentration of silicon as the filament-substrate distance decrease. The value of x decreases indicating an increase in the content of silicon as shown in Figure 2(b), where we plot the composition values of the silicon oxide phase obtained by FTIR and the composition of the whole film found by EDAX.

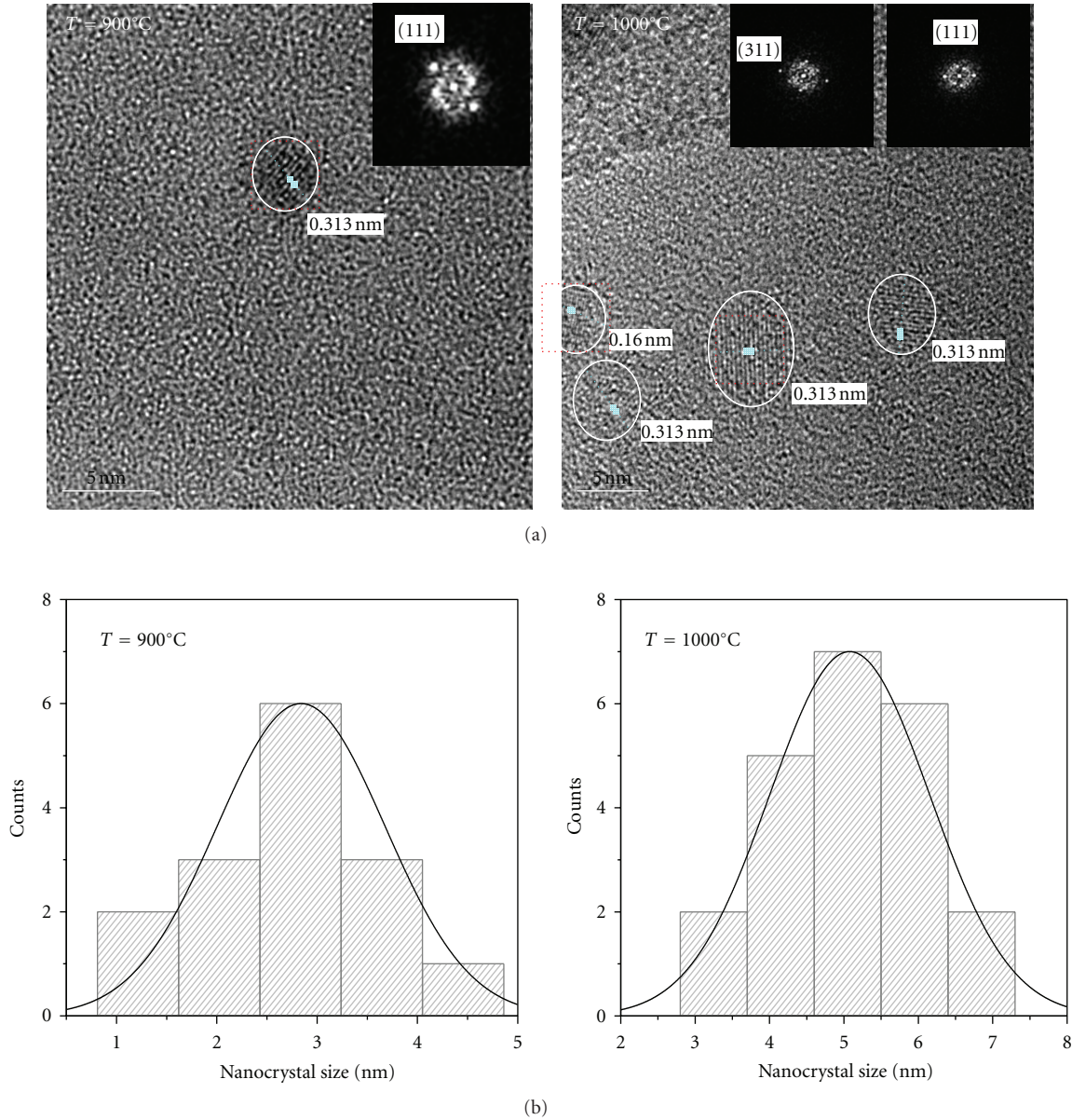


FIGURE 4: (a) HRTEM images of the samples grown at 900°C and 1000°C, (b) histograms corresponding to the samples grown at 900 and 1000°C.

Thus, it is suggested to have a mixture of two phases, using the relationship $\text{SiO}_x = a\text{Si} + b\text{SiO}_x$ for the composition of both silicon and silicon dioxide phases, we obtain coefficients a , b , which are called the silicon separation coefficient and silicon oxide matrix coefficient, respectively [22]. Coefficients a , b are shown in Table 2. We can deduce that the relatively high growth temperatures (800–1000°C) may induce diffusion of silicon atoms in silicon oxide structure, causing phase separation and the formation of silicon clusters embedded in a matrix of SiO_x . This way, for the film deposited at 800°C, it is gotten a composition of $\text{SiO}_{1.2} \rightarrow 0.34\text{Si} + 0.65\text{SiO}_{1.82}$.

Silicon clusters in amorphous phase or amorphous-nanocrystalline phase are found in SiO_x films. These

amorphous-nanocrystalline phases are detected by micro-Raman measurements. In Figure 3, micro-Raman spectra of the SiO_x films grown at 800, 900, and 1000°C; are presented. The spectrum of the sample grown at 800°C presents two bands around 180 cm^{-1} and 480 cm^{-1} . These bands are related to disorder-activated modes in amorphous silicon [23, 24]. For samples grown at 900 and 1000°C: a reduction in the amorphous bands takes place and a small peak appears at 521.84 cm^{-1} [25]. The peak centered around 521.84 cm^{-1} has a full width at half maximum (FWHM) of 6.58 cm^{-1} and 9.54 cm^{-1} for samples grown at 900 and 1000°C respectively; these peak shows the presence of Si-ncs, so the increase in substrate temperature helps to promote the phase of Si-ncs. This effect could be explained as follow:

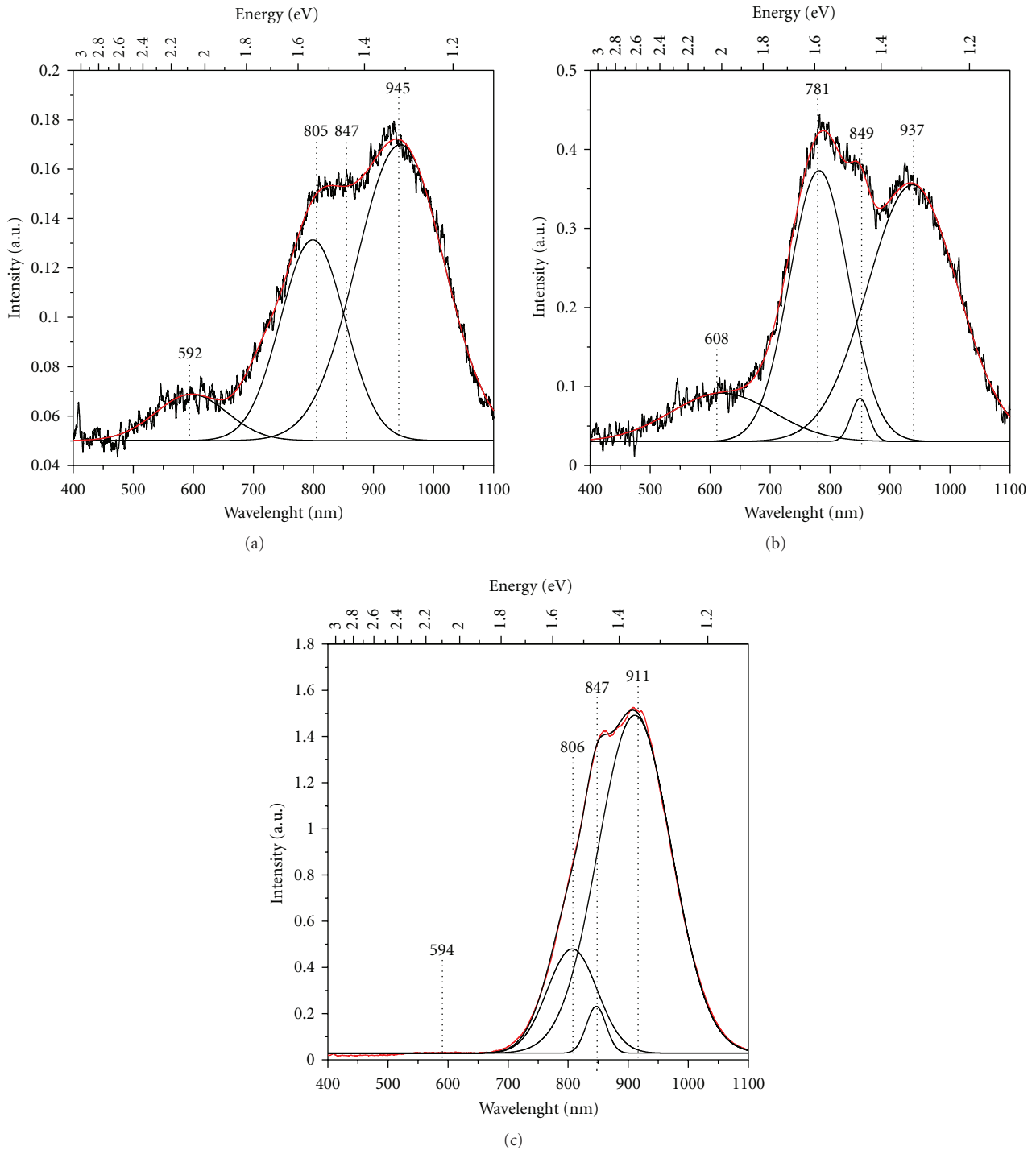


FIGURE 5: PL of SiO_x films grown at (a) 800°C , (b) 900°C , and (c) 1000°C .

we assume that high temperature induces diffusion of silicon to the formation of silicon clusters embedded in a matrix SiO_x , so while the process is taking place, exist an in situ annealing caused by the high growth temperature. Thus, when growth temperature significantly increases the clusters start to crystallize to form the Si-ncs.

It has been reported that crystallization of silicon clusters on annealing processes takes place at high temperatures

($1000\text{--}1300^\circ\text{C}$) [15, 16]. In the highlights of these SiO_x films obtained by HWCVD, the crystallization of silicon clusters was obtained at growth temperatures of 900°C as suggested the micro-Raman results.

Figure 4(a), shows the HRTEM images for samples grown at 900°C and 1000°C . HRTEM images confirmed the existence of Si-ncs with a mean square value about 5 nm. The average size found for sample grown at 900°C was 3 nm and

for sample grown at 1000°C varied between 3 and 6 nm as shown the histograms in Figure 4(b).

Amorphous silicon clusters detected by Micro-Raman cannot be observed by HRTEM, only silicon crystals of nanometer size are observed. For SiO_x films grown at 800°C, we suggest that the growth temperature is not enough to achieve crystallization in the silicon clusters. For films grown at 900 and 1000°C the silicon clusters begins to crystallize, suggesting the formation of a nanocrystalline core in silicon clusters. Thus, we proposed that silicon clusters consist in Si-ncs (nanocrystalline cores) surrounded by an amorphous silicon shell, where the size of the Si-ncs depends of the growth temperature. The formation of silicon clusters is carried out entirely by diffusion mechanism of silicon in SiO₂ [26]. This diffusion is dependent on growth temperature, so the higher growth temperature the diffusion of silicon atoms is higher and clusters should therefore be larger.

Nanocrystal lattice spacing in HRTEM images was estimated using the digital micrograph 3.7 software. Interplanar distances of 0.313, 0.16 nm were measured; these distances correspond to (111) and (311) planes of silicon [27]; respectively. Fast Fourier transform (FFT) of the selected area in the HRTEM images (red squares) produces a diffractogram, in which it was possible to determine the structure of the crystals formed (upper right side in Figure 4(a)).

PL measurements were performed at room temperature in a range of emission from 400 to 1100 nm. SiO_x films grown at 800, 900 and 1000°C show a broad PL emission from 450 to 1100 nm (Figure 5). Peaks around 600, 800, 847 and 930 nm are observed after applying the appropriate deconvolution. As is well known, several hypotheses have been proposed to explain the PL origin of Si-ncs in SiO_x films. Quantum confinement (QC) and the model that relates the PL with the presence of defects in the SiO₂/Si-ncs matrix and/or interface [7–9] are two of the main mechanisms responsible for efficient light emission from nano-sized structures based in silicon. In the SiO_x films grown by HWCVD, some interface defects may exist: the one between crystalline core and amorphous silicon shell and the one between silicon amorphous shell and the surrounding matrix (SiO_x).

Si-ncs observed by HRTEM are sufficiently small to observe QC effect. PL peaks at 600, 800, and 847 nm are generally attributed to the presence of silicon nanoparticles [28, 29]. However this does not exclude the possibility that defects such as Neutral Charged Oxygen Vacancies (NOV) (Si–Si bonds), No Bridging Oxygen Hole Center (NBOHC), positively charged oxygen vacancies (E_c-centers), interstitial oxygen molecules, and peroxide radicals [30–32] may be responsible for the PL, because the emissions are located in the same range of wavelengths.

The band emission in the infrared region with peak main at 930 nm is related to defects, this range of emissions is not allowed for emissions due to Si-ncs because there is a reduced likelihood of QC. There is a linear relation between the PL peak energy and the reciprocal of the square of crystallite size [33], Thus for an peak energy around 930 nm, it is likely estimated by the ratio $d^{-1.39}$ [31, 33] a diameter of the nanocrystal, $d > 5$ nm, which do not agree to the Bohr radius

of the bulk silicon (5 nm) [34], which is necessary for the quantum confinement.

We propose that both effects must be responsible for the phenomenon of PL; however a thorough study is needed to support these assumptions.

4. Conclusion

Silicon nanocrystals in a SiO_x matrix were synthesized by the HWCVD technique. Characteristic peaks of SiO₂ as well as peaks due to the presence of hydrogen are detected by FTIR. Using EDAX and FTIR characterization was obtained the composition of the SiO_x films, this composition is a mixture of two phases; a phase due to the silicon and the other phase due to silicon oxide. The crystallization temperature of silicon clusters occurs around 900 and 1000°C, this crystallization results in the formation of Si-ncs. It is proposed that the Si-ncs observed by HRTEM are surrounded by amorphous silicon. It is likely that the Si-ncs observed by HRTEM between 3 and 6 nm are responsible of the photoluminescence in films, however the Si-ncs should be surrounded by defects which cause part of the emission, so we proposed that both effects are producing the emission in SiO_x films.

Acknowledgments

A. Coyopol acknowledges the support received from CONACYT and ICUAP-BUAP. The authors would like to thank the technicians from IPYCIT HRTEM measurements performed.

References

- [1] L. T. Canham, “Silicon quantum wire array fabrication by electrochemical and chemical dissolution of wafers,” *Applied Physics Letters*, vol. 57, no. 10, article 1046, 3 pages, 1990.
- [2] P. M. Anbarasan, P. Senthilkumar, S. Manimegalai et al., “Spectral and morphological studies of nanocrystalline silicon thin films synthesized by PECVD for solar cells,” *Silicon*, vol. 2, no. 1, pp. 7–17, 2010.
- [3] C. D. Presti, A. Irrera, G. Franzó et al., “Photonic-crystal silicon-nanocluster light-emitting device,” *Applied Physics Letters*, vol. 88, no. 3, Article ID 033501, 3 pages, 2006.
- [4] D. J. Lockwood, “Optical properties of porous silicon,” *Solid State Communications*, vol. 92, no. 1-2, pp. 101–112, 1994.
- [5] M. S. Brandt, H. D. Fuchs, M. Stutzmann, J. Weber, and M. Cardona, “The origin of visible luminescence from “porous silicon”: a new interpretation,” *Solid State Communications*, vol. 81, no. 4, pp. 307–312, 1992.
- [6] J. F. Du, T. Wan, and B. Zhou, “Visible light emission at room temperature from PECVD a-Si:H:O,” *Journal of Non-Crystalline Solids*, vol. 164–166, no. 2, pp. 945–948, 1993.
- [7] H. Z. Song and X. M. Bao, “Visible photoluminescence from silicon-ion-implanted SiO₂ film and its multiple mechanisms,” *Physical Review B*, vol. 55, no. 11, pp. 6988–6993, 1997.
- [8] N. Daldosso, M. Luppi, S. Ossicini et al., “Role of the interface region on the optoelectronic properties of silicon nanocrystals embedded in SiO₂,” *Physical Review B*, vol. 68, no. 8, Article ID 085327, 2003.

- [9] H. Z. Song, X. M. Bao, N. S. Li, and J. Y. Zhang, "Relation between electroluminescence and photoluminescence of Si⁺-implanted SiO₂," *Journal of Applied Physics*, vol. 82, no. 8, Article ID 4028, 5 pages, 1997.
- [10] M. Zacharias and P. Streitenberger, "Crystallization of amorphous superlattices in the limit of ultrathin films with oxide interfaces," *Physical Review B*, vol. 62, no. 12, pp. 8391–8396, 2000.
- [11] T. Shimizu-Iwayama, S. Nakao, and K. Saitoh, "Visible photoluminescence in Si⁺-implanted thermal oxide films on crystalline Si," *Applied Physics Letters*, vol. 65, no. 14, pp. 1814–1816, 1994.
- [12] Y. Matsumoto, S. Godavarthi, M. Ortega, V. Sánchez, S. Velumani, and P. S. Mallick, "Size modulation of nanocrystalline silicon embedded in amorphous silicon oxide by Cat-CVD," *Thin Solid Films*, vol. 519, no. 14, pp. 4498–4501, 2011.
- [13] Z. X. Ma, X. B. Liao, J. He et al., "Annealing behaviors of photoluminescence from SiO_x:H," *Journal of Applied Physics*, vol. 83, no. 12, pp. 7934–7939, 1998.
- [14] P. Salazar, F. Chávez, F. Silva-Andrade, A. V. Ilinskii, N. Morales, and R. Peña-Sierra, "Photoluminescence from amorphous silicon oxide films prepared by HFCVD technique," *Modern Physics Letters B*, vol. 15, no. 17–19, pp. 756–759, 2001.
- [15] G. Franzó, M. Miritello, S. Boninelli et al., "Microstructural evolution of SiO_x films and its effect on the luminescence of Si nanoclusters," *Journal of Applied Physics*, vol. 104, no. 9, Article ID 094306, 5 pages, 2008.
- [16] D. Riabinina, C. Durand, J. Margot, M. Chaker, G. A. Botton, and F. Rosei, "Nucleation and growth of Si nanocrystals in an amorphous SiO₂ matrix," *Physical Review B*, vol. 74, no. 7, Article ID 075334, 7 pages, 2006.
- [17] P. G. Pai, S. S. Chao, Y. Takagi et al., "Infrared spectroscopic study of SiO_x films produced by plasma enhanced chemical vapor deposition," *Journal of Vacuum Science & Technology A*, vol. 4, no. 3, pp. 689–694, 1986.
- [18] H. J. Cheong, J. H. Kang, J. K. Kim et al., "Formation of luminescent Si nanocrystals by high-temperature rapid thermal chemical vapor deposition," *Applied Physics Letters*, vol. 83, no. 14, pp. 2922–2924, 2003.
- [19] Y. Fukuda, W. Zhou, K. Furuya, and H. Suzuki, "Photoluminescence change of as-prepared and aged porous silicon with NaOH treatment," *Journal of the Electrochemical Society*, vol. 146, no. 7, pp. 2697–2701, 1999.
- [20] N. Jeyakumaran, B. Natarajan, S. Ramamurthy, and V. Vasu, "Effect of nitrogen on optical properties of porous silicon," *Journal for Bloomers of Research*, vol. 2, no. 2, p. 116, 2010.
- [21] M. Molinari, H. Rinnert, and M. Vergnat, "Visible photoluminescence in amorphous SiO_x thin films prepared by silicon evaporation under a molecular oxygen atmosphere," *Applied Physics Letters*, vol. 82, no. 22, pp. 3877–3879, 2003.
- [22] C.-T. Lee, Y.-F. Chen, and C.-H. Lin, "Phase-separated Si nanoclusters from Si oxide matrix grown by laser-assisted chemical vapor deposition," *Nanotechnology*, vol. 20, no. 2, Article ID 025702, 2009.
- [23] R. Tubino, L. Piseri, and G. Zerbi, "Lattice dynamics and spectroscopic properties by a valence force potential of diamondlike crystals: C, Si, Ge, and Sn," *The Journal of Chemical Physics*, vol. 56, no. 3, pp. 1022–1039, 1972.
- [24] Y. Yang, L. Xu, F. Yang et al., "Enhanced visible photoluminescence from nc-Si/SiO_x films deposited by electron beam evaporation," *Journal of Non-Crystalline Solids*, vol. 356, no. 50–51, pp. 2790–2793, 2010.
- [25] S. Hernández, A. Martínez, P. Pellegrino et al., "Silicon nanocluster crystallization in SiO_x films studied by Raman scattering," *Journal of Applied Physics*, vol. 104, no. 4, Article ID 044304, 5 pages, 2008.
- [26] L. A. Nesbit, "Annealing characteristics of Si-rich SiO₂ films," *Applied Physics Letters*, vol. 46, no. 1, pp. 38–40, 1985.
- [27] W. F. McClune, Ed., *Powder Diffraction File*, International Centre for Diffraction Data, Newtown Square, Pa, USA, 2006.
- [28] X. Y. Chen, Y. F. Lua, L. J. Tang et al., "Annealing and oxidation of silicon oxide films prepared by plasma-enhanced chemical vapor deposition," *Journal of Applied Physics*, vol. 97, no. 1, Article ID 014913, 10 pages, 2005.
- [29] H. Takagi, H. Owada, Y. Yamazaki, A. Ishizaky, and T. Nakagiri, "Quantum size effects on photoluminescence in ultrafine Si particles," *Applied Physics Letters*, vol. 56, no. 24, p. 2379, 1990.
- [30] T. Inokuma, Y. Wakayama, T. Muramoto, R. Aoki, Y. Kurata, and S. Hasegawa, "Optical properties of Si clusters and Si nanocrystallites in high-temperature annealed SiO_x films," *Journal of Applied Physics*, vol. 83, no. 4, pp. 2228–2234, 1998.
- [31] G.-R. Lin, C.-J. Lin, C.-K. Lin et al., "Oxygen defect and Si nanocrystal dependent white-light and near-infrared electroluminescence of Si-implanted and plasma-enhanced chemical-vapor deposition-grown Si-rich SiO₂," *Journal of Applied Physics*, vol. 97, no. 9, Article ID 094306, 8 pages, 2005.
- [32] A. Morales-Sánchez, J. Barreto, C. Domínguez, M. Aceves, Z. Yu, and J. A. Luna López, "Charge trapping and de-trapping in Si-nanoparticles embedded in silicon oxide films," *Physica Status Solidi C*, vol. 5, no. 12, pp. 3651–3654, 2008.
- [33] C. Delerue, G. Allan, and M. Lannoo, "Theoretical aspects of the luminescence of porous silicon," *Physical Review B*, vol. 48, no. 15, pp. 11024–11036, 1993.
- [34] C. Kittel, *Introduction to Solid State Physics*, John Wiley & Sons, New York, NY, USA, 1986.

Research Article

Nanomechanics of Nonideal Single- and Double-Walled Carbon Nanotubes

C. H. Wong and V. Vijayaraghavan

School of Mechanical and Aerospace Engineering, Nanyang Technological University, 50 Nanyang Avenue, Singapore 639798

Correspondence should be addressed to C. H. Wong, chwong@ntu.edu.sg

Received 24 March 2012; Accepted 12 June 2012

Academic Editor: Leonard Deepak Francis

Copyright © 2012 C. H. Wong and V. Vijayaraghavan. This is an open access article distributed under the Creative Commons Attribution License, which permits unrestricted use, distribution, and reproduction in any medium, provided the original work is properly cited.

The buckling characteristics of nonideal single- and double-walled carbon nanotubes were studied in this work via molecular dynamics simulation method. An imperfectly straight nonideal single-walled carbon nanotube (SWCNT) with a bent along the tube axis was used to form an array which is subjected to compression. The change in orientation of bends will result in a variation of nonbonded interactions in an SWCNT array system. We find that these variations in the nonbonded interactions strongly affect the buckling resistance of the SWCNT array. Similarly, a nonideal double-walled carbon nanotube (DWCNT) is constructed by varying the interlayer distance by introducing a center offset on the inner core SWCNT. The inclusion of offset along the tube axis in such nonideal DWCNT can enhance or deteriorate the mechanical qualities of the DWCNT under compression. Our numerical studies on nonideal CNT systems suggest a possibility of designing high-performing CNTs for applications involving fiber reinforcements.

1. Introduction

Carbon nanotubes (CNTs) have attracted a significant research interest in the academic and industry circles due to its remarkable characteristics [1]. Extensive application of CNTs has been in the field of structural engineering due to its high tensile strength [2–4]. Most investigations on the mechanical characteristics of CNTs have been performed theoretically by deploying continuum mechanics or molecular dynamics (MD) simulation technique. The release in strain energy of CNTs subjected to large deformations has been explained by making use of a continuum shell model proposed by Yacobson et al. [5]. The variation of the buckling load with the CNT diameter has been analyzed by Liew et al. [6]. The REBO potential was further modified to include the long-range effects to study the effect of van der Waal forces on the compressive strength of CNT by Che et al. [7]. Ru [8] developed an elastic double-shell model to describe the infinitesimal buckling of a double-walled carbon nanotube (DWCNT). A systematic analysis on the buckling of multiwalled CNT (MWCNT) under radial pressure was investigated by Wang et al. [9]. They

introduced an approximate method to replace MWCNT by few layered elastic shell. The effect of boundary conditions on the buckling behavior of MWCNTs has been studied by Tong et al. [10]. They found that clamping the outermost CNT in an MWCNT can enhance the critical strain up to four times the original value. The buckling of DWCNTs subjected to torsion or compression has been studied by Lu et al. [11]. They developed a continuum model to account for the van der Waals interactions that act in between the layers of the DWCNT. The effect of tube radius on the critical buckling load of a MWCNT has been investigated by He et al. [12]. They derived explicit formulas to describe the interlayer van der Waals interaction in an MWCNT. A molecular structural mechanics approach was utilized to explain the elastic buckling behavior of carbon nanotubes by Li and Chou [13]. The results from this study indicate the improvement in the critical axial compressive load of a double-walled CNT (DWCNT) to that of a single-walled CNT (SWCNT). Though all the previously mentioned studies suggest superior mechanical qualities of CNTs, the observed mechanical strengths [14, 15] are always lower than the theoretical predictions. This observation is attributed

mainly due to the poor load transfer in between the layers of the MWCNT [16] and those of the interspatial layers in a CNT bundle [14]. We further need to note that the fabricated CNTs [17] are seldom perfectly straight in the laboratory conditions resulting in its nonideal nature. The effect of these curvatures on the elastic properties of CNTs with large aspect ratio can never be ignored [18]. In the first part of our present study, we report the elastic properties of a nonideal SWCNT array comprising long imperfectly straight SWCNTs [18] with a single bent along the tube axis. We find that the buckling characteristics are strongly affected by the interspatial distance of the SWCNT array due to the variations in arranging a bent orientation. Based on this understanding, we define a nonideal DWCNT in which the center core SWCNT is arranged at an offset distance to the outer SWCNT. MD simulation technique is employed to investigate the buckling characteristics of the nonideal DWCNT. The results clearly indicate that the resistance to buckling in a DWCNT arises mainly from the interlayer van der Waals interactions which are strongly influenced by the interlayer spacing. It should further be noted that close spacing of the adjacent CNT layers in a nonideal MWCNT introduces cross-links [19] which enhance the interwall shear strength. Liew et al. [20] performed buckling analysis of abnormal MWCNT by deploying a multishell continuum model with a refined van der Waal force model. Their investigations revealed that the effect of the van der Waals interaction is more significant for abnormal MWCNT than for normal MWCNT. Additionally, Song et al. [21] performed numerical simulation analysis to investigate the torsional responses of an abnormal MWCNT. They found that the critical torsional moments of DWCNTs are considerably enhanced due to the abnormal interlayer spacing of the CNT. Their results were significant due to the fact that the critical torsional moment does not always increase with decrease in the interlayer distance of DWCNTs. Zhang et al. [22] proposed a computer simulation model of novel DWCNTs with an interlayer distance of less than 3.4 Å with improved compressive stability. The MD studies on DWCNTs with abnormal interlayer distances by Song and Zhi [23] further confirmed that the small interlayer spacing provides an effective channel for load transfer of outer and inner tubes and permits mechanical participation of two walls. Therefore, an optimum design of the interlayer spacing in a DWCNT will result in a superior mechanical performance. We would however like to remark that the current study aims to propose only a numerical model of nonideal DWCNT, and its fabrication method still needs to be investigated. The following section presents the computational model employed in our current work. The studies on the compressive characteristics of SWCNT array are described next followed by our research on the DWCNT. Finally we summarized our findings in the conclusion section.

2. Numerical Simulation and Model

In the current study, the interatomic forces that act in between the covalently bonded carbon atoms of the CNT were computed using the Brenner's second generation

reactive empirical bond order function [25]. The long range Lennard-Jones 12–6 potential [26] is further deployed to account for the non-bonded interactions in an SWCNT array and the DWCNT. The mathematical representation of the previously mentioned potentials is given as

$$E_{\text{REBO}} = V_R(r_{ij}) - b_{ij}V_A(r_{ij}), \quad (1)$$

where the repulsive and attractive pair terms are given by V_R and V_A , respectively. The b_{ij} term is used to include the reactive empirical bond order between the atoms. And the Lennard-Jones (12–6) potential is given as

$$E_{\text{LJ}} = 4\varepsilon \left[\left(\frac{\sigma}{r_{ij}} \right)^{12} - \left(\frac{\sigma}{r_{ij}} \right)^6 \right], \quad (2)$$

where $\varepsilon = 4.55$ meV which is the well depth parameter and $\sigma = 3.4$ Å is the collision diameter between two atoms [27].

The complete form of the potential employed is therefore given by

$$E_{\text{CNT}} = E_{\text{REBO}} + E_{\text{vdW}}. \quad (3)$$

The contribution due to the van der Waals interaction (E_{vdW}) is accounted for when the covalent potential given by E_{REBO} becomes zero for bond lengths exceeding 2.0 Å. E_{vdW} is therefore defined as [28]

$$E_{\text{vdW}} = \begin{cases} 0, & r_{ij} \leq 2.0 \text{ \AA}, \\ c_{3,k}(r_{ij} - r_k)^3 + c_{2,k}(r_{ij} - r_k)^2, & 2.0 \text{ \AA} < r_{ij} \leq 3.2 \text{ \AA}, \\ E_{\text{LJ}}(r_{ij}), & 3.2 \text{ \AA} < r_{ij} \leq 10.0 \text{ \AA}, \end{cases} \quad (4)$$

where $c_{n,k}$ are the cubic spline coefficients for computation of the potential [28] when it turns repulsive when $2.0 \text{ \AA} < r_{ij} \leq 3.2 \text{ \AA}$.

The mechanical properties of the nonideal SWCNT and DWCNT were investigated using MD simulation. The simulation procedure consists of defining the initial positions of atoms after which it is subjected to relaxation using the potential model represented above to obtain the relaxed energy positions using conjugate gradient technique in an NVE ensemble. The carbon atoms at both ends of the system are fixed not to move in the plane normal to the tube axis and subjected to a finite inward displacement. The remaining atoms are subjected to relaxation after every 1000 time steps where the data is extracted. The procedure is repeated until the system buckles completely. This simulation consists of a total of 200,000 time steps with each time step equivalent to 1 fs.

3. Studies on SWCNT Array

3.1. Description of the Array System. It is evident from our previous study [18] that the critical compressive strain in a nonideal imperfectly straight SWCNT will depend strongly

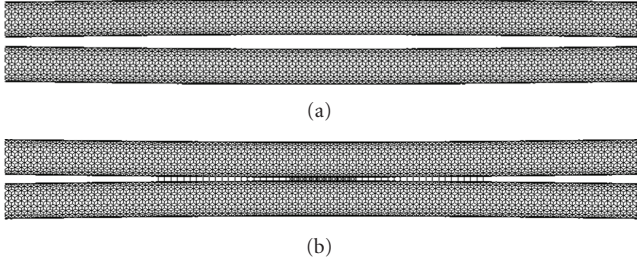


FIGURE 1: System of two “C” shaped CNTs arranged to form (a) a convex array and (b) a concave array.

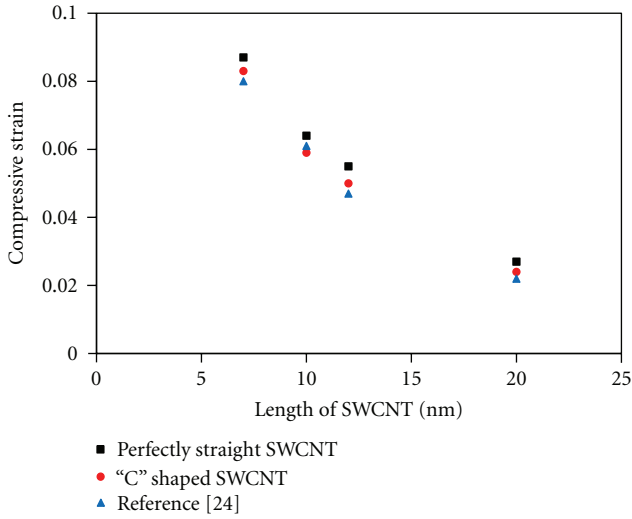


FIGURE 2: The variation in the compressive strain of the (16,0) SWCNT and its comparison with the virtual experiment results of [24].

on the number of bends present along the axis of CNT. As an extension, we have investigated the effect of bend orientation on the buckling properties of nonideal CNT array system comprising imperfectly straight SWCNTs. Using the same naming convention as in [18], we define an imperfectly straight (10,10) SWCNT with a single bent along its tube axis as a “C” shaped SWCNT with length $l = 245 \text{ \AA}$. Two sets of SWCNT array configurations are deployed and are hence described.

- (1) Array comprising two “C” shaped SWCNTs in which the bends face away from each other to form a convex system (referred to as convex array).
- (2) Array of two “C” shaped SWCNTs in which the bends face towards each other to form a concave system (represented as concave array).

The two “C” shaped SWCNTs are arranged with an interspatial gap of 3.4 \AA along the x -axis, with the array configuration illustrated in Figure 1.

The buckling characteristic of an SWCNT is considered first in our study. For this purpose, we chose a (16,0) SWCNT of “C” shaped and perfectly straight pristine configurations of various lengths. The variation in the compressive

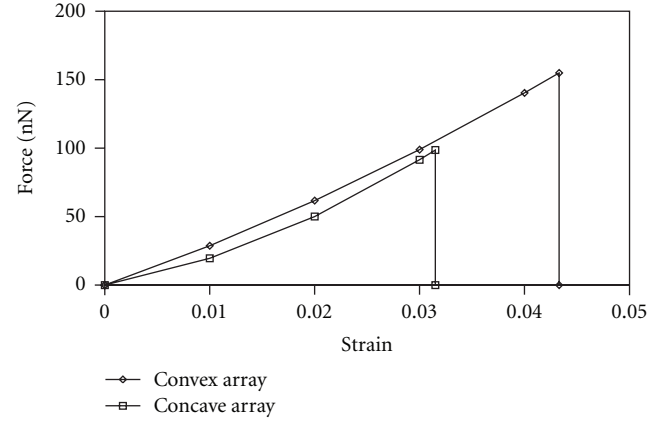


FIGURE 3: Force-strain plot of concave and convex SWCNT array.

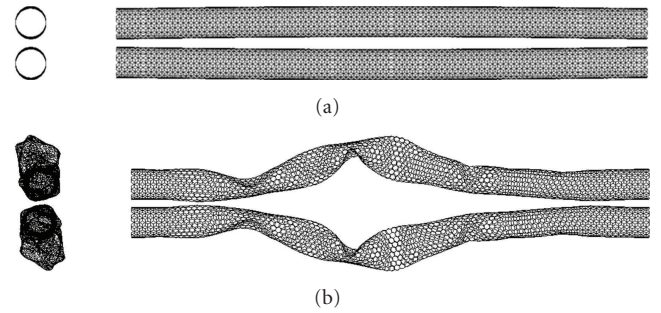


FIGURE 4: Morphological structural deformation of the convex array at (a) strain $\epsilon = 0.00$ and (b) at $\epsilon = 0.0433$.

strain of the SWCNT with length is depicted in Figure 2. We also compared the results with the virtual experiment results of the (16,0) SWCNT performed by Sears and Batra [24]. As described in [24], the virtual experiment follows a procedure that closely mimics traditional macroscopic material tests. It can be seen from Figure 2 that the variation in the compressive strain reduces due to the inclusion of a curvature along the tube axis. Additionally, this procedure also helps us to validate our simulation model as described in Section 2.

We commence our study on nonideal CNT array comprising imperfectly straight SWCNTs by investigating the buckling characteristics of the convex array. The force-strain plot of the array system deployed in the study is given in Figure 3. For the array in which the two “C” shaped SWCNTs form a convex arrangement, the critical buckling load that the system can withstand is $P_{cr} = 150 \times 10^{-9} \text{ N}$, and the corresponding critical strain value is $\epsilon = 0.0433$. This is certainly a much improved performance over the concaved system which buckles at $\epsilon = 0.0315$. The load-carrying capacity of the system is $P_{cr} = 97 \times 10^{-9} \text{ N}$, a reduction by about 33%. The morphological structural deformation of the convex and concave array is depicted in Figures 4 and 5, respectively.

3.2. Discussion. The simulation results of the array of imperfectly straight SWCNTs reveal that the buckling characteristics show a marked variation with which the bends

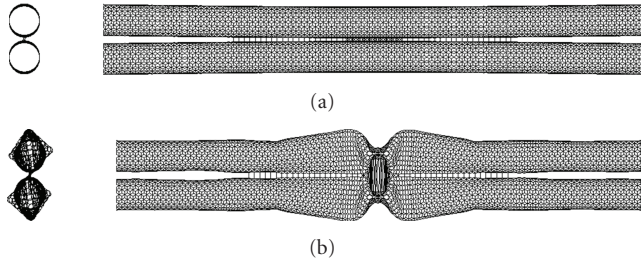


FIGURE 5: Morphological structural deformation of the concave array at (a) strain $\varepsilon = 0.00$ and (b) at $\varepsilon = 0.0315$.

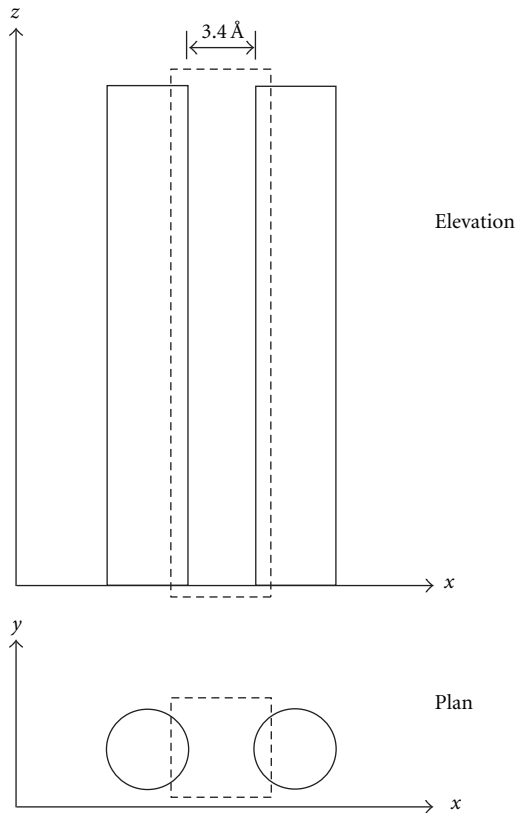


FIGURE 6: Measurement of the inter-tube van der Waals force component. The force components due to the van der Waals interaction are measured in between the atoms from adjacent facets of the SWCNTs in an array. This region is marked by the dashed rectangle. The interfacial spacing is at 3.4 \AA along the x axis.

are arranged. A quantitative explanation to the buckling behavior of the SWCNT array is explained by making use of the intertube van der Waals forces in the array system. This is due to the fact that in a system of CNT array or MWCNT, van der Waals interaction becomes a decisive component [18, 29, 30] that decides the mode of buckling.

The buckling load of a CNT array is increased due to the intertube van der Waals interaction by about $3.8 \sim 5.2\%$, as reported in [29]. This interactive force is measured by considering the reaction in between the atoms that belong to the adjacent opposite walls of the two “C” shaped SWCNTs that

face each other as indicated by the region enclosed within the dashed rectangle as shown in Figure 6. The intertube van der Waals force has three mutually perpendicular components directed along the x , y , and z direction respectively. We have considered only the x component of the force because the tube spacing is across the x -axis, and the force components along the y and z axis are negligible.

Figures 7 and 8 show the macroscopic view of the central interspatial region that separates the two “C” shaped CNTs for both the array systems considered in our study. We observe from the figure that for a convex array, due to the bends facing opposite direction, the interspatial distance will be greater than 3.4 \AA . Similarly, for the concave array the distance will be lesser than 3.4 \AA due to the bends facing each other. This variation in distance affects the interatomic distance in between the two adjacent facets as explained earlier, which in turn affects the inter-tube van der Waals forces. The x component of the inter-tube van der Waals force is denoted by F_x^{vdW} in our study. The relationship between F_x^{vdW} and the strain is depicted in Figure 9 for the convex and concave array systems. It can be seen from Figure 9 that the value of F_x^{vdW} for a convex array is always higher than that of the concave array. This shows a strong correlation between the van der Waals force and the interspatial distance that separates the two “C” shaped SWCNTs. We can also observe that near the point of critical strain, a steep drop in F_x^{vdW} is observed which indicates that the tube has buckled. It is evident that with the decrease in the van der Waals force, the strengthening effect of the SWCNT array becomes weaker, and it initiates buckling at that particular value of critical strain. Additionally, we also observe that the concave nature of arrangement in the CNT array results in the formation of inter-tube bonds to be formed. These inter-tube bonds are formed mainly due to the reduction in the C-C bond distance resulting in the formation of more sp^3 configuration bonds. These sp^3 bonds increase the strain energy of the concave array system (Figure 10) when compared to the convex array. This can be observed by the strain energy increase corresponding to the concave array system in Figure 10 for compressive strain value approaching the plastic limit. This increase in the internal strain energy causes the rapid failure under the application of compressive forces.

4. Studies on DWCNT

4.1. Description of the DWCNT System. It is evident from Section 3 that the variation in the interspatial distance strongly influences the nonbonded interaction. This in turn affects the elastic properties of a nonbonded CNT system. In this section, we aim to study the variation in the buckling characteristics of a DWCNT by varying the interlayer distance in between the two SWCNTs and hence resulting in a nonideal DWCNT. The DWCNT used in our study consists of a (10, 10) SWCNT nested inside a (15, 15) SWCNT of a shorter length $l = 98.5 \text{ \AA}$. Due to the shorter length, we assumed that the DWCNT is perfectly straight, that is, pristine. A schematic of the DWCNT system is given in Figure 11 where the interlayer region between the two

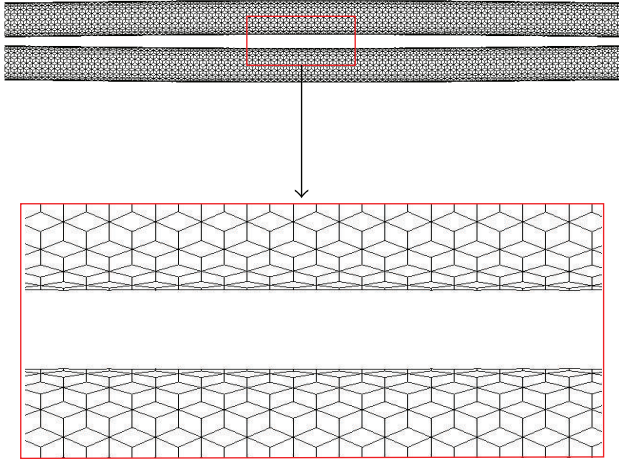


FIGURE 7: Illustration of the inter-tube spacing in the convex array. Even though the inter-spatial distance in between the tubes at both ends of the convex array is kept at 3.4 Å, the corresponding distance at the central region is greater than 3.4 Å.

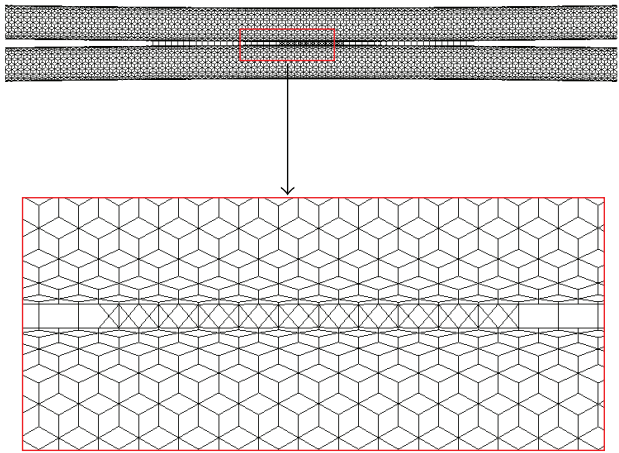


FIGURE 8: Illustration of the inter-tube spacing in a concave array. Atoms near the central region of a nonideal concave SWCNT array are more closely spaced resulting in the formation of C-C bonds.

SWCNTs in the top half is represented as region 1 and those in the bottom half as region 2. Three different classes of DWCNTs are deployed in our study, namely, classes “A,” “B” and “C.” The classification is based on the interlayer distance in region 1 and region 2 as given in Table 1. It should be noted from Table 1 that class “B” is an ideal DWCNT while classes “A” and “C” are categorized as nonideal DWCNTs with nonconcentric constituent SWCNTs. The class “B” DWCNT is equilibrated using conjugate gradient technique in an NVE ensemble. It should be noted that energy relaxation of class “A” and class “C” DWCNT will result in a concentric arrangement (i.e., class “B”). Hence to maintain the non-concentricity of class “A” and class “C” DWCNT structure, we did not perform any energy minimization operations and these two classes of DWCNTs are left as a pre-stressed structure before they were subjected to compression.

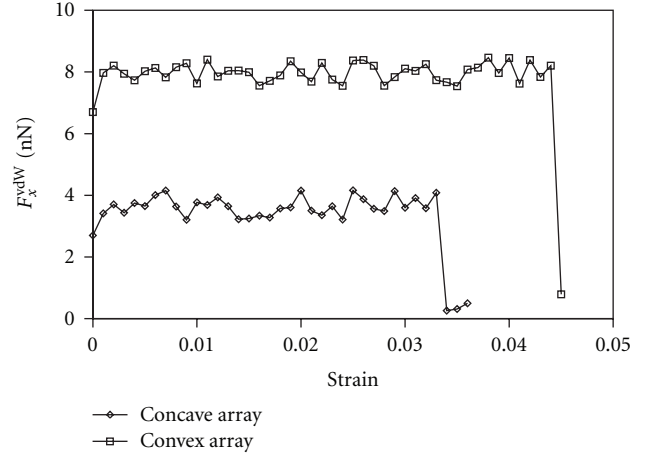


FIGURE 9: The inter-tube van der Waals force versus the strain acting across the inter-tube spacing between the atoms in the x -direction from adjacent facets of the convex and concave array systems.

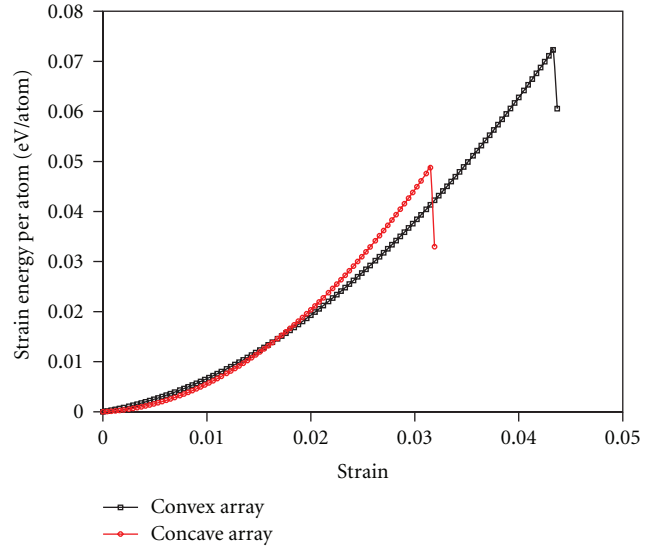


FIGURE 10: Strain energy per atom plot of the concave and convex array of (10, 10) SWCNT. Formation of inter-tube bonds in a concave array increases the strain energy of the concave array SWCNT system.

TABLE 1: Description of the classes of DWCNTs considered in our study classified based on the inter-layer distance in region 1 and region 2 as described in Figure 11.

DWCNT	Interlayer Distance (Å)	
	Region 1	Region 2
Class A	4.86	1.92
Class B	3.38	3.39
Class C	3.78	3.00

4.2. Results. The buckling characteristic of non-concentric DWCNTs is described by making use of the force-strain plot as depicted in Figure 12. From this plot we observe that the normal class “B” DWCNT is able to resist the compression

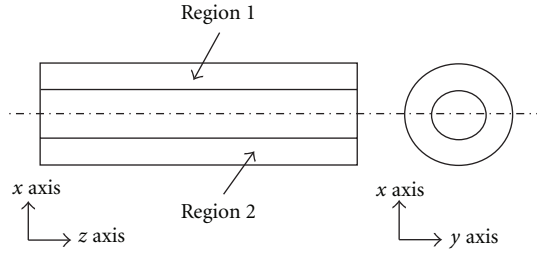


FIGURE 11: Schematic view of a DWCNT used in our study with the interlayer regions marked as region 1 and region 2.

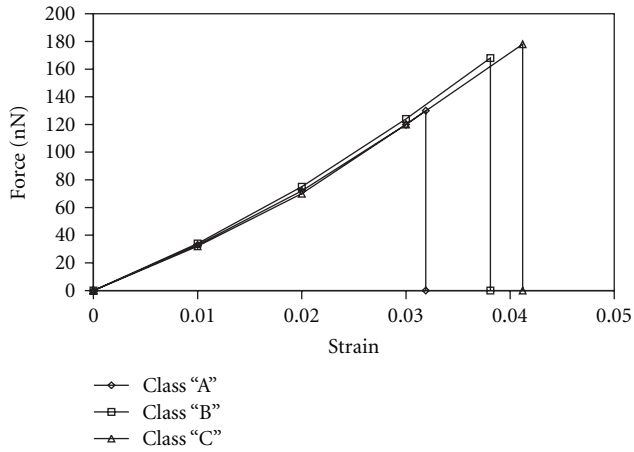


FIGURE 12: Force-strain plot of the DWCNT classes used in our study subjected to compression.

forces for an extended period compared to that of the class "A" DWCNT with abnormal interlayer distance. The critical buckling load of the class "B" DWCNT is 168 nN and its critical buckling strain is $\epsilon = 0.0381$. Superior elastic properties are observed in a class "C" DWCNT system which buckles at a critical buckling strain of $\epsilon = 0.0412$ and critical buckling load of 178 nN. The class "A" DWCNT exhibits the least resistance to the buckling when compared to class "B" and class "C" DWCNT systems and it buckles at a critical strain of $\epsilon = 0.0319$ with the critical buckling load of 130 nN. The morphological variations of the three classes of DWCNT under compression are depicted in Figure 13.

4.3. Discussion

4.3.1. Inter-Tube van der Waals Interaction. The variation in elastic properties of the three classes of DWCNTs can once again be explained by the non-bonded interactions that act in between the adjacent layers of the DWCNT. Since in our current study, the nesting of DWCNT is oriented along the x - y plane (Figure 11), we have considered the resultant of the x and y components of the van der Waals force that act in between the two component SWCNTs. Mathematically this resultant force is represented as F_{xy}^{vdW} . It is evident from the plot (Figure 14) that the magnitude of the inter-tube van der Waals force for the class "C" DWCNT is the highest which results in its superior performance under compression when

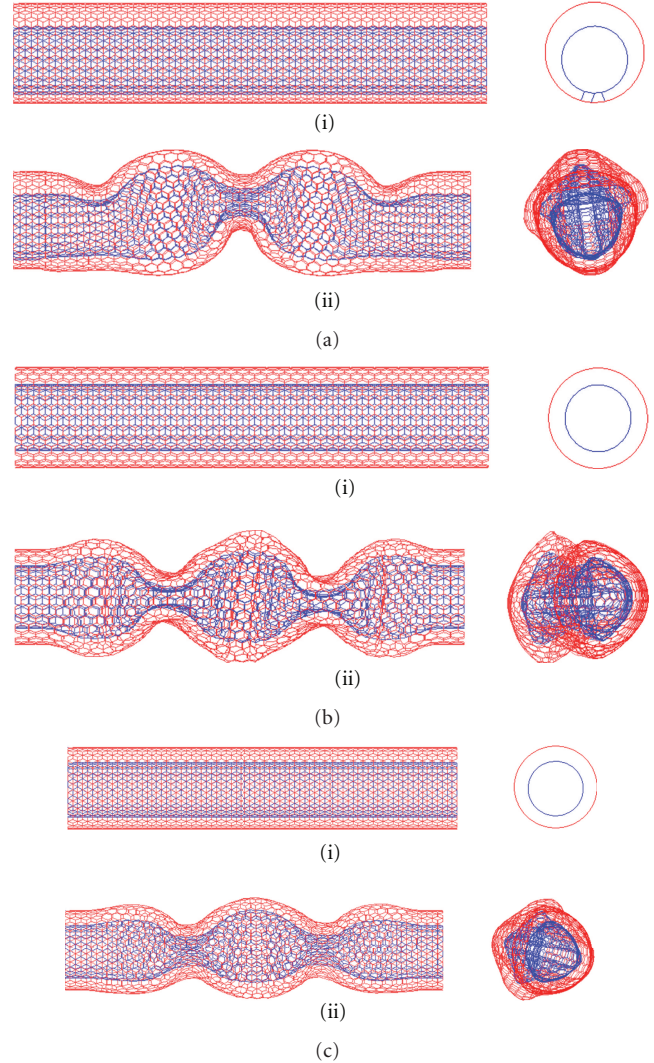


FIGURE 13: Morphological changes of the three classes of DWCNTs under buckling. (a) A class "A" DWCNT at (i) strain, $\epsilon = 0.0$, (ii) strain, $\epsilon = 0.0319$, (b) A class "B" DWCNT at (i) strain, $\epsilon = 0.0$, (ii) strain, $\epsilon = 0.0381$ and (c) A class "C" DWCNT at (i) strain, $\epsilon = 0.0$, (ii) strain, $\epsilon = 0.0412$.

compared to the class "A" and class "B" counterparts. Similar to what we observe in a CNT array system, a steep decrease in van der Waals forces indicate the onset of buckling. Resistance to buckling is affected by the stability of these non-bonded forces during the period of elasticity after which the DWCNT will buckle when the inter-tube van der Waals force becomes zero.

4.3.2. Interwall Separation. It is also useful to consider the effect of interwall spacing to describe the compressive behavior of the non-concentric DWCNTs. Since from Figure 11 the offset alignment is oriented across the x direction, let us focus on the x component of the inter-tube van der Waals forces that act in region 1 and region 2. These force components are denoted as $[F_x^{vdW}]_{\text{region1}}$ and $[F_x^{vdW}]_{\text{region2}}$, and the corresponding plots are given in Figures 15 and 16,

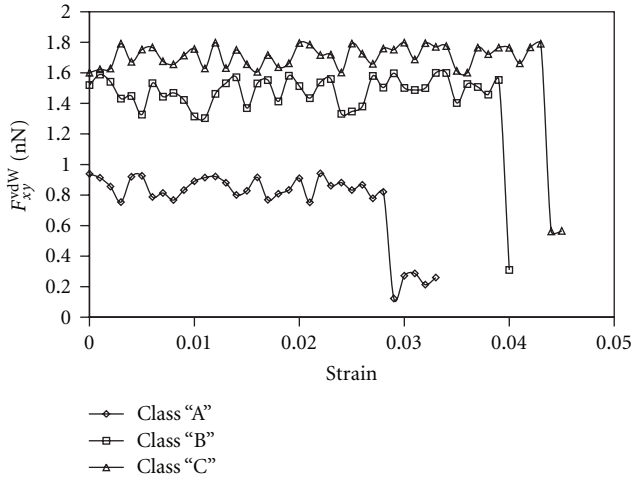


FIGURE 14: The resultant of the x and y components of the inter-tube van der Waals force acting across the inter-tube spacing between the atoms from adjacent layers of the inner (10, 10) SWCNT and the outer (15, 15) SWCNT.

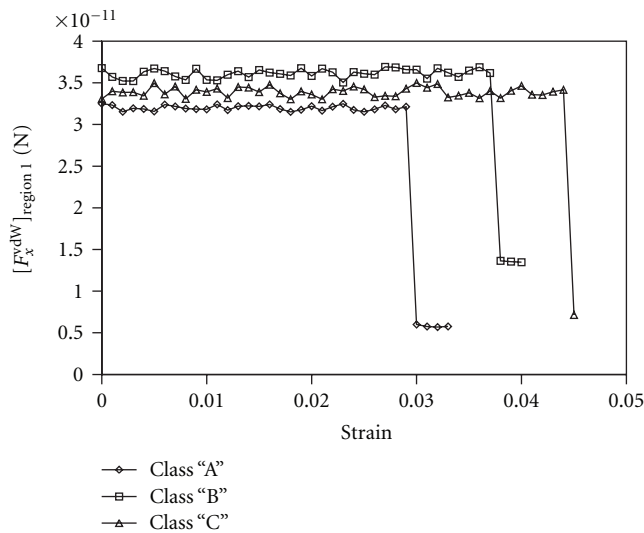


FIGURE 15: The x component of the inter-tube van der Waals force acting across the atoms from adjacent layers of the inner (10, 10) SWCNT and the outer (15, 15) SWCNT in the region 1 for the three classes of DWCNT considered in our study.

respectively. We note from (4) that the interlayer spacing in region 1 falls in between 3.2, and 10.0 Å, and the governing interaction is mainly due to the $E_{LJ}(r_{ij})$ term and this interactive potential decreases with increasing interatomic distance. Since the inter-layer spacing for the class “B” DWCNT in region 1 is the lowest for all three classes of DWCNT which is at about 3.4 Å, it exhibits a higher value of interactive van der Waals force in region 1.

It is interesting to observe the interaction forces in region 2 of all the three classes of DWCNT (Figure 16). The interlayer spacing of three classes of DWCNT in this region is distinct which will cause a functional variation in the interactive potential as described in (4). For a class “A”

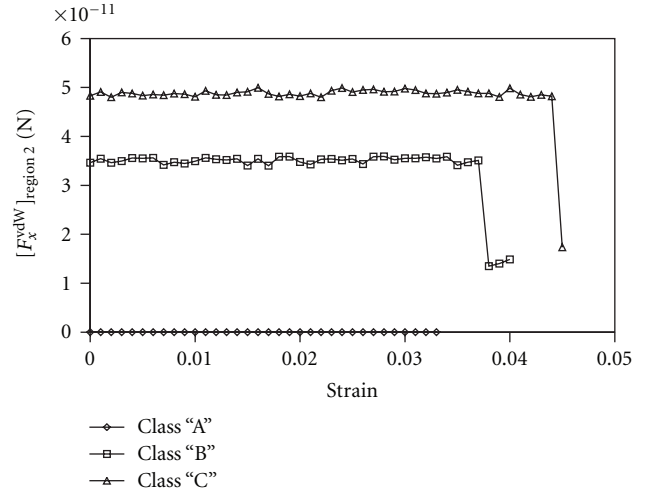


FIGURE 16: The x component of the inter-tube van der Waals force acting across the atoms from adjacent layers of the inner (10, 10) SWCNT and the outer (15, 15) SWCNT in the region 2 for the three classes of DWCNT considered in our study.

DWCNT in which the interlayer separation is below 2.0 Å, the value of $[F_x^{\text{vdW}}]_{\text{region2}}$ is zero. Since the resistance to buckling in a DWCNT is caused by the intertube van der Waals interaction, we can conclude that there is effectively no contribution to the resistive forces from the region 2 of the class “A” DWCNT which aids in its premature buckling. Furthermore, superior resistance to the buckling of a class “C” DWCNT is offered by the interaction forces from the region 2 which are spaced at 3.0 Å as described by the cubic spline polynomial in (4). A nominal performance is expected from the normal class “B” DWCNT where the interaction among the layers spaced at 3.4 Å is determined by the $E_{LJ}(r_{ij})$ term.

4.3.3. Strain Energy. Figure 17 shows the plot of strain energy per atom of the inside (10, 10) SWCNT in all three classes of DWCNT considered in our study. We can observe that until all three DWCNTs collapse due to compressive forces, the magnitude of strain energy per atom for the class “C” DWCNT is always smaller than the other two classes, namely, “A” and “B”. Furthermore, at the point of critical buckling strain, there is a sudden increase in strain energy for class “B” and class “C” DWCNT. This increase in strain energy is due to the spontaneous increase in potential energy of atoms in the DWCNT [6]. However, in the case of the class “A” DWCNT, a drop in strain energy is observed during buckling due to spontaneous plastic collapse [31]. This nature is due to the fact that the arrangement of class “A” DWCNT results in the formation of inter-tube bonds which are composed of sp^3 hybridized configuration. As explained in Section 3.2, we see that these inter-tube bonds play prominent role in increasing the strain energy of the class “A” DWCNT. Hence, we deduce from Figure 17 that application of compressive forces on a class “A” DWCNT will result in accelerated accumulation of strain energy that enhances the system instability leading to its premature failure.

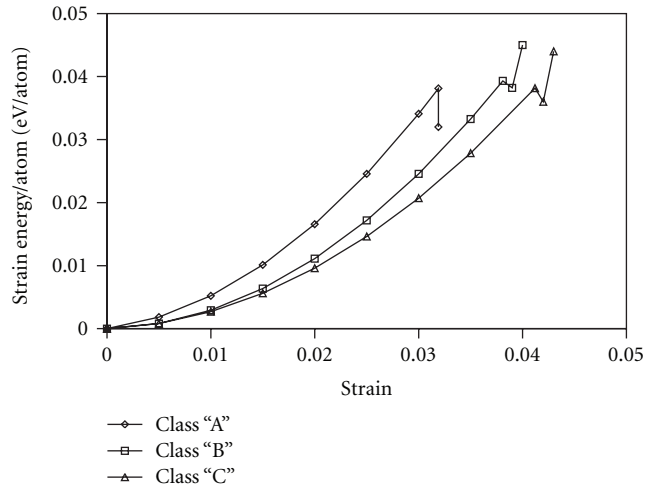


FIGURE 17: Plot of the strain energy per atom for the inside (10, 10) SWCNT in the three classes of DWCNT considered in our study.

5. Conclusion

We performed a theoretical investigation on the structural properties of the nonbonded CNT systems using molecular dynamics simulation technique. We constructed an array of two “C” shaped SWCNTs oriented in mutually opposite directions and reported a variation in the buckling characteristics. Our results show that these orientations affect the interspatial distance which in turn affects the nonbonded interactive forces in the adjacent facets of the CNT array. Resistance to buckling of an SWCNT array is caused due to the van der Waals forces which are explained quantitatively in our research. Similarly, our studies on the compressive characteristics of DWCNT also show the influence of the interlayer van der Waals forces to the compressive stability of the DWCNT. Suitable placement of the central SWCNT in a DWCNT system will result in enhanced mechanical performance as is evident from the buckling characteristics of the “class C” DWCNT. With recent developments in the fabrication process of carbon nanotubes, we hope that the findings obtained from this work may help in designing high-performing DWCNT and CNT array systems.

References

- [1] E. T. Thostenson, Z. Ren, and T. W. Chou, “Advances in the science and technology of carbon nanotubes and their composites: a review,” *Composites Science and Technology*, vol. 61, no. 13, pp. 1899–1912, 2001.
- [2] A. Krishnan, E. Dujardin, T. W. Ebbesen, P. N. Yianilos, and M. M. J. Treacy, “Young’s modulus of single-walled nanotubes,” *Physical Review B*, vol. 58, no. 20, pp. 14013–14019, 1998.
- [3] K. M. Liew, X. Q. He, and C. H. Wong, “On the study of elastic and plastic properties of multi-walled carbon nanotubes under axial tension using molecular dynamics simulation,” *Acta Materialia*, vol. 52, no. 9, pp. 2521–2527, 2004.
- [4] M. M. J. Treacy, T. W. Ebbesen, and J. M. Gibson, “Exceptionally high Young’s modulus observed for individual carbon nanotubes,” *Nature*, vol. 381, no. 6584, pp. 678–680, 1996.
- [5] B. I. Yakobson, C. J. Brabec, and J. Bernholc, “Nanomechanics of carbon tubes: instabilities beyond linear response,” *Physical Review Letters*, vol. 76, no. 14, pp. 2511–2514, 1996.
- [6] K. M. Liew, C. H. Wong, X. Q. He, M. J. Tan, and S. A. Meguid, “Nanomechanics of single and multiwalled carbon nanotubes,” *Physical Review B*, vol. 69, no. 11, Article ID 115429, 8 pages, 2004.
- [7] J. Che, T. Çağın, and W. A. Goddard, “Studies of fullerenes and carbon nanotubes by an extended bond order potential,” *Nanotechnology*, vol. 10, no. 3, pp. 263–268, 1999.
- [8] C. Q. Ru, “Axially compressed buckling of a doublewalled carbon nanotube embedded in an elastic medium,” *Journal of the Mechanics and Physics of Solids*, vol. 49, no. 6, pp. 1265–1279, 2001.
- [9] C. Y. Wang, C. Q. Ru, and A. Mioduchowski, “Axially compressed buckling of pressured multiwall carbon nanotubes,” *International Journal of Solids and Structures*, vol. 40, no. 15, pp. 3893–3911, 2003.
- [10] F. M. Tong, C. Y. Wang, and S. Adhikari, “Axial buckling of multiwall carbon nanotubes with heterogeneous boundaries,” *Journal of Applied Physics*, vol. 105, no. 9, Article ID 094325, 7 pages, 2009.
- [11] W. B. Lu, J. Wu, X. Feng, K. C. Hwang, and Y. Huang, “Buckling analyses of double-wall carbon nanotubes: a shell theory based on the interatomic potential,” *Journal of Applied Mechanics*, vol. 77, no. 6, Article ID 061016, 6 pages, 2010.
- [12] X. Q. He, S. Kitipornchai, and K. M. Liew, “Buckling analysis of multi-walled carbon nanotubes: a continuum model accounting for van der Waals interaction,” *Journal of the Mechanics and Physics of Solids*, vol. 53, no. 2, pp. 303–326, 2005.
- [13] C. Y. Li and T. W. Chou, “Modeling of elastic buckling of carbon nanotubes by molecular structural mechanics approach,” *Mechanics of Materials*, vol. 36, no. 11, pp. 1047–1055, 2004.
- [14] M. F. Yu, B. S. Files, S. Arepalli, and R. S. Ruoff, “Tensile loading of ropes of single wall carbon nanotubes and their mechanical properties,” *Physical Review Letters*, vol. 84, no. 24, pp. 5552–5555, 2000.
- [15] M. F. Yu, O. Lourie, M. J. Dyer, K. Moloni, T. F. Kelly, and R. S. Ruoff, “Strength and breaking mechanism of multiwalled carbon nanotubes under tensile load,” *Science*, vol. 287, no. 5453, pp. 637–640, 2000.
- [16] J. Cumings and A. Zettl, “Low-friction nanoscale linear bearing realized from multiwall carbon nanotubes,” *Science*, vol. 289, no. 5479, pp. 602–604, 2000.
- [17] S. Iijima and T. Ichihashi, “Erratum: single-shell carbon nanotubes of 1-nm diameter (Nature (1993) 363 (603-605)),” *Nature*, vol. 364, no. 6439, p. 737, 1993.
- [18] C. H. Wong and V. Vijayaraghavan, “Nanomechanics of imperfectly straight single walled carbon nanotubes under axial compression by using molecular dynamics simulation,” *Computational Materials Science*, vol. 53, no. 1, pp. 268–277, 2011.
- [19] A. J. R. da Silva, A. Fazzio, and A. Antonelli, “Bundling up carbon nanotubes through wigner defects,” *Nano Letters*, vol. 5, no. 6, pp. 1045–1049, 2005.
- [20] K. M. Liew, J. B. Wang, X. Q. He, and H. W. Zhang, “Buckling analysis of abnormal multiwalled carbon nanotubes,” *Journal of Applied Physics*, vol. 102, no. 5, Article ID 053511, 6 pages, 2007.
- [21] H. Y. Song, L. F. Li, and F. Feng, “Torsional behaviour of carbon nanotubes with abnormal interlayer distances,” *Journal of Physics D*, vol. 42, no. 5, Article ID 055414, 2009.

- [22] H. W. Zhang, L. Wang, and J. B. Wang, "Computer simulation of buckling behavior of double-walled carbon nanotubes with abnormal interlayer distances," *Computational Materials Science*, vol. 39, no. 3, pp. 664–672, 2007.
- [23] H. Y. Song and X. W. Zha, "Molecular dynamics study of effects of intertube spacing on sliding behaviors of multi-walled carbon nanotube," *Computational Materials Science*, vol. 50, no. 3, pp. 971–974, 2011.
- [24] A. Sears and R. C. Batra, "Buckling of multiwalled carbon nanotubes under axial compression," *Physical Review B*, vol. 73, no. 8, Article ID 085410, 11 pages, 2006.
- [25] D. W. Brenner, O. A. Shenderova, J. A. Harrison, S. J. Stuart, B. Ni, and S. B. Sinnott, "A second-generation reactive empirical bond order (REBO) potential energy expression for hydrocarbons," *Journal of Physics Condensed Matter*, vol. 14, no. 4, pp. 783–802, 2002.
- [26] L. E. Lennard-Jones, "On the determination of molecular fields. I. From the variation of the viscosity of a gas with temperature," *Proceedings of the Royal Society A*, vol. 106, no. 738, pp. 441–463, 1924.
- [27] A. K. Rappé, C. J. Casewit, K. S. Colwell, W. A. Goddard, and W. M. Skiff, "UFF, a full periodic table force field for molecular mechanics and molecular dynamics simulations," *Journal of the American Chemical Society*, vol. 114, no. 25, pp. 10024–10035, 1992.
- [28] Z. G. Mao, A. Garg, and S. B. Sinnott, "Molecular dynamics simulations of the filling and decorating of carbon nanotubes," *Nanotechnology*, vol. 10, no. 3, pp. 273–277, 1999.
- [29] K. M. Liew, C. H. Wong, and M. J. Tan, "Buckling properties of carbon nanotube bundles," *Applied Physics Letters*, vol. 87, no. 4, Article ID 041901, 3 pages, 2005.
- [30] Y. Y. Jiang, W. Zhou, T. Kim, Y. Huang, and J. M. Zuo, "Measurement of radial deformation of single-wall carbon nanotubes induced by intertube van der Waals forces," *Physical Review B*, vol. 77, no. 15, Article ID 153405, 4 pages, 2008.
- [31] O. Lourie and H. D. Wagner, "Transmission electron microscopy observations of fracture of single-wall carbon nanotubes under axial tension," *Applied Physics Letters*, vol. 73, no. 24, pp. 3527–3529, 1998.

Research Article

Size-Dependent Dynamic Behavior of a Microcantilever Plate

Xiaoming Wang and Fei Wang

School of Mechanical and Electronic Engineering, Harbin Institute of Technology, Harbin 150001, China

Correspondence should be addressed to Fei Wang, wangfeivc@gmail.com

Received 18 February 2012; Revised 10 May 2012; Accepted 16 May 2012

Academic Editor: Grégory Guisbiers

Copyright © 2012 X. Wang and F. Wang. This is an open access article distributed under the Creative Commons Attribution License, which permits unrestricted use, distribution, and reproduction in any medium, provided the original work is properly cited.

Material length scale considerably affects the mechanical properties of microcantilever components. Recently, cantilever-plate-like structures have been commonly used, whereas the lack of studies on their size effects constrains the design, testing, and application of these structures. We have studied the size-dependent dynamic behavior of a cantilever plate based on a modified couple stress theory and the differential quadrature method in this note. The numerical solutions of microcantilever plate equation involving the size effect have been presented. We have also analyzed the bending and vibration of the microcantilever plates considering the size effect and discussed the dependence of the size effect on their geometric dimensions. The results have shown that (1) the mechanical characteristics of the cantilever plate show obvious size effects; as a result, the bending deflection of a microcantilever plate reduces whereas the natural frequency increases effectively and (2) for the plates with the same material, the size effect becomes more obvious when the plates are thinner.

The miniaturized cantilever device is one of the fastest developing and most efficient types of micro-nano devices; it is widely used in the chemistry, physical, and biological fields [1–3]. In these applications, the dimensions of the cantilever are typically on the order of microns or even sub-microns. And the performance of cantilever device depends on the accurate extract of static bending and resonant frequency. Using test measurements and theoretical studies, scholars have recently proved that the mechanical properties of miniaturized structures critically depend on material length-scale. The size effect shown in the mechanical properties considerably affects the static bending and resonant frequency shift of cantilever devices [4–6]. Therefore, studying the size-dependent behavior of cantilever devices is important.

Couple stress theory is an effective method for studying the size effect [7, 8]. By rotating the gradient, the theory introduces material length-scale parameters to the constitutive equation. Lam et al. [9] proposed a modified couple stress model in which only one material length parameter is needed to capture the size effect, and the model has attracted many researchers in the past years. Kong et al. [10] used this theory to study the size effect of the Euler-Bernoulli beam natural frequency. Ma et al. [11] then studied

the Timoshenko size effect that accounts for axial deformation and the Poisson effect.

Most widely known miniaturized devices are typical cantilever plate structures. Compared with a cantilever beam, a cantilever plate with a large surface area has higher sensitivity. However, current studies focus only on micro-beam structures, and few studies on the size effect of cantilever plates have been reported. Tsiatas [12] developed a new Kirchhoff plate model for the static analysis of isotropic microplates with arbitrary shape based on a modified couple stress theory. Yin et al. [13] proposed a non-classical Kirchhoff plate model for the dynamic analysis of microscale. However, they have not studied the cantilever plate.

In this letter, we use the modified couple stress theory and the differential quadrature (DQ) method to study the size effect of a microcantilever plate. The characteristic length effect on static bending deflection and natural frequency of plate under uniform loads is analyzed. Furthermore, we discuss the dependence of the size effect on the geometric dimensions of the plate.

We study a rectangular Kirchhoff cantilever plate and assuming that the initial state of the microplate is flat and thin. The plate is subjected to a uniform distributed

transverse load q and hence undergoes a three-dimensional deformation state. The w represents the deflection of the z direction.

Based on the modified couple stress theory, the governing equation of the static bending of a microcantilever plate is [12]

$$(D + D') \left(\frac{\partial^4 w(x, y)}{\partial x^4} + 2 \frac{\partial^4 w(x, y)}{\partial x^2 \partial y^2} + \frac{\partial^4 w(x, y)}{\partial y^4} \right) = q(x, y), \quad (1)$$

where D is the classical bending rigidity of the plate and D' is the contribution of rotation gradients to the bending rigidity. The two parameters can be expressed as

$$D = \frac{Eh^3}{12(1 - \nu^2)}, \quad D' = \frac{El^2 h}{2(1 + \nu)}, \quad (2)$$

where E is Young's modulus, ν is Poisson's ratio, and l denotes the material length-scale parameter representing the size effect, usually in the micro-nano order.

On the basis of (2), the governing equation for the vibration of the plate under uniform loads can be expressed as

$$(D + D') \left(\frac{\partial^4 w(x, y, t)}{\partial x^4} + 2 \frac{\partial^4 w(x, y, t)}{\partial x^2 \partial y^2} + \frac{\partial^4 w(x, y, t)}{\partial y^4} \right) + \rho h \frac{\partial^2 w(x, y, t)}{\partial t^2} = q(x, y), \quad (3)$$

where ρ is the plate density and h is the thickness of microcantilever.

The equation based on the modified couple stress theory contains only one material length-scale parameter. Therefore, the size effect can be well characterized. Meanwhile, (2) shows that when l is zero, the equation degenerates to the classical equations of the Kirchhoff plate. It should be noted, in this letter we focus on the size effect and therefore ignored surface effect and induce residual stress.

For solving the equation of microplate, the analytical method is well-known cumbersome, and with the change of boundary and loading conditions, the difficulty of solving a sharp increase even cannot solve. In commonly used finite difference method and finite element method, the solving regional needs to be divided into fairly large number of grid or node, leading to large amount of calculation. However, as an effective numerical approach to solving boundary value problems, the DQ method can get enough precision of the calculation results using a few grid points, and this is the most significant advantage in comparison to other methods. We obtain the numerical solutions of static bending and vibration equations using this method.

By setting $\xi = x/L$, $\eta = y/b$ ($0 < \xi < 1$, $0 < \eta < 1$), where L and b are the length and width of the plate, respectively. The coordinate dimensionless form of (1) can be expressed as

$$(D + D') \left(\frac{1}{L^4} \frac{\partial^4 w}{\partial \xi^4} + 2 \frac{1}{L^2 b^2} \frac{\partial^4 w}{\partial \xi^2 \partial \eta^2} + \frac{1}{b^4} \frac{\partial^4 w}{\partial \eta^4} \right) = q(\xi, \eta). \quad (4)$$

In the DQ method, the value of function partial derivative at one point can be approximately to weighted summation of function value of all the nodes, and the n -order derivative of function $g(x)$ at node x_i is expressed as [14]:

$$g^{(n)}(x_i) = \sum_{j=1}^N C_{ij}^{(n)} g(x_j) \quad n = 1, 2, \dots, N_x - 1, \quad (5)$$

where $C_{ij}(n)$ is the n -order weighting coefficient and N is the number of nodes.

By substituting (5) into (4), we can obtain the microplate static bending equation in DQ form:

$$\left[\frac{1}{L^4} \sum_{k=1}^{N_x} C_{ik}^{(4)} w(\xi_k, \eta_j) + 2 \frac{1}{L^2 b^2} \sum_{k=1}^{N_x} \sum_{l=1}^{N_y} C_{ik}^{(2)} \bar{C}_{jl}^{(2)} w(\xi_k, \eta_l) + \frac{1}{b^4} \sum_{l=1}^{N_y} \bar{C}_{jl}^{(4)} w(\xi_i, \eta_l) \right] = \frac{q(\xi_i, \eta_j)}{(D + D')}, \quad (6)$$

where $i = 1, 2, \dots, N_x$, $j = 1, 2, \dots, N_y$. N_x and N_y are the number of nodes along the x and y directions of the plate. When (6) is expressed in matrix form, the equation becomes

$$C \cdot w = q, \quad (7)$$

where C is the weight coefficient matrix, w is the nodal displacement array, and q is the load vector.

The boundary conditions of the cantilever plate are

$$\begin{aligned} \omega = 0, \quad \frac{\partial w}{\partial \xi} = 0; \quad \xi = 0, \\ \frac{\partial^2 w}{\partial \xi^2} + \nu \frac{\partial^2 w}{\partial \eta^2} = 0, \quad \frac{\partial^3 w}{\partial \xi^3} + (2 - \nu) \frac{\partial^3 w}{\partial \xi \partial \eta^2} = 0; \quad \xi = 1, \\ \frac{\partial^2 w}{\partial \eta^2} + \nu \frac{\partial^2 w}{\partial \xi^2} = 0, \quad \frac{\partial^3 w}{\partial \eta^3} + (2 - \nu) \frac{\partial^3 w}{\partial \xi^2 \partial \eta} = 0; \quad \eta = 0, \\ \frac{\partial^2 w}{\partial \eta^2} + \nu \frac{\partial^2 w}{\partial \xi^2} = 0, \quad \frac{\partial^3 w}{\partial \eta^3} + (2 - \nu) \frac{\partial^3 w}{\partial \xi^2 \partial \eta} = 0; \quad \eta = 1. \end{aligned} \quad (8)$$

We use the equation substitution method to processing boundary conditions. Based on this method, the DQ equations in (8) substituted the nodes equation on $i = 1, 2, N_x - 1, N_x$; $j = 1, 2, N_y - 1, N_y$ in (6). The correctional weight coefficient matrix C' is obtained. The boundary conditions are introduced into (7).

We can see that C' and q are known matrixes in (7), and then we can obtain the nodal displacement array w under uniform loads. Finally, we can obtain the full displacement fields using a higher-order Lagrange interpolation.

Similarly, by transforming and arranging (3), the cantilever vibration equation in DQ form becomes

$$\left[\frac{1}{L^4} \sum_{k=1}^{N_x} C_{ik}^{(4)} W(\xi_k, \eta_j) + 2 \frac{1}{L^2 b^2} \sum_{k=1}^{N_x} \sum_{l=1}^{N_y} C_{ik}^{(2)} \bar{C}_{jl}^{(2)} W(\xi_k, \eta_l) + \frac{1}{b^4} \sum_{l=1}^{N_y} \bar{C}_{jl}^{(4)} W(\xi_i, \eta_l) \right] - \frac{\rho h \omega^2}{(D + D')} W(\xi_i, \eta_j) = \frac{q(\xi_i, \eta_j)}{(D + D')}, \quad (9)$$

where $W(x, y)$ is the mode function and ω is the angular frequency. The matrix form of (8) is

$$C \cdot W - \rho h \omega^2 \cdot W = q. \quad (10)$$

According to the approach in (7), the natural frequency of the cantilever vibration can be obtained. Because the uniform load does not affect the natural frequency of the plate, the obtained value of the natural frequency is the natural frequency of the free vibration of the plate.

We present the numerical solution of the mechanical equations of a cantilever plate by the DQ method, then we expect to bring value to further analyses of the size effects of cantilever plates.

We set both length L and width b as $50 \mu\text{m}$, thickness h as $5 \mu\text{m}$, modulus of elasticity E as 50 GPa , density ρ as 2700 kg/m^3 , and uniform load q as $1 \text{ N}/\mu\text{m}$. The 9×9 nodes were chosen for the grid point in solving regional, and node distributions are taken based on well-accepted Gauss-Chebyshev-Lobatto points [14].

In order to verify the effectiveness of the DQ method, we present the comparison results of analytical and DQ solution for deflection on $y = 25 \mu\text{m}$, as shown in Table 1. We can see that, compared with analytical solutions, the error of DQ solution is less than 1% at different position x . It shows the satisfactory accuracy with a few grid points and full performances the characteristics of little computation quantity and high precision.

This letter is the first to present an investigation of the size effect of a cantilever plate by numerical simulation. The following issues are analyzed: (1) the changes in the cantilever deflection and natural frequency of the plate with certain geometric dimensions caused by the size effect and (2) the influence of the geometric dimensions of a plate on the strength of the size effect.

Figure 1 is obtained using (7), when Poisson's ratio as 0.3, a thickness as $5 \mu\text{m}$, at different length-scale parameters, the bending deflection of the cantilever plate along the x direction ($y = 25 \mu\text{m}$). Here, l has values of 0, 1.5, 3, and $4.5 \mu\text{m}$. Figure 1 shows that when the length-scale parameter l increases, the deflection of the plate considerably decreases at the same location. For $x = 25 \mu\text{m}$, when the length-scale parameter increases from 0 to $4.5 \mu\text{m}$, the bending deflection decreases from 0.15 to $0.03 \mu\text{m}$ —a reduction of 80%. This reduction indicates an obvious size effect. We emphasize that when the length-scale parameter is zero ($l = 0$), the bending deflection is the classical elasticity solution. Therefore, the data show that, in considering the influence of the size effect, the deflection of the plate is substantially reduced.

TABLE 1: The comparison of analytical and DQ solution for deflection on $y = 25 \mu\text{m}$.

Position x	Static bending deflection (10^{-8} m)			
	$12.5 \mu\text{m}$	$25 \mu\text{m}$	$37.5 \mu\text{m}$	$50 \mu\text{m}$
Analytical solution	5.214	14.925	24.051	32.014
DQ solution	5.171	14.805	23.845	31.720
Error %	0.827	0.809	0.858	0.919

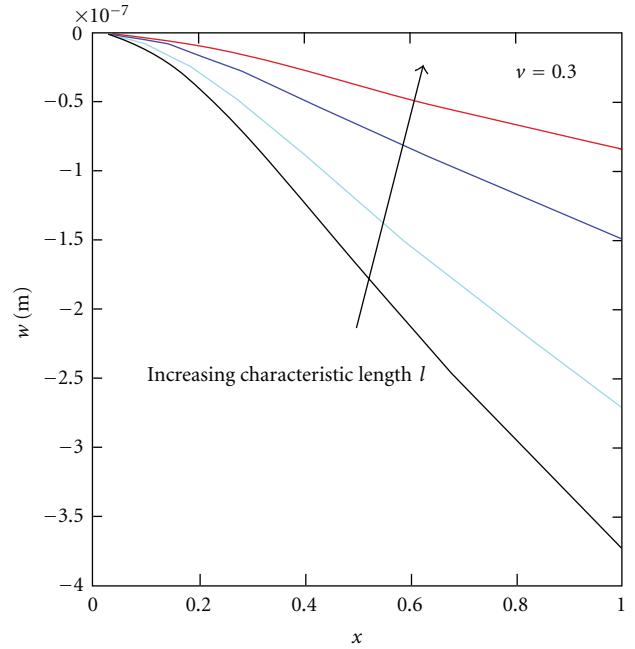


FIGURE 1: Deflection curve in the x direction of a cantilever plate subjected to uniform loads; $l = 0, 1.5, 3,$ and $4.5 \mu\text{m}$; $\nu = 0.3$.

Table 2 is obtained using (9), when having Poisson's ratio as 0.3, a thickness as $5 \mu\text{m}$, at different length-scale parameters, the first four orders of the natural frequencies of the cantilever plate; l has values of 0, 1.5, 3, and $4.5 \mu\text{m}$. Table 1 shows that when the length-scale parameters increase, the natural frequency of each order mode considerably increases. For the first-order mode, when the length-scale parameters increase from 0 to $4.5 \mu\text{m}$, the natural frequency increases from 14 to 30 MHz—an increase of 114%. Similarly, in considering the influence of the size effect, the natural frequency of the plate considerably increases.

Equation (2) can explain the phenomenon above, that is, when the length-scale parameters increases, the bending stiffness of the cantilever bending plate increases. Therefore, the plate bending deflection decreases and the natural frequency increases. In summary, when the length-scale parameters and plate thickness are in the same order of magnitude, the size effect cannot be disregarded. In addition, with the increase in length-scale parameters, the size effect becomes increasingly apparent. These results are in accordance with the size effect of microcantilever beams.

TABLE 2: First four orders of the natural frequencies of the plate under uniform loads at different length-scale parameters.

Mode	Natural frequency of vibration (10^8Hz)			
	$l = 0 \mu\text{m}$	$l = 1.5 \mu\text{m}$	$l = 3 \mu\text{m}$	$l = 4.5 \mu\text{m}$
1	0.14	0.17	0.23	0.30
2	0.47	0.56	0.76	1.01
3	0.69	0.81	1.10	1.45
4	1.49	1.74	2.36	2.59

To study the dependence of the size effect on the geometric dimensions of the cantilever plate, we set the definitions of the relative change in deflection as $(w - w_0)/w_0$ and the relative change in frequency as $(\omega - \omega_0)/\omega_0$, where w_0 and ω_0 are respectively the bending deflection and natural frequency that do not consider the size effect ($l = 0$), and w and ω are, respectively, the bending deflection and natural frequency that consider the size effect. By this definition, for the certain length-scale parameters, the influence of the size effect on mechanical properties is more substantial when relative change is greater.

The size effects of each point on the plate under the same conditions are the same. Thus, a fixed point ($x = 25 \mu\text{m}$, $y = 25 \mu\text{m}$) is chosen. Figure 2 and Table 3 show the same material (with $l = 5 \mu\text{m}$), and the relative changes in deflection and natural frequency with thickness and Poisson's ratios. The thickness is between 1 to $5 \mu\text{m}$, and Poisson's ratios are 0.25, 0.3, and 0.35.

We can see that, the size effect on mechanical properties weakens with the increase in thickness. For a Poisson's ratio of 0.3, when the thickness of the cantilever plate increases from 1 to $5 \mu\text{m}$, the relative change in deflection is reduced from 0.98 to 0.79 and the relative natural frequency decreases from 9.44 to 1.28. These results indicate a considerably reduced size effect. In addition, for the cantilever plate of a certain thickness, the relative changes in deflection and natural frequency increase with the decrease in Poisson's ratio.

Based on the modified couple stress theory and the differential quadrature (DQ) method, we studied the size-dependent dynamic behavior of a rectangular cantilever plate. We provide numerical solutions to the static bending deflection and natural frequency and analyzed static bending deflection and the natural frequency vibration under the size effect and discussed the dependence of the size effect on the geometric dimensions of the plate. The results show that the DQ solution seems quite well to approach analytical solution and performs the satisfactory accuracy with a few grid points. When the length-scale parameters and the thickness are in the same magnitude, the size effect cannot be disregarded. Under the influence of the size effect, the bending deflection decreases and the natural frequency increases. For the cantilever plate with the same material, the size effect on the mechanical properties gradually increases when thickness decreases. This study provided data on the size effect of cantilever plates and serves as basis for future research.

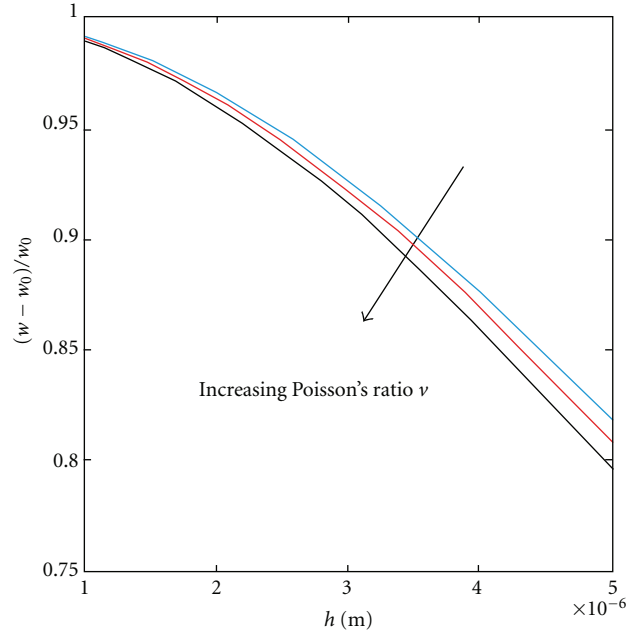


FIGURE 2: Relative change in the deflection of the plate with different thicknesses; $\nu = 0.25, 0.3, 0.35$.

TABLE 3: Relative change in the first orders of the natural frequencies of the plate with different thicknesses.

Poisson's ratio	Relative change in natural frequencies			
	$h = 1 \mu\text{m}$	$h = 2 \mu\text{m}$	$h = 3.5 \mu\text{m}$	$h = 5 \mu\text{m}$
0.25	9.63	4.39	2.20	1.34
0.30	9.44	4.22	2.09	1.28
0.35	8.90	4.03	1.99	1.20

Acknowledgment

This work is supported by the National Natural Science Foundation of China Project no. 10902031 and China Postdoctoral Science Foundation Project no. 20090451001.

References

- [1] F. Wang, J. Y. Chen, and X. Z. Zhao, "Comment on 'Mechanism of flexural resonance frequency shift of a piezoelectric microcantilever sensor during humidity detection,'" *Applied Physics Letters*, vol. 93, no. 9, Article ID 096101, 2008.
- [2] D. Maraldo and R. Mutharasan, "Mass-change sensitivity of high-order mode of piezoelectric-excited millimeter-sized cantilever (PEMC) sensors: theory and experiments," *Sensors and Actuators B*, vol. 143, no. 2, pp. 731–739, 2010.
- [3] F. Sansoz and T. Gang, "A force-matching method for quantitative hardness measurements by atomic force microscopy with diamond-tipped sapphire cantilevers," *Ultramicroscopy*, vol. 111, no. 1, pp. 11–19, 2010.
- [4] S. Cuenot, C. Frétygny, S. Demoustier-Champagne, and B. Nysten, "Surface tension effect on the mechanical properties of nanomaterials measured by atomic force microscopy," *Physical Review B*, vol. 69, no. 16, Article ID 165410, p. 1, 2004.

- [5] L. G. Zhou and H. Huang, "Are surfaces elastically softer or stiffer?" *Applied Physics Letters*, vol. 84, no. 11, Article ID 1940, 3 pages, 2004.
- [6] J. G. Guo and Y. P. Zhao, "The size-dependent elastic properties of nanofilm with surface effects," *Journal of Applied Physics*, vol. 98, Article ID 074306, 2005.
- [7] Q. Ma and D. R. Clarke, "Size dependent hardness of silver single crystals," *Journal of Materials Research*, vol. 10, no. 4, pp. 853–863, 1995.
- [8] W. J. Poole, M. F. Ashby, and N. A. Fleck, "Micro-hardness of annealed and work-hardened copper polycrystals," *Scripta Metallurgica et Materialia*, vol. 34, p. 559, 1996.
- [9] D. C. C. Lam, F. Yang, A. C. M. Chong, J. Wang, and P. Tong, "Experiments and theory in strain gradient elasticity," *Journal of the Mechanics and Physics of Solids*, vol. 51, no. 8, pp. 1477–1508, 2003.
- [10] S. Kong, S. Zhou, Z. Nie, and K. Wang, "The size-dependent natural frequency of Bernoulli-Euler micro-beams," *International Journal of Engineering Science*, vol. 46, no. 5, pp. 427–437, 2008.
- [11] H. M. Ma, X. L. Gao, and J. N. Reddy, "A microstructure-dependent Timoshenko beam model based on a modified couple stress theory," *Journal of the Mechanics and Physics of Solids*, vol. 56, no. 12, pp. 3379–3391, 2008.
- [12] G. C. Tsiatas, "A new Kirchhoff plate model based on a modified couple stress theory," *International Journal of Solids and Structures*, vol. 46, no. 13, pp. 2757–2764, 2009.
- [13] L. Yin, Q. Qian, L. Wang, and W. Xia, "Vibration analysis of microscale plates based on modified couple stress theory," *Acta Mechanica Sinica*, vol. 23, no. 5, pp. 386–393, 2010.
- [14] T. Murmu and S. C. Pradhan, "Vibration analysis of nanoplates under uniaxial prestressed conditions via nonlocal elasticity," *Journal of Applied Physics*, vol. 106, no. 10, Article ID 104301, 2009.

Research Article

SnO₂ Nanoparticle-Based Passive Capacitive Sensor for Ethylene Detection

Mangilal Agarwal,¹ Mercyma D. Balachandran,² Sudhir Shrestha,¹ and Kody Varahramyan¹

¹Integrated Nanosystems Development Institute (INDI), Indiana University-Purdue University Indianapolis (IUPUI),
723 W. Michigan Street, Indianapolis, IN 46202, USA

²Foxconn International Holdings (FIH), 1551 Sawgrass Corporate Parkway, Sunrise, FL 33323, USA

Correspondence should be addressed to Mangilal Agarwal, agarwal@iupui.edu

Received 24 March 2012; Accepted 1 June 2012

Academic Editor: Grégory Guisbiers

Copyright © 2012 Mangilal Agarwal et al. This is an open access article distributed under the Creative Commons Attribution License, which permits unrestricted use, distribution, and reproduction in any medium, provided the original work is properly cited.

A passive capacitor-based ethylene sensor using SnO₂ nanoparticles is presented for the detection of ethylene gas. The nanoscale particle size (10 nm to 15 nm) and film thickness (1300 nm) of the sensing dielectric layer in the capacitor model aid in sensing ethylene at room temperature and eliminate the need for microhotplates used in existing bulk SnO₂-resistive sensors. The SnO₂-sensing layer is deposited using room temperature dip coating process on flexible polyimide substrates with copper as the top and bottom plates of the capacitor. The capacitive sensor fabricated with SnO₂ nanoparticles as the dielectric showed a total decrease in capacitance of 5 pF when ethylene gas concentration was increased from 0 to 100 ppm. A 7 pF decrease in capacitance was achieved by introducing a 10 nm layer of platinum (Pt) and palladium (Pd) alloy deposited on the SnO₂ layer. This also improved the response time by 40%, recovery time by 28%, and selectivity of the sensor to ethylene mixed in a CO₂ gas environment by 66%.

1. Introduction

In the United States, almost 23 percent wastage of fruit occurs every year in the postharvest handling [1]. Ethylene gas is the key factor for initiating the ripening process in climacteric fruits and for accelerating the aging process, thereby reducing the quality and shelf life of production during postharvest transits. Climacteric fruits, such as, apples, peaches tend to emit different concentrations of ethylene at various stages of ripening [2, 3]. Thus, by using ethylene gas sensors, the condition of the fruit can be monitored based on the concentrations of ethylene emitted.

The most common material used for sensing ethylene in the ethylene sensor is tin dioxide [4–6]. Other materials used are tungsten trioxide [7], palladium [8], platinum [9], titanium dioxide [10], and zinc oxide [11]. Most of these materials are used to model resistor-based devices, where the conductivity of these materials either increases or decreases based on the exposure to different concentrations of ethylene gas. The usual techniques followed to fabricate the sensing layer are ceramic paste [12], thick film printing [13], sol gel [6], and chemical vapor deposition [14] which requires

high-temperature heating and complex material mixing techniques. Further, the ethylene detection also requires expensive and complex methods like Quantum-cascade laser [15], gas chromatography [16], photoluminescence [17], and chemiluminescence [18].

The ethylene sensor presented in this paper is a simple capacitor-based sensor fabricated and tested at room temperature. The active sensing layer is tin dioxide used as the dielectric material, fabricated at room temperature using low-cost dip coating technique or layer-by-layer (LbL) self-assembly technique [19]. These fabrication techniques that are used for coating nanolayer thickness of active layers also allow the ease of coating the sensing layer on any surface, even on surface-like plastic, flexible polyimide sheets, or paper. The coated nanoorganized-sensitive layers have thickness of ca. 1300 nm and can be further reduced down to 600 nm which is less than the traditionally used coating technologies. The SnO₂ nanoparticle used for fabrication in this work has a particle diameter of 10 to 15 nm. This nm particle size aids in enhancing the sensitivity of SnO₂ as studied by Korotcenkov [20]. The increase in grain boundary area to grain volume ratio of the SnO₂ nanoparticles,

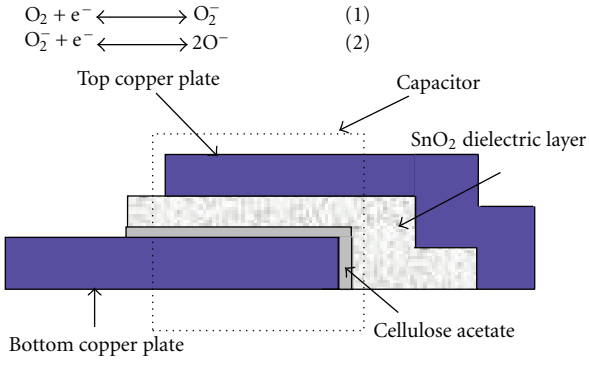


FIGURE 1: Model of ethylene gas sensor.

exceeding a certain threshold value, increases the sensitivity [21, 22]. In addition the adsorption of Pd and Pt ions to the SnO₂ nanoparticles reduces the threshold value thereby increasing the sensitivity as described by Straumal et al. in [22]. Moreover, the passive nature of the SnO₂ capacitive ethylene sensor aids in the integrated with a triangular microstrip patch antenna which represents a one of a kind passive wireless sensor tag used for detecting freshness of climacteric fruit [23].

2. Theory

The capacitive ethylene sensor developed has a top and bottom copper plate. Cellulose acetate is used as an insulating layer to prevent shorting of plates (see Figure 1). The sensing material is SnO₂ nanoparticles coated as the dielectric layer. In this work, the SnO₂ nanoparticles are n-type material with electrons (e⁻) as the majority carriers. In air, for the nanoparticles where oxygen is absorbed, a depletion layer (depleted of e⁻) consisting of O⁻ ionic species is formed [24]. This reaction mechanism is given by (1) and (2):



As more oxygen is absorbed, the depletion region increases and the conduction region decreases in thickness. When ethylene is encountered, the depleted electrons are replenished back to the SnO₂ surface, thereby increasing the conduction region and reducing the depletion region (3) [6]:



Figure 2 shows a schematic representation of the top view of a portion of the dielectric region containing the SnO₂ nanoparticles with depletion region and conduction region as seen through the top copper plate before and after exposure to ethylene gas. In this model, the diffusion of ethylene and air is only through the sides of the device. Moreover, complete diffusion of ethylene and air over the entire sensing dielectric region occurs in this case because of the selected size of SnO₂ nanoparticles. The change in the depletion region of the SnO₂ nanoparticles in the presence of ethylene changes the capacitance of the sensor.

Let us assume that the particles are closely packed next to each other with the nanoparticles of the bottom layer

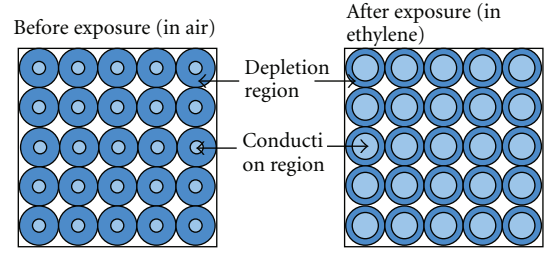


FIGURE 2: Top view of dielectric region with SnO₂ nanoparticles seen through the top copper plate before and after exposure to ethylene gas.

aligning vertically below the top layer of nanoparticles. Let C_B be the initial capacitance of the capacitive sensor before exposure to ethylene gas:

$$C_B = \frac{\epsilon_0 \epsilon_r A_1}{d}, \quad (4)$$

where, ϵ_0 is the permittivity of free space, ϵ_r is the dielectric constant of SnO₂ nanoparticles, A_1 is the area of the dielectric, that is, sum of the total depletion region of the nanoparticles and the dielectric regions between nanoparticles before exposure to ethylene gas (in air), and d is the thickness of the dielectric region. Let C_A be the capacitance of the capacitive sensor after exposure to ethylene, thus,

$$C_A = \frac{\epsilon_0 \epsilon_r A_2}{d}, \quad (5)$$

where, A_2 is the area of the dielectric, that is, sum of the total depletion region of the nanoparticles and the dielectric regions between nanoparticles after exposure to ethylene gas. The dielectric thickness d remains the same after exposure to ethylene gas as the changes in the depletion thickness after exposure to ethylene happen inside the nanoparticles and the overall thickness of the nanoparticles still remains the same.

As shown in Figure 2, the depletion region reduces in the presence of ethylene, which causes the plate area A_2 to decrease in value. If we assume that the depletion region reduces in thickness by about 1.5 nm, the capacitance is reduced by 5 pF, which is similar to the reduction in capacitance obtained experimentally. The use of nanoparticles increases the grain surface area to grain volume ratio. The addition of Pd/Pt layer creates a contact between the nanoparticle and the metals which induces adsorption of Pd and Pt ions to the SnO₂ nanoparticles reducing the threshold value thus increases the sensitivity of the sensor [22].

3. Fabrication

The deposition of the insulator and sensing layers of the capacitor has been done using dip coating, spin coating, and LbL nanoassembly technique. The ethylene sensor given in this paper is fabricated by dip coating technique on a flexible polyimide substrate (Pyrulux FR copper-clad laminate, DuPont). The bottom plate is the copper layer of the substrate, and the top plate of the capacitor is copper of thickness 300 nm deposited by E-beam evaporation technique. The thickness of the insulator (cellulose acetate) is about 1200 nm

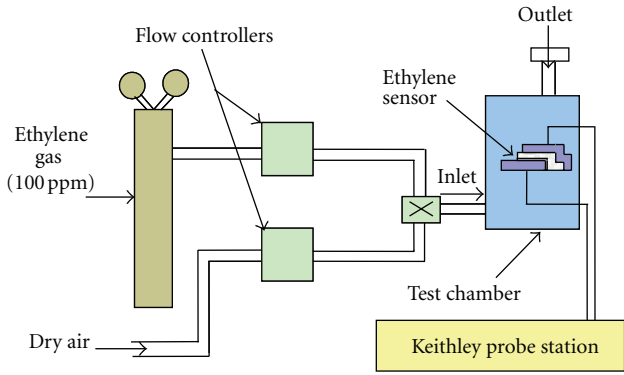


FIGURE 3: Experimental set-up for measuring ethylene sensors characteristics.

and SnO₂ coated is about 1300 nm. Initially the cellulose acetate is dip coated and dried at room temperature (in acetone solvent). The sensing layer of SnO₂ colloids (Nyacol Colloidal Tin 10 to 15 nm particle size and counter ion concentration of 0.23% NH₃) was mixed with 50%, and DI water was coated using simple dip coating technique and dried at room temperature. For uniform coating of SnO₂ and for better adherence of the sensing layer to the substrate, a very thin layer of poly(diallyldimethylammonium chloride) (PDDA) of thickness 100 nm with polycationic property was used as in LbL fabrication technique [19]. A 10 nm layer of Pd/Pt nanoparticles deposited using sputtering technique was coated on the SnO₂ sensing layer to increase sensitivity and selectivity of the ethylene sensor.

4. Results and Discussions

The SnO₂ capacitors were tested for capacitance using Keithley electrical probe station using the set-up shown in Figure 3. The ethylene gas concentration from 0 ppm to 100 ppm was used for testing purpose. Dry air was used to flush the experimental chamber to bring the sensor back to the original value. As Pt and Pd particles are known for their catalytic effect to enhance the sensitivity of SnO₂ nanoparticles to ethylene gas stimulant [4], a layer of 10 nm thickness of Pt/Pd alloy (80 : 20) was deposited by sputtering technique. Thus, two sets of sensors were developed, with and without the Pt/Pd layer. The sensor characteristics were measured and compared for both pure SnO₂ and SnO₂ with Pt/Pd layer devices (see Figure 4)

From the results obtained, it is observed that the capacitance of the sensor device decreases linearly with different concentration of ethylene. ΔC represents the amount of change in capacitance when ethylene is sensed compared to the original value of sensor capacitance in air, as given below:

$$\Delta C = C - C_0, \quad (6)$$

where, C_0 is the capacitance of the sensor in air (0 ppm) and C is the capacitance at varying ethylene gas concentrations. The negative value indicates that the capacitance decreases for an increase in ethylene concentration. From Figure 4, we can see that the overall change in capacitance of pure SnO₂ device to ethylene gas concentration from 0 to 100 ppm is

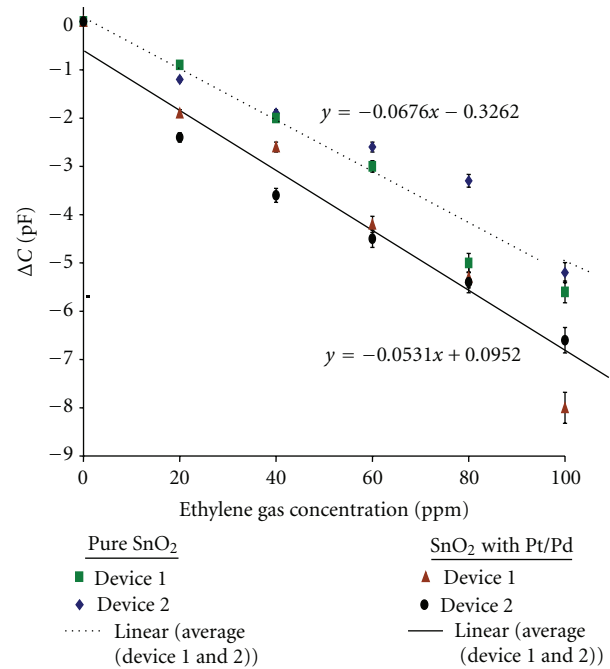


FIGURE 4: Sensitivity and reproducibility of capacitive ethylene sensor to ethylene gas.

5 pF and for SnO₂ with Pt/Pd device is 7 pF, thus showing that the Pt/Pd layer on the SnO₂ has enhanced the sensitivity of SnO₂ nanoparticles to ethylene gas by 39%. This is attributed to the absorption of Pt and Pd ions into the SnO₂ nanoparticles which reduces the threshold value as described by Straumal et al. in [22]. During measurements, it was observed that SnO₂ with Pt/Pd layer showed hysteresis similar to the hysteresis effect observed by Dennis et al. [25], the cause of which is attributed to the imbalances in the catalytic nature of Pd nanoparticles dissociating oxygen and producing O⁻ ions.

Figure 5 shows the degradation of the sensor over time. The same device was tested for 5 days under the same testing condition. The dotted line indicates the pure SnO₂ device and the solid line indicates the SnO₂ with Pt/Pd device, showing an overall change of 5 pF and 7.5 pF for pure SnO₂ and SnO₂ with Pt/Pd devices, respectively.

From Figure 5, it can be observed that the device with pure SnO₂ has slightly less degradation than the SnO₂ device with the Pt/Pd layer. The variations in the data points for 20 ppm and 40 ppm for the SnO₂ device with the Pt/Pd layer can be attributed to the variations in the oxygen dissociation on Pd particle surface at room temperature [26]. Oxygen dissociates into O⁻ ions when it encounters Pd which acts as a catalyst. This atomic oxygen spills over from the Pd to the SnO₂ surface enhancing the reaction of ethylene gas with the SnO₂ nanoparticles. The effect can be clearly observed from Figure 5, as only the first two ethylene concentrations show more variations in data values which later stabilize to more repeatable data values.

The sensor response time and recovery time are given in Figure 6. From the figure we can see that SnO₂ with the Pt/Pd layer has the faster response time of about 3 min

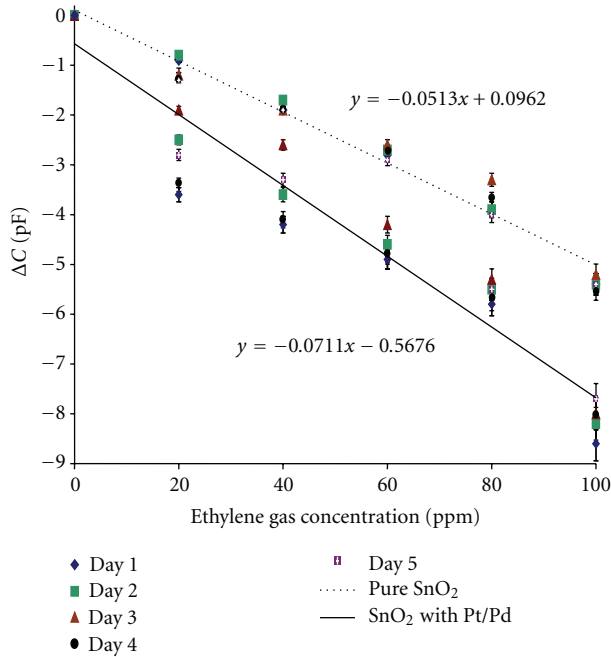


FIGURE 5: Degradation of ethylene sensor for varying ethylene concentrations.

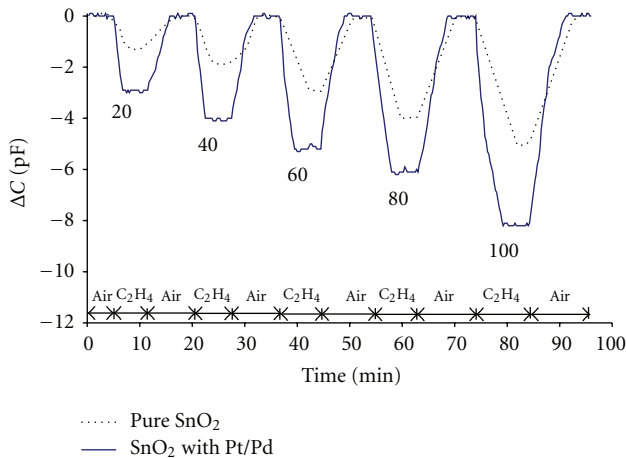


FIGURE 6: Response time and recovery time of pure SnO_2 and SnO_2 with Pt/Pd to ethylene concentration.

as compared to the pure SnO_2 device with 5 min response time. The recovery time for pure SnO_2 is higher at 7 min as compared to SnO_2 with the Pt/Pd layer which has a faster recovery time of 5 min. Therefore, the overall response time and recovery time are improved by 40% and 28%, respectively. The faster response time and recovery time are also attributed to the catalytic effect of platinum and palladium in SnO_2 to ethylene gas.

In this work, the developed sensor is proposed to sense ethylene emanated from fruits, which also means that it should be able to detect ethylene from among other gases present in the environment. As given in [27], carbon dioxide (CO_2) is another gas most commonly present in environments as in warehouses. CO_2 emanates from both

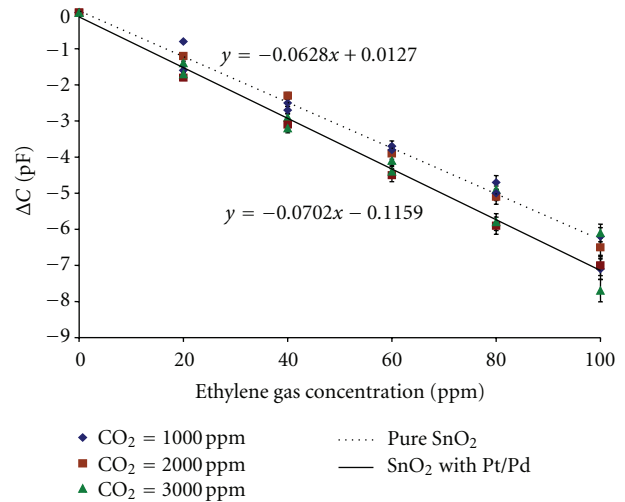


FIGURE 7: Sensitivity of pure SnO_2 and SnO_2 with Pt/Pd layer to ethylene gas concentration mixed with CO_2 gas.

climacteric and nonclimacteric fruits. Therefore, we have checked the sensor's sensitivity to ethylene in a carrier CO_2 gas concentration of 1000, 2000, and 3000 ppm (see Figure 7).

The capacitive sensor with pure SnO_2 dielectric layer shows an overall decrease of 6 pF in capacitance and SnO_2 with Pt/Pd shows an overall decrease of 7.2 pF for an increase in concentration of ethylene from 0 to 100 ppm. When comparing Figures 4 and 7, the overall change of pure SnO_2 has increased from 5 pF to 6 pF, whereas for SnO_2 with a Pt/Pd layer the capacitance has almost remained the same. This clearly indicates that pure SnO_2 has cross sensitivities to CO_2 gas and that the addition of Pt/Pd layer to SnO_2 has increased the sensor selectivity by 66%.

5. Conclusion

A capacitor-based ethylene sensor fabricated at room temperature with SnO_2 nanoparticles as the active dielectric layer is presented. Devices with dielectric layer as SnO_2 and SnO_2 with Pd/Pt were tested. The use of Pd/Pt nanoparticles with SnO_2 improved the sensor's sensitivity (39%), selectivity (66%), response time (40%), and recovery time (28%) when compared to pure SnO_2 devices. The proposed sensor is a low cost, passive and planar, and capacitor-based device, which make it possible to be easily integrated with passive RFID tags for wireless detection.

Acknowledgments

The authors are thankful to Louisiana Tech University and its Institute for Micromanufacturing (IfM) for providing the facilities and laboratory resources for this work.

References

- [1] A. A. Kader, "Increasing food availability by reducing postharvest losses of fresh produce," in *Proceedings of the 5th*

- International Postharvest Symposium*, Acta Horticulturae, pp. 2169–2176, 2005.
- [2] D. M. Tieman and A. K. Handa, “Immunocytolocalization of polygalacturonase in ripening tomato fruit,” *Plant Physiology*, vol. 90, pp. 17–20, 1989.
- [3] S. M. Cristescu, D. De Martinis, S. Te Lintel Hekkert, D. H. Parker, and F. J. M. Harren, “Ethylene production by *Botrytis cinerea* in vitro and in tomatoes,” *Applied and Environmental Microbiology*, vol. 68, no. 11, pp. 5342–5350, 2002.
- [4] P. Ivanov, E. Llobet, A. Vergara et al., “Towards a micro-system for monitoring ethylene in warehouses,” *Sensors and Actuators B*, vol. 111–112, pp. 63–70, 2005.
- [5] C. H. Kwon, H. Hong, S. T. Kim et al., “Vegetable freshness keeping device having a sensor,” US Patent, 5 609 096, 1997.
- [6] A. Giberti, M. C. Carotta, V. Guidi, C. Malag?, M. Piga, and G. Martinelli, “Monitoring of ethylene for agro-alimentary applications and compensation of humidity effects,” in *Proceedings of the Eurosensor XVII*, September 2003.
- [7] S. Pitcher, J. A. Thiele, H. Ren, and J. F. Vetelino, “Current/voltage characteristics of a semiconductor metal oxide gas sensor,” *Sensors and Actuators B*, vol. 93, no. 1–3, pp. 454–462, 2003.
- [8] B. Pietrucha and B. Lalevic, “Detection of hydrocarbon gases using PdMnO₂ capacitors,” *Sensors and Actuators*, vol. 13, no. 3, pp. 275–286, 1988.
- [9] F. Winquist and I. Lundström, “Thin metal film-oxide-semiconductor structures with temperature-dependent sensitivity for unsaturated hydrocarbons,” *Sensors and Actuators*, vol. 12, no. 3, pp. 255–261, 1987.
- [10] R. Zhang, M. I. Tejedor, M. A. Anderson, M. Paulose, and C. A. Grimes, “Ethylene detection using nanoporous PtTiO₂ coatings applied to magnetoelastic thick films,” *Sensors*, vol. 2, no. 8, pp. 331–338, 2002.
- [11] B. S. Kang, S. Kim, F. Ren et al., “Detection of C₂H₄ using wide-bandgap semiconductor sensors: AlGaIn/GaN MOS diodes and bulk ZnO schottky rectifiers,” *Journal of the Electrochemical Society*, vol. 151, no. 7, pp. G468–G471, 2004.
- [12] K. Ihokura, “Tin oxide gas sensor for deoxidizing gases,” *New Materials and New Processes in Electrochemical Technology*, vol. 1, pp. 43–50, 1981.
- [13] R. Srivastava, R. Dwivedi, and S. K. Srivastava, “Effect of oxygen, nitrogen and hydrogen plasma processing on palladium doped tin oxide thick film gas sensors,” in *The International Society for Optical Engineering*, vol. 3316 of *Proceedings of SPIE*, pp. 526–528, 1998.
- [14] L. R. Jordan, P. C. Hauser, and G. A. Dawson, “Humidity and temperature effects on the response to ethylene of an amperometric sensor utilizing a gold-nafion electrode,” *Electroanalysis*, vol. 9, no. 15, pp. 1159–1162, 1997.
- [15] D. Weidmann, A. A. Kosterev, C. Roller, R. F. Curl, M. P. Fraser, and F. K. Tittel, “Monitoring of ethylene by a pulsed quantum cascade laser,” *Applied Optics*, vol. 43, no. 16, pp. 3329–3334, 2004.
- [16] E. D. Butrym and T. G. Hartman, “Determination of ethylene by adsorbent trapping and thermal desorption-gas chromatography,” in *Proceedings of the (Pittcon '98)*, March 1998.
- [17] J. N. Burstyn, A. B. Ellis, O. Green, and N. A. Smith, “Photoluminescent ethylene sensors,” US Patent 20 050 031 985, 2005.
- [18] B. N. Nelson, R. V. Richard, and J. A. Kanc, “Ethylene monitoring and control system,” US Patent 6 105 416, 2000.
- [19] R. C. Ghan, Y. Lvov, and R. S. Besser, “Characterization of self-assembled SnO₂ nanoparticles for fabrication of a high sensitivity and high selectivity micro-gas sensor,” in *Proceedings of the Materials Research Society Symposium*, vol. 703, pp. 297–302, April 2002.
- [20] G. Korotcenkov, “Gas response control through structural and chemical modification of metal oxide films: state of the art and approaches,” *Sensors and Actuators B*, vol. 107, no. 1, pp. 209–232, 2005.
- [21] R. L. Van der Wal, G. M. Berger, G. W. Hunter, J. C. Xu, L. J. Evans, and C. C. Liu, “A comparison between SnO₂ nanowires and nanofibers for advanced environmental sensing,” in *Proceedings of the Annual Meeting and Fall Showcase (AIChE '05)*, p. 11922, November 2005.
- [22] B. B. Straumal, S. G. Protasova, A. A. Mazilkin et al., “Ferromagnetic properties of the Mn-doped nanograined ZnO films,” *Journal of Applied Physics*, vol. 108, no. 7, Article ID 073923, 6 pages, 2010.
- [23] M. D. Balachandran, S. Shrestha, M. Agarwal, Y. Lvov, and K. Varahramyan, “SnO₂ capacitive sensor integrated with microstrip patch antenna for passive wireless detection of ethylene gas,” *Electronics Letters*, vol. 44, no. 7, pp. 464–466, 2008.
- [24] H. Molero, D. Stacchiola, and W. T. Tysoe, “The kinetics of ethylene hydrogenation catalyzed by metallic palladium,” *Catalysis Letters*, vol. 101, no. 3–4, pp. 145–149, 2005.
- [25] J. O. Dennis, M. M. .A. Karim, Z. Ibrahim, and M. K. Saidin, “Hysteresis behavior of sensitivity in CH₄ detection in air using SnO₂ with Pd as sensitizing additive,” *Jurnal Teknologi C*, vol. 36, pp. 55–60, 2002.
- [26] G. Korotcenkov, V. Brinzari, Y. Boris, M. Ivanov, J. Schwank, and J. Morante, “Influence of surface Pd doping on gas sensing characteristics of SnO₂ thin films deposited by spray pyrolysis,” *Thin Solid Films*, vol. 436, no. 1, pp. 119–126, 2003.
- [27] T. Thomas and M. Skaria, “Air quality parameters in ethylene degreening rooms in the valley influence citrus fruit decay,” Tech. Rep., Department of Agriculture, Texas A & M University, College Station, Tex, USA.

Research Article

Structural Properties of Zn-ZnO Core-Shell Microspheres Grown by Hot-Filament CVD Technique

R. López,¹ T. Díaz,¹ G. García,¹ R. Galeazzi,¹ E. Rosendo,¹ A. Coyopol,¹
M. Pacio,¹ H. Juárez,¹ and A. I. Oliva²

¹Centro de Investigaciones en Dispositivos Semiconductores, Benemérita Universidad Autónoma de Puebla, 14 sur y Avenida, San Claudio, Edif. 137, 72570, PUE, Mexico

²Departamento de Física Aplicada, CINVESTAV del IPN, Unidad Mérida, A.P. 73, Cordemex, 97310 Mérida, YUC, Mexico

Correspondence should be addressed to R. López, lorr810813@gmail.com

Received 25 February 2012; Accepted 22 May 2012

Academic Editor: Grégory Guisbiers

Copyright © 2012 R. López et al. This is an open access article distributed under the Creative Commons Attribution License, which permits unrestricted use, distribution, and reproduction in any medium, provided the original work is properly cited.

We report the hot-filament chemical vapor deposition (HFCVD) growth of Zn-ZnO core-shell microspheres in the temperature range of 350–650°C only using ZnO pellets as raw material. The samples were characterized by scanning electron microscope (SEM), energy dispersive spectroscopy (EDS), and X-ray diffraction (XRD) techniques. SEM micrographs showed the presence of solid microspheres and a Zn-ZnO layer in all samples. The observed heterogeneous morphology on each sample suggested two different growth mechanisms. On the one hand, solid microspheres were formed by means of gas phase nucleation of Zn atoms. The Zn-ZnO layer was formed on the substrate as result of surface reactions. It is possible that Zn microspheres condensed during the natural cooling of the HFCVD reactor as they were observed on the Zn-ZnO layer.

1. Introduction

Over the last few years, nanotechnology has emerged as an important research field of materials science, since nanostructures exhibit superior physical properties compared to their counterpart bulk materials. Nowadays, nanotechnology has focused on the understanding of the physical properties of nanomaterials and their consequent applications. The controlled fabrication of functional nanostructured materials is an important objective of fundamental and applied research. In addition to nanostructures, spherical-like structures such as hollow microspheres and hemispheres have attracted great interest due to their particular properties such as low density and distinct optical properties. The microspheres are technologically very important among nanostructures because of their large surface-to-volume ratio which is useful in gas sensors and drug delivery [1, 2]. For many years, ZnO has been recognized as a promising material. It is a compound that shows unique physical properties for direct application in varistors [3], optical

devices [4], gas sensors [5], and so forth. ZnO has been extensively used as a gas sensing material due to its high electron mobility and good chemical and thermal stability under the sensors operating conditions [6]. Therefore, the synthesis of ZnO microspheres can be an alternative to gas sensing applications due to the interesting properties that exhibit the ZnO material and the microsphere structures.

Lately, various techniques have been employed to synthesize nano- and microstructures; however, some of them are complex and considerably expensive. The HFCVD technique is a low cost method with interesting properties. This technique has been a common method in the growth of diamond films due to its simple design and easy scaleup to deposit materials on substrates with large areas. The production of nanoscale materials by the HFCVD technique has focused on the carbon nanotubes synthesis [7–10]. In fact, the HFCVD technique has usually been more efficient in fast synthesis of long carbon nanotubes than other complex CVD techniques such as plasma-enhanced CVD [11–13]. One remarkable characteristic of using the HFCVD technique in the growth

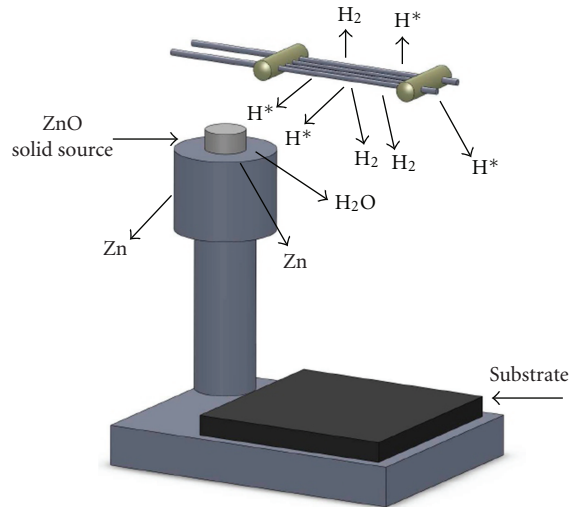


FIGURE 1: Schematic diagram of the experimental configuration of the filament, the ZnO pellet, and the substrate holder.

of diamond films and carbon nanotubes is that it uses atomic hydrogen as a volatile radical to generate gas-phase active species which, in large numbers, can lead into a possible increase in the growth rate. The above-mentioned advantages suggest this technique as an easy, reproducible, and low-cost alternative for the production of structures at the micro- or nanoscale. In the present work, Zn-ZnO microspheres were obtained by the HFCVD technique, but instead of using reactant gases, we used ZnO pellets as the only source in the formation of gas active species. We also used atomic hydrogen atoms in order to increase the decomposition rate of the ZnO pellet. We consider that this experimental setup can be a cheaper option to avoid the use of reactant gases that in some cases may be expensive.

2. Experimental Procedure

Zn-ZnO microstructures were synthesized in a home-made HFCVD system in the temperature range of 350–650°C. Commercial ZnO powder (Mallinckrodt) was compressed to obtain ZnO pellets (0.3 g), which served as raw material. Molecular H was used as reactant gas. P-type (100) oriented silicon wafers (area 4 cm²) and resistivity $\rho = 1 - 3 \Omega\text{-cm}$ were used as substrates. The ZnO pellets were loaded into the center of the HFCVD reactor (diameter 60 mm, length 350 mm) and under of the tungsten filament. The scheme of the configuration of the filament, the ZnO pellets, and the substrate is shown in Figure 1. Using an AC voltage of 83.4 V, the filament was heated up to 2000°C and kept parallel to the substrate holder with a distance of 9, 7, and 5 mm on each experiment to reach substrate temperatures of 350, 500, and 650°C, respectively. The process time was 10 seconds in all samples. The ZnO pellets were placed 2 mm away from the filament and kept at a temperature of 1500°C. The filament and the ZnO pellet temperature zones were monitored by an infrared optical pyrometer. The substrate

temperature was measured using a K-type thermocouple. During the microstructures formation, H₂ gas is introduced into the reactor, and it is then activated by contact with the hot filament. This generates a quantity of atomic H (H*) [14], which is able to decompose the ZnO pellet into Zn gas and water vapor precursors that diffuse towards to the substrate where the reaction takes place.

After the end of the growth process, the HFCVD reactor was naturally cooled down to room temperature. The XRD diffractograms were measured with a Bruker D8 Discover diffractometer using Cu K α radiation (1.5418 Å). The morphology and elemental analysis of the products were characterized using a scanning electron microscopy (SEM) Phillips XL-30.

3. Results and Discussion

3.1. SEM and EDS Measurements

3.1.1. Sample Grown at 350°C. Figure 2 shows the SEM images of the sample grown at 350°C by the HFCVD technique. We can see in Figure 2(a) a fibrous-like morphology with localized surface formation of dispersed micrometer clusters. High-magnification image (Figure 2(b)) clearly shows a heterogeneous morphology. Clusters located at the top of the structure show a sphere-like morphology. The surface under spheres presents a porous and nonuniform structure. The formation of spherical particles suggests that the material was liquid (droplet-like) before solidification. However, the growth process for this sample (350°C) was carried out at lower temperature than the melting point of Zn (419°C); therefore, the liquid assisted growth mechanism is ruled out since liquid droplets are not formed onto substrate surface at this temperature [15]. Thus, homogeneous nucleation of Zn during gas diffusion and its condensation is a strong argument to justify the obtained morphology. Besides, the formation of sphere particles seems to be independent from the substrate because the spheres were observed on the fibrous structure which grows onto the substrate surface, suggesting that they condensed during the natural coolingdown stage. Figure 2(c) shows that the spheres have a mean diameter around 10 micrometers. It can also be seen that they have an irregular surface. High magnification image (Figure 2(d)) shows that the fibrous morphology consists of entangled wire-like structures with irregular surface, and that they are connected with each other. The mean thickness of the wires was about 500 nanometers. Considering the one-dimensional vapor-solid (VS) growth of the wires [16] at 350°C, their irregular surfaces are ascribed to the formation of clusters that grow by nucleation of some species that do not reach the end of the wire because of their mobility drastically decreases with the natural cooling of the HFCVD reactor.

EDS spectrum of the microspheres (Figure 3(a)) shows only Zn signals, which may confirms the gas phase nucleation of Zn. In the case of the wires, EDS spectrum (Figure 3(b)) reveals the presence of Zn and a very little concentration of oxygen. This suggests that wires have Zn core with a thin ZnO

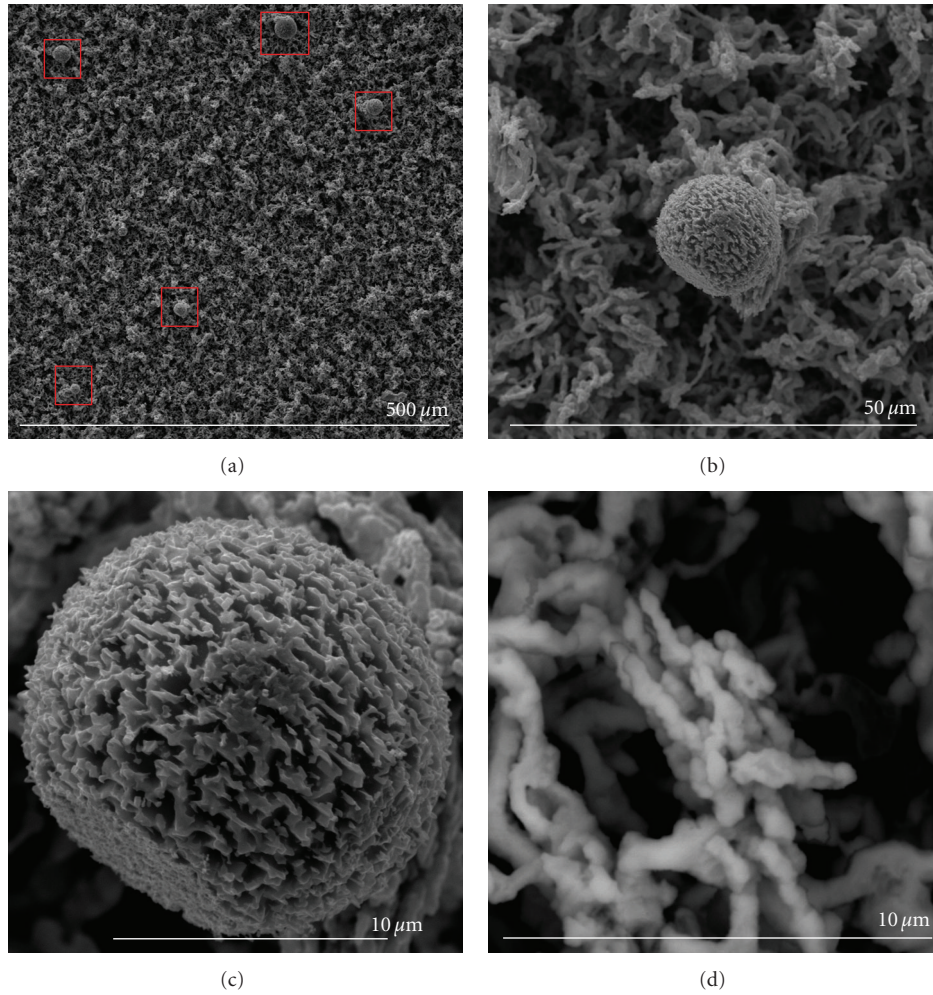


FIGURE 2: SEM micrographs of the sample grown at 350°C; the Zn microspheres on a Zn-ZnO layer composed by wire-like structures are observed in this figure.

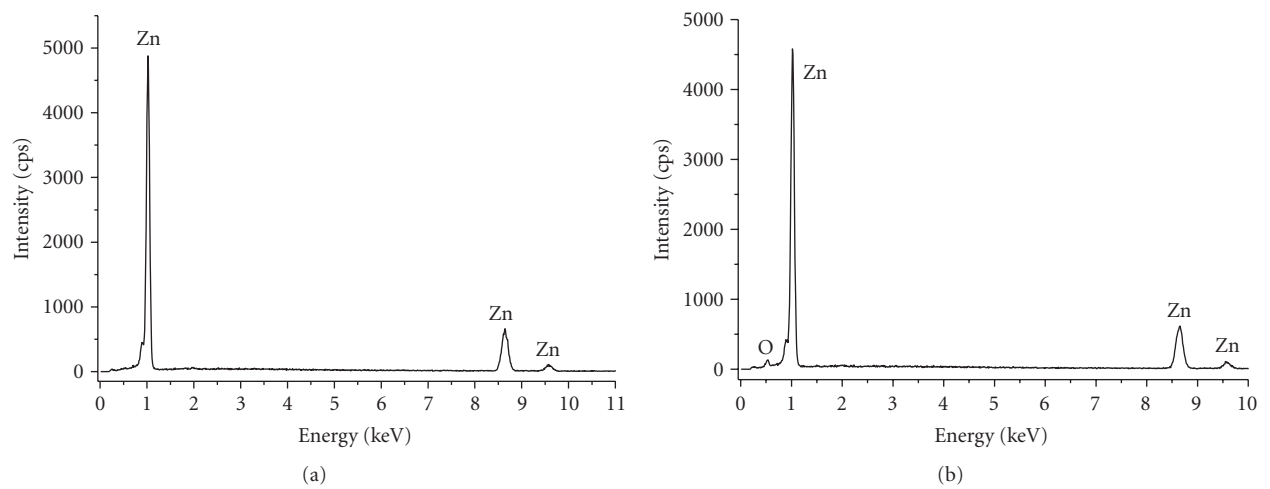


FIGURE 3: EDS spectra of sample grown at 350°C: (a) elemental analysis from a single microsphere and (b) from the wires.

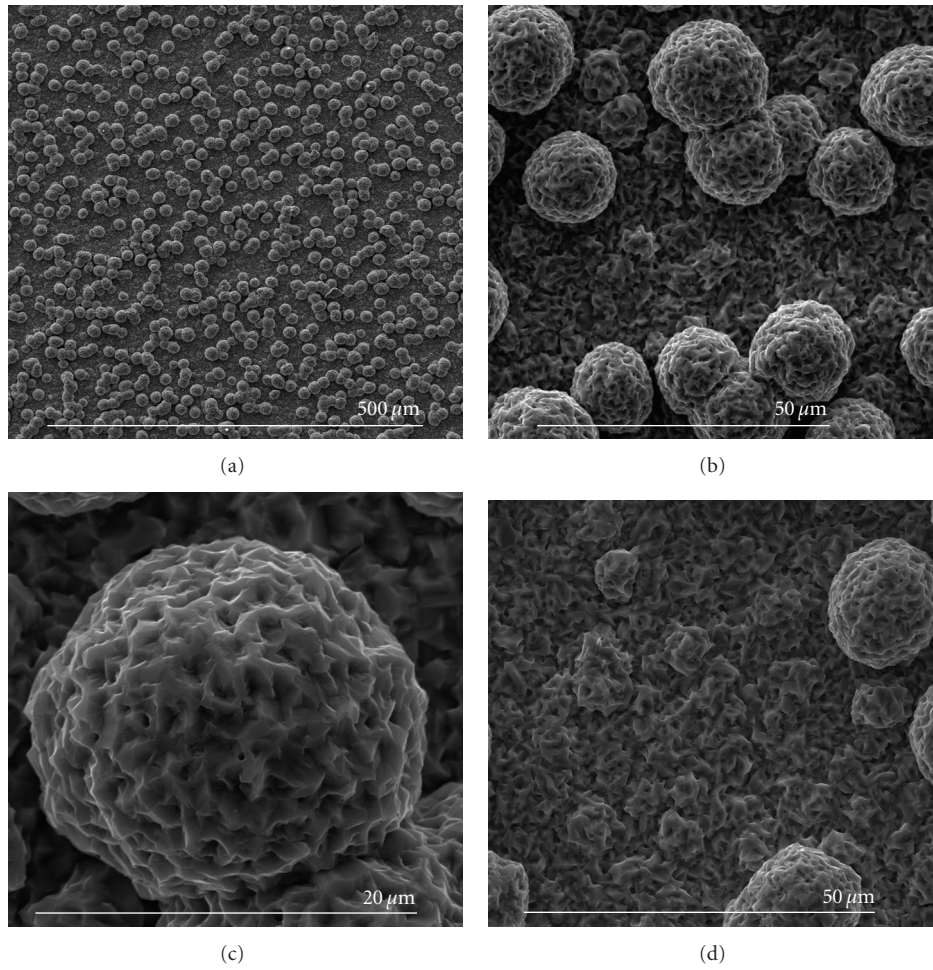


FIGURE 4: SEM micrographs of the sample grown at 500°C; the Zn-ZnO microspheres on a compact layer are observed in this figure.

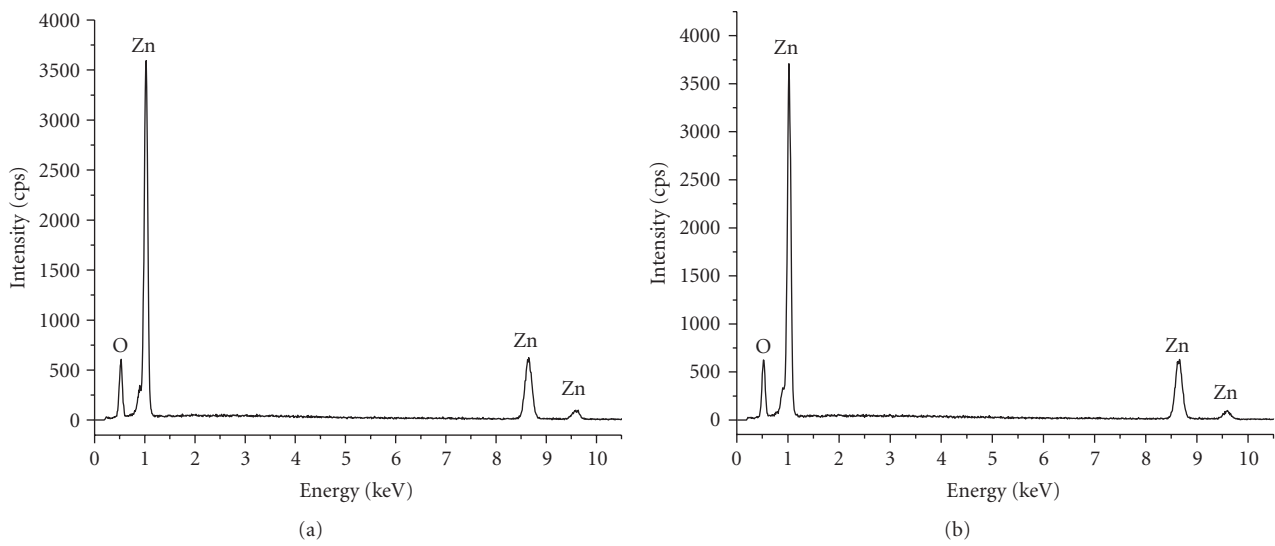


FIGURE 5: EDS spectra of sample grown at 500°C: (a) elemental analysis from a single microsphere and (b) from layer under microspheres.

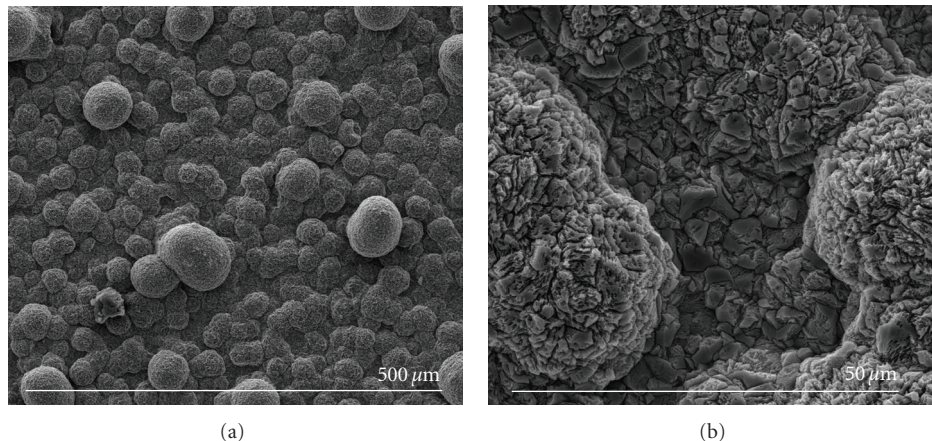


FIGURE 6: SEM micrographs of sample grown at 650°C. The large number of microspheres covers the layer grown onto the substrate surface completely.

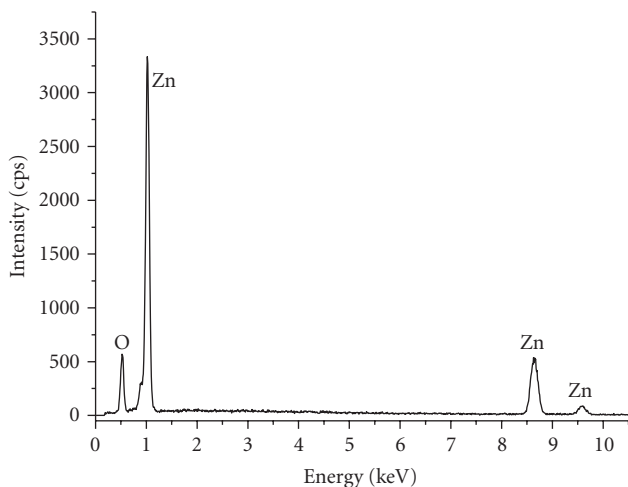


FIGURE 7: EDS spectra of sample grown at 650°C.

surface layer as was observed by some previous authors [17]. The wires are only partially oxidized due to its surface oxide layer that inhibits the oxidation of the bulk Zn by forming a protective layer, leading to a very slow oxidation.

3.1.2. Sample Grown at 500°C. SEM micrographs shown in Figure 4 illustrate the morphology of product grown at 500°C. Figure 4(a) shows the formation of a large number of microspheres distributed on a compact layer. The number of microspheres is considerably higher than that for sample grown at 350°C. It is observed that surfaces of both microspheres and the compact layer are very similar and relatively rough (Figure 4(b)). Also, the microspheres have relatively uniform sizes with a mean diameter about 20 micrometers (Figure 4(c)), and some of them are self-assembled leading to spherical packing. The layer under

microspheres (Figure 4(d)) exhibits a film-like structure, which is different than the wires formed at 350°C.

EDS analysis of the microspheres shows Zn and O peaks (Figure 5(a)). Although microspheres principally formed in the gas phase and condensed at the slow cooling-down stage at the end of the process, it is possible that some water vapor species oxidizes their surface because the substrate is closer from the hot filament. Therefore, a Zn microsphere with a ZnO shell can be obtained by increasing the substrate temperature at 500°C. EDS measurements of the compact layer formed under the microspheres (Figure 5(b)) show Zn and O peaks, indicating again that substrate surface reaction includes Zn layer formation and a postsurface oxidation process. Additionally, this result suggests that this compact layer is sufficiently thick to prevent the silicon substrate contribution.

3.1.3. Sample Grown at 650°C. Figure 6 shows SEM micrographs of the sample grown at 650°C. The obtained product exhibits a dense structure composed by solid microspheres (Figure 6(a)). The microspheres have uniform sizes of approximately 50 μm. This image shows no further layer under microspheres as seen for samples grown at 350 and 500°C. It could be suggested that the large number of condensed microspheres and its coalescence lead the microspheres to cover the layer grown onto the substrate completely. High magnification SEM image of the microspheres is shown in Figure 6(b). It is observed that the shape of some microspheres is lost by coalescence with the tendency to integrate to the under layer. EDS spectrum (Figure 7) of this sample shows Zn peaks with a low contribution of oxygen, which confirms the presence of a Zn-ZnO structure.

3.2. XRD Measurements. Figure 8 shows the XRD spectra of the microspheres grown at 350, 500, and 650°C by the HFCVD technique. The observed diffraction peaks in all recorded XRD patterns are in agreement with the

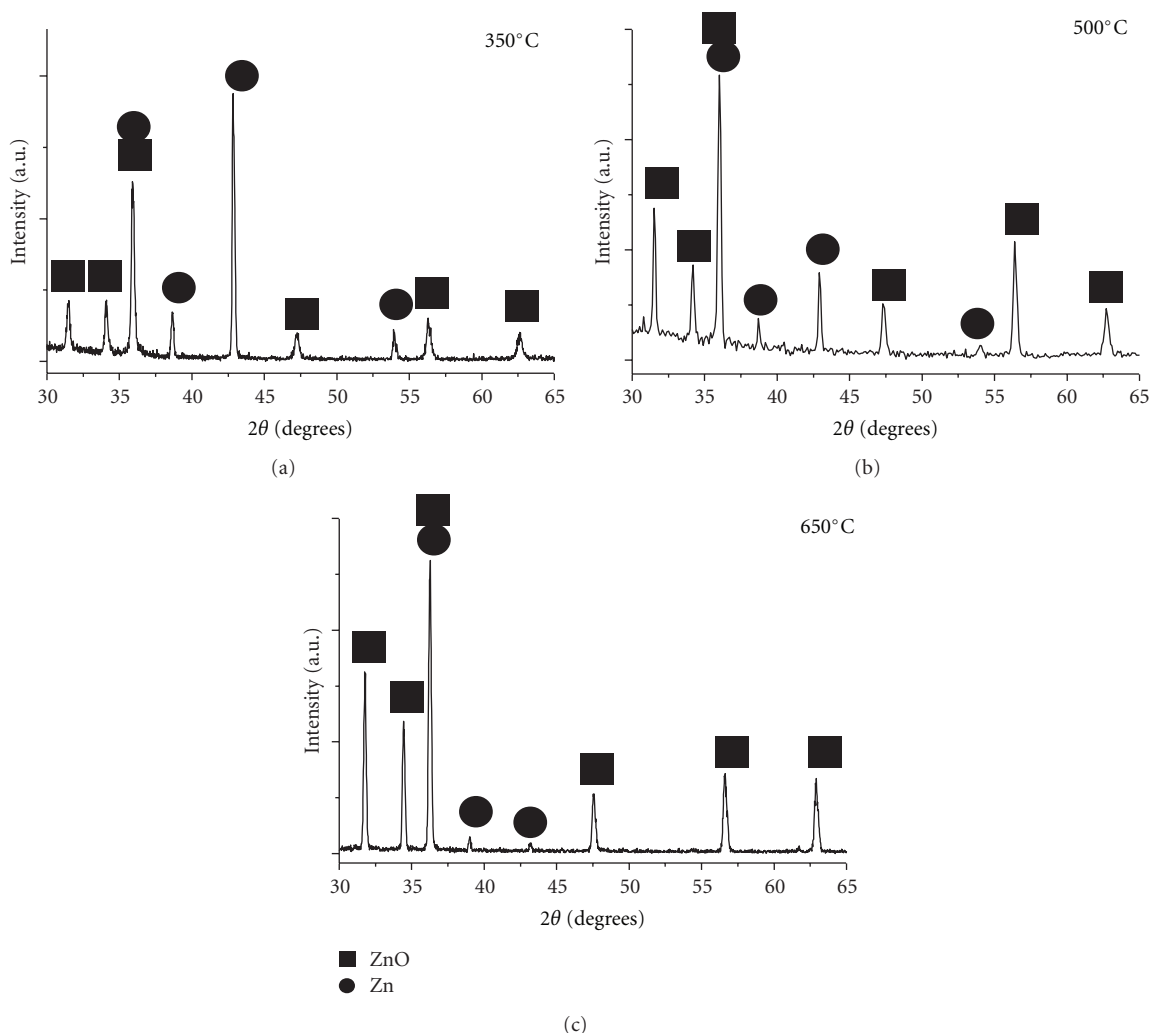


FIGURE 8: XRD spectra of samples grown at 350, 500, and 650 °C by the HFCVD technique.

JCPDS 00-035-1451 and 00-004-0831 cards corresponding to ZnO and Zn hexagonal crystal structures, respectively. No peaks of any other phase were detected; this rules out the possibility of sample contamination by the tungsten filament. The presence of ZnO and Zn phases in all XRD spectra corroborates the fact that both microspheres and the layer that grow on the substrate are only superficially oxidized independently from the substrate temperature. It is observed that peak at 43.10° corresponding to Zn (101) plane in the XRD diffractogram of sample grown at 350 °C is the strongest. We suggest that the main contribution of Zn crystals on this sample comes from the bulk Zn of the wires due to the low number of Zn microspheres placed at the top of the structure. At higher substrate temperatures, the intensity ratio of the Zn peaks to the ZnO peaks decreases, suggesting a better oxidation characteristic. It is known that in Zn-ZnO structures, the bulk oxidation is controlled by the outdiffusion of Zn through the surface ZnO layer [18, 19]. Thus, the increase of the substrate temperature enhances the

mobility of Zn, leading to the outdiffusion of these atoms across of the thin ZnO layer from the microspheres and from the layer under microspheres. This results in bigger Zn-ZnO microspheres as a result of this physical mechanism.

4. Conclusion

Zn microspheres and Zn-ZnO core-shell microspheres were obtained in the temperature range of 350–650 °C by HFCVD technique. The Zn microspheres were observed on a Zn-ZnO surface layer, which is formed on the silicon substrate during the experimental process. XRD and EDS results suggested that all grown Zn microspheres are only partially oxidized independently of the substrate temperature. We suggest that the Zn-ZnO microspheres condensed during the natural cooling of the HFCVD reactor, and they are not formed as a result of the vapor-liquid-solid growth mechanism. The formation of Zn-ZnO microspheres by the HFCVD technique could be an easy

and low cost way to produce these structures at the large scale.

Acknowledgments

This work was financially supported by CONACYT, VIEP-BUAP, and ICUAP-BUAP. The authors also acknowledge S&C Associates for proofreading of the paper.

References

- [1] K. M. Sulieman, X. Huang, J. Liu, and M. Tang, "Controllable synthesis and characterization of hollow-opened ZnO/Zn and solid Zn/ZnO single crystal microspheres," *Nanotechnology*, vol. 17, no. 19, pp. 4950–4955, 2006.
- [2] W. Ding, F. Chun, X. Qiang, and P. Yi, "Gas sensing properties of hollow SnO₂ microspheres prepared by a template process," *Sensor Letters*, vol. 9, pp. 184–187, 2011.
- [3] M. H. Aslan, A. Y. Oral, E. Menşur, A. Gül, and E. Başaran, "Preparation of C-axis-oriented zinc-oxide thin films and the study of their microstructure and optical properties," *Solar Energy Materials and Solar Cells*, vol. 82, no. 4, pp. 543–552, 2004.
- [4] A. E. Jimenez and J. A. Soto, "Optical transmittance and photoconductivity studies on ZnO : Al thin films prepared by the sol-gel technique," *Solar Energy Materials and Solar Cells*, vol. 52, no. 3-4, pp. 345–353, 1998.
- [5] M. Sucheá, S. Christoulakis, K. Moschovis, N. Katsarakis, and G. Kiriakidis, "ZnO transparent thin films for gas sensor applications," *Thin Solid Films*, vol. 515, no. 2, pp. 551–554, 2006.
- [6] Q. Wan, Q. H. Li, Y. J. Chen et al., "Fabrication and ethanol sensing characteristics of ZnO nanowire gas sensors," *Applied Physics Letters*, vol. 84, pp. 3654–3656, 2004.
- [7] B. Gan, J. Ahn, Q. Zhang et al., "Branching carbon nanotubes deposited in HFCVD system," *Diamond and Related Materials*, vol. 9, no. 3, pp. 897–900, 2000.
- [8] K. H. Kim, E. Lefevre, M. Châtelet, D. Pribat, and C. S. Cojocar, "Laterally organized carbon nanotube arrays based on hot-filament chemical vapor deposition," *Thin Solid Films*, vol. 519, no. 14, pp. 4598–4602, 2011.
- [9] S. L. Katar, D. Hernandez, A. B. Labiosa et al., "SiN/bamboo like carbon nanotube composite electrodes for lithium ion rechargeable batteries," *Electrochimica Acta*, vol. 55, no. 7, pp. 2269–2274, 2010.
- [10] W. W. Yi and Q. Q. Yang, "Aligned growth and alignment mechanism of carbon nanotubes by hot filament chemical vapor deposition," *Applied Physics A*, vol. 98, no. 3, pp. 659–669, 2010.
- [11] J. H. Yim, S. Choi, S. Lee, and K. H. Koh, "Synthesis of very dense carbon nanotube bundles using silica supported metal catalyst," *Journal of Vacuum Science and Technology B*, vol. 22, pp. 1308–1311, 2004.
- [12] K. H. Park, J. H. Yim, S. Lee, and K. H. Koh, "Catalyst-assisted hot filament chemical vapor deposition and characterization of carbon nanostructures," *Thin Solid Films*, vol. 501, no. 1-2, pp. 233–237, 2006.
- [13] H. Umemoto, K. Ohara, D. Morita, Y. Nozaki, A. Masuda, and H. Matsumura, "Direct detection of H atoms in the catalytic chemical vapor deposition of the SiH₄/H₂ system," *Journal of Applied Physics*, vol. 91, no. 3, pp. 1650–1656, 2002.
- [14] S. J. Harris and A. M. Weiner, "Reaction kinetics on diamond: measurement of H atom destruction rates," *Journal of Applied Physics*, vol. 74, pp. 1022–1026, 1993.
- [15] T. W. Kim, T. Kawazoe, S. Yamazaki, M. Ohtsu, and T. Sekiguchi, "Low-temperature orientation-selective growth and ultraviolet emission of single-crystal ZnO nanowires," *Applied Physics Letters*, vol. 84, no. 17, pp. 3358–3360, 2004.
- [16] S. Kar, T. Ghoshal, and S. Chaudhuri, "Simple thermal evaporation route to synthesize Zn and Cd metal nanowires," *Chemical Physics Letters*, vol. 419, no. 1–3, pp. 174–178, 2006.
- [17] J. G. Wang, M. L. Tian, N. Kumar, and T. E. Mallouk, "Controllable template synthesis of superconducting Zn nanowires with different microstructures by electrochemical deposition," *Nano Letters*, vol. 5, no. 7, pp. 1247–1253, 2005.
- [18] J. O. Cope, "Kinetics of the oxidation of molten zinc," *Transactions of the Faraday Society*, vol. 57, pp. 493–503, 1961.
- [19] A. C. S. Sabioni, "About the oxygen diffusion mechanism in ZnO," *Solid State Ionics*, vol. 170, no. 1-2, pp. 145–148, 2004.

Research Article

Solubility of Carbon in Nanocrystalline α -Iron

Alexander Kirchner and Bernd Kieback

Institute of Materials Science, Technische Universität Dresden, 01062 Dresden, Germany

Correspondence should be addressed to Alexander Kirchner, alexander.kirchner@tu-dresden.de

Received 24 February 2012; Accepted 3 May 2012

Academic Editor: Grégory Guisbiers

Copyright © 2012 A. Kirchner and B. Kieback. This is an open access article distributed under the Creative Commons Attribution License, which permits unrestricted use, distribution, and reproduction in any medium, provided the original work is properly cited.

A thermodynamic model for nanocrystalline interstitial alloys is presented. The equilibrium solid solubility of carbon in α -iron is calculated for given grain size. Inside the strained nanograins local variation of the carbon content is predicted. Due to the nonlinear relation between strain and solubility, the averaged solubility in the grain interior increases with decreasing grain size. The majority of the global solubility enhancement is due to grain boundary enrichment however. Therefore the size effect on carbon solubility in nanocrystalline α -iron scales with the inverse grain size.

1. Introduction

An enhancement of solid solubility has been found in many bulk nanocrystalline materials, for instance [1, 2]. Often the bigger part of the effect can be attributed to nonequilibrium processing such as mechanical alloying [3]. However quantifying the impact of grain refinement on equilibrium solid solubility is important for understanding the behavior of nanocrystalline alloys upon thermal activation. In this context equilibrium shall be constrained by the assumption of a stable grain size.

The scope of this work is to develop a thermodynamic model of nanocrystalline alloys. It has to comprise both the nanoscale grains and the grain boundary regions, since the fraction of atoms located in those cannot be neglected. The description is based upon the previously published thermodynamic treatment of alloy grain boundaries [4]. There the grain boundaries are approximated by a uniformly dilated lattice retaining the symmetry of the bulk material [5, 6] and are characterized by their volumetric strain $\Delta V/V_0$.

The interstitial solution of carbon in α -iron is chosen as an alloy of practical relevance and experimental accessibility. In pure iron the nanocrystalline state is retained even after prolonged annealing at 650 K [7]. At this temperature and a time of 3600 s, the diffusion length of carbon in bulk iron exceeds 50 μm [8]. Since the carbon diffusivity will be larger

in nanocrystalline iron, this enables chemical equilibration without strong grain growth.

2. Thermodynamic Model of Nanocrystalline Fe-C

The thermodynamic description of a binary Fe-C alloy under volumetric strain is based upon Kaufman and Schlosser's expression [9] for the Helmholtz free energy F . The free energy of the strained solid consists of F° at zero pressure and a second term that accounts for the elastic energy depending on the parameter $\chi = (V/V_0)^{1/3}$ using the Vinet et al. universal equation of state [10]. The isothermal bulk modulus B_0 , the molar volume V_0 , and the anharmonicity parameter η_0 are given at zero pressure:

$$F = F^\circ + \frac{9B_0V_0}{\eta_0^2} \left[\left\{ \eta_0(1-\chi) - 1 \right\} e^{\eta_0(1-\chi)} + 1 \right]. \quad (1)$$

A two-sublattice model $\text{Fe}(\text{Va},\text{C})_3$ is used to describe the interstitial solution of carbon in α -iron. In the second sublattice carbon substitutes normally vacant octahedral sites. Here y_C marks the molar fraction of carbon in the sublattice. Its relation to the carbon content given as the molar fraction x_C is $y_C = x_C/(3(1-x_C))$. Conveniently choosing pure α -iron and graphite as the reference state,

the molar free energy F° of the unstrained alloy is stated by [11] in units of Joule where T is the temperature in Kelvin:

$$F^\circ = (322050 + 75.667T)y_C + 3RT(y_C \ln y_C + (1 - y_C) \ln(1 - y_C)) - 190T(1 - y_C)y_C. \quad (2)$$

Assuming a dilute alloy, B_0 and η_0 of pure α -iron are used in (1). Values of $B_0 = 178.6$ GPa, $V_0 = 7.09 \cdot 10^{-6}$ m³/mol [12], and $\eta_0 = 5.16$ [13] at $T = 298$ K are employed. Their temperature dependence is calculated according to Vinet and coworkers [10] using the coefficient of volumetric thermal expansion $\alpha_0 = 36.9 \cdot 10^{-6}$ K⁻¹ [12]. At low solute concentration the molar volume V_0 of the alloy varies linearly with x_C , and

$$\chi = \sqrt[3]{\frac{1 + \Delta V/V_0}{1 + x_C \Omega_C^{\text{Fe,bcc}}}} \quad (3)$$

is obtained. The volume size factor of carbon in α -iron $\Omega_C^{\text{Fe,bcc}} = 0.825$ is averaged from two publications [14, 15]. The equilibrium between carbon in strained α -iron and the reference state graphite is given by $F + (1 - x_C) \cdot (\partial F / \partial x_C) = 0$.

The strain of the crystallite interior is calculated using Weissmüller's model [16]. Accordingly local strain in bulk nanocrystalline materials is caused by the fact that the cavities defined by the adjacent grains need to accommodate a finite number of lattice planes. The maximum linear strain ε_{max} is given by the interatomic distance r_{NN} (for iron $r_{\text{NN}} = 0.252$ nm [12]) and the grain size D :

$$|\varepsilon_{\text{max}}| = \frac{1}{4} \sqrt{\frac{3}{2}} \frac{r_{\text{NN}}}{D}. \quad (4)$$

The predicted root mean square strain is in good agreement with strain measured in nc-Fe by X-ray diffraction [17, 18]. Here the mean strain $\langle \varepsilon \rangle_V = -2 \langle f \rangle_A / (3B_0 D)$ is neglected, because with a grain-boundary stress $\langle f \rangle_A$ of 1.1 N/m [19] it is more than a magnitude of order smaller than $|\varepsilon_{\text{max}}|$. The volumetric strain is given by the superposition of the linear strain in three dimensions $\Delta V/V_0 \cong \varepsilon_x + \varepsilon_y + \varepsilon_z$.

Furthermore a thickness w of 0.7 nm representing 3-4 monolayers and a value of $\Delta V/V_0 = 0.12$ is used to describe average grain boundaries. This choice of parameters yields a good agreement with an experimental value of the interface free energy of 468 mJ/m² at 1723 K [20].

Finally the resulting global solubility x_C^{global} is calculated from the grain boundary and interior compositions with their respective molar fractions as weighting factors:

$$x_C^{\text{global}} = f x_C^{\text{GB}} + (1 - f) \bar{x}_C^{\text{interior}}, \quad (5)$$

$$f = \frac{(D + w)^3 - D^3}{(D + w)^3 + D^3 (\Delta V/V_0)}. \quad (6)$$

The molar fraction of the atoms located in grain boundaries f is corrected for the different atomic densities and converges for $\Delta V/V_0 = 0$ and large grain sizes toward $3w/D$.

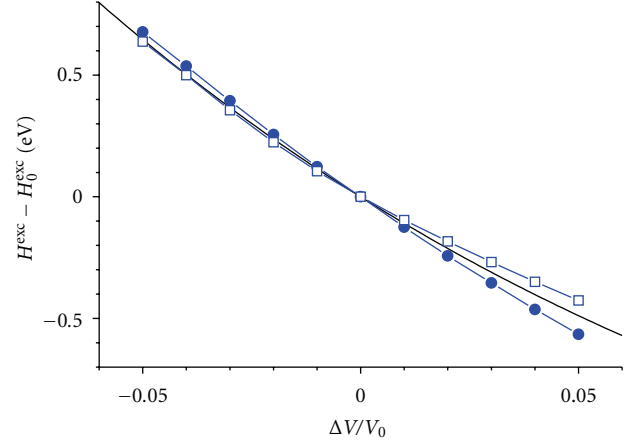


FIGURE 1: Difference of the excess enthalpies of a carbon atom in strained and strain-free iron. Results from [21] are marked as filled circles (DFT) and open squares (MEAM).

3. Results and Discussion

Recently *ab initio* methods based on density-functional theory (DFT) allow for highly accurate simulation of carbon solution in α -iron. The excess enthalpy of carbon in iron as defined by [21] depending on volumetric strain was calculated at $T = 0$ K and infinite carbon dilution. The result is presented in Figure 1. Good agreement with the strain dependence of excess enthalpies computed by DFT and a modified embedded-atom method (MEAM) is observed. The calculated derivative of the excess enthalpy with respect to the atomic volume at $\Delta V/V_0 = 0$ is -0.95 eV/Å³ as compared to -1.08 eV/Å³ (DFT) and -0.84 eV/Å³ (MEAM).

The maximum linear strain of the grain interior given by (4) can be used to calculate the local volumetric strain assuming three independent axes. For a grain size of 20 nm the linear strain varies locally between $-3.8 \cdot 10^{-3}$ and $+3.8 \cdot 10^{-3}$ and the volumetric strain between -0.011 and $+0.011$ with the frequency distribution shown in Figure 2. Close to $\Delta V/V_0 = 0$ the calculated carbon concentration in equilibrium with graphite at 673 K coincides with the linear theory of thermochemical equilibrium of solids under stress [22]. For large strains nonlinear behavior is observed. At lower values of $\Delta V/V_0$ indicating strong compression, the carbon concentration converges towards zero, which is the physically reasonable behavior.

The expected variation in composition between individual nanograins can be deduced from the range of values calculated for x_C^{interior} . For a grain size of 20 nm the ratio between the maximum ($9.8 \cdot 10^{-4}$ at.%) and the minimum carbon concentration ($1.7 \cdot 10^{-5}$ at.%) is 59. This ratio will be even larger for smaller grain sizes. Another notable consequence of the nonlinear trend of x_C^{interior} is that weighted averaging yields a deviation from bulk solubility despite the strain distribution symmetry. Figure 3 shows the average carbon solubility in the grain interior as a function of inverse grain size. It increases with decreasing grain size slightly.

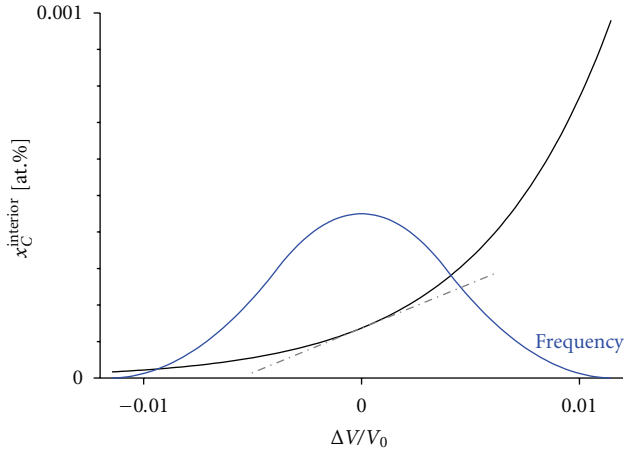


FIGURE 2: Solubility of carbon in the strained grain interior at 673 K. The range and frequency distribution of the local strain is calculated for a grain size of 20 nm. The broken line represents the result of the theory by Larché and Cahn [22].

$\bar{x}_C^{\text{interior}}$ is doubled with respect to the bulk solubility for 11 nm grains.

The carbon concentration in grain boundaries was calculated in equilibrium with graphite assuming it to be independent of curvature and grain size. At a temperature of 673 K the computed value of x_C^{GB} is 3.9 at.%. This means that carbon is enriched by a factor of $3 \cdot 10^4$ in the grain boundaries with respect to the bulk. Atom probe microscopy measurements confirm the presence of a minimum of 2 at.% carbon in α -iron grain boundaries [23]. Other experiments at 873 K [24, 25] yielded higher values, expressed as excess densities of carbon at the interface of $\Gamma_C^{\text{GB}} \approx 20 \mu\text{mol}/\text{m}^2$. The corresponding theoretical prediction is lower at $\Gamma_C^{\text{GB}} = 5 \mu\text{mol}/\text{m}^2$. The difference may be explained by the strong variation between individual grain boundaries and the information depth of the analytical methods employed. In the case of autoradiography it exceeds the grain boundary thickness of approximately 1 nm by far. The detected amount is likely to include carbon enriched at stress fields around grain boundaries as well. Then the concentration in the grain boundary core is lower than Γ_C^{GB} suggests.

Calculating the global solubility according to (5) yields an almost linear relation with the inverse grain size as Figure 3 illustrates. The reason is that the contribution of enriched grain boundaries dominates the size effect. Figure 4 shows the calculated solubility of carbon in nanocrystalline α -iron of various grain sizes. Thereafter a pronounced increase in equilibrium carbon solubility is to be expected in nanocrystalline iron in comparison to bulk iron.

4. Conclusions

A thermodynamic model for nanocrystalline α -phase Fe-C alloys has been presented. Considering the strained grain interior in equilibrium with graphite local variation of the carbon concentration but only a weak size effect on the average carbon solubility is found. While the extent of

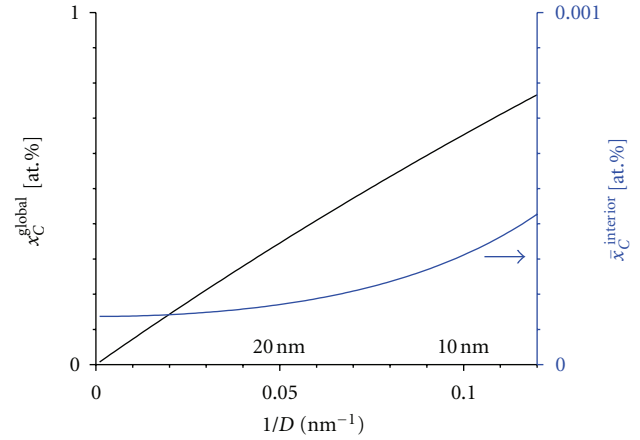


FIGURE 3: Average solubility of carbon in the grain interior $\bar{x}_C^{\text{interior}}$ and resulting solubility x_C^{global} in nanocrystalline α -iron at 673 K as a function of grain size. Note that the axis of $\bar{x}_C^{\text{interior}}$ is scaled by a factor 1000.

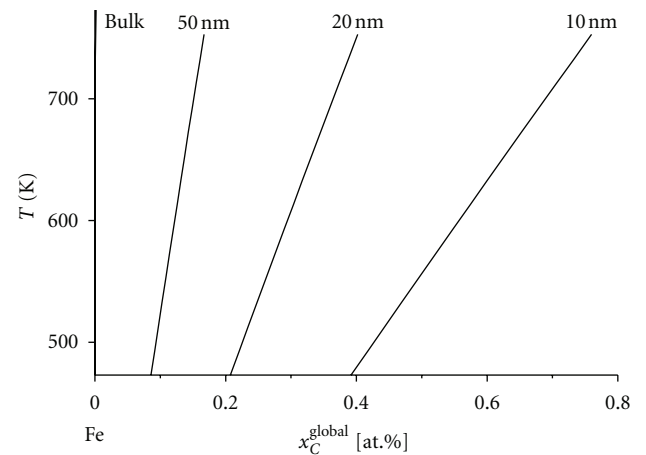


FIGURE 4: Calculated solvus lines of carbon in nanocrystalline α -iron of 10, 20, and 50 nm grain size compared to bulk iron.

enrichment at grain boundaries is not precisely established, grain boundary segregation dominates the solubility increase in the nanocrystalline state. It is concluded that the excess carbon solubility in nanocrystalline iron over bulk iron is proportional to the inverse grain size. At a given temperature the overall solubility follows

$$x_C^{\text{global}} \approx x_C^{\text{bulk}} + \frac{\text{const}}{D}. \quad (7)$$

Acknowledgments

The research of A. Kirchner was supported by Deutsche Forschungsgemeinschaft via the Emmy Noether Programme.

References

- [1] H. Gleiter, "Nanocrystalline solids," *Journal of Applied Crystallography*, vol. 24, no. 2, pp. 79–90, 1991.
- [2] C. D. Terwilliger and Y. M. Chiang, "Size-dependent solute segregation and total solubility in ultrafine polycrystals: Ca in TiO₂," *Acta Metallurgica Et Materialia*, vol. 43, no. 1, pp. 319–328, 1995.
- [3] C. Suryanarayana, "Mechanical alloying and milling," *Progress in Materials Science*, vol. 46, no. 1–2, pp. 1–184, 2001.
- [4] A. Kirchner and B. Kieback, "Thermodynamic model of alloy grain boundaries," *Scripta Materialia*, vol. 64, no. 5, pp. 406–409, 2011.
- [5] H. J. Fecht, "Intrinsic instability and entropy stabilization of grain boundaries," *Physical Review Letters*, vol. 65, no. 5, pp. 610–613, 1990.
- [6] M. Wagner, "Structure and thermodynamic properties of nanocrystalline metals," *Physical Review B*, vol. 45, no. 2, pp. 635–639, 1992.
- [7] T. R. Malow and C. C. Koch, "Grain growth in nanocrystalline iron prepared by mechanical attrition," *Acta Materialia*, vol. 45, no. 5, pp. 2177–2186, 1997.
- [8] E. A. Brandes and G. B. Brook, Eds., *Smithells Metals Reference Book*, Butterworth Heinemann, Oxford, UK, 1999.
- [9] M. Kaufman and H. Schlosser, "A thermodynamic model for pressurized solids," *Journal of Physics*, vol. 7, no. 11, article 03, pp. 2259–2264, 1995.
- [10] P. Vinet, J. R. Smith, J. Ferrante, and J. H. Rose, "Temperature effects on the universal equation of state of solids," *Physical Review B*, vol. 35, no. 4, pp. 1945–1953, 1987.
- [11] P. Gustafson, "A thermodynamic evaluation of the Fe-C system," *Scandinavian Journal of Metallurgy*, vol. 14, no. 5, pp. 259–267, 1985.
- [12] W. Martienssen and H. Warlimont, Eds., *Handbook of Condensed Matter and Materials Data*, Springer, Berlin, Germany, 2005.
- [13] J. H. Rose, J. R. Smith, F. Guinea, and J. Ferrante, "Universal features of the equation of state of metals," *Physical Review B*, vol. 29, no. 6, pp. 2963–2969, 1984.
- [14] E. J. Fasiska and H. Wagenblast, "Dilation of alpha iron by carbon," *Transactions of the Metallurgical Society of AIME*, vol. 239, no. 11, pp. 1818–1820, 1967.
- [15] H. W. King, "Quantitative size-factors for interstitial solid solutions," *Journal of Materials Science*, vol. 6, no. 9, pp. 1157–1167, 1971.
- [16] J. Weissmüller, "Thermodynamics of nanocrystalline solids," in *Nanocrystalline Metals and Oxides*, P. Knauth and J. Schoonman, Eds., Kluwer Academic, New York, NY, USA, 2002.
- [17] E. Bonetti, L. Del Bianco, L. Pasquini, and E. Sampaoli, "Thermal evolution of ball milled nanocrystalline iron," *Nanostructured Materials*, vol. 12, no. 5, pp. 685–688, 1999.
- [18] Y. H. Zhao, H. W. Sheng, and K. Lu, "Microstructure evolution and thermal properties in nanocrystalline Fe during mechanical attrition," *Acta Materialia*, vol. 49, no. 2, pp. 365–375, 2001.
- [19] P. Zimmer and R. Birringer, "Measuring the interface stress of nanocrystalline iron," *Applied Physics Letters*, vol. 92, no. 8, Article ID 081912, 3 pages, 2008.
- [20] L. E. Murr, *Interfacial Phenomena in Metals and Alloys*, Addison-Wesley, New York, NY, USA, 1975.
- [21] E. Hristova, R. Janisch, R. Drautz, and A. Hartmaier, "Solubility of carbon in α -iron under volumetric strain and close to the $\Sigma 5(310)[001]$ grain boundary: comparison of DFT and empirical potential methods," *Computational Materials Science*, vol. 50, no. 3, pp. 1088–1096, 2011.
- [22] F. Larché and J. W. Cahn, "A linear theory of thermochemical equilibrium of solids under stress," *Acta Metallurgica*, vol. 21, no. 8, pp. 1051–1063, 1973.
- [23] A. Atrens, J. Q. Wang, K. Stiller, and H. O. Andren, "Atom probe field ion microscope measurements of carbon segregation at an α/α grain boundary and service failures by intergranular stress corrosion cracking," *Corrosion Science*, vol. 48, no. 1, pp. 79–92, 2006.
- [24] J. M. Papazian and D. N. Besherb, "Grain boundary segregation of carbon in iron," *Metallurgical Transactions*, vol. 2, no. 2, pp. 497–503, 1971.
- [25] H. Hänsel and H. J. Grabke, "Grain boundary segregation of phosphorus and carbon in ferritic iron," *Scripta Metallurgica*, vol. 20, no. 11, pp. 1641–1644, 1986.

Research Article

Elastic Analysis for Nanocontact Problem with Surface Stress Effects under Shear Load

D. X. Lei, L. Y. Wang, and Z. Y. Ou

School of Science, Lanzhou University of Technology, Lanzhou 730050, China

Correspondence should be addressed to Z. Y. Ou, zhiyingou@163.com

Received 24 February 2012; Accepted 15 May 2012

Academic Editor: Sergio J. Mejía-Rosales

Copyright © 2012 D. X. Lei et al. This is an open access article distributed under the Creative Commons Attribution License, which permits unrestricted use, distribution, and reproduction in any medium, provided the original work is properly cited.

Consideration of surface stress effects on the elastic field of nanocontact problem has extensive applications in several modern problems of solid mechanics. In this paper, the effects of surface stress on the contact problem at nanometers are studied in the frame of surface elasticity theory. Fourier integral transform method is adopted to derive the fundamental solution of the nanocontact problem under shear load. As two special cases, the deformations induced by a uniformly distributed shear load and a concentrated shear force are discussed in detail, respectively. The results indicate some interesting characteristics in nanocontact mechanics, which are distinctly different from those in macrocontact problem. At nanoscale, both the contact stresses and the displacements on the deformed surface transit continuously across the uniform distributed shear load boundary as a result of surface stress. In addition, the indent depth and the contact stress depend strongly on the surface stress for nanoindentation.

1. Introduction

Contact problems of an elastic half-space by applied loads on its plane surface are the subject of extensive literature [1]. The greater parts of these works of literature are concerned with the responses subjected to surface loads with only existing residual surface tension [2]. Corresponding problems of complete effects of surface stress (nonzero surface tension and surface elastic properties) have also attracted the attention of a number of authors and a considerable body of literature exists on this class of problems [3]. The surface of solids is a special region with very small thickness (a few times of atom-spacing). Since the equilibrium lattice spacing in the surface is different from that in the bulk, surface stress appears. For solids with large characteristic dimensions, the volume ratios of surface region to the bulk material is small; the effect of surface stress then can be neglected because of its relatively tiny contribution. However, for microsolids with large surface-to-bulk ratio the significance of surfaces is likely to be important, such as nanocontact problem [4]. This is extremely true for nanoscale materials or structures.

When the characteristic size of an element or a solid approaches nanometers, its mechanical behavior displays

remarkable size-dependent phenomena [5]. However, as there is no intrinsic length scale involved in the constitutive laws, the classical elastic theory cannot predict the size-dependent behavior of solids. Owing to the increasing ratio of surface-to-bulk volume, the effect of surface stress has been considered as one of the major factors contributing to the exceptional behaviors at nanoscale [2, 6–12].

To account for the effect of surface stress in solid mechanics, Gurtin and Ian Murdoch [13, 14] developed a continuum theory of surface elasticity. For some elementary deformation modes, the prediction of surface elasticity showed a good agreement with directly atomic simulation. Therefore, the surface elasticity has been widely adopted to investigate the mechanical phenomena at nanoscale. Miller and Shenoy [15] studied the size-dependent elastic stiffness of structural elements such as nanobars, nanobeams, and nanoplates. Cammarata et al. [16] considered the size-dependent deformation in thin film with surface effect. Through atomic simulation, Shenoy [17] calculated the surface elastic constants of metallic fcc crystal surfaces. Gao et al. [18] developed a finite-element method to account for the effect of surface elasticity. Zhang and Wang [19, 20] investigated the effect of surface energy on the yield strength of

nanoporous materials and nanowires. Wang and Feng [2] studied the response of a half-plane subjected to normal pressures with constant residual surface tension. Ou et al. [9–11] studied how the size dependence can be considered in the mechanical performance of nanoscale structures and devices. Zhao and Rajapakse [21] derived the fundamental solution of an elastic layer bonded to a rigid substrate with surface effects. Due to the complexity of the problem, however, until now there has been no systematic investigation into the complete effects of stress (nonzero surface tension and surface elastic properties) on an isotropic elastic bulk. In this paper, Fourier integral transform method is used to solve the nonclassical boundary-value problems with complete surface effects.

In the present paper, the fundamental nanocontact problem of an isotropic elastic bulk with complete surface stress effects (nonzero surface tension and surface elastic properties) subjected to surface shear load is considered. The Fourier integral transform method is employed to obtain the fundamental solution of nanocontact problem with surface effects. This method allows us to easily extend our analysis to problems involving half-plane subjected to both concentrated shear load and uniformly distributed shear load on a finite region. The outline of the paper is organized as follows. The basic equations of surface elasticity are reviewed briefly in Section 2. In Section 3, the Fourier integral transform method is adopted to solve the nanocontact problem with surface effects subjected to shear loads. The detailed results for the cases of uniformly distributed shear load and concentrated forces are discussed in Sections 4 and 5, respectively, and concluding remarks are presented in Section 6.

2. Basic Equations of Surface Elasticity

In surface elasticity theory, a surface is regarded as a negligibly thin membrane that has material constants different from the bulk material and is adhered to the bulk without slipping. The equilibrium and constitutive equations in the bulk of material are the same as those in classical elastic theory, but the presence of surface stresses gives rise to a nonclassical boundary condition. For further details, the reader may refer to Gurtin and Ian Murdoch [13, 14]. Here only several basic equations of surface elasticity theory are reviewed.

In the absence of body force, the equilibrium equations, constitutive law, and geometry relations in the bulk are as follows:

$$\begin{aligned} \sigma_{ij,j} &= 0 \\ \sigma_{ij} &= 2G \left(\varepsilon_{ij} + \frac{\nu}{1-2\nu} \varepsilon_{kk} \delta_{ij} \right), \end{aligned} \quad (1)$$

where G and ν are the shear modulus and Poisson's ratio of the bulk material, σ_{ij} and ε_{ij} are the stress tensor and strain tensor in the bulk material, respectively. Throughout the paper, Einstein's summation convention is adopted for all repeated Latin indices (1, 2, 3) and Greek indices (1, 2).

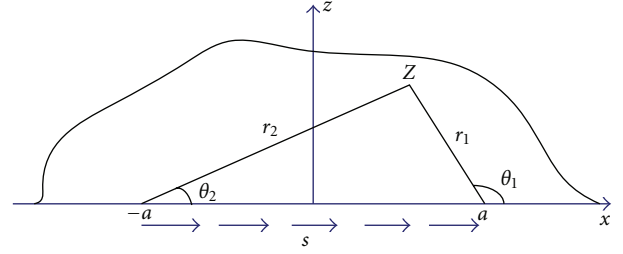


FIGURE 1: Schematic of contact problem under uniform shear load.

The strain tensor is related to the displacement vector u_i by

$$\varepsilon_{ij} = \frac{1}{2} (u_{i,j} + u_{j,i}). \quad (2)$$

Assume that the surface of the material adheres perfectly to its bulk without slipping. Then the equilibrium conditions on the surface are expressed as

$$\begin{aligned} \sigma_{\beta\alpha} n_\beta + \sigma_{\beta\alpha,\beta}^s &= 0, \\ \sigma_{ij} n_i n_j &= \sigma_{\alpha\beta}^s \kappa_{\alpha\beta}, \end{aligned} \quad (3)$$

where n_i denotes the normal to the surface, $\kappa_{\alpha\beta}$ the curvature tensor of the surface, and $\sigma_{\alpha\beta}^s$ the surface stress tensor.

The surface stress tensor is related to the surface strain tensor by

$$\sigma_{\beta\alpha}^s = \tau^s \delta_{\beta\alpha} + 2(\mu^s - \tau^s) \varepsilon_{\beta\alpha} + (\lambda^s + \tau^s) \varepsilon_{\gamma\gamma} \delta_{\beta\alpha}, \quad (4)$$

where τ^s is the residual surface tension under unstrained conditions, μ^s and λ^s are surface Lamé constants which can be determined by atom simulations or experiments [17].

3. Nanocontact Model with Surface Effects

Considering a material occupying the upper half-plane $z > 0$, we refer to a Cartesian coordinate system $(o-xyz)$, as shown in Figure 1, where the x -axis is along the surface, and the z -axis perpendicular to the surface. The plane-strain conditions are assumed to $\varepsilon_{2i} = 0$, and the contact is assumed to be frictionless. In this case, the boundary conditions (3) on the contact surface $z = 0$ are simplified to

$$\begin{aligned} \sigma_{zz} &= 0 \\ \sigma_{xz} + s(x) &= - \left(\frac{d\tau^s}{dx} + k^s \frac{d^2 u}{dx^2} \right), \end{aligned} \quad (5)$$

where $s(x)$ is the shear load applied on the surface, and $k^s = 2\mu^s + \lambda^s$ is a surface material constant.

For the considered plane problem, the equilibrium equations and Hooke's law in the bulk reduce to

$$\frac{\partial \sigma_{xx}}{\partial x} + \frac{\partial \sigma_{xz}}{\partial z} = 0, \quad \frac{\partial \sigma_{zz}}{\partial z} + \frac{\partial \sigma_{xz}}{\partial x} = 0, \quad (6)$$

$$\begin{aligned} \varepsilon_{xx} &= \frac{1}{2G} [(1-\nu)\sigma_{xx} - \nu\sigma_{zz}], \\ \varepsilon_{zz} &= \frac{1}{2G} [(1-\nu)\sigma_{zz} - \nu\sigma_{xx}], \\ \varepsilon_{xz} &= \frac{\sigma_{xz}}{2G}. \end{aligned} \quad (7)$$

The strains are related to the displacements by

$$\varepsilon_{xx} = \frac{\partial u}{\partial x}, \quad \varepsilon_{zz} = \frac{\partial w}{\partial z}, \quad \varepsilon_{xz} = \frac{1}{2} \left(\frac{\partial u}{\partial z} + \frac{\partial w}{\partial x} \right). \quad (8)$$

which satisfy the following compatibility condition:

$$\frac{\partial^2 \varepsilon_{xx}}{\partial z^2} + \frac{\partial^2 \varepsilon_{zz}}{\partial x^2} = 2 \frac{\partial^2 \varepsilon_{xz}}{\partial x \partial z}. \quad (9)$$

As in classical theory of elasticity, the Airy stress function $\chi(x, z)$ is defined by

$$\sigma_{xx} = \frac{\partial^2 \chi}{\partial z^2}, \quad \sigma_{zz} = \frac{\partial^2 \chi}{\partial x^2}, \quad \sigma_{xz} = -\frac{\partial^2 \chi}{\partial x \partial z}. \quad (10)$$

Then the equilibrium equations in (6) are satisfied automatically, and the compatibility equation in (9) becomes

$$\left(\frac{\partial^2}{\partial x^2} + \frac{\partial^2}{\partial z^2} \right) \left(\frac{\partial^2 \chi}{\partial x^2} + \frac{\partial^2 \chi}{\partial z^2} \right) = 0. \quad (11)$$

To solve the boundary-value problem, the Fourier integral transformation method is adopted to the coordinate x . Then, the Airy-stress function $\chi(x, z)$ and its Fourier transformation $\tilde{\chi}(\xi, z)$ can be expressed as

$$\tilde{\chi}(\xi, z) = \frac{1}{\sqrt{2\pi}} \int_{-\infty}^{\infty} \chi(x, z) e^{ix\xi} d\xi, \quad (12)$$

$$\chi(\xi, z) = \frac{1}{\sqrt{2\pi}} \int_{-\infty}^{\infty} \tilde{\chi}(x, z) e^{-ix\xi} d\xi.$$

Substituting (12) into (11) and considering the condition that the stresses vanish at infinity, one obtains

$$\tilde{\chi}(\xi, z) = (A + Bz)e^{-z|\xi|}, \quad (13)$$

where A and B are generally functions of ξ as yet to be determined.

Substituting (13) and (12) into (10), the stresses can be written as

$$\sigma_{xx} = \frac{1}{\sqrt{2\pi}} \int_{-\infty}^{\infty} \xi^2 [A(\xi) + (z-2|\xi|)B(\xi)] e^{-ix\xi - z|\xi|} d\xi,$$

$$\sigma_{zz} = -\frac{1}{\sqrt{2\pi}} \int_{-\infty}^{\infty} \xi^2 [A(\xi) + zB(\xi)] e^{-ix\xi - z|\xi|} d\xi,$$

$$\sigma_{xz} = \frac{i}{\sqrt{2\pi}} \int_{-\infty}^{\infty} \xi [(1-|\xi|z)B(\xi) - |\xi|A(\xi)] e^{-ix\xi - z|\xi|} d\xi. \quad (14)$$

By substituting the stresses into (7) and using (8), the displacements are derived as

$$\begin{aligned} w(x, z) &= \frac{1}{2\sqrt{2\pi}G} \int_{-\infty}^{\infty} [|\xi|A(\xi) + (1-2\nu+z|\xi|)B(\xi)] \\ &\quad \times e^{-ix\xi - z|\xi|} d\xi, \\ u(x, z) &= \frac{i}{2\sqrt{2\pi}G} \int_{-\infty}^{\infty} [(2-\nu)|\xi|A(\xi) + (z|\xi| - 2(1-\nu)) \\ &\quad \times B(\xi)] e^{-ix\xi - z|\xi|} d\xi. \end{aligned} \quad (15)$$

Substituting (15) and (14) into the surface condition (5) leads to

$$A(\xi) = 0, \quad B(\xi) = i \frac{\tilde{s}(\xi)}{\xi} \frac{1}{1+b\xi}. \quad (16)$$

Here

$$b = \frac{k^s(1-\nu)}{G}, \quad (17)$$

$$\tilde{s}(\xi) = \frac{1}{\sqrt{2\pi}} \int_{-\infty}^{\infty} s(x) e^{ix\xi} dx,$$

where b is a length parameter depending on the surface property and material elastic constants. It should be pointed out that this parameter indicates the thickness size of the zone where the surface effect is significant and plays a critical role in the surface elasticity. For metals, b is estimated on the order of nanometers [15, 19, 22].

In what follows, the two special cases including a uniform distributed shear load over a finite region and a concentrated shear force will be discussed in detail, respectively.

4. Uniform Distributed Shear Load

In the case a uniform shear load s acts over the region $|x| \leq a$, one has

$$\tilde{s}(\xi) = \sqrt{\frac{2}{\pi}} \frac{s \sin(a\xi)}{\xi}. \quad (18)$$

Therefore $B(\xi)$ is given by

$$B(\xi) = i \sqrt{\frac{2}{\pi}} \frac{s \sin(a\xi)}{\xi^2} \frac{1}{1+b\xi}. \quad (19)$$

Then the stresses are obtained as

$$\sigma_{xx} = \frac{2s}{\pi} \int_0^{\infty} \left[\frac{z\xi - 2}{\xi(1+b\xi)} \right] \sin(a\xi) \sin(x\xi) e^{-z\xi} d\xi,$$

$$\sigma_{zz} = -\frac{2s}{\pi} \int_0^{\infty} \left[\frac{z}{1+b\xi} \right] \sin(a\xi) \sin(x\xi) e^{-z\xi} d\xi,$$

$$\sigma_{xz} = -\frac{2s}{\pi} \int_0^{\infty} \left[\frac{1-z\xi}{\xi(1+b\xi)} \right] \sin(a\xi) \sin(x\xi) e^{-z\xi} d\xi. \quad (20)$$

The corresponding displacements are expressed as

$$u(x, z) = -\frac{s}{\pi G} \int_0^\infty \left[\frac{(2-\nu)z\xi - 2(1-\nu)}{\xi^2(1+b\xi)} \right] \times \sin(a\xi) \cos(x\xi) e^{-z\xi} d\xi, \quad (21)$$

$$w(x, z) = \frac{s}{\pi G} \int_0^\infty \frac{1-2\nu+z\xi}{\xi^2(1+b\xi)} \sin(a\xi) \sin(x\xi) e^{-z\xi} d\xi.$$

On the contact surface $z = 0$, the stresses is given by

$$\sigma_{xx} = -\frac{4s}{\pi} \int_0^\infty \left(\frac{b}{a}t + 1 \right)^{-1} \frac{\sin(t)}{t} \sin\left(\frac{x}{a}t\right) dt, \quad (22)$$

$$\sigma_{xz} = -\frac{2s}{\pi} \int_0^\infty \left(\frac{b}{a}t + 1 \right)^{-1} \frac{\sin(t)}{t} \cos\left(\frac{x}{a}t\right) dt.$$

A closed-form solution for the elastic field of the half-plane cannot be obtained due to the complexity of the integrals involved in the solution. However, when $b = 0$, that is, the surface influence is ignored in (22), the stresses of the half-plane are in agreement with those in the classical elastic results [1], and are expressed as

$$\sigma_{xx} = \frac{s}{2\pi} \left[4 \ln\left(\frac{r_1}{r_2}\right) - (\cos(2\theta_1) - \cos(2\theta_2)) \right], \quad (23)$$

$$\sigma_{xz} = -\frac{s}{2\pi} [2(\theta_2 - \theta_1) + (\sin(2\theta_1) - \sin(2\theta_2))],$$

where $\tan \theta_{1,2} = z/(x \mp a)$ and $r_{1,2} = [(x \mp a)^2 + z^2]^{1/2}$.

Assuming that the origin has no displacement in the z direction, that is, $w(0, 0) = 0$, one obtains

$$w(x, 0) = \frac{(1-2\nu)as}{\pi G} \int_0^\infty \left(\frac{b}{a}t + 1 \right)^{-1} \frac{\sin(t)}{t^2} \sin\left(\frac{x}{a}t\right) dt. \quad (24)$$

If the shear displacement u is specified to be zero at a distance l on the contact surface, that is, $u(l, 0) = 0$, the displacement on the surface is derived as

$$u(x, 0) = \frac{2(1-\nu)as}{\pi G} \int_0^\infty \left(\frac{b}{a}t + 1 \right)^{-1} \frac{\sin(t)}{t^2} \times \left[\cos\left(\frac{x}{a}t\right) - \cos\left(\frac{l}{a}t\right) \right] dt. \quad (25)$$

It is instructive to examine the influence of the surface stress on the stresses and displacements of the contact surface and compare them with those in classical contact problem. Surface stress can be obtained from experiments [2] or atomic simulations [15]. According to these results, the influence of surface stresses, characterized by the intrinsic length, $b = k^s(1-\nu)/G$, becomes significant at nanoscale. For the illustration of the effects of surface energy, b/a is taken as 0, 0.2, 0.5, and 2 in our calculations. Figures 2 and 3 show the distribution of the stresses σ_{xx} and σ_{xz} on the contact surface, where the solution of $b/a = 0$ is consistent with the classical elastic result. When the loading size a is comparable to the parameter b , that is, of the order of nanometers, the influence

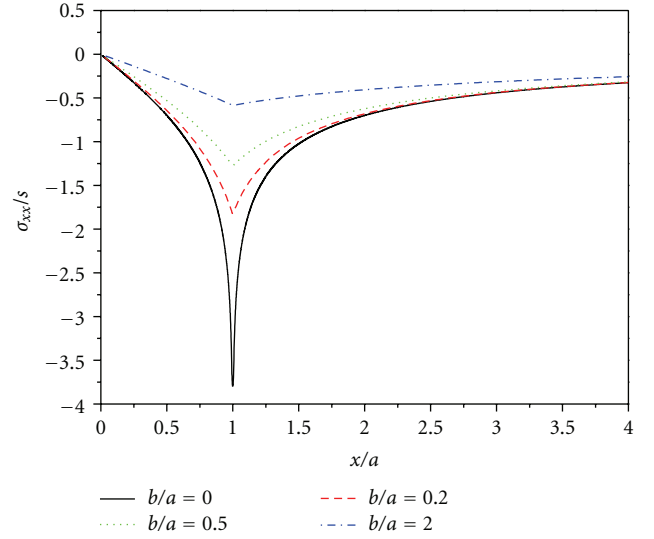


FIGURE 2: Distribution of contact normal stress under a uniform shear load.

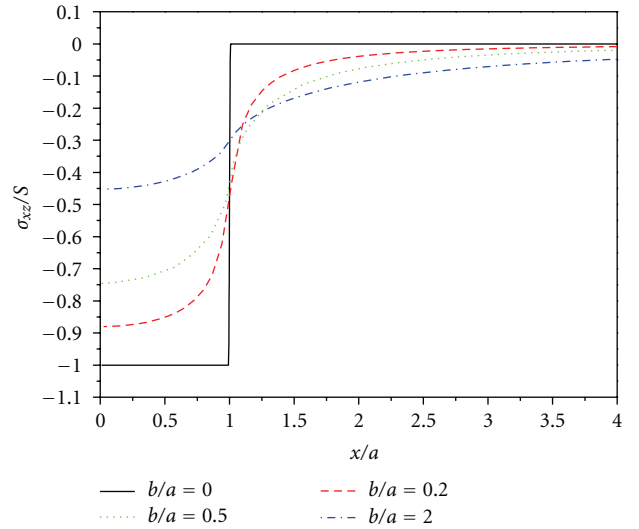


FIGURE 3: Distribution of contact shear stress under a uniform shear load.

of surface stress is evidently significant. It can be seen from Figure 2 that the normal stress transits continuously across the loading boundary $x = \pm a$, which is opposed to a singularity predicted by classical elasticity. In addition, the maximum normal stress in the bulk increases with an increase in surface stress. In the loading region ($|x/a| < 1.0$), the normal stress is decreasing monotonically with respect to x , and the inverse is observed outside the loading region ($|x/a| > 1.0$). It is also found in Figure 3 that shear stress changes smoothly across the loading boundary $x = \pm a$, which is different from a rapid jump from zero outside the load region to s inside the load region predicted by the classical contact problem. In addition, the maximum shear

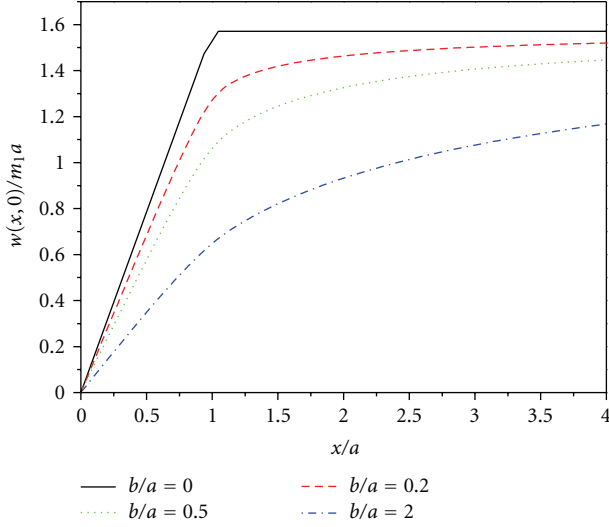


FIGURE 4: Surface displacement under a uniform shear load.

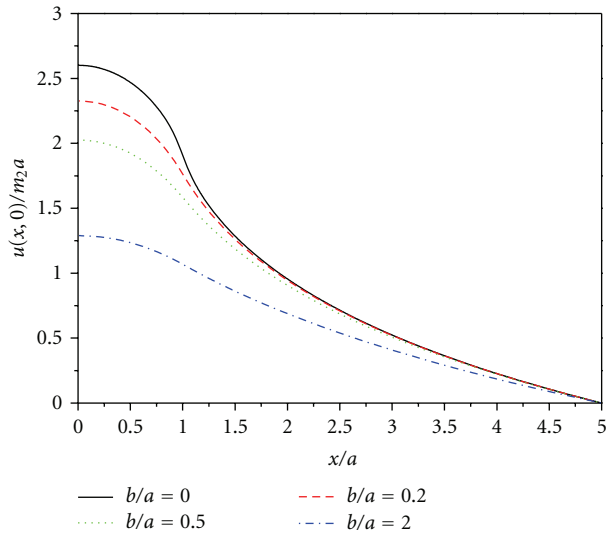


FIGURE 5: Surface indentation under a uniform shear load.

stress in the bulk decreases continuously with the increase of surface stress.

Due to the different surface stress value, the surface displacement on the contact surface is plotted in Figure 4 with $m_1 = (1 - 2\nu)s/\pi G$ which also shows that the gradient of the surface displacement is continuous everywhere on the deformed surface, though the classical elasticity gives only discontinuous displacement gradient at $x = \pm a$. With the increase of surface stress, the indent depth decreases continuously. The horizontal displacement is displayed in Figure 5, where we set $l = 5a$. and $m_2 = 2(1 - \nu)s/\pi G$. It is seen that the slope of the deformed surface for $a > 0$ is continuous everywhere. However, the classical elasticity theory predicted unreasonably that the gradient of the deformed surface is infinite at the load boundary $x = \pm a$, as seen from the curve of $b/a = 0$.

5. Concentrated Shear Load

Now the extreme situation that a point force S acts on the surface at the origin is considered by setting $2sa \rightarrow S$ as $a \rightarrow 0$. Thus, one has

$$B(\xi) = i\sqrt{\frac{1}{2\pi}} \frac{S}{\xi} \frac{1}{1 + b\xi}. \quad (26)$$

Substituting (26) into (14) and (15), the corresponding stress and displacement distributions are given as follows, respectively,

$$\begin{aligned} \sigma_{xx} &= \frac{S}{\pi} \int_0^\infty \frac{z\xi - 2}{1 + b\xi} \sin(x\xi) e^{-z\xi} d\xi, \\ \sigma_{zz} &= -\frac{S}{\pi} \int_0^\infty \frac{z\xi}{1 + b\xi} \sin(x\xi) e^{-z\xi} d\xi, \\ \sigma_{xz} &= -\frac{S}{\pi} \int_0^\infty \frac{1 - z\xi}{1 + b\xi} \cos(x\xi) e^{-z\xi} d\xi, \end{aligned} \quad (27)$$

$$u(x, z) = -\frac{S}{\pi G} \int_0^\infty \frac{(2 - \nu)z\xi - 2(1 - \nu)}{\xi(1 + b\xi)} \cos(x\xi) e^{-z\xi} d\xi,$$

$$w(x, z) = \frac{S}{\pi G} \int_0^\infty \frac{1 - 2\nu + z\xi}{\xi(1 + b\xi)} \sin(x\xi) e^{-z\xi} d\xi. \quad (28)$$

However, when $b = 0$, which implies that the surface influence is ignored, the stresses of the half-plane can be obtained as

$$\begin{aligned} \sigma_{xx} &= -\frac{2S}{\pi} \frac{x^3}{(x^2 + z^2)^2}, \\ \sigma_{xz} &= -\frac{2S}{\pi} \frac{x^2 z}{(x^2 + z^2)^2} \end{aligned} \quad (29)$$

which are consistent with those in classical contact mechanics [1].

On the contact surface, the stresses and displacements are

$$\begin{aligned} \sigma_{xx} &= -\frac{G}{1 - \nu} \int_0^\infty \left(\frac{b}{\Lambda_2} t + 1\right)^{-1} \sin\left(\frac{x}{\Lambda_2} t\right) dt, \\ \sigma_{xz} &= -\frac{G}{1 - 2\nu} \int_0^\infty \left(\frac{b}{\Lambda_2} t + 1\right)^{-1} \cos\left(\frac{x}{\Lambda_2} t\right) dt, \\ u(x, 0) &= \Lambda_1 \int_0^\infty \frac{1}{t} \left(\frac{b}{\Lambda_2} t + 1\right)^{-1} \left[\cos\left(\frac{x}{\Lambda_2} t\right) - \cos\left(\frac{l}{\Lambda_2} t\right)\right] dt, \\ w(x, 0) &= \Lambda_2 \int_0^\infty \frac{1}{t} \left(\frac{b}{\Lambda_2} t + 1\right)^{-1} \sin\left(\frac{x}{\Lambda_2} t\right) dt, \end{aligned} \quad (31)$$

where

$$\Lambda_1 = \frac{2(1 - \nu)S}{\pi G}, \quad \Lambda_2 = \frac{(1 - 2\nu)S}{\pi G}. \quad (32)$$

The variation of the distribution of stresses on the contact surface subjected to a concentrated shear force with

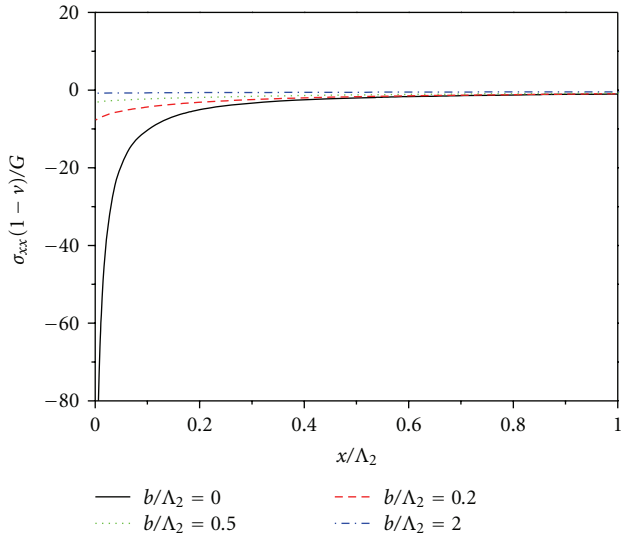


FIGURE 6: Distribution of the contact normal stress under a concentrated shear load.

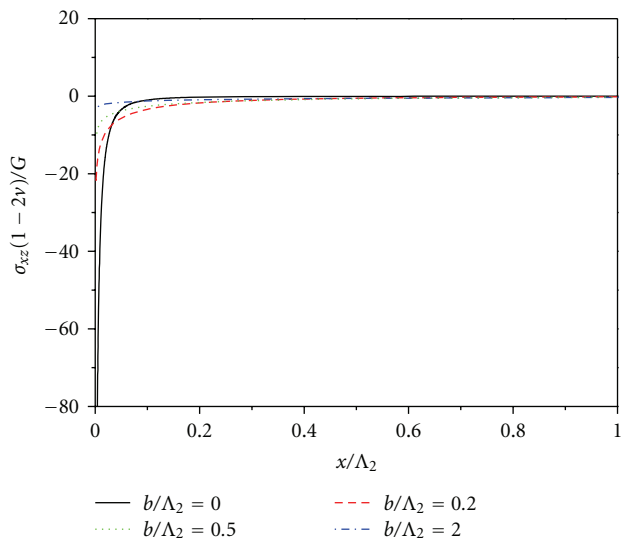


FIGURE 7: Distribution of the contact shear stress under a concentrated shear load.

various values of b/Λ_2 is shown in Figures 6 and 7. In classical elasticity without surface effect (i.e., $b/\Lambda_2 = 0$), the stresses tend to infinity at the loading point $x = 0$, while it approaches finite values when surface stresses are present. And the stresses σ_{xz} and σ_{xx} at $x = 0$ decrease with the increase of surface stress characterized by b/Λ_2 . Figure 8 shows the maximum surface displacement in the bulk decreases with the increase of surface stress. Figure 9 shows the surface indentation for several representative values of surface stresses. Different from the classical elastic solution without surface effects (i.e., $b/\Lambda_2 = 0$), in which the indent depth at $x = 0$ is maximum, the indent depth will decrease when the effect of surface stress is taken into

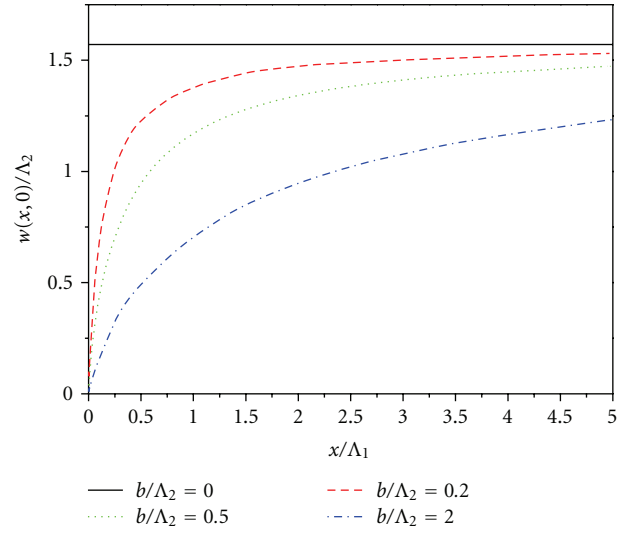


FIGURE 8: Surface displacement under a concentrated shear load.

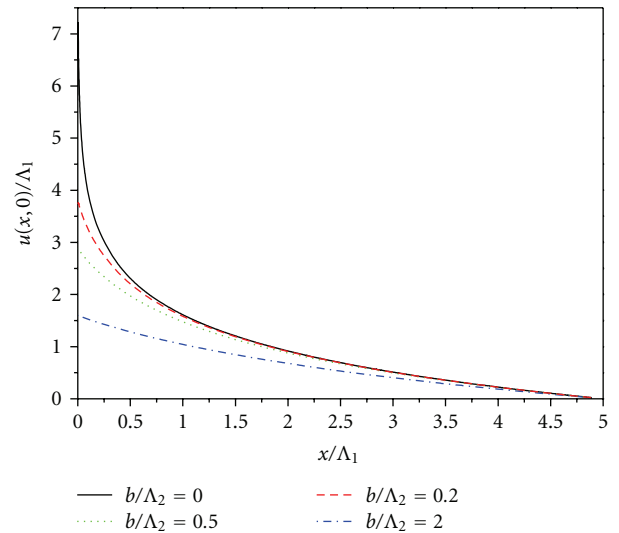


FIGURE 9: Surface indentation under a concentrated shear load.

account. The indent depth decreases as the surface stress increases.

Though only two special cases have been considered in contact problems with surface stresses, based on the solution of a point force applied on a semi-infinite body, one can deal with various types of contact problems by solving an integral equation, as those have been done in the classical contact mechanics.

6. Conclusions

The two-dimensional nanocontact problems for elastic bulk materials subjected to surface shear loads are investigated with completed surface stress effect (nonzero surface tension and surface elastic properties). A set of analytical solutions are presented by using Fourier integral transform method.

The closed-form solution can be derived for the case of a half-plane. For the two particular cases of a uniform distributed shear load and a concentrated shear force, the results are analyzed in detail and compared with the classical linear elastic solutions. It is found that the surface elasticity theory illuminates some interesting characteristics of nanocontact problems, which are distinctly different from the classical solutions of elasticity without surface effects. The contact stresses and the displacements of the deformed surface change smoothly across the loading boundary; moreover the stress and the indent depth show a significant dependence on the surface stress. Therefore the effects of surface stresses should be considered for nanocontact problems.

Acknowledgments

The supports from the National Natural Science Foundation (Grant no. 11062004), the Natural Science Foundation of Gansu province (1010RJZA021) and the Doctoral Foundation of Lanzhou University of Technology are acknowledged.

References

- [1] K. L. Johnson, *Contact Mechanics*, Cambridge University Press, Cambridge, Mass, USA, 1985.
- [2] G. F. Wang and X. Q. Feng, "Effects of surface stresses on contact problems at nanoscale," *Journal of Applied Physics*, vol. 101, Article ID 013510, 2007.
- [3] M. E. Kassner, S. Nemat-Nasser, Z. Suo et al., "New directions in mechanics," *Mechanics of Materials*, vol. 37, no. 2-3, pp. 231–259, 2005.
- [4] Y. Huang, F. Zhang, K. C. Hwang, W. D. Nix, G. M. Pharr, and G. Feng, "A model of size effects in nano-indentation," *Journal of the Mechanics and Physics of Solids*, vol. 54, no. 8, pp. 1668–1686, 2006.
- [5] R. Dingreville, J. Qu, and M. Cherkaoui, "Surface free energy and its effect on the elastic behavior of nano-sized particles, wires and films," *Journal of the Mechanics and Physics of Solids*, vol. 53, no. 8, pp. 1827–1854, 2005.
- [6] A. J. Kulkarni and M. Zhou, "Surface-effects-dominated thermal and mechanical responses of zinc oxide nanobelts," *Acta Mechanica Sinica*, vol. 22, pp. 217–224, 2006.
- [7] B. Movchan and I. S. Jones, "Asymptotic and numerical study of a surface breaking crack subject to a transient thermal loading," *Acta Mechanica Sinica*, vol. 22, pp. 22–27, 2006.
- [8] G. F. Wang and X. Q. Feng, "Interface effects on effective elastic moduli of nanocrystalline materials," *Materials Science and Engineering A*, vol. 363, pp. 1–8, 2003.
- [9] Z. Y. Ou, G. F. Wang, and T. J. Wang, "Effect of residual surface tension on the stress concentration around a nanosized spheroidal cavity," *International Journal of Engineering Science*, vol. 46, pp. 475–485, 2008.
- [10] Z. Y. Ou, G. F. Wang, and T. J. Wang, "Elastic fields around a nanosized spheroidal cavity under arbitrary uniform remote loadings," *European Journal of Mechanics A/Solids*, vol. 28, pp. 110–120, 2009.
- [11] Z. Y. Ou, G. F. Wang, and T. J. Wang, "An analytical solution for the elastic fields near spheroidal nano-inclusions," *Acta Mechanica Sinica*, vol. 25, pp. 821–830, 2009.
- [12] Z. Y. Ou and S. D. Pang, "A screw dislocation interacting with a coated nano-inhomogeneity incorporating interface stress," *Materials Science and Engineering A*, vol. 528, no. 6, pp. 2762–2775, 2011.
- [13] M. E. Gurtin and A. Ian Murdoch, "A continuum theory of elastic material surfaces," *Archive for Rational Mechanics and Analysis*, vol. 57, no. 4, pp. 291–323, 1975.
- [14] M. E. Gurtin and A. Ian Murdoch, "Surface stress in solids," *International Journal of Solids and Structures*, vol. 14, no. 6, pp. 431–440, 1978.
- [15] R. E. Miller and V. B. Shenoy, "Size-dependent elastic properties of nanosized structural elements," *Nanotechnology*, vol. 11, no. 3, pp. 139–147, 2000.
- [16] R. C. Cammarata, K. Sieradzki, and F. Spaepen, "Simple model for interface stresses with application to misfit dislocation generation in epitaxial thin films," *Journal of Applied Physics*, vol. 87, no. 3, pp. 1227–1234, 2000.
- [17] V. B. Shenoy, "Atomistic calculations of elastic properties of metallic fcc crystal surfaces," *Physical Review B*, vol. 71, Article ID 094104, 2005.
- [18] W. Gao, S. Yu, and G. Huang, "Finite element characterization of the size-dependent mechanical behaviour in nanosystems," *Nanotechnology*, vol. 17, no. 4, pp. 1118–1122, 2006.
- [19] W. X. Zhang and T. J. Wang, "Effect of surface energy on the yield strength of nanoporous materials," *Applied Physics Letters*, vol. 90, Article ID 063104, 2007.
- [20] W. X. Zhang, T. J. Wang, and X. Chen, "Effect of surface stress on the asymmetric yield strength of nanowires," *Journal of Applied Physics*, vol. 103, Article ID 123527, 2008.
- [21] X. J. Zhao and R. K. N. D. Rajapakse, "Analytical solutions for a surface-loaded isotropic elastic layer with surface energy effects," *International Journal of Engineering Science*, vol. 47, pp. 1433–1444, 2009.
- [22] F. Q. Yang and, "Size-dependent effective modulus of elastic composite materials: spherical nanocavities at dilute concentrations," *Journal of Applied Physics*, vol. 95, pp. 3516–3520, 2004.

Research Article

One-Step Method for Preparation of Magnetic Nanoparticles Coated with Chitosan

Karla M. Gregorio-Jauregui,¹ Ma. Guadalupe Pineda,¹ Jorge E. Rivera-Salinas,¹ Gil Hurtado,² Hened Saade,² José L. Martínez,¹ Anna Ilyina,¹ and Raúl G. López²

¹Departamento de Biotecnología, Facultad de Ciencias Químicas, Universidad Autónoma de Coahuila, Boulevard V. Carranza y José Cárdenas Valdés, 25280 Saltillo, COAH, Mexico

²Departamento de Procesos de Polimerización, Centro de Investigación en Química Aplicada, Boulevard Enrique Reyna No. 140, 25294 Saltillo, COAH, Mexico

Correspondence should be addressed to Raúl G. López, glopez@ciqa.mx

Received 1 March 2012; Accepted 23 April 2012

Academic Editor: Sergio J. Mejía-Rosales

Copyright © 2012 Karla M. Gregorio-Jauregui et al. This is an open access article distributed under the Creative Commons Attribution License, which permits unrestricted use, distribution, and reproduction in any medium, provided the original work is properly cited.

Preparation of magnetic nanoparticles coated with chitosan in one step by the coprecipitation method in the presence of different chitosan concentrations is reported here. Obtaining of magnetic superparamagnetic nanoparticles was confirmed by X-ray diffraction and magnetic measurements. Scanning transmission electron microscopy allowed to identify spheroidal nanoparticles with around 10–11 nm in average diameter. Characterization of the products by Fourier transform infrared spectroscopy demonstrated that composite chitosan-magnetic nanoparticles were obtained. Chitosan content in obtained nanocomposites was estimated by thermogravimetric analysis. The nanocomposites were tested in Pb²⁺ removal from a PbCl₂ aqueous solution, showing a removal efficacy up to 53.6%. This work provides a simple method for chitosan-coated nanoparticles obtaining, which could be useful for heavy metal ions removal from water.

1. Introduction

Magnetic iron oxides, like magnetite (Fe₃O₄) and maghemite (γ -Fe₂O₃) are a widely known materials because of their superparamagnetism when the particles are smaller enough [1]. This property, along their low toxicity and a great surface/area ratio, makes magnetic nanoparticles attractive for a number of actual and potential applications [2–8]. For applications in biomedical and environmental fields, magnetic nanoparticles are usually coated with polymers, bounded to the particle through organic linkers [9]. This type of coating is able to recognize specific molecules and ions for their binding and removal. Furthermore, in some cases it offers enhanced stability [10].

Chitosan is a partially deacetylated form of chitin obtained by thermochemical treatment. It has been identified as a versatile biopolymer, nontoxic, and biodegradable, which is used for a number of agriculture, food, and biopharmaceutical applications [11, 12]. Free amino and hydroxyl groups

are responsible for the reactivity of this polymer. Magnetic nanoparticles coated with chitosan can provide a convenient tool for exploring separation techniques as well as novel applications in fields such as protein and metal adsorption [2, 13, 14].

Obtaining of magnetic nanoparticles coated with chitosan by coprecipitation of magnetic material followed by polymer coating is a well-documented method [13, 15–18]. Using this approach, chitosan-coated magnetic nanoparticles from 14 [17] to 25–30 nm [13, 15, 16] in average diameter and different coating degrees were obtained.

An attractive option to obtain this type of particles is carrying out precipitation and coating in one step. To our best knowledge, there are very few reports on this subject [19, 20]. Hong and Rhee [19] prepared chitosan-coated magnetic nanoparticles with 28 wt. % in theoretical chitosan content by coprecipitation in a solution containing Fe⁺², Fe⁺³, and chitosan. However, particle size as determined by quasi-elastic light dispersion was relatively large, 67 nm in average

diameter, despite that uncoated magnetic nanoparticles were very small, with average diameter around 7.5 nm. The cause of this increase in size was not discussed in the paper. Furthermore, additional characterization of coated nanoparticles was not included. Rather, the attention was focused on establishing the effect of chitosan-coated magnetic nanoparticles on the relaxation times of hydrogen protons of water molecules in a dispersion of this type of particles in water. On the other hand, Wu et al. [20] reported the *in situ* preparation of chitosan-coated magnetic nanoparticles for lipase immobilization. The nanoparticles were obtained by precipitation of $\text{Fe}(\text{OH})_2$ and further controlled oxidation to Fe_3O_4 in an aqueous solution containing crosslinked chitosan. It is noteworthy that the weight ratio chitosan in the formulation to the theoretical Fe_3O_4 was very high (≈ 8.7). In contrast with the report of Hong and Rhee [19], Wu et al. [20], based on the characterization by vibrating sample magnetization and the thermogravimetric analysis of the nanoparticles, concluded that chitosan-coated magnetic nanoparticles were prepared. According to the measurements by transmission electron microscopy, particle diameters of Fe_3O_4 ranged between 10 and 20 nm and those of chitosan-coated magnetic nanoparticles, between 50 and 100 nm.

We report in this paper the coprecipitation of magnetic nanoparticles in the presence of different chitosan concentrations. A detailed characterization of the products was carried out to demonstrate the feasibility of this method for obtaining chitosan-coated magnetic nanoparticles in one step. Moreover, the kinetics of interaction between selected nanocomposites and Pb^{+2} ions was determined to evaluate their ability to ions removal.

2. Materials and Methods

2.1. Materials. All reagents were high-purity grades from Aldrich and used without further purification: chitosan with low molecular weight and 75% deacetylation degree, ferric chloride ($\text{FeCl}_3 \cdot 6\text{H}_2\text{O}$, 99%), ferrous chloride ($\text{FeCl}_2 \cdot 4\text{H}_2\text{O}$, 98%), and aqueous ammonia (NH_4OH , 57.6 wt. %). De-ionized and triple-distilled water was drawn from a Millipore system.

2.2. Preparation of Coated Magnetic Nanoparticles. The process was carried out in a 150 mL jacketed glass reactor equipped with a reflux condenser, mechanical agitation (400 rpm), and an inlet for the feed of aqueous ammonia. All the reactions were performed in duplicate (set 1 and set 2). The procedure started with mixing in the reactor 50 mL of $\text{FeCl}_3 \cdot 6\text{H}_2\text{O}$ (0.32 M) and 50 mL of $\text{FeCl}_2 \cdot 4\text{H}_2\text{O}$ (0.2 M). Then, the required amount of chitosan was added to the reaction mixture, raising the mixture temperature to 50°C. Three concentrations of chitosan were used: 0.125, 0.25, and 0.5% (w/v). Coprecipitation reaction without chitosan was also carried out as a control. Once Fe^{+2} , Fe^{+3} , and chitosan solution reached the desired temperature (50°C), the dosing of 20 mL of the aqueous ammonia at 0.67 mL/min was started. After dosing was over, the completion reaction was allowed to proceed for 20 min. At the end of the reaction, the particles were recovered by using a permanent magnet,

washed 25 times with de-ionized water, and lyophilized to obtain the final product.

2.3. Nanocomposites Characterization. X-ray analysis of the products were carried out with a Siemens D-5000 diffractometer using $\text{Cu-K}\alpha$ ($\lambda = 1.5418 \text{ \AA}$) as incident radiation. The size and morphology of the particles were determined in a JEOL JSM-7401F scanning-transmission electron microscope (STEM), for which samples were prepared by dispersing the resulting powders in water with ultrasonication and then depositing the dispersion on a copper grid. The magnetic properties of the nanoparticles were determined using a Physical Properties Measurement System from Quantum Design, model 6000 in mode-vibrating sample magnetometer (VSM), with an applied field between -20.0 to 20.0 kOe at room temperature. Attenuated total reflectance (ATR) Fourier transform infrared spectrometry (FTIR) was carried out in a Magna IR 550 from Nicolet with germanium crystal. Thermogravimetric analysis (TGA) of nanocomposite and chitosan was performed in a TGA Q500 from TA Instruments. Analyzed samples were heated from 30 to 800°C at a heating rate of 10°C/min under a nitrogen flow of 50 mL/min.

2.4. Pb^{+2} Removal by Using Chitosan-Coated Magnetic Nanoparticles. Typically, 60 mg of dried nanoparticles were added to 50 mL of 10 ppm Pb^{+2} aqueous solution. Then, this mixture was ultrasonicated for 50 min at room temperature taking samples during the process each 10 min. After the magnetic chitosan nanocomposites were removed, the concentration of Pb^{+2} in the samples was measured by atomic absorption spectroscopy in a Varian Spectra 250 AA equipment.

3. Results and Discussion

All reactions rendered a black powder at the end of the process. There was no visually detected difference between the nanoparticles prepared with and without chitosan. Figure 1 shows the X-ray diffraction pattern (XRDP) of the final products obtained in set 1 of precipitation reactions. XRDP of the products from set 2 (not included) shows the same signals pattern. As is well-known, precipitation reactions from $\text{Fe}^{+2} + \text{Fe}^{+3}$ aqueous solution using aqueous ammonia usually produce a mixture of magnetite and maghemite. To compare with the obtained results, the standard patterns of these species, taken from the library of our X-ray equipment, were included in Figure 1. From this figure, it is evident that product patterns match pretty well those of maghemite and magnetite. Although differentiation between both species is not possible from the X-ray data in Figure 1, magnetite presence is evident due to the black color of the final products. It is noteworthy that there is no difference in the patterns of the products obtained with and without chitosan, which leads to conclude that the presence of this polymer does not affect the crystallinity of the precipitation reaction products.

The average grain sizes of the magnetic nanoparticles obtained in set 1 and 2 of precipitation reactions were

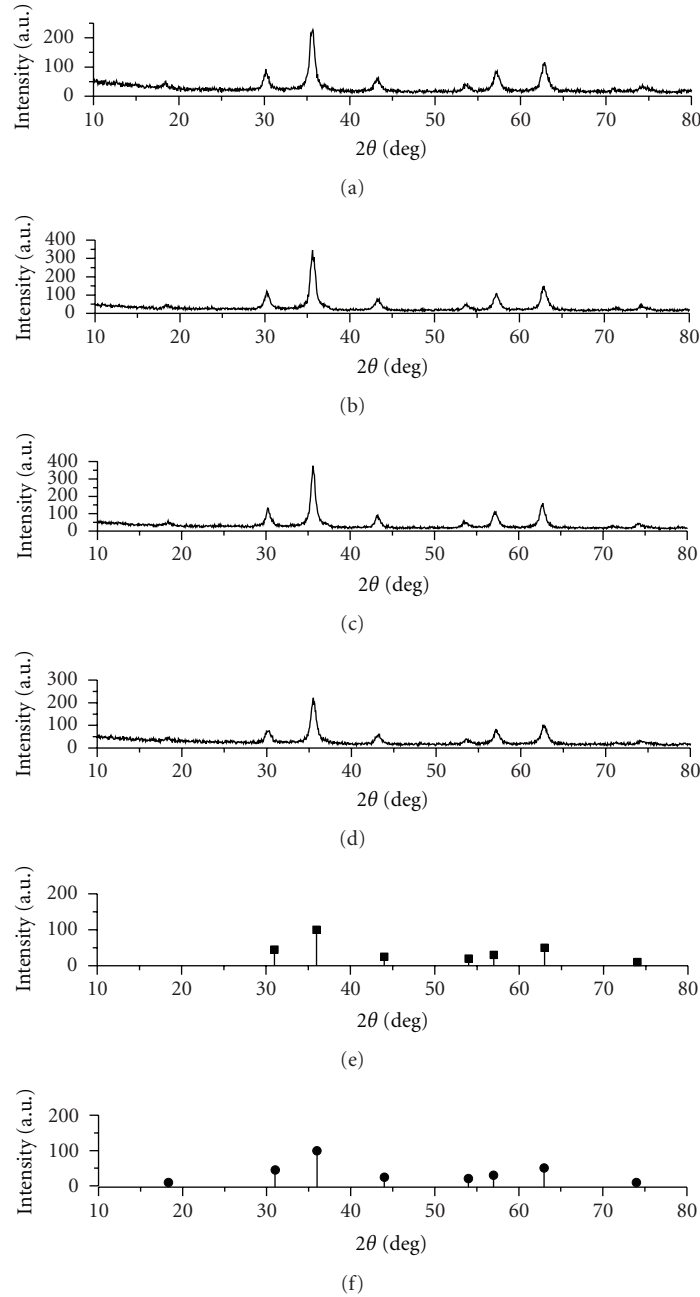


FIGURE 1: X-ray patterns of magnetic nanoparticles prepared by coprecipitation method (at 50°C) without chitosan and with different chitosan concentrations: (a) without chitosan; (b) 0.125; (c) 0.25; (d) 0.5 (w/v %); (e) magnetite standard pattern; (f) maghemite standard pattern.

calculated by using data from their XRDs and the well-known Scherrer equation, which is represented as

$$d = \frac{K\lambda}{\beta \cos \theta}, \quad (1)$$

where d is the average diameter of grain in nm; K is the dimensional factor (0.9); λ is the X-ray wavelength (0.154 nm); β is the line broadening at half the maximum intensity in radians and θ is the Bragg's angle. Calculated values of average diameter of grain were 11.1 ± 0.6 , $11.6 \pm$

1.3 , 12.6 ± 0.5 , and 10.6 ± 0.3 for products prepared with 0, 0.125, 0.25, and 0.5% (w/v) chitosan, respectively. These results indicate an absence of effect of chitosan on the grain size of magnetic nanoparticles.

Micrographs of the final products prepared with and without chitosan (set 1) are shown in Figure 2. Particles in this figure show a spheroidal morphology, but a difference between the particles obtained with and without chitosan is not evident. To characterize these particles, the sizes of more than 1000 of them were measured from different

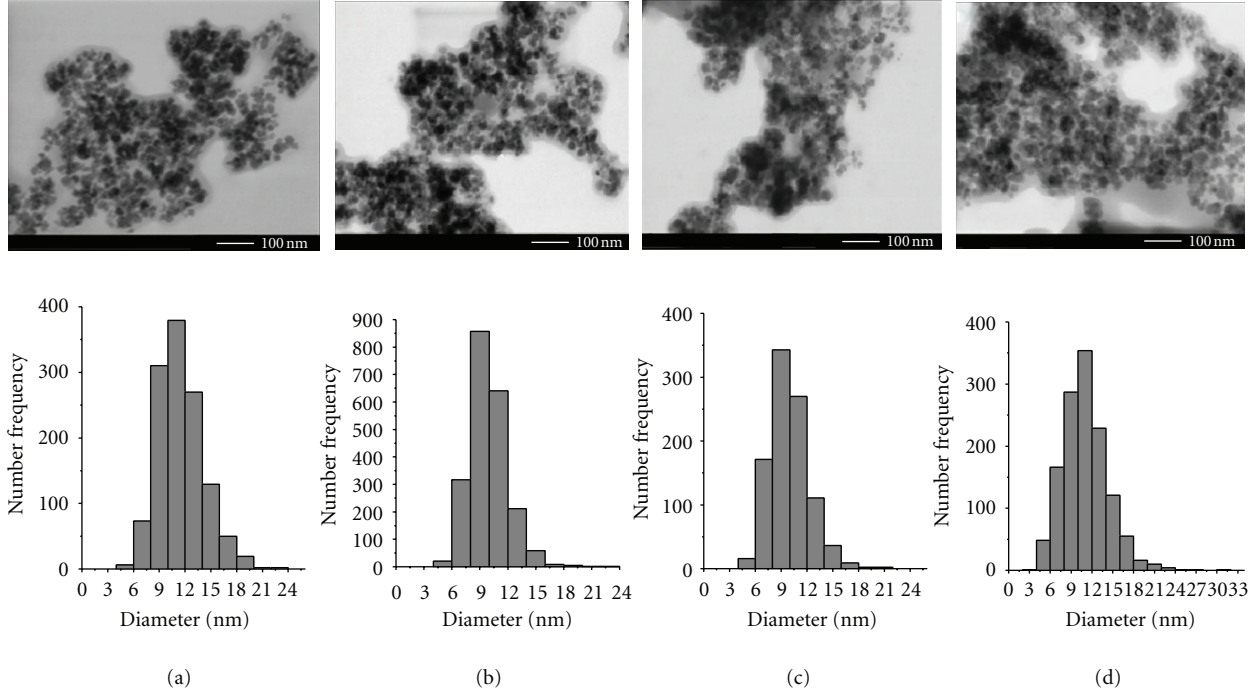


FIGURE 2: STEM micrographs and their corresponding particle diameter histograms of particles prepared by coprecipitation method (at 50°C) without chitosan and with different chitosan concentrations: (a) without chitosan; (b) 0.125; (c) 0.25; (d) 0.5 (w/v %).

micrographs of each of the samples using an image analysis program (ImageJ 1.37 c). The results of this analysis were presented as the corresponding histograms of particle diameters and included in Figure 2. Furthermore, the number-average diameter (D_n), the weight-average diameter (D_w), and the polydispersity index (D_w/D_n) were calculated by using the following equations [21]:

$$D_n = \frac{\sum n_i D_i}{\sum n_i}, \quad (2)$$

$$D_w = \frac{\sum (n_i D_i)^4}{\sum (n_i D_i)^3}, \quad (3)$$

where n_i is the number of particles of diameter d_i .

D_n and polydispersity values from products (set 1) are shown in Table 1. It should be clarified that the data in this table correspond to the sizes of magnetic nanoparticles, that is, the nanoparticles without chitosan coating. As it can be seen, D_n of magnetic nanoparticles obtained in this study when chitosan was used in their preparation ranges from 9.9 to 11 nm, a very small range to consider that a direct relation between the particle size and the chitosan used in the formulation exists. It is noteworthy that these particle diameters are smaller than those reported in the preparation of magnetic nanoparticles by coprecipitation method, which ranges from 14 [17] to 25–30 nm [13, 15, 16]. Although, it cannot be excluded that other authors using this method have obtained magnetic nanoparticles with similar sizes to those obtained in this work, they were not identified in the search in the specialized literature.

TABLE 1: Average diameters and polydispersity index of particles prepared by coprecipitation method determined: (a) from XRD data; (b) and (c) from STEM micrographs.

Chitosan content in reaction mixture (w/v %)	$D_p^{(a)}$ (nm)	$D_n^{(b)}$ (nm)	$D_w/D_n^{(c)}$
0	11.1 ± 0.6	11.5	1.2
0.125	11.6 ± 1.3	9.9	1.1
0.250	12.6 ± 0.5	10.0	1.2
0.500	10.6 ± 0.3	11.0	1.3

For comparison, the values of grain average diameters calculated with Scherrer equation are also included in Table 1. Data in this table indicate that sizes from X-ray information and those measured by STEM are very similar. This suggests that no aggregation of the grains during magnetic nanoparticles forming was occurred, even in the presence of chitosan.

To this point, it is clear that a mixture of magnetite-maghemite nanoparticles was obtained in presence of chitosan. It is assumed that at least part of chitosan used in the process is coating these nanoparticles. This assumption comes from the expected bond between the hydroxyl groups in the chitosan and the oxygen atoms of Fe_3O_4 (magnetite) and Fe_2O_3 (maghemite). Unfortunately, it was not possible to demonstrate this assumption by STEM. Nevertheless, in the following, the obtaining of a composite chitosan-magnetic nanoparticles will be demonstrated.

TABLE 2: Results of magnetic characterization of nanoparticles obtained at 50°C without chitosan and with different chitosan concentrations.

Chitosan content in reaction mixture (w/v %)	Magnetization at 20 kOe (emu/g)	Remnant magnetization (emu/g)	Coercivity (Oe)
0	70.13 ± 0.01	2.33 ± 1.32	26.85 ± 13.62
0.125	66.35 ± 2.10	2.29 ± 0.41	27.09 ± 4.24
0.250	61.57 ± 5.04	4.61 ± 2.03	64.39 ± 41.98
0.500	45.07 ± 3.73	3.10 ± 0.29	40.91 ± 0.49

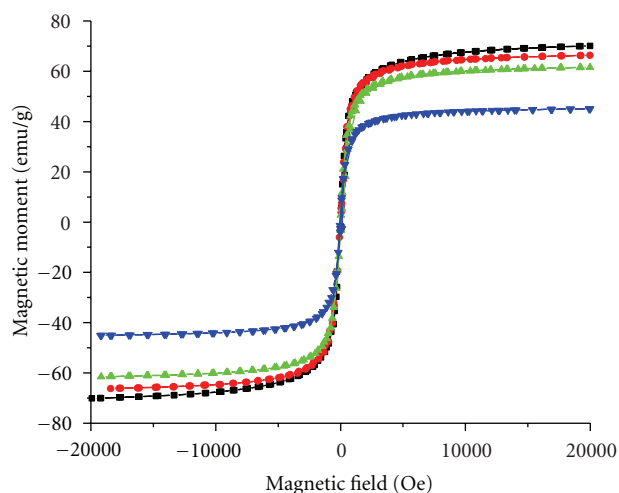


FIGURE 3: Magnetization curves determined at room temperature for particles prepared by coprecipitation method (at 50°C) without chitosan and different chitosan concentrations: (■) without chitosan; (●) 0.125; (▲) 0.25; (▼) 0.5 (w/v %).

The results of magnetic measurements of the nanoparticles prepared in set 1 are depicted in Figure 3. None of the curves in this figure shows magnetic saturation up to 20 kOe, which is understandable taken into account that the surface atoms in very small particles, which constitute a great fraction of the total atoms, have difficulties for aligning the magnetic moments in the direction of applied magnetic field [22]. The results of magnetic characterization of nanoparticles from set 2 (not shown) are very similar to those described for nanoparticles from set 1. Table 2 shows the mean values of the magnetic properties for the products obtained in precipitation reactions (set 1 and set 2).

Obtained results (Figure 3 and Table 2) demonstrate that nanoparticles prepared without chitosan are characterized by the highest final magnetization value (70.1 emu/g) and that this value decrease between 66.4 and 45.1 emu/g, as chitosan content in the precipitation reactions increases. Furthermore, the very small values for remnant magnetization (2.3–4.6 emu/g) and coercivity field (26.9–64.4 Oe) suggest a superparamagnetic behavior of all the nanoparticles prepared in this study [23]. In fact, this behavior is typical of magnetite and maghemite nanoparticles smaller than 10–15 nm in diameter [23]. The decrease of the nanoparticles final magnetization as the chitosan content used in the precipitation reactions increased indicates that

the proportion of the nonmagnetic material (in this case, chitosan) in nanoparticles increased. A comparison of the results of magnetic characterization obtained in this study with those reported in the specialized literature indicates that the final magnetization value of the naked particles prepared in this study is higher than those reported by Ge et al. [17] and Wu et al. [20]. Furthermore, they are similar to that obtained by Pan et al. [16] but lower than those reported by Liu et al. [13] and Kuo et al. [18], who obtained values of magnetic saturation around 80 emu/g. Nevertheless, due to the relatively large size of the nanoparticles (≈ 25 nm in average diameter) obtained by Liu et al., they presented a ferromagnetic behavior, which is not attractive for some applications where reuse of nanoparticles is required, because their high values of remnant magnetization. Regarding to chitosan-coated nanoparticles, the final magnetization values obtained in this study are similar to those reported by other authors [16–18] and higher than that reported by Wu et al. [20], who obtained a value of 35.5 emu/g. It is noteworthy the relatively high values of final magnetization were obtained in this study, despite that the sizes of magnetic nanoparticles are in the bottom of the sizes range reported in the literature on preparation of magnetic nanoparticles by coprecipitation method [13, 15–20]. In accordance with the known fact that the magnetization of small particles (diameters smaller than ca. 15 nm) decreases as particle size decreases [24, 25], smaller values of magnetization should be expected. Based on the reported direct relation between crystallinity and magnetization in magnetic particles [26], the higher magnetization values obtained in this study could be tentatively ascribed to an improved crystallinity of the magnetic nanoparticles.

Conclusive evidence of the obtaining of chitosan-coated magnetic nanoparticles in this study arose from FTIR results (Figure 4). This figure includes the IR spectra for all the prepared nanoparticles (set 1). In accordance with Figure 4, the characteristic absorption bands for chitosan appeared at 3363 (O–H and N–H stretching vibrations), 2874 (C–H stretching vibrations), 1653 (N–H bending vibrations), and 1070 cm^{-1} (C–O–C stretching vibrations) [27, 28]. The spectra of the products obtained using chitosan show the four characteristic absorption bands for this polymer. Taken into account that the products of the reactions were exhaustively washed and magnetically recovered, it was concluded that all the chitosan in the final products are chemically bound to the magnetic nanoparticles. Results of FTIR demonstrated that the precipitation reactions carried out with chitosan led to obtain a composite chitosan-magnetic nanoparticles.

TABLE 3: Immobilization of chitosan on the nanoparticles obtained by coprecipitation method at 50°C.

Chitosan content in reaction mixture (w/v %)	Theoretical immobilized chitosan on the nanoparticles ^a (mg/g)	Immobilized chitosan on the nanoparticles ^b (mg/g)
0.125	60.67	135.85
0.250	121.58	148.5
0.500	243.00	584.79

^aCalculated from the recipe of precipitation reactions.

^bEstimated from TGA results.

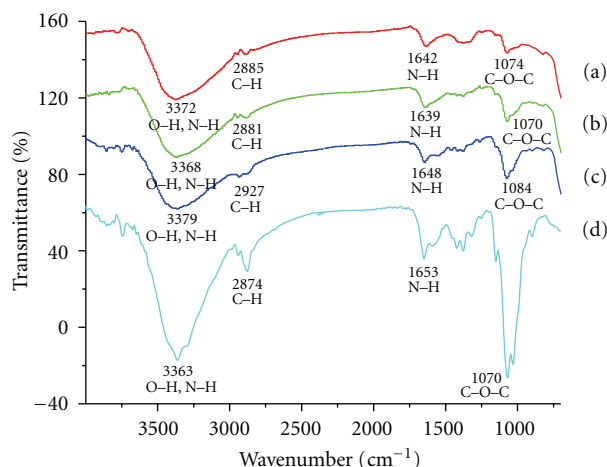


FIGURE 4: FTIR spectra of particles prepared by coprecipitation method (at 50°C) with different chitosan concentrations: (a) 0.125; (b) 0.25; (c) 0.5 (w/v %); (d) pure chitosan FTIR spectra.

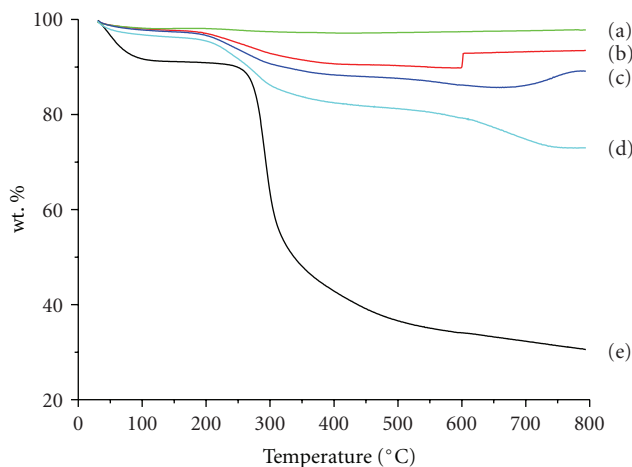


FIGURE 5: Thermal degradation curves of particles prepared by coprecipitation method (at 50°C) without chitosan and with different chitosan concentrations: (a) without chitosan; (b) 0.125; (c) 0.25; (d) 0.5 (w/v %); (e) pure chitosan thermal degradation curve.

The results of characterization by TGA of the products obtained in set 1 (Figure 5) were used for the estimation of the amount of chitosan immobilized on the nanoparticles. As it can be seen in this figure, the product prepared without chitosan, that is, the mixture magnetite-maghemite, showed 2.16% in weight loss when it was heated from 30 to 800°C. Pan et al. [16] reported that a sample of Fe_3O_4 lost 1.3 wt. % when it was heated from 30 to 300°C in a TGA equipment under similar conditions to those used in this study. As indicated by Pan et al. [16], this weight loss can be ascribed to the removal of free and chemically adsorbed water. On the other hand, a sample of pure chitosan, whose thermogram was also included in Figure 5, showed a weight loss of 69.4%. As it was expected, the composites showed weight losses intermediate between those of the mixture magnetite-maghemite and pure chitosan: 10, 11, and 27% for the products prepared with 0.125, 0.25, and 0.5% (w/v), respectively. Using these results and the weight of the samples before and after TGA characterization, the quantities of chitosan immobilized on the nanoparticles were estimated (Table 3). For comparison, the theoretical values of immobilized chitosan calculated from the recipe of precipitation reactions, assuming that the reactions proceeded to 100% and only magnetite was obtained, were also included in Table 3. In accordance with the data in this table, the amounts of chitosan immobilized on the nanoparticles

estimated from TGA measurements were consistently higher than the theoretical values. This difference can be explained if the precipitation reactions do not proceed to 100%, which would lead to increase the chitosan/nanoparticles ratio.

Having demonstrated the preparation of magnetic nanoparticles with average diameters around 10-11 nm covered with chitosan in one step, the final test in this study was to evaluate the efficacy of the obtained composites in Pb^{+2} removal from a $\text{Pb}(\text{NO}_3)_2$ aqueous solution. This test is based on the ability of chitosan to chelate heavy metal ions through its amino groups. For this, the composites prepared with 0.125 and 0.5% (w/v) chitosan in set 1 were evaluated. Figure 6 shows that the Pb^{+2} concentration drops from its initial value (10 ppm) to around 6.2 in the first 10 minutes in the assay when the composite was prepared with 0.125% (w/v) chitosan. Then, it slowly decreases to attain a final value of 4.6 ppm at the end of the test. In the assay carried out with the composite prepared with 0.5% (w/v) chitosan, values of 8.3 and 6.0 ppm were attained in the first 10 minutes and at the end of the assay, respectively. From here, a removal efficacy of 53.6% for the chitosan-coated magnetic nanoparticles prepared with 0.125% (w/v) chitosan and of 39.8% for those prepared with 0.5% (w/v) were calculated, which is surprising, because of a direct

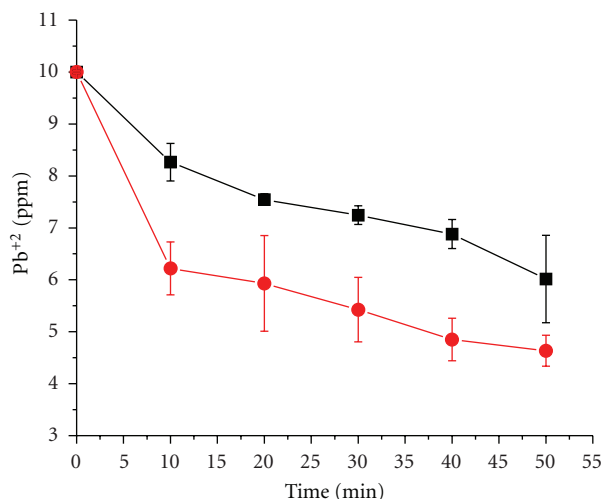


FIGURE 6: Pb²⁺ removal as a function of time using chitosan-coated magnetic nanoparticles prepared with (●) 0.125 and (■) 0.5% (w/v) chitosan.

relation between removal efficacy and chitosan content in the evaluated composites was expected. This indicates that the nanoparticles prepared with the higher chitosan content have a smaller total amount of amino groups on their surface, which really means that they have less total surface area than the nanoparticles prepared with 0.125% (w/v) chitosan. A possible explanation for this behavior is that contents of chitosan as higher as 0.5% (w/v), under the conditions used in this study, favor the aggregation of chitosan-coated nanoparticles. In turn, this would lead to an increase in the final nanocomposite size and, as a consequence, to a decrease in the total surface area.

Finally it should highlight the difference between the productivity in this study and those in the other reports on preparation of chitosan-coated magnetic nanoparticles in one step [19, 20]. Calculations based on the formulations in the reports of Hong and Rhee [19] and Wu et al. [20] indicate theoretical productivities of around 0.1 g of magnetic nanoparticles per 100 g of reaction mixture. In contrast, theoretical productivity in this study is around 1.7 g per 100 g of reaction mixture. Furthermore, the weight ratio chitosan in the formulation/theoretical magnetic nanoparticles is close to 0.4 and 8.7 in the reports of Hong and Rhee and Wu et al., respectively. These values are higher than those calculated in this study, which range from 0.06 to 0.24, depending on the used formulation. The highlighted differences indicate that the preparation of chitosan-coated magnetic nanoparticles in one step is a method able to attain relatively high productivities. Also, they suggest that an optimal ratio chitosan/magnetic nanoparticles should exist, which would lead to a minimization of particle aggregation.

4. Conclusions

A one-step method comprising the coprecipitation of magnetic nanoparticles in the presence of different chitosan

concentrations allowed to obtain chitosan-coated magnetic nanoparticles with average diameter around 10–11 nm, as demonstrated by X-ray diffraction, magnetic measurements, STEM, and FTIR. The ratios chitosan/magnetic nanoparticles were estimated, from the results of TGA, between 135.9 and 584.8 mg/g. When evaluated for Pb²⁺ ions removal from a Pb(NO₃)₂ aqueous solution, chitosan-coated magnetic nanoparticles showed up to 53.6% in removal efficacy. This value corresponds to the composites with the lower chitosan content. It is believed that particle aggregation and, as a consequence, a decrease in the total surface area was favored when a higher chitosan content was used during the magnetic nanoparticles precipitation.

Acknowledgments

National Council of Science and Technology (CONACyT) supported this research through Grant 2007-84009. The authors are grateful to Jesús A. Cepeda, Alejandro Espinoza, and Blanca Huerta for their technical assistance in characterization work.

References

- [1] S. J. Schneider, *Engineered Materials Handbook: Ceramics and Glasses*, ASM International, Materials Park, Ohio, USA, 1991.
- [2] L. Zhu, J. Ma, N. Jia, Y. Zhao, and H. Shen, "Chitosan-coated magnetic nanoparticles as carriers of 5-fluorouracil: preparation, characterization and cytotoxicity studies," *Colloids and Surfaces B*, vol. 68, no. 1, pp. 1–6, 2009.
- [3] T. Osaka, T. Matsunaga, T. Nakanishi, A. Arakaki, D. Niwa, and H. Iida, "Synthesis of magnetic nanoparticles and their application to bioassays," *Analytical and Bioanalytical Chemistry*, vol. 384, no. 3, pp. 593–600, 2006.
- [4] S. Wan, J. Huang, H. Yan, and K. Liu, "Size-controlled preparation of magnetite nanoparticles in the presence of graft copolymers," *Journal of Materials Chemistry*, vol. 16, no. 3, pp. 298–303, 2006.
- [5] K. Naka, A. Narita, H. Tanaka et al., "Biomedical applications of imidazolium cation-modified iron oxide nanoparticles," *Polymers for Advanced Technologies*, vol. 19, no. 10, pp. 1421–1429, 2008.
- [6] A. G. Roca, R. Costo, A. F. Rebolledo et al., "Progress in the preparation of magnetic nanoparticles for applications in biomedicine," *Journal of Physics D*, vol. 42, no. 22, Article ID 224002, 2009.
- [7] C. C. Berry, "Progress in functionalization of magnetic nanoparticles for applications in biomedicine," *Journal of Physics D*, vol. 42, no. 22, Article ID 224003, 2009.
- [8] Q. A. Pankhurst, N. K. T. Thanh, S. K. Jones, and J. Dobson, "Progress in applications of magnetic nanoparticles in biomedicine," *Journal of Physics D*, vol. 42, no. 22, Article ID 224001, 2009.
- [9] P. Li, A. M. Zhu, Q. L. Liu, and Q. G. Zhang, "Fe₃O₄/poly(N-isopropylacrylamide)/chitosan composite microspheres with multiresponsive properties," *Industrial and Engineering Chemistry Research*, vol. 47, no. 20, pp. 7700–7706, 2008.
- [10] V. Kekkonen, N. Lafreniere, M. Ebara, A. Saito, Y. Sawa, and R. Narain, "Synthesis and characterization of biocompatible magnetic glyconanoparticles," *Journal of Magnetism and Magnetic Materials*, vol. 321, no. 10, pp. 1393–1396, 2009.

- [11] V. Maghsoodi, J. Razavi, and S. Yaghmaei, "Production of chitosan by submerged fermentation from *Aspergillus niger*," *Scientia Iranica*, vol. 16, no. 2, pp. 145–148, 2009.
- [12] Y. Zhuo, P. X. Yuan, R. Yuan, Y. Q. Chai, and C. L. Hong, "Bionzyme functionalized three-layer composite magnetic nanoparticles for electrochemical immunosensors," *Biomaterials*, vol. 30, no. 12, pp. 2284–2290, 2009.
- [13] X. Liu, Q. Hu, Z. Fang, X. Zhang, and B. Zhang, "Magnetic chitosan nanocomposites: a useful recyclable tool for heavy metal ion removal," *Langmuir*, vol. 25, no. 1, pp. 3–8, 2009.
- [14] Y. T. Zhou, H. L. Nie, C. Branford-White, Z. Y. He, and L. M. Zhu, "Removal of Cu^{2+} from aqueous solution by chitosan-coated magnetic nanoparticles modified with α -ketoglutaric acid," *Journal of Colloid and Interface Science*, vol. 330, no. 1, pp. 29–37, 2009.
- [15] D. T. K. Dung, T. H. Hai, L. H. Phuc, B. D. Long, L. K. Vinh, and P. N. Truc, "Preparation and characterization of magnetic nanoparticles with chitosan coating," *Journal of Physics: Conference Series*, vol. 187, no. 1, Article ID 012036, 2009.
- [16] C. Pan, B. Hu, W. Li, Y. Sun, H. Ye, and X. Zeng, "Novel and efficient method for immobilization and stabilization of β -D-galactosidase by covalent attachment onto magnetic Fe_3O_4 -chitosan nanoparticles," *Journal of Molecular Catalysis B*, vol. 61, no. 3-4, pp. 208–215, 2009.
- [17] Y. Ge, Y. Zhang, S. He, F. Nie, G. Teng, and N. Gu, "Fluorescence modified chitosan-coated magnetic nanoparticles for high-efficient cellular imaging," *Nanoscale Research Letters*, vol. 4, no. 4, pp. 287–295, 2009.
- [18] C. Kuo, Y. Liu, C. Liu et al., "Optimum conditions for lipase immobilization on chitosan coated Fe_3O_4 nanoparticles," *Carbohydrate Polymers*, vol. 87, no. 4, pp. 2538–2545, 2012.
- [19] S. Hong and I. Rhee, "Relaxivity of hydrogen protons of water molecules in the aqueous solutions of dextran and chitosan coated ferrite nanoparticles," *International Journal of Magnetic Resonance Imaging*, vol. 1, no. 1, pp. 15–20, 2007.
- [20] Y. Wu, Y. Wang, G. Luo, and Y. Dai, "In situ preparation of magnetic Fe_3O_4 -chitosan nanoparticles for lipase immobilization by cross-linking and oxidation in aqueous solution," *Bioresource Technology*, vol. 100, no. 14, pp. 3459–3464, 2009.
- [21] E. A. Collins, *Emulsion Polymerization and Emulsion Polymers*, John Wiley & Sons, Chichester, UK, 1997.
- [22] R. H. Kodama, "Magnetic nanoparticles," *Journal of Magnetism and Magnetic Materials*, vol. 200, no. 1, pp. 359–372, 1999.
- [23] R.M. Cornell and U. Schwertmann, *The Iron Oxides: Structure, Properties, Reactions, Occurrence and Uses*, Wiley-VCH, Weinheim, Germany, 1996.
- [24] L. Liz, M. A. López Quintela, J. Mira, and J. Rivas, "Preparation of colloidal Fe_3O_4 ultrafine particles in microemulsions," *Journal of Materials Science*, vol. 29, no. 14, pp. 3797–3801, 1994.
- [25] S. Santra, R. Tapeç, N. Theodoropoulou, J. Dobson, A. Hebard, and W. Tan, "Synthesis and characterization of silica-coated iron oxide nanoparticles in microemulsion: the effect of nonionic surfactants," *Langmuir*, vol. 17, no. 10, pp. 2900–2906, 2001.
- [26] H. Qi, J. Ye, N. Tao, M. Wen, and Q. Chen, "Synthesis of octahedral magnetite microcrystals with high crystallinity and low coercive field," *Journal of Crystal Growth*, vol. 311, no. 2, pp. 394–398, 2009.
- [27] L. Guo, G. Liu, R. Y. Hong, and H. Z. Li, "Preparation and characterization of chitosan poly(acrylic acid) magnetic microspheres," *Marine Drugs*, vol. 8, no. 7, pp. 2212–2222, 2010.
- [28] L. Chen, C. Y. Tang, N. Y. Ning, C. Y. Wang, Q. Fu, and Q. Zhang, "Preparation and properties of chitosan/lignin composite films," *Chinese Journal of Polymer Science*, vol. 27, no. 5, pp. 739–746, 2009.

Research Article

A First-Principle Study of B- and P-Doped Silicon Quantum Dots

Jieqiong Zeng and Hong Yu

Key Laboratory of MEMS of Ministry of Education, Southeast University, Nanjing 210096, China

Correspondence should be addressed to Hong Yu, h_yu@seu.edu.cn

Received 24 February 2012; Accepted 26 April 2012

Academic Editor: Sergio J. Mejía-Rosales

Copyright © 2012 J. Zeng and H. Yu. This is an open access article distributed under the Creative Commons Attribution License, which permits unrestricted use, distribution, and reproduction in any medium, provided the original work is properly cited.

Doping of silicon quantum dots (Si QDs) is important for realizing the potential applications of Si QDs in the fields of Si QDs-based all-Si tandem solar cells, thin-film transistors, and optoelectronic devices. Based on the first-principle calculations, structural and electronic properties of hydrogen terminated Si QDs doped with single Boron (B) or phosphorus (P) are investigated. It is found out that the structural distortion induced by impurity doping is related to the impurity characteristic, impurity position, and the QD size according to the structural analysis. The relative energetic stability of Si QDs with a single impurity in different locations has been discussed, too. Furthermore, our calculations of the band structure and electronic densities of state (DOS) associated with the considered Si QDs show that impurity doping will introduce impurity states within the energy gap, and spin split occurs for some configurations. A detailed analysis of the influences of impurity position and QD size on the impurity levels has been made, too.

1. Introduction

As we all know, the ultimate reduction in the dimensionality of a semiconductor device will result in a quantum dot. Much attention has been drawn to Si QDs, with promising applications in fields such as optoelectronics [1], photovoltaics [2], and data storage [3]. In order to realize these potential applications of Si QDs, it is essential to develop techniques to control the electronic and optical properties of Si QDs. One such technique currently being investigated is impurity doping [4, 5]. Doping of Si QDs is expected to introduce additional levels close to the HOMO (highest occupied molecular orbital) or LUMO (lowest unoccupied molecular orbital) in the same fashion as it does for bulk Si; for instance, a nanoscaled P-N junction formed by doping Si QDs embedded in a dielectric is proposed as a way to dissociate photogenerated electron-hole pairs [6].

Lots of experimental works have been made to study the electronic and optical properties of doped Si QDs. However, several factors contribute to making these studies difficult tasks. For instance, QDs synthesized by using different techniques often show different properties in size, shape, and in the interface structure. Moreover, it is tremendously challenging to control over impurity concentration and precise positioning by experiments. This leads to the

imperative need for theoretical calculations to predict the properties of doped Si QDs. Compared with calculations for pure, undoped systems, calculations for doped Si QDs are much more complicated and time consuming owing to the variety of atoms and low symmetry. To date, only few first-principle studies devoted to doped Si QDs are presented in the literature. Melnikov and Chelikowsky [7] investigated the electronic properties of hydrogenated Si QDs doped with a single phosphorus atom using a real-space *ab initio* pseudopotential method, and the ionization energy and binding energy of the defect were calculated. Cantele et al. [8] reported on a detailed first-principle calculation of the impurity states in B- and P-doped Si QDs; the formation energies for neutral impurities were discussed. Although the size effect on the impurity levels were often studied in the previous work, the influences of different impurity positions on the band structures and DOSs of doped Si QDs were not very often examined.

In this paper, we carry out first-principle calculations of impurity states in spherical Si QDs doped with single B or P atom. Both the structural and electronic properties (band structure and DOS) are investigated as functions of the QD size and of the impurity position within the Si QD. Since it has been demonstrated that the properties of doped Si QDs critically depend on the location of the impurity atom

[9, 10], the relative energetic stability of Si QDs with a single impurity in all the possible locations has been discussed. Owing to the highly demanding computational costs, we limit our calculations to Si QDs with two different sizes; one is $\text{Si}_{35}\text{H}_{36}$ -based QD (approximately 1.1 nm in diameter), and the other is $\text{Si}_{87}\text{H}_{76}$ -based QD (approximately 1.6 nm in diameter). The B or P impurity is considered in substitution site, which is the most stable site for these two impurities [11].

2. Modeling and Calculation

Our first-principle calculations are performed by the CASTEP software package [12] which employs the plane-wave pseudopotentials method based on the density functional theory (DFT). The generalized gradient approximation (GGA) with ultrasoft pseudopotentials in reciprocal space is adopted, and exchange-correlation potential is parametrized by the Perdew-Burke-Ernzerhof scheme (PBE) [13]. Since for a single B- or P-doping, the doped QDs have an odd number of electrons, spin polarization is included in our calculations. The cutoff energy for the wave functions is 190 eV. It has been shown that the results are well converged at this cutoff energy. The SCF tolerance is $2.0e-6$ eV/atom, and the k-points for the Brillouin-zone sampling are set as Gamma point only in all cases.

As mentioned above, we consider Si QDs with two different sizes here; one is $\text{Si}_{35}\text{H}_{36}$ -based QD (approximately 1.1 nm in diameter), and the other is $\text{Si}_{87}\text{H}_{76}$ -based QD (approximately 1.6 nm in diameter). Initial undoped dots have been obtained by taking all the bulk Si atoms contained within a sphere of a given radius and passivating the surface dangling bonds with hydrogen. For doped dots, we use the optimized undoped geometry as a base and substitute a Si atom with an impurity atom. A simple-cubic supercell of vacuum is built for each considered dot which is placed at the center in order to prevent interactions between the periodic replicas. In this work we choose 30 Å and 35 Å as the supercell side lengths for $\text{Si}_{35}\text{H}_{36}$ -based QDs and $\text{Si}_{87}\text{H}_{76}$ -based QDs, respectively.

Since the details of the QD surface are different for QDs synthesized by using different techniques, here the impurity atom is not allowed to replace an Si atom on the surface of the QD that is passivated by one or two H atoms. For the remaining sites, there are two different sites within the QD for a single substitution impurity in the case of $\text{Si}_{35}\text{H}_{36}$, whereas in the case of $\text{Si}_{87}\text{H}_{76}$ there are five. These different sites within the dots are shown in Figure 1. All these geometries are examined for impurity doping to investigate the effects of the impurity position. Here we assign $\text{Si}_{34}\text{XH}_{36}$ -1, $\text{Si}_{34}\text{XH}_{36}$ -2, and $\text{Si}_{86}\text{XH}_{76}$ -1, $\text{Si}_{86}\text{XH}_{76}$ -2, $\text{Si}_{86}\text{XH}_{76}$ -3, $\text{Si}_{86}\text{XH}_{76}$ -4, $\text{Si}_{86}\text{XH}_{76}$ -5 (X represents B or P) corresponding to the doped Si QD whose impurity atom situates in the site marked by 1, 2 in Figure 1(a), and 1, 2, 3, 4, 5 in Figure 1(b), respectively.

For each model, the first step is to relax the structure with all the freedom. Once the optimization is achieved, the related properties are calculated. However, even accurate

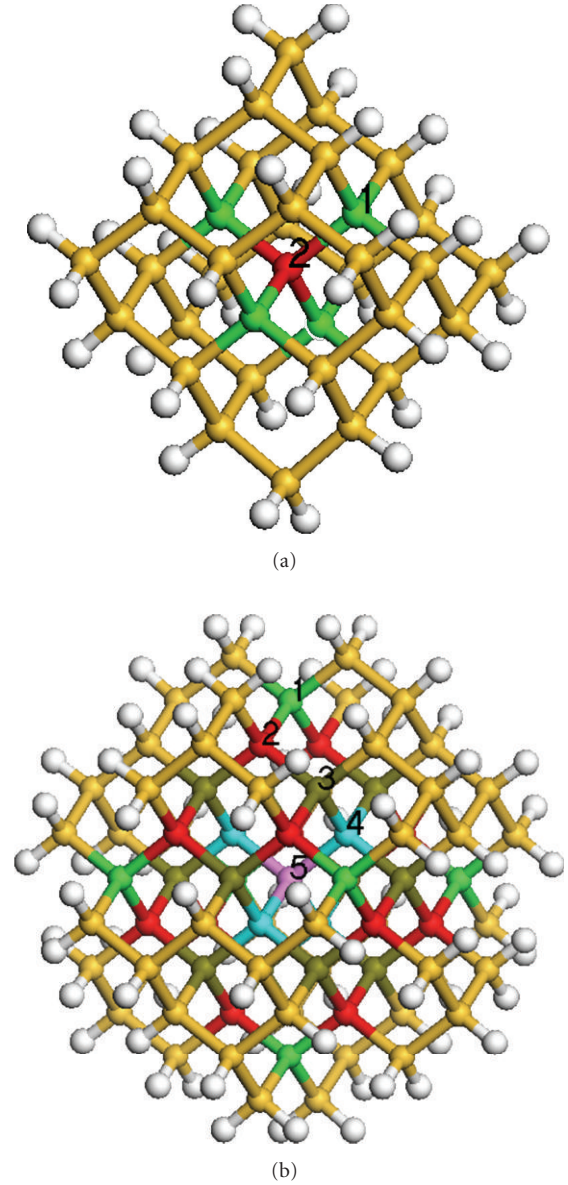


FIGURE 1: A schematic representation of different sites within the QDs for a single substitution impurity. H and Si atoms are denoted by white and yellow balls, respectively. The sites shaded by a same color within the QDs correspond to equivalent doping sites. (a) Model of a 1.1 nm Si QD ($\text{Si}_{35}\text{H}_{36}$); the two different sites within the QD are marked by 1 and 2; (b) model of a 1.6 nm Si QD ($\text{Si}_{87}\text{H}_{76}$); the five different sites within the QD are marked by 1, 2, 3, 4, and 5.

ab initio calculations performed within GGA will suffer from the well-known underestimation of the energy gap. Here we leave the underestimation of energy gap uncorrected and do not discuss the absolute value of the energy gap but focus on how the band structure and DOS are affected by a single impurity doping. Thus it can provide some guidance to properly utilizing impurity doping to control the electronic and optical properties of Si QDs.

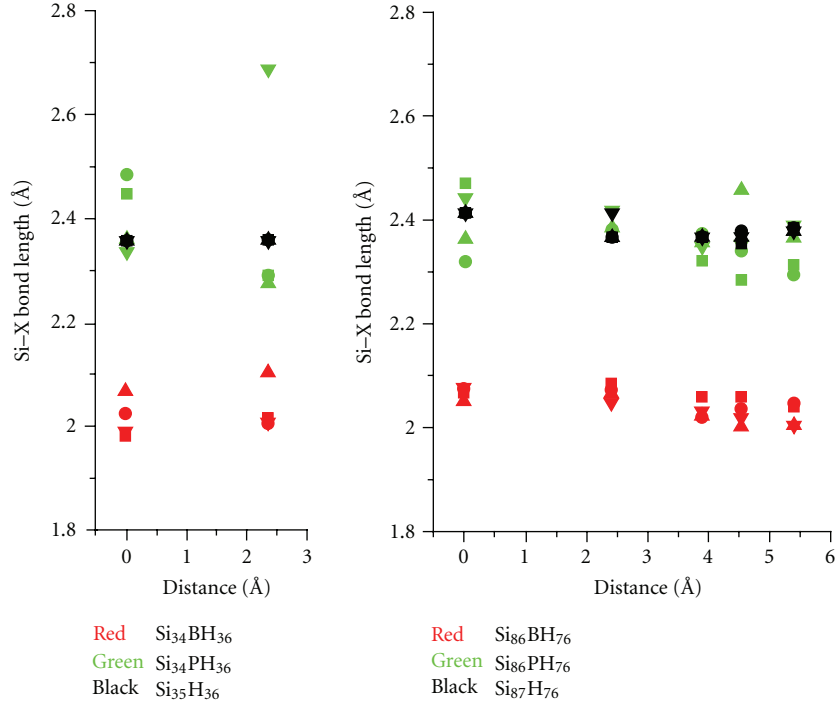


FIGURE 2: The optimized bond lengths around the impurity site for the undoped Si QDs (black ones, X = Si), B-doped Si QDs (red ones, X = B), and P-doped Si QDs (green ones, X = P). The x-axis measures the distance from the center to the replaced Si atom in undoped QDs. The four different Si–X bond lengths are indicated by ●, ■, ▲, and ▼, respectively.

3. Results and Discussion

3.1. Structural Properties. The structural changes induced by the presence of a single impurity with respect to the corresponding undoped ones have been investigated. It is observed that with the insertion of one impurity, some variations in the bond lengths occur around the impurity site, whereas the Si–Si bond lengths remain almost unchanged. Figure 2 shows the optimized bond lengths around the impurity site for the doped and undoped Si QDs. Our results for the bond lengths are in very good agreement with the results reported by Iori et al. [14]. From Figure 2 it can be seen that, compared with undoped cases in which the four Si–Si bond lengths are practically the same, there is a general trend to a significant decrease of the bond lengths for B-doped Si QDs. However, for P-doped cases there exists expansion of the bond lengths with respect to the undoped cases, and the changes are less than B-doped cases. Moreover, for P-doped cases the structural distortion is strongly dependent on the QD size; the larger the size, the less the distortion, while for B-doped cases the distortion is nearly independent of the size. In addition, as is shown in Figure 2, the relaxation around the impurity is also related to the impurity position. By comparing the Si₃₅H₃₆-based cases and Si₈₇H₇₆-based cases, we find out that with the decrease of the QD size the impact of impurity position on the structure relaxation becomes more significant.

From the discussion above, we know that the configurations for single doped Si QDs are different from each other due to different impurity positions. So it is needed to explore

which configuration is the most stable one. The relative energetic stability of these Si QDs can be evaluated through the calculation of the formation energy (FE). Starting from the Si_nH_m nanocluster, the FE for the neutral X impurity can be depicted in (1) [8]:

$$FE = E(\text{Si}_{n-1}\text{XH}_m) - E(\text{Si}_n\text{H}_m) + \mu_{\text{Si}} - \mu_{\text{X}}, \quad (1)$$

where E is the total energy of the system, μ_{Si} is the total energy per atom of bulk Si, and μ_{X} is the total energy per atom of the impurity. From (1), we find out that the relative value of the FE for doped Si QDs with all kinds of B (or P) configurations does not depend on μ_{Si} and μ_{B} (or μ_{P}). It is proportional to the difference between $E(\text{Si}_{n-1}\text{XH}_m)$ and $E(\text{Si}_n\text{H}_m)$. Thus, the relative stability may be determined by simply comparing the differences of total energies between doped QDs and corresponding undoped ones.

The calculated differences of total energies as functions of the impurity position are shown in Figure 3. We observe that the energies required for impurity X (X = B, P) doping into Si QDs increase in the order Si₃₄XH₃₆₋₁ < Si₃₄XH₃₆₋₂ for Si₃₅H₃₆-based QDs. While in the case of Si₈₇H₇₆-based QDs, for B-doping the order is Si₈₆BH₇₆₋₂ < Si₈₆BH₇₆₋₄ < Si₈₆BH₇₆₋₅ < Si₈₆BH₇₆₋₁ < Si₈₆BH₇₆₋₃, and for P-doping the order is Si₈₆PH₇₆₋₂ < Si₈₆PH₇₆₋₅ < Si₈₆PH₇₆₋₁ < Si₈₆PH₇₆₋₄ < Si₈₆PH₇₆₋₃. This means that Si₃₄XH₃₆₋₁ (Si₈₆XH₇₆₋₂) is energetically the most favorable configuration for either B- or P-doping in Si₃₅H₃₆ (Si₈₇H₇₆) owing to the smallest formation energy. So we find out that for either B- or P-doping, the impurity atom tends to substitute Si atom near

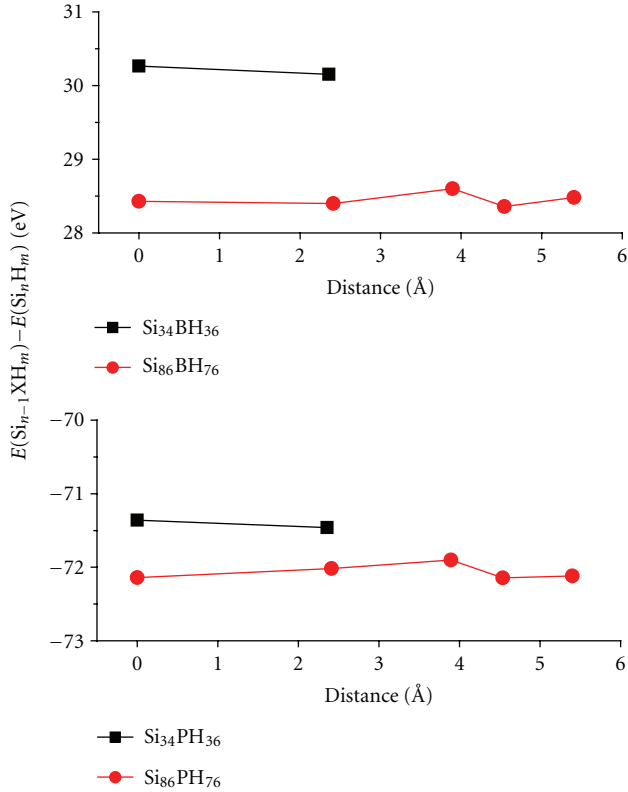


FIGURE 3: Differences of total energies between doped QDs with different impurity positions and corresponding undoped ones. The x -axis measures the distance from the center to the replaced Si atom in undoped QDs. Different x value corresponds different impurity position. Along the increasing direction of x -axis, they are in the order of $\text{Si}_{34}\text{XH}_{36-2}$, $\text{Si}_{34}\text{XH}_{36-1}$ for $\text{Si}_{35}\text{H}_{36}$ -based QDs, and for $\text{Si}_{87}\text{H}_{76}$ -based QDs the order is $\text{Si}_{86}\text{XH}_{76-5}$, $\text{Si}_{86}\text{XH}_{76-4}$, $\text{Si}_{86}\text{XH}_{76-3}$, $\text{Si}_{86}\text{XH}_{76-2}$, $\text{Si}_{86}\text{XH}_{76-1}$.

the surface. Moreover, it can be observed that the energy required for impurity X ($X = \text{B}, \text{P}$) doping is smaller for $\text{Si}_{87}\text{H}_{76}$ than for $\text{Si}_{35}\text{H}_{36}$, demonstrating that with a decrease of the QD size the insertion of a substitution impurity becomes more difficult. In addition, we find out that this influence of size is much more evident for B-doping than for P-doping (see Figure 3), meaning that it would be even harder to conduct B-doping for Si QD with smaller size.

3.2. Electronic Properties. The calculated energy levels for doped and undoped Si QDs are depicted in Figure 4. As can be seen, the B-doping gives rise to impurity states located above the valence band, whereas the P-doping gives rise to impurity states located below the conduction band. These impurity-related levels falling within the gap are strongly focused either on B or P impurity atom, as one can see from Figure 5 where the localization of these impurity states is shown.

One can see from Figure 4 that owing to the impurity doping, spin split occurs for some doped QD configurations. It is obvious that the energy differences between spin-up and spin-down levels in smaller doped Si QDs are more

pronounced than the ones in the bigger doped QDs case. Besides, for QDs with the same size but different impurity positions, the situations of spin split are different from each other, particularly for $\text{Si}_{87}\text{H}_{76}$ -based QDs in which split disappears in several configurations. So spin split induced by doping depends on not only the QD size but also the impurity position. In addition, it is observed that the impurity position also has an impact on the position of impurity levels. For $\text{Si}_{35}\text{H}_{36}$ -based QDs, as the impurity moves from the QD subsurface toward the center, the impurity states become deeper (shallower) for B-doping (P-doping). However, in the case of $\text{Si}_{87}\text{H}_{76}$ -based QDs, as the impurity moves from the QD subsurface toward the center, the impurity states become shallower (deeper) for B-doping (P-doping). This indicates that the impurity position has opposite effects on the impurity levels for B-doping and for P-doping, and the ultimate effects also closely depend on the QD size. Furthermore, we find out that although B (or P) introduces shallow acceptor (or donor) states in bulk silicon, either B- or P-doping introduces deep energy levels in the energy gap of Si QD. By comparing the impurity levels of the QDs with two different sizes, it can be easily found out that with a decrease of the QD size the acceptor (B-doping) and donor (P-doping) levels become even deeper.

The electronic densities of states (DOSs) for the investigated Si QDs have also been calculated to get a better understanding of the effect of impurity doping on the electronic properties of Si QDs. The DOSs shown in Figure 6 for the B- and P-doped Si QDs are compared with the ones of corresponding undoped Si QDs. As can be seen, the peaks in the DOSs for either B- or P-doped Si QDs show a similar structure with that of the undoped cases out of the energy range of the HOMO-LUMO gap. However, some impurity-related peaks appear just above the HOMO of the undoped QD for B-doped cases, while for P-doped cases the peaks located just below the LUMO of the undoped QD. In addition, it can be seen from Figure 6 that for $\text{Si}_{35}\text{H}_{36}$ -based QDs, as the impurity moves from the QD subsurface toward the center, the impurity-related peaks move toward the midgap region (LUMO) for B-doping (P-doping). While for $\text{Si}_{87}\text{H}_{76}$ -based QDs, as the impurity moves from the QD subsurface toward the center, the impurity-related peaks move toward the HOMO (midgap region) for B-doping (P-doping). Moreover, it is obvious that with a decrease of the QD size the impurity-related peaks are closer to the midgap region. All these characteristics show a good agreement with the ones of energy levels discussed before.

4. Conclusion

The structural and electronic properties of B- and P-doped Si QDs are investigated by means of first-principle calculations. All the possible locations for a single substitution impurity inside Si QDs are considered. According to the structural analysis, it is found out that for P-doped case the structural distortion is less significant than that for B-doped case. The distortion is strongly dependent on the QD size for P-doped case; the larger the size, the less the distortion. While for

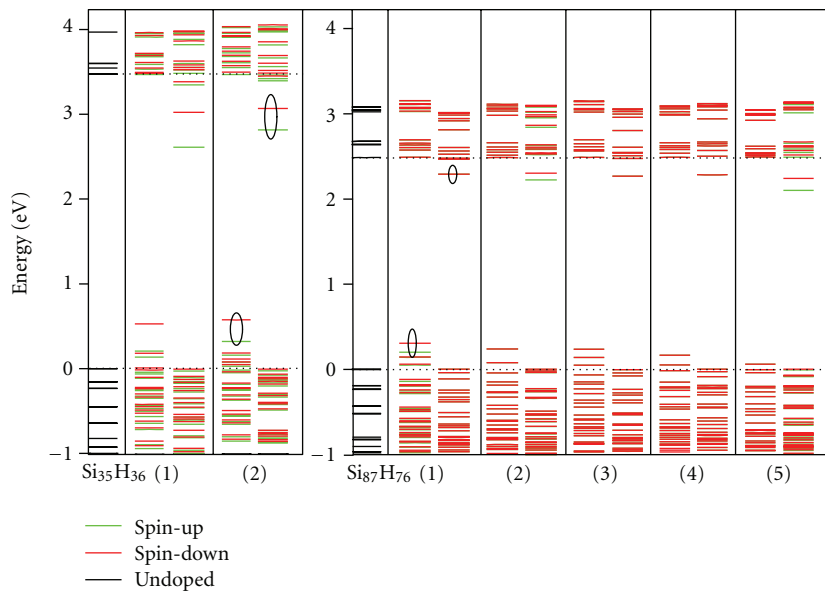


FIGURE 4: Energy level diagram for doped (red and green) and undoped (black) Si QDs. From left to right it is arranged in the order $\text{Si}_{35}\text{H}_{36}$, $\text{Si}_{34}\text{BH}_{36}-1$, $\text{Si}_{34}\text{PH}_{36}-1$, $\text{Si}_{34}\text{BH}_{36}-2$, $\text{Si}_{34}\text{PH}_{36}-2$, $\text{Si}_{87}\text{H}_{76}$, $\text{Si}_{86}\text{BH}_{76}-1$, $\text{Si}_{86}\text{PH}_{76}-1$, $\text{Si}_{86}\text{BH}_{76}-2$, $\text{Si}_{86}\text{PH}_{76}-2$, $\text{Si}_{86}\text{BH}_{76}-3$, $\text{Si}_{86}\text{PH}_{76}-3$, $\text{Si}_{86}\text{BH}_{76}-4$, $\text{Si}_{86}\text{PH}_{76}-4$, $\text{Si}_{86}\text{BH}_{76}-5$, $\text{Si}_{86}\text{PH}_{76}-5$. Spin-up (spin down) states of doped Si QDs are indicated by green (red). If spin-up state and spin-down state overlap, the overlap turns out to be red. So if the energy levels are all red, it means that there does not exist spin split; otherwise it means that spin split occurs. The dotted lines represent the HOMO and LUMO states of the undoped QD.

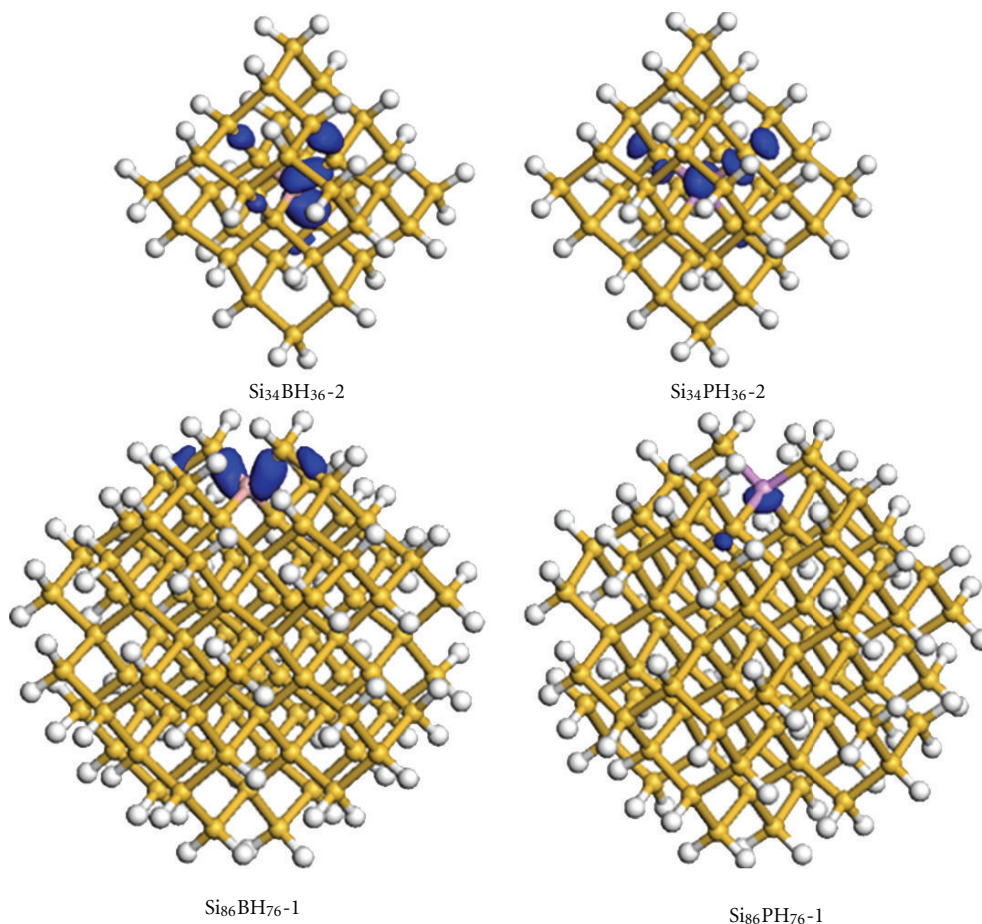


FIGURE 5: The orbital analysis of defect states (denoted by circles in Figure 4) for doped Si QDs. The isovalue is set as 0.02 for each case.

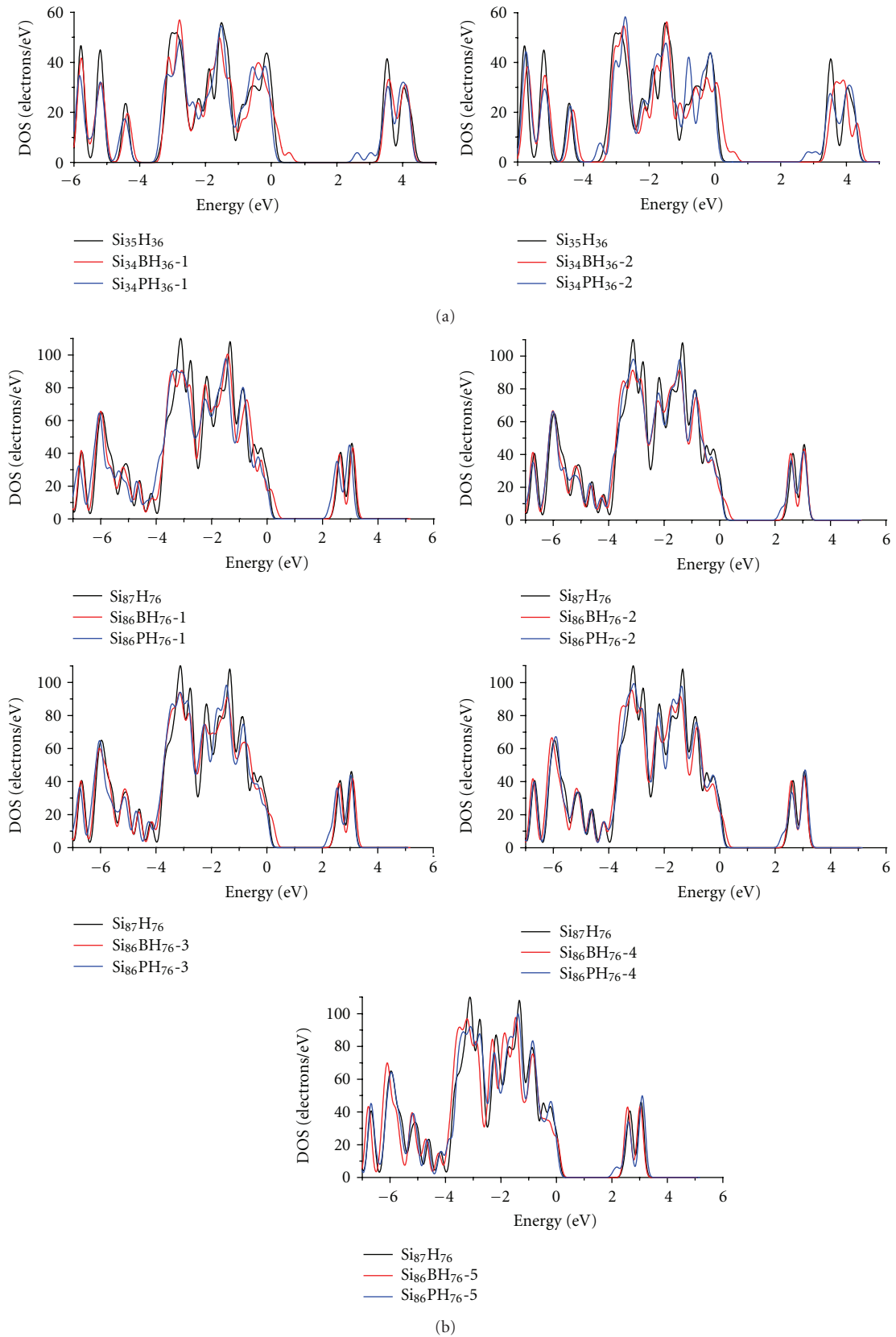


FIGURE 6: Electronic density of states for undoped Si QDs (black), B-doped Si QDs (red), and P-doped Si QDs (blue). From left to right, from top to bottom, the impurity position moves from the QD subsurface toward the center. (a) The DOSs for $\text{Si}_{35}\text{H}_{36}$ -based QDs; (b) the DOSs for $\text{Si}_{87}\text{H}_{76}$ -based QDs.

B-doped case the distortion is nearly independent of the size. The relaxation around the impurity is also related to the impurity position, and the impact of impurity position becomes more significant with a decrease of the QD size. The most stable configuration is explored in all these single doped configurations by the energy calculations. The results show that for either B- or P-doping, the impurity atom tends to substitute Si atom near the surface. Besides, we find out that with a decrease of the QD size the insertion of a substitution impurity becomes more difficult, and this size effect is much more evident for B-doping than P-doping. In addition, our calculations of the band structure and DOS associated with the considered Si QDs show that the presence of P atom (or B atom) introduces donor (or acceptor) states within the energy gap, and spin split occurs for some doped QD configurations. Moreover, the influence of impurity position on the impurity levels has been discussed. It is indicated that the impurity position has opposite effects on the impurity levels for B-doping and for P-doping. Furthermore, it is demonstrated that either B- or P-doping introduces deep energy levels in the energy gap of Si QDs, and with a decrease of the QD size the acceptor (B-doping) and donor (P-doping) levels become even deeper.

These insights gained in our study show the possibility of an impurity-based engineering of the Si QD electronic properties, which are of great help to the realization of related Si QD-based potential applications.

Acknowledgments

This project is partially supported by the National Science Foundation of China (Grant no. 61001044). The authors are grateful to Shanghai Supercomputer Center for providing computation resources.

References

- [1] M. Cazzanelli, D. Navarro-Urriós, F. Riboli et al., "Optical gain in monodispersed silicon nanocrystals," *Journal of Applied Physics*, vol. 96, no. 6, pp. 3164–3171, 2004.
- [2] E. C. Cho, M. A. Green, G. Conibeer et al., "Silicon quantum dots in a dielectric matrix for all-silicon tandem solar cells," *Advances in OptoElectronics*, vol. 2007, Article ID 69578, 11 pages, 2007.
- [3] Z. J. Horváth, "Semiconductor nanocrystals in dielectrics: optoelectronic and memory applications of related silicon-based MIS devices," *Current Applied Physics*, vol. 6, no. 2, pp. 145–148, 2006.
- [4] E. Srinivasan and G. N. Parsons, "Hydrogen elimination and phase transitions in pulsed-gas plasma deposition of amorphous and microcrystalline silicon," *Journal of Applied Physics*, vol. 81, no. 6, pp. 2847–2855, 1997.
- [5] E. A. G. Hamers, A. Fontcuberta I Morral, C. Niikura, R. Brenot, and P. Roca I Cabarrocas, "Contribution of ions to the growth of amorphous, polymorphous, and microcrystalline silicon thin films," *Journal of Applied Physics*, vol. 88, no. 6, pp. 3674–3688, 2000.
- [6] X. J. Hao, E. C. Cho, C. Flynn, Y. S. Shen, G. Conibeer, and M. A. Green, "Effects of boron doping on the structural and optical properties of silicon nanocrystals in a silicon dioxide matrix," *Nanotechnology*, vol. 19, no. 42, Article ID 424019, 2008.
- [7] D. V. Melnikov and J. R. Chelikowsky, "Quantum confinement in phosphorus-doped silicon nanocrystals," *Physical Review Letters*, vol. 92, no. 4, pp. 468021–468024, 2004.
- [8] G. Cantele, E. Degoli, E. Luppi et al., "First-principles study of n- and p-doped silicon nanoclusters," *Physical Review B*, vol. 72, no. 11, Article ID 113303, 4 pages, 2005.
- [9] X. Pi, X. Chen, and D. Yang, "First-principles study of 2.2 nm silicon nanocrystals doped with boron," *Journal of Physical Chemistry C*, vol. 115, no. 20, pp. 9838–9843, 2011.
- [10] X. Chen, X. Pi, and D. Yang, "Critical role of dopant location for P-doped Si nanocrystals," *Journal of Physical Chemistry C*, vol. 115, no. 3, pp. 661–666, 2011.
- [11] F. Iori, E. Degoli, R. Magri et al., "Engineering silicon nanocrystals: theoretical study of the effect of codoping with boron and phosphorus," *Physical Review B*, vol. 76, no. 8, Article ID 085302, 14 pages, 2007.
- [12] M. D. Segall, P. J. D. Lindan, M. J. Probert et al., "First-principles simulation: ideas, illustrations and the CASTEP code," *Journal of Physics Condensed Matter*, vol. 14, no. 11, pp. 2717–2744, 2002.
- [13] J. P. Perdew, K. Burke, and M. Ernzerhof, "Generalized gradient approximation made simple," *Physical Review Letters*, vol. 77, no. 18, pp. 3865–3868, 1996.
- [14] F. Iori, E. Degoli, E. Luppi et al., "Doping in silicon nanocrystals: an ab initio study of the structural, electronic and optical properties," *Journal of Luminescence*, vol. 121, no. 2, pp. 335–339, 2006.

Research Article

Particle Size Effect on TL Emission of ZnS Nanoparticles and Determination of Its Kinetic Parameters

L. Robindro Singh^{1,2} and S. Dorendrajit Singh³

¹ Department of Physics, Mizoram University, P U College, Aizawl 796 001, India

² Department of Nanotechnology, North-Eastern Hill University, Shillong 793 002, India

³ Department of Physics, Manipur University, Manipur 795 003, Canchipur, India

Correspondence should be addressed to L. Robindro Singh, robindro001@yahoo.co.in

Received 17 March 2012; Accepted 3 May 2012

Academic Editor: Leonard Deepak Francis

Copyright © 2012 L. R. Singh and S. D. Singh. This is an open access article distributed under the Creative Commons Attribution License, which permits unrestricted use, distribution, and reproduction in any medium, provided the original work is properly cited.

Nanoparticles have large surface area, and most of the ions are lying on its surface. Could these surface ions be contributed in thermoluminescence emission or enhanced nonradiative transition? In view of this, we have prepared small sizes of ZnS nanoparticles at low temperature and made two samples, one as-prepared (size ~3 nm) and the other heat-treated at 1073 K (size ~32 nm). Characterization of the samples shows that the prepared phosphors are pure. Thermoluminescence (TL) glow curves could not be recorded in both samples without irradiation. Even for higher dose of γ -radiation the as-prepared samples could not show TL signal, but 1073 K heat-treated sample shows the TL signal. This may be due to the fact that smaller particles have large surface area compared to bigger particles, the surface ions may produce the nonradiative transitions. The kinetic parameters of the TL glow curves are evaluated by the conventional methods and compared with curve fitting computerised glow curve deconvolution (CGCD) technique. The variations in both techniques are found only ± 0.02 . The shape factor of all the glow curves ~0.48, and these TL glow curves could be fitted with order of kinetics 1.5.

1. Introduction

The semiconductor nanoparticles in the groups II–VI have been studied extensively due to their intriguing physical properties compared to their bulk counterparts [1–10]. Optical properties of such materials can be tuned due to quantum size effects which effectively lead to a size-dependent variation of band gap. Among the most studied II–VI semiconductors are ZnO, CdS, ZnS, and so forth [11–15] for their wide range of luminescence emissions from ultraviolet to infrared regions. ZnS is a blue emitting direct band gap semiconductor of energy gap 3.6 eV with low phonon energy suitable in display devices and lighting applications. Extensive studies on the luminescence emissions of ZnS nanoparticles doped with transition metals or lanthanide ions at different sizes, pH, capping agents, and so forth have been carried out since the past decades [16–22]. There are few reports on the study of thermoluminescence characteristics of these materials in nanosize; in view of this, the present

paper is prepared to study their luminescence characteristics at different particle sizes.

Thermoluminescence (TL) continues to be an active area of research because of its immense contribution in the fields of personnel and environmental dosimetry, dating of archeological artifacts, sediments and study of defects in solids. Irradiation on many insulating and semiconducting materials creates sufficient defects to act as trap centers for electron and holes. Upon heating the materials containing large number of electrons and holes trapped in their respective trap centers, these electrons and holes are released and recombine with opposite charges resulting luminescence called TL (thermoluminescence). In the case of nanomaterials, the surface-to-volume ratio is large resulting in larger concentrations of surface states. The surface states are responsible for the production of TL glow curves, that is why Chen et al. [23] record TL glow curves in ZnS nanoparticle prior to irradiation. They also observed that the TL intensity increases with the decrease of particle sizes and concluded that the surface

ions on the nanoparticles were responsible for the production of TL glow curves. Crystalline sizes of the particles take important role in producing luminescence emission of the phosphors, many researchers are working in this regard on different phosphors [24–29]. Studying the luminescence characteristics of phosphors on particle sizes will be beneficial in lighting applications.

The present work studies the photoluminescence and thermoluminescence (TL) of as-prepared and 1073 K heat-treated undoped (pure) ZnS nanoparticles. Kinetic parameters such as the activation energy (E), order of kinetics (b), and frequency factor (s) of the glow peaks are determined by initial rise [30], curve fitting [31] and compared with computerised glow curve deconvolution method [32].

2. Experimental Section

2.1. Preparation. Quantum sizes of undoped (pure) ZnS nanoparticles were prepared by coprecipitation reaction at low temperature. In order to get small sizes of the particles, slow release of the reactants at controlled manner would be needed [33, 34]. Ethylene glycol acts as the reaction medium as well as the capping ligand. The precursors used for the production of Zn^{2+} was $Zn(CH_3COO)_2 \cdot 2H_2O$ (99.05%, E-Merck), and thiourea (AR) for the production of S^{2-} . 1 gm of $Zn(CH_3COO)_2 \cdot 2H_2O$ was dissolved in 25 mL ethylene glycol; warming the solution, a clear solution could be observed. This solution contained Zn^{2+} ions. In this solution, 2.0 g of thiourea (AR) was simply added and warmed the mixture at 353 K, the solution again became transparent. The reaction medium was kept in nitrogen atmosphere, in order to avoid oxidation during reaction. The whole mixture was heated linearly up to 403 K. After half an hour, light yellowish-white colloidal precipitate could be observed, the reaction temperature maintained at this temperature and continues another two hours. The precipitates so obtained are extracted by centrifugation and washed several times in excess methanol (AR). Special care has been taken to avoid oxidation, the powder samples so obtained were dried at room temperature.

2.2. Characterization. X-ray diffraction studies were carried out using a Philips powder X-ray diffractometer (model PW 1071) with Ni-filtered $Cu-k_\alpha$ radiation. The lattice parameters were calculated from the least square fitting of the diffraction peaks. The average crystallite sizes were calculated from the diffraction line-width based on Scherrer relation: $d = 0.9\lambda/\beta \cos \theta$, where λ is the wavelength of X-rays, and β is the half maximum line width. To record UV-visible spectra, EDX and AFM, the powder samples were dispersed in dimethyl formide (DMF), then multiple dipping were carried out on ultrasonically cleaned glass slides.

Photoluminescence measurements were carried out at room temperature with a resolution of 3 nm, using a Hitachi Instrument (F-4500) having a 150 W Xe lamp as the excitation source. Powder samples (5 mg) were mixed with methanol, spread over a quartz plate, dried at 373 K, and mounted inside the sample chamber for photoluminescence

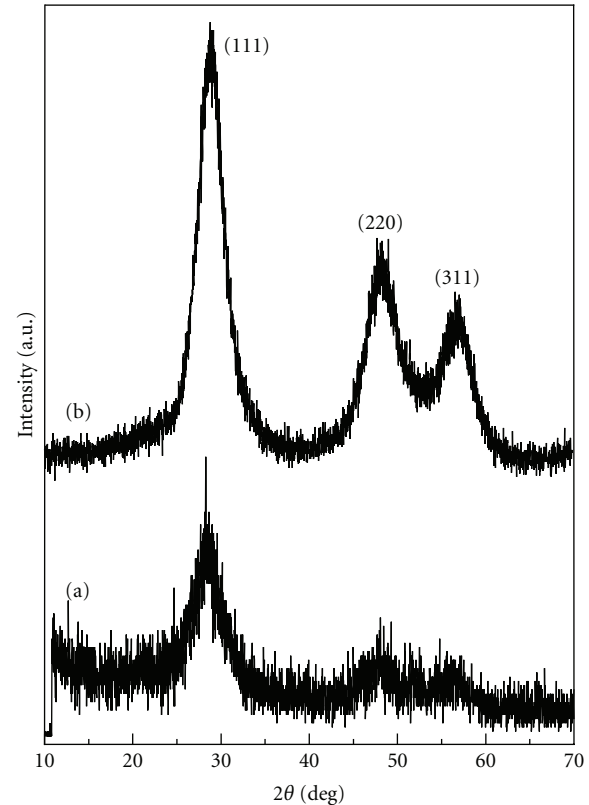


FIGURE 1: XRD pattern of (a) as-prepared and (b) 1073 K heat-treated ZnS nanoparticles.

measurements. Thermoluminescence glow curves of the powder samples were recorded using TLD-1404 recorder.

3. Results and Discussion

3.1. X-Ray Diffraction (XRD) Study. Figure 1 shows the X-ray diffraction patterns of (a) as-prepared and (b) 1073 K heat-treated ZnS nanoparticles and corresponds to cubic phase (JCPDS-77-2100) of space group $F43m$. No extra peaks of impurity could be detected even for higher heat-treated sample within the resolution of limit diffractometer. The lattice parameter of the as-prepared ZnS nanoparticle is $a = 5.359(1)$ Å with unit cell volume $153.948(1)$ Å³ and that of 1073 K heat-treated ZnS nanoparticle is $a = 5.369(1)$ Å with unit cell volume $V = 154.825(1)$ Å³. The unit cell volume of heat-treated ZnS gives higher value compared to as-prepared ZnS nanoparticle. The increase of the unit cell volume with the increase of heat-treatment temperature may be due to the decrease in ionicity. The particle sizes calculated from Scherrer relation are found to be 3 and 32 nm, respectively for as-prepared and 1073 K heat-treatment samples, respectively. The intensity of the diffraction peaks increases with the increase of the heat-treatment temperature showing an increase in the crystallinity of the samples with heat-treatment.

3.2. EDX (Energy Dispersive X-ray) and AFM (Atomic Force Microscopy) Study. Figure 2 shows the EDX of as-prepared

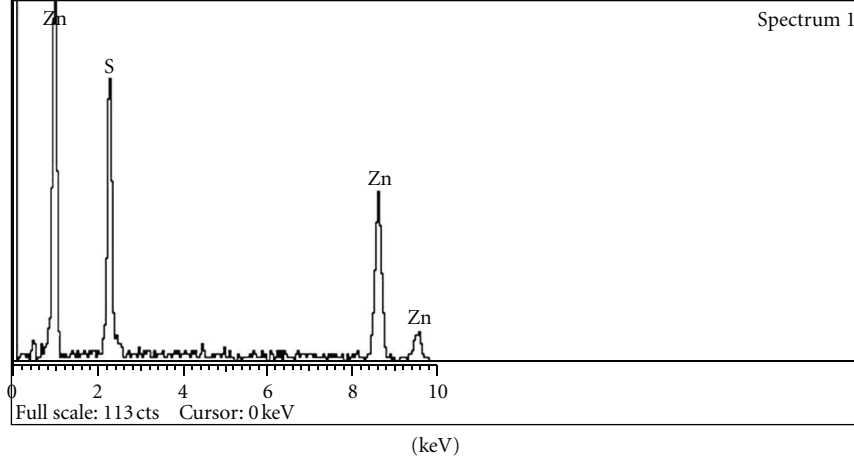


FIGURE 2: EDX spectra of as-prepared ZnS nanoparticles.

ZnS nanoparticles. As-prepared sample gives the atomic %Zn = 54 and S = 46, while the heat-treated sample gives atomic %Zn = 51 and S = 49. Figure 3 shows the 2-dimensional AFM picture of (a) as-prepared and (b) 1073 K heat-treated ZnS nanoparticles. The particles sizes determined by AFM are 12 and 87 nm, respectively for the as-prepared and heat-treated ZnS nanocrystals. The particles in as-prepared samples are spherical in shape and agglomerated. Figure 3(c) is the log-normal distribution of as-prepared sample showing the particle size of this sample is 13 nm. In the 1073 K heat-treated samples, the particles are spherical in shape and homogenous. It is obvious that the ethylene glycol can significantly resist agglomeration of nanoparticles.

4. Luminescence Study

4.1. TL Theory. Thermoluminescence is the thermally stimulated emission of light from insulators or semiconductors following previous absorption of energy from radiation. The electrons in the valance band gain energy due to exposure in radiation may come either to the conduction band or trapped in a metastable state as trapped electrons causing defect states in the material. On heating the phosphor, the trapped electrons in the metastable gain in energy then are released from the trapped level, if these electrons return to ground state with radiative recombination with the holes near the ground state, there is observation of thermoluminescence. When the recombination probability dominates the retrapping probability or retrapping probability is zero, Randall and Wilkins [35] had reported an expression for TL intensity of the first-order kinetics ($b = 1$) at a temperature T as

$$I(T) = n_0 s \exp\left(-\frac{E}{kT}\right) \exp\left[-\frac{s}{\beta} \int_{T_0}^T \exp\left(-\frac{E}{kT'}\right) dT'\right], \quad (1)$$

where n_0 is the initial concentration of trap electrons, s the frequency factor, E the activation energy, k the Boltzmann constant, and β the linear heating rate.

When the retrapping probability is the same as recombination probability then the expression for TL intensity of the second-order kinetics is given by [30]:

$$I(T) = \frac{n_0^2 s' \exp(-E/kT)}{\left[1 + (n_0 s' / \beta) \int_{T_0}^T \exp(-E/kT') dT'\right]^2}, \quad (2)$$

where $s = n_0 s'$.

For the non-first-order kinetics ($b \neq 1$), Gartia et al. [36] and Rasheedy [37] reported an expression for TL intensity as

$$I(T) = N f^b s \exp\left(-\frac{E}{kT}\right) \times \left[1 + (b-1) f^{b-1} \frac{s}{\beta} \int_{T_0}^T \exp\left(-\frac{E}{kT'}\right) dT'\right]^{-b/(b-1)}, \quad (3)$$

where N is the electron traps and filling factor $f = n_0/N$.

The condition for maximum intensity for the glow curve obeying (3) is given by

$$1 + (b-1) f^{b-1} \left(\frac{s}{\beta}\right) \int_{T_0}^{T_m} \exp\left(-\frac{E}{kT'}\right) dT' = \frac{b s k T_m^2}{\beta E} f^{b-1} \exp\left(-\frac{E}{kT_m}\right). \quad (4)$$

The shape factor μ_g , of the glow curve can also be determined from the relation [32]:

$$\mu_g = \frac{\delta}{\omega} = \frac{(T_2 - T_m)}{(T_2 - T_1)}, \quad (5)$$

where T_m is the peak temperature of the glow curve, and T_1 , and T_2 are the temperatures at half of the maximum intensity on the rising and falling sides of the glow curves.

4.2. Photoluminescence and Thermoluminescence Study. Figure 4 shows the photoluminescence emissions of as-prepared and 1073 K heat-treated ZnS nanoparticles excited at

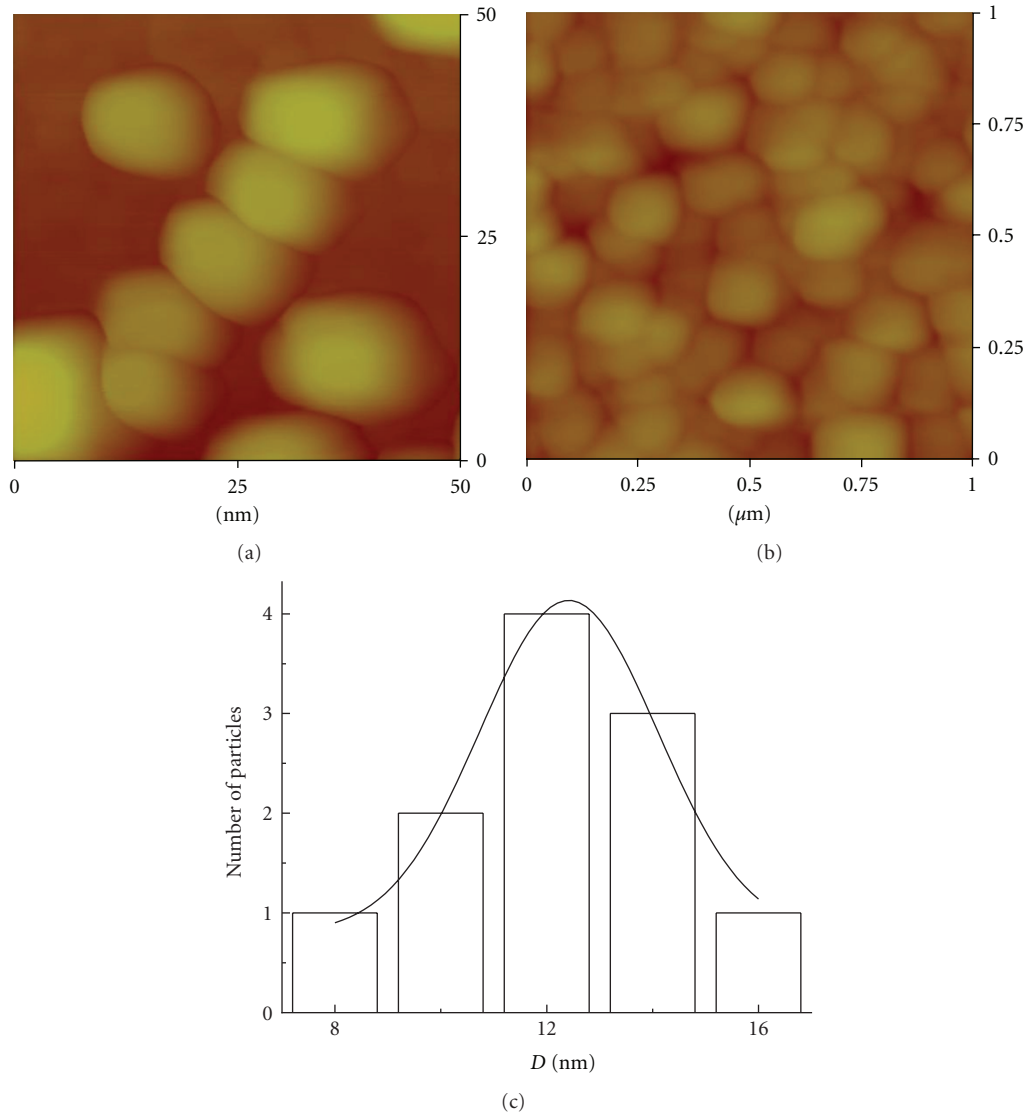


FIGURE 3: AFM picture of (a) as-prepared, (b) 1073 K heat-treated ZnS nanoparticles, and (c) log-normal distribution of the as-prepared nanoparticles showing that most of the particles are 13 nm in size.

290 nm. Strong blue emissions are observed, these emissions are due to native intrinsic defects such as vacancies and interstitials forming energy levels in ZnS, such as donor levels of V_S and Z_{ni} and acceptor level of V_{zn} . The emission intensity increases with the increase of heat-treatment temperature, this observation may be due to an increase in crystallinity of the particles which in turn reduces the ionicity and the surface effects of the nanoparticles.

Thermoluminescence (TL) glow curves were recorded for both as-prepared and heat-treated ZnS nanoparticles without irradiation, but no TL signal could be recorded. Both the as-prepared and heat-treated samples were irradiated with different doses of γ radiation, but the as-prepared sample does not show TL signals even for a higher dose of γ radiation. The 1073 K heat-treated ZnS nanoparticles were irradiated with 126 and 252 Gy of γ -rays, and TL glow curves could be recorded. Chen et al. [23] could get TL glow curves of

ZnS nanoparticles without irradiation. They observed that the TL intensity increases with the reduction of particle sizes. Their observations had open vehement argument for further understandings on the luminescence characteristics of small particles. They suggested that the surface ions on the nanoparticles took a vital role in the production of TL signals. But our observations are contrary to their findings. It is expected that the surface ions on the surface of nanoparticles enhance the nonradiative transition that is why TL signal cannot be detected for as-prepared samples. It is well accepted that small particles have large surface area, and most of the ions lie on its surface. To confirm these observations, the as-prepared nanoparticles are heat-treated at 1073 K for one hour to get bigger particle sizes. Bigger nanoparticles have less number of surface ions and the non-radiative transition due to phonon-phonon interactions could be reduced extensively. Even this sample

TABLE 1: Peak parameters of the TL glow curves irradiated with 126 and 252 Gy of γ -rays.

Dose	T_m (K)	I_m	τ	$\delta = T_2 - T_m$	$\omega = T_2 - T_1$	$\mu_g = \delta/\omega$
126	374.0	66.3	43.5	50.5	101.0	0.50
252	390.0	112.9	43.5	39.5	83.0	0.48

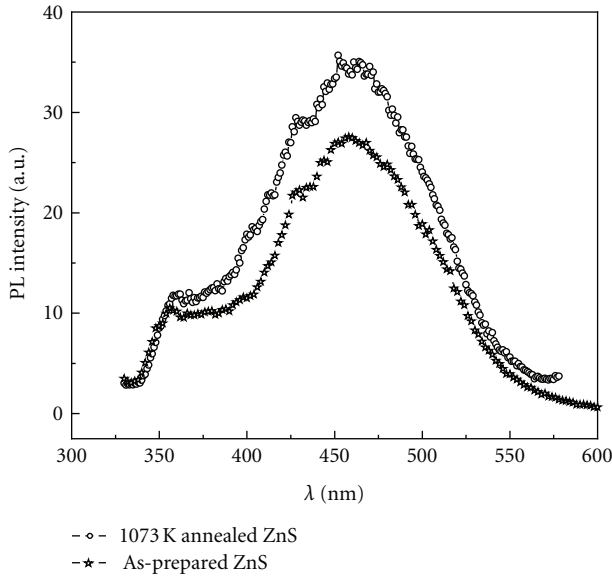
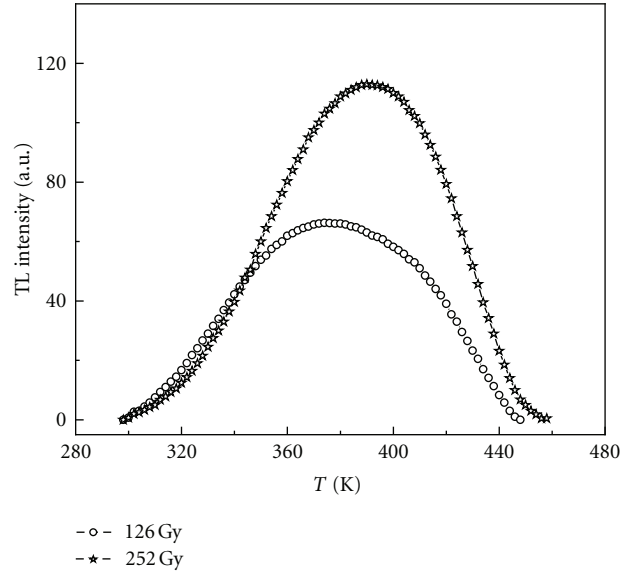


FIGURE 4: Photoluminescence emission spectra of as-prepared and 1073 K heat-treatment ZnS nanoparticles showing the native blue emission.

FIGURE 5: TL glow curves of nanoparticle ZnS irradiated with (a) 126 Gy and (b) 252 Gy of γ -rays with a linear heating rate $\beta = 1.73^\circ\text{C/s}$.

the TL signal could not be recorded prior to irradiation. Then the samples are again irradiated with γ radiations, and TL signal could be recorded for different doses of radiations. With irradiation different trap centers could be developed, even though there are surface ions on the nanoparticles. The radiative transitions due to trap levels dominates over the non-radiative transitions due to surface ions. That is why, TL signals could be recorded in heat-treated and irradiated samples. The above observations revealed that the surface ions on the surface of the nanoparticles could not contribute to the luminescence emissions, but only the trap centers could give luminescence emissions. Figure 5 shows the TL glow curves of 1073 K heat-treated ZnS nanoparticle irradiated with 126 and 252 Gy of γ -rays with a linear heating rate of 1.73 K/s, and the peak temperatures of the glow curves are around 374 and 390 K, respectively. The TL intensity of the glow curves varies with the different doses of γ -rays. The sample irradiated with higher dose of γ -ray has more intense in TL signal than the sample irradiated with lower γ dose. The full widths (ω) of the glow curves are found to be 83 K and 101 K, which are exceptionally large. In general, such a broad peak must contain at least two or more TL peaks. The shape factor μ_g is found to be 0.48, which are the characteristics of the non-first-order kinetics model [30, 31]. Table 1 indicates the characteristic peak parameters of the recorded glow curves of Figure 7.

Figure 6 shows the TL glow curves of 1073 K heat-treated ZnS nanoparticles irradiated with 126 Gy and 252 Gy of γ -rays after thermal cleaning up to 393 K. The peak temperatures of the glow curves (126 Gy and 252 Gy) are observed around 419 K, and the full widths at half maximum (ω) of the glow curves become 41 and 47 K, respectively. The shape factors of the glow curves are still at 0.48. The 252 Gy irradiated sample has been thermally cleaned to different temperatures 373, 393, 413, and 443 K, and then the glow curves are recorded. The peak temperatures of the recorded glow curves are 409.15, 415.82, 423.38, and 434.2 K, respectively as shown in Figure 7. The full width (ω) becomes narrower as compared to the glow curves before thermal cleaning. The value of the shape factor of the glow curves is at ~ 0.48 , which is the characteristic of the non-first-order kinetics. Physically, it signifies that during heating parts of the electrons released from the traps are recombining with the holes in the hole centers resulting TL, and the remaining part of electrons are retrapped back to the electron traps. If significant numbers of electrons are retrapped back to the earlier electron trap centres such that retrapping probability is equal to recombination probability, the shape factor should be nearly 0.52. Table 2 describes the peak parameters of the glow curves, which are thermally cleaned at temperatures 373, 393, 413, and 443 K. It is clearly observed that all the peaks are non-first-order kinetics.

TABLE 2: Peak parameters of γ -irradiated TL glow curves of 1073 K heat-treatment ZnS nanoparticles recorded with different thermal cleaning (T_c).

T_c (K)	T_m (K)	I_m	τ	$\delta = T_2 - T_m$	$\omega = T_2 - T_1$	$\mu_g = \delta/\omega$
373	409.15	99.2	38.4	30.0	64.8	0.47
393	415.82	89.6	36.1	29.1	60.8	0.48
413	423.38	63	31.4	24.6	51.4	0.48
443	434.20	16.6	16.1	22.35	44.7	0.50

TABLE 3: Comparison of activation energies calculated from CGCD and peak shape method of the γ -irradiated ZnS nanoparticles.

Dose (Gy)	T_m (K)	E_c (eV)	E_δ	b	s (sec ⁻¹)	FOM
	396.92	0.67	0.634	1.5	5.9×10^7	
126	427.16	0.95	0.891	1.5	2.3×10^{10}	0.0869
	391.25	0.70	0.732	1.5	1.5×10^7	
252	421.5	1.00	0.992	1.5	2.0×10^{10}	

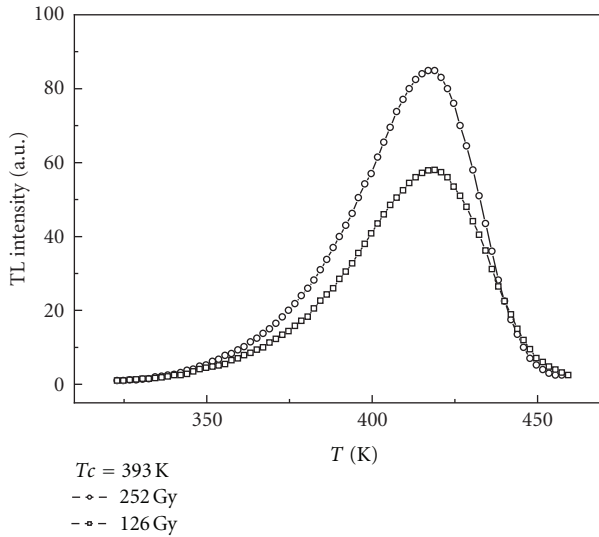


FIGURE 6: TL glow curves of nanoparticle ZnS irradiated with (a) 126 Gy and (b) 252 Gy of γ -rays recorded after thermal cleaning up to 393 K ($\beta = 1.73^\circ\text{C/s}$).

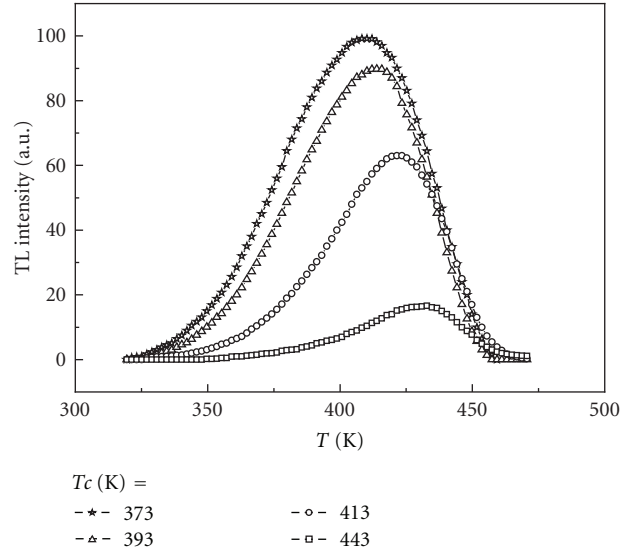


FIGURE 7: TL glow curves of ZnS irradiated with 252 Gy of γ -rays recorded after thermal cleaning at (a) 373 K, (b) 393 K, (c) 413 K, and (d) 443 K with linear heating rate 1.73°C/s .

To determine kinetic parameters such as activation energy (E), order of kinetics (b), and frequency factor (s) of the observed TL glow curves, we have used the conventional methods such as initial rise (IR) [30], peak shape method [31], and CGCD technique [32, 36, 38]. A series of initial rise (IR) thermoluminescence curves are recorded for the sample irradiated with 252 Gy of γ -ray by keeping the voltage across the photomultiplier tube to a high value such that TL intensity becomes large. The magnitude of the slope of $\ln(I)$ versus $1/T$ gives E/k , and consequently E (activation energy) can be evaluated. The mean value of activation energy by using IR method is 0.78 eV. It is to be noted that the IR method to determine E is independent of the order of kinetics. Again the activation energy is evaluated using the peak shape formula of Gartia et al. [39]. The comparison between trapping parameters of ZnS nanoparticles evaluated by peak shape method and CGCD is shown in Table 3.

Figure 8 shows curve fitting of the glow curve of ZnS irradiated with 126 Gy of γ -rays after thermally cleaned up to 393 K. It can be fitted with two peaks with peak temperatures 396.92 and 427.16 K. The thermal activation energies of the deconvoluted curves are 0.7 and 1.0 eV, and frequency factors of the deconvoluted curves are 5.9×10^7 and $2.3 \times 10^{10} \text{ s}^{-1}$. Both the deconvoluted peaks are non-first-order of kinetics $b = 1.5$. Similar pattern can be observed for higher T_c samples. Similar patterns can also be observed for 252 Gy γ -ray irradiated sample. The deconvoluted glow curves have peak temperatures at 391.25 and 421.5 K, with order of kinetics $b = 1.5$. Table 3 indicates the activation energies calculated from CGCD and shape factor technique of ZnS nanoparticle irradiated with 126 and 252 Gy of γ -rays. The activation energy (E_c) determined from CGCD and shape factor (E_δ) is almost consistent, the difference is ± 0.02 .

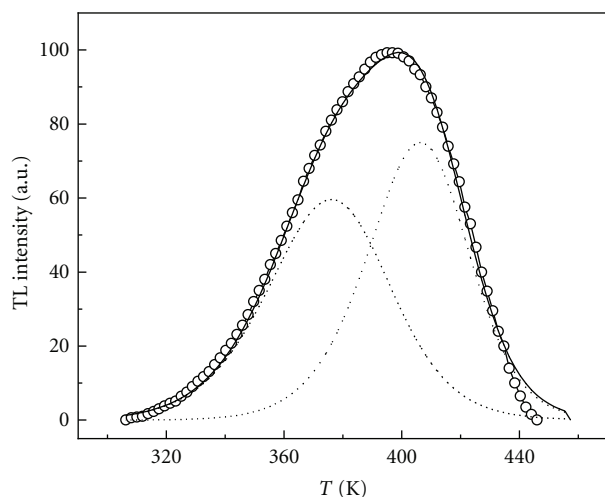


FIGURE 8: Computerised glow curve deconvolution of ZnS nanoparticles irradiated with 252 Gy of γ after thermal cleaning of 393 K with linear heating rate of 1.73°C/s, (ooo) Expt. Glow curve (—) sum of deconvoluted curves and (· · ·) deconvoluted curves.

5. Conclusion

Small sizes of ZnS nanoparticles could be prepared successfully at low temperature, it is evident that ethylene glycol can significantly resist agglomeration of the nanoparticles even heated at higher temperatures. As-prepared and 1073 K heat-treatment samples could not show TL signal without irradiation, reduction of surface ions on the nanoparticles might be responsible for the production of TL signals. The order of kinetics as evaluated by shape factor (non-first-order of kinetics) has the same pattern as evaluated by curve fitting technique. Peak shape method could be suitable to determine activation energy of the glow curves. Order of kinetics of the glow curves has the same value on order of kinetics $b = 1.5$ even for different doses of irradiation. The calculated value of activation energy using peak shape formula is in agreement with that of fitted value.

Acknowledgments

The authors owe R. S. Ningthoujam, scientific officer E. Chemistry Division, BARC, Mumbai for providing the facilities of characterizations and luminescence measurements. L. R. Singh thanks Dr. T. D. Singh, Swambung College, Imphal for his constant encouragement and suggestions while preparing this work. L. R. Singh thanks to DST-New Delhi for financial assistance under the scheme of DST Fast Tract Scheme for Young Scientist during execution of the present work.

References

- [1] A. Balandin, K. L. Wang, N. Kouklin, and S. Bandyopadhyay, "Raman spectroscopy of electrochemically self-assembled CdS quantum dots," *Applied Physics Letters*, vol. 76, no. 2, pp. 137–140, 2000.
- [2] R. N. Bhargava, D. Gallagher, X. Hong, and A. Nurmikko, "Optical properties of manganese-doped nanocrystals of ZnS," *Physical Review Letters*, vol. 72, no. 3, pp. 416–419, 1994.
- [3] L. E. Brus, "Zero dimensional "excitons" in semiconductor clusters IEEE," *Journal of Quantum Electronics*, vol. 22, no. 9, pp. 1909–1926, 1986.
- [4] N. Taghavinia and T. Yao, "ZnS nanocrystals embedded in SiO₂ matrix," *Physica E*, vol. 21, no. 1, pp. 96–102, 2004.
- [5] M. J. Natan, J. W. Thackeray, and M. S. Wrighton, "Interaction of thiols with n-type cadmium sulfide and n-type cadmium selenide in aqueous solutions: adsorption of thiolate anion and efficient photoelectrochemical oxidation to disulfides," *Journal of Physical Chemistry*, vol. 90, no. 17, pp. 4089–4098, 1986.
- [6] M. Ihara, T. Igarashi, T. Kusunoki, and K. Ohno, "Cathodoluminescence and photoluminescence of nanocrystal phosphors," *Journal of the Electrochemical Society*, vol. 149, no. 3, pp. H72–H75, 2002.
- [7] A. A. Bol and A. Meijerink, "Long-lived Mn²⁺ emission in nanocrystalline ZnS:Mn²⁺," *Physical Review B*, vol. 58, no. 24, pp. R15997–R16000, 1998.
- [8] W. L. Wilson, P. F. Szajowski, and L. E. Brus, "Quantum confinement in size-selected, surface-oxidized silicon nanocrystals," *Science*, vol. 262, no. 5137, pp. 1242–1244, 1993.
- [9] R. S. Ningthoujam, V. Sudarsan, S. V. Godbole, L. Kienle, S. K. Kulshreshtha, and A. K. Tyagi, "Sn O₂:Eu³⁺ nanoparticles dispersed in TiO₂ matrix: improved energy transfer between semiconductor host and Eu³⁺ ions for the low temperature synthesized samples," *Applied Physics Letters*, vol. 90, no. 17, Article ID 173113, 3 pages, 2007.
- [10] A. D. Yoffe, "Low-dimensional systems: Quantum size effects and electronic properties of semiconductor microcrystallites (zero-dimensional systems) and some quasi-two-dimensional systems," *Advances in Physics*, vol. 42, no. 2, pp. 173–266, 1993.
- [11] A. P. Alivisatos, "Semiconductor nanocrystals," *MRS Bulletin*, vol. 20, no. 8, pp. 23–32, 1995.
- [12] C. C. Yang, S. Y. Cheng, H. Y. Lee, and S. Y. Chen, "Effects of phase transformation on photoluminescence behavior of ZnO:Eu prepared in different solvents," *Ceramics International*, vol. 32, no. 1, pp. 37–41, 2006.
- [13] M. Lomascolo, A. Creti, G. Leo, L. Vasanelli, and L. Manna, "Exciton relaxation processes in colloidal core/shell ZnSe/ZnS nanocrystals," *Applied Physics Letters*, vol. 82, no. 3, article 418, 3 pages, 2003.
- [14] N. Karar, F. Singh, B. R. Mehata et al., "Structure and Photoluminescence studies on ZnS:Mn nanoparticles," *Journal of Applied Physics*, vol. 95, no. 2, pp. 656–661, 2004.
- [15] K. K. Nanda and S. N. Sahu, "Photoluminescence of CdS nanocrystals: effect of ageing," *Solid State Communications*, vol. 111, no. 12, pp. 671–674, 1999.
- [16] B. A. Smith, J. Z. Zhang, A. Joly, and J. Liu, "Luminescence decay kinetics of Mn²⁺-doped ZnS nanoclusters grown in reverse micelles," *Physical Review B*, vol. 62, no. 3, pp. 2021–2028, 2000.
- [17] I. V. Kityk, M. Makowska-Janusik, J. Ebothé, A. El Hichou, B. El Idrissi, and M. Addou, "Photoinduced non-linear optical effects in the ZnS-Al, In-Sn doped film-glass nanometer-sized interfaces," *Applied Surface Science*, vol. 202, no. 1-2, pp. 24–32, 2002.
- [18] A. A. Bol, J. Ferwerda, J. A. Bergwerff, and A. Meijerink, "Luminescence of nanocrystalline ZnS:Cu²⁺," *Journal of Luminescence*, vol. 99, no. 4, pp. 325–334, 2002.
- [19] L. Xu, X. Huang, H. Huang, H. Chen, J. Xu, and K. Chen, "Surface modification and enhancement of luminescence due to

- quantum effects in coated CdSe/CuSe semiconductor nanocrystals,” *Japanese Journal of Applied Physics, Part 1*, vol. 37, no. 6, pp. 3491–3494, 1998.
- [20] S. L. Cumberland, K. M. Hanif, A. Javier et al., “Inorganic clusters as single-source precursors for preparation of CdSe, ZnSe, and CdSe/ZnS nanomaterials,” *Chemistry of Materials*, vol. 14, no. 4, pp. 1576–1584, 2002.
- [21] H. Benisty, C. M. Sotomayor-Torrès, and C. Weisbuch, “Intrinsic mechanism for the poor luminescence properties of quantum-box systems,” *Physical Review B*, vol. 44, no. 19, pp. 10945–10948, 1991.
- [22] J. F. Suyver, R. Bakker, A. Meijerink, J. J. Kelly et al., “Photoelectrochemical characterization of nanocrystalline ZnS:Mn²⁺ layer,” *Physica Status Solidi*, vol. 224, no. 1, pp. 307–312, 2001.
- [23] W. Chen, Z. Wang, Z. Lin, and L. Lin, “Absorption and luminescence of the surface states in ZnS nanoparticles,” *Journal of Applied Physics*, vol. 82, no. 6, pp. 3111–3115, 1997.
- [24] S. J. Dhoble, P. M. Bhujbal, N. S. Dhoble, and S. V. Moharil, “Lyoluminescence, thermoluminescence and photodecomposition in microcrystalline powder of KCl, KBr, KI and KI:KNO₃ crystals,” *Nuclear Instruments and Methods in Physics Research, Section B*, vol. 192, no. 3, pp. 280–290, 2002.
- [25] R. Sharma, D. P. Bisen, S. J. Dhoble, N. Brahme, and B. P. Chandra, “Mechanoluminescence and thermoluminescence of Mn doped ZnS nanocrystals,” *Journal of Luminescence*, vol. 131, no. 10, pp. 2089–2092, 2011.
- [26] A. Jagannatha Reddy, M. K. Kokila, H. Nagabhushana et al., “Structural, EPR, photo and thermoluminescence properties of ZnO:Fe nanoparticles,” *Spectrochimica Acta—Part A*, vol. 133, no. 2-3, pp. 876–883, 2011.
- [27] A. N. Yazici, M. Öztaş, and M. Bedir, “The thermoluminescence properties of copper doped ZnS nanophosphor,” *Optical Materials*, vol. 29, no. 8, pp. 1091–1096, 2007.
- [28] A. B. de Carvalho Jr., P. L. Guzzob, H. L. Sullasic, H. J. Khoury et al., “Effect of particle size in the TL response of natural quartz sensitized by high dose of gamma radiation and heat-treatments,” *Materials Research*, vol. 13, no. 2, pp. 265–271, 2010.
- [29] A. N. Yazici, M. Öztaş, and M. Bedir, “Effect of sample producing conditions on the thermoluminescence properties of ZnS thin films developed by spray pyrolysis method,” *Journal of Luminescence*, vol. 104, no. 1-2, pp. 115–122, 2003.
- [30] G. F. J. Garlick and A. F. Gibson, “The electron trap mechanism of luminescence in sulphide and silicate phosphors,” *Proceedings of the Physical Society*, vol. 60, no. 6, pp. 574–590, 1948.
- [31] S. Mahajna and Y. S. Horowitz, “The unified interaction model applied to the gamma ray induced supralinearity and sensitization of peak 5 in LiF:Mg,Ti (TLD-100),” *Journal of Physics D*, vol. 30, no. 18, pp. 2603–2619, 1997.
- [32] R. K. Gartia, S. J. Singh, T. S. C. Singh, and P. S. Mazumdar, “On the peak shape method for the determination of activation energy in TSL and TSC,” *Journal of Physics D*, vol. 26, no. 4, pp. 694–696, 1993.
- [33] L. R. Singh, R. S. Ningthoujam, and S. D. Singh, “Tuning of ultra-violet to green emission by choosing suitable excitation wavelength in ZnO: quantum dot, nanocrystals and bulk,” *Journal of Alloys and Compounds*, vol. 487, no. 1-2, pp. 466–471, 2009.
- [34] L. Robindro Singh, R. S. Ningthoujam, V. Sudarsan et al., “Luminescence study on Eu³⁺ doped Y₂O₃ nanoparticles: particle size, concentration and core-shell formation effects,” *Nanotechnology*, vol. 19, no. 5, Article ID 055201, 2008.
- [35] J. T. Randall and M. H. F. Wilkins, “The phosphorescence of Various solids,” *MHF*, vol. 184, no. 999, pp. 347–367, 1945.
- [36] R. G. Gartia, S. D. Singh, and P. S. Mazumdar, “On the glow curve shape and plateau test: the case of non-first-order kinetics,” *Physica Status Solidi*, vol. 138, no. 1, pp. 319–326, 1993.
- [37] M. S. Rasheedy, “On the general-order kinetics of the thermoluminescence glow peak,” *Journal of Physics*, vol. 5, no. 5, pp. 633–636, 1993.
- [38] R. Chen and Y. Kirsh, *Analysis of Thermally Stimulated Process*, Pergamon, Oxford, UK, 1981.
- [39] R. K. Gartia, S. J. Singh, and P. S. Mazumdar, “Determination of the activation energy of thermally stimulated luminescence peaks obeying general-order kinetics,” *Physica Status Solidi (A)*, vol. 114, no. 1, pp. 407–411, 1989.

Research Article

Catalysis of Methanol-Air Mixture Using Platinum Nanoparticles for Microscale Combustion

James R. Applegate,¹ Howard Pearlman,² and Smitesh D. Bakrania¹

¹Mechanical Engineering Department, Rowan University, 201 Mullica Hill Road, Glassboro, NJ 08028, USA

²Advanced Cooling Technologies, Inc., 1046 New Holland Avenue, Lancaster, PA 17601, USA

Correspondence should be addressed to Smitesh D. Bakrania, bakrania@rowan.edu

Received 24 February 2012; Accepted 10 April 2012

Academic Editor: Grégory Guisbiers

Copyright © 2012 James R. Applegate et al. This is an open access article distributed under the Creative Commons Attribution License, which permits unrestricted use, distribution, and reproduction in any medium, provided the original work is properly cited.

High surface area, active catalysts containing dispersed catalytic platinum nanoparticles ($d_p \sim 11.6$ nm) on a cordierite substrate were fabricated and characterized using TEM, XRD, and SEM. The catalyst activity was evaluated for methanol oxidation. Experimental results were obtained in a miniature-scale continuous flow reactor. Subsequent studies on the effect of catalyst loading and reactor flow parameters are reported. Repeat tests were performed to assess the stability of the catalyst and the extent of deactivation, if any, that occurred due to restructuring and sintering of the particles. SEM characterization studies performed on the postreaction catalysts following repeat tests at reasonably high operating temperatures ($\sim 500^\circ\text{C}$ corresponding to $\sim 0.3T_m$ for bulk platinum) showed evidence of sintering, yet the associated loss of surface area had minimal effect on the overall catalyst activity, as determined from bulk temperature measurements. The potential application of this work for improving catalytic devices including microscale reactors is also briefly discussed.

1. Introduction

Catalytic nanoparticles offer a substantial increase in surface area to volume ratio relative to their bulk counterparts and are important in a variety of energy-related applications and chemical processes. Platinum nanoparticles, for example, are embedded in the membranes of proton exchange membrane (PEM) fuel cells [1–3] and used in other systems including micropower generation [4, 5], automotive exhaust cleanup [6], and oxidation of volatile organic compounds (VOCs) [7]. Platinum nanoparticles are also being explored for use as radiosensitizers and new medical applications including targeted cancer treatments [8]. Regarding the use of nano-sized catalysts, their high surface energy is responsible for their high catalyst activity [9–12]. Increased catalyst activity offers the potential to reduce the amount of catalyst needed and reduce the operating temperature of the catalyst. In turn, knowing that the sintering temperature of nanoparticles is size dependent, sintering may be less of an issue for catalysts that operate at low temperature, yet special consideration must be given before such a conclusion can be drawn.

Typically, the sintering temperature is 0.2–0.3 of the melting temperature T_m for nanoparticles and 0.5–0.6 T_m for larger size particles [10, 13].

In this study, platinum nanoparticles are synthesized, dispersed on a cordierite substrate, tested in a continuous flow reactor, and characterized before and after use in the reactor. The results obtained in this fundamental study will also potentially be used to enhance the performance and sustain chemical reaction in a microscale combustor. In the past 10 years, much research has been performed on microscale combustion aimed at developing a small-scale generator that can replace batteries and rapidly be recharged by simply adding fuel [4, 4–17]. Since hydrocarbon fuels have an energy density of ~ 40 MJ/kg, a device having an overall system-level efficiency (chemical-to-electrical energy) in excess of 1% would have a comparable energy density to the state-of-the-art Li-ion batteries (~ 0.5 MJ/kg) [18, 19]. Sustaining combustion, however, in small-scale channels necessitates the use of catalysts or advanced heat recirculating strategies, otherwise conduction heat loss owed to the high surface area of the device exceeds the heat generation rate (\sim volume of

the device), and self-sustained operation cannot be achieved [20–23]. In this application, it is envisioned that nano-sized platinum catalysts can be used to sustain combustion at low operating temperatures, alleviating concerns with quenching.

Platinum nanoparticles have been previously demonstrated to self-ignite small alcohols, notably methanol-air, at room temperature and their reactivity is particle size dependent [24]. Nominal particle sizes, as large as 500 nm, have been tested with methanol-air premixtures and nearly complete oxidation was achieved without the need to preheat the catalyst [24, 25]. Additionally, size-dependent catalyst activity was also established, with increased activity observed for smaller nanoparticles [2, 25]. Beck and coworkers [11] have further shown that peak catalytic activity exists for 2 nm Pt nanoparticles during methane oxidation, explained by the competing effect of oxidized and metallic platinum species on catalyst activity [11]. Coalescence or sintering, however, becomes major concerns using nanoparticles since they are exposed to relatively high temperatures [10, 26, 27]. To improve stability and hinder degradation of catalyst, several strategies are pursued including alloying and composite structures for improved sintering resistance [27–29]. While such modified Pt catalysts show appreciable success, pure platinum nanoparticles remain attractive due to their high catalytic activity. Pt nanoparticles therefore warrant further investigation.

Several studies have reported synthesis techniques for Pt and other metal nanoparticles, yet systematic studies aimed at evaluating their initial and long-term catalyst activity in real-world systems are limited. This study therefore focussed on repeated catalytic cycling from room temperature ignition to stable catalysis temperatures and its influence on the Pt catalyst nanoparticles. The outcomes are directly applicable to development of devices that integrate microscale combustion as an energy source.

2. Experimental

2.1. Material Synthesis. Platinum nanoparticles were synthesized via a colloidal synthesis technique described by Bonet, et al. [30]. Briefly, 45 mL of ethylene glycol (EG, 99.8% purity, Sigma Aldrich) was heated up to 150°C in a reflux reactor. Hexachloroplatinic acid (500 mg) (H_2PtCl_6 , ACS reagent grade, Sigma Aldrich) was first dissolved in 5 mL of EG, at which time, the solution was then combined with the remaining heated EG. Then, 100 mg of polyvinylpyrrolidone (PVP, M.W. 29,000, Sigma Aldrich) was dissolved in 25 mL of EG and added to the heated solution with the aid of a syringe pump at a rate of 1.5 mL/min. The solution was maintained at 150°C for a period of one hour.

To clean the Pt nanoparticles in solution, a centrifuge tube containing 25 mL of methanol (99.8%, Sigma Aldrich) was added to 5 mL of the EG-PVP-Pt nanoparticle solution. The solution was agitated by hand for one minute and then centrifuged for 2 min at 3,000 rpm. After pouring off the supernatant, 25 mL of distilled water was substituted. The precipitate was agitated mechanically until a suspension of Pt nanoparticles was achieved. The resulting solution was then

centrifuged for another 2 min at 3,000 rpm. The supernatant was again discarded and replaced with 5 mL of distilled water. The precipitate was agitated mechanically and sonicated for one minute.

2.2. Substrate Preparation. The substrate for the nanoparticles was an extruded cordierite monolith (900 cells per square inch, Corning Inc.). The monolith had square channels with a width of 0.85 mm and wall thickness of 0.05 mm. The overall dimensions of the monoliths were 19 mm in length and the cross section contained 14 cells; the cross-sectional shape was octagonal and the maximum dimension across the cross-section was 13.5 mm.

The Pt nanoparticles, synthesized and suspended in solution, were deposited on the substrates using a draw-coat method. In particular, the Pt colloidal suspension was drawn through the open cells of the substrate, which was vertically mounted, using a 10 mL syringe connected directly to the substrate using a flexible clay coupling. The substrates were subsequently placed horizontally (with respect to the channel length) in an open petridish and dried at ambient conditions. Using this technique, a single dispersion of Pt nanoparticles was deposited on the bottom wall (base) of the channel. To coat adjacent walls, the substrate was rotated 90°, 180°, and 270° and a second, third, and fourth application of the Pt solution was applied, each done in succession and allowed to dry prior to application of each sequential coat. Molar conversion calculations indicated that approximately 10 mg of Pt particles were deposited per deposition step. Consequently, mass loading studies described later refer to the number of coatings during this step of substrate preparation.

2.3. Catalysis Experiments. The catalysts were tested in a continuous flow reactor fabricated with an aluminum housing as schematically shown in Figure 1. The reactor was 55.4 mm long and 20.3 mm in external diameter. Quartz wool was used as a filler in the gap between the reactor and the substrate so not to allow the gases to take a lower pressure drop bypass and flow through the honeycomb catalyst. The reactor inlet was designed to enable different catalyst materials to easily be inserted and removed. The inlet to the portion of the reactor containing the catalyst was 14.3 mm (KF-16 flange), which was tapered to a 1/4-20 NPT fitting through which the reactants were introduced.

The experiments were conducted by bubbling compressed air (99.9% purity, Air Gas) through a methanol reservoir (99.8% purity, Sigma Aldrich) at a metered flow rate of 200–1100 mL/min using a 30 mL glass bubbler. Calculated velocities through the substrate channels ranged from 2.3 cm/s to 12.8 cm/s. The methanol saturated air flowed through the Pt-coated substrate channels and the products exited from the reactor. A coated 0.5 mm diameter K-type thermocouple (KMTXL-020G, Omega) was cemented 7.6 mm from the exit of the center channel using high temperature cement (Omega) to monitor the bulk temperature of the catalyst substrate at the center. Temperature measurements were acquired at 10 Hz using a LabView DAQ system. External reactor temperatures were obtained

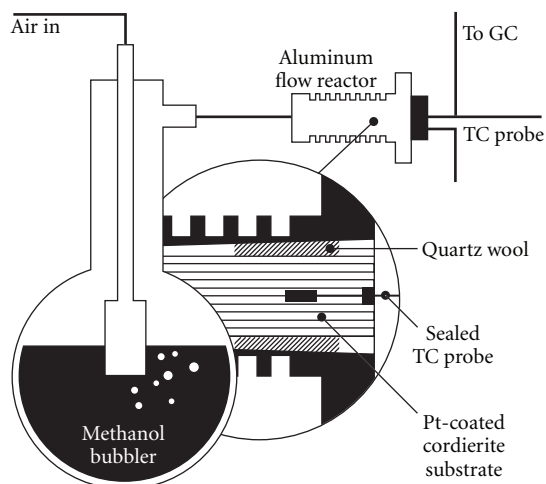


FIGURE 1: The experimental setup for Pt nanoparticle catalysis of methanol-air mixture. The inset provides details of the reactor and the catalyst substrate with an embedded sealed thermocouple.

by placing a thermocouple on the surface of the aluminum reactor.

2.4. Material Characterization. The nanoparticles were analyzed using an X-ray diffractometer (XRD, PANalytical 9430), a transmission electron microscope (TEM, Hitachi H-600ABi), and a scanning electron microscope (SEM, Zeiss Supra 50VP). XRD reflection scans were obtained by dispersing Pt nanoparticles on a glass slide and analyzed at a scan rate of $2^\circ/\text{min}$ using continuous scan mode and a $\text{CuK}\alpha$ source ($\lambda = 1.5405 \text{ \AA}$). Scherrer analysis was used to obtain average crystallite size. TEM samples were prepared by placing a drop-coat of the as-synthesized Pt colloidal solution on a 3 mm carbon-coated copper grid. A semiautomated program described elsewhere [31] was used to analyze particle size distributions. The deposited catalysts were analyzed on an SEM by removing fragments of pre- and post-catalysis substrate channel walls and placing them on a piece of carbon tape for imaging.

3. Results and Discussion

The measured temperature of the reactant gases at the inlet was 22°C . Based on methanol vapor pressure at the measured temperature, the saturated methanol-air mixture yields an effective equivalence ratio ϕ of 1.18. However, previous work by Ma and coworkers [25] with identical methanol delivery system indicates that the equivalence ratio is a weak function of the air inlet velocity. Considering the flow rates used for this study, a slightly fuel lean mixture ($\phi = 0.9\text{--}0.95$) of methanol-air was being introduced to the catalyst substrate.

Figure 2 displays the temperature history for a typical catalysis run lasting three hours. It should be noted that the temperature here indicates the bulk substrate temperature and not the Pt catalyst temperature; it is possible to have higher localized temperatures on the nanoparticles. The results presented in Figure 2 were generated using a substrate

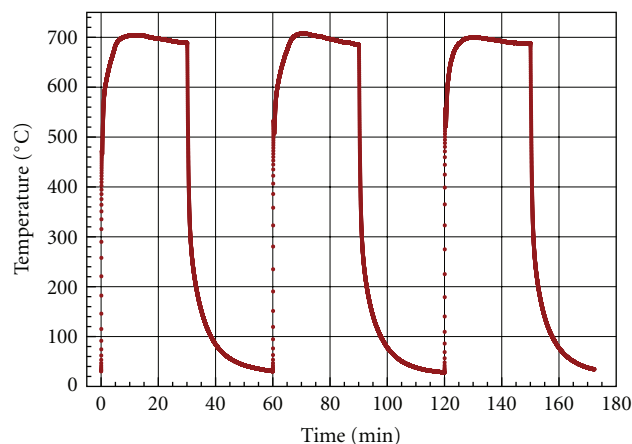


FIGURE 2: Temperature versus time graph of a substrate with four coatings of Pt nanoparticles demonstrating room temperature ignition and highly repeatable catalytic cycling. A constant flow rate of 600 mL/min was maintained.

with four Pt-coated sides and a nominal flow rate of 600 mL/min . The introduction of methanol-saturated air into the reactor produces a simultaneous rise in substrate temperature that peaks at 700°C . Figure 2, therefore, demonstrates room temperature ignition of methanol-air mixture due to the presence of Pt nanoparticles. When the flow of methanol-air mixture was halted, the substrate temperature approached room temperature within 30 minutes. After a total of an hour, a second catalysis cycle began. The temperature at the exterior of the reactor was approximately $200\text{--}300^\circ\text{C}$ lower than the substrate temperature suggesting notable heat loss to the ambient air through the reactor walls. The subsequent cycles in Figure 2 represent repeatable catalysis runs highlighting the self-ignition and nominally stable peak temperatures using Pt nanoparticles.

Identical results were obtained for all samples prepared using the same synthesis procedure; that is, the results presented in Figure 2 were reproducible with respect to ignition and stable high temperatures. It should be noted that even though the catalysis temperatures demonstrate a slight downward drift in temperatures, the overall behavior was repeatable. The catalysis cycling on a single catalysis sample was repeatable for over 30 cycles (with each cycle lasting 1 hr) without any sign of catalyst degradation. To explore the drift in stable temperature a prolonged single cycle experiment was conducted for six hours. Figure 3 shows how a stable temperature of around 450°C is obtained beyond the initial peak in exothermicity. The stable temperature is maintained for over three hours before instabilities in temperature are observed. The substrate selected for the stability study had two opposite sides of the channel coated with Pt nanoparticles. It is assumed that the prolonged exposure to the high temperature eventually yields microstructural and hence surface area changes that in turn influence the catalytic stable temperatures. The extended stability tests beyond the test presented were limited by the bubbler capacity. The catalyst substrates involved in the standard cycling tests were

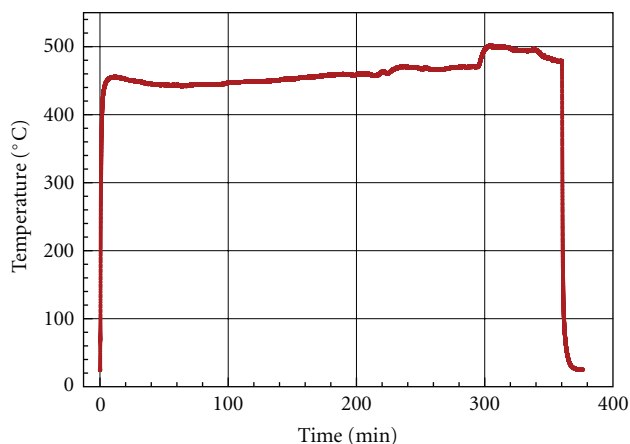


FIGURE 3: Temperature history of a substrate with two opposite channel walls coated with Pt nanoparticles experiencing catalysis reaction over prolonged period of time. A constant flow rate of 400 mL/min was maintained.

observed to be reusable as long as the period between two experimental runs did not exceed 48 hours. It is assumed that the catalyst material experiences poisoning or degradation when exposed to ambient air for prolonged period of time, as suggested by other researchers [24, 27, 32].

Extensive work has been performed in the field of nanoparticle catalysis on preventing degradation of these nanometer sized particles when exposed to relatively high temperatures. The degradation occurs due to the high temperature sintering or coalescence of metallic particles in the nanometer size range [9–11, 25, 27]. To counter this effect of high temperatures, researchers have explored supported Pt nanoparticles to prevent significant coalescence and therefore improve stability with some notable success [28, 29]. On the other hand, the highly repeatable nature of Pt nanoparticle catalysis behavior observed for the current study has been rarely reported. Material characterization was performed to assess the state of the catalyst materials before and after the catalysis runs.

3.1. Catalyst Material Characterization. The synthesized Pt nanoparticles when analyzed for crystallite sizes using XRD yielded an average of $d_{\text{XRD}} = 8.9$ nm. The same particles when observed under a TEM showed discrete unsintered spherical nanoparticles as depicted in Figure 4(a). It should be noted that the agglomerated nature of the particles seen in the TEM was potentially a result of the grid sample preparation which was analogous to the catalyst substrate preparation method. In other words, the agglomerated nature of the particles in the TEM images can be used as a representative sample of how the particles would look on the cordierite substrate. TEM image analysis of the nearly 200 particles produced an average particle size d_p of 11.6 nm. Figure 4(c) provides the output of the semiautomated image analysis showing a Pt nanoparticle distribution ranging from 7 to 20 nm. Both d_{XRD} and d_p were in good agreement considering the biases involved with the two approaches.

The as-deposited nanoparticle coatings were investigated using SEM imaging. Figures 5(a) and 5(b) display precatalysis SEM images of the substrate wall fragment. Due to the limited resolving power offered by the SEM, it is difficult to distinguish individual Pt nanoparticles near the 10 nm size range; however it is clear from the images that significant catalyst coverage was achieved. Porous Pt-aggregated films were observed on the cordierite substrate represented by micron sized smooth structures in the background. The aggregated films observed using SEM were similar in structure to the particles observed using the TEM in Figure 4(a). The films of particles were identified as elemental platinum using XEDS mapping.

In order to investigate the effect of catalysis and the resulting high combustion temperatures on Pt nanoparticles, fragments of a postcatalysis substrate sample were analyzed using the SEM. Figure 5(c) shows SEM images of a substrate coated on four sides that experienced a peak temperature of 500°C for two cycles. As observed from the sample images, the overall structure of Pt films seen in the precatalysis images is still present, however the structure is noticeably less porous and coalesced in nature. The same Pt nanoparticles that subsequently experienced 1120°C peak temperature yielded significantly coalesced spherical particles shown in Figure 5(d). XEDS analysis confirmed the bright spherical particles as the Pt nanoparticles in Figure 5(d). Image analysis of over 500 of the fully coalesced particles yielded an average particle size of 88 nm. Assuming the clusters of adjoined nanoparticles coalesced to yield the larger particles, estimated 600 particles constituted the porous films observed in Figures 5(a)–5(c).

Based on the catalyst structural observations, there is discernible catalyst degradation with respect to coalescence and thus the loss of surface area as a function of stable catalysis temperatures. However, from the catalysis temperature studies (Figure 2) which depict repeatable catalytic cycling of the material, the effect of coalescence is minimal when low-to-moderate operating temperatures (less than 1000°C) are maintained. In other words, the loss in Pt porosity and specific surface area, such as seen in Figure 5(c), demonstrated only minor influence on the reactivity of the catalyst for the conditions and materials tested. Catalyst stability similar to that observed here has been demonstrated before by Karim and coworkers [15] with Pt nanoparticles deposited on anodized alumina substrate. However, the higher operating stable temperatures with the repeatable cycling studies make these results unique and warrant further investigation of operational regimes for this system as required for potential applications in a portable power production device.

3.2. Flow Rate Dependence. To investigate the behavior of the catalyst substrate as a function of methanol-air mixture flow rate, a sample with four sides coated with Pt nanoparticles was tested. Figure 6 shows the dependence of the substrate temperature on volumetric flow rate of the reactants. As the compressed air flow rate was increased from 200 mL/min to 1000 mL/min in increments of 100 mL/min, the stable temperature of the substrate increased from 500°C to almost 900°C. These results are in agreement with similar studies

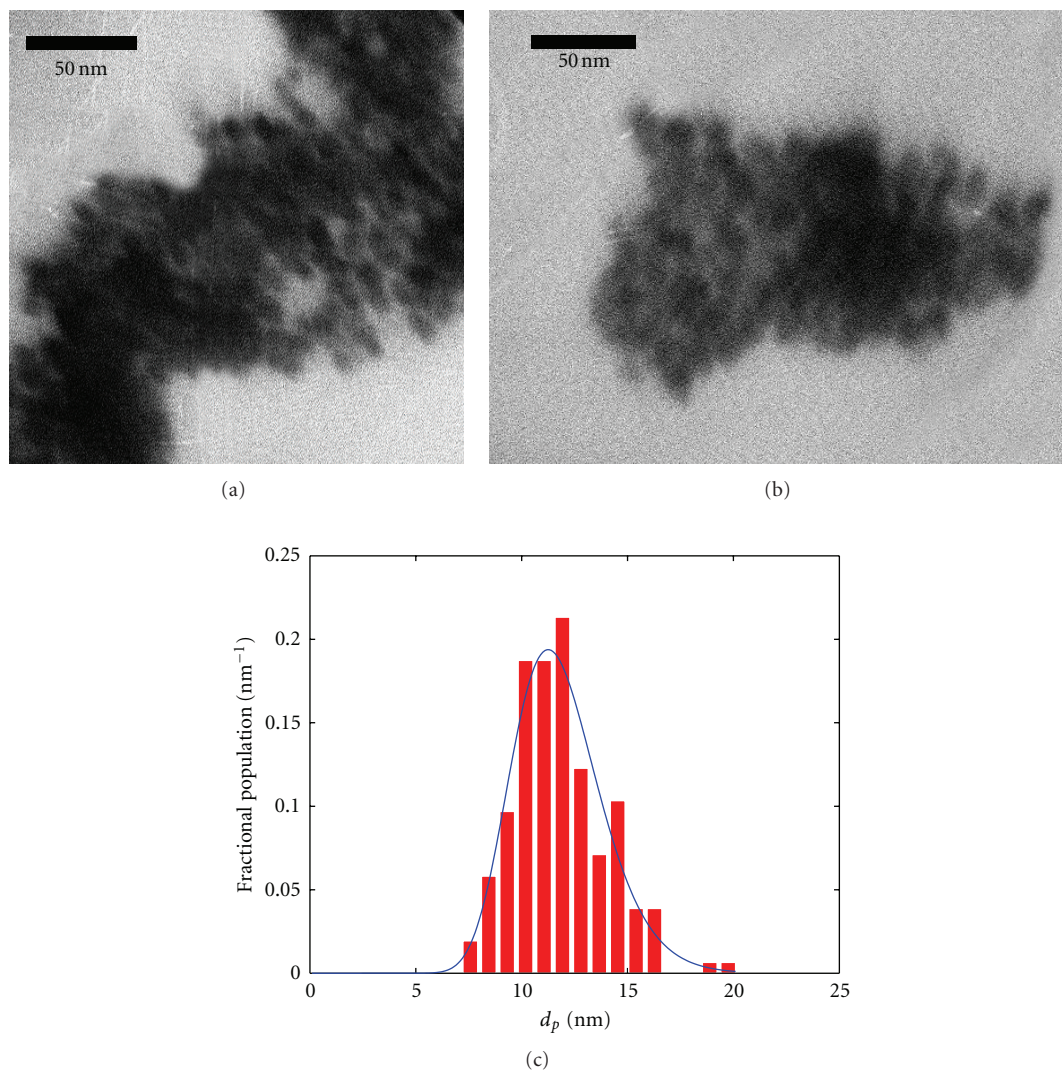


FIGURE 4: (a) and (b) TEM images of unreacted platinum nanoparticles. (c) Particle distribution plot of Pt nanoparticles analyzed using a semiautomated sizing approach based on TEM images.

that show higher fuel-air flow rate results in higher rate of heat release by the catalysis reaction manifested as an elevated stable temperature [15, 25]. The diminishing rate of corresponding increase in temperature can be attributed to the saturation of the active catalytic sites leading to incomplete conversion of reactants to products. For stable temperatures beyond 700°C, an initial peak in temperature appeared before plateauing to the stable temperature. Such behavior was documented by Ma and coworkers using Pt nanoparticles supported on quartz wool [25]. Beyond 800°C however, a rapid spike in temperature emerged that indicated substrate temperature reaching 1100–1150°C before returning to the shape of temperature history at lower flow rates. The rapid spikes were observed for compressed air flow rates of greater than 800 mL/min. While these samples with high flow rates showed repeatable catalytic cycling, their lifespan was dramatically reduced due to catalyst degradation. Samples tested at flow rates greater than

1000 mL/min were unable to demonstrate self-ignition for the second cycle, suggesting significant degradation of the catalyst substrate due to the high temperatures.

3.3. Mass Loading Dependence. A mass loading study was conducted by varying the number of coatings within the channels of the cordierite substrate. Since a single coating was applied to each wall of the square channel, mass loading study involved up to four Pt-coated sides. The mass loading study was carried out at the minimum compressed air flow rate of 200 mL/min to maintain low stable temperatures. With the combination of low flow rate and the low mass loading, the single Pt-coated substrate did not ignite at room temperature. Facilitating room temperature ignition required a minimum of two coatings. As seen in Figure 7, the increase in number of Pt-coated sides is accompanied by corresponding increase in stable temperature. Again, the heat release is a function of fuel conversion rate which

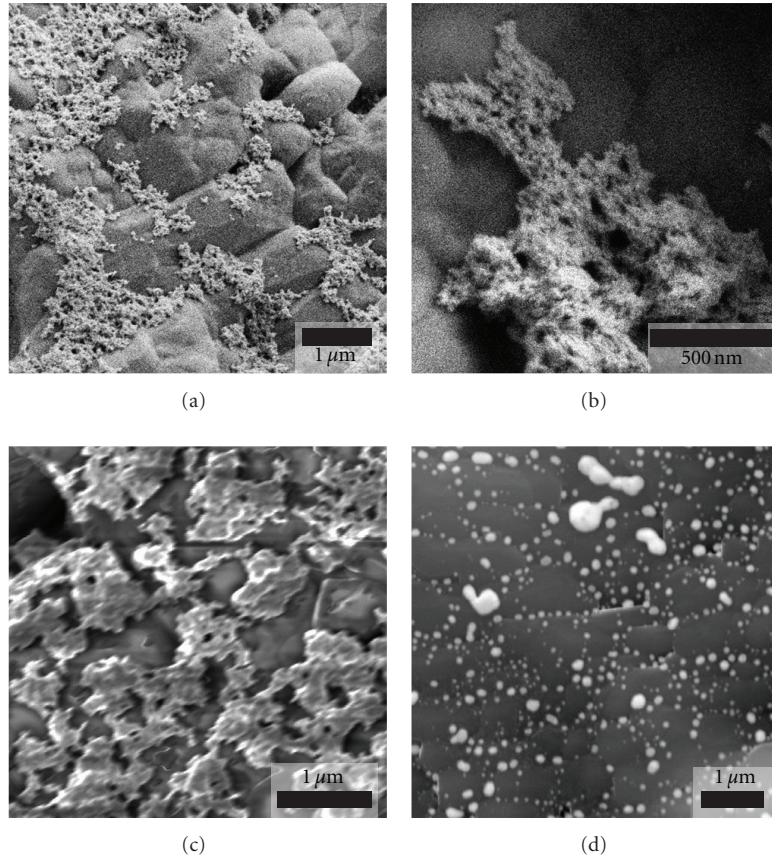


FIGURE 5: (a) and (b) are SEM images of Pt particles deposited on the substrate walls prior to catalysis (precatalysis). (c) Postcatalysis SEM image of Pt nanoparticles with moderate sintering with peak temperatures of 500°C after two cycles (1 hr cycle time). (d) Coalesced spheres of metallic Pt after experiencing peak temperatures of 1120°C over 25 cycles.

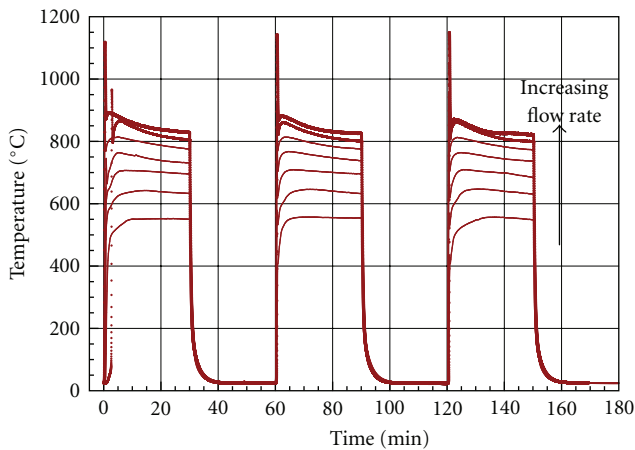


FIGURE 6: Temperature histories for air flow rates ranging from 200 to 1000 mL/min with 100 mL/min increments. Catalyst substrates with four Pt-coated were sides used in this study.

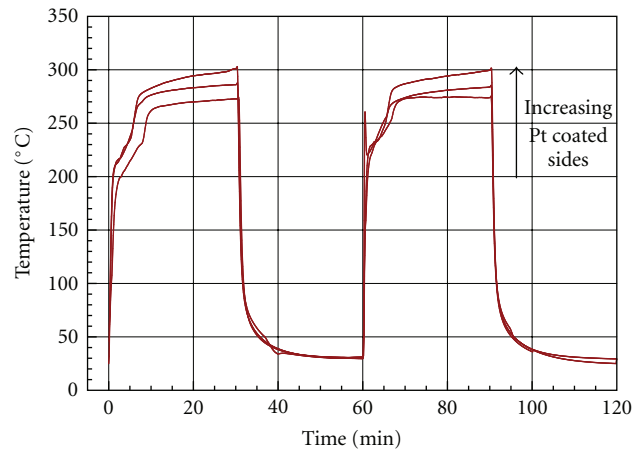


FIGURE 7: Temperature histories for substrates with two, three, and four Pt-coated sides with air flow rate at 200 mL/min.

is dependent on the available active catalytic sites. As the number of coatings increased, the active sites increased driving higher rate of heat released.

3.4. Device Performance Implications. For catalytic micro-scale combustion applications, typically long residence time channel reactors are employed, such as the swiss-roll type reactor [4, 22]. Considering the short catalytic substrate

sample (19 mm) and the high reactant flow rates (200–1000 mL/min) used here, it is expected that only fractional conversion of the fuel and oxidizer mixture is achieved. Within a device however, the excess methanol fuel can be combusted by extending the catalytic channel to allow longer residence times for the fuel to react. In addition, due to the catalytic stability offered by the cycling approach used here, the peak temperatures of the overall device can be easily controlled by tuning the catalytic cycling to match the thermal requirements of the device. Alternatively, the mass loading study indicated that substrates coated with a single layer of Pt nanoparticles failed to ignite potentially as a result of the low heat generation rate compared to the heat loss to the surroundings. Therefore, strategies used to diminish heat loss in microreactors can significantly reduce the Pt mass loadings required to sustain combustion. Furthermore, the size-dependent catalytic reactivity of Pt nanoparticles can provide an additional control parameter for targeted device operation conditions and is currently being explored [11, 25].

4. Conclusion

Platinum nanoparticles have been previously identified as strong candidates for sustaining microscale combustion and have been used for many years in automotive catalytic converters for exhaust gas cleanup. However, their vulnerability to sintering at high combustion temperatures results in a decrease in the catalyst activity and limits the catalyst lifetime. Therefore, the demonstration of repeatable Pt nanoparticle catalysis over numerous cycles in this work is an important step towards achieving controlled catalytic combustion. The cycling studies showed that nanoparticle sintering can be dramatically reduced to cause minimal or negligible change in the activity of the catalyst particles. The flow rate and mass loading studies provided additional insights into operational regimes of a potential microreactor. As next steps, quantitative investigation of the product gases as a function of cycling periods, particle size, and catalyst distribution can provide data necessary to model and design functional efficient microcombustor systems.

Acknowledgments

The authors would like to acknowledge the support of the National Science Foundation CBET Grant 0755740. The authors would like to thank Rowan University's Materials Research Laboratory for allowing the use of instrumentation.

References

- [1] S. Litster and G. McLean, "PEM fuel cell electrodes," *Journal of Power Sources*, vol. 130, no. 1-2, pp. 61–76, 2004.
- [2] T. Frelink, W. Visscher, and J. A. R. van Veen, "Particle size effect of carbon-supported platinum catalysts for the electrooxidation of methanol," *Journal of Electroanalytical Chemistry*, vol. 382, no. 1-2, pp. 65–72, 1995.
- [3] M. C. Orilall, F. Matsumoto, Q. Zhou et al., "One-pot synthesis of platinum-based nanoparticles incorporated into mesoporous niobium oxide-carbon composites for fuel cell electrodes," *Journal of the American Chemical Society*, vol. 131, no. 26, pp. 9389–9395, 2009.
- [4] Y. Ju and K. Maruta, "Microscale combustion: technology development and fundamental research," *Progress in Energy and Combustion Science*, vol. 37, no. 6, pp. 669–715, 2011.
- [5] A. Mitsos, B. Chachuat, and P. I. Barton, "What is the design objective for portable power generation: efficiency or energy density?" *Journal of Power Sources*, vol. 164, no. 2, pp. 678–687, 2007.
- [6] W. C. Pfefferle and L. D. Pfefferle, "Catalytically stabilized combustion," *Progress in Energy and Combustion Science*, vol. 12, no. 1, pp. 25–41, 1986.
- [7] J. Tsou, L. Pinard, P. Magnoux, J. L. Figueiredo, and M. Guisnet, "Catalytic oxidation of volatile organic compounds (VOCs) Oxidation of o-xylene over Pt/HBEA catalysts," *Applied Catalysis B*, vol. 46, no. 2, pp. 371–379, 2003.
- [8] E. Porcel, S. Liehn, H. Remita et al., "Platinum nanoparticles: a promising material for future cancer therapy?" *Nanotechnology*, vol. 21, no. 8, Article ID 085103, 2010.
- [9] M. Xiaofei, L. Liu, N. Aronhime, and M. R. Zachariah, "Ignition catalyzed by unsupported metal nanoparticles," *Energy & Fuels*, vol. 25, no. 9, pp. 3925–3933, 2011.
- [10] M. A. Asoro, D. Kovar, Y. Shao-Horn, L. F. Allard, and P. J. Ferreira, "Coalescence and sintering of Pt nanoparticles: in situ observation by aberration-corrected HAADF STEM," *Nanotechnology*, vol. 21, no. 2, p. 025701, 2010.
- [11] I. E. Beck, V. I. Bukhtiyarov, I. Y. Pakharukov, V. I. Zaikovskiy, V. V. Kriventsov, and V. N. Parmon, "Platinum nanoparticles on Al₂O₃: correlation between the particle size and activity in total methane oxidation," *Journal of Catalysis*, vol. 268, no. 1, pp. 60–67, 2009.
- [12] S. Mostafa, F. Behafarid, J. R. Croy et al., "Shape-dependent catalytic properties of Pt nanoparticles," *Journal of the American Chemical Society*, vol. 132, no. 44, pp. 15714–15719, 2010.
- [13] G. Guisbiers, G. Abudukelimu, and D. Hourlier, "Size-dependent catalytic and melting properties of platinum-palladium nanoparticles," *Nanoscale Research Letters*, vol. 6, no. 1, p. 396, 2011.
- [14] M. Broussely and G. Archdale, "Li-ion batteries and portable power source prospects for the next 5–10 years," *Journal of Power Sources*, vol. 136, no. 1, pp. 386–394, 2004.
- [15] A. M. Karim, J. A. Federici, and D. G. Vlachos, "Portable power production from methanol in an integrated thermoelectric/microreactor system," *Journal of Power Sources*, vol. 179, no. 1, pp. 113–120, 2008.
- [16] J. A. Federici, D. G. Norton, T. Brüggemann, K. W. Voit, E. D. Wetzel, and D. G. Vlachos, "Catalytic microcombustors with integrated thermoelectric elements for portable power production," *Journal of Power Sources*, vol. 161, no. 2, pp. 1469–1478, 2006.
- [17] J. T. Wiswall, M. S. Wooldridge, and H. G. Im, "An experimental study of the effects of platinum on methane/air and propane/air mixtures in a stagnation point flow reactor," *Journal of Heat Transfer*, vol. 131, no. 11, pp. 1–8, 2009.
- [18] J. D. Holladay, E. O. Jones, M. Phelps, and J. Hu, "Microfuel processor for use in a miniature power supply," *Journal of Power Sources*, vol. 108, no. 1-2, pp. 21–27, 2002.
- [19] A. C. Fernandez-Pello, "Micropower generation using combustion: Issues and approaches," *Proceedings of the Combustion Institute*, vol. 29, no. 1, pp. 883–898, 2002.
- [20] J. A. Federici and D. G. Vlachos, "A computational fluid dynamics study of propane/air microflame stability in a heat

- recirculation reactor,” *Combustion and Flame*, vol. 153, no. 1-2, pp. 258–269, 2008.
- [21] K. Bijjula and D. Vlachos, “Catalytic ignition and autothermal combustion of JP-8 and its surrogates over a Pt/ γ -Al₂O₃ catalyst,” *Proceedings of the Combustion Institute*, vol. 33, pp. 1801–1807, 2011.
- [22] J. Ahn, C. Eastwood, L. Sitzki, and P. D. Ronney, “Gas-phase and catalytic combustion in heat-recirculating burners,” in *Proceedings of the 30th International Symposium on Combustion*, vol. 30, pp. 2463–2472, July 2004.
- [23] M. J. Lee and N. I. Kim, “Experiment on the effect of Pt-catalyst on the characteristics of a small heat-regenerative CH₄-air premixed combustor,” *Applied Energy*, vol. 87, no. 11, pp. 3409–3416, 2010.
- [24] Z. Hu, V. Boiadjev, and T. Thundat, “Nanocatalytic spontaneous ignition and self-supporting room-temperature combustion,” *Energy and Fuels*, vol. 19, no. 3, pp. 855–858, 2005.
- [25] Y. Ma, C. Ricciuti, T. Miller, J. Kadlowec, and H. Pearlman, “Enhanced catalytic combustion using sub-micrometer and nano-size platinum particles,” *Energy and Fuels*, vol. 22, no. 6, pp. 3695–3700, 2008.
- [26] K. Dick, T. Dhanasekaran, Z. Zhang, and D. Meisel, “Size-dependent melting of silica-encapsulated gold nanoparticles,” *Journal of the American Chemical Society*, vol. 124, no. 10, pp. 2312–2317, 2002.
- [27] P. Forzatti and L. Lietti, “Catalyst deactivation,” *Catalysis Today*, vol. 52, no. 2-3, pp. 165–181, 1999.
- [28] T. Sanders, P. Papas, and G. Veser, “Supported nanocomposite catalysts for high-temperature partial oxidation of methane,” *Chemical Engineering Journal*, vol. 142, no. 1, pp. 122–132, 2008.
- [29] T. Mitsui, T. Matsui, H. Miyata et al., “Formation of layered Al₂O₃ and its inhibitory effect on the sintering of supported platinum particles,” *Applied Catalysis A*, vol. 348, no. 1, pp. 121–128, 2008.
- [30] F. Bonet, V. Delmas, S. Grugeon, R. H. Urbina, and P.-Y. Silvert, “Synthesis of monodisperse Au, Pt, Pd, Ru and Ir nanoparticles in glycol,” *Acta Metallurgica*, vol. 11, no. 8, pp. 1277–1284, 2000.
- [31] S. D. Bakrania, T. A. Miller, C. Perez, and M. S. Wooldridge, “Combustion of multiphase reactants for the synthesis of nanocomposite materials,” *Combustion and Flame*, vol. 148, no. 1-2, pp. 76–87, 2007.
- [32] J. Li, J. Zhang, Z. Lei, and B. Chen, “Pd-Co coating onto cordierite monoliths as structured catalysts for methane catalytic combustion,” *Energy and Fuels*, vol. 26, no. 1, pp. 443–450, 2012.

Research Article

Effect of Size, Shape, and Surface Modification on Cytotoxicity of Gold Nanoparticles to Human HEP-2 and Canine MDCK Cells

Yinan Zhang,¹ Dan Xu,^{2,3} Wenqin Li,^{1,2} Jun Yu,² and Yu Chen¹

¹Department of Physics, University of Strathclyde, John Anderson Building, 107 Rottenrow, Glasgow G4 0NG, UK

²Strathclyde Institute of Pharmacy and Biomedical Sciences, University of Strathclyde, Glasgow G4 0RE, UK

³Institute of Immunopathology, School of Life Science & Technology, Xi'an Jiaotong University, Shanxi 710061, China

Correspondence should be addressed to Yu Chen, y.chen@strath.ac.uk

Received 25 March 2012; Revised 20 April 2012; Accepted 23 April 2012

Academic Editor: Grégory Guisbiers

Copyright © 2012 Yinan Zhang et al. This is an open access article distributed under the Creative Commons Attribution License, which permits unrestricted use, distribution, and reproduction in any medium, provided the original work is properly cited.

There have been increasing interests in applying gold nanoparticles in biological research, drug delivery, and therapy. As the interaction of gold nanoparticles with cells relies on properties of nanoparticles, the cytotoxicity is complex and still under debating. In this work, we investigate the cytotoxicity of gold nanoparticles of different encapsulations, surface charge states, sizes and shapes to both human HEP-2 and canine MDCK cells. We found that cetyltrimethylammonium-bromide- (CTAB-) encapsulated gold nanorods (GNRs) were relatively higher cytotoxic than GNRs undergone further polymer coating and citrate stabilized gold nanospheres (GNSs). The toxicity of CTAB-encapsulated GNRs was mainly caused by CTAB on GNRs' surface but not free CTAB in the solution. No obvious difference was found among GNRs of different aspect ratios. Time-lapse study revealed that cell death caused by GNRs occurred predominately within one hour through apoptosis, whereas cell death by free CTAB was in a time- and dose-dependent manner. Both positively and negatively surface-charged polymer-coated GNRs (PSS-GNRs and PAH-PSS-GNRs) showed similar levels of cytotoxic, suggesting the significance of surface functionality rather than surface charge in this case.

1. Introduction

Gold nanoparticles have been demonstrated to have extraordinary potential in biomedical applications including biological imaging, sensing, thermal therapy, drug and gene delivery [1–11]. Compared to gold nanospheres (GNSs), gold nanorods (GNRs) are especially beneficial in biological imaging and sensing due to their unique optical properties [12–14]. Cytotoxicity of gold nanoparticles, as the premise of any further biological study, is a key issue to be investigated. There have been intensive studies from different point of views focusing on the cytotoxicity of gold nanoparticles, which are complex and still under debating. Compared to GNSs, GNRs have been found to be toxic to cell culture, but almost nontoxic after being coated with polymer molecules [10, 15–27]. This is because the cytotoxicity depends on the particle size, shape, surface charge and modification, agglomeration, as well as the mechanisms of cellular uptake and toxicity response [28–30]. Despite difference in particle

shape, one primary concerns about GNRs in biological research is cetyltrimethylammonium bromide (CTAB), the surfactant which is essential for nanorods growth in popularly used seed-growth GNRs synthesis method, but toxic to cell lines [26, 31–33]. CTAB is important in controlling the particle size and shape to achieve designed localized surface plasmon resonance bands for spectroscopic and microscopic applications in biological research [34–36]. As removal of CTAB will cause instability of GNRs, polymers, such as poly(acrylic acid) (PAA), poly(diallyldimethylammonium chloride)-poly(4-styrenesulfonic acid) (PDADMAC-PSS), and poly(ethylene glycol) (PEG), have been introduced to functionalize the GNRs surface [31, 32, 37, 38].

Optical properties of gold nanoparticles critically depend on their sizes, shapes, and surface conditions. On the other hand, incubation time and particle concentration are key parameters in controlling the internalization process of nanoparticles into cells, as well as cell normal functions. In this paper, we intended to investigate the cytotoxicity

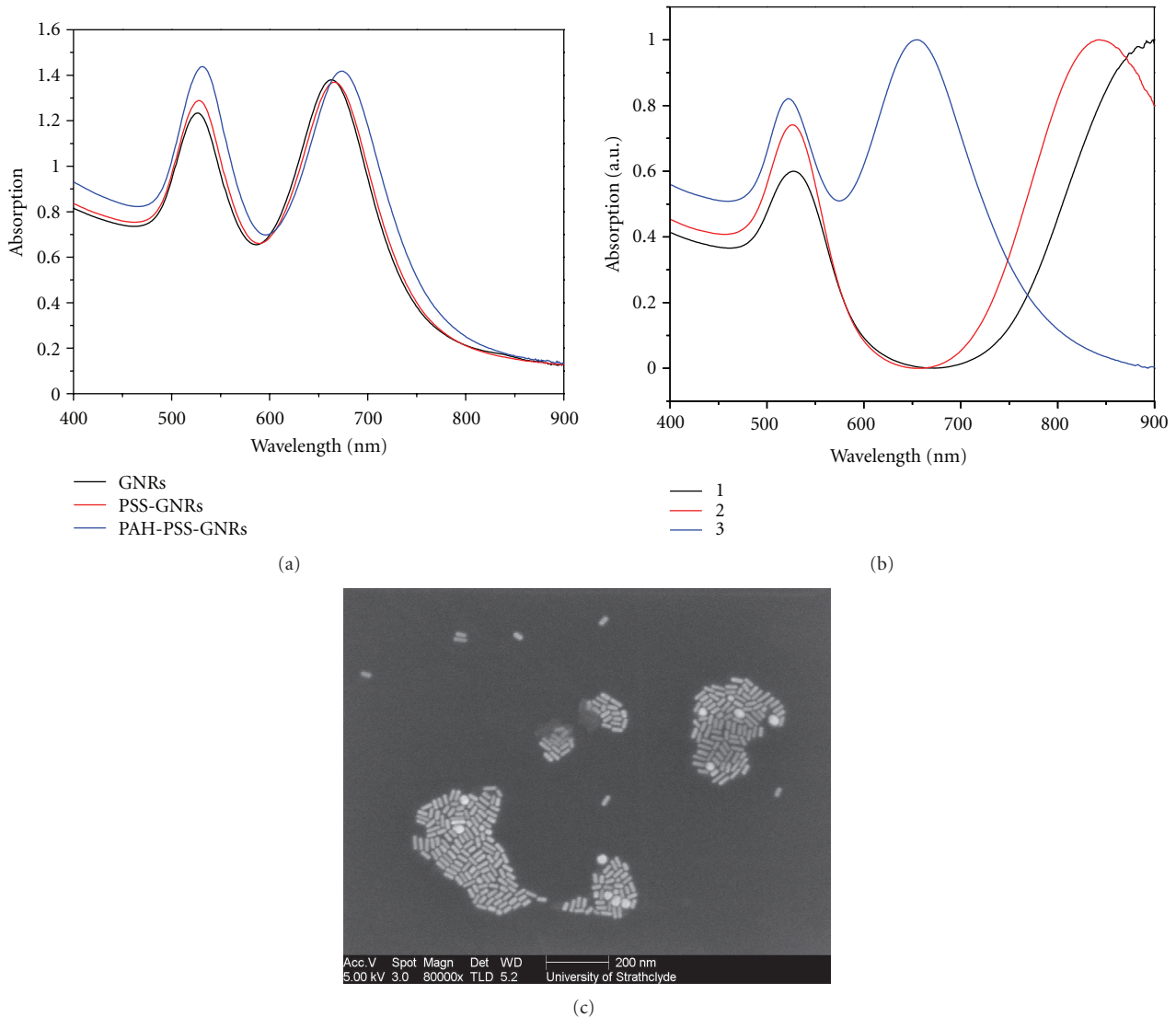


FIGURE 1: (a) Absorption spectrum of GNRs and polymer-coated GNRs; (b) absorption spectrum of GNR-1, GNR-2, and GNR-3; (c) scanning electron microscopic image of GNR-1.

of gold nanoparticles in a systematic manner. GNRs were synthesized via the same procedure but with 4 different aspect ratios, GNSs, and polymer- (polystyrenesulfonate (PSS) and poly(allylamine) hydrochloride(PAH)) coated GNRs have been applied to two cell lines at different exposure time and particle dosages. GNRs of aspect ratio of 3 are approximately 40 nm long, which had excellent potential in biological imaging and sensing applications [39–41]. PSS and PAH have been used in multilayer membrane for long-term graft transplantation [42]. The layer-by-layer polyelectrolyte coating using PSS/PAH not only changes the surface condition of gold particles inducing changes in particle optical properties but also plays important roles in functionalizing new types of bioimaging tools, such as SPASER (surface plasmon amplification by stimulated emission of radiation), a surface-plasmon-based nanolaser providing localized intensive excitation [43–45]. The dosage levels and

incubation time selected for 3-(4,5-Dimethylthiazol-2-yl)-2,5-diphenyltetrazolium bromide MTT assay analysis was based on the previous imaging study [39, 41]. In addition to reveal the intrinsic cytotoxicity of gold nanoparticles, this study also provide insights on managing the cytotoxicity of gold nanoparticles in further biological research.

2. Material and Method

GNRs were synthesized by the seeded growth method [46], and GNSs were prepared by Turkevich method [47]. Further coating on GNRs was proceeded via electrostatic layer-by-layer growth using PSS and PAH. Single layer of PSS and double layers of PSS/PAH coating were carried out following a process described by Omura et al. (denoted as PSS-GNRs and PAH-PSS-GNRs) [45]. Successful coating is proven by

the shift of surface plasmon bands as shown in Figure 1(a). All particles were centrifuged to remove the excess CTAB/polymers and redispersed in deionised water with a final concentration around 10^{-10} M.

MDCK (ATCC CCL-34) and HEP-2 (ATCC CCL-23) cell lines were obtained from American Type Culture Collection. Cell culture medium was high-glucose (4.5 g/L) DMEM containing fetal calf serum (10%), L-glutamine (2.9 mg/mL), antibiotic-antimycotic solution (GIBCO). Cells were routinely cultured at 37°C under 5% CO_2 .

MTT assay was carried out in the following procedure. Briefly, both MDCK and HEP-2 cells were seeded at 1×10^4 cells per well in 96-well plates. After 24 h of incubation (37°C , 5% CO_2), a series of concentrations of GNRs (in water) was added in each well. The cells were further incubated to appropriate time intervals. At appropriate time intervals, $20 \mu\text{L}$ of MTT (3-(4,5-Dimethylthiazol-2-yl)-2,5-diphenyltetrazolium bromide, 4 mg/mL in PBS) was added to each well and incubated for up to 4 h at 37°C , 5% CO_2 . After careful removal of the media, $150 \mu\text{L}$ of DMSO was added into each well to solubilise the purple crystals. After being incubated at 37°C for 10 min, $\text{OD}_{540\text{nm}}$ was measured with a plate reader (LabSystems Genesis).

For fluorescent microscopic observation of apoptosis, cells were seeded onto cover slides 1×10^5 cells per slide in 24-well plates and cultured for 24 h at 37°C under 5% CO_2 . After exposure to GNRs for 5 h, the spent medium was discarded and cells were incubated for 1 h in fresh media containing sulforhodaminyl-L-valylalanylasparyl fluoromethyl ketone (SR-VA-DFMK) according to manufacturer's instructions (Immunochemistry Technologies). Cells were washed with PBS and fixed with 3.7% paraformaldehyde (in PBS) for 10 min at 37°C . The coverslips were mounted onto microscope slides with Prolong Gold antifade reagent containing 4',6'-diamidino-2-phenylindole (DAPI) (Invitrogen). Images were captured using a confocal microscope LSM 510 (Carl Zeiss).

3. Results and Discussion

Figure 1(a) displays absorption spectra taken from GNRs, PSS-GNRs, and PAH-PSS-GNRs. Absorption of three GRNs of different aspect ratios, 5, 4.5, and 3, are shown in Figure 1(b), where a typical SEM image of GNR-1 is displayed in Figure 1(c). Figure 2 shows the MTT assay results on HEP-2 cells incubated for 1 h with different types of gold nanoparticles. The dosage is calculated as the volume percentage of cell medium, for gold particles, concentration of 1% is approximately 10^{-12} M. Contribution in absorption from gold nanoparticles in MTT assay has been subtracted taking into account the absorption coefficient of different gold nanoparticles at 540 nm and number of nanoparticles in cell culture.

Based on results displayed in Figure 2, GNRs have shown much higher toxicity compared to GNSs. The (Citrate stabilized) GNSs showed no significant cytotoxicity under all dosage levels used, while for CTAB-capped GNRs, high cytotoxicity was found especially at large dosages. It cannot

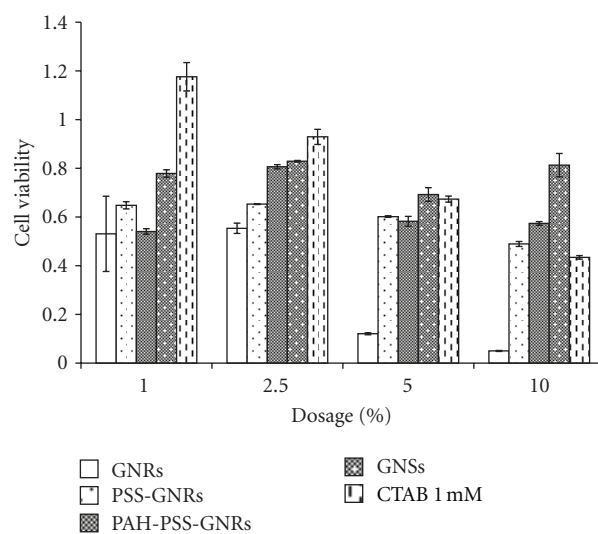


FIGURE 2: Cytotoxicity of different types of gold particles and free CTAB based on MTT assay outlined above.

be simply explained as shape effect, as GNSs and GNRs have different surfactants and surface charge states. To elucidate the effects from capped CTAB, polymer-coated GNRs have been compared with CTAB capped GNRs. Figure 2 shows that both PSS-GNRs and PAH-PSS-GNRs are less toxic than GNRs, which becomes more apparent at higher dosages.

The above observation is in line with the previous finding that CTAB is the major reason for cytotoxicity [31, 32]. Nevertheless, the cause of the cytotoxicity, either the free CTAB in solution or surfactant ones, is still debatable. To bring insights into this issue, toxicity of free CTAB to Hep2 was examined. Figure 2 shows that free CTAB solution is less toxic than CTAB capped GNRs. We thus propose that the toxicity of GNRs is mainly related to the surface CTAB on GNRs rather than free form in the solution based on three facts. Firstly, as polymer-coated GNRs were centrifuged under the same condition as GNRs, concentration of free CTAB in the solution can be considered at a similar level. Therefore, the different cytotoxic properties should be originated from different surface conditions. Secondly, 1 mM of CTAB used here is 1% of the concentration used for GNRs synthesis and considered to be the upper limit of remaining CTAB in GNRs solution after centrifuge. This is because GNRs solution was diluted roughly 10 times after each centrifugation and concentration of free CTAB is below 1/100 of the original concentration after two times of centrifugations. Figure 2 shows that 1 mM CTAB has only moderate cytotoxicity, much lower than GNRs, implying that toxicity of GNRs is not mainly due to free CTAB. This result is consistent with that of the time-lapse toxicity shown in Figure 3(b), as cell survival of samples treated with 1 mM CTAB solution from 1% to 10% of medium volume (actual concentration 1×10^{-5} M to 1×10^{-4} M) decreased from more than 90% to around 60%. At last, time-lapse toxicity study reveals different cytotoxic behaviour between GRNs and free

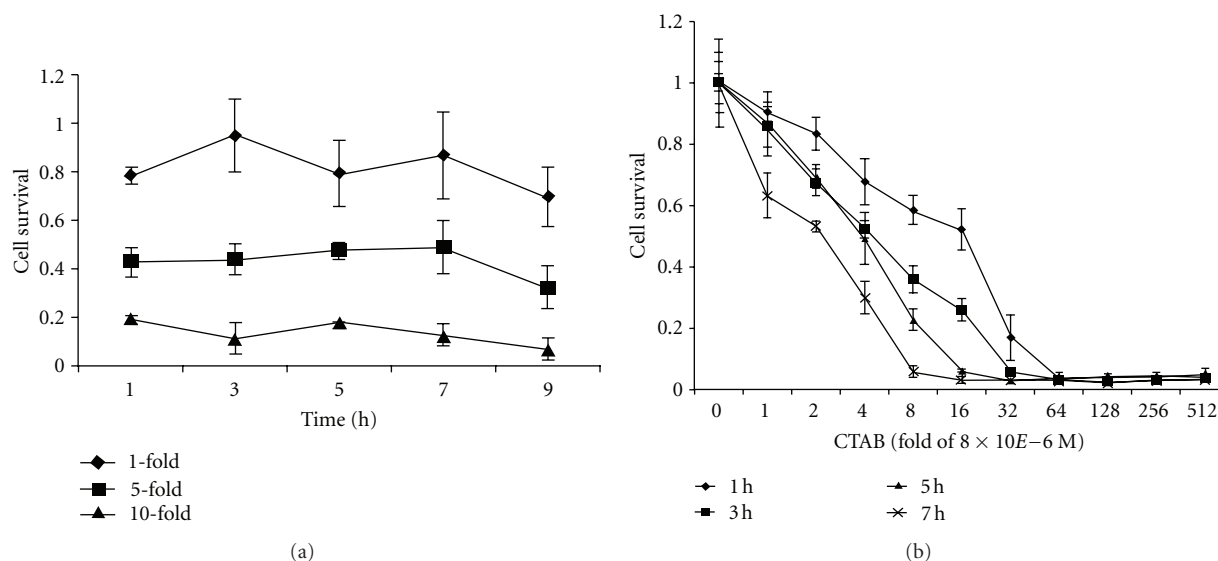


FIGURE 3: Time lapse cytotoxicity of GNRs (a) and free CTAB (b) to HEP-2, 1 h, 3 h, 5 h, and 7 h indicate different incubation times, and 1-fold of 8×10^{-6} M CTAB is comparable to the 1% concentration in the form of volume concentration in Figure 2.

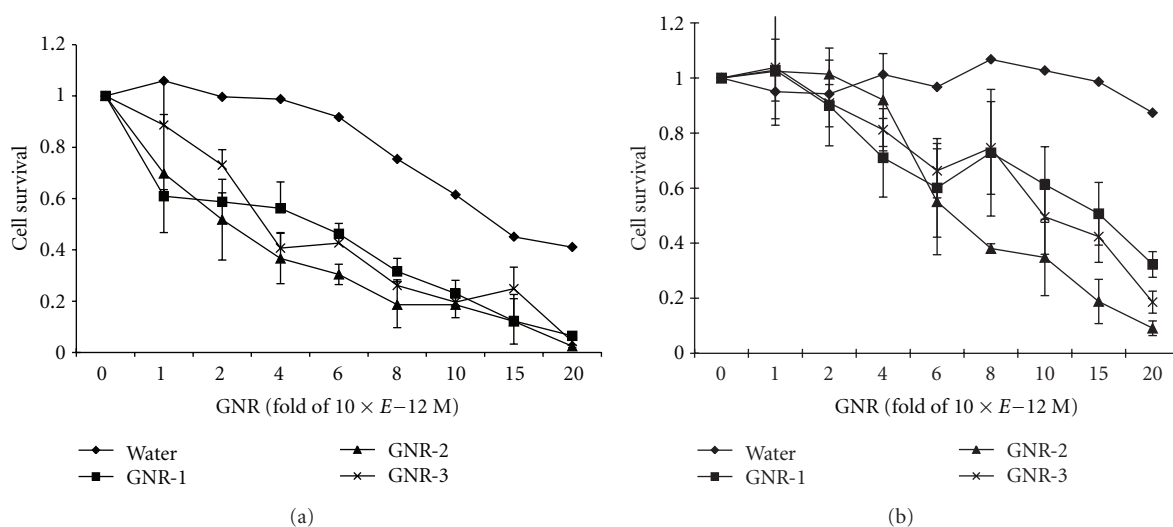


FIGURE 4: MTT assay for HEP-2 (a) and MDCK (b) cells.

CTAB. Figure 3(a) shows that cell survival value reaches a stable number in the first hour, and further incubation only results in slight reduction in cell survival up to 9 hrs. While by incubating a series of concentrations of free CTAB solution to the cells for 1, 3, 5, and 7 hours, a dependence on both concentration and incubation time was observed in Figure 3(b).

Additional polymer coating of GNRs not only prevents direct interaction of CTAB with cell membrane but also modifies the surface charge state. Previous work suggests that cationic gold particles are moderately toxic, whereas anionic ones are relatively nontoxic [25, 48]. This phenomenon can be explained as the cell membrane is negatively charged in which case cationic particles are prone to adsorb. Furthermore, it has also been reported that cationic particles are more likely to follow a direct diffusion pathway while

anionic GNPs are internalized by endocytosis [25, 49]. In this work, negatively charged PSS-GNRs perform less toxic on all dosages, and no significant difference was observed between PSS-GNRs and positively charged PAH-PSS-GNRs. Considering both PAH-PSS-GNRs and GNRs have positive surface charge, the discrepancy in cytotoxicity between CTAB capped and polymer-coated GNRs should be related to the surface CTAB on GNRs. With GNRs sizing around 50 nm, surface modification and interaction with membrane functional parts may play a more important role than surface charge property.

To study the influence of size and shape on the cytotoxicity, GNRs of different aspect ratios were examined. It is found that all three types of GNRs exhibited cytotoxicity to both MDCK and HEP-2 cells in a dose-dependent manner as shown in Figures 4(a) and 4(b), but no significant

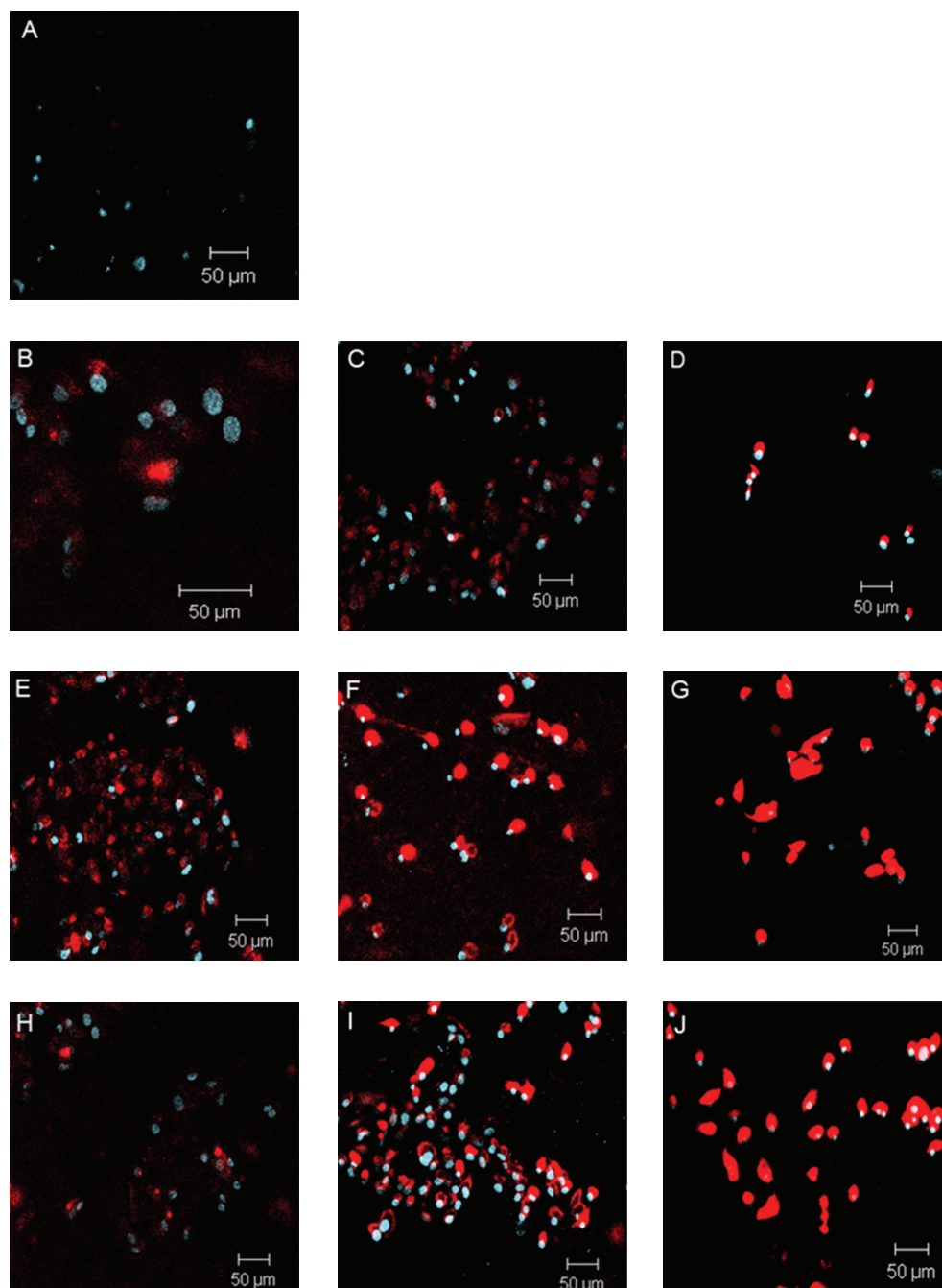


FIGURE 5: Confocal microscopy on HEp-2 cells for activated caspases (in red) and nuclei (in blue). All images were taken 5 h after GNR treatment. (A) negative control (untreated cells); (B), (C), and (D), respectively, were cells treated with GNR-1 at the concentration of 1-, 5- and 10-fold of 10^{-12} M of stock solution. Similarly, (E), (F), and (G) were cells treated with GNR-2, and (H), (I), (J) were cells treated with GNR-3, respectively, at the concentrations of 1-, 5-, and 10-fold of the 10^{-12} M solutions.

difference were found between GNRs. The viability of the cells decreased as the concentrations of GNRs increased. However, the two cell lines had significant difference in susceptibility to GNR-1 and GNR-2 at 2-fold of 10^{-12} M (Student *t*-test, $P < 0.1$ in both cases): viability of HEp-2 cells dropped below 60%, whereas MDCK cells remained above 90% in both cases. Based on gold particle concentration and cell counts, we estimated that at 10^{-12} M GNRs

concentration, the particle cell ratio is approximately 300 GNRs per cell, which reduced cell viability by $\sim 20\%$ in all cases and may be used as an upper limit reference for cellular research.

To detect apoptosis, cells were stained with SR-VAD-FMK, which detect all activated caspases. The activation of caspases can be quantitatively correlated with the intensity of the fluorescent intensity. All three types of GNRs were

confirmed to induce the activation of caspases in both cell lines with different capacity as is shown in Figure 5. In general, the accumulation of activated caspases depends on the dosage of GNRs, which is in accordance with the MTT assay. Even at low dosage, activated caspases were detected in HEp-2 cells. The signal intensity increased with the rising dosage, and in the cases of treatment with high dose (10-fold of 10^{-12} M), all cells were all stained strongly and many cells were detached at this stage. All these results suggest that GNRs have triggered apoptotic process. For MDCK cells, figures not shown here, a similar trend has been observed, while the stain was relatively weaker compared to Hep-2 cells and did not increase as drastically as HEp-2 cells when higher concentrations of GNRs applied, which is in accordance with the MTT assay results.

In conclusion, GNRs show relative higher cytotoxicity compared to GNSs and PSS/PAH-coated GNRs to HEp-2 cells, which is mainly related to the CTAB on particle surface rather than the free ones in solution. Furthermore, dosage rather than time scale is more important in GNRs-induced cytotoxicity. The majority cell death occurs within one hour of incubation via GNRs-induced apoptosis processes. Change in the aspect ratio up to 5 has little influence on GNRs' cytotoxicity. Additional polymer (PSS/PAH) coating can significantly improve cell survival, which seems not due to the change of surface charge properties but isolation of CTAB from cell membrane by additional layer(s) of barrier.

Acknowledgments

This work was supported by an EPSRC Science and Innovation Award and a Pump Priming Award from SPIBS University of Strathclyde. D. Xu was supported by a Ph.D. mobility program from the Chinese Government. The authors also thank Alison McLintock and Dr. Alastair Ward for their support on GNSs synthesis. The authors do not have a direct financial relation with the commercial identity mentioned in the paper that might lead to a conflict of interests for any of the authors.

References

- [1] P. K. Jain, I. H. ElSayed, and M. A. El-Sayed, "Au nanoparticles target cancer," *Nano Today*, vol. 2, no. 1, pp. 18–29, 2007.
- [2] X. Liu, Q. Dai, L. Austin et al., "A one-step homogeneous immunoassay for cancer biomarker detection using gold nanoparticle probes coupled with dynamic light scattering," *Journal of the American Chemical Society*, vol. 130, no. 9, pp. 2780–2782, 2008.
- [3] C. Yu and J. Irudayaraj, "Multiplex biosensor using gold nanorods," *Analytical Chemistry*, vol. 79, no. 2, pp. 572–579, 2007.
- [4] A. K. Salem, P. C. Searson, and K. W. Leong, "Multifunctional nanorods for gene delivery," *Nature Materials*, vol. 2, no. 10, pp. 668–671, 2003.
- [5] C. C. Chen, Y. P. Lin, C. W. Wang et al., "DNA-gold nanorod conjugates for remote control of localized gene expression by near infrared irradiation," *Journal of the American Chemical Society*, vol. 128, no. 11, pp. 3709–3715, 2006.
- [6] N. J. Durr, T. Larson, D. K. Smith, B. A. Korgel, K. Sokolov, and A. Ben-Yakar, "Two-photon luminescence imaging of cancer cells using molecularly targeted gold nanorods," *Nano Letters*, vol. 7, no. 4, pp. 941–945, 2007.
- [7] K. Imura, T. Nagahara, and H. Okamoto, "Near-field optical imaging of plasmon modes in gold nanorods," *Journal of Chemical Physics*, vol. 122, no. 15, Article ID 154701, pp. 1–5, 2005.
- [8] K. Imura, T. Nagahara, and H. Okamoto, "Near-field two-photon-induced photoluminescence from single gold nanorods and imaging of plasmon modes," *Journal of Physical Chemistry B*, vol. 109, no. 27, pp. 13214–13220, 2005.
- [9] P. K. Jain, X. Huang, I. H. El-Sayed, and M. A. El-Sayed, "Noble metals on the nanoscale: optical and photothermal properties and some applications in imaging, sensing, biology, and medicine," *Accounts of Chemical Research*, vol. 41, no. 12, pp. 1578–1586, 2008.
- [10] C. J. Murphy, A. M. Gole, J. W. Stone et al., "Gold nanoparticles in biology: beyond toxicity to cellular imaging," *Accounts of Chemical Research*, vol. 41, no. 12, pp. 1721–1730, 2008.
- [11] X. Huang, I. H. El-Sayed, W. Qian, and M. A. El-Sayed, "Cancer cell imaging and photothermal therapy in the near-infrared region by using gold nanorods," *Journal of the American Chemical Society*, vol. 128, no. 6, pp. 2115–2120, 2006.
- [12] K. S. Lee and M. A. El-Sayed, "Gold and silver nanoparticles in sensing and imaging: sensitivity of plasmon response to size, shape, and metal composition," *Journal of Physical Chemistry B*, vol. 110, no. 39, pp. 19220–19225, 2006.
- [13] P. K. Jain, K. S. Lee, I. H. El-Sayed, and M. A. El-Sayed, "Calculated absorption and scattering properties of gold nanoparticles of different size, shape, and composition: applications in biological imaging and biomedicine," *Journal of Physical Chemistry B*, vol. 110, no. 14, pp. 7238–7248, 2006.
- [14] H. Wang, T. B. Huff, D. A. Zweifel et al., "In vitro and in vivo two-photon luminescence imaging of single gold nanorods," *Proceedings of the National Academy of Sciences of the United States of America*, vol. 102, no. 44, pp. 15752–15756, 2005.
- [15] N. Lewinski, V. Colvin, and R. Drezek, "Cytotoxicity of nanoparticles," *Small*, vol. 4, no. 1, pp. 26–49, 2008.
- [16] H. J. Johnston, G. Hutchison, F. M. Christensen, S. Peters, S. Hankin, and V. Stone, "A review of the in vivo and in vitro toxicity of silver and gold particulates: particle attributes and biological mechanisms responsible for the observed toxicity," *Critical Reviews in Toxicology*, vol. 40, no. 4, pp. 328–346, 2010.
- [17] M. Thomas and A. M. Klibanov, "Conjugation to gold nanoparticles enhances polyethylenimine's transfer of plasmid dna into mammalian cells," *Proceedings of the National Academy of Sciences of the United States of America*, vol. 100, no. 16, pp. 9138–9143, 2003.
- [18] N. L. Rosi, D. A. Giljohann, C. S. Thaxton, A. K. R. Lytton-Jean, M. S. Han, and C. A. Mirkin, "Oligonucleotide-modified gold nanoparticles for intracellular gene regulation," *Science*, vol. 312, no. 5776, pp. 1027–1030, 2006.
- [19] B. D. Chithrani and W. C. W. Chan, "Elucidating the mechanism of cellular uptake and removal of protein-coated gold nanoparticles of different sizes and shapes," *Nano Letters*, vol. 7, no. 6, pp. 1542–1550, 2007.
- [20] Y. Pan, S. Neuss, A. Leifert et al., "Size-dependent cytotoxicity of gold nanoparticles," *Small*, vol. 3, no. 11, pp. 1941–1949, 2007.
- [21] E. Boisselier and D. Astruc, "Gold nanoparticles in nanomedicine: preparations, imaging, diagnostics, therapies and

- toxicity," *Chemical Society Reviews*, vol. 38, no. 6, pp. 1759–1782, 2009.
- [22] X. Huang, P. K. Jain, I. H. El-Sayed, and M. A. El-Sayed, "Gold nanoparticles: interesting optical properties and recent applications in cancer diagnostics and therapy," *Nanomedicine*, vol. 2, no. 5, pp. 681–693, 2007.
- [23] W. Cui, J. Li, Y. Zhang, H. Rong, W. Lu, and L. Jiang, "Effects of aggregation and the surface properties of gold nanoparticles on cytotoxicity and cell growth," *Nanomedicine*, vol. 8, no. 1, pp. 46–53, 2012.
- [24] Y. Hao, X. Yang, S. Song et al., "Exploring the cell uptake mechanism of phospholipid and polyethylene glycol coated gold nanoparticles," *Nanotechnology*, vol. 23, no. 4, Article ID 045103, 2012.
- [25] X. M. Jiang, L. M. Wang, and C. Y. Chen, "Cellular uptake, intracellular trafficking and biological responses of gold nanoparticles," *Journal of the Chinese Chemical Society*, vol. 58, no. 3, pp. 273–281, 2011.
- [26] Y. Qiu, Y. Liu, L. Wang et al., "Surface chemistry and aspect ratio mediated cellular uptake of Au nanorods," *Biomaterials*, vol. 31, no. 30, pp. 7606–7619, 2010.
- [27] N. M. Schaeublin, L. K. Braydich-Stolle, E. I. Maurer et al., "Does shape matter? Bioeffects of gold nanomaterials in a human skin cell model," *Langmuir*, vol. 28, no. 6, pp. 3248–3258, 2012.
- [28] B. Nikoobakht and M. A. El-Sayed, "Preparation and growth mechanism of gold nanorods (NRs) using seed-mediated growth method," *Chemistry of Materials*, vol. 15, no. 10, pp. 1957–1962, 2003.
- [29] C. J. Johnson, E. Dujardin, S. A. Davis, C. J. Murphy, and S. Mann, "Growth and form of gold nanorods prepared by seed-mediated, surfactant-directed synthesis," *Journal of Materials Chemistry*, vol. 12, no. 6, pp. 1765–1770, 2002.
- [30] N. R. Jana, L. Gearheart, and C. J. Murphy, "Wet chemical synthesis of high aspect ratio cylindrical gold nanorods," *Journal of Physical Chemistry B*, vol. 105, no. 19, pp. 4065–4067, 2001.
- [31] S. Wang, W. Lu, O. Tovmachenko, U. S. Rai, H. Yu, and P. C. Ray, "Challenge in understanding size and shape dependent toxicity of gold nanomaterials in human skin keratinocytes," *Chemical Physics Letters*, vol. 463, no. 1–3, pp. 145–149, 2008.
- [32] A. M. Alkilany, P. K. Nagaria, C. R. Hexel, T. J. Shaw, C. J. Murphy, and M. D. Wyatt, "Cellular uptake and cytotoxicity of gold nanorods: molecular origin of cytotoxicity and surface effects," *Small*, vol. 5, no. 6, pp. 701–708, 2009.
- [33] T. Niidome, M. Yamagata, Y. Okamoto et al., "PEG-modified gold nanorods with a stealth character for in vivo applications," *Journal of Controlled Release*, vol. 114, no. 3, pp. 343–347, 2006.
- [34] D. Mirska, K. Schirmer, S. S. Funari, A. Langner, B. Dobner, and G. Brezesinski, "Biophysical and biochemical properties of a binary lipid mixture for DNA transfection," *Colloids and Surfaces B*, vol. 40, no. 1, pp. 51–59, 2005.
- [35] H. Takahashi, Y. Niidome, T. Niidome, K. Kaneko, H. Kawasaki, and S. Yamada, "Modification of gold nanorods using phosphatidylcholine to reduce cytotoxicity," *Langmuir*, vol. 22, no. 1, pp. 2–5, 2006.
- [36] E. E. Connor, J. Mwamuka, A. Gole, C. J. Murphy, and M. D. Wyatt, "Gold nanoparticles are taken up by human cells but do not cause acute cytotoxicity," *Small*, vol. 1, no. 3, pp. 325–327, 2005.
- [37] S. C. Boca and S. Astilean, "Detoxification of gold nanorods by conjugation with thiolated poly(ethylene glycol) and their assessment as SERS-active carriers of Raman tags," *Nanotechnology*, vol. 21, no. 23, Article ID 235601, 2010.
- [38] C. Grabinski, N. Schaeublin, A. Wijaya et al., "Effect of gold nanorod surface chemistry on cellular response," *ACS Nano*, vol. 5, no. 4, pp. 2870–2879, 2011.
- [39] Y. Zhang, J. Yu, D. J. Birch, and Y. Chen, "Gold nanorods for fluorescence lifetime imaging in biology," *Journal of Biomedical Optics*, vol. 15, no. 2, p. 020504-3, 2010.
- [40] Y. Zhang, J. Yu, D. J. S. Birch, and Y. Chen, "Gold nanorods for applications in biological imaging," in *Proceedings of the SPIE*, January 2011.
- [41] Y. Zhang, D. J. S. Birch, and Y. Chen, "Two-photon excited surface plasmon enhanced energy transfer between DAPI and gold nanoparticles: opportunities in intra-cellular imaging and sensing," *Applied Physics Letters*, vol. 99, no. 10, Article ID 103701, 2011.
- [42] A. Leung, M. Trau, and L. K. Nielsen, "Assembly of multilayer PSS/PAH membrane on coherent alginate/PLO microcapsule for long-term graft transplantation," *Journal of Biomedical Materials Research A*, vol. 88, no. 1, pp. 226–237, 2009.
- [43] D. J. Bergman and M. I. Stockman, "Surface plasmon amplification by stimulated emission of radiation: quantum generation of coherent surface plasmons in nanosystems," *Physical Review Letters*, vol. 90, no. 2, pp. 027402/1–027402/4, 2003.
- [44] M. A. Noginov, G. Zhu, A. M. Belgrave et al., "Demonstration of a spaser-based nanolaser," *Nature*, vol. 460, no. 7259, pp. 1110–1112, 2009.
- [45] N. Omura, I. Uechi, and S. Yamada, "Comparison of plasmonic sensing between polymer-and silica-coated gold nanorods," *Analytical Sciences*, vol. 25, no. 2, pp. 255–259, 2009.
- [46] C. J. Murphy, T. K. Sau, A. M. Gole et al., "Anisotropic metal nanoparticles: synthesis, assembly, and optical applications," *Journal of Physical Chemistry B*, vol. 109, no. 29, pp. 13857–13870, 2005.
- [47] J. Kimling, M. Maier, B. Okenve, V. Kotaidis, H. Ballot, and A. Plech, "Turkevich method for gold nanoparticle synthesis revisited," *Journal of Physical Chemistry B*, vol. 110, no. 32, pp. 15700–15707, 2006.
- [48] C. M. Goodman, C. D. McCusker, T. Yilmaz, and V. M. Rotello, "Toxicity of gold nanoparticles functionalized with cationic and anionic side chains," *Bioconjugate Chemistry*, vol. 15, no. 4, pp. 897–900, 2004.
- [49] J. Lin, H. Zhang, Z. Chen, and Y. Zheng, "Penetration of lipid membranes by gold nanoparticles: insights into cellular uptake, cytotoxicity, and their relationship," *ACS Nano*, vol. 4, no. 9, pp. 5421–5429, 2010.

Research Article

Magnetic Properties of FePt Nanoparticles Prepared by Sonoelectrodeposition

Nguyen Hoang Nam, Nguyen Thi Thanh Van, Nguyen Dang Phu, Tran Thi Hong, Nguyen Hoang Hai, and Nguyen Hoang Luong

VNU University of Science, 334 Nguyen Trai Road, Hanoi, Vietnam

Correspondence should be addressed to Nguyen Hoang Luong, luongnh@vnu.edu.vn

Received 24 March 2012; Accepted 26 April 2012

Academic Editor: Leonard Deepak Francis

Copyright © 2012 Nguyen Hoang Nam et al. This is an open access article distributed under the Creative Commons Attribution License, which permits unrestricted use, distribution, and reproduction in any medium, provided the original work is properly cited.

Sonoelectrodeposition is a useful technique to make metallic nanoparticles, using ultrasound during electrodeposition to remove nanoparticles as they grow on the cathode surface. This paper reports some structural and magnetic properties of FePt nanoparticles prepared by this method. The as-prepared Fe₄₅Pt₅₅ nanoparticles were ferromagnetic at room temperature. Upon annealing at 700°C for 1 h under H₂ atmosphere, the saturation magnetization and the coercivity of the nanoparticles were improved significantly. The annealed nanoparticles showed a high coercivity of 13.5 kOe at 2 K and of 9 kOe at room temperature. Sonoelectrodeposition is a promising technique to make large quantity of FePt nanoparticles.

1. Introduction

The ordered face-centered tetragonal (fct) L1₀ FePt materials are normally obtained from the disordered face-centered cubic (fcc) materials via the order-disorder transition. The ordered FePt alloys possess excellent hard magnetic properties with the saturation magnetization, $\mu_0 M_s$, of 1.4 T, the Currie temperature, T_c , of 750 K, and the crystalline anisotropy K_1 , of 7 MJ/m³ [1]. Despite the high cost of Pt, FePt thin films or particles have been paid much attention to their use as ultrahigh density magnetic storage media and microelectronic mechanical system (MEMS) due to the mechanical and chemical stability of the ordered fct L1₀ structure.

There are several ways to make FePt-nanostructured materials including physical techniques such as mechanical deformation [2], arc-melting [3], vacuum evaporation (sputtering and thermal evaporation) [4, 5], laser ablation pulse [6], chemical methods [7–9], and physicochemical method such as electrodeposition [10, 11]. Up to now, the vacuum evaporation is the most used method. Electrodeposition is a promising way to obtain FePt thin films because it is less expensive than physical methods, less complicated than chemical methods. But by this technique, it is difficult to

get nanoparticles with large quantity. Sonoelectrochemistry was developed to make nanoparticles [12]. It combined the advantages of sonochemistry and electrodeposition. Sonochemistry is a very useful synthetic method which was discovered as early as 1934 that the application of ultrasonic energy could increase the rate of electrolytic water cleavage. The effects of ultrasonic radiation on chemical reactions are due to the very high temperatures and pressures, which develop in and around the collapsing bubble [13]. Sonoelectrochemistry has the potential benefit of combining sonochemistry with electrochemistry. Some of these beneficial effects include acceleration of mass transport, cleaning and degassing of the electrode surface, and an increased reaction rate [14]. In this paper, we report the use of the sonoelectrochemical method for the preparation of FePt nanoparticles. Recently, CoPt nanoparticles encapsulated in carbon cages prepared by sonoelectrodeposition have been reported by Luong et al. [15].

2. Experimental

The sonoelectrochemical device employed is similar to that described in [16]. A titanium horn with diameter of 1.3 cm acted as both the cathode and ultrasound emitter (Sonics

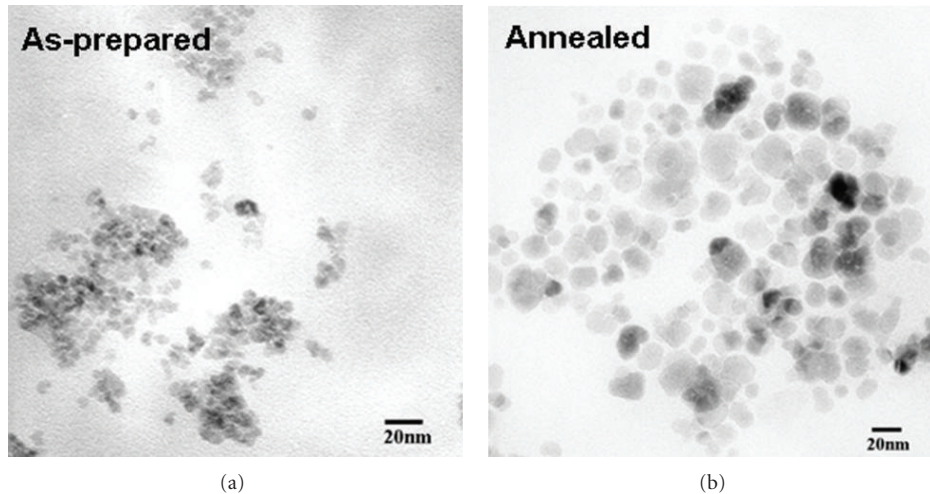


FIGURE 1: TEM images of the as-prepared (a) and annealed (b) $\text{Fe}_{45}\text{Pt}_{55}$ nanoparticles ($700^\circ\text{C}/1\text{ h}$).

VCX 750). The electroactive part of the sonoelectrode was the planar circular surface at the bottom of the Ti horn. An isolating plastic jacket covered the immersed cylindrical part. This sonoelectrode produced a sonic pulse that immediately followed a current pulse. One pulse driver was used to control a galvanostat and the ultrasonic processor, which was adapted to work in the pulse mode. A home-made galvanostat (without using a reference electrode) was used to control the constant current regime. A platinum plate with a square of 1 cm^2 was used as a counter electrode. The current pulse was $15\text{ mA}/\text{cm}^2$. The ultrasound power density was $100\text{ W}/\text{cm}^2$. The duration t_{on} of the current pulse was $0.5\text{--}0.8\text{ s}$, then the current was turned off for a fixed duration t_{off} of 0.5 s . During t_{on} , FePt nanoparticles were deposited on the surface of the electrode. When the current was switched off, an ultrasound was activated to remove the nanoparticles from the electrode. The time of ultrasound was 0.3 s . The temperature during the reaction was room temperature. The volume of the electrolysis cell was 80 mL containing $1\text{ mM H}_2\text{PtCl}_6$, 0.1 M FeSO_4 , and $0.525\text{ M Na}_2\text{SO}_4$. The chemicals were mixed under N_2 atmosphere. The $\text{pH} = 3$ of the solution was controlled by H_2SO_4 . After deposition, FePt nanoparticles were collected by using a centrifuge (Hettich Universal 320, 9000 rpm , 20 min). Nanoparticles were dried in air at 80°C for 20 min . All samples were annealed at 700°C for 1 h under H_2 atmosphere. The structure of the nanoparticles was analyzed by using a Bruker D5005 X-ray diffractometer (XRD). The particle morphology was obtained from a transmission electron microscope (TEM JEM1010-JEOL). The chemical composition of the FePt nanoparticles was studied by using an energy dispersion spectroscopy (EDS OXFORD-ISIS 300) and revealed that the chemical composition of our sample is $\text{Fe}_{45}\text{Pt}_{55}$. Magnetic measurements were conducted by using Quantum Design's superconducting quantum interference device (SQUID) with a magnetic field up to 50 kOe at temperature range from 2 K to 300 K .

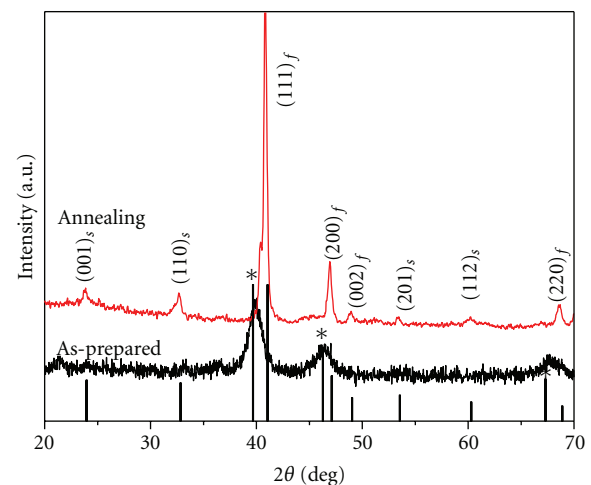


FIGURE 2: XRD patterns ($\text{Cu K}\alpha$ radiation) of the as-prepared (bottom) and annealed (top) $\text{Fe}_{45}\text{Pt}_{55}$ nanoparticles compared to those of the intensities for L1_0 FePt (PDF file 431359) and for Pt (marked by the asterisks, PDF file 04-0802). The fundamental peaks of FePt structure were denoted by “f,” and the superlattice peaks were denoted by “s.”

3. Results and Discussion

Figure 1 is the TEM images of typical as-prepared and annealed samples. Particle size of the as-prepared $\text{Fe}_{45}\text{Pt}_{55}$ sample was $5\text{--}10\text{ nm}$. After annealing the particle size increased to $10\text{--}25\text{ nm}$ due to the aggregation and particle growth. In addition, the size distribution of the annealed particles was larger than that of the as-prepared samples.

Figure 2 shows the XRD patterns of the as-prepared and the annealed $\text{Fe}_{45}\text{Pt}_{55}$ nanoparticles (700°C for 1 h). Before annealing, the XRD results showed the reflections of pure Pt structure, which is similar to other FePt thin films produced by electrodeposition [17]. However, authors in

[17] thought that the reflections were from the disordered fcc phase. For the fcc phase, XRD results present only the fundamental reflections which are (111), (200), and (220). The fundamental reflections of the fcc FePt are close to the (111), (200), and (220) reflections of the Pt that make some scientists thought that they are of the fcc structure. We propose that XRD results from our as-prepared nanoparticles and from [17] are the peaks of only Pt. The reflections from Fe are very weak due to the fact that their atomic weight is much less than that of Pt which is similar to the XRD result of FePt foils prepared by cold deformation [18]. The Pt peaks in the as-prepared samples are broad due to the small size of the particles. Using the Scherrer formula with the full width at half maximum of the strongest peak (111), the mean particle size of Pt particles was deduced to be 5.2 nm, which is much smaller than the particle size obtained from the TEM image. The particles were not disordered FePt, but they can be formed by many small domains of pure Fe and Pt. The formation of FePt by electrodeposition did not occur and may be ascribed to the large difference in the standard electrode potential of the Fe^{2+}/Fe (-0.44 V [19]) and Pt^{4+}/Pt (0.742 V [20]). Upon annealing, the formation of the ordered L1_0 fct phase happened by the diffusion process between Fe and Pt domains.

Magnetic measurements revealed low-saturation magnetization (M_s) and coercivity (H_c) in all as-prepared samples (data not shown). The saturation magnetization of the unannealed particles was about few emu/g and the coercivity was 20–80 kOe. The low value of M_s of the as-prepared nanoparticles may be explained by the oxidation or hydroxidation of Fe atoms in nanoparticles, which can result in the weak magnetic iron oxides and iron hydroxides. This is in agreement with the suggestion of separated Fe and Pt domains in as-prepared nanoparticles. It is known that FePt with high-saturation magnetization is a chemically stable material. Therefore, it is difficult to be oxidized to form weak ferromagnetic materials. After annealing, the hard magnetic FePt phase was formed. Figure 3 presents the magnetic curves of the annealed $\text{Fe}_{45}\text{Pt}_{55}$ at different temperatures. The curves show a typical hard magnetic hysteresis loops with high H_c . Beside, form of the magnetic curves shows that a small soft magnetic phase, probably FePt_3 , exists in the sample. The as-prepared $\text{Fe}_{45}\text{Pt}_{55}$ nanoparticles were ferromagnetic at room temperature. Upon annealing at 700°C for 1 h, the saturation magnetization and the coercivity of the nanoparticles were improved significantly. Coercivity of annealed $\text{Fe}_{45}\text{Pt}_{55}$ nanoparticles as a function of temperature is shown in Figure 4. At 2 K, the coercivity is 13.5 kOe and slightly decreases with increasing temperature to the value of 9 kOe at 300 K.

Magnetic squareness $S = M_r/M_s$ of annealed $\text{Fe}_{45}\text{Pt}_{55}$ nanoparticles as a function of temperature is shown in Figure 5. The temperature dependence of S is similar to that of H_c . At 2 K, the magnetic squareness is 0.78, slightly decreases with increasing temperature, and has a value of 0.745 at 300 K. This value of S is very close to that obtained for $\text{L1}_0\text{CoPt}$ nanoparticles at room temperature [15].

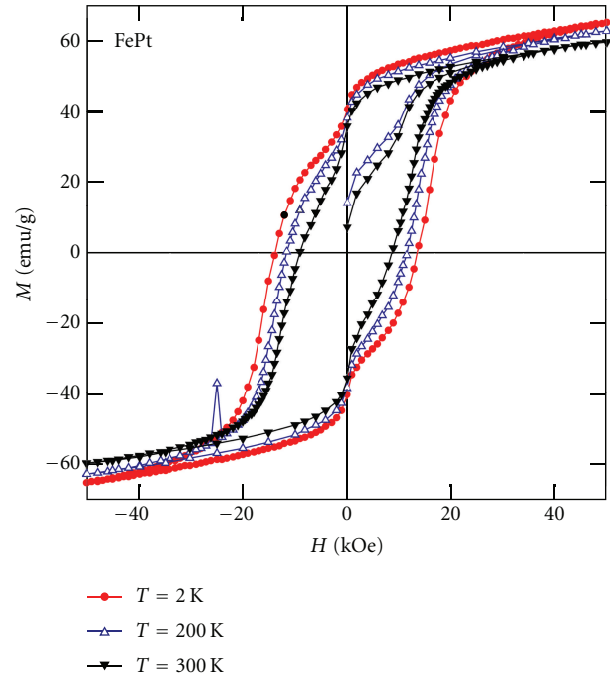


FIGURE 3: Magnetic curves of annealed $\text{Fe}_{45}\text{Pt}_{55}$ nanoparticles at different temperatures.

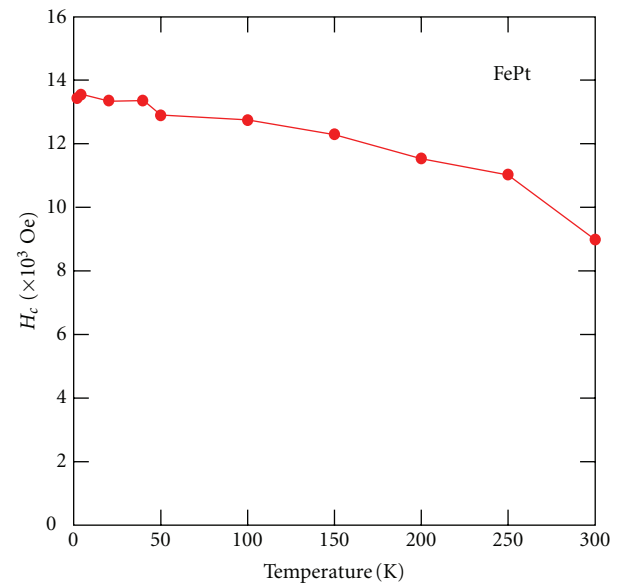


FIGURE 4: Coercivity of annealed $\text{Fe}_{45}\text{Pt}_{55}$ nanoparticles as a function of temperature.

4. Conclusion

Sonoelectrochemistry is a promising method to make FePt magnetic nanoparticles. The annealed FePt nanoparticles made by this technique had the size of 10–25 nm. After annealing, the nanoparticles showed a high coercivity of 13.5 kOe at 2 K and 9 kOe at room temperature. This method possesses some advantages compared to common methods

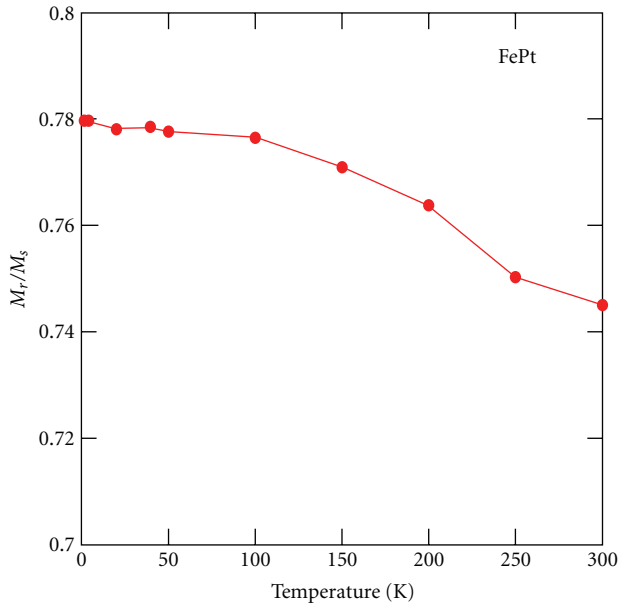


FIGURE 5: Magnetic squareness $S = M_r/M_s$ of annealed $\text{Fe}_{45}\text{Pt}_{55}$ nanoparticles as a function of temperature.

such as simple preparation, low-cost equipment, and easy scaleup.

Acknowledgments

The authors would like to thank the National Foundation for Science and Technology Development of Vietnam-NAFOSTED (project 103.02.72.09) for financial support. N. H. Nam is grateful to the TRIG A Project of Hanoi University of Science, Vietnam National University, Hanoi for support to complete the paper at Nottingham University, Nottingham, United Kingdom. The authors would like to thank Professor Y. Nozue of Osaka University, Japan, for providing SQUID.

References

- [1] A. Cebollada, R. F. C. Farrow, and M. F. Toney, "Structure and magnetic properties of chemically ordered magnetic binary alloys in thin film form," in *Magnetic Nanostructure*, H. S. Nalwa, Ed., p. 93, American Scientific, Stevenson Ranch, Calif, USA, 2002.
- [2] N. H. Hai, N. M. Dempsey, M. Veron, M. Verdier, and D. Givord, "An original route for the preparation of hard FePt," *Journal of Magnetism and Magnetic Materials*, vol. 257, no. 2-3, pp. L139–L145, 2003.
- [3] Q. I. Xiao, P. D. Thang, E. Brück, F. R. De Boer, and K. H. J. Buschow, "Effect of phase transformation on remanence enhancement in bulk Fe-Pt magnets," *Applied Physics Letters*, vol. 78, no. 23, pp. 3672–3674, 2001.
- [4] N. T. T. Van, N. H. Hai, N. H. Luong, V. V. Hiep, and N. Chau, "Magnetic properties of $(\text{FePt})_{100-x}\text{Cu}_x$ thin films," *Journal of the Korean Physical Society*, vol. 52, no. 5, pp. 1435–1438, 2008.
- [5] N. H. Luong, V. V. Hiep, D. M. Hong et al., "High-coercivity FePt sputtered films," *Journal of Magnetism and Magnetic Materials*, vol. 290-291, pp. 559–561, 2005.
- [6] L. J. Qiu, J. Ding, A. O. Adeyeye et al., "FePt patterned media fabricated by deep UV lithography followed by sputtering or PLD," *IEEE Transactions on Magnetics*, vol. 43, no. 6, pp. 2157–2159, 2007.
- [7] S. Saita and S. Maenosono, "FePt nanoparticles with a narrow composition distribution synthesized via pyrolysis of iron(III) ethoxide and platinum(II) acetylacetonate," *Chemistry of Materials*, vol. 17, no. 14, pp. 3705–3710, 2005.
- [8] R. Harpeness and A. Gedanken, "The microwave-assisted polyol synthesis of nanosized hard magnetic material, FePt," *Journal of Materials Chemistry*, vol. 15, pp. 698–702, 2005.
- [9] S. Sun, C. B. Murray, D. Weller, L. Folks, and A. Moser, "Monodisperse FePt nanoparticles and ferromagnetic FePt nanocrystal superlattices," *Science*, vol. 287, no. 5460, pp. 1989–1992, 2000.
- [10] K. Žužek Rožman, A. Krause, K. Leistner, S. Fähler, L. Schultz, and H. Schlörb, "Electrodeposition and hard magnetic properties of Co-Pt films in comparison to Fe-Pt films," *Journal of Magnetism and Magnetic Materials*, vol. 314, no. 2, pp. 116–121, 2007.
- [11] F. M. F. Rhen, G. Hinds, C. O'Reilly, and J. M. D. Coey, "Electrodeposited FePt films," *IEEE Transactions on Magnetics*, vol. 39, no. 5, pp. 2699–2701, 2003.
- [12] A. Gedanken, "Novel methods (sonochemistry, microwave heating, and sonoelectrochemistry) for the preparation of nanosized inorganic compounds," in *Inorganic Materials: Recent Advances*, D. Bahadur, S. Vitta, and O. Prakash, Eds., p. 302, Narosa Publishing, Delhi, India, 2002.
- [13] K. S. Suslick, S. B. Choe, A. A. Cichowlas, and M. W. Grinstaff, "Sonochemical synthesis of amorphous iron," *Nature*, vol. 353, no. 6343, pp. 414–416, 1991.
- [14] T. J. Mason, J. P. Lorimer, and D. J. Walton, "Sonoelectrochemistry," *Ultrasonics*, vol. 28, no. 5, pp. 333–337, 1990.
- [15] N. H. Luong, N. H. Hai, N. D. Phu, and D. A. MacLaren, "Co-Pt nanoparticles encapsulated in carbon cages prepared by sonoelectrodeposition," *Nanotechnology*, vol. 22, no. 28, Article ID 285603, 2011.
- [16] J. Zhu, S. T. Aruna, Y. Koltypin, and A. Gedanken, "A novel method for the preparation of lead selenide: pulse sonoelectrochemical synthesis of lead selenide nanoparticles," *Chemistry of Materials*, vol. 12, no. 1, pp. 143–147, 2000.
- [17] Q. Zeng, Y. Zhang, H. L. Wang, V. Papaefthymiou, and G. C. Hadjipanayis, "Magnetic properties and microstructure of fine Fe-Pt nanoparticles prepared by chemical reduction," *Journal of Magnetism and Magnetic Materials*, vol. 272–276, no. 1, pp. e1223–e1225, 2004.
- [18] N. H. Hai, N. M. Dempsey, and D. Givord, "Hard magnetic FePt alloys prepared by cold-deformation," *Journal of Magnetism and Magnetic Materials*, vol. 262, no. 3, pp. 353–360, 2003.
- [19] P. Atkins, *Physical Chemistry*, W.H. Freeman and Company, New York, NY, USA, 6th edition, 1997.
- [20] A. J. Bard and L. R. Faulkner, *Electrochemical Methods: Fundamentals and Applications*, John Wiley and Sons, New York, NY, USA, 2nd edition, 2001.

Research Article

Study on Vibration Behavior of Doubly Clamped Silicon Nanowires by Molecular Dynamics

H. Yu, W. W. Zhang, S. Y. Lei, L. B. Lu, C. Sun, and Q. A. Huang

Key Lab of MEMS of Ministry of Education, Southeast University, Nanjing 210096, China

Correspondence should be addressed to H. Yu, h_yu@seu.edu.cn

Received 25 February 2012; Revised 1 April 2012; Accepted 19 April 2012

Academic Editor: Sergio J. Mejía-Rosales

Copyright © 2012 H. Yu et al. This is an open access article distributed under the Creative Commons Attribution License, which permits unrestricted use, distribution, and reproduction in any medium, provided the original work is properly cited.

The vibration behavior of doubly clamped silicon nanowires with square cross sections is studied by molecular dynamics method. Silicon nanowires have lengths ranging from 4.888 to 12.491 nm and cross sections ranging from $1.22 \text{ nm} \times 1.22 \text{ nm}$ to $3.39 \text{ nm} \times 3.39 \text{ nm}$. The size dependence of the resonant frequency is studied in detail. The results show that the vibration behavior of Si nanowire is quite different from the macroscopic beam, and the resonant frequency is much higher than the result based on the continuum theory, but close to the theoretical result based on the semicontinuum approach. Surface reconstruction can strongly affect on vibration behavior. These results demonstrate that the classic theory may not be suitable for analysis of performances of nanostructures, and the conclusion of the study has a certain practical significance on related fields.

1. Introduction

In last decade, resonant nanoelectromechanical systems (NEMSs) have been found in a variety of important applications, including ultrasensitive mass and force sensing [1, 2], ultralow-power radio frequency (RF) signal generation, timing [3–5], and switch [6]. Silicon-based nanowires and nanobeams with very small dimensions and high-performance form the basis of most experimental demonstrations in these applications, where the nanowires or the nanobeams appear either in cantilever or in doubly clamped beam resonators. Nanoscale cantilevers are preferred to be resonators in mass sensing and ultrahigh frequency applications. For example, the nanothick resonant cantilever is used to detect ppm level trace trimethylamine vapor via specific molecular adsorption by measuring the resonant frequency shift of the cantilever [7]. On the other hand, doubly clamped silicon nanowire or nanobeam is another type of resonators in nanomechanical systems. They are also very attractive to researchers. As early as the year 2007, the fundamental resonance of 215 MHz of the doubly clamped silicon nanowire was demonstrated by Feng et al. [3]. The demonstration of mass spectrometry based on single biological molecule detection by using a doubly clamped silicon resonant nanobeam was reported in 2009 [8]. Therefore, the

resonant or vibration behavior of the silicon nanowire is very important to the mass sensing and other applications and has been widely studied by researchers.

In the aspect of theoretical study, some of researches applied equations and software based on continuum assumption to nanowires when they studied the resonance of silicon nanowires and the relationship between resonant frequency and Young's modulus [3, 9, 10]. However, because of the low dimension of the nanowire, the mechanical properties and thus the vibration behavior may deviate from their microscopic and macroscopic counterparts. It means that classical theories based on continuum assumptions or computational design tools, which have been developed for microstructures and macrostructures, may not be directly applicable for the nanostructures. Some approaches have been proposed to extend classical continuum theories to nanostructured materials. By considering the discrete nature of nanomaterial, Sun and Zhang developed a semicontinuum model to calculate Young's modulus of the ultrathin film with a simple cubic lattice [11]. This approach was then developed to study Young's modulus of silicon nanoplate [12]. Based on this approach, a multiscale model was built to analyze the deflection and resonant frequency of silicon nanobeam [13, 14]. On the other hand, molecular dynamics method

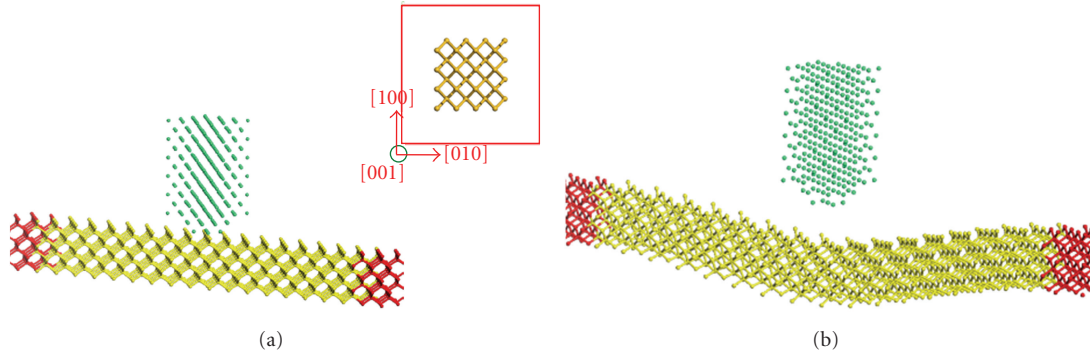


FIGURE 1: Model of a doubly clamped silicon nanowire and one AFM probe: (a) before optimization and (b) after optimization.

is often used to study and simulate the mechanical and resonant properties of nanowires. Park et al. and Kim et al. [15, 16] simulated the flexural and longitudinal vibrations of silicon nanocantilevers by molecular dynamics method. They deduced the elastic modulus and Young's modulus for nanothick silicon cantilevers from the natural frequency equation based on the continuum theory.

In this paper, we study the resonant behavior of doubly clamped silicon nanowires by using a specific computer code, Forcite, which is based on molecular dynamics method. Our results are in well agreement with the results based on the multiscale model but much higher than those based on continuum theory.

2. Construction of Simulation Model

Simulation model of one doubly clamped silicon nanowire with a square cross section is built as shown in Figure 1(a) (yellow atoms). The red atoms at two ends of the silicon nanowire are clamped. The cross section and the orientation of the silicon nanowire are depicted in Figure 1, too. Periodic boundary condition is used in the longitudinal direction of Si nanowire, and lateral surfaces are under free boundary conditions in vacuum. The simulation has been carried out at the average temperature of 298 K with a time step of 1 fs. Compass (Condensed-phase Optimized Molecular Potential for Atomistic Simulation Studies) force-field is selected when simulation is performed.

To actuate the nanowire, an AFM probe is constructed above the nanowire, which is denoted by green atoms in Figure 1. After structure optimization, the nanowire begins to deflection as shown in Figure 1(b), because Van der Waals force exists between the AFM and the nanowire. Then the AFM is removed and the simulation starts. Because of the initial deflection, the nanowire will vibrate freely.

3. Simulation Results and Discussion

Figure 2 shows the kinetic and potential energy of the silicon nanowire when the nanowire is vibrating. It can be seen that after undergoing very short transient oscillations, the kinetic energy and potential energy start oscillating almost in one uniform period. At the maximum point of the kinetic

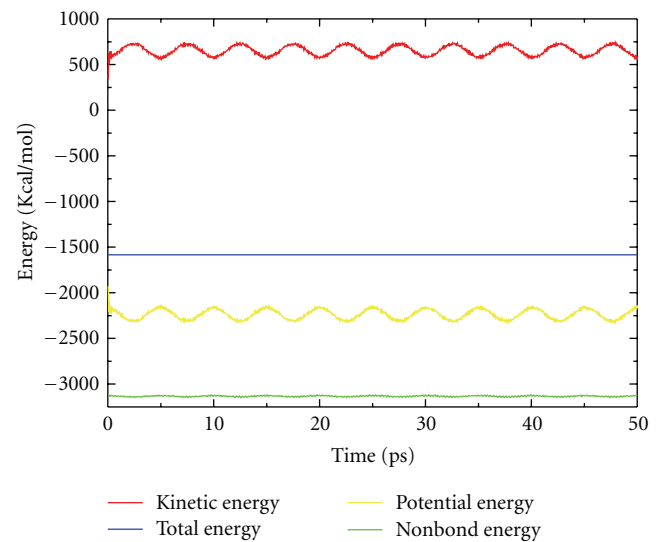


FIGURE 2: Energy of the nanowire while vibrating.

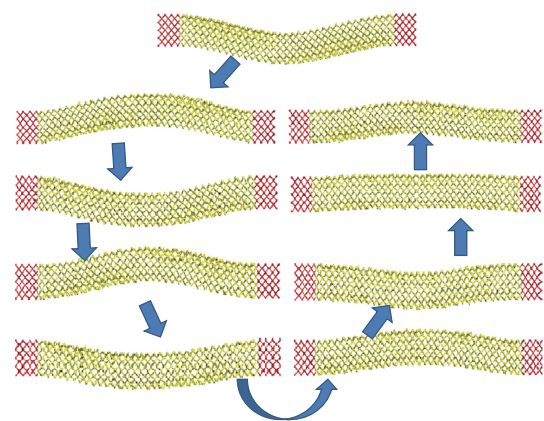


FIGURE 3: Vibration traces of the silicon nanowire in one oscillation period.

energy, the potential energy reaches to the minimum, and vice versa. Exchange between the kinetic energy and the potential energy occurs during one period.

Figure 3 shows the vibration traces of the nanowire in the successive time moment during one oscillation period. It is

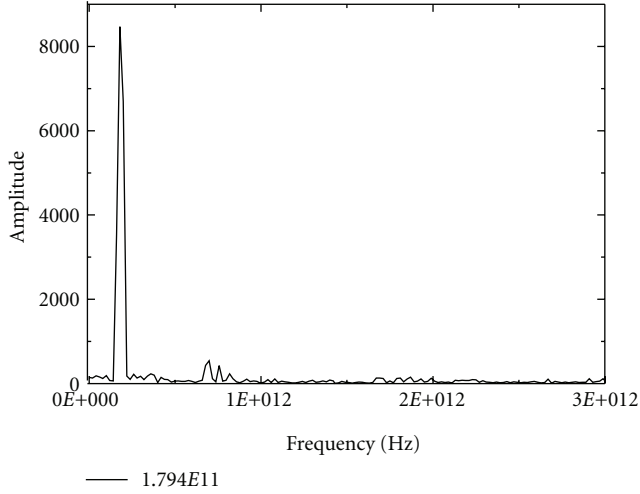


FIGURE 4: Frequency response of a silicon nanowire.

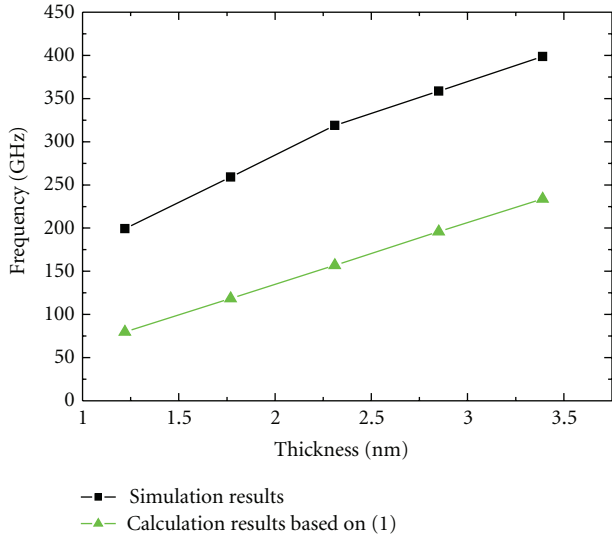


FIGURE 5: Fundamental frequency as a function of nanowire thickness: simulation results by MD software (black), and calculation results based on (1) (green) while Young's modulus coming from [15, 16]. All nanowires keep the same length of 9.232 nm and the same width of 2.85 nm.

seen that the vibration mode is the first mode and the motion of the nanowire in one oscillation period is different from that of a macroscopic beam.

The frequency response of the silicon nanowire can be obtained by performing FFT of the kinetic energy or the potential energy. Figure 4 shows the frequency response of the nanowire with a length of 9.232 nm. The cross section is 1.22 nm \times 1.22 nm. It can be seen that the fundamental frequency is about 179.4 GHz.

The vibrations of nanowires with different thicknesses are studied. The fundamental frequency as a function of thickness of the nanowire is shown in Figure 5 (black).

As we have known, the first mode frequency ω_0 and the j th mode frequency ω_j for a doubly clamped Euler-Bernoulli beam can be written as [17]

$$\omega_0 = \sqrt{\frac{EI}{ml^4}}, \quad (1)$$

$$\omega_j = (j\pi)^2 \omega_0 \quad (j = 1, 2, \dots), \quad (2)$$

where E is Young's modulus, m is mass per unit length, $m = \rho A$, ρ is the density of the beam, A is the area of the cross section, and l and I are the beam length and the mass moment of inertia, respectively. Now we apply this model to calculate fundamental frequencies of doubly clamped silicon nanowires. Young's modulus in (1) takes the value obtained by Park et al. [15, 16] for silicon nanowire. The results calculated from (1) for nanowires with different thicknesses are also shown in Figure 5 (green).

It is noticed that there is a big deviation between simulation results and calculation results based on (1). The deviation is larger than 60%. This means that the classic theory may not be suitable for analysis of performance of nanostructures, since (1) is built based on continuum assumption, and the discrete nature must be considered in the model for nanostructures. By considering the discrete nature in thickness direction of nanobeam, a multiscale model is proposed to study the vibration frequency of silicon nanobeam [14]. In this model, the fundamental frequency of the doubly clamped silicon nanobeam is described as

$$f_0 = \frac{\omega_0}{2\pi} = \begin{cases} \frac{\pi}{3l^2 t} \sqrt{\frac{2ka}{\rho} \times \frac{(N+1)(2N+1)}{2+t^2}}, & N \leq 3, \\ 2\pi \sqrt{\frac{ka}{l^2} \left[\frac{1}{18} \frac{(N-3)(N-2)(2N-5)}{3(N-3)^2 + 12(N-3)t + 14t^2} \right]}, & N > 3, \end{cases} \quad (3)$$

where l , ρ , and a are the length, the density, and the lattice constant of the silicon nanobeam, respectively. N is the number of lattices in thickness, k is the spring constant between two silicon atoms, 2.614×10^2 N/m, and t is the relaxation constant. For nonsurface relaxation, $t = 1$. Based on this multiscale approach, resonant frequencies for silicon nanowires are calculated and compared with our simulation results, as shown in Figure 6. It is clear that the discrepancy between them is smaller than the deviation in Figure 5. The deviation here is smaller than 20%. This figure shows that our results are in well agreement with the multiscale model results.

When the length of the nanowire is changed, the vibration behavior will change, too. The fundamental frequencies of doubly clamped silicon nanowires with different lengths are studied. Figure 7 shows the resonant frequency as a function of length of the silicon nanowire. The fundamental

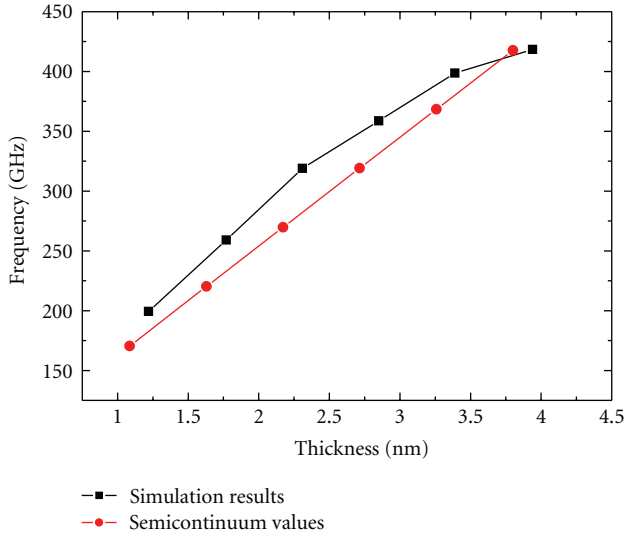


FIGURE 6: Fundamental frequency as a function of nanowire thickness: simulation results by MD software (black), and calculation results based on multiscale model (red). The length of nanowire is 9.232 nm.

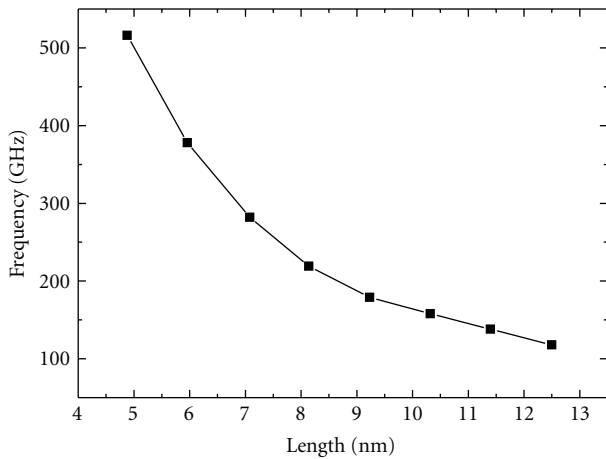


FIGURE 7: Fundamental frequency as a function of length of silicon nanowire. The width and thickness of nanowires are both of 1.22 nm.

frequency decreases monotonically with the length increasing.

When the width is changed, the frequency response of the nanowire does not change significantly, as shown in Figure 8. This concludes that the transverse vibration frequency is not related to the width of nanowire too much, which is similar with the result based on continuum theory.

Surface reconstruction can strongly impact on the elasticity of silicon nanoplate [18–20]. Therefore, the effect of surface reconstruction on vibration frequency of silicon nanowire is also studied in detail. The (2×1) dimer reconstruction is considered on four of lateral surfaces of the silicon nanowire. Figure 9 shows the vibration frequencies with and without reconstruction for nanowires with different cross sections. It can be seen that the frequency under surface

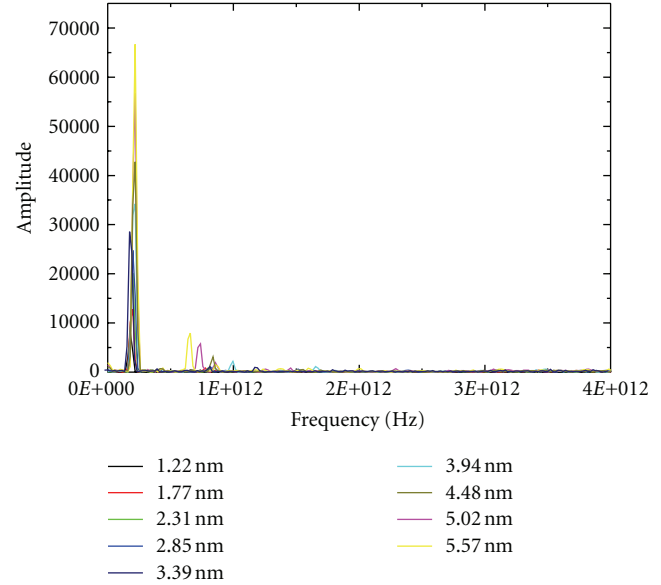


FIGURE 8: Frequency responses of doubly clamped nanowires with different widths.

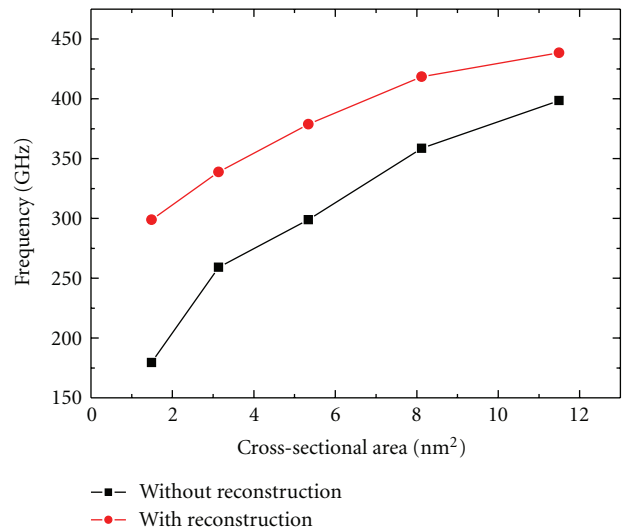


FIGURE 9: Resonant frequency for nanowires with different cross sections with and without reconstructions on lateral surfaces.

reconstruction is much higher than that without reconstruction. The frequency is almost doubled by surface reconstruction for the nanowire with the cross section of 1.488 nm². Because of the surface reconstruction, the nanowire becomes stiffer, and Young's modulus becomes larger, resulting in the resonant frequency increasing significantly. The size of cross section is smaller, the change of resonant frequency is greater, since the surface-to-volume ratio is higher for the nanowire with a smaller cross section.

4. Conclusions

Vibration behavior of doubly clamped silicon nanowires is studied by molecular dynamics software. The results are

different from those based on classic continuum theory but are close to the results obtained from semicontinuum approach. Resonant frequency of doubly clamped silicon nanowires strongly depends on the length and thickness of the nanowire. Surface reconstruction has strong impact on the vibration behavior of the silicon nanowire, especially on the nanowire with smaller size. The results show that the classic theory may not be suitable for analysis of the vibration of silicon nanowires.

Acknowledgment

This project is supported by the National Science Foundation of China (Grant no. 61001044).

References

- [1] Y. T. Yang, C. Callegari, X. L. Feng, K. L. Ekinici, and M. L. Roukes, "Zeptogram-scale nanomechanical mass sensing," *Nano Letters*, vol. 6, no. 4, pp. 583–586, 2006.
- [2] K. L. Ekinici and M. L. Roukes, "Nanoelectromechanical systems," *Review of Scientific Instruments*, vol. 76, no. 6, Article ID 061101, 12 pages, 2005.
- [3] X. L. Feng, R. R. He, P. D. Yang, and M. L. Roukes, "Very high frequency silicon nanowire electromechanical resonators," *Nano Letters*, vol. 7, no. 7, pp. 1953–1959, 2007.
- [4] X. L. Feng, C. J. White, A. Hajimiri, and M. L. Roukes, "A self-sustaining ultrahigh-frequency nanoelectromechanical oscillator," *Nature Nanotechnology*, vol. 3, no. 6, pp. 342–346, 2008.
- [5] N. Liu, F. Giesen, M. Belov et al., "Time-domain control of ultrahigh-frequency nanomechanical systems," *Nature Nanotechnology*, vol. 3, no. 12, pp. 715–719, 2008.
- [6] E. F. Arkan, D. Sacchetto, I. Yildiz, Y. Leblebici, and B. E. Alaca, "Monolithic integration of Si nanowires with metallic electrodes: NEMS resonator and switch applications," *Journal of Micromechanics and Microengineering*, vol. 21, Article ID 125018, 9 pages, 2011.
- [7] Y. L. Yang, X. Y. Xia, X. H. Gan, P. C. Xu, H. T. Yu, and X. X. Li, "Nano-thick resonant cantilevers with a novel specific reaction-induced frequency-increase effect for ultra-sensitive chemical detection," *Journal of Micromechanics and Microengineering*, vol. 20, no. 5, Article ID 055022, 5 pages, 2010.
- [8] A. K. Naik, M. S. Hanay, W. K. Hiebert, X. L. Feng, and M. L. Roukes, "Towards single-molecule nanomechanical mass spectrometry," *Nature Nanotechnology*, vol. 4, no. 7, pp. 445–450, 2009.
- [9] M. Belov, N. J. Quidron, S. Sharma, W. K. Hiebert, T. I. Kamins, and S. Evoy, "Mechanical resonance of clamped silicon nanowires measured by optical interferometry," *Journal of Applied Physics*, vol. 103, no. 7, Article ID 074304, 7 pages, 2008.
- [10] Y. K. Feng, Y. L. Liu, and B. Wang, "Finite element analysis of resonant properties of silicon nanowires with consideration of surface effects," *Acta Mechanica*, vol. 217, no. 1-2, pp. 149–155, 2011.
- [11] C. T. Sun and H. T. Zhang, "Size-dependent elastic moduli of platelike nanomaterials," *Journal of Applied Physics*, vol. 93, no. 2, pp. 1212–1218, 2003.
- [12] J. Wang, Q. A. Huang, and H. Yu, "Size and temperature dependence of Young's modulus of a silicon nano-plate," *Journal of Physics D*, vol. 41, no. 16, Article ID 165406, 5 pages, 2008.
- [13] F. Bao, H. Yu, Q. R. Lu, and Q. A. Huang, "Multi-scale model for load-deflection of Si nanobeams," *Chinese Journal of Semiconductors*, vol. 28, no. 12, pp. 1979–1982, 2007.
- [14] Q. R. Lu, F. Bao, H. Yu, and Q. A. Huang, "A semicontinuum model of nature frequency for nanoscaled clamped silicon beam," *Chinese Journal of Sensors and Actuators*, vol. 21, no. 3, pp. 469–472, 2008.
- [15] S. H. Park, J. S. Kim, J. H. Park, J. S. Lee, Y. K. Choi, and O. M. Kwon, "Molecular dynamics study on size-dependent elastic properties of silicon nanocantilevers," *Thin Solid Films*, vol. 492, no. 1-2, pp. 285–289, 2005.
- [16] J. S. Kim, S. H. Park, J. H. Park, and J. S. Lee, "Molecular dynamics simulation of elastic properties of silicon nanocantilevers," *Nanoscale and Microscale Thermophysical Engineering*, vol. 10, no. 1, pp. 55–65, 2006.
- [17] W. J. Bottega, *Engineering Vibrations*, CRC Taylor & Francis, 2006.
- [18] H. W. Shim, L. G. Zhou, H. C. Huang, and T. S. Cale, "Nanoplate elasticity under surface reconstruction," *Applied Physics Letters*, vol. 86, no. 15, Article ID 151912, 3 pages, 2005.
- [19] L. G. Zhou and H. C. Huang, "Are surfaces elastically softer or stiffer?" *Applied Physics Letters*, vol. 84, no. 11, pp. 1940–1942, 2004.
- [20] W. W. Zhang, Q. A. Huang, H. Yu, and L. B. Lu, "Size-dependent elasticity of silicon nanowires," *Advanced Materials Research*, vol. 60-61, pp. 315–319, 2009.

Research Article

Size and Shape Dependence on Melting Temperature of Gallium Nitride Nanoparticles

Paneerselvam Antoniammal and Dakshanamoorthy Arivuoli

Crystal Growth Centre, Anna University, Chennai, Tamil Nadu 600 025, India

Correspondence should be addressed to Dakshanamoorthy Arivuoli, arivuoli@annauniv.edu

Received 19 January 2012; Revised 6 March 2012; Accepted 7 March 2012

Academic Editor: Grégory Guisbiers

Copyright © 2012 P. Antoniammal and D. Arivuoli. This is an open access article distributed under the Creative Commons Attribution License, which permits unrestricted use, distribution, and reproduction in any medium, provided the original work is properly cited.

The study of variation of the size and shape effect on the melting property of gallium nitride nanoparticles with their spherical and cylindrical geometrical feature is theoretically explored. A numerical thermodynamical model has been devoted for the study. A comparative investigation is made between the two shapes, at the range of ~ 3 nm dia. The cylindrical GaN nanoparticles, whose melting point has been reported to decrease with decreasing particle radius, become larger than spherical-shaped nanoparticles. The melting temperature obtained in the present study is in line with the function of radius of curvature.

1. Introduction

It has been well established both experimentally and theoretically that the melting temperature (T) of nanoparticles depends on the particle size [1–11]. Pawlow in 1909 developed a thermodynamical model that predicts a point depression of nanoparticles with the particle size. An attempt to confirm this experimentally has been made first by Pawlow [12] in 1910. Subsequently, other researchers have investigated the variation of melting temperature with particle size [13–17].

A numerical thermodynamical model is implemented for our exploration of the temperature distribution with respect to other size of the spherical and cylindrical nanoparticles of gallium nitride (GaN). In the last decade, GaN has been investigated intensively, both experimentally and theoretically [18–22]. It is a wide bandgap semiconductor that exists in both wurtzite and zinc blende crystal structure. All devices, currently constructed for applications with the use of wurtzite structure. Because of the wide bandgap, the intrinsic carrier concentration n_i of GaN is essentially Zero at $T = 300$ K, and n_i remains small enough so as to have a negligible effect on the operation of most of the devices until $T \approx 1000$ K. This property makes this wide bandgap material suitable for use in high-temperature environments. GaN is a very hard, mechanically stable wide bandgap

semiconductor material with high heat capacity and thermal conductivity [18]. GaN can be doped with silicon (Si) or with oxygen to n-type and with magnesium (Mg) to p-type [19]; however, the Si and Mg atoms change the way GaN crystals grow, introducing tensile stresses and making them brittle [20]. GaN compounds also tend to have a high spatial defect frequency, on the order of a hundred million to ten billion defects per square centimeter. The crystalline quality GaN led to the discovery of p-type GaN [19], p-n junction blue/UV-LEDs [19], and room-temperature-stimulated emission. The very high breakdown voltage [21] high electron mobility, and saturation velocity of GaN has also made it an ideal candidate for high-power and high-temperature microwave applications, as evidenced by its high Johnson's figure of merit. Moreover, GaN-based MOSFET and MESFET transistors also offer many advantages in high-power electronics, especially in automotive and electric car applications [22]. Nanotubes of GaN are proposed for applications in nanoscale electronics, optoelectronics, and biochemical-sensing applications. They are also useful in military electronics such as active electronically scanned array radars. A GaN nanoparticle in a BN matrix by nitridation with urea has a lot of applications. Bionanotechnology is the use of biomolecules for applications in nanotechnology, including use of viruses.

The interest has been heightened recently at the nanoscale, because nanostructures are pervasive in nature and in modern industry. We depict that the variation of the properties of GaN material with its geometrical feature size has a long history because of its importance in many fields. In physics and chemistry, the effect of particle size on melting has been discussed since 1900s, and this effect is not restricted to any particular material; rather, it is observed in a variety of materials from metals and alloys, and the typical size range over which the melting temperature undergoes a large change in the range 5–100 nm [23–31]. Many phenomena in solid-state physics and materials science also exhibit size dependence. For example, the elastic constants of Ag and Pb nanowires of diameter 30 nm are nearly twice those of the bulk metals [32]. Such increase in stiffness cannot be explained by structural modifications of the materials as the nanoscale reduction in the size of the solids also results in a change of their failure mode.

Thus, when the size of brittle calcium carbonate particles is reduced to a critical value of 850 nm [33, 34], the particles behave as if they were ductile. Size dependence of the melting temperature at nanoscale has enormous implications in the production of nanocrystals and in the thermal stability of quantum dots. A large data has accumulated on this size dependence, and a number of theoretical models have been proposed to explain it. Thermodynamically, the melting temperature of nanoparticles has been described by three models: (1) the homogeneous melting and growth, (2) the liquid shell nucleation, and (3) the liquid nucleation and growth. All the three models predict a size-dependent melting temperature.

The melting temperature of the nanoparticles will be different in different shapes when considering the radius of curvature of nanoparticles; especially the particle size is mentioned with respect to its radius of curvature. Therefore, an indispensable course of action to take the particle size into consideration is when one develops the models for the melting temperature of nanoparticles. In the present work, the radius of curvature is considered to account for the particle shape difference and develop the model for the cylindrical nanoparticles. According to the relation between the melting temperature and radius of curvature of the nanoparticles, an expression (15) for the size- and shape-dependent melting temperature of nanoparticles is developed. The theoretical prediction of this expression for the melting temperature of GaN nanoparticles is compared between spherical and cylindrical shapes.

2. Model of Calculation

2.1. Surface Energy Calculation. It is known that the total surface energy involved in any heterogeneous nucleation is given as

$$\begin{aligned} \text{total surface energy} &= \text{free surface energy} \\ &+ \text{interfacial energy} \\ &+ \text{substrate energy.} \end{aligned} \quad (1)$$

It has been assumed that the geometry of the heterogeneous nucleation is that of the cylindrical-shaped particle. So the equation can be written as

$$\Gamma = 2\pi RH\gamma_s + \pi H(2R - H)(\gamma_{sb} - \gamma_b) + \Gamma_b, \quad (2)$$

where R, H are the radius and the height of the cylindrical nanoparticle on the substrate, γ_s is the surface energy of the solid vapor interface, γ_b is the surface energy of the bare substrate, γ_{sb} is the interfacial energy between the solid and the substrate and Γ_b is the total energy of the substrate.

Now, (2) can be minimized by using the condition

$$\frac{\partial \Gamma}{\partial R} + \frac{\partial \Gamma}{\partial H} = 0. \quad (3)$$

To find the relationship between R and H , substituting (2) in (3), we get

$$H = \frac{\Delta\gamma_{sb}}{\gamma_s} R, \quad (4)$$

where $\Delta\gamma_{sb}$ is a parameter called wetting or spreading parameter which is given by

$$\Delta\gamma_{sb} = \gamma_b - \gamma_s - \gamma_{sb}. \quad (5)$$

The magnitude of the wetting or spreading parameter ($\Delta\gamma_{sb}$) is used to determine whether the surface melting takes place or not in the given substrate. If the magnitude of the spreading parameter is positive, that is, $\Delta\gamma_{sb} > 0$, then there is a possibility of wetting the substrate, and if it is negative, that is, $\Delta\gamma_{sb} < 0$, then the surface melting takes place.

In the case of nanofilms, the free surface energy of the solid is always higher than the energy density of the bare substrate, thus, $\Delta\gamma_{sb}$ is always less than zero and it is negative. From (5), it is seen clearly that if $\Delta\gamma_{sb}$ is negative, then H is also negative, and this is not possible. Thus, to keep H positive, a negative sign is included in (4), that is,

$$H = -\frac{\Delta\gamma_{sb}}{\gamma_s} R. \quad (6)$$

Substituting the value of H (height of the spherical nanoparticle on the substrate) in (3), we get

$$\Gamma^* = 2\pi\gamma_s \left(\frac{a}{R_s}\right) a^2 + \Gamma_b. \quad (7)$$

R_s^* is the corresponding radius of curvature of supported spherical nanoparticle, and it is given by

$$R_s^* = \left[\frac{1}{2}\right]^{1/3} \left[\frac{2\gamma_s}{\Delta\gamma_{sb}}\right]^{2/3} \frac{a}{[3 + \Delta\gamma_{sb}/\gamma_s]^{1/3}}, \quad (8)$$

where Γ^* is the equilibrium surface energy, and R_s^* is the corresponding radius of curvature of the supported gallium

nitride (GaN) solid spherical nanoparticles [35] and it is given by

$$R_s^* = L_G \left(1 - \frac{\delta(4\gamma_s^2\pi^2)^3}{[r(4\gamma_s^2\pi^2) + (\gamma_b - \gamma_s - \gamma_{sb})^2]^3} \right), \quad (9)$$

where L_G is latent heat of melting material of GaN, δ is fitting parameter, and it is a measure of GaN solid shell.

Similarly, the corresponding radius of curvature of the GaN nanoparticle with liquid film surrounding the solid [35] R_l^* is given as

$$R_l^* = L_G \left(1 - \frac{\delta(4\gamma_l^2\pi^2)^3}{[r(4\gamma_l^2\pi^2) + (\gamma_b - \gamma_l - \gamma_{lb})^2]^3} \right), \quad (10)$$

where γ_l is the free surface energy of the liquid-vapors interface, and γ_{lb} is the interfacial energy between the liquid and substrate. The basic formula for the radius of curvature of cylindrical nanoparticle which is used in the above expression has been attached in the Appendix [35].

2.2. Melting Point Calculation. The expression for the melting of nanoparticle can be derived using free energies density of solid and liquid. The free energy density expression for the solid (F_s) and the corresponding liquid (F_l) are given as follows [36]:

$$\begin{aligned} F_s &= \frac{4}{3}\pi a^3 \rho f_s + 4\pi a^3 \rho \frac{\gamma_s}{R_s^*}, \\ F_l &= \frac{4}{3}\pi a^3 \rho f_l + 4\pi a^3 \rho \frac{\gamma_l}{R_l^*}, \end{aligned} \quad (11)$$

where a is the radius of the melting of nanoparticle, f_s is the surface energy of solid, and f_l is the surface energy of liquid. Now the difference in free energies (ΔF) is calculated to be

$$\begin{aligned} \Delta F &= F_s - F_l, \\ \Delta F &= \frac{4}{3}\pi a^3 \rho \left[(f_s - f_l) + 3 \left(\frac{\gamma_s}{R_s^*} - \frac{\gamma_l}{R_l^*} \right) \right]. \end{aligned} \quad (12)$$

It is already known that

$$f_l - f_s = \rho L \left(1 - \frac{T}{T_c} \right), \quad (13)$$

where ρ is the density of the materials, L is the latent heat of the material, T_c is the bulk melting temperature, and T is the melting point of the nanomaterial as a function of size. At melting point the difference in free energies is zero, that is, $\Delta F = 0$. Substituting the above two equations, we get

$$T_m = T_c \left(1 - \frac{2}{\rho L} \left(\frac{\gamma_s}{R_s^*} - \frac{\gamma_l}{R_l^*} \right) \right). \quad (14)$$

If $R_s^* = R_l^* = R^*$, that is, if no surface melting takes place then, $T_m = T_m^{\text{free}}(R^*)$. T_m^{free} is the melting point of nanofilms with free interfacial energy between liquid and substrate.

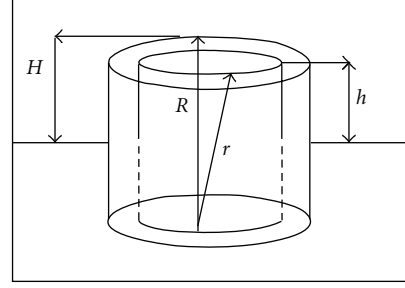


FIGURE 1: H : height of cylindrical particle with quasiliquid film. R : radius of curvature of quasi liquid film formed on the core cylindrical solid particle. r : radius of curvature of the core cylindrical solid particle. h : height of the core cylindrical solid particle.

Thus, the expression for melting point for nanofilms (T_m) as a function of radius of the particle is given as follows:

$$T_m = T_m^{\text{free}} \left(1 - \frac{2}{\rho L} \left(\frac{\gamma_s}{R_s^*} - \frac{\gamma_l}{R_l^*} \right) \right). \quad (15)$$

Using the expression above, the variation of the melting point with respect to the GaN particle can be plotted.

Similarly, the expression for the melting point GaN nanofilms as a function of the radius of the particle [35] is given as

$$T_{\text{GN}} = T \left[1 - \frac{2}{\rho_s L_G} \left(\frac{\gamma_s}{R_s} - \frac{\gamma_l}{R_l} \left(\frac{\rho_s}{\rho_l} \right)^{2/3} \right) \right], \quad (16)$$

where T_{GN} is the temperature of nanoparticle of GaN, T is the Bulk melting temperature of GaN, ρ_s Density of GaN solid phase, ρ_l is the density of GaN liquid phase, L_G is the latent heat of melting GaN material, γ_s is the surface energy of solid GaN, γ_l is the surface energy of liquid GaN, R_s is the radius of curvature of supported GaN nanoparticle, and R_l is the radius of curvature of nanoparticle with liquid film.

2.3. Surface Melting Calculations. The schematic diagram for the surface melting is as shown in Figure 1. A quasiliquid film of radius R is formed on the core solid particle of radius r . The difference between R and r gives the thickness of the liquid film.

At the onset of surface melting, we assume that the geometry is close to that of the solid particle in a quasiliquid film of radius of curvature R formed on the core solid particle of radius of curvature r . The difference between R and r gives the thickness of the liquid film. The solid particle is in its equilibrium geometry and it is initially wet by a molten layer with uniform thickness. The radius of curvature of solid particle is r and height is h [35].

Liquid film thickness is given as

$$\delta = H - h = R - r. \quad (17)$$

The total energy of the surface-melted particle is then a function of δ and is given as

$$F(\delta) = V_s(\delta)(f_s - f_l) + V_l f_l + \Gamma(\delta), \quad (18)$$

where V_s is the volume of the solid, V_l is the volume of the liquid, $\Gamma(\delta)$ is the thickness-dependent surface energy.

3. Results and Discussion

The crystal shape and the supporting substrate influence the size dependence of melting point, where the cylindrical shape is considered. The mentioned gallium nitride (GaN) nanoparticles are extremely small in 1–100 nm range. There is a considerable difference in the calculated values of the melting point as a function of size of the particle. It is known that the radius of curvature varies according to the shapes of the nanoparticle which decide the size of the particle.

The main difference between (8) and other expression (9) for the size-dependent melting temperature is that the radius of curvature of spherical and cylindrical shape is considered in (8) and (9), respectively, and derived using a separate helical method which is given in the Appendix. Based on expression (8), corresponding melting point for GaN is obtained in expression (15).

Using the expressions (8) and (15), the size of the supported spherical nanoparticle is calculated and also the variation of the melting point, which is listed in Table 1.

Similarly, using the expressions (9) and (16), the size of the supported cylindrical nanoparticle is calculated and also the variation of the melting point, which is listed in Table 2. The thickness of the quasiliquid film is plotted as a function of the size of the supported nanoparticles.

3.1. Melting Point versus Radius of the Particle. Using the data for the gallium nitride (GaN) nanofilms in the expression that is derived for melting point, the variation of the melting point with respect to the size of the supported nanoparticles can be tabulated. Using Tables 1 and 2, the melting point can be plotted against the radius of the supported spherical and cylindrical nanoparticles, respectively.

From Figures 2 and 3, it can be clearly seen that with decrease in size of the supported nanoparticles, the melting point reduces. It is also seen that there is a variation in the melting point for free nanoparticles and the nanofilms. Thus, the effect of substrate is determined.

An important part of our present work is a comparative study of GaN film between spherical and cylindrical nanoparticles has been done, and the theoretical calculated values are tabulated in Table 3, comparative Figure 4 plotted by the tabulated values shows the variation of melting point of GaN nanofilms against the size of the spherical and cylindrical nanoparticles.

In this, it is clearly shown that the melting temperature decreases when the particle size reduces little more in the case of cylindrical than the spherical nanoparticle. At nanoscales, particles exhibit many thermophysical features distinct from those found at microscales. As the size decreases beyond

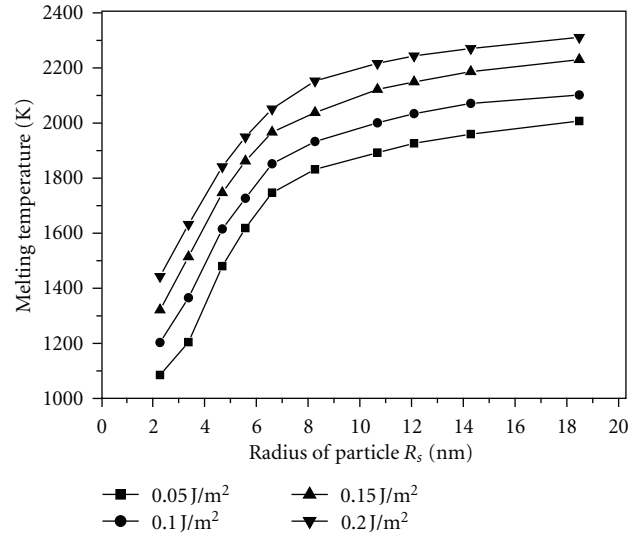


FIGURE 2: Variation of melting point of GaN spherical nanoparticles against the size of the particles.

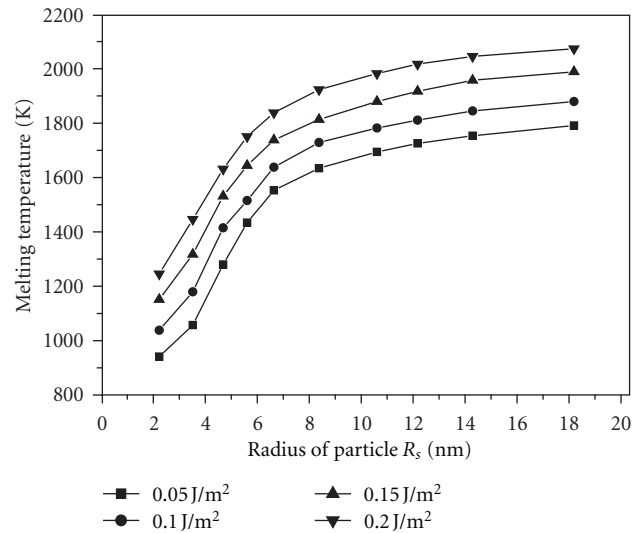


FIGURE 3: Variation of melting point of GaN cylindrical nanoparticles against the size of the particles.

a critical value, due to the increase in the surface-to-volume ratio, the melting temperature deviates from the bulk values and becomes a size-dependent property. This phenomenon has been studied experimentally by means of transmission electron diffraction by Wronski for nanosized tin [37]. The melting point agrees reasonably well with the predictions based on classical theories, which show a nonlinear relationship with the reciprocal of the particle size. The melting temperature of gallium nitride (GaN) becomes size dependent for particles smaller than 10 nm, reducing from 1618 K range for a 5 nm particle.

Pawlow [1] improved the Gibbs-Thompson model by considering the equilibrium of a liquid spherical drop with both a solid spherical particle of the same material and

TABLE 1: Variations in melting point of GaN spherical nanoparticles against the size of the particles.

S. no.	R_s (nm)	$1/R_s$ (nm) ⁻¹	T_{GN} (K)			
			$\gamma_{lb} = 0.05$ J/m ²	$\gamma_{lb} = 0.10$ J/m ²	$\gamma_{lb} = 0.15$ J/m ²	$\gamma_{lb} = 0.20$ J/m ²
1	2.28	0.439	1085.07	1203.18	1321.29	1443.12
2	3.38	0.296	1204.39	1365.48	1514.15	1632.27
3	4.69	0.213	1480.29	1615.33	1747.07	1841.65
4	5.58	0.179	1618.64	1726.84	1861.88	1949.85
5	6.61	0.151	1747.07	1851.97	1966.78	2051.33
6	8.27	0.121	1831.74	1932.92	2037.81	2152.92
7	10.68	0.094	1892.44	2000.64	2122.06	2216.63
8	12.10	0.083	1926.31	2034.11	2149.32	2243.89
9	14.29	0.069	1959.76	2071.26	2186.48	2270.73
10	18.48	0.054	2007.25	2101.82	2230.26	2311.21

TABLE 2: Variations in melting point of GaN cylindrical nanoparticles against the size of the particles.

S. no.	R_s (nm)	$1/R_s$ (nm) ⁻¹	T_{GN} (K)			
			$\gamma_{lb} = 0.05$ J/m ²	$\gamma_{lb} = 0.10$ J/m ²	$\gamma_{lb} = 0.15$ J/m ²	$\gamma_{lb} = 0.20$ J/m ²
1	2.23	0.448	941.41	1038.43	1151.56	1245.51
2	3.52	0.284	1057.22	1179.55	1317.61	1446.46
3	4.69	0.213	1280.02	1415.01	1531.21	1631.29
4	5.61	0.178	1433.81	1515.48	1643.95	1750.56
5	6.64	0.151	1553.06	1637.81	1737.91	1838.37
6	8.38	0.118	1634.36	1728.71	1813.45	1923.12
7	10.61	0.094	1694.18	1782.01	1879.41	1982.56
8	12.17	0.082	1725.63	1810.98	1916.99	2017.07
9	14.29	0.071	1753.62	1844.89	1957.64	2045.45
10	18.19	0.055	1791.21	1879.41	1989.08	2073.83

its vapor. This model leads to the following Well-Lenon Equation (15). The suggestion that the melting point of a particle should depend on its size is implicit in the work Thomson [38].

It is well known that the melting temperature of Au (1064 K) decreases when particle dimensions are reduced to the nanoscale. Therefore, at ~ 3 nm diameter, Au particle can melt at temperature ~ 500 K [23, 39, 40]. Similarly, the melting temperature of B₄C (2450 K) lowered to ~ 764 K range with spherical-shaped and ~ 495 K ranges with cylindrical shaped nanoparticles at ~ 3 nm dia [35]. In the present work, the melting temperature of GaN (2770 K) decreases significantly when the particle dimensions are reduced to the nanoscale and we got that an ~ 3 nm diameter of GaN spherical shaped particle melted at temperature ~ 1747 K range, but the same particle with an ~ 3 nm diameter melted at the temperature ~ 1553 K range, since the particle shape is considered in cylindrical shape.

3.2. Melting Point versus Inverse of the Radius of the Particle. In Figures 5 and 6 there are two regions namely, logarithmic increases at low values of radius and an exponential increase at the higher values of radius. A linear figure (Figures 5 and 6)

between melting point and the inverse of the radius of the particle is drawn.

3.3. Thickness of the Liquid Film versus Radius of the Particle. From Figure 2 it can be seen clearly that with increased in the radius of the supported nanoparticles, it increases up to certain limit after which it is saturated. The melting temperature is a function of the particle radius evaluated from the calculations and the analytical formulation reported in Buffat and Borel [23]. In that, the calculation of latent heat is a function of the particle radius, which is valid for small particle with spherical shape, and it is the radius of curvature varies according to the shape of the particle. The obtained expression (9) because is for the corresponding radius of curvature of the GaN solid cylindrical nanoparticle. Similarly, the expression (16) obtained for the melting point of GaN nanofilms is a function of radius of the particle.

Melting-point depression is most evident in nanowires, nanotubes, and nanoparticles, which all melt at lower temperatures than bulk amounts of the same material. Changes in melting point occur because nanoscale materials have a much larger surface-to-volume ratio than bulk materials, drastically altering their thermodynamic and thermal properties. The decrease in melting temperature can be on

TABLE 3: Comparative study of GaN film between spherical and cylindrical nanoparticle.

S. no.	R_s (nm)		T_m (K)							
			$\gamma_{lb} = 0.05 \text{ J/m}^2$		$\gamma_{lb} = 0.10 \text{ J/m}^2$		$\gamma_{lb} = 0.15 \text{ J/m}^2$		$\gamma_{lb} = 0.20 \text{ J/m}^2$	
	S	C	S	C	S	C	S	C	S	C
1	2.28	2.23	1085.07	941.41	1203.18	1038.43	1321.29	1151.56	1443.12	1245.51
2	3.38	3.52	1204.39	1057.22	1365.48	1179.55	1514.15	1317.61	1632.27	1446.46
3	4.69	4.69	1480.29	1280.02	1615.33	1415.01	1747.07	1531.21	1841.65	1631.29
4	5.58	5.61	1618.64	1433.81	1726.84	1515.48	1861.88	1643.95	1949.85	1750.56
5	6.61	6.64	1747.07	1553.06	1851.97	1637.81	1966.78	1737.91	2051.33	1838.37
6	8.27	8.38	1831.70	1634.36	1932.92	1728.71	2037.81	1813.45	2152.92	1923.12
7	10.68	10.61	1892.44	1694.18	2000.64	1782.01	2122.06	1879.41	2216.63	1982.56
8	12.10	12.17	1926.31	1725.63	2034.11	1810.98	2149.32	1916.99	2243.89	2017.07
9	14.29	14.29	1959.76	1753.62	2071.26	1844.89	2186.48	1957.64	2270.73	2045.45
10	18.48	18.19	2007.25	1791.21	2101.82	1879.41	2230.26	1989.08	2311.21	2073.83

Note: C: cylindrical Nanoparticle/S: spherical Nanoparticle.

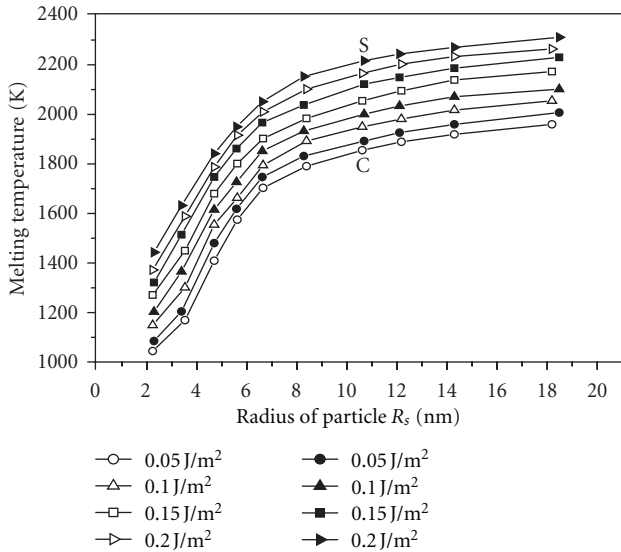


FIGURE 4: Comparative study of GaN film between spherical and cylindrical nanoparticles.

the order of tens to hundreds of degrees for metals with nanometer dimensions [41–44]. Surface atoms bind in the solid phase with less cohesive energy because they have fewer neighboring atoms in close proximity compared to atoms in the bulk of the solid. Each chemical bond an atom shares with a neighboring atom provides cohesive energy, so atoms with fewer bonds and neighboring atoms have lower cohesive energy. The average cohesive energy per atom of a nanoparticle has been theoretically calculated as a function of particle size [45].

Atoms located at or near the surface of the nanoparticle have reduced cohesive energy due to a reduced number of cohesive bonds. An atom experiences an attractive force with all nearby atoms according to the Lennard-Jones potentials [46]. The cohesive energy of an atom is directly related to

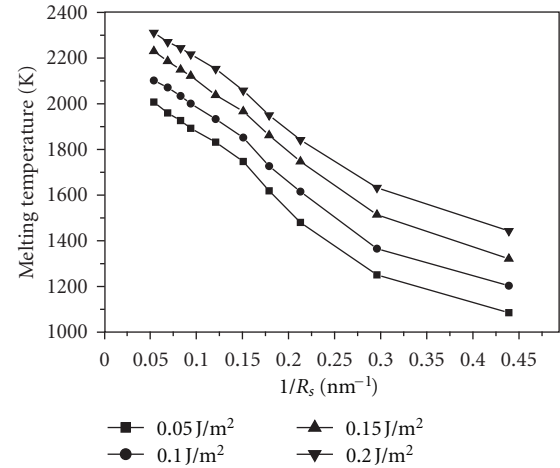


FIGURE 5: Variation of the melting point of GaN with inverse of radius of the particle in the spherical shape.

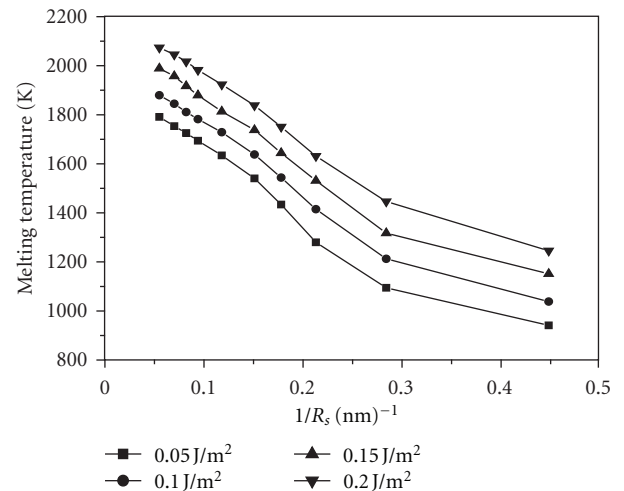


FIGURE 6: Variation of the melting point of GaN with inverse of radius of the particle in the cylindrical shape.

the thermal energy required to free the atom from the solid. Since atoms near the surface have fewer bonds and reduced cohesive energy, they require less energy to be free from the solid phase. Melting point depression of high surface-to-volume ratio materials results from this effect [47]. The liquid drop model (LDM) represents the binding energy of a nanoparticle as a function of the free energies of the volume and surface [46]. The liquid shell nucleation model (LSN) predicts that a surface layer of atoms melts prior to the bulk of the particle [48]. The melting temperature of a nanoparticle is a function of its radius of curvature according to the LSN. The bond-order-length-strength (BOLS) model calculates the melting temperature for individual atoms from the sum of their cohesive bonds. As a result, the BOLS predicts the surface layers of a nanoparticle melt at lower temperatures than the bulk of the nanoparticle [49]. The lowered coordination number changes the equilibrium bond length between atoms near the surface of the nanoparticle. The integrated cohesive energy for surface atoms is much lower than bulk atoms due to the reduced coordination number and overall decrease in cohesive energy.

Nanoparticle shape impacts the melting point of a nanoparticle. Facets, edges, and deviations from a perfect sphere all change the magnitude of melting point depression [46]. These shape changes affect the surface-to-volume ratio, which affects the cohesive energy and thermal properties of a nanostructure. The cohesive energy of nanocrystals, which can be determined by experiment [50] and computed by different theoretical models such as the SE model [51], the BE model [52], the Lennard-Jones potential model [53], Jiang's model [54], the liquid-drop model [55–57], and the bond-OLS model [58, 59], is regarded as directly related to the nature of the thermal stability of nanocrystals [60].

In observing the evolution of numerical thermodynamical model yields the calculated data, which is compared to the melting point of spherical nanoparticle, the cylindrical nanoparticle has low melting point, since the surface area of cylindrical nanoparticle (169.56 nm^2 at $\sim 3 \text{ nm}$ radius range) is larger than the spherical (113.04 nm^2 at $\sim 3 \text{ nm}$ radius range). The number of atoms present on the surface will have only fewer neighboring atoms. Hence, on the larger surface, the more number of atoms will have fewer neighboring atoms in close proximity compared to atoms in the bulk of the nanomaterial. Each chemical bond of an atom shared with a neighboring atom provides cohesive energy, so atom with fewer bonds and neighboring atoms have lower cohesive energy; they require less energy to be free from the solid phase. Hence, melting point depression of high surface (cylindrical shape) is reduced more than the lower surface (spherical shape) nanoparticles. It should be mentioned that the radius of curvature with respect to the shape of the nanoparticle and as the present work describes the melting temperature effect on the shape difference between the spherical nanoparticles and cylindrical nanoparticles. This same property of GaN nanowires with triangular cross-section has been studied using molecular dynamics simulation, in that it was reported that the melting temperature of the GaN nanowires increases with increasing cross-sectional area to a saturation value [61]. The “approximately” is

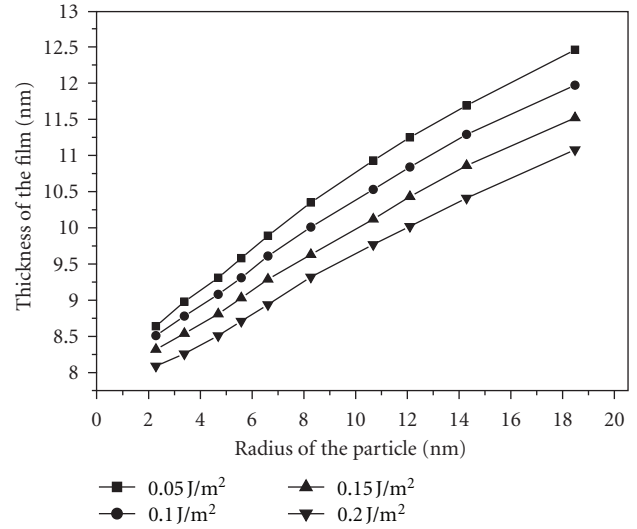


FIGURE 7: Variation of the thickness of the liquid film against radius of GaN spherical particles.

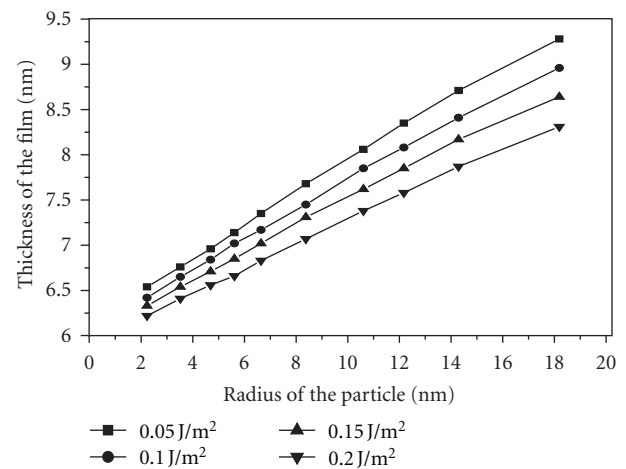


FIGURE 8: Variation of the thickness of the liquid film against radius of GaN cylindrical particles.

stressed here due to the fact that some different shape of the nanoparticle may have different radius of curvature which decides the particle size. However, present calculation shows that the present radius of curvature expression is enough for predicting the shape-dependent size effect on the temperature of nanoparticle. This method could be used to study the nanoparticles, and it can be experimentally determined by measuring the particle shape with radius of curvature, which is subjected to future experiments.

It is reported that the atomic radius of metallic nanoparticles contracts with decreasing their particle size, which means that the atomic radius will change a little if the particle size is small. The thickness of the liquid film against the radius of the supported nanoparticle is also done for GaN which has been given in the tabulation (Tables 4 and 5) and in Figures 7 and 8.

TABLE 4: The thickness of the liquid films is tabulated against the radius of the supported spherical nanoparticles.

S. no.	R_s (nm)	δ (nm)			
		$\gamma_{lb} = 0.05 \text{ J/m}^2$	$\gamma_{lb} = 0.10 \text{ J/m}^2$	$\gamma_{lb} = 0.15 \text{ J/m}^2$	$\gamma_{lb} = 0.20 \text{ J/m}^2$
1	2.28	8.64	8.51	8.32	8.09
2	3.38	8.98	8.78	8.54	8.26
3	4.69	9.31	9.08	8.81	8.51
4	5.58	9.58	9.31	9.03	8.71
5	6.61	9.89	9.61	9.29	8.94
6	8.27	10.35	10.01	9.63	9.32
7	10.68	10.93	10.53	10.12	9.77
8	12.10	11.25	10.84	10.43	10.02
9	14.29	11.69	11.29	10.86	10.41
10	18.48	12.46	11.97	11.52	11.08

TABLE 5: The thickness of the liquid films is tabulated against the radius of the supported cylindrical nanoparticles.

S. no.	R_s (nm)	δ (nm)			
		$\gamma_{lb} = 0.05 \text{ J/m}^2$	$\gamma_{lb} = 0.10 \text{ J/m}^2$	$\gamma_{lb} = 0.15 \text{ J/m}^2$	$\gamma_{lb} = 0.20 \text{ J/m}^2$
1	2.23	6.54	6.42	6.33	6.22
2	3.52	6.76	6.65	6.54	6.41
3	4.69	6.96	6.84	6.71	6.56
4	5.61	7.14	7.02	6.85	6.66
5	6.64	7.35	7.17	7.02	6.83
6	8.38	7.68	7.45	7.31	7.07
7	10.61	8.06	7.85	7.62	7.38
8	12.17	8.35	8.08	7.85	7.58
9	14.29	8.71	8.41	8.17	7.87
10	18.19	9.28	8.96	8.64	8.31

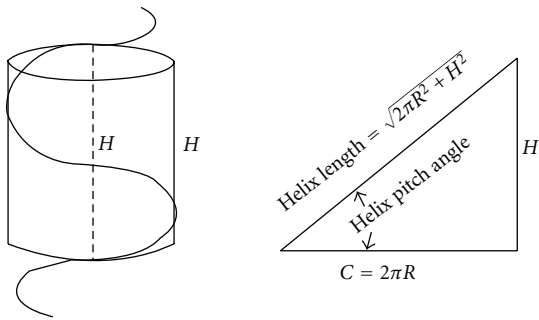


FIGURE 9

The regulation of nanotechnology has made a growing debate related to the human health and safety risks associated with nanotechnology [62]. An important property of the material, the melting temperature of GaN, was predicted by top-down approach through classical thermodynamics [63]. Hence, the phenomenon of size and shape effect on melting temperature of nanoparticles is utilized in nanotechnology field. The expression for the size-dependent melting temperature of nanoparticles in present work is derived from their size-dependent radius of curvature according to the shape of the nanoparticles. It should be mentioned that, according to

the shape of the nanoparticles, the radius of curvature varies. And it should be noted that the particle size-dependent on its radius of curvature. Similar melting phenomena have been reported for Au nanoparticles [19], and the melting temperature of prism-shaped nanoparticles [26] and especially for B4C nanoparticles [45] had been analyzed. It has been argued that substrate-particle interaction plays a significant role in the melting behavior of nanoparticles. It has also been shown that the extrapolated bulk melting temperature is lower than the experimental value. It has also been noted by different researchers that the bulk melting temperature cannot be extrapolated from the nanoscale results [64]. In our present work, we showed that the melting temperature of GaN decreased when the size of the nanoparticle reduced. Moreover this reduction is little more in cylindrical nanoparticle when compared with spherical nanoparticle.

4. Conclusion

The present exploration showed, the size- and shape-dependent temperature of GaN nanoparticles, using the numerical thermodynamical model, where spherical and cylindrical shapes of the nanoparticle are considered with respect to its radius of curvature. It is shown that the present

results of the melting temperature of GaN nanoparticles consistently decrease with the size of the nanoparticle. The cylindrical GaN nanoparticles, whose melting point has been decreased with decreasing particle radius, become larger than spherical-shaped nanoparticle. Further, it is found that the particle shape can affect the melting temperature of nanoparticles, and this effect on the melting temperature becomes larger with decreasing particle size. Because melting temperature is a very important parameter, the model developed in the present investigation may have potential applications in the temperature-related phenomena of nanoparticles.

Appendix

The following formula for radius of curvature of a cylinder (by Helix method) (see Figure 9):

$$\begin{aligned} \text{Helix length} &= c \times \frac{c}{\text{helix length}}, \\ C = \text{helix length} \times \frac{\text{helix length}}{c} &= 2\pi R^*, \\ R^* &= \frac{\sqrt{(2\pi R^*)^2 + H^2} \times \sqrt{(2\pi R)^2 + H^2}}{2\pi \times 2\pi R}, \\ 2\pi R^* &= \sqrt{(2\pi R^*)^2 + H^2} \times \sqrt{\frac{(2\pi R)^2 + H^2}{2\pi R}}, \\ R^* &= \frac{(\pi/2)^2 R^2 + (H/4)^2}{(\pi/2)^2 R}, \end{aligned} \quad (\text{A.1})$$

where H : Height required for helix to complete one revolution about the cylinder, c : Circumference of cylinder, R : Radius of cylinder, C : Circumference of baluster circle, R^* : Radius of curvature of cylinder.

By using the above expression, the radius of curvature of solid cylindrical nanoparticle is obtained as

$$R_s^* = \frac{R \left[(4\gamma_s^2 \pi^2) + (\gamma_b - \gamma_s - \gamma_{sb})^2 \right]}{4\gamma_s^2 \pi^2}. \quad (\text{A.2})$$

Similarly, the corresponding radius of curvature of the nanoparticle with a liquid film surrounding the solid is calculated to be

$$R_l^* = \frac{R \left[(4\gamma_l^2 \pi^2) + (\gamma_b - \gamma_s - \gamma_{lb})^2 \right]}{4\gamma_l^2 \pi^2}. \quad (\text{A.3})$$

where γ_l is the free surface energy of the liquid-vapor interface and is the interfacial energy between the liquid and substrate.

References

- [1] P. Pawlow, "The dependency of the melting point on the surface energy of a solid body," *Zeitschrift für Physikalische Chemie*, vol. 65, no. 5, pp. 545–548, 1909.
- [2] D. K. Sar, P. Nayak, and K. K. Nanda, "Thermodynamic model for the size-dependent melting of prism-shaped nanoparticles," *Physics Letters A*, vol. 372, no. 25, pp. 4627–4629, 2008.
- [3] I. Gulseren and J. N. Coupland, "Surface melting in alkane emulsion droplets as affected by surfactant type," *Journal of the American Oil Chemists' Society*, vol. 85, no. 5, pp. 413–419, 2008.
- [4] W. H. Qi, "Size effect on melting temperature of nanosolids," *Physica B*, vol. 368, no. 1–4, pp. 46–50, 2005.
- [5] G. Guisbiers and M. Wautelet, "Size and stress effects on the melting temperature of nano-polyhedral grains on a substrate," *Nanotechnology*, vol. 17, no. 8, pp. 2008–2011, 2006.
- [6] A. S. Shirinyan, A. M. Gusak, and M. Wautelet, "Melting and superheating of nanowires," *Acta Materialia*, vol. 55, article 5025, 2005.
- [7] G. Guisbiers, O. van Overschelde, and M. Wautelet, "Nanoparticulate origin of intrinsic residual stresses in thin films," *Acta Materialia*, vol. 55, article 3541, 2007.
- [8] C. Q. Sun, Y. Wang, B. K. Tay, S. Li, H. Huang, and Y. B. Zhang, "Correlation between the melting point of a nanosolid and the cohesive energy of a surface atom," *Journal of Physical Chemistry B*, vol. 106, no. 41, pp. 10701–10705, 2002.
- [9] C. Kan, G. Wang, X. Zhu, C. Li, and B. Cao, "Structural and thermal stability of gold nanoparticle," *Applied Physics Letters*, vol. 88, Article ID 071904, 2006.
- [10] H. H. Farrell, "Surface bonding effects in compound semiconductor nanoparticles: II," *Journal of Vacuum Science and Technology B*, vol. 26, no. 4, pp. 1534–1541, 2008.
- [11] A. Jiang, N. Awasthi, A. N. Kolmogorov et al., "Theoretical study of the thermal behavior of free and alumina-supported Fe–C nanoparticles," *Physical Review B*, vol. 75, no. 20, Article ID 205426, 2007.
- [12] P. Pawlow, "Size dependent melting properties of Bi nanoparticles by molecular dynamics simulation," *Physical Chemistry*, vol. 74, article 562, 1910.
- [13] T. Bachelis, H. J. Guntherodt, and R. Schafer, "Melting of isolated tin nanoparticles," *Physical Review Letters*, vol. 85, no. 6, pp. 1250–1253, 2000.
- [14] E. A. Olsan, M. Yu. Efremov, M. Zhang, Z. Zhang, and L. H. Allen, "Size-dependent melting of Bi nanoparticles," *Journal of Applied Physics*, vol. 97, no. 3, Article ID 034304, 9 pages, 2005.
- [15] M. Zhang, M. Y. Efremov, F. Schiettekatte et al., "Size-dependent melting point depression of nanostructures: nanocalorimetric measurements," *Physical Review B*, vol. 62, no. 15, pp. 10548–10557, 2000.
- [16] M. D. McCluckey, Y. M. Gupta, C. G. van de Walle, D. P. Bour, M. Kneissl, and N. M. Johnson, "Band gap changes of GaN shackled to BGpa," *Applied Physics Letters*, vol. 80, pp. 1912–1914, 2002.
- [17] X. W. Wang, G. T. Fei, K. Zheng, Z. Jin, and L. de Zhang, "Size-dependent melting behavior of Zn nanowire arrays," *Applied Physics Letters*, vol. 88, no. 17, Article ID 173114, 2006.
- [18] G. Mula, C. Adelman, S. Moehl, J. Oullier, and B. Daudin, "Surfactant effect of gallium during molecular-beam epitaxy of GaN on AlN (0001)," *Physical Review B*, vol. 64, no. 19, Article ID 195406, pp. 1954061–19540612, 2001.
- [19] B. Heying, R. Aeverbeck, L. F. Chen, E. Haus, H. Riechert, and J. S. Speck, "Control of GaN surface morphologies using plasma-assisted molecular beam epitaxy," *Journal of Applied Physics*, vol. 88, no. 4, pp. 1855–1860, 2000.
- [20] L. X. Zheng, M. H. Xie, S. M. Seutter, S. H. Cheung, and S. Y. Tong, "Observation of 'ghost' islands and surfactant effect of surface gallium atoms during GaN growth by molecular beam epitaxy," *Physical Review Letters*, vol. 85, no. 11, pp. 2352–2355, 2000.

- [21] C. Adelman, J. Brault, G. Mula, B. Daudin, L. Lymperakis, and J. Neugebauer, "Gallium adsorption on (0001) GaN surfaces," *Physical Review B*, vol. 67, no. 16, Article ID 165419, pp. 1654191–1654199, 2003.
- [22] G. Koblmüller, R. Averbeck, H. Riechert, and P. Pongratz, "Direct observation of different equilibrium Ga adlayer coverages and their desorption kinetics on GaN (0001) and (0001) surfaces," *Physical Review B*, vol. 69, no. 3, Article ID 035325, pp. 353251–353259, 2004.
- [23] P. H. Buffat and J. P. Borel, "Size effect on the melting temperature of gold particles," *Physical Review A*, vol. 13, no. 6, pp. 2287–2298, 1976.
- [24] P. R. Couchman and W. A. Jesser, "Thermodynamic theory of size dependence of melting temperature in metals," *Nature*, vol. 269, no. 5628, pp. 481–483, 1977.
- [25] T. Castro, R. Reifengerger, E. Choi, and R. P. Andres, "Size-dependent melting temperature of individual nanometer-sized metallic clusters," *Physical Review B*, vol. 42, no. 13, pp. 8548–8556, 1990.
- [26] K. F. Peters, J. B. Cohen, and Y. W. Chung, "Melting of Pb nanocrystals," *Physical Review B*, vol. 57, no. 21, pp. 13430–13438, 1998.
- [27] M. Zhao, X. H. Zhou, and Q. Jiang, "Comparison of different models for melting point change of metallic nanocrystals," *Journal of Materials Research*, vol. 16, no. 11, pp. 3304–3307, 2001.
- [28] K. Dick, T. Dhanasekaran, Z. Zhang, and D. Meisel, "Size-dependent melting of silica-encapsulated gold nanoparticles," *Journal of the American Chemical Society*, vol. 124, no. 10, pp. 2312–2317, 2002.
- [29] K. K. Nanda and S. C. Vanithakumari, "A universal relation for the cohesive energy of nanoparticles," *Physics Letters A*, vol. 372, no. 46, pp. 6930–6934, 2008.
- [30] C. Q. Sun, Y. Wang, B. K. Tay, S. Li, H. Huang, and Y. B. Zhang, "Correlation between the melting point of a nanosolid and the cohesive energy of a surface atom," *Journal of Physical Chemistry B*, vol. 106, no. 41, pp. 10701–10705, 2002.
- [31] W. A. Jesser, R. Z. Shneck, and W. W. Gile, "Solid-liquid equilibria in nanoparticles of Pb–Bi alloys," *Physical Review B*, vol. 69, no. 14, Article ID 144121, 13 pages, 2004.
- [32] S. Cuenot, C. Fretigny, S. D. Champagne, and B. Nysten, "Surface tension effect on the mechanical properties of nanomaterials measured by atomic force microscopy," *Physical Review B*, vol. 69, no. 16, Article ID 165410, 5 pages, 2004.
- [33] K. Kendall, "The impossibility of comminuting small particles by compression," *Nature*, vol. 272, no. 5655, pp. 710–711, 1978.
- [34] B. L. Karihaloo, "Scaling laws for properties of materials with imperfect interfaces," *Nature*, vol. 279, article 169, 1979.
- [35] P. Antoniammal and D. Arivuoli, "A thermo dynamical model for the shape and size effect on melting of boron carbide nanoparticles," *Journal of Nanoscience and Nanotechnology*, vol. 11, pp. 1–8, 2011.
- [36] S. C. Hendy, "A thermodynamic model for the melting of supported metal nanoparticles," *Nanotechnology*, vol. 18, no. 17, Article ID 175703, 2007.
- [37] C. R. M. Wronski, "The size dependence of the melting point of small particles of tin," *British Journal of Applied Physics*, vol. 18, no. 12, pp. 1731–1737, 1967.
- [38] D. Kashchey and G. M. van Rosmalen, "Nucleation in solutions revisited," *Crystal Research and Technology*, vol. 38, no. 7–8, pp. 555–574, 2003.
- [39] F. Ercolessi, W. Andreoni, and E. Tosatti, "Melting of small gold particles: Mechanism and size effects," *Physical Review Letters*, vol. 66, no. 7, pp. 911–914, 1991.
- [40] L. J. P. Lewis, P. Jensen, and J. L. Barrat, "Melting, freezing, and coalescence of gold nanoclusters," *Physical Review B*, vol. 56, no. 4, pp. 2248–2257, 1997.
- [41] G. L. Allen, R. A. Bayles, W. W. Gile, and W. A. Jesser, "Small particle melting of pure metals," *Thin Solid Films*, vol. 144, no. 2, pp. 297–308, 1986.
- [42] J. Sun and S. L. Simon, "The melting behavior of aluminum nanoparticles," *Thermochimica Acta*, vol. 463, no. 1–2, pp. 32–40, 2007.
- [43] F. Lopeandia and J. Rodriguez-Viejo, "Size-dependent melting and supercooling of Ge nanoparticles embedded in a SiO₂ thin film," *Thermochimica Acta*, vol. 461, no. 1–2, pp. 82–87, 2007.
- [44] M. Takagi, "Electron-diffraction study of liquid-solid transition of thin metal films," *Journal of the Physical Society of Japan*, vol. 9, no. 3, pp. 359–363, 1954.
- [45] W. H. Qi and M. P. Wang, "Size effect on the cohesive energy of nanoparticle," *Journal of Materials Science Letters*, vol. 21, no. 22, pp. 1743–1745, 2002.
- [46] K. K. Nanda, S. N. Sahu, and S. N. Behera, "Liquid-drop model for the size-dependent melting of low-dimensional systems," *Physical Review A*, vol. 66, no. 1, Article ID 013208, 2002.
- [47] J. W. M. Frenken and J. F. van der Veen, "Observation of surface melting," *Physical Review Letters*, vol. 54, no. 2, pp. 134–137, 1985.
- [48] H. Sakai, "Surface-induced melting of small particles," *Surface Science*, vol. 351, no. 1–3, pp. 285–291, 1996.
- [49] C. Q. Sun, Y. Wang, B. K. Tay, S. Li, H. Huang, and Y. B. Zhang, "Correlation between the melting point of a nanosolid and the cohesive energy of a surface atom," *Journal of Physical Chemistry B*, vol. 106, no. 41, pp. 10701–10705, 2002.
- [50] H. K. Kim, S. H. Huh, J. W. Park, J. W. Jeong, and G. H. Lee, "Modeling the cohesive energy and melting point of nanoparticles," *Chemical Physics Letters*, vol. 354, article 165, 2002.
- [51] W. H. Qi and M. P. Wang, "A simplified model to calculate the surface-to-volume atomic ratio dependent cohesive energy of nanocrystals," *Journal of Materials Science Letters*, vol. 21, article 1743, 2002.
- [52] W. H. Qi, M. P. Wang, and G. Y. Xu, "An investigation of the size-dependent cohesive energy and the structural stability of spherical metallic nanoparticles," *Chemical Physics Letters*, vol. 372, article 632, 2003.
- [53] W. H. Qi, M. P. Wang, and W. Y. Hu, "Nano structured materials for advanced technological applications," *Materials Letters*, vol. 58, article 1745, 2004.
- [54] Q. Jiang, J. C. Li, and B. Q. Chi, "Size-dependent cohesive energy of nanocrystals," *Chemical Physics Letters*, vol. 366, no. 5–6, pp. 551–554, 2002.
- [55] K. K. Nanda, F. E. Kruis, and H. Fissan, "Evaporation of free PbN nanoparticles: evidence of the Kelvin effect," *Physical Review Letters*, vol. 89, no. 25, Article ID 256103, 4 pages, 2002.
- [56] C. Brechignac, H. Busch, P. H. Cahuzac, and J. Leygnier, "Dissociation pathways and binding energies of lithium clusters from evaporation experiments," *The Journal of Chemical Physics*, vol. 101, no. 8, pp. 6992–7002, 1994.
- [57] F. Chandezon, P. M. Hansen, C. Ristori, J. Pedersen, J. Westergaard, and S. Bjørnholm, "Evaporation of clusters in a heat bath," *Chemical Physics Letters*, vol. 277, no. 5–6, pp. 450–455, 1997.

- [58] S. L. Lai, J. Y. Guo, V. Petrova, G. Ramanath, and L. H. Allen, "Size-dependent melting properties of small tin particles: nanocalorimetric measurements," *Physical Review Letters*, vol. 77, no. 1, pp. 99–102, 1996.
- [59] C. Q. Sun, B. K. Tay, X. T. Zeng et al., "A nanosolid and the cohesive energy of a surface atoms," *Journal of Physics*, vol. 14, article 7781, 2002.
- [60] D. Xie, W. H. Qi, L. F. Cao, and M. P. Wang, "Thermal stability of indium nanocrystals: a theoretical study," *Materials Chemistry and Physics*, vol. 96, no. 2-3, pp. 418–421, 2006.
- [61] Z. Wang, X. Zu, F. Gao, and W. J. Weber, "Size dependence of melting of GaN nanowires with triangular cross sections," *Journal of Applied Physics*, vol. 101, no. 4, Article ID 043511, 2007.
- [62] K. Rollins, "Nanobiotechnology regulation: a proposal for self-regulation with limited oversight," *Nems Memos Works, LLC*, vol. 6, no. 2, 2010.
- [63] G. Guisbiers, D. Liu, Q. Jiang, and L. Buchailot, "Theoretical predictions of wurtzite III-nitride nano-materials properties," *Physical Chemistry Chemical Physics*, vol. 12, no. 26, pp. 7203–7210, 2010.
- [64] Y. H. Wen, Z. Zhu, R. Zhu, and G. F. Shao, "Size-dependent melting of nanoparticles," *Physica E*, vol. 25, article 47, 2004.

Research Article

Top-Down Processing of NaNbO_3 Nanopowder

Jurij Koruza,^{1,2} Barbara Malič,¹ Oleksandr Noshchenko,¹ and Marija Kosec^{1,2}

¹ Electronic Ceramics Department, Jožef Stefan Institute, Jamova cesta 39, 1000 Ljubljana, Slovenia

² Centre of Excellence NAMASTE, Jamova cesta 39, 1000 Ljubljana, Slovenia

Correspondence should be addressed to Jurij Koruza, jurij.koruza@ijs.si

Received 23 February 2012; Accepted 5 April 2012

Academic Editor: Sergio J. Mejía-Rosales

Copyright © 2012 Jurij Koruza et al. This is an open access article distributed under the Creative Commons Attribution License, which permits unrestricted use, distribution, and reproduction in any medium, provided the original work is properly cited.

We report the processing of NaNbO_3 nanopowder by combining the solid-state synthesis and subsequent milling in the agitator bead mill. The effect of different rotation speeds of the agitator shaft on the comminution process was followed by laser granulometry. The morphology and specific surface area of the powders were investigated by scanning electron microscopy and the N_2 adsorption method, respectively. With the optimized milling parameters, we obtained NaNbO_3 nanoparticles with an average size of 25 nm and a narrow particle size distribution. The result is comparable to other processing techniques, such as solution-based chemical routes or mechanochemical synthesis; however, the presented method does not require any complicated processing and it can be easily upscaled to yield large quantities of the NaNbO_3 nanopowder. Furthermore, the compaction behaviour of the obtained nanopowder was investigated, and a compaction-response diagram was constructed revealing good compactability of the powder. The green compacts, isostatically pressed at 740 MPa, had a relative density of 70% and a narrow pore size distribution with an average pore radius of 4 nm.

1. Introduction

Antiferroelectric materials have gained increased attention due to their large energy storage capacity, required for high-performance capacitors [1], and a large volume change accompanying the field-induced phase transition, which may be used in high-strain actuator and transducer applications [2]. Lead zirconate (PbZrO_3) is a prototype antiferroelectric [3, 4]; however, due to increased environmental concerns [5], lead-free antiferroelectrics, such as sodium niobate (NaNbO_3), are considered [6]. The phase transition behaviour of NaNbO_3 is quite complicated [7]. Beside the temperature and electric-field-induced phase transitions, size-induced phase transition phenomena have been recently observed [8, 9]. In order to investigate the effect of the particle/grain sizes on the polymorphism, and consequently on the functional properties, dense NaNbO_3 ceramics with a wide grain size range should be prepared. A necessary condition for the preparation of ultrafine-grained ceramics is the NaNbO_3 nanopowder.

Nobre et al. prepared NaNbO_3 nanoparticles by the Pechini route and calcination of the precursor at 700°C for 5 h. The powder had the particle size of around 60 nm, as determined by the Brunauer-Emmet-Teller (BET) method [10]. Lanfredi et al. prepared the NaNbO_3 nanoparticles from the solution of an oxalatonioibium complex, sodium nitrate, oxalic acid, and ammonium hydroxide. The particle size of the powder, obtained by calcining the precursor at 900°C for 5 h, was 85 nm, as calculated from the X-ray diffraction (XRD) data by the Sherrer equation. However, some impurities could be observed in the XRD pattern [11]. In both studies, dense NaNbO_3 ceramics were obtained after sintering at lower temperatures than usually needed for the solid-state synthesized powder, which was connected to the small particle size and to a high concentration of defects, such as oxygen vacancies. The latter were presumably created due to the incomplete oxidation of organic precursors. In 2005, Pithan et al. introduced a microemulsion-mediated hydrolytic decomposition of a mixed-alkoxide solution, followed by Soxhlet extraction, and subsequent calcining at

400°C to prepare the nanopowder with the particle size of a few 10 nm as observed by scanning electron microscopy (SEM) and the BET size of a few 100 nm [12].

Solution-based chemical routes, applied to prepare NaNbO_3 nanopowders, suffer various deficiencies, such as complicated processing, small product yield, difficult upscaling, and sometimes difficulties in a complete removal of residual carbon. In addition, they typically require additional calcination steps to obtain the crystalline product.

An alternative approach was introduced by Rojac et al. who prepared the NaNbO_3 nanopowder by mechanochemical synthesis [13]. After 40 h of high-energy milling of Na_2CO_3 and Nb_2O_5 in a planetary mill, the product consisted of agglomerates of 100–300 nm in size, while the crystallites were in the range of 10–20 nm, as determined from the transmission electron microscope images. The process however introduced impurities in the powder due to wear of the ZrO_2 milling vial and balls.

The aim of the present work was to establish a simple and effective processing route for the preparation of NaNbO_3 nanopowder by combining conventional and well established ceramic processing techniques, such as the solid-state synthesis of submicron-sized powder [9] and subsequent efficient milling to nanorange in an agitator bead mill. The influences of the milling time and different rotation speeds of the agitator shaft were followed by measurements of the particle size and size distribution and specific surface area. The optimization of the process resulted in a successful preparation of NaNbO_3 nanopowder. Furthermore, the nanopowder was isostatically pressed between 250 MPa and 740 MPa and its compaction-response diagram was constructed.

2. Experimental Work

The NaNbO_3 powder was prepared by solid-state synthesis from the high-purity Nb_2O_5 (99.9%, Sigma-Aldrich, Taufkirchen, Germany) and mechanically activated Na_2CO_3 (anhydrous 99.9%, Chempur, Karlsruhe, Germany). The submicron-sized starting powders were mixed in a stoichiometric ratio and homogenized in a planetary mill (Fritsch Pulverisette 4 Vario-Mill, Fritsch GmbH, Idar-Oberstein, Germany) for 4 h, using a zirconia vial and balls, and acetone as the liquid medium (p. A., AppliChem, Darmstadt, Germany). After drying, the powder mixture was pressed into pellets and calcined twice in a closed alumina crucible at 700°C for 4 h with intermediate milling. The product was crushed in an agate mortar and milled in a planetary mill for 4 h, as described above. The particle size distributions of the powders were determined from the area distribution, measured by a static light-scattering granulometer (Microtrac S3500 Particle Size Analyzer, Montgomeryville, PA, USA). The phase purity of the obtained powder was analysed by a PANalytical X'Pert PRO MPD diffractometer equipped with a graphite monochromator (Almelo, The Netherlands), and the material was found to be single phase, since all the peaks could be described with the crystallographic card of the orthorhombic NaNbO_3 (Figure 1) [14]. A detailed description of the synthesis and phase analysis can be found elsewhere [9].

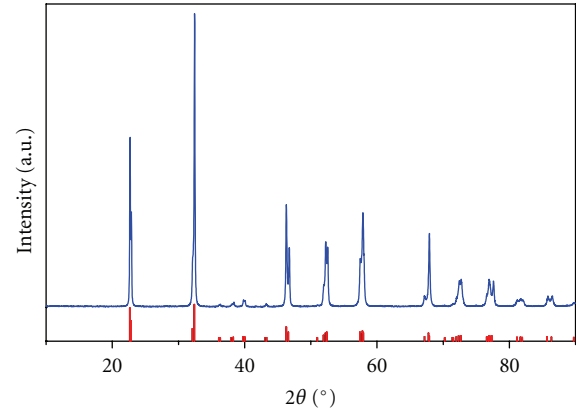


FIGURE 1: XRD pattern of the solid-state synthesis prepared NaNbO_3 (blue line). All the peaks could be described with the crystallographic card of the orthorhombic NaNbO_3 (red tick marks).

For milling the NaNbO_3 to nanorange, we used the Mini-Cer agitator bead mill (Netzsch Feinmahltechnik GmbH, Selb, Germany), where the grinding medium is accelerated in the chamber by an agitator shaft. Prior milling the as-synthesized powder was dispersed in isopropyl alcohol (p. A., AppliChem, Darmstadt, Germany) in an ultrasonic bath. The suspension was fed through the grinding chamber by a peristaltic hose pump (Verderlab, Haan, Germany), and zirconia beads with a diameter of 0.5 mm (Tosoh Corporation, Tokyo, Japan) were used as the grinding medium. The milling process was followed by the granulometer. The particle size distributions are described with the 90% particle size limit (d_{90}), 50% particle size limit (d_{50} , median value), and 10% particle size limit (d_{10}).

The powder morphology was investigated by a field emission scanning electron microscope (FE-SEM JSM-7600F, Jeol, Tokyo, Japan) with an operating voltage of 5 kV, while the specific surface area was analysed using the N_2 adsorption BET method (NOVA 2200E, Quantachrome Instruments, Boynton Beach, FL, USA). The BET equivalent particle diameters were calculated by the following equation:

$$d_{\text{BET}} = \frac{\psi_A/\psi_V}{S_M \cdot \rho_t}, \quad (1)$$

where S_M is the specific surface area, ρ_t is the theoretical density of NaNbO_3 (4.55 g/cm^3 [14]), and ψ_A/ψ_V is the shape factor ratio, for which a value of 6 was assumed [15].

The compaction behaviour of the powders was studied by uniaxial pressing the pellets with a pressure of 100 MPa and subsequently isostatically with pressures ranging from 250 MPa to 740 MPa. The relative densities were calculated from the dimensions and mass of the sample.

The pore size measurements of the compacted pellets were performed using the N_2 sorption equipment described above. The samples were dried at 250°C for 4 h and subsequently degassed at 200°C for 2 h prior to the measurement. The pore size distributions were calculated from the desorption curves using the method proposed by Barrett, Joyner, and Halenda (BJH) [16].

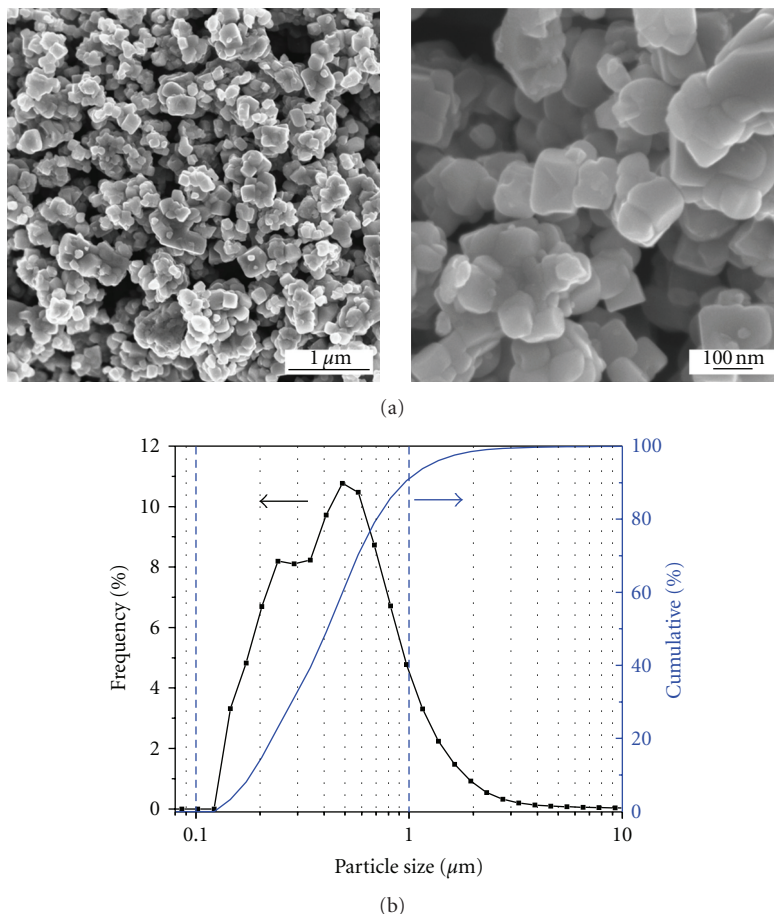


FIGURE 2: The reference-NN powder prepared by the solid-state synthesis and milled in a planetary mill for 4 h: (a) FE-SEM images and (b) particle size distribution, as measured by laser granulometry.

3. Results and Discussion

The FE-SEM images of the NaNbO_3 powder, obtained after the solid-state synthesis and subsequent milling in a planetary mill, are presented in Figure 2(a). This powder is further denoted as “reference-NN.” The estimated primary particle size was around 200–300 nm; however, some agglomerates of around 400–700 nm could be observed. This was confirmed by the granulometric measurement (Figure 2(b)), with two maxima at around 150–200 nm and 400–500 nm, attributed to the primary particles and to the agglomerates, respectively. The milling in the planetary mill after the calcination obviously failed to break strong agglomerates, created during the calcination process.

In order to prepare the NaNbO_3 nanopowder, we milled the reference-NN powder in the agitator bead mill. Different rotation speeds of the agitator shaft, that is, 1000 rpm, 1500 rpm, and 2000 rpm, were applied. The milled powders are denoted as “nano-NN-1000,” “nano-NN-1500,” and “nano-NN-2000,” respectively. The milling process was followed by measuring the particle size distributions by laser granulometry which allowed a quick evaluation of the milling process, since the samples could be rapidly transported in the form of a suspension directly from the mill to

the granulometer. The results of the milling process with different rotation speeds of the agitator shaft for times up to 75 min are presented in Figure 3. We observed a considerable narrowing of the size distributions and a major decrease of the d -values during the first 30 min of the milling process, while the size reduction was much smaller with further increase of the milling time. The milling process was stopped after 75 min, since a further increase of the time did not considerably reduce the particle size or in some cases even resulted in increasing the d -values due to increased particle agglomeration. This is partially observed for the nano-NN-1000 in Figure 3. In addition, long milling times could cause the wear of the zirconia beads and subsequent contamination of the powder and should therefore be avoided. The optimal conditions for the milling were identified to be the rotation speed of 2000 rpm and the milling time of around 75 min.

The NaNbO_3 nanopowders, milled for 75 min, were investigated by FE-SEM (Figure 4). The primary particle size was below 100 nm in all samples, and the images confirm the decrease of the particle size with increased rotation speed. In addition, some larger particles of around 200–400 nm could be observed; however, it was not clear, if they were agglomerates or particles. The amount of large particles decreased with increasing rotation speed.

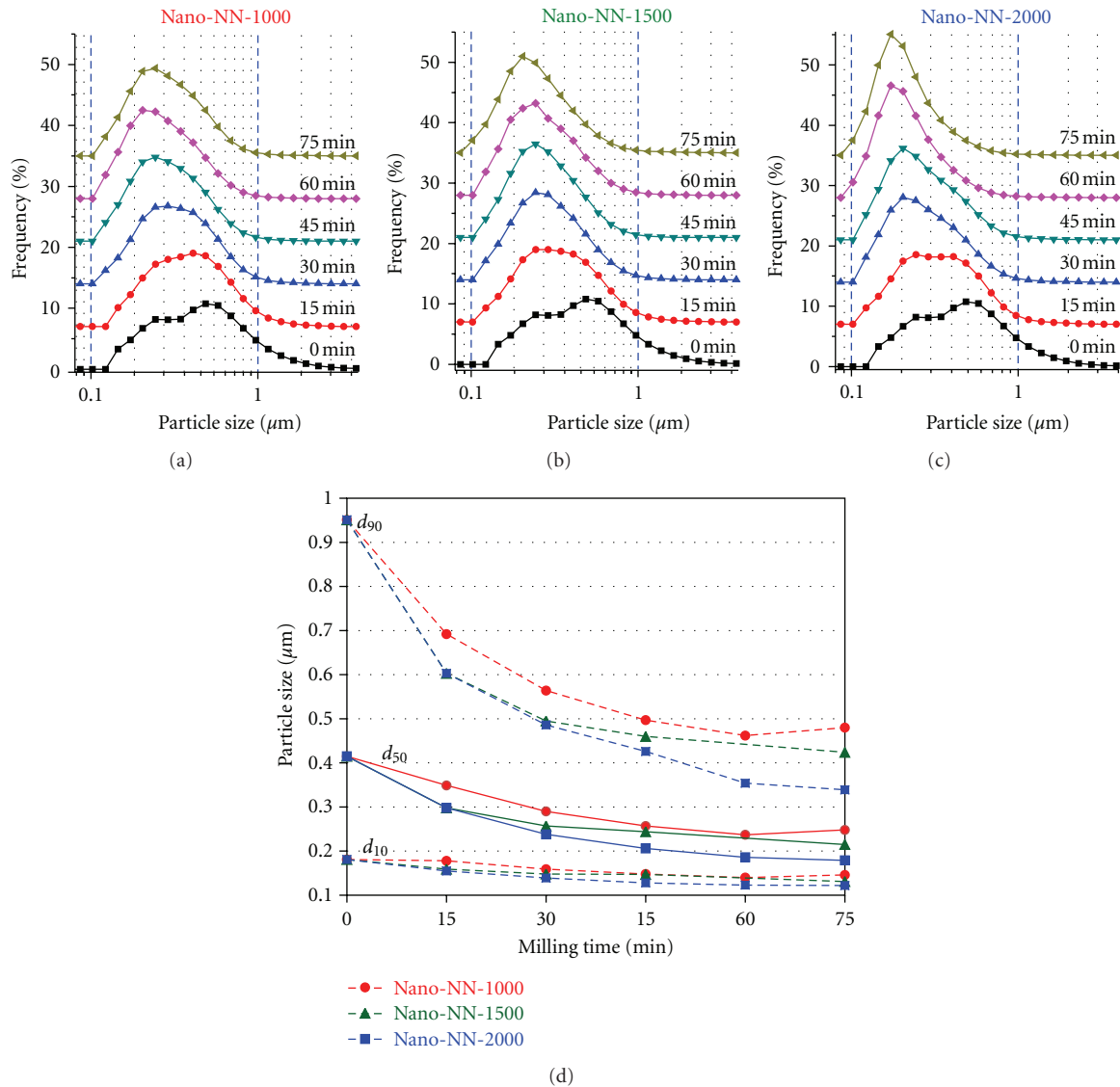


FIGURE 3: The effect of different rotation speeds of the agitator shaft on the milling process of NaNbO_3 powders: 1000 rpm (nano-NN-1000), 1500 rpm (nano-NN-1500), and 2000 rpm (nano-NN-2000).

The specific surface areas of the powders, milled for 75 min at different rotation speeds, were measured by the N_2 adsorption method. The results are summarized in Figure 5. The reference-NN powder had the specific surface area of $5.81 \text{ m}^2/\text{g}$. After the 1000 rpm milling, the specific surface area increased for about 6 times, while the milling with 2000 rpm resulted in nanopowder with an almost 10 times larger specific surface area. In addition, the d_{BET} primary particle sizes, calculated by (1), are added to Figure 5. The primary particle sizes decrease from 41 nm to 25 nm with increasing rotation speed, which is in agreement with the FE-SEM observations (Figure 4). The particle size of the obtained nano-NN powders is within the ranges reported for solution methods [10–12] and mechanochemical synthesis [13].

The compaction behaviour of the reference-NN and the nano-NN-2000 powders is presented in Figure 6 in the form

of a compaction-response diagram [17]. The curve of the reference-NN has a constant slope throughout the whole investigated isostatic pressure range between 250 MPa and 740 MPa, where the highest relative density of about 69% was obtained. A different compaction behaviour was observed in the case of the nano-NN-2000 powder, where lower relative densities were obtained in the lower pressure region up to about 550 MPa; however, a steeper slope, revealing a better compactability of this powder, resulted in higher relative densities at pressures above 550 MPa, as compared to the reference-NN powder. The interpolated value of around 64% relative density at 450 MPa for the nano-NN-2000 powder is comparable to the value reported for the compaction of the solution-derived NaNbO_3 nanopowder by Lanfredi et al., that is, 65% at a uniaxial pressure of 450 MPa [11]. However, the authors reported that this relative density was the limiting value, since the compaction rate at pressures above 320 MPa

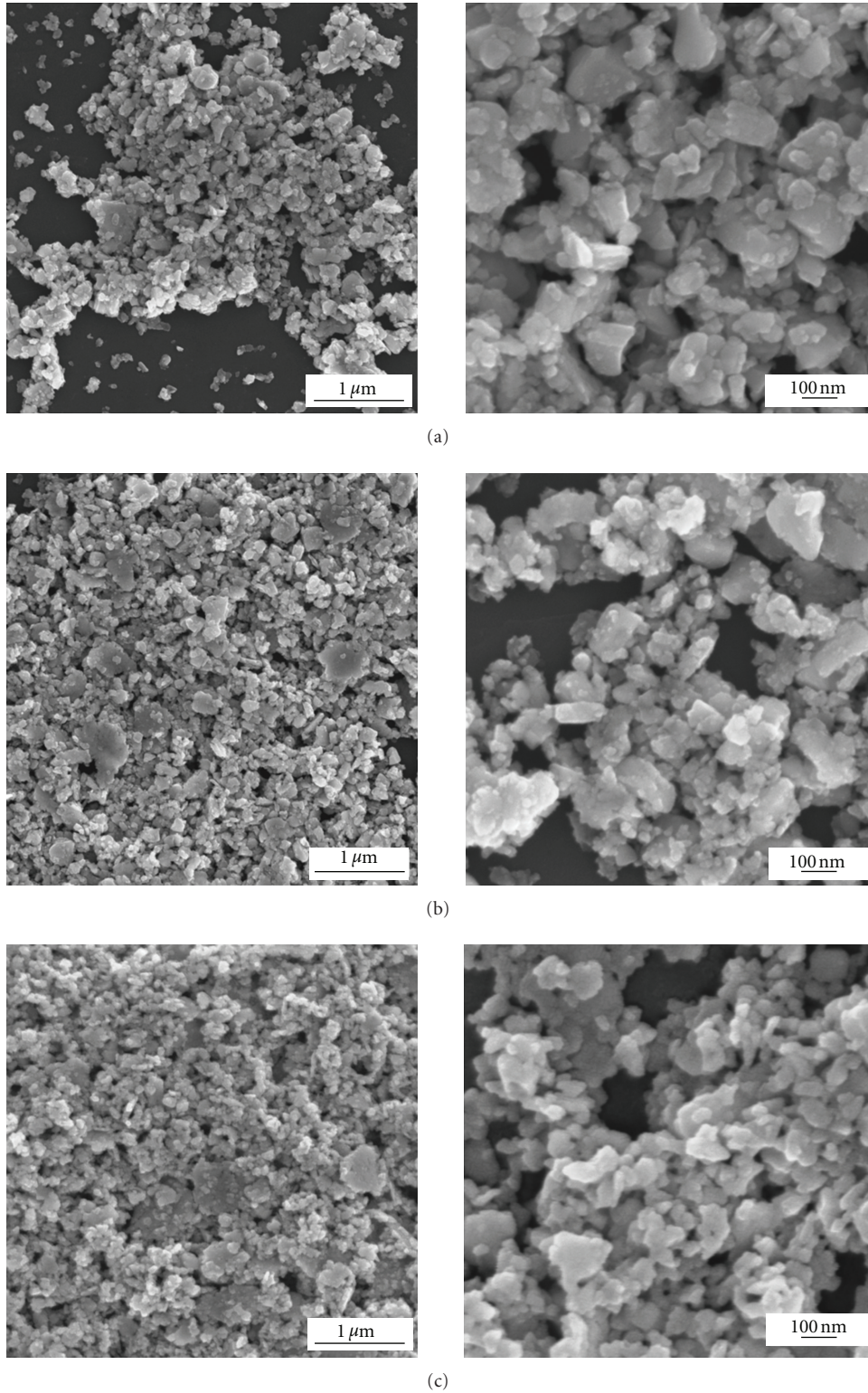


FIGURE 4: FE-SEM images of the nano-NN-1000 (a), nano-NN-1500 (b), and nano-NN-2000 (c) powders.

was very small. In our case, the limiting value seems to be at higher pressures, since a considerable increase of the relative density was observed with increasing the pressure up to about 650 MPa, where a relative density of around 69.2%

was measured. The highest relative density of about 70.2% was achieved at the pressure of 740 MPa.

The pore size and size distribution within the green body are important parameters of the sintering process,

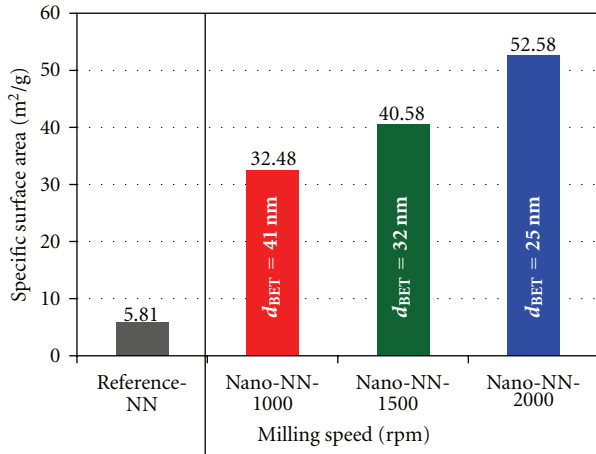


FIGURE 5: Specific surface areas of the obtained nano-NN-1000, nano-NN-1500, and nano-NN-2000 powders, as measured by the BET method. The calculated d_{BET} values are included in the corresponding columns. The specific surface area of the reference-NN powder is added for comparison.

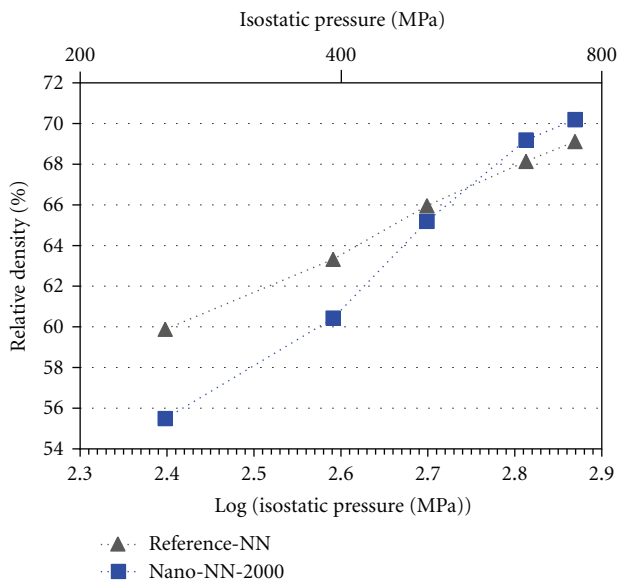


FIGURE 6: The compaction-response diagram of the reference-NN and nano-NN-2000 powders. Note that the dotted lines are a guide for the eye only.

and, clearly, a uniform pore size distribution is a reflection of a uniform packing of particles, which should promote sintering and densification [18]. The pore size distributions of the reference-NN and nano-NN-2000 green samples, compacted with the pressure of 740 MPa, were determined using the N₂ desorption curves and are presented in Figure 7. The average pore radius is reduced from about 24 nm to about 4 nm, for the reference-NN and the nano-NN-2000 compacts, respectively. Moreover, a much narrower pore size distribution was obtained in the latter case. It is also

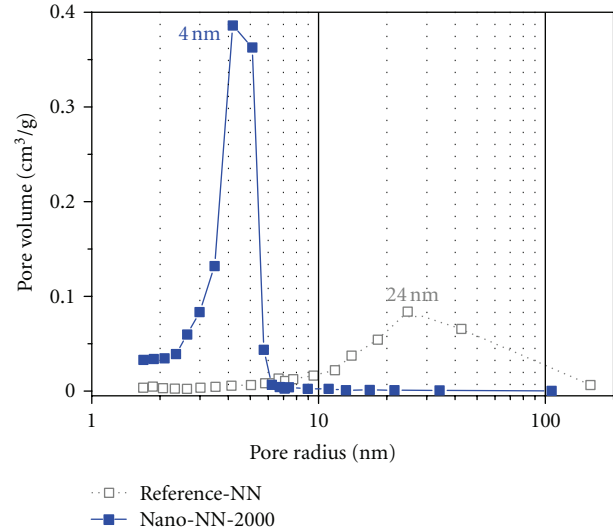


FIGURE 7: Pore size distribution of the reference-NN and nano-NN-2000 green samples, compacted with an isostatic pressure of 740 MPa. The numbers above the distributions represent the average pore radius.

important to note that both distributions were unimodal, since only one peak was observed in each distribution up to the detection limit of this method, which is at a pore diameter of 400 nm [19]. This could indicate the absence of agglomerates in these green samples; however, further analysis should be performed to confirm this. The fracture surfaces of the two samples, shown in Figure 8, reveal an obvious particle size decrease obtained by efficient bead milling. A detailed study of the sintering behaviour of the nanopowder is in progress.

4. Summary

NaNbO₃ nanopowder was prepared by simple top-down processing, combining the solid-state synthesis and subsequent bead milling. The milling process was optimized to yield nanoparticles with the average size of around 25 nm, which is comparable to the particle sizes obtained by solution-based chemical routes or mechanochemical synthesis. The proposed approach does not require any expensive reactants or high-energy milling and, as it is easily upscaled, it could yield a large quantity of the NaNbO₃ nanopowder. The compaction behaviour of the nanopowder was investigated in order to establish a suitable starting point for further research of the sintering process. The NaNbO₃ nanopowder exhibited a better compactability than the submicron NaNbO₃ powder, with an about six times lower average pore radius, and a narrower pore size distribution in the green samples.

Acknowledgments

The authors would like to thank Brigita Kužnik, Katarina Korenčan, Edi Kranjc, and Gregor Trefalt. This work was

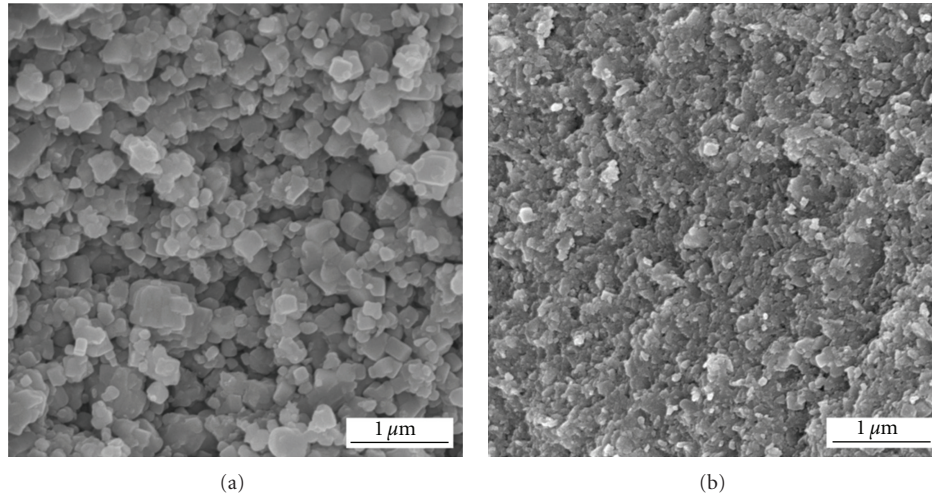


FIGURE 8: FE-SEM images of the fracture surfaces of the green compacts pressed with a pressure of 740 MPa: (a) reference-NN, (b) nano-NN-2000.

supported by the Slovenian Research Agency, under Grant no. 1000-08-310121, P2-0105, and J2-1227, and the Centre of Excellence NAMASTE under the Project RRP6.

References

- [1] N. H. Fletcher, A. D. Hilton, and B. W. Ricketts, "Optimization of energy storage density in ceramic capacitors," *Journal of Physics D*, vol. 29, no. 1, pp. 253–258, 1996.
- [2] W. Y. Pan, C. Q. Dam, Q. M. Zhang, and L. E. Cross, "Large displacement transducers based on electric field forced phase transitions in the tetragonal $(\text{Pb}_{0.97}\text{La}_{0.02})(\text{Ti,Zr,Sn})\text{O}_3$ family of ceramics," *Journal of Applied Physics*, vol. 66, no. 12, pp. 6014–6023, 1989.
- [3] G. Shirane, E. Sawaguchi, and Y. Takagi, "Dielectric properties of lead zirconate," *Physical Review*, vol. 84, no. 3, pp. 476–481, 1951.
- [4] H. Liu and B. Dkhil, "A brief review on the model antiferroelectric PbZrO_3 perovskite-like material," *Zeitschrift für Kristallographie*, vol. 226, no. 2, pp. 163–170, 2011.
- [5] E. P. a. t. E. Council, "Directive 2011/65/EU on the restriction of the use of certain hazardous substances in electrical and electronic equipment," in *Directive 2011/65/EU*, E. Union, Ed., p. 23, Official Journal of the European Union, Strasbourg, France, 2011.
- [6] B. Jaffe, W.R. Cook Jr., and H. Jaffe, *Piezoelectric Ceramics*, Academic Press, London, UK, 1971.
- [7] H. D. Megaw, "The seven phases of sodium niobate," *Ferroelectrics*, vol. 7, no. 1–4, pp. 87–89, 1974.
- [8] Y. Shiratori, A. Magrez, J. Dornseiffer, F. H. Haegel, C. Pithan, and R. Waser, "Polymorphism in micro-, Submicro-, and nanocrystalline NaNbO_3 ," *Journal of Physical Chemistry B*, vol. 109, no. 43, pp. 20122–20130, 2005.
- [9] J. Koruza, J. Tellier, B. Malič, V. Bobnar, and M. Kosec, "Phase transitions of sodium niobate powder and ceramics, prepared by solid state synthesis," *Journal of Applied Physics*, vol. 108, no. 11, Article ID 113509, 2010.
- [10] M. A. L. Nobre, E. Longo, E. R. Leite, and J. A. Varela, "Synthesis and sintering of ultra fine NaNbO_3 powder by use of polymeric precursors," *Materials Letters*, vol. 28, no. 1-3, pp. 215–220, 1996.
- [11] S. Lanfredi, L. Dessemond, and A. C. Martins Rodrigues, "Dense ceramics of NaNbO_3 produced from powders prepared by a new chemical route," *Journal of the European Ceramic Society*, vol. 20, no. 7, pp. 983–990, 2000.
- [12] C. Pithan, Y. Shiratori, J. Dornseiffer, F. H. Haegel, A. Magrez, and R. Waser, "Microemulsion mediated synthesis of nanocrystalline $(\text{K}_x\text{Na}_{1-x})\text{NbO}_3$ powders," *Journal of Crystal Growth*, vol. 280, no. 1-2, pp. 191–200, 2005.
- [13] T. Rojac, M. Kosec, B. Malič, and J. Holc, "Mechanochemical synthesis of NaNbO_3 ," *Materials Research Bulletin*, vol. 40, no. 2, pp. 341–345, 2005.
- [14] J.-I. 01-082-0606, *PCPDFWin, PDF-ICDD*, International Center for Diffraction Data, 2002.
- [15] J. S. Reed, *Principles of Ceramics Processing*, John Wiley & Sons, New York, NY, USA, 1995.
- [16] E. P. Barrett, L. G. Joyner, and P. P. Halenda, "The determination of pore volume and area distributions in porous substances. I. Computations from nitrogen isotherms," *Journal of the American Chemical Society*, vol. 73, no. 1, pp. 373–380, 1951.
- [17] R. L. K. Matsumoto, "Generation of powder compaction response diagrams," *Journal of the American Ceramic Society*, vol. 69, no. 10, pp. C246–C247, 1986.
- [18] M. N. Rahaman, *Ceramic Processing and Sintering*, Marcel Dekker, New York, NY, USA, 2003.
- [19] T. Allen, *Particle Size Measurement: Surface Area and Pore Size Determination*, Chapman & Hall, London, UK, 1997.

Research Article

The Size and Shape Dependence of Ferromagnetism in Nanomagnets

Ying Li,¹ Yongfeng Li,^{2,3} and Tianxing Wang⁴

¹ School of Materials Science and Engineering, Hebei University of Technology, Tianjin 300130, China

² School of Mathematics, Physics and Biological Engineering, Inner Mongolia University of Science and Technology, Baotou 014010, China

³ Inner Mongolia Key Laboratory for Utilization of Bayan Obo Multi-Metallic Resources, Elected State Key Laboratory, Inner Mongolia University of Science and Technology, Baotou 014010, China

⁴ College of Physics and Information Engineering, Henan Normal University, Xinxiang 453007, China

Correspondence should be addressed to Ying Li, liyingphy@126.com

Received 16 February 2012; Accepted 15 March 2012

Academic Editor: Chang Sun

Copyright © 2012 Ying Li et al. This is an open access article distributed under the Creative Commons Attribution License, which permits unrestricted use, distribution, and reproduction in any medium, provided the original work is properly cited.

The size and shape dependence of dynamic behaviors of nanomagnets is studied by the kinetic Monte Carlo method based on the transition state theory. We analyze the hysteresis curves of the nanomagnet systems with different shapes (or spin array patterns) in the presence of an external magnetic field. The results show that the magnetization of the chain-shaped nanomagnet is more sensitive to the applied field than that of the oblong-shaped or bulk-shaped systems. For the same magnetic nanostructure, the coercive field presents an exponential decay with temperature. Moreover, the coercive field is found to be strongly dependent on the effective coordination number, which has different values corresponding to those systems of different size and shapes (spin array patterns).

1. Introduction

The need for the increase of data-recording densities in the magnetic recording technique has driven the size of magnetic particles used down into the nanometer range [1, 2]. As the dimensions of magnetic materials decrease from the bulk size down to the nanometer scale, the magnetic properties will undergo a dramatic transition. The magnetism depends strongly on the shape and size of magnetic nanostructures [3–10]. It was well known that the continual decrease of the size of the magnetic nanoparticles will lead to the emergence of the superparamagnetic limit, below which the random magnetization reversal in particles will frequently occur, and consequently degrade the recorded information. On the other hand, an experimental study showed that the superparamagnetic limit of out-of-plane magnetized particles is strongly shape dependent, for example, oblong particles switch much more often than compact, almost circular particles of equal volume [9]. The superparamagnetic limit is a key factor in the magnetic recording industry, and it directly

determines the maximum achievable recording density. In order to extend the physical understanding of the superparamagnetic limit, it is essential to obtain a complete view of magnetic properties of nanomagnets through theoretical studies as well as experimental investigations [11–13].

In the present work, with the kinetic Monte Carlo method based on the transition state theory we study the dynamic behavior of magnetization reversal in the chain-shaped, oblong-shaped, and bulk-shaped nanomagnets with giant uniaxial anisotropy under the action of an external field at different temperatures. The aim of the work is first to provide a systematic understanding of the influence of shape on the magnetization reversal behavior and second to discuss the changes in coercive field with various spin array patterns of the system. Our study shows that magnetization reversal is much easier to occur in finite chain than in the oblong-shaped and bulk-shaped systems. This indicates that the magnetization of the elongated particles is more sensitive to the applied field than that of the compact particles. Furthermore, it is found that the coercive field and magnetic

order transition temperature in nanomagnets are strongly dependent on the effective coordination number.

2. Model and Method

Consider the nanomagnets of size $N = L_x \times L_y \times L_z$, where $L_x \neq 1, L_y = L_z = 1$ reduces to a one-dimensional magnetic chain, $L_x \neq 1, L_y \neq 1, L_z = 1$ indicates a two-dimensional oblong-shaped system, and $L_x \neq 1, L_y \neq 1, L_z \neq 1$ is a three-dimensional bulk-shaped system while the values of L_x, L_y , and L_z are finite. In this paper the uniaxial axis of the system is labelled by the $\pm z$ direction and the single-ion anisotropy energy has a large value. An external magnetic field is applied along the easy axis. We use a Heisenberg model with an extremely large uniaxial magnetic anisotropy to describe the magnetic properties of the system. The Hamiltonian of the system can be written as

$$\mathcal{H} = -J \sum_{\langle ij \rangle} \mathbf{S}_i \cdot \mathbf{S}_j - k_u \sum_i (\mathbf{S}_{i,z})^2 - \mathbf{H} \cdot \sum_i \mathbf{S}_i, \quad (1)$$

where \mathbf{S}_i is the normalized spin variable at site i . In the first term, the sum runs over all the nearest-neighbor spin pairs with J being ferromagnetic exchange coupling constant. The second term denotes the uniaxial anisotropy energy with k_u being the single-ion anisotropy constant. The last term is the coupling of spin magnetic moment to the applied field \mathbf{H} , that is, Zeeman energy. The magnetization of the system is defined as $m = (1/N) \sum_{i=1}^N \langle S_i \rangle$, where N is the total number of all spin sites and $\langle \dots \rangle$ denotes the thermodynamical average.

Owing to the fact that each atom has a large magnetic anisotropy, two metastable states of a spin will prefer to orient along the easy axis. The spin variable \mathbf{S}_i can reduce to the s_i , which takes values $+1$ and -1 , corresponding to the spin orientation in $+z$ and $-z$ direction, respectively. We use an angle θ_i to describe the angular deviation of the spin at site i between its current state and its initial state. A transition state begins at $\theta_i = 0$ ($\cos \theta_i = 1$) and ends at $\theta_i = \pi$ ($\cos \theta_i = -1$). From the Hamiltonian (1), a nonzero θ_i will produce an energy increment

$$e_i = k_u \sin^2 \theta - h_i (\cos \theta_i - 1), \quad (2)$$

where $h_i = (J \sum_j s_j + \mu H) s_i$. The energy increment yields a transition-state barrier, $\Delta E_i = (2k_u + h_i)^2 / 4k_u$ at $\cos \theta_i = h_i / 2k_u$ when $2k_u > |h_i|$ [14–16]. The reversal rate of the spin can be expressed as the Arrhenius law [17] $R = R_0 \exp(-\Delta E_i / k_B T)$, where k_B is Boltzmann constant and T is temperature. For $2k_u \leq |h_i|$, the transition state barriers disappear for some spin reversal processes where we use the Glauber method [18] to treat the exponential factor of the rates, with the prefactor being kept [14]. The expression of the rate implies that our spin processes are thermal activated. This scheme is justified for our simulation because dipolar interactions can be ignored [6, 19] and quantum tunnelling comes into action at very low temperature only [20].

By the kinetic Monte Carlo method, we carry out simulation on the magnetization responses to the applied field

for the systems with chain, oblong, and bulk shape. The simulation uses a single-spin flip algorithm under free boundary conditions. Starting from an initial state with all spins $s_i = -1$, we computed the local field for a randomly chosen spin and flipped the spin state according to the transition rates mentioned above. The spin flip may change the local field of the neighboring spins, thereby affecting the stability of other spins. The local fields of other spins are computed again and another spin is flipped. To reduce error each data point is averaged over at least 500 independent runs.

In our simulation, the exchange interaction between the nearest-neighbor spins is taken as $J = 7$ meV, and the anisotropy energy is $k_u = 0.3J = 2.1$ meV/spin. Here, it is worth noting that the experimental studies have revealed that the magnetic anisotropy energy per Co atom can reach 2.0 meV in one-dimensional Co chains on Pt(997) surface [21], and the magnetic anisotropy energy per Fe atom is up to 1.6 meV in FePt nanoparticles embedded in Al [22]. The larger the magnetic anisotropy energy, the smaller the critical particle size for stable magnetization at room temperature. So the nanomagnets with a giant magnetic anisotropy energy have been considered as the prime candidate for future data storage media application. The magnetic parameters such as J and k_u remain unchanged for all systems unless specified otherwise. The magnetic field sweeping rate is taken as 132 T/s. We sweep the magnetic field, starting from a strong field $H = -H_0$, at which all spin magnetic moments are aligned along the $-z$ direction. The field strength is then gradually increased in increments of ΔH to $+H_0$, followed by a decrease back to $-H_0$. Thus, a magnetic field sweeping cycle is completed.

3. Results and Discussions

Figure 1 shows the magnetization curves of chain-shaped and oblong-shaped systems with fixed atoms and varying arrays, that is, $40 \times 1, 20 \times 2, 10 \times 4, 8 \times 5$, at 10, 16, and 25 K. Clearly, the results from the chain $L_x \times L_y = 40 \times 1$, that is, the mostly inner hysteresis curves, are very different from those of oblong-shaped arrays. At a fixed temperature, the magnetization of spin arrays with a larger length-to-width ratio, that is, $\eta = L_x / L_y$, is more sensitive to the applied field so that the value of the coercive field of elongated arrays is smaller than that of nearly square-shaped arrays. On the other hand, the difference between the magnetization curves for different spin arrays changes with temperature.

In Figure 2, we plot the variation of the coercive field with temperature for spin arrays $40 \times 1, 20 \times 2, 10 \times 4, 8 \times 5$. It is clear that the crossover temperature for chain-shaped arrays is smaller than that of the oblong-shaped arrays. The relationship between the coercive field and temperature can be described by a fit function

$$H_c = H_0 \exp \left[- \left(\frac{T}{T_0} \right)^g \right], \quad (3)$$

where H_c and T represent the coercive field and temperature and H_0, T_0 , and g are fit parameters whose values are shown in Table 1.

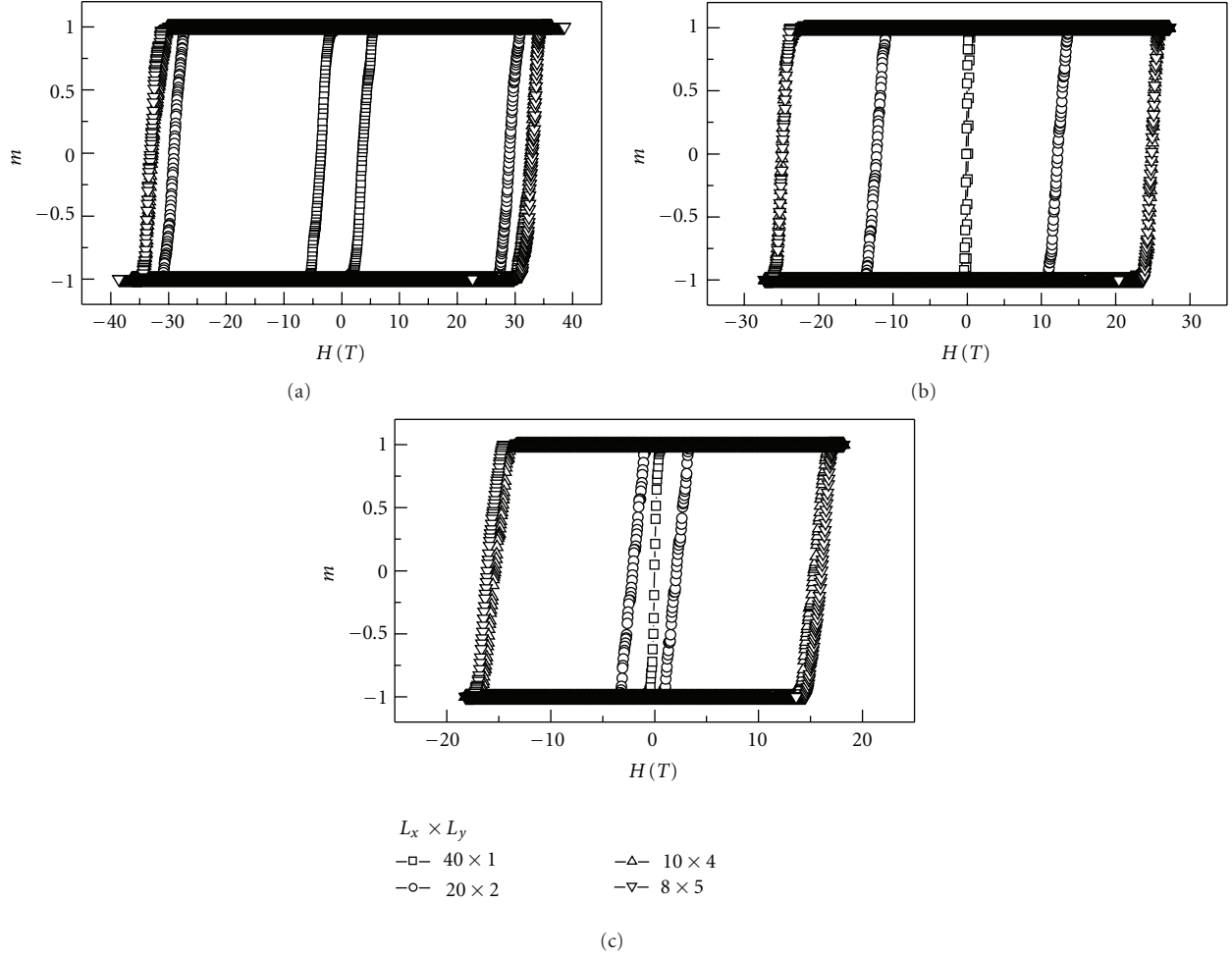


FIGURE 1: The magnetization responses to the applied field for chain-shaped arrays $L_x \times L_y = 40 \times 1$ and oblong-shaped arrays 20×2 , 10×4 , 8×5 at (a) $T = 10$ K, (b) $T = 16$ K, and (c) $T = 25$ K.

TABLE 1: Parameters corresponding to the fit curves in Figure 2.

$L_x \times L_y$	H_0 (T)	T_0 (K)	g
40×1	25.9561	7.27	2.0896
20×2	53.1599	13.1625	1.8299
10×4	40.2432	25.4633	1.6579
8×5	43.6804	25.0683	1.3370

In addition, we further study the magnetization reversal properties for nanomagnets of chain shape and oblong shape including 60, 80, and 120 atoms. In Table 2, we give various spin arrays of $N = 40, 60, 80$, and 120 atoms, their length-to-width ratio η , their coercive fields $H_c(T)$ at $T = 25$ K, and standard deviations of the coercive fields. We can see that the coercive fields have a decreasing tendency with increasing η for arrays with a fixed width and varying length. This implies that the elongated particles switch more easily than the nearly square-shaped particles, which is in agreement with the results from the literature [9]. Additionally, for the system with a fixed number of total spins, the coercive field of the compact-shaped array is large compared with that

of the oblong-shaped array, but the coercive field exhibits a nonmonotonic increase with η decreasing, as shown in Table 2. We think that the slight decrease of the coercive field with η should be induced by standard deviations, which are given in Table 2.

In order to gain a systematical understanding of the effects of the shape (or spin array pattern) of nanomagnets on the magnetization reversal, we also study the magnetic properties of bulk-shaped systems with various spin arrays $L_x \times L_y \times L_z = 30 \times 2 \times 2, 20 \times 3 \times 2, 15 \times 4 \times 2, 5 \times 12 \times 2, 6 \times 10 \times 2, 10 \times 4 \times 3, 5 \times 8 \times 3, 5 \times 4 \times 6$. Bringing together the results from the chain-shaped, oblong-shaped, and bulk-shaped systems, we found that at a fixed temperature the coercive field is closely dependent on the shape (or spin array pattern) of the system. The dependence relation can be explained in the following way. For the systems comprising of the same atoms, the transitions both from chain to oblong shape and from oblong to bulk shape lead to an increase in the number of effective nearest neighbors for each spin, which in turn raises the coercive field. Here, the number of effective nearest neighbors per spin, also called the effective coordination number Z_{eff} , is defined as twice the ratio of

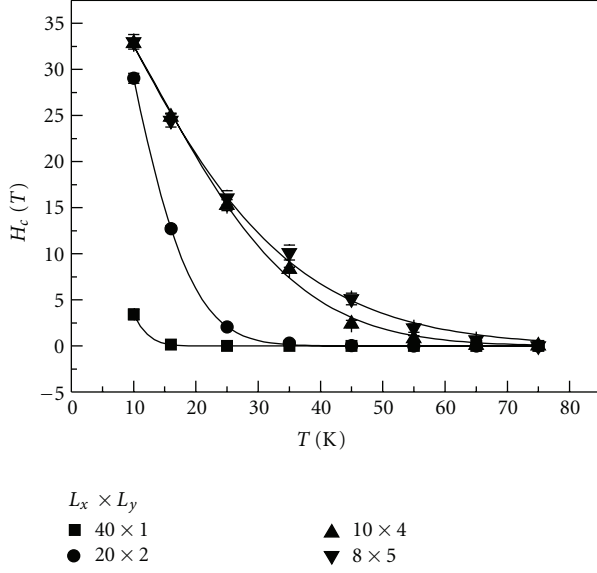


FIGURE 2: The coercive field versus temperature for $L_x \times L_y = 40 \times 1, 20 \times 2, 10 \times 4, 8 \times 5$, in which the solid lines represent fits to data by (3). The corresponding fit parameters are listed in Table 1 (see text).

TABLE 2: The various chain-shaped and oblong-shaped spin arrays, their ratio of length to width η , the coercive field at $T = 25$ K, and standard deviations of the coercive field.

$L_x \times L_y$	η	$H_c(T)$	Standard deviation (T)
40×1	40	0	0
20×2	10	2.05745	0.15
10×4	2.5	15.27256	0.6
8×5	1.6	16.06252	0.3788
60×1	60	0	0
30×2	15	2.97262	0.5
20×3	6.666	10.76375	0.7
15×4	3.75	15.17215	0.6
12×5	2.4	15.97444	0.6884
10×6	1.6667	15.61092	0.745
80×1	80	0	0
40×2	20	3.16916	0.88
20×4	5	15.40603	0.8985
16×5	3.2	16.61719	0.9339
10×8	1.25	15.46548	0.7772
120×1	120	0	0
60×2	30	3.68	0.8
40×3	13.33	10.1	0.8
30×4	7.5	16.1	0.9
24×5	4.8	17.1	0.95
20×6	3.33	16.05	0.6
15×8	1.875	15.46	0.9
12×10	1.2	15.49	0.85

the number of total bonds to the number of total spins in the system. Hence, the values of Z_{eff} are not more than 2, 4, and

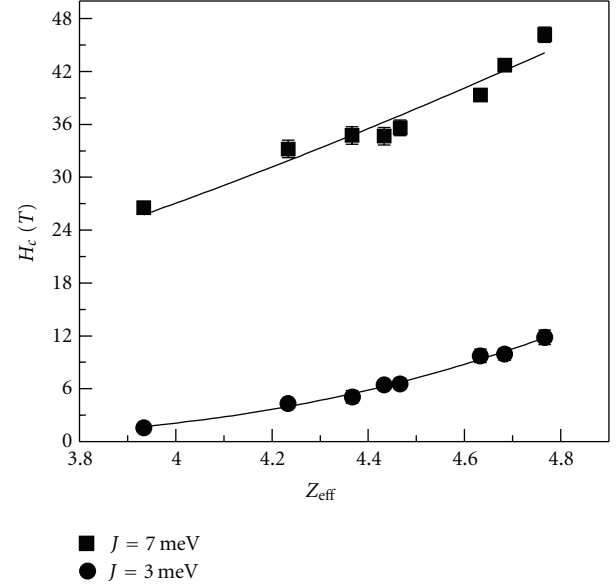


FIGURE 3: The Z_{eff} dependence of the coercive field for the bulk-shaped system of $L_x \times L_y \times L_z = 30 \times 2 \times 2, 20 \times 3 \times 2, 15 \times 4 \times 2, 5 \times 12 \times 2, 6 \times 10 \times 2, 10 \times 4 \times 3, 5 \times 8 \times 3, 5 \times 4 \times 6$ with $J = 7$ meV and $J = 3$ meV at $T = 25$ K. The solid lines are fits to data by (4), as discussed in the text.

6 in chain-shaped, oblong-shaped, and bulk-shaped systems. For bulk-shaped systems, if we treat those spins having the largest coordination number as the inner spins (or interior atoms) and other spins as outer spins (or surface atoms), Z_{eff} is in some sense analogous but inversely proportional to the surface-to-volume ratio of nanomagnets [11]. Taking $N = 120$ for example, in Table 3 we display the values of Z_{eff} for various spin array patterns corresponding to chain-shaped, oblong-shaped, and bulk-shaped systems.

In Figure 3 we show the coercive field as a function of Z_{eff} for bulk-shaped arrays $L_x \times L_y \times L_z = 30 \times 2 \times 2, 20 \times 3 \times 2, 15 \times 4 \times 2, 5 \times 12 \times 2, 6 \times 10 \times 2, 10 \times 4 \times 3, 5 \times 8 \times 3, 5 \times 4 \times 6$ of $N = 120$ in the cases of $J = 7$ meV and $J = 3$ meV at 25 K. The anisotropy energy remains unchanged in both cases. From Figure 3 it follows that the coercive field increases with Z_{eff} and becomes small for relatively small exchange interaction J . The Z_{eff} dependence of H_c can be described by the function expression

$$H_c = H_{c0} \exp \left[- \left(\frac{Z_{\text{eff}}}{Z_{\text{eff}0}} \right)^\lambda \right], \quad (4)$$

where H_{c0} and $Z_{\text{eff}0}$ represent the fit parameters and λ is a minus power exponent. We also find that the relation between the coercive field and Z_{eff} is also true for those systems with larger anisotropy or smaller exchange coupling. The coercive field increases with increasing the anisotropy energy, but when the anisotropy energy increases to the extent to which the transition between two metastable states involves transition states with barriers only, the influence of Z_{eff} on the coercive field becomes small.

TABLE 3: The Z_{eff} for chain-shaped, oblong-shaped, and bulk-shaped systems.

L_x	120							
Z_{eff}	1.9834							
$L_x \times L_y$	60×2	40×3	30×4	24×5	20×6	15×8	12×10	
Z_{eff}	2.9666	3.2834	3.4334	3.5186	3.5666	3.6166	3.6334	
$L_x \times L_y \times L_z$	$30 \times 2 \times 2$	$20 \times 3 \times 2$	$15 \times 4 \times 2$	$5 \times 12 \times 2$	$6 \times 10 \times 2$	$10 \times 4 \times 3$	$5 \times 8 \times 3$	$5 \times 4 \times 6$
Z_{eff}	3.9334	4.2334	4.3666	4.4334	4.4666	4.6334	4.6834	4.7666

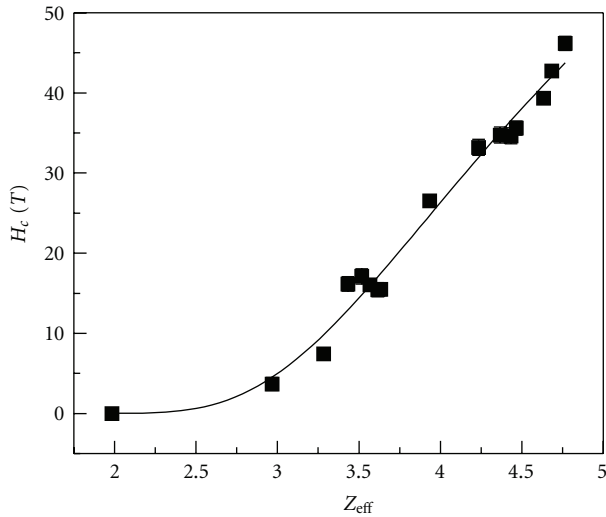


FIGURE 4: The coercive field as a function of Z_{eff} at 25 K for chain-shaped, oblong-shaped, and bulk-shaped systems including equal atoms $N = 120$ with $J = 7$ meV. The values of Z_{eff} are shown in Table 3. The solid line is fit to data by (4), as discussed in the text.

For the purpose of comparison, in Figure 4 we display the coercive field as a function of Z_{eff} for chain-shaped, oblong-shaped, and bulk-shaped systems containing the same atoms $N = 120$ with $J = 7$ meV. The solid line is fit to data by (4). The values of Z_{eff} correspond to those of Table 3. It can be seen that the coercive field tends to increase with Z_{eff} increasing. This indicates that the coercivity or the magnetic order transition temperature of nanomagnets is closely related to the effective coordination number.

For the case of bulk-shaped nanomagnets, our simulated results are qualitatively consistent with the experimental ones [10], where the order-disorder transition temperature of oblong nanoparticles (with 4 and 1.5 nm for the size and the thickness) was found to be lower than that of spherical nanoparticles (with 3 nm for the size). Besides, our results are also in qualitative agreement with the theoretical ones, where the order transition temperature decreases with the increase of surface-to-volume ratio for nanodots, rod, plate, and icosahedra [11].

4. Conclusions

In conclusion, we have investigated the size and shape dependence of magnetic dynamic behaviors in chain-shaped, oblong-shaped, and bulk-shaped nanomagnets. The coercive

fields are found to be strongly dependent on the size and shape (or spin array patterns) of the nanomagnets. The magnetization of the elongated array is more sensitive to the applied field than the nearly square-shaped arrays and bulk-shaped arrays. We propose that the coercive field is closely associated with the number of effective nearest neighbors for each spin (or effective coordination number), which has different values corresponding to different systems such as chain-shaped, oblong-shaped, and bulk-shaped systems.

Acknowledgments

This work is supported by the Nature Science Foundation of Hebei Province (Grant no. A201000013) and by the National Natural Science Foundation of China, and by 100 Excellent Innovative Talents Programme of Hebei Province (Grant no. 50901027).

References

- [1] H. N. Bertram, *Theory of Magnetic Recording*, Cambridge University Press, Cambridge, UK, 1994.
- [2] S. Y. Chou, M. S. Wei, P. R. Krauss, and P. B. Fischer, "Single-domain magnetic pillar array of 35 nm diameter and 65 Gbits/in. 2 density for ultrahigh density quantum magnetic storage," *Journal of Applied Physics*, vol. 76, no. 10, pp. 6673–6675, 1994.
- [3] C. Xu, P. M. Hui, L. F. Zhang, Y.Q. Ma, J. H. Zhou, and Z. Y. Li, "Hysteresis in small arrays of interacting magnetic nanoparticles," *European Physical Journal*, vol. 46, no. 4, pp. 475–480, 2005.
- [4] S. T. Chui, "Shape dependence of the switching field in small structures," *IEEE Transactions on Magnetics*, vol. 34, no. 4, pp. 1000–1002, 1998.
- [5] D. Q. Li, B. R. Cuenya, J. Pearson, S. D. Bader, and W. Keune, "Magnetism of step-decorated Fe on Pd(110)," *Physical Review B*, vol. 64, no. 14, pp. 1444101–1444105, 2001.
- [6] M. Pratzner and H. J. Elmers, "Domain wall energy in quasi-one-dimensional Fe/W(110) nanostripes," *Physical Review B*, vol. 67, no. 9, Article ID 094416, 7 pages, 2003.
- [7] H.-B. Braun, "Thermally activated magnetization reversal in elongated ferromagnetic particles," *Physical Review Letters*, vol. 71, no. 21, pp. 3557–3560, 1993.
- [8] E. Y. Vedmedenko, N. Mikuszeit, H. P. Oepen, and R. Wiesendanger, "Multipolar ordering and magnetization reversal in two-dimensional nanomagnet arrays," *Physical Review Letters*, vol. 95, no. 20, Article ID 207202, pp. 1–4, 2005.
- [9] M. Bode, O. Pietzsch, A. Kubetzka, and R. Wiesendanger, "Shape-dependent thermal switching behavior of superparamagnetic nanoislands," *Physical Review Letters*, vol. 92, no. 6, Article ID 067201, 4 pages, 2004.

- [10] D. Alloyeau, C. Ricolleau, C. Mottet et al., "Size and shape effects on the order-disorder phase transition in CoPt nanoparticles," *Nature Materials*, vol. 8, no. 12, pp. 940–946, 2009.
- [11] W. H. Zhong, C. Q. Sun, S. Li, H. L. Bai, and E. Y. Jiang, "Impact of bond-order loss on surface and nanosolid magnetism," *Acta Materialia*, vol. 53, no. 11, pp. 3207–3214, 2005.
- [12] V. Skumryev, S. Stoyanov, Y. Zhang, G. Hadjipanayis, D. Givord, and J. Nogués, "Beating the superparamagnetic limit with exchange bias," *Nature*, vol. 423, no. 6942, pp. 850–853, 2003.
- [13] J. Y. Yang, K. S. Yoon, Y. H. Do et al., "Magnetic properties of cobalt nanodots fabricated by a new laser irradiation method: anisotropy and superparamagnetism," *IEEE Transactions on Magnetics*, vol. 41, no. 10, pp. 3313–3315, 2005.
- [14] Y. Li and B. G. Liu, "Long-range ferromagnetism in one-dimensional monatomic spin chains," *Physical Review B*, vol. 73, no. 17, Article ID 174418, 5 pages, 2006.
- [15] Y. Li and B. G. Liu, "Current controlled spin reversal of nanomagnets with giant uniaxial anisotropy," *Physical Review Letters*, vol. 96, no. 21, Article ID 217201, 2006.
- [16] K. C. Zhang and B. G. Liu, "Dynamical ferromagnetism of interacting tiny magnets with strong anisotropy," *Physics Letters A*, vol. 374, no. 19–20, pp. 2058–2061, 2010.
- [17] T. A. Wittern and L. M. Sander, "Diffusion-limited aggregation, a kinetic critical phenomenon," *Physical Review Letters*, vol. 47, no. 19, pp. 1400–1403, 1981.
- [18] R. J. Glauber, "Time-dependent statistics of the Ising model," *Journal of Mathematical Physics*, vol. 4, no. 2, pp. 294–307, 1963.
- [19] J. Hauschild, H. J. Elmers, and U. Gradmann, "Dipolar superferromagnetism in monolayer nanostripes of Fe(110) on vicinal W(110) surfaces," *Physical Review B*, vol. 57, no. 2, pp. R677–R680, 1998.
- [20] W. Wernsdorfer, R. Clerac, C. Coulon, L. Lecren, and H. Miyasaka, "Quantum nucleation in a single-chain magnet," *Physical Review Letters*, vol. 95, no. 23, Article ID 237203, 4 pages, 2005.
- [21] P. Gambardella, A. Dallmeyer, K. Maiti et al., "Ferromagnetism in one-dimensional monatomic metal chains," *Nature*, vol. 416, no. 6878, pp. 301–304, 2002.
- [22] C. Antoniak, M. E. Gruner, M. Spasova et al., "A guideline for atomistic design and understanding of ultrahard nanomagnets," *Nature Communications*, vol. 2, article 528, 2011.

Research Article

Layer-by-Layer Self-Assembled Metal-Ion- (Ag-, Co-, Ni-, and Pd-) Doped TiO₂ Nanoparticles: Synthesis, Characterisation, and Visible Light Degradation of Rhodamine B

Mphilisi M. Mahlambi,¹ Ajay K. Mishra,¹ Shivani B. Mishra,¹ Ashok M. Raichur,^{1,2} Bhekhe B. Mamba,¹ and Rui W. Krause¹

¹ Department of Applied Chemistry, University of Johannesburg, P.O. Box 17011, Doornfontein 2028, South Africa

² Department of Materials Engineering, Indian Institute of Science, Bangalore 560012, India

Correspondence should be addressed to Ashok M. Raichur, amr@materials.iisc.ernet.in

Received 25 January 2012; Revised 13 March 2012; Accepted 13 March 2012

Academic Editor: Grégory Guisbiers

Copyright © 2012 Mphilisi M. Mahlambi et al. This is an open access article distributed under the Creative Commons Attribution License, which permits unrestricted use, distribution, and reproduction in any medium, provided the original work is properly cited.

Metal-ion- (Ag, Co, Ni and Pd) doped titania nanocatalysts were successfully deposited on glass slides by layer-by-layer (LbL) self-assembly technique using a poly(styrene sulfonate sodium salt) (PSS) and poly(allylamine hydrochloride) (PAH) polyelectrolyte system. Solid diffuse reflectance (SDR) studies showed a linear increase in absorbance at 416 nm with increase in the number of m-TiO₂ thin films. The LbL assembled thin films were tested for their photocatalytic activity through the degradation of Rhodamine B under visible-light illumination. From the scanning electron microscope (SEM), the thin films had a porous morphology and the atomic force microscope (AFM) studies showed “rough” surfaces. The porous and rough surface morphology resulted in high surface areas hence the high photocatalytic degradation (up to 97% over a 6.5 h irradiation period) using visible-light observed. Increasing the number of multilayers deposited on the glass slides resulted in increased film thickness and an increased rate of photodegradation due to increase in the availability of more nanocatalysts (more sites for photodegradation). The LbL assembled thin films had strong adhesion properties which made them highly stable thus displaying the same efficiencies after five (5) reusability cycles.

1. Introduction

Photocatalytic reaction-based processes are becoming more attractive to industry because they provide an alternative avenue for the decomposition of environmental pollutants. Growth in industrial development can be directly linked to the emergence of toxic pollutants which are deposited into aqueous streams [1, 2]. Among the semiconductor catalysts, TiO₂ (titanium dioxide or titania) is close to the ideal benchmark in environmental photocatalytic applications because of its outstanding chemical and biological stability, abundance, high oxidative power and, it is comparably less expensive [3–9].

Although the use of TiO₂ in suspension form is more feasible due to its large surface area, there are four major technical challenges that restrict large-scale application of

titania. Firstly, it has a relatively wide band gap (~3.2 eV, which falls in the UV range of the solar spectrum); therefore, it has minimal absorption of visible light and is unable to harness visible light hence ruling out sunlight as the energy source of photoactivation [7, 8, 10–14]. Secondly, it has low quantum efficiency due to the low rate of electron transfer to oxygen resulting in a high recombination of the photo generated electron-hole pairs [5, 7, 10]. Therefore, the effective utilisation of visible light for photocatalytic processes has become the ultimate goal. To achieve this, various methods like substitutional doping (N, C, F, etc.), dye sensitizing, using narrow band-gap quantum dots, binary oxides, and noble and transition metal nanoparticles have been developed [15, 16]. Also, the photoactivity of TiO₂ nanoparticles has been tailored by exposing the {001} facets which are very active [17]. Although these facets are very

active, they easily diminish crystal during nucleation and growth due to that they possess a high surface [17, 18]. Doping metals into the TiO_2 lattice is an effective strategy to reduce the band gap and shift the absorption edge towards visible-light region as they create energy states within the band gap by providing a “cushion” on the valence band (the donor level), resulting in a “decrease” in the band gap and also by acting as electron scavengers hence resulting in increased photocatalysis [7, 19–25]. However, it is imperative to take into consideration the amount of the dopant (metal) when preparing doped titania because when the dopant level surpasses the optimal limit, which usually lies at a very low dopant concentration ($\sim 0.4\%$), the metal ions act as recombination centres resulting in reduced photoactivity [23, 26]. Thirdly, when used in a suspension, titanium dioxide aggregates rapidly due to its small size (4–30 nm) suspended particles may scatter the light beam thus reducing its catalytic efficiency [8, 27, 28]. Lastly, the application of powdered TiO_2 catalysts requires posttreatment separation to recover the catalyst which is normally difficult, energy consuming, and economically not viable [1, 5, 8, 27, 29].

These technical challenges have led to more research activities on the fabrication of different types of titania thin films [6, 8, 9, 30–33]. Generally, thin films are known to be chemically stable and possess a high dielectric constant, a high refractive index, and excellent transmittance [9]. The most common methods for synthesising thin films include among others chemical vapour deposition (CVD), spray pyrolysis, dip coating, spin coating, liquid-phase deposition (LPD), ion-assisted deposition, arc-ion planting, sputtering, and sol-gel [11, 19, 32, 34–39]. However, these methods have some drawbacks. For example, although the sol-gel technique is the most widely used method, its disadvantage is the difficulty to control film thickness. The CVD method requires high temperatures while cracking and peeling off of the catalyst layer is usually observed due to poor adherence of the photocatalyst on the support [1, 8], and LPD requires special raw materials [38], hence they are not suitable for industrial applications.

In our laboratories we have used an alternative thin film synthesis method, layer-by-layer (LbL) self-assembly technique, to synthesise TiO_2 thin films of high quality [1]. The LbL technique can be used to deposit different types of materials on various substrates with good control of the thickness of the materials deposited on the substrate at nanometer-scale precision [1, 40–42]. The technique allows for alternate layer-by-layer growth of films through adsorption of polycation and polyanion monolayers from their aqueous solutions. The ionic attraction between opposite charges is the driving force for the multilayer buildup [40, 43–45]. This approach has been found to be a more economic alternative method compared to other methods for the direct preparation of thin films because it is simple, cheap, deposition occurs at low temperatures (room temperature), ease of control of film thickness (from nanometers to micrometers), and does not require complex equipment to execute [42, 44, 46, 47].

Layer-by-layer synthesised thin films have found applications, in a variety of scientific applications, and these include

biosensors, controlled drug delivery, surface coatings, and environmental applications in the degradation of toxic pollutants [8, 44, 48–52]. TiO_2 nanoparticles have also been successfully assembled on substrates using electrolytic polymers resulting in improved photocatalytic performances [1, 36, 53, 54]. These photocatalytic processes were performed under UV irradiation. However, most research activities in semiconductor photocatalysis focus on the development of a system that employs natural solar energy to degrade toxic pollutants in an aqueous medium. To achieve this, we have synthesised metal-ion- (Ag-, Co-, Ni-, and Pd-) doped titania thin films through the LbL self-assembly technique. Pd is highly reactive, and Ni is almost the same size as Ti. Pd and Ni are also abundant in South Africa hence are readily available and inexpensive. Ag and Co were used for comparative purposes. Metal-ion-doped TiO_2 (m- TiO_2) thin films have been previously synthesised using either sol-gel, liquid-phase deposition or colloidal sol techniques [5, 7, 10, 19, 28] but not using the layer-by-layer self-assembly deposition. To the best of our knowledge, the application of the LbL technique and the polyelectrolyte system used to immobilise the catalysts as described in this study has not been reported in the literature.

The photocatalytic efficiencies of these metal-ion-doped titania thin films were determined by the degradation of Rhodamine B, a xanthene group dye, under visible light. Rhodamine B (Rh B) was chosen because it is one of the major pollutants found in the textile and photographic industry effluents [55, 56]. Furthermore, it is estimated that approximately 1 to 20% of the total world produce of dyes is lost to the environment during synthesis and dyeing processes. These textile effluents are an environmental burden as they contain large amounts of azoic, anthraquinonic, and heteropolyaromatic dyes [55]. The discharge of these highly pigmented synthetic dyes to the ecosystem causes aesthetic pollution, eutrophication, and perturbations of aquatic life. Therefore, in this study we have used Rhodamine B as a model pollutant.

In this paper, we report on the photodegradation of Rhodamine B by poly(styrene sulfonate/metal-ion-doped titania (PSS/m- TiO_2)) multilayer thin films. The presence of the metals on the titania lattice shifts the absorption edge of titania to the visible-light region while the thin films eliminate the problems of suspension aggregation and posttreatment. The value-add of this work is the development of a system that can be potentially used in daylight to degrade pollutants in an aqueous media without leaving residual nanoparticles in the treated media. Poly(styrene sulfonate) was chosen because it is a strong polyelectrolyte that is negatively charged at all pH values. To study the cost effectiveness and sustainability of the prepared thin films, catalyst reusability studies were also performed.

2. Experimental

2.1. Materials and Methods. A Model Orion 5 star digital pH (Thermo Electron Corporation, USA) was used for determining the pH of the solutions. HCl or NaOH (1 M)

was used to adjust the pH of the prepared solutions. Microscopic glass slides (25.4 × 63.5 mm) were used as catalyst substrates. Poly(styrene sulfonate) (PSS, $M_W = 70\,000$ g/mol) and poly(allylamine hydrochloride) (PAH, $M_W = 70\,000$ g/mol) were purchased from Sigma-Aldrich (USA). Metal-ion-doped TiO₂ nanoparticles were synthesised by modifying a sol-gel method reported by Zhu et al. [57]. Titanium (IV), tetraisopropoxide (TTIP) (99%), and NiNO₃ were bought from Sigma-Aldrich (Germany) and used without further purification. Formic acid (98%) was purchased at Merck, and AR grade *n*-propanol was sourced from SD's Fine Chemicals (Pty) Ltd. and was distilled before usage. PdCl₂ and Rhodamine B were supplied by Finar Chemicals (Mumbai, India), AgNO₃ was procured from Associated Chemicals Enterprises (Pty) Ltd., whereas Co(NO₃)₂ was sourced from Hopkins and Williams Ltd., Essex, UK.

2.1.1. Synthesis of Catalysts. Titanium (IV) tetraisopropoxide (10 mL, 0.334 mol) was dissolved in propanol (48 mL, 0.642 mol), and the reaction mixture was stirred for 20 min. The metal salt AgNO₃ (0.4%) was dissolved in water (5 mL) while the other salts (PdCl₂, Co(NO₃)₂, and NiNO₃) (0.4%) were dissolved in *n*-propanol (5 mL) and were added dropwise to the reaction mixture of TTIP and propanol. Formic acid (13 mL, 0.535 mol) was gradually added while stirring gently. After stirring the reaction mixture for a further 20 min, a precipitate (metal-ion-doped titanium hydroxide) was gradually formed. The precipitated solution was stirred for a further 2 h period, aged at room temperature for another 2 h, and filtered. The filtered residue was then repeatedly washed with copious amounts of propanol and deionised water; thereafter, it was dried overnight in an oven at 80°C. The precipitate was then ground into fine powder using a mortar and pestle and then calcined at 450°C for 6 hrs at a heating rate of 2° min⁻¹ to obtain nanosized metal ion-doped TiO₂ photocatalysts. All experiments were carried out at room temperature.

2.1.2. LbL Thin Film Synthesis. The thin films were immobilised on glass slides using the method described by Decher et al. [41]. The glass slides were cleaned by first sonicating for 10 min in a 2 : 1 (v/v) ratio of isopropanol and water followed by rinsing with deionised water. Poly(allylamine hydrochloride), and poly(styrene sulfonate) solutions (1 g L⁻¹) were prepared using deionised water, and the pH of the solutions was adjusted to 2.5. The pH of the water used for rinsing was also adjusted to the same pH. A metal-ion-doped TiO₂ colloidal suspension was made in deionised water, and its pH was adjusted to that of the electrolyte solutions for the deposition of the thin films by the LbL technique. Polyelectrolyte solutions (PELs, 100 mg L⁻¹) and metal-ion-doped TiO₂ colloidal suspensions of 4 g L⁻¹ concentration, that is, 0.4% wt were prepared in deionised water and deposited on both sides of the glass slides. Based on the isoelectric point of TiO₂ (6.6), TiO₂ is positive and stable at pH 2.5, and PSS is negative at all pH values while PAH is positive below pH = 4. Before deposition of the films on

the substrates, the charge (on the substrates) was reversed (positive) by the deposition of a PAH monolayer. Thereafter, alternate layers of PSS and m-TiO₂ were deposited with m-TiO₂ being the last layer to be deposited in all instances.

2.2. Characterisation

2.2.1. UV-Visible Diffuse Reflectance Spectroscopy. The absorbance spectra of the prepared PSS/m-TiO₂ were obtained from a T60U spectrophotometer (PG Instruments Ltd., London, UK) and were recorded from 600 nm to 300 nm range. Since the film deposition was on both sides of the slide, the absorbance reported is also for the two sides of the glass slide.

2.2.2. SEM and EDX Analysis. A field emission microscope (FEI SIRION SEM, Eindhoven, The Netherlands) was used to analyse and visualise the quality and morphology of the synthesised thin films. The extent of LbL thin film deposition was also studied by the scanning electron microscope. The thin films were coated with gold prior to analysis. The SEM was coupled with an EDX detector in order to confirm the elemental composition of the thin films.

2.2.3. AFM Analysis. A Nanosurf EasyScan 2 (Switzerland), atomic force microscope (AFM) was employed to view the topography of the thin films. The AFM was also used to verify the effectiveness of the LbL technique on the deposition of thin films. The AFM was operated in the contact mode with the cantilever being in contact with the thin film surface.

2.3. Visible-Light Degradation Studies

2.3.1. Visible-Light Degradation. The ability of the thin films to degrade Rhodamine B under visible light was studied using a high-pressure powerball HCI-T 70W/NDL mercury vapour lamp with a maximum wavelength range of 410–460 nm (Osram, Germany). The photocatalytic degradation experiments were carried out in a photoreactor chamber. The photoreactor was set up and enclosed in a wooden box. It had a jacketed quartz tube with dimensions of 3.4 cm (inner diameter), 4 cm (outer diameter), and 21 cm (length). A submersible water pump was used to propel and circulate water through the quartz tube to avoid heating up of the photodegradation chamber due to the visible-light irradiation. The immobilised catalysts were placed in the dye solution, and the solution was continuously stirred with a magnetic stirrer. The stirring ensured a continuous flow of the solution over the catalysts during the photocatalytic experiments and hence promote the degradation process.

2.3.2. UV-Vis (Quantification) and Kinetics. The photocatalytic activity of the PSS/m-TiO₂ nanophotocatalysts was studied using Rhodamine B dye (100 mL, 10 mg L⁻¹). The red dye was poured into a beaker, placed in the photoreactor, and the solution was stirred using a magnetic stirrer for 30 min prior to irradiation with visible light to obtain a catalyst/dye adsorption-desorption equilibrium. Aliquots of

2 mL were extracted from the reaction chamber at 30 min intervals for 6.5 h to measure the extent of the degradation.

The kinetics of the photodegradation process was studied using the apparent rate constant. The apparent rate constant allows for the determination of photocatalytic activity independent of the previous adsorption period and the concentration of the Rh B remaining in the solution [58]. The data was fitted into the first order kinetic equation. The apparent first order kinetic equation is $-\ln(C_t/C_0) = K_{app}t$, where K_{app} is the apparent rate constant, C_t , the solution phase concentration, and C_0 , the concentration at $t = 0$, and it was used to fit the experimental data [26].

2.3.3. Catalyst Reusability. The importance of catalyst reusability is important when considering cost and economic implications. To study the reusability of the m-TiO₂ thin films, the degraded dye solution was removed after the first cycle, without removing the catalyst. A fresh solution of the dye was poured into the beaker, and the irradiation was started. This procedure was repeated over five (5) cycles for 6.5 h, and the solution was analysed after each cycle to determine the extent of degradation by the recycled catalysts.

3. Results and Discussions

3.1. UV-Visible Diffuse Reflectance Spectroscopy. Figure 1 shows the UV-Visible solid diffuse reflectance (SDR) spectra of the thin films. For the SDR measurements, 1, 3, 5, and 10 m-TiO₂ layers were each deposited on glass slides. Poly(allylamine hydrochloride) was the initial layer followed by alternate layers of PSS and m-TiO₂, respectively. Glass absorbs UV light, but it gives specious peaks below 300 nm, thus, a wavelength of 300 nm to 600 nm was chosen. The maximum UV absorbance of metal-ion-doped titania is 416 nm [59], and PSS has a characteristic absorption peaks at 220 nm while PAH shows negligible absorbance under the UV-vis region [1]. Hence, the absorption spectra recorded were characteristic of only m-TiO₂. From Figure 1 it can be seen that as the number of the deposited bilayers increased the absorbance also increased [1, 47, 53]. Also, the insert graph further reveals that the absorbance increased linearly as the number of metal-ion-doped titania bi-layers were increased.

3.2. SEM and EDX Analysis. The SEM micrographs of the synthesised thin films (1 to 5 bi-layers) in Figure 2 demonstrate that as the number of depositions of the thin films increased, there was also an increase in the metal-ion-doped titania nanoparticles assembled on the glass substrates. This observation can also be used to explain the increase in the absorbance noted in the UV-Vis spectroscopy. Furthermore, as the number of the deposited bilayers was increased from 1 to 10, the thin films assumed a more uniform distribution of the nanoparticles, a special trend exhibited by layer-by-layer self-assembled thin films [60]. Furthermore, SEM characterisation showed a smooth surface morphology as a result of a network of crosslinked polyelectrolytes, and m-TiO₂ nanoparticles [61]. Also, a high degree of porosity of

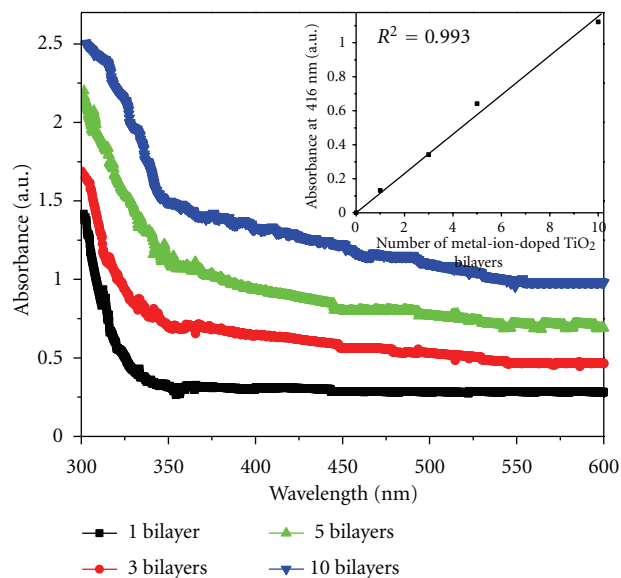


FIGURE 1: Absorption spectra of PSS/m-TiO₂ showing increase in absorbance with increase in number of layers (0.4% wt%). Insert: number of PSS/m-TiO₂ versus absorbance.

the thin films was observed on the SEM micrographs, and this property plays an important role in the photocatalytic activity of the assembled m-TiO₂ nanoparticles [1, 53]. The porosity nature of the thin films confirms the presence of a large surface area which results in an increased photocatalytic activity.

Electron dispersive X-ray spectroscopy (Figure 3) provided evidence of the successful synthesis of the metal-ion-doped titania thin films. The presence of the metal ions (Ag, Co, Ni, and Pd) is further indication that doped metal ions formed part of the titania lattice. The Si and Ca peaks observed from the EDX spectra of the thin films emanate from the glass slides used as the substrate used for assembling the metal-ion-doped titania nanoparticles [62].

3.3. AFM Analysis. The AFM images revealed an increase in surface coverage of metal-ion-doped titania nanoparticles as the number of the deposited bi-layers increased from 1 to 10. Also, the topography of the thin films showed patches and gaps between the nanocatalysts which became smaller and eventually became closely packed as the number of bi-layers increased. This is as a result of the overlap of the nanocatalyst layers forming a network as they adhere to oppositely charged surfaces (self-assembly) due to the presence of free charges from the previous depositions [40]. Also, from the 3D AFM images there seems to be an increased roughness of the thin film topography as the number of the bi-layers increased [63]. This suggests that the thin films had an increased surface area which is desirable for increased photocatalytic activity.

Furthermore, the AFM images confirm that there is an increase in film thickness as the number of deposited layers is increased (Figure 4). The linear fit (Figure 5) had a regression value of 0.994 which indicates a uniform growth

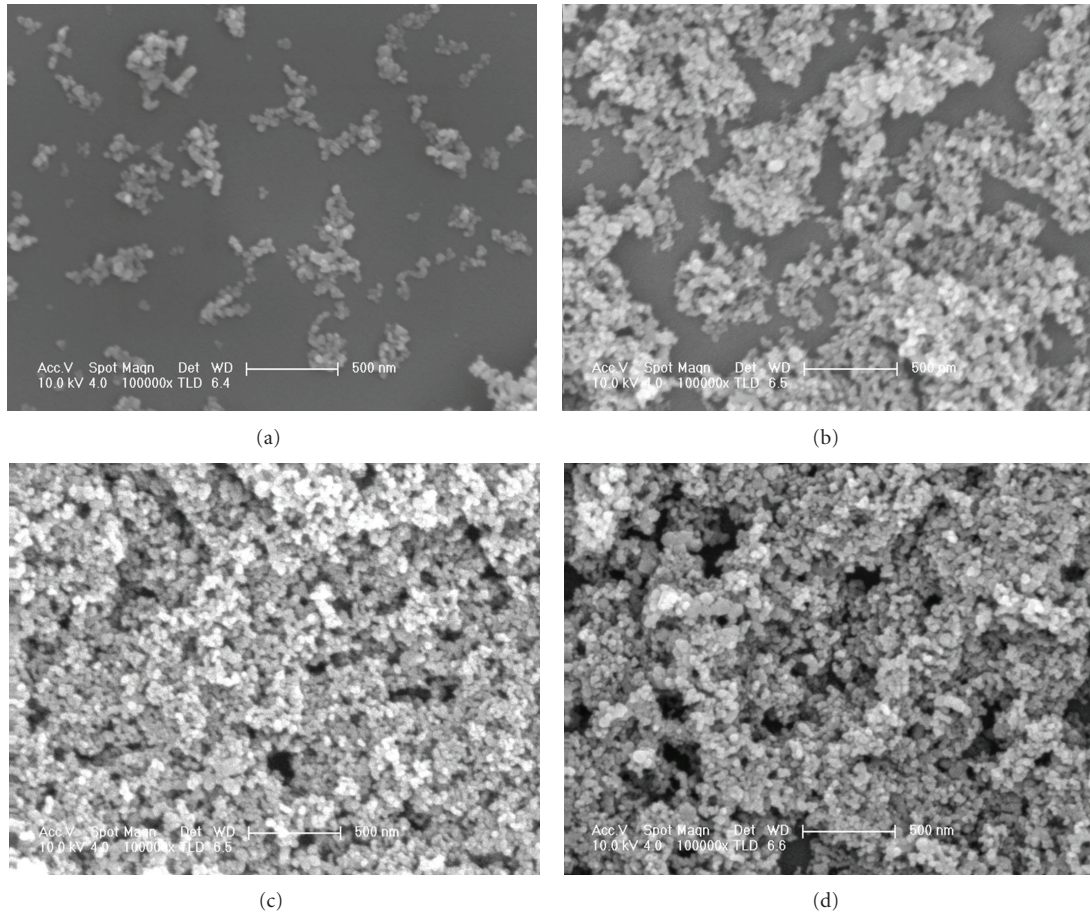
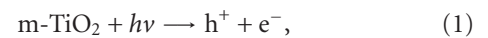


FIGURE 2: SEM images of $(\text{PSS}/\text{m-TiO}_2)_n$, where n = number of deposited layers, 1 (a), 3 (b), 5 (c), and 10 (d) immobilised on glass slides by LbL self-assembly technique.

of the PSS/TiO_2 thin films. The average thickness of the m-TiO_2 thin films was estimated to be 19.2 nm. Generally, the thickness of PSS/TiO_2 bi-layer thin films is estimated to be approximately 19 nm [1]. Film thickness is largely dependent on the polyelectrolyte used, the pH during deposition, and the size of the nanoparticles deposited because this is directly related to the amount of TiO_2 deposited on the substrate. For example, a single bi-layer of PAA/TiO_2 and PDAC/TiO_2 thin films is estimated to be around 18 nm and 38 nm, respectively [1, 64]. Since one (1) bi-layer of PSS/TiO_2 is estimated to be 19 nm, theoretically PSS/TiO_2 thin films having three (3) and ten (10) bi-layers are expected to be 57 nm and 190 nm thick, respectively, hence the values of 58.3 nm and 186 nm obtained for the synthesised $\text{PSS}/\text{m-TiO}_2$ thin films compare favourably to the reported values.

3.4. Visible Light Degradation of Rhodamine B and Kinetic Studies. The photodegradation process of Rhodamine B can be summarised in (1) to (3) when disregarding the role of the electrons (e^-) which is in the oxidation of metal ions. The titania nanocatalysts absorb a photon ($h\nu$) resulting in the excitation of an electron (e^-) from the valence band (VB) to the conduction band (CB) leaving an electron vacancy or a

hole (h^+) in the valence band (1). The holes then migrate to the surface of the titania where they react with surface hydroxyl groups in the TiO_2 lattice or water to produce hydroxyl radicals (2).



The hydroxyl radicals then react with the Rhodamine B producing intermediates, carbon dioxide, water, and inorganic ions (3).

UV-visible spectroscopy was used to quantify the amount of Rhodamine B photodegraded by the m-TiO_2 layer-by-layer thin films assembled on glass slides. Glass slides with different thin film thicknesses, that is, 1 to 10 bi-layers were investigated for the photodegradation of Rhodamine B. Five immobilised catalysts (i.e., 5 glass slides) of each bi-layer sequence were put in Rhodamine B solution (100 mL of 100 mg L^{-1}) and stirred for 30 min in the dark to attain an adsorption-desorption equilibrium between the

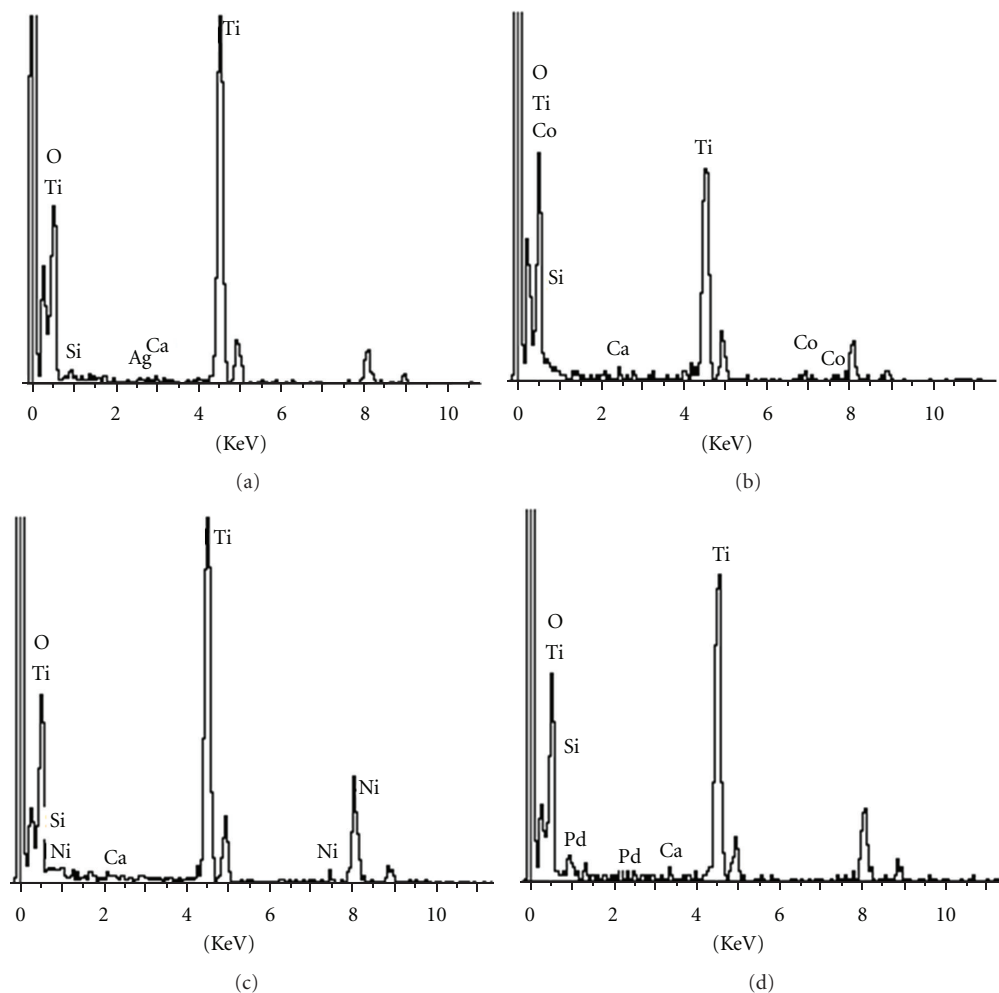


FIGURE 3: EDX spectra of $(\text{PSS}/\text{m-TiO}_2)_{10}$ for Ag-, Co-, Ni-, and Pd-, doped titania immobilised on glass slides by LbL self-assembly technique.

catalyst and the Rhodamine B. The reaction mixture was then illuminated for 6.5 h, and 2 mL aliquots of the dye were taken to study the extent of the photodegradation. Visible-light illumination without the semiconductor catalyst produced no photodegradation of the dye without. Poly(styrene sulfonate) and PAH do not take part in the photodegradation of Rhodamine B by TiO_2 nanoparticles [1]. The photodegradation kinetic studies were studied using the first order apparent rate law equation ($-\ln C_t/C_0 = K_{\text{app}}t$).

3.4.1. Ag- TiO_2 Thin Films. The photodegradation experiments showed that 5 of catalysts 1 bi-layer degraded 33%, 3 bi-layers had degraded 48%, 5 bi-layers had degraded 79%, and 10 bi-layers had degraded 96% of Rhodamine B after 6.5 h of visible-light irradiation (Figure 6). These results confirm that as the number of bi-layers is increased, there is also an increase in the rate of photocatalytic degradation of Rhodamine B. Further confirmation can be drawn from the apparent rate constants obtained from the linear transform graph. As the number of bi-layers increased from 1 to 10, the

apparent rate constant also increased from 0.0012 min^{-1} to 0.0102 min^{-1} as shown in Table 1.

3.4.2. Co- TiO_2 Thin Films. For the Co- TiO_2 immobilised thin films, photodegradation efficiencies of 33%, 51%, 76%, and 97% were observed for 1, 3, 5, and 10 bi-layers after 6.5 h of visible-light irradiation. Increasing the number of bi-layers resulted in an increase in the rate of photocatalytic degradation of Rhodamine B. The apparent rate constants observed for these photocatalytic degradation efficiencies were 0.0012 min^{-1} for a single bi-layer, 0.0022 min^{-1} for 3 bi-layers, 0.0043 min^{-1} for 5 bi-layers, and 0.0102 min^{-1} for 10 bi-layers.

3.4.3. Ni- TiO_2 Thin Films. The same photodegradation trend was observed for Ni- TiO_2 LbL assembled thin films. After 6.5 h of visible-light irradiation, it was observed that 1 bi-layer of the Ni-titania film has degraded only 3.5 mg L^{-1} (35%), 3 bi-layers had degraded 5.6 mg L^{-1} (56%), and 5 bi-layers had degraded 6.2 mg L^{-1} , an equivalent of 62% of Rhodamine B. The highest photodegradation efficiency

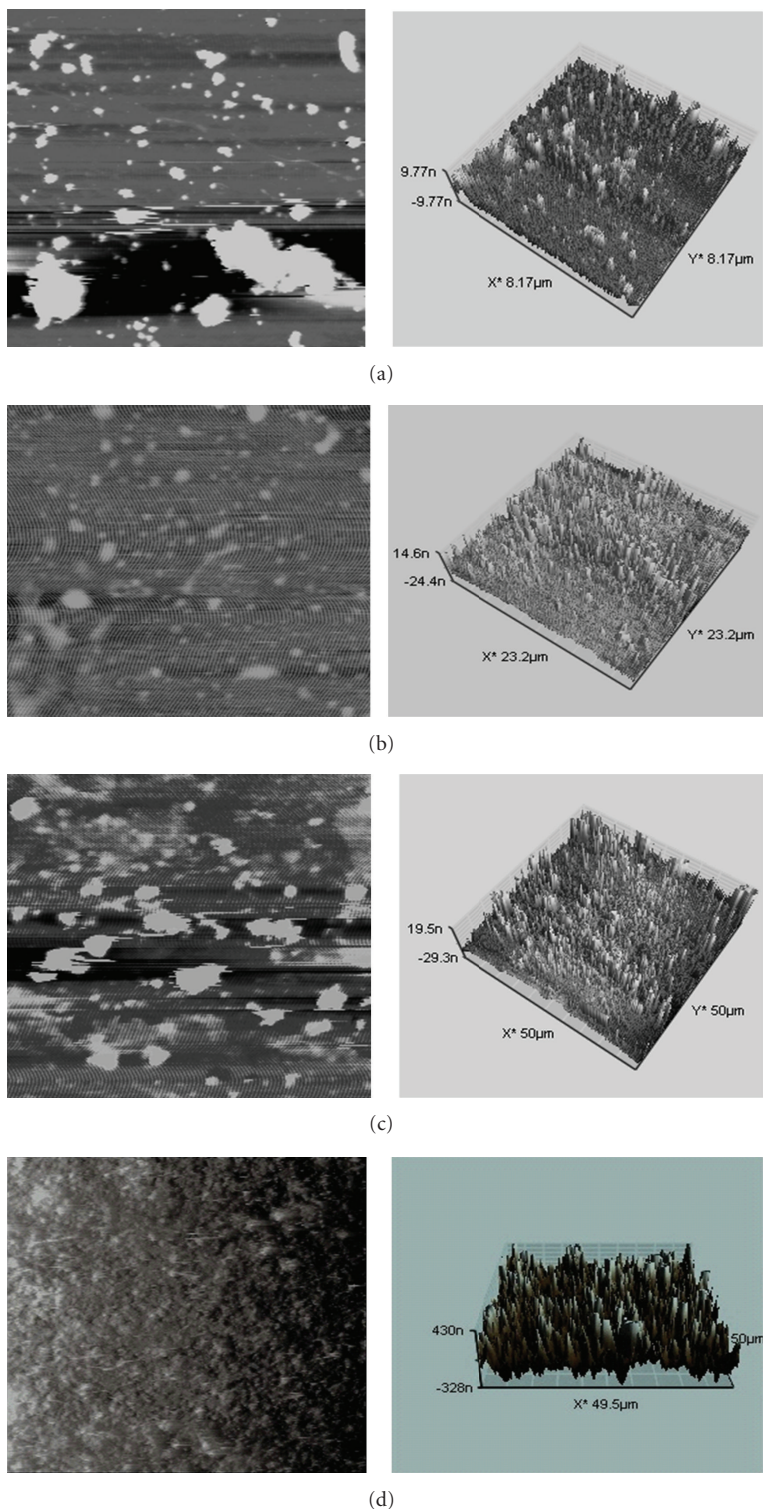


FIGURE 4: 2D and 3D AFM images of $(\text{PSS}/\text{m-TiO}_2)_n$, where $n = 1$ (a), 3 (b), 5 (c), and 10 (d) immobilised on glass slides by LbL self-assembly technique.

was observed for the 10 bi-layers (85%). This confirms that enhancement of the initial rate of photodegradation (apparent rate) of Rhodamine B corresponds to an increase in the number of bi-layers (Table 1).

3.4.4. Pd-TiO₂ Thin Films. The Pd-TiO₂ thin films also produced the same photodegradation pattern that was observed for the Ag-, Co-, and Ni-TiO₂ thin films, that is, there was an increase in the rate of photodegradation

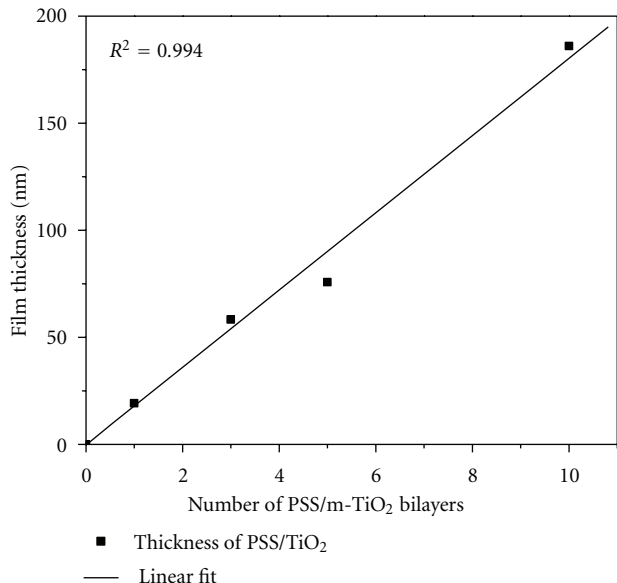


FIGURE 5: Number of PAH(PSS/m-TiO₂)_n bilayers versus film thickness ($n = 1, 3, 5,$ and 10).

TABLE 1: Photocatalytic degradation efficiencies and apparent rate constants of the thin films.

Catalyst	No. of bi-layers	Apparent rate constant (min ⁻¹)	Degradation after 6.5 h (%)
Degussa P25	10	0.0008	20
Ag-TiO ₂	1	0.0012	33
	3	0.0019	48
	5	0.0047	79
	10	0.0092	96
Co-TiO ₂	1	0.0012	33
	3	0.0022	51
	5	0.0043	76
	10	0.0102	97
Ni-TiO ₂	1	0.0013	35
	3	0.0025	56
	5	0.0029	62
	10	0.0059	85
Pd-TiO ₂	1	0.0013	35
	3	0.0022	51
	5	0.0029	61
	10	0.0083	94

as the number of bi-layers increased. The photocatalytic efficiencies obtained after 6.5 h of visible-light irradiation increased from 35% to 94% as the number bi-layers increased from 1 to 10, respectively. These efficiencies corresponded to apparent rate constants of 0.0013 min⁻¹ and 0.0083 min⁻¹, respectively. The rest of the apparent rate constants and photodegradation efficiencies are shown in Table 1.

The increase in the absorption efficiencies observed with increase in the number of bi-layers is most probably due to increase and availability of more surface area of the catalyst. Furthermore, as the number of bi-layers increase, there was a direct increase in the amount of catalysts embedded on the substrate as shown by the SEM and AFM images. The initial rate, that is, the apparent rate constant of degradation of Rhodamine B was observed to increase with increasing number of bi-layers. This is an indication that the photodegradation is not only affected by the outermost layer but also the inner preceding layers. The participation of the inner layers in the photodegradation is possible due to the high degree of porosity and roughness exhibited by the thin films as shown by the SEM and AFM images, respectively. These resulted in an increased surface area for Rhodamine B adsorption and hence an increased rate of photocatalytic degradation.

To further ascertain the reactivity of the synthesised metal-ion-doped thin film catalysts, their photocatalytic activities were compared with the Degussa P25 titania nanocatalysts. The synthesised thin films were found to be superior to the Degussa P25 thin films which could only degrade up to 20% Rhodamine B under visible-light irradiation over a 6.5 h period (Table 1). Although these Degussa P25 thin films show high degradation efficiencies under UV-light irradiation [1], they fail to possess the same under visible-light. This therefore proves that the presence of the metal ions on the titania lattice has played a pivotal role in shifting the absorption edge of the titania nanocatalysts towards visible light. Hence, this study provides a major stride towards the use of solar energy (visible light) for the activation of titania nanoparticles for use in environmental remediation processes.

3.4.5. Effect of Metal-Ion on the Rate of Photodegradation.

The results of Rhodamine B photodegradation show average degradation efficiencies of about 33%, 50%, 70%, and 93% for the 5 catalysts of 1, 3, 5, and 10 bi-layers of m-TiO₂ thin films (Figure 7), respectively. These average degradation efficiencies were irrespective of the metal ion used during the 6.5 h of visible-light irradiation. The only metal-ion-doped catalyst that showed lower absorption efficiencies for 10 bi-layer thin films was Ni-TiO₂ titania (shown by the larger error bar on the 10 bi-layer thin films (Figure 7)). This could be as a result of the photocatalytic activity of m-TiO₂ being affected by the slide orientation. Although the incident visible-light intensity was the same for all the experiments, the slides might not have been identically oriented hence the absorption of visible light by the slides might not be the similar. This suggests that the rate of production of radicals was not identical for all the glass slides thus resulting in slight differences in the photodegradation efficiencies.

3.5. Catalyst Reusability. To investigate the catalyst reusability studies, PAH(PSS/m-TiO₂)₁₀ (where $m = \text{Ag, Co, Ni, or Pd}$) thin films were used. The catalyst reusability studies were performed over five (5) cycles (Figure 8). The results

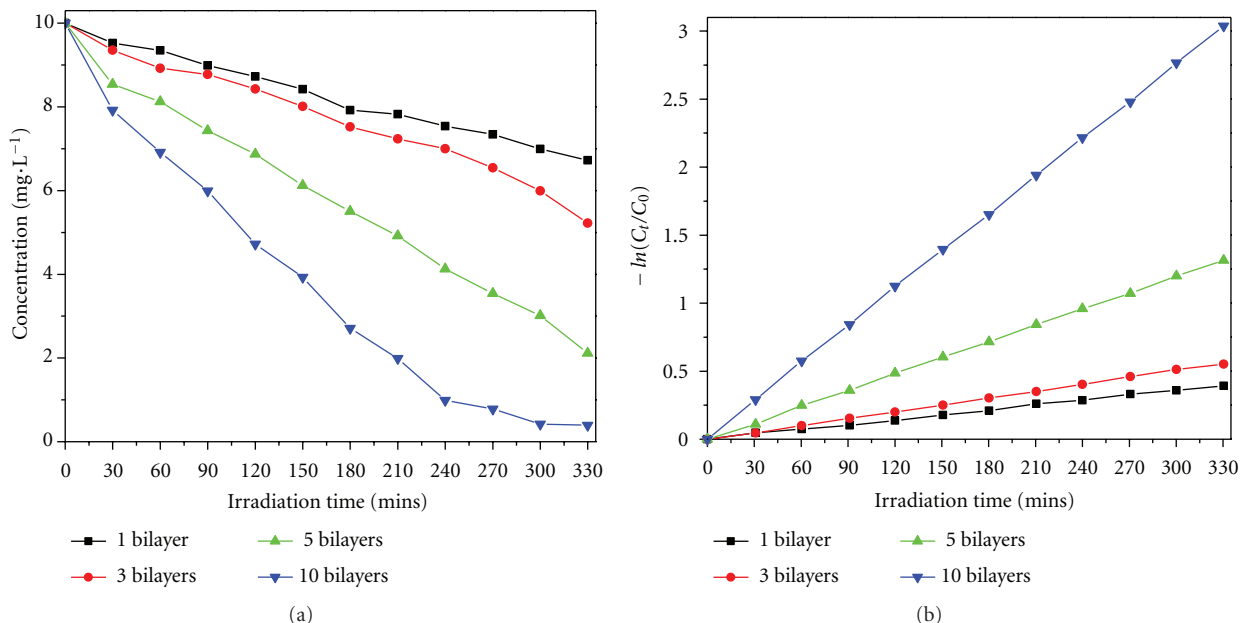


FIGURE 6: Photocatalytic degradation of Rh B and the linear transform, $-\ln(C_t/C_0) = f(t)$, of the kinetic curves of Rh B disappearance by Ag-TiO₂ thin films (1–10 bi-layers).

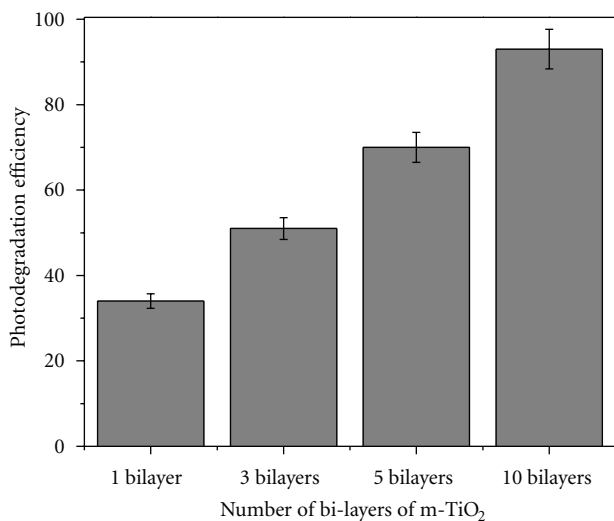


FIGURE 7: Absorption efficiencies exhibited by the m-TiO₂ thin films.

obtained show that the LbL synthesised thin films did not lose their photocatalytic efficiencies even after the five cycles, that is, the photodegradation results of Rhodamine B were still reproducible even after the five cycles. The LbL self-assembled thin films therefore exhibited film stability. This is important because this observation suggests that the LbL assembled m-TiO₂ thin films could be potentially used in continuous water treatment systems. In addition, the reusability of the thin films means could result in a reduction in the cost of water treatment if m-TiO₂ thin films were to be utilised and if scaling up would still be as efficient and economically viable.

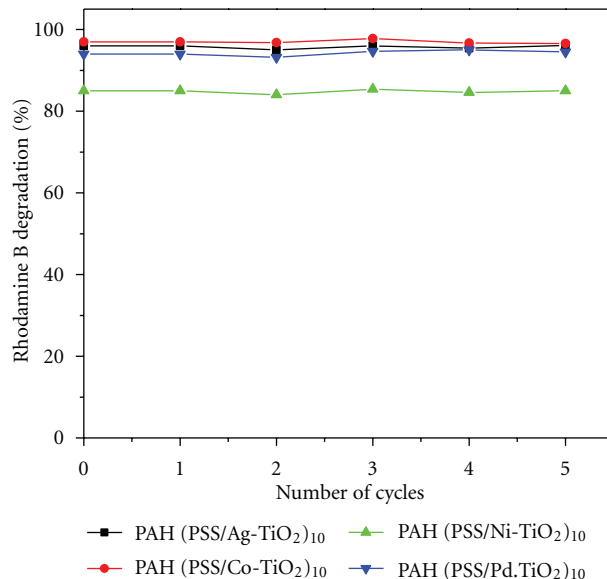


FIGURE 8: Catalyst reusability studies by the m-TiO₂ LbL assembled thin films.

4. Conclusions

The m-TiO₂ LbL assembled thin films (PAH(PSS/m-TiO₂)_n) were successfully synthesised, and there was a linear increase in thickness as the number of multilayer deposition increased. These thin films exhibited high photodegradation efficiencies (up to 95%) of Rhodamine B under visible-light illumination. Although the illumination time was longer than when the suspension form is used, this can be overcome by increasing the number of thin film multilayers

to cause an increase in the rate of photocatalytic degradation of Rhodamine B. Catalyst reusability studies revealed that the LbL synthesised thin films were highly stable as they could maintain the equivalent photodegradation efficiencies for the five cycles that were tested. The high stability, reusability, and visible-light illumination of the m-TiO₂ make the LbL assembled m-TiO₂ thin films a potentially viable technique for application in water treatment processes where solar energy can be used as the source of energy for the illumination of photodegradation of pollutants in the presence of titania nanocatalysts.

Acknowledgments

The authors are grateful to the University of Johannesburg for financial support and the Indian Institute of Science, Bangalore, for providing the infrastructure to carry out most of this research work.

References

- [1] D. N. Priya, J. M. Modak, and A. M. Raichur, "LbL fabricated poly(styrene sulfonate)/TiO₂ multilayer thin films for environmental applications," *ACS Applied Materials & Interfaces*, vol. 1, no. 1, pp. 2684–2693, 2009.
- [2] R. S. Sonawane and M. K. Dongare, "Sol-gel synthesis of Au/TiO₂ thin films for photocatalytic degradation of phenol in sunlight," *Journal of Molecular Catalysis A*, vol. 243, no. 1, pp. 68–76, 2006.
- [3] Z. He, C. Sun, S. Yang, Y. Ding, H. He, and Z. Wang, "Photocatalytic degradation of rhodamine B by Bi₂WO₆ with electron accepting agent under microwave irradiation: mechanism and pathway," *Journal of Hazardous Materials*, vol. 162, no. 2-3, pp. 1477–1486, 2009.
- [4] A. Murakami, T. Yamaguchi, S. I. Hirano, and K. Kikuta, "Synthesis of porous titania thin films using carbonation reaction and its hydrophilic property," *Thin Solid Films*, vol. 516, no. 12, pp. 3888–3892, 2008.
- [5] L. Ge, M. Xu, and H. Fang, "Synthesis and characterization of the Pd/InVO₄-TiO₂ co-doped thin films with visible light photocatalytic activities," *Applied Surface Science*, vol. 253, no. 4, pp. 2257–2263, 2006.
- [6] F. Ren, K. He, Y. Ling, and J. Feng, "Novel fabrication of net-like and flake-like Fe doped TiO₂ thin films," *Applied Surface Science*, vol. 257, pp. 9621–9625, 2011.
- [7] B. Zhao and Y. Chen, "Ag/TiO₂ sol prepared by a sol-gel method and its photocatalytic activity," *Journal of Physics and Chemistry of Solids*, vol. 72, pp. 1312–1318, 2011.
- [8] M. A. Nawari, A. H. Jawad, S. Sabar, and W. S. W. Ngah, "Immobilized bilayer TiO₂/chitosan system for the removal of phenol under irradiation by a 45 watt compact fluorescent lamp," *Desalination*, vol. 280, pp. 288–296, 2011.
- [9] G. A. Battiston, R. Gerbasi, M. Porchia, and A. Marigo, "Influence of substrate on structural properties of TiO₂ thin films obtained via MOCVD," *Thin Solid Films*, vol. 239, no. 2, pp. 186–191, 1994.
- [10] X. Hou, X. Wu, and A. Liu, "Studies on photocatalytic activity of Ag/TiO₂ films," *Frontiers of Chemistry in China*, vol. 1, no. 4, pp. 402–407, 2006.
- [11] M. C. Kao, H. Z. Chen, S. L. Young, C. Y. Kung, C. C. Lin, and Z. Y. Hong, "Microstructure and optical properties of tantalum modified TiO₂ thin films prepared by the sol-gel process," *Journal of Superconductivity and Novel Magnetism*, vol. 23, no. 5, pp. 843–845, 2010.
- [12] P. Romero-Gómez, V. Rico, J. P. Espinós, A. R. González-Elipe, R. G. Palgrave, and R. G. Egdell, "Nitridation of nanocrystalline TiO₂ thin films by treatment with ammonia," *Thin Solid Films*, vol. 519, no. 11, pp. 3587–3595, 2011.
- [13] P. Wang, T. Zhou, R. Wang, and T. T. Lim, "Carbon-sensitized and nitrogen-doped TiO₂ for photocatalytic degradation of sulfanilamide under visible-light irradiation," *Water Research*, vol. 45, pp. 5015–5026, 2011.
- [14] A. Bai, W. Liang, G. Zheng, and J. Xue, "Preparation and enhanced daylight-induced photo-catalytic activity of transparent C-Doped TiO₂ thin films," *Journal Wuhan University of Technology, Materials Science Edition*, vol. 25, no. 5, pp. 738–742, 2010.
- [15] J. Yu, J. Xiong, B. Cheng, and S. Liu, "Fabrication and characterization of Ag-TiO₂ multiphase nanocomposite thin films with enhanced photocatalytic activity," *Applied Catalysis B*, vol. 60, no. 3-4, pp. 211–221, 2005.
- [16] J. Yu, G. Dai, and B. Huang, "Fabrication and characterization of visible-light-driven plasmonic photocatalyst Ag/AgCl/TiO₂ nanotube arrays," *Journal of Physical Chemistry C*, vol. 113, no. 37, pp. 16394–16401, 2009.
- [17] W. Q. Fang, J. Z. Zhou, J. Liu et al., "Hierarchical structures of single-crystalline anatase TiO₂ nanosheets dominated by 001 facets," *Chemistry*, vol. 17, no. 5, pp. 1423–1427, 2011.
- [18] Q. Xiang, J. Yu, and M. Jaroniec, "Tunable photocatalytic selectivity of TiO₂ films consisted of flower-like microspheres with exposed 001 facets," *Chemical Communications*, vol. 47, no. 15, pp. 4532–4534, 2011.
- [19] N. S. Begum, H. M. F. Ahmed, and K. R. Gunashekar, "Effects of Ni doping on photocatalytic activity of TiO₂ thin films prepared by liquid phase deposition technique," *Bulletin of Materials Science*, vol. 31, no. 5, pp. 747–751, 2008.
- [20] W. Weng, M. Ma, P. Du et al., "Superhydrophilic Fe doped titanium dioxide thin films prepared by a spray pyrolysis deposition," *Surface and Coatings Technology*, vol. 198, no. 1–3, pp. 340–344, 2005.
- [21] F. Meng, X. Song, and Z. Sun, "Photocatalytic activity of TiO₂ thin films deposited by RF magnetron sputtering," *Vacuum*, vol. 83, no. 9, pp. 1147–1151, 2009.
- [22] Y. Cao, H. Tan, T. Shi, T. Shi, T. Tang, and J. Li, "Preparation of Ag-doped TiO₂ nanoparticles for photocatalytic degradation of acetamiprid in water," *Journal of Chemical Technology and Biotechnology*, vol. 83, no. 4, pp. 546–552, 2008.
- [23] P. Bouras, E. Stathatos, and P. Lianos, "Pure versus metal-ion-doped nanocrystalline titania for photocatalysis," *Applied Catalysis B*, vol. 73, no. 1-2, pp. 51–59, 2007.
- [24] E. Bae and W. Choi, "Highly enhanced photoreductive degradation of perchlorinated compounds on dye-sensitized metal/TiO₂ under visible light," *Environmental Science and Technology*, vol. 37, no. 1, pp. 147–152, 2003.
- [25] T. Umehayashi, T. Yamaki, H. Itoh, and K. Asai, "Analysis of electronic structures of 3d transition metal-doped TiO₂ based on band calculations," *Journal of Physics and Chemistry of Solids*, vol. 63, no. 10, pp. 1909–1920, 2002.
- [26] M. Stir, R. Nicula, and E. Burkel, "Pressure-temperature phase diagrams of pure and Ag-doped nanocrystalline TiO₂ photocatalysts," *Journal of the European Ceramic Society*, vol. 26, no. 9, pp. 1547–1553, 2006.
- [27] A. Bhattacharyya, S. Kawi, and M. B. Ray, "Photocatalytic degradation of orange II by TiO₂ catalysts supported on adsorbents," *Catalysis Today*, vol. 98, no. 3, pp. 431–439, 2004.

- [28] J. Yu, J. C. Yu, B. Cheng, and X. Zhao, "Photocatalytic activity and characterization of the sol-gel derived Pb-doped TiO₂ thin films," *Journal of Sol-Gel Science and Technology*, vol. 24, no. 1, pp. 39–48, 2002.
- [29] A. López, D. Acosta, A. I. Martínez, and J. Santiago, "Nanostructured low crystallized titanium dioxide thin films with good photocatalytic activity," *Powder Technology*, vol. 202, no. 1–3, pp. 111–117, 2010.
- [30] C. Zhang, R. Chen, J. Zhou, J. Cheng, and Q. Xia, "Synthesis of TiO₂ films on glass slides by the sol-gel method and their photocatalytic activity," *Rare Metals*, vol. 28, no. 4, pp. 378–384, 2009.
- [31] X. S. Zhou, L. J. Li, Y. H. Lin, and C. W. Nan, "Characterization and properties of anatase TiO₂ film prepared via colloidal sol method under low temperature," *Journal of Electroceramics*, vol. 21, no. 1–4, pp. 795–797, 2008.
- [32] Z. He, Z. Yu, H. Miao, G. Tan, and Y. Liu, "Preparation of TiO₂ thin film by the LPD method on functionalized organic self-assembled monolayers," *Science in China, Series E*, vol. 52, no. 1, pp. 137–140, 2009.
- [33] J. Yu, X. Zhao, and Q. Zhao, "Effect of film thickness on the grain size and photocatalytic activity of the sol-gel derived nanometer TiO₂ thin films," *Journal of Materials Science Letters*, vol. 19, no. 12, pp. 1015–1017, 2000.
- [34] A. Nakaruk and C. C. Sorrell, "Conceptual model for spray pyrolysis mechanism: fabrication and annealing of titania thin films," *Journal of Coatings Technology Research*, vol. 7, no. 5, pp. 665–676, 2010.
- [35] D. Dumitriu, A. R. Bally, C. Ballif et al., "Photocatalytic degradation of phenol by TiO₂ thin films prepared by sputtering," *Applied Catalysis B*, vol. 25, no. 2–3, pp. 83–92, 2000.
- [36] S.-H. Nam, S.-J. Cho, C.-K. Jung et al., "Comparison of hydrophilic properties of TiO₂ thin films prepared by sol-gel method and reactive magnetron sputtering system," *Thin Solid Films*, vol. 519, pp. 6944–6950, 2011.
- [37] M. Guglielmi, A. Martucci, E. Menegazzo et al., "Control of semiconductor particle size in sol-gel thin films," *Journal of Sol-Gel Science and Technology*, vol. 8, no. 1–3, pp. 1017–1021, 1997.
- [38] J. G. Yu, H. G. Yu, B. Cheng, X. J. Zhao, J. C. Yu, and W. K. Ho, "The effect of calcination temperature on the surface microstructure and photocatalytic activity of TiO₂ thin films prepared by liquid phase deposition," *Journal of Physical Chemistry B*, vol. 107, no. 50, pp. 13871–13879, 2003.
- [39] J. Yu and B. Wang, "Effect of calcination temperature on morphology and photoelectrochemical properties of anodized titanium dioxide nanotube arrays," *Applied Catalysis B*, vol. 94, pp. 295–302, 2010.
- [40] T. Sasaki, Y. Ebina, T. Tanaka, M. Harada, M. Watanabe, and G. Decher, "Layer-by-layer assembly of titania nanosheet/polycation composite films," *Chemistry of Materials*, vol. 13, no. 12, pp. 4661–4667, 2001.
- [41] G. Decher, J. D. Hong, and J. Schmitt, "Buildup of ultrathin multilayer films by a self-assembly process—III. Consecutively alternating adsorption of anionic and cationic polyelectrolytes on charged surfaces," *Thin Solid Films*, vol. 210–211, no. 2, pp. 831–835, 1992.
- [42] Y. Guo, W. Geng, and J. Sun, "Layer-by-layer deposition of polyelectrolyte-polyelectrolyte complexes for multilayer film fabrication," *Langmuir*, vol. 25, no. 2, pp. 1004–1010, 2009.
- [43] M. E. Mahmoud, S. S. Haggag, and T. M. Abdel-Fattah, "Surface layer-by-layer chemical deposition reaction for thin film formation of nano-sized metal 8-hydroxyquinolate complexes," *Polyhedron*, vol. 28, no. 1, pp. 181–187, 2009.
- [44] P. G. Su and Y. S. Chuang, "Flexible H₂ sensors fabricated by layer-by-layer self-assembly thin film of multi-walled carbon nanotubes and modified in situ with Pd nanoparticles," *Sensors and Actuators B*, vol. 145, no. 1, pp. 521–526, 2010.
- [45] G. B. Sukhorukov, E. Donath, H. Lichtenfeld et al., "Layer-by-layer self assembly of polyelectrolytes on colloidal particles," *Colloids and Surfaces A*, vol. 137, no. 1–3, pp. 253–266, 1998.
- [46] M. Yin, J. Qian, Q. An, Q. Zhao, Z. Gui, and J. Li, "Polyelectrolyte layer-by-layer self-assembly at vibration condition and the pervaporation performance of assembly multilayer films in dehydration of isopropanol," *Journal of Membrane Science*, vol. 358, no. 1–2, pp. 43–50, 2010.
- [47] J. A. He, R. Mosurkal, L. A. Samuelson, L. Li, and J. Kumar, "Dye-sensitized solar cell fabricated by electrostatic layer-by-layer assembly of amphoteric TiO₂ nanoparticles," *Langmuir*, vol. 19, no. 6, pp. 2169–2174, 2003.
- [48] X. Yang, X. Han, and Y. Zhu, "(PAH/PSS)₅ microcapsules templated on silica core: encapsulation of anticancer drug DOX and controlled release study," *Colloids and Surfaces A*, vol. 264, no. 1–3, pp. 49–54, 2005.
- [49] M. M. De Villiers, D. P. Otto, S. J. Strydom, and Y. M. Lvov, "Introduction to nanocoatings produced by layer-by-layer (LbL) self-assembly," *Advanced Drug Delivery Reviews*, vol. 63, no. 9, pp. 701–715, 2011.
- [50] K. Murugan, T. N. Rao, G. V. N. Rao, A. S. Gandhi, and B. S. Murty, "Effect of dehydration rate on non-hydrolytic TiO₂ thin film processing: structure, optical and photocatalytic performance studies," *Materials Chemistry and Physics*, vol. 129, no. 3, pp. 810–815, 2011.
- [51] S. Suárez, N. Arconada, Y. Castro et al., "Photocatalytic degradation of TCE in dry and wet air conditions with TiO₂ porous thin films," *Applied Catalysis B*, vol. 108–109, pp. 14–21, 2011.
- [52] P. G. Su, W. C. Li, J. Y. Tseng, and C. J. Ho, "Fully transparent and flexible humidity sensors fabricated by layer-by-layer self-assembly of thin film of poly(2-acrylamido-2-methylpropane sulfonate) and its salt complex," *Sensors and Actuators B*, vol. 153, no. 1, pp. 29–36, 2011.
- [53] T. H. Kim and B. H. Sohn, "Photocatalytic thin films containing TiO₂ nanoparticles by the layer-by-layer self-assembling method," *Applied Surface Science*, vol. 201, no. 1–4, pp. 109–114, 2002.
- [54] C. Pan, L. Dong, L. Q. Ge, J. Wang, and Z. Z. Gu, "Highly active TiO₂/polyelectrolytes hybrid multilayered hollow nanofibrous photocatalyst prepared from electrospun fibers using electrostatic layer-by-layer technique," *Journal of Macromolecular Science Part B*, vol. 48, no. 1, pp. 92–105, 2009.
- [55] T. S. Natarajan, M. Thomas, K. Natarajan, H. C. Bajaj, and R. J. Tayade, "Study on UV-LED/TiO₂ process for degradation of Rhodamine B dye," *Chemical Engineering Journal*, vol. 169, no. 1–3, pp. 126–134, 2011.
- [56] M. Akarsu, M. Asiltürk, F. Sayilkan, N. Kiraz, E. Arpaç, and H. Sayilkan, "A novel approach to the hydrothermal synthesis of anatase titania nanoparticles and the photocatalytic degradation of Rhodamine B," *Turkish Journal of Chemistry*, vol. 30, no. 3, pp. 333–343, 2006.
- [57] J. Zhu, J. Zhang, F. Chen, K. Iino, and M. Anpo, "High activity TiO₂ photocatalysts prepared by a modified sol-gel method: characterization and their photocatalytic activity for the degradation of XRG and X-GL," *Topics in Catalysis*, vol. 35, no. 3–4, pp. 261–268, 2005.

- [58] Y. Ao, J. Xu, D. Fu, and C. Yuan, "Preparation of Ag-doped mesoporous titania and its enhanced photocatalytic activity under UV light irradiation," *Journal of Physics and Chemistry of Solids*, vol. 69, no. 11, pp. 2660–2664, 2008.
- [59] J. A. Navio, G. Colon, M. Macias, C. Real, and M. I. Litter, "Iron-doped titania semiconductor powders prepared by a sol-gel method—part I: synthesis and characterization," *Applied Catalysis A*, vol. 177, pp. 111–120, 1999.
- [60] K. Katagiri, T. Suzuki, H. Muto, M. Sakai, and A. Matsuda, "Low temperature crystallization of TiO₂ in layer-by-layer assembled thin films formed from water-soluble Ti-complex and polycations," *Colloids and Surfaces A*, vol. 321, no. 1–3, pp. 233–237, 2008.
- [61] G. Decher, B. Lehr, K. Lowack, Y. Lvov, and J. Schmitt, "New nanocomposite films for biosensors: layer-by-layer adsorbed films of polyelectrolytes, proteins or DNA," *Biosensors and Bioelectronics*, vol. 9, no. 9-10, pp. 677–684, 1994.
- [62] P. Ding, F. M. Liu, X. A. Yang, and J. Q. Li, "Characterization of structure and distortion in the manganese ions implanted TiO₂ thin films," *Nuclear Instruments and Methods in Physics Research Section B*, vol. 267, no. 18, pp. 3109–3113, 2009.
- [63] J. H. Kim, S. Fujita, and S. Shiratori, "Fabrication and characterization of TiO₂ thin film prepared by a layer-by-layer self-assembly method," *Thin Solid Films*, vol. 499, no. 1-2, pp. 83–89, 2006.
- [64] A. Izquierdo, S. S. Ono, J. C. Voegel, P. Schaaf, and G. Decher, "Dipping versus spraying: exploring the deposition conditions for speeding up layer-by-layer assembly," *Langmuir*, vol. 21, no. 16, pp. 7558–7567, 2005.

Research Article

Cubic-to-Tetragonal Phase Transitions in Ag–Cu Nanorods

Francesco Delogu and Michele Mascia

Dipartimento di Ingegneria Chimica e Materiali, Università degli Studi di Cagliari, Piazza d'Armi, 09123 Cagliari, Italy

Correspondence should be addressed to Francesco Delogu, delogu@dicm.unica.it

Received 19 December 2011; Accepted 13 February 2012

Academic Editor: Grégory Guisbiers

Copyright © 2012 F. Delogu and M. Mascia. This is an open access article distributed under the Creative Commons Attribution License, which permits unrestricted use, distribution, and reproduction in any medium, provided the original work is properly cited.

Molecular dynamics simulations have been used to investigate the structural behavior of nanorods with square cross section. The nanorods consist of pure Ag and Cu phases or of three Ag and Cu domains in the sequence Ag–Cu–Ag or Cu–Ag–Cu. Ag and Cu domains are separated by coherent interfaces. Depending on the side length and the size of individual domains, Ag and Cu can undergo a transition from the usual face-centered cubic structure to a body-centered tetragonal one. Such transition can involve the whole nanorod, or only the Ag domains. In the latter case, the transition is accompanied by a loss of coherency at the Ag–Cu interfaces, with a consequent release of elastic energy. The observed behaviors are connected with the stresses developed at the nanorod surfaces.

1. Introduction

It is well known that surface and bulk atoms exhibit different properties due to their different coordination numbers [1, 2]. For example, surface atoms have a potential energy higher than bulk ones as a consequence of their smaller number of neighbors [1, 2]. It follows that the overall physical and chemical behavior of a given system depends on the fractions of surface and bulk atoms [1, 2], which are in turn affected by the characteristic system lengths [1–5]. Whenever at least one of these lengths is in the nanometer range, the fractions of surface and bulk atoms become comparable [1–5]. For this reason, nanometer-sized systems must be expected to exhibit unusual properties ascribable to surface effects [3–5].

One of the most striking examples of surface effects in nanometer-sized systems is provided by the change in the relative thermodynamic stability of different crystalline structures [6, 7]. Provided that the free energy difference between the crystalline structures is on the order of surface free energies, the crystalline phase thermodynamically less favored in the bulk can become the most stable one at the nanoscale [6, 7]. This is the case of Pd nanocubes compressed in a diamond anvil cell, which exhibit a face-centered tetragonal structure even though massive Pd under similar conditions keep the face-centered cubic (fcc) lattice [6]. Numerical simulations also indicate that isolated Ag and Au

nanorods (NRs) can exhibit a body-centered tetragonal (bct) structure, unstable in the bulk, due to intrinsic surface stresses [7, 8]. Along the same line, fcc Pd NRs have been shown to transform into either a bct or a hexagonal close-packed (hcp) structure [9, 10]. Other examples can be found in the behavior of Ni nanometer-sized systems [11, 12]. Experimental work has shown that highly strained hcp Ni islands form by heteroepitaxial growth on the (001) face of MgO [11], whereas numerical simulations have given the necessary theoretical support and extended the predictions to Co, Pd, and Pt [12]. Furthermore, it has been demonstrated that intrinsic surface stresses are sensitive to both surface composition and curvature [13–15].

Starting from the afore mentioned results, the present work aims at deepening the insight into the effect of chemical composition on the intrinsic surface stresses arising in NRs. Attention is focused on Ag and Cu NRs as well as on composite NRs with three alternate Ag and Cu domains according to the sequences Ag–Cu–Ag and Cu–Ag–Cu. Molecular dynamics simulations have been used to investigate the stability of the different NRs as a function of their cross-sectional area and, in the case of composite NRs, of the size of chemical domains. It is shown that the smallest Ag NRs exhibit an unusual bct structure. It is also shown that the presence of Cu domains can significantly affect the phase stability of Ag in composite NRs. Depending on the

composite NR size, Cu can also undergo a fcc-to-bct transition unobserved in both Cu bulk phases and NRs.

2. Computational Outline

Interactions were described by using a semiempirical tight-binding (TB) potential based on the second-moment approximation to the density of electronic states [16, 17]. Accordingly, the cohesive energy E is expressed as

$$E = \sum_{\alpha} \sum_{i_{\alpha}=1}^{N_{\alpha}} \left\{ \sum_{\beta} \sum_{j_{\beta}=1}^{N_{\beta}} A_{\alpha\beta} e^{-p_{\alpha\beta}((r_{ij}^{\alpha\beta}/d_{\alpha\beta})-1)} - \left[\sum_{\beta} \sum_{j_{\beta}=1}^{N_{\beta}} \xi_{\alpha\beta}^2 e^{-p_{\alpha\beta}((r_{ij}^{\alpha\beta}/d_{\alpha\beta})-1)} \right]^{1/2} \right\}, \quad (1)$$

where i_{α} and j_{β} run over the N_{α} and N_{β} atoms of species α and β , $r_{ij}^{\alpha\beta} = |r_{i\alpha} - r_{j\beta}|$ is the distance between two atoms, the parameters $A_{\alpha\beta}$, $\xi_{\alpha\beta}$, $p_{\alpha\beta}$, and $q_{\alpha\beta}$ quantify the potential energy, and $d_{\alpha\beta}$ is the distance between α - β nearest neighbor pairs at 0 K. The first member on the right-hand side describes the repulsive part of the potential as a Born-Mayer pairwise interaction, while the second member accounts for the attractive part in the framework of the second-moment approximation of the TB band energy [16, 17]. Interactions were computed within a cutoff distance r_c of 0.67 nm. The potential parameter values were taken from literature [17, 18].

The selected TB potential exhibits a remarkable capability in reproducing the structural, thermodynamic, and mechanical properties of both massive and nanometer-sized transition metals and their alloys [1, 2, 16–19]. It has been successfully employed to study Ag and Cu systems, including metastable solid solutions at the nanometer scale [1, 2, 16–19]. However, the present work has qualitative purposes, and the obtained results should be regarded as a rough approximation of real behavior.

Ag and Cu NRs as well as composite Ag–Cu–Ag and Cu–Ag–Cu ones were created starting from relaxed Ag and Cu bulk phases containing 256000 Ag or Cu atoms arranged in $40 \times 40 \times 40$ cF4 fcc elementary cells. The bulk systems were relaxed at 200 K in the isobaric-isothermal statistical ensemble with number of atoms, pressure, and temperature T constant [20, 21]. The Parrinello-Rahman scheme was employed to suitably deal with possible phase transitions [22]. Periodic boundary conditions were applied along the three Cartesian directions [23]. Equations of motion were solved with a fifth-order predictor-corrector algorithm [23] and a time step of 2 fs. The fluctuations of volume as well as of potential and kinetic energies were used to monitor the equilibration process, which attained completion after approximately 0.2 ns.

Five Ag NRs and five Cu NRs about 15 nm long and with square cross section were created by selecting parallelepipedic regions at the center of the Ag and Cu bulk phases, respectively. The side length s of the square cross section was given values roughly equal to 1.2, 1.6, 2.0, 2.4, and

2.8 nm. The NR main axis was chosen coincident with the $\langle 100 \rangle$ crystallographic direction, so that free surfaces exhibit (100), (010), and (001) crystallographic facets, respectively. The choice of investigating $\langle 100 \rangle$ NRs with (100), (010), and (001) crystallographic facets is motivated by the fact that only such orientation and facets allow the fcc-to-bct phase transition in Ag and Au NRs [7, 15, 24]. Although (111) crystallographic facets are in principle more stable than (100) ones [25], these seem to be necessary to reach intrinsic surface stresses large enough to affect the stability of the fcc crystalline phase and promote a change to the bct crystalline lattice.

The unsupported Ag and Cu NRs were obtained by isolating the selected parallelepipeds from the parent matrices. To such aim, the interactions between the atoms inside and outside the parallelepiped were progressively canceled by reducing linearly to zero in 50 ps, the A and ξ potential parameters for the involved atomic pairs.

Although computationally cumbersome, the afore mentioned procedure allows the gradual relaxation of NRs already during the process of formation [8, 18]. In particular, it permits equilibrating the excess energy appearing at free surfaces as a consequence of the disappearance of the matrix [8, 18]. Correspondingly, the unsupported NRs exhibit relaxed free surfaces [8, 18].

The unsupported Ag and Cu NRs were used to fabricate, respectively, the composite Ag–Cu–Ag and Cu–Ag–Cu NRs. The composite Ag–Cu–Ag NRs were created by selecting k atomic planes at the center of the Ag NRs and replacing the Ag atoms there located with Cu ones. An analogous procedure was followed to create the composite Cu–Ag–Cu NRs. The number k of Ag or Cu atomic planes defines the size of the central domains. It was given integer values in the range between 2 and 24, with consecutive values differing by two units. 72 being the total number of atomic planes included in any given NR, the number of atomic planes in the Ag or Cu end portions varied between 24 and 35. Information on the composite Ag–Cu–Ag NRs is given in Table 1.

The replacement of Ag atoms with Cu ones, and *vice versa*, induces a considerable strain at the Ag–Cu interfaces due to the different elementary cell parameters of Ag and Cu. The result is the formation of highly strained interfacial regions in which Ag and Cu lattices, even though affected by compressive and tensile respectively, keep the initial coherency [26].

Structural features were studied by comparing the distances and the spatial arrangement of neighboring atoms to point out any departure from the equilibrium fcc arrangement and to identify the attained crystalline structure [27].

The average stress f at the NR surfaces was estimated by the first derivatives of the interatomic potential [13]. Although relatively simple and direct, this method is sensitive to the shape of the potential curve [8, 13]. Therefore, small differences in the f values obtained by using different potentials must be expected. Also, it must be noted that the evaluation of the average surface stress f is further complicated by the presence of different chemical domains along

TABLE 1: The side length s , the cross-sectional area A_{NR} , the total number N of atoms and the total number N_{plane} of atoms in individual atomic planes. A_{NR} values refer to the initial configuration of the different composite Ag–Cu–Ag NRs investigated with fcc crystallographic structure. The NRs are about 15 nm long, that is, include 72 atomic planes perpendicular to the NR main axis. For each given NR, the number k of Cu atomic planes was varied of two units in the range between 2 and 24. The number N_{Cu} of Cu atoms in composite Ag–Cu–Ag NRs can be evaluated by the product of the number k of Cu atomic planes in the NR with the number N_{plane} of atoms in individual atomic planes. The number N_{Ag} of Ag atoms can be evaluated as the difference between the total number N of atoms in the NR and N_{Cu} .

s (nm)	A_{NR} (nm ²)	N	N_{plane}
1.2	1.44	1800	25
1.6	2.56	2952	41
2.0	4.00	4392	61
2.4	5.76	6120	85
2.8	7.84	8136	113

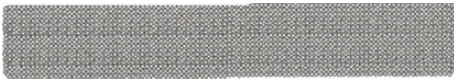


FIGURE 1: The relaxed atomic configuration of the unsupported Ag NR with sides about 2.8 nm long.

the NR axis, which results in an inhomogeneous distribution of local strains at the NR surfaces.

The induced compressive stress σ_{NR} along the NR axis can be indirectly estimated from the average surface stress f by calculating the ratio $4f/A_{NR}$ [24], where l and A_{NR} represent, respectively, the total length and the cross-sectional area of NRs.

All of the results discussed in the following were obtained from at least two simulations, aimed at ascertaining the reliability of results and their dependence on the initial configuration.

3. Ag and Cu NRs

The relaxed atomic configuration of the unsupported Ag NR with sides about 2.8 nm long is shown in Figure 1. It can be seen that the system has kept the fcc crystalline structure typical of Ag bulk phases. The stability of this structure depends on the size of the NR. As observed in previous work [8], the fcc structure is replaced by a bct one as the side length s of the Ag NR becomes equal to 2.0 nm or smaller. The analysis of the atomic arrangements indicates that the bct structure exhibits elementary cell parameters a_{bct} and c_{bct} equal to about 0.347 and 0.286 nm, respectively.

Information on the mechanism of the phase transition is obtained by visualizing the atomic configurations of Ag NRs at different times. The images of a few configurations are shown in Figure 2. They clearly point out that the fcc-to-bct phase transition nucleates at the free (100) surfaces

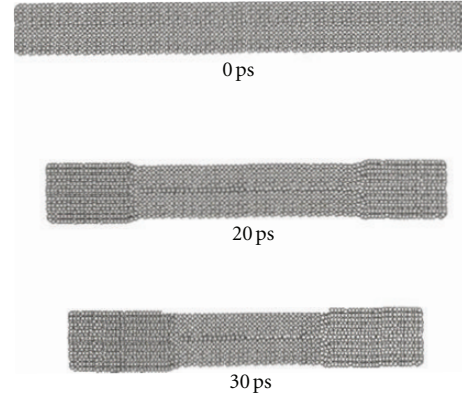


FIGURE 2: Atomic configurations of the Ag NR with side length s equal to about 2.0 nm taken at the indicated times.

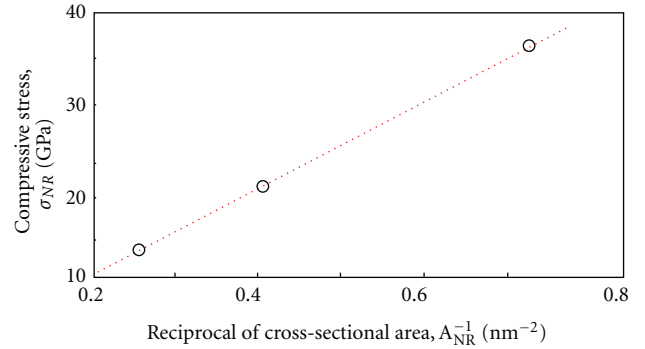


FIGURE 3: The surface-induced compressive stress σ_{NR} as a function of the reciprocal of the NR cross-sectional area A_{NR} , A_{NR}^{-1} . The best-fitted line is also shown.

perpendicular to the NR main axis and progressively propagates inwards at a rate of about 400 nm ns⁻¹.

Following previous work [7, 15], the fcc-to-bct phase transition in NRs with cross-sectional area A_{NR} smaller than about 4 nm² has been connected with the surface stress f . Calculations point out that the average surface stress f exhibited by the (100) free surfaces of the Ag NRs amounts approximately to -1.3 J m⁻². This f value is on the same order of magnitude than the ones reported in literature for Au nanowires [7]. The negative sign of the f estimate indicates that the Ag NRs undergo a contraction along their main axis. The extent to which their length contracts depends on the intensity of the compressive stress σ_{NR} induced by the surface stress f . The compressive stress σ_{NR} varies with the NR size as shown in Figure 3, where σ_{NR} is plotted as a function of the reciprocal of the NR cross-sectional area A_{NR} , A_{NR}^{-1} . The largest NR able to undergo the fcc-to-bct phase transition is the one with cross-sectional area A_{NR} equal to about 4 nm². In this case, the surface-induced compressive stress σ_{NR} amounts to about 13 GPa. This value can be also regarded as the minimum surface-induced compressive stress σ_{NR} able to promote a fcc-to-bct phase transition in Ag NRs with square cross section.

In contrast with the behavior exhibited by Ag NRs, Cu NRs do not undergo any fcc-to-bct phase transition. In all

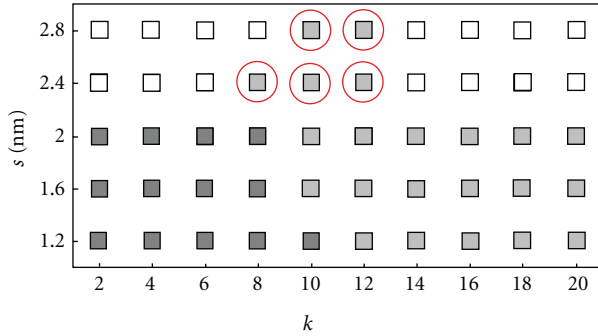


FIGURE 4: A grid showing the different combination of side length s and number k of Cu atomic planes for all of the composite Ag–Cu–Ag NRs considered. Dark and light gray indicate, respectively, the NRs entirely and partially involved in fcc-to-bct phase transitions. The red circles point out the NRs in which the fcc-to-bct phase transition of Ag end portions does not find counterpart in pure Ag NRs of the same size.

of the examined cases, that is, Cu NRs with roughly the same size of Ag NRs, the fcc structure exhibits the highest stability. Therefore, it is kept by all of the unsupported Cu NRs irrespective of their cross sectional area.

The behavior of Ag and Cu NRs described previously represents the starting point to analyze the behavior of composite Ag–Cu–Ag and Cu–Ag–Cu NRs.

4. Composite Ag–Cu–Ag NRs

In the case of Ag–Cu–Ag NRs, considerable lattice distortions are observed at the interfacial regions. On the one hand, the Cu side of the Ag–Cu interface undergoes a tensile deformation, which results in a cell parameter slightly larger than the equilibrium one. On the other hand, the Ag atoms at the interface are submitted to a compressive stress, and their local cell parameter is smaller than the equilibrium one. The same is true for all of the Ag–Cu–Ag NRs investigated.

The central Cu domain is expected to affect the fcc-to-bct phase transition behavior of the composite NRs. The stacking of k Cu atomic planes between the Ag domains can be regarded as a perturbation of the NR including only Ag atoms. The consequence of such perturbation can be readily visualized from the grid shown in Figure 4. The grid is constructed by correlating the NR side length s with the number k of Cu atomic planes and allows to mark the composite Ag–Cu–Ag NRs affected by structural changes. Four different regions can be identified. For composite Ag–Cu–Ag NRs with s equal to 2.0 nm or smaller and k equal to 8 or smaller, a fcc-to-bct phase transition takes place that also involves the Cu domain. Within the same s range, the Cu domain is no longer affected by the fcc-to-bct transition when k becomes larger than 8. The Ag–Cu–Ag NRs with side length s larger than 2.0 nm and number k of Cu atomic planes around 10 also exhibits the same behavior. This is quite surprising, since the corresponding Ag NRs do not undergo any structural transformation. Therefore, it must be inferred that the phase transition is due to the central Cu domain. For all of the remaining Ag–Cu–Ag NRs, no phase transition occurs.

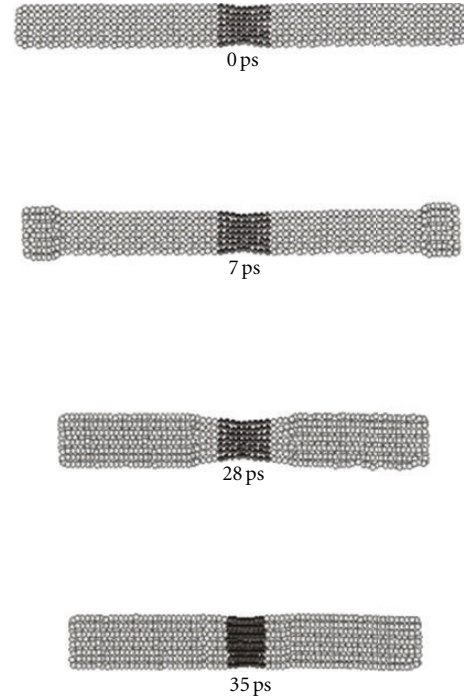


FIGURE 5: The atomic configurations of the composite Ag–Cu–Ag NR with sides about 1.2 nm long and 8 Cu atomic planes in the central region. Ag and Cu atoms are shown in light and dark gray, respectively. Configurations are taken at the times indicated.

For simplicity, hereafter the cases in which transformations take place will be indicated as A, B, and C. Case A will include the Ag–Cu–Ag NRs in which both Ag and Cu domains undergo a fcc-to-bct phase transition. Case B will refer to NRs in which only the Ag domain participates in the transition. Finally, Case C will refer to the NRs in which the Ag domains transform even though the corresponding Ag NRs do not.

4.1. Case A. The atomic configurations of the composite Ag–Cu–Ag NR with side length s equal to 1.2 nm and k equal to 8 are shown in Figure 5 at different times after the isolation from the parent matrix. It can be seen that, as in the case of Ag NRs, the fcc-to-bct phase transition starts at the Ag-free surfaces perpendicular to the main NR axis. Once the phase transition has started, the transition front propagates along the NR axis at rates of about 400 nm ns^{-1} . The Cu atomic planes in the central region do not arrest the transition front. On the contrary, it overcomes the strained coherent interfaces between Ag and Cu and forces the Cu domain to take a bct arrangement. The analysis of the arrangement of nearest neighbors indicates that the Cu bct phase exhibits elementary cell parameters a_{bct} and c_{bct} equal to about 0.309 and 0.261 nm, respectively. Correspondingly, the contraction of the Cu lattice along the main NR axis and its dilatation perpendicular to it, are similar in percentage to the ones observed in Ag NRs.

As a whole, case A NRs and Ag NRs share a similar behavior. The fcc arrangement is replaced by the bct one along the whole NR length, and the Ag–Cu interfaces keep

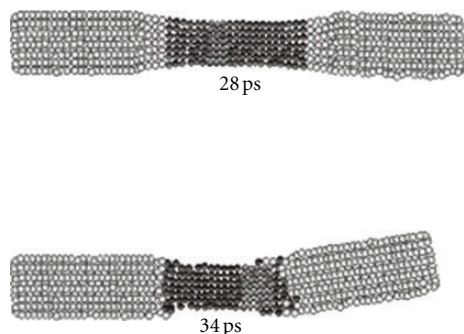


FIGURE 6: The atomic configurations of the composite Ag–Cu–Ag NR with sides about 1.2 nm long and 20 Cu atomic planes in the central region. Ag and Cu atoms are shown in light and dark gray, respectively. Configurations are taken at the times indicated.

coherent. After the transition, the composite Ag–Cu–Ag NRs still exhibit a thinner central region. Indeed, although it withstands considerable strain, the Cu domain exhibits elementary bct cell parameters smaller than Ag.

The difference between the elementary bct cell parameters of Ag and Cu depends on the size of the Cu domain. It decreases as the number k of Cu atomic planes decreases and almost disappears when k is equal to 2. The afore mentioned findings suggest that the behavior of case A NRs is dominated by the coherency of the Ag–Cu interfaces. In contrast, when the number k of Cu atomic planes increases, the Case A behavior is replaced by the Case B one.

4.2. Case B. As the number k of Cu atomic planes in the central region of the composite Ag–Cu–Ag NR with side length s equal to 2.0 nm becomes larger than 8, the fcc-to-bct phase transition no longer involves the Cu domain. The structural evolution of these NRs is exemplified by the atomic configurations shown in Figure 6, regarding the composite Ag–Cu–Ag NR with side length s equal to 1.2 nm and k equal to 20. The Ag–Cu–Ag NRs with s values equal to 1.6 and 1.2 nm and k values, respectively, equal to 8 and 10 exhibit a similar behavior.

In Case A and Ag NRs, the fcc-to-bct phase transition nucleates at the free Ag surfaces perpendicular to the main NR axis. As far as the transition fronts undergo their axial displacements within the Ag portions, the propagation rate is comparable with the one of about 400 nm ns^{-1} observed in Case A and Ag NRs. The fcc-to-bct phase transition progressively involves the entire Ag domains, but it arrests at the Ag–Cu interfaces. The Cu domain keeps its initial fcc structure, although disordering processes take place at interfaces. These determine the loss of interface coherency, and a modification of the overall structure of the NRs. The final configuration in Figure 6 clearly shows that the two Ag portions no longer share the same main axis, exhibiting a misalignment of about 10° .

A similar behavior is observed in all of the Case B NRs. The extent to which the NR structure is modified depends on the number k of Cu atomic planes. The smaller the Cu domain, the more disordered the final arrangement of the Cu and Ag portions.

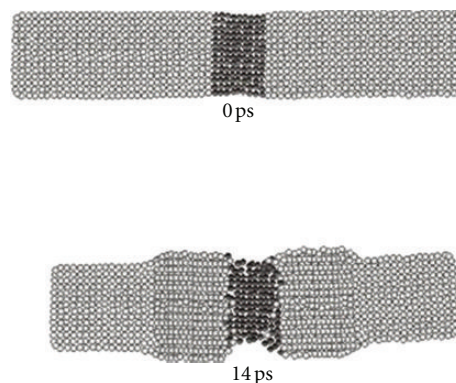


FIGURE 7: The atomic configurations of the composite Ag–Cu–Ag NR with sides about 2.4 nm long and 10 Cu atomic planes in the central region. Ag and Cu atoms are shown in light and dark gray, respectively. Configurations are taken at the times indicated.

The Ag–Cu interfaces rapidly disorder as the fcc-to-bct phase transition takes place. The structural modifications affecting the Ag domains induce a considerable strain on the adjacent Cu atomic planes. Although the Cu lattice is no longer able to follow the dilatation of the Ag one, the interfacial interactions are intense enough to induce the nucleation of lattice defects and the displacement of atomic species. This results in a limited mixing of Ag and Cu atoms at interfaces, aimed at lowering the surface energy.

4.3. Case C. A few composite Ag–Cu–Ag NRs with side length s larger than 2.0 nm also undergo structural modifications. In the light of the Ag NR behavior, this is somewhat unexpected. In fact, only Ag NRs with s values equal to 2.0 nm or smaller undergo a phase transition. Therefore, the phase transitions in the composite Ag–Cu–Ag NRs can be reasonably ascribed to the presence of the central Cu domain.

The observed structural modification is exemplified by the atomic configurations shown in Figure 7 for the composite Ag–Cu–Ag NR with side length s equal to 2.4 nm and 10 Cu atomic planes in the middle. The Ag end portions undergo the fcc-to-bct phase transition, whereas the Cu central domain is not involved. However, different from Case A and Case B NRs, the bct phase no longer nucleates at the free Ag surfaces perpendicular to the main NR axis. Rather, the phase transition starts in the neighborhood of the Ag–Cu interfaces. Thus, it appears that the transition behavior should be connected with the stress induced by the strained coherent Ag–Cu interface.

5. Composite Cu–Ag–Cu NRs

The composite Cu–Ag–Cu NRs have roughly the same size of the Ag–Cu–Ag ones, but opposite compositional profile. Simulations indicate that the central Ag domain still undergoes the fcc-to-bct phase transition, provided that the side length s is equal to 2.0 nm or smaller and the number k of Ag atomic planes is larger than 6. In the other cases, the Ag domain keeps its usual fcc structure.

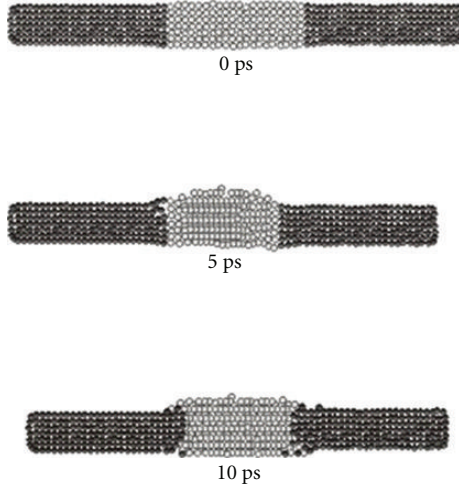


FIGURE 8: The atomic configurations of the composite Cu–Ag–Cu NR with sides about 1.2 nm long and 20 Ag atomic planes in the central region. Ag and Cu atoms are shown in light and dark gray, respectively. Configurations are taken at the times indicated.

The structural evolution of the Cu–Ag–Cu NR with side length s equal to 1.2 nm and number k of Ag atomic planes equal to 20 is exemplified by the atomic configurations shown in Figure 8. It can be seen that the phase transition nucleates homogeneously in the Ag domain. No transition front is observed. The coherency of Ag–Cu interfaces is rapidly lost, which induces the disordering of interfacial regions and the misalignment of Ag and Cu domains.

6. Discussion

The different behaviors exhibited by Ag and Cu NRs, as well as by composite Ag–Cu–Ag and Cu–Ag–Cu NRs, are determined by size effects. In the case of Ag and Cu NRs, size effects can be substantially identified with the stress f intrinsically associated with the NR free surfaces. The surface stress f can take quite large values, inducing a significant compressive stress σ_{NR} along the main NR axis. In turn, this compressive stress can be large enough to stabilize the bct structure over the fcc one. Provided that the cross-sectional area of the NRs becomes smaller than a threshold of about 4.0 nm^2 , a fcc-to-bct phase transition is actually observed in the case of Ag NRs. Conversely, no such transition takes place in the case of Cu NRs. In fact, Cu keeps its usual fcc structure irrespective of the NR cross-sectional area.

Although a similar mechanism can be expected to operate in composite Ag–Cu–Ag and Cu–Ag–Cu NRs, the situation is further complicated by the structural heterogeneity. In particular, it must be expected that size effects connected with the side length s of the NRs are modulated by the size, that is, the number k of atomic planes, of the central Cu or Ag domains. The numerical findings clearly show that, depending on the s and k values, the NRs can undergo a fcc-to-bct phase transition. This phase transition can involve either the whole NR or only the Ag domains. It must be noted that, different from the case of Ag NRs, Ag domains

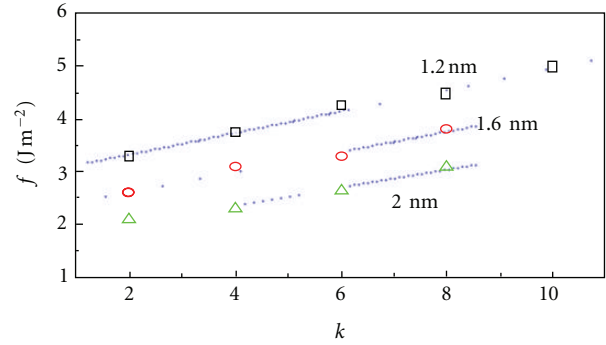


FIGURE 9: The average surface stress f as a function of the number k of Cu atomic planes for the Case A composite Ag–Cu–Ag NRs. Data refer to the case of NRs with side length s equal to 1.2, 1.6, and 2.0 nm as indicated. Best-fitted lines are also shown.

can undergo the fcc-to-bct phase transition also when their side length s is larger than 2.0 nm.

The average surface stress f for Case A composite Ag–Cu–Ag NRs that undergo the fcc-to-bct phase transformation is shown in Figure 9 as a function of the number k of Cu atomic planes. The f estimates exhibit a simple dependence on the size of the Cu domain, increasing almost linearly with k . The minimum f value allowing the fcc-to-bct phase transition amounts roughly to 2.1 J m^{-2} . This value is not far from the one observed in the case of Ag NRs, equal to about 1.7 J m^{-2} , and close to the f estimate obtained for Ag NRs submitted to a hydrostatic pressure of roughly 0.3 GPa [8]. The NRs with the shortest side length s exhibit an intrinsic surface stress f as large as 4.9 J m^{-2} . As a whole, it follows that the free surfaces of composite Ag–Cu–Ag are considerably more strained than the ones of the Ag NRs of similar size.

The large intrinsic surface stress f exhibited by case A NRs can be tentatively rationalized in terms of local strains generated by coherent Ag–Cu interfaces. The Cu fcc lattice has an elementary cell parameter of about 0.362 nm, remarkably smaller than the one of about 0.410 nm characteristic of the Ag fcc lattice. The difference between these two values induces tensile and compressive loadings, respectively, on the Cu and Ag domains, particularly in the region neighboring the coherent interface. Locally, such local strain further enhances the compressive stresses σ_{NW} , already present due to the reduced size of NRs.

A consequence of the large average values of the intrinsic surface stress f is the involvement of the central Cu domains of composite Ag–Cu–Ag NRs in the fcc-to-bct phase transition. This never occurs in bulk Cu phases and in Cu NRs, irrespective of their size. It follows that the relative stability of the bct Cu domain must be ascribed to a combination of effects connected with surface stresses and Ag–Cu coherent interfaces.

Case B and Case C NRs present different aspects. Cu domains keep their fcc structure unchanged despite the fcc-to-bct phase transition involving the Ag ones. This determines the release of the elastic energy associated with coherent Ag–Cu interfaces. Such energy was roughly estimated by calculating the potential energy difference between

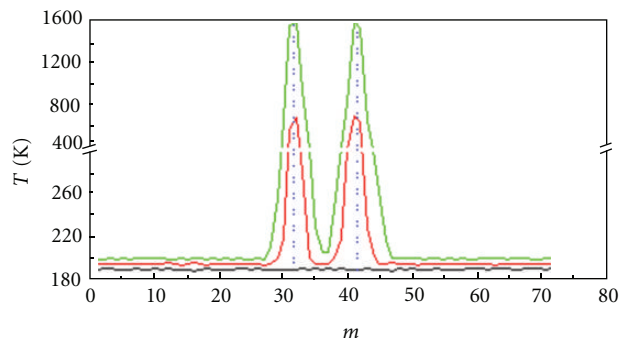


FIGURE 10: The average temperature T of the m individual atomic planes of the composite Ag–Cu–Ag NR with side length s equal to 1.6 and 10 Cu atomic planes. The vertical dotted lines ideally locate the Ag–Cu interfaces. The curves are downshifted of 5 and 10 K for avoiding superposition. From bottom to top, the data refer to the temperature profiles at the beginning of the fcc-to-bct phase transition in Ag end portions, after about 29 ps, and after about 30 ps. At longer times, the temperature of interfacial planes starts decreasing.

coherent and incoherent Ag–Cu interfaces. In turn, these were evaluated by comparing the total energies of Ag and Cu NRs of suitable size with the ones of composite Ag–Cu–Ag NRs of the same size containing either coherent or incoherent interfaces. The obtained energies for coherent and incoherent Ag–Cu interfaces with (100) topology amount roughly to 1.2 and 0.8 J m^{-2} respectively, in substantial agreement with literature values [26, 28]. It follows that the elastic energy released when the Ag domains of case B and case C NRs undergo the fcc-to-bct phase transition is on the order of 0.4 J m^{-2} . The same is true for the case of central Ag domains undergoing the fcc-to-bct transition in composite Cu–Ag–Cu NRs.

The elastic energy is released almost instantaneously at the phase transition. As a consequence, the local temperature T at Ag–Cu interfaces also rises almost instantaneously. Local temperatures T were estimated by monitoring the average kinetic energy in the m individual atomic planes forming the NRs [26]. The T estimates obtained at different times for the composite Ag–Cu–Ag NR with side length s equal to 1.6 nm and number k of Cu atomic planes equal to 10 are shown in Figure 10. It can be seen that the Ag and Cu planes at interfaces undergo a rapid T increase immediately after the loss of coherency at the Ag–Cu interfaces. The temperature T of the interfacial atomic planes rises up to about 1600 K, which is roughly 400 K points $T_{m,\text{Ag}}$ and $T_{m,\text{Cu}}$ of Ag and Cu, respectively. Although T keeps higher than $T_{m,\text{Ag}}$ and $T_{m,\text{Cu}}$ for about 5 ps only, such time interval is sufficient to allow a certain mobility to interface atoms, which undergo intermixing and disordering phenomena. The same phenomena occur in the other composite Ag–Cu–Ag NRs as well as in composite Cu–Ag–Cu NRs in which the central Ag domain undergoes the fcc-to-bct transition.

7. Conclusions

Numerical findings indicate that as the intrinsic surface stresses reach a threshold value, the fcc structure of Ag NRs

becomes unstable, and a fcc-to-bct phase transition takes place. The transition starts at the surfaces perpendicular to the main NR axis and propagates to the rest of the NR. Conversely, Cu NRs always keep the fcc structure.

Whereas the structural behavior of Ag and Cu NRs depends only on their size, in the case of composite Ag–Cu–Ag and Cu–Ag–Cu NRs, the size of the central Cu or Ag domains also plays an important role. Three different structural behaviors emerge in composite NRs as a function of the NR side length s and of the number k of atomic planes in the central Ag or Cu domain. The Ag–Cu–Ag NRs with side length $s \geq 2.4 \text{ nm}$ do not undergo structural modifications, in agreement with the case of Ag NRs of similar size. In contrast, an fcc-to-bct phase transition takes place in composite Ag–Cu–Ag NRs with side length $s \leq 2.0 \text{ nm}$ and 8 or 10 Cu atomic planes. In these cases, the transition also involves the central Cu domain, although the bct structure is unstable in both bulk Cu and pure Cu NRs of similar size.

The fcc-to-bct phase transition is also observed in Ag–Cu–Ag NRs with more than 10 Cu atomic planes and in Cu–Ag–Cu NRs with more than 6 Ag atomic planes. However, the transition only involves the Ag domains, leaving the Cu ones unaffected. The Ag–Cu interfaces lose their coherency and almost instantaneously release the associated elastic energy. The temperature of interfaces suddenly rises up to about 1600 K, which allows a significant local disordering and the loss of coaxiality of Ag and Cu domains.

Acknowledgments

A. Ermini, ExtraInformatica s.r.l., is gratefully acknowledged for his kind assistance and support. Financial support has been given by the University of Cagliari.

References

- [1] F. Baletto and R. Ferrando, “Structural properties of nanoclusters: energetic, thermodynamic, and kinetic effects,” *Reviews of Modern Physics*, vol. 77, no. 1, pp. 371–423, 2005.
- [2] R. Ferrando, J. Jellinek, and R. L. Johnston, “Nanoalloys: From theory to applications of alloy clusters and nanoparticles,” *Chemical Reviews*, vol. 108, no. 3, pp. 845–910, 2008.
- [3] P. Moriarty, “Nanostructured materials,” *Reports on Progress in Physics*, vol. 64, no. 3, pp. 297–381, 2001.
- [4] J. Jortner and C. N. R. Rao, “Nanostructured advanced materials. Perspectives and directions,” *Pure and Applied Chemistry*, vol. 74, no. 9, pp. 1491–1506, 2002.
- [5] G. A. Ozin and A. C. Arsenault, *Nanochemistry. A Chemical Approach to Nanomaterials*, RSC Publishing, Cambridge, UK, 2005.
- [6] Q. Guo, Y. Zhao, W. L. Mao, Z. Wang, Y. Xiong, and Y. Xia, “Cubic to tetragonal phase transformation in cold-compressed Pd nanocubes,” *Nano Letters*, vol. 8, no. 3, pp. 972–975, 2008.
- [7] K. Gall, J. Diao, M. L. Dunn, M. Hafel, N. Bernstein, and M. J. Mehl, “Tetragonal phase transformation in gold nanowires,” *Journal of Engineering Materials and Technology*, vol. 127, no. 4, pp. 417–422, 2005.
- [8] F. Delogu, “Numerical investigation of the cubic-to-tetragonal phase transition in Ag nanorods,” *Journal of Physical Chemistry*

- C, vol. 114, no. 8, pp. 3364–3370, 2010.
- [9] J. Lao and D. Moldovan, “Surface stress induced structural transformations and pseudoelastic effects in palladium nanowires,” *Applied Physics Letters*, vol. 93, no. 9, Article ID 093108, 2008.
- [10] V. K. Sutrarakar and D. R. Mahapatra, “Comment on “surface stress induced structural transformations and pseudoelastic effects in palladium nanowires” [Appl. Phys. Lett. 93, 093108 (2008)],” *Applied Physics Letters*, vol. 97, no. 14, Article ID 146101, 2010.
- [11] W. Tian, H. P. Sun, X. Q. Pan et al., “Hexagonal close-packed Ni nanostructures grown on the (001) surface of MgO,” *Applied Physics Letters*, vol. 86, no. 13, Article ID 131915, 3 pages, 2005.
- [12] R. Ferrando, G. Rossi, F. Nita, G. Barcaro, and A. Fortunelli, “Interface-stabilized phases of metal-on-oxide nanodots,” *ACS Nano*, vol. 2, no. 9, pp. 1849–1856, 2008.
- [13] G. J. Ackland and M. W. Finnis, “Semi-empirical calculation of solid surface tensions in body-centred cubic transition metals,” *Philosophical Magazine A*, vol. 54, no. 2, pp. 301–315, 1986.
- [14] F. H. Streitz, R. C. Cammarata, and K. Sieradzki, “Surface-stress effects on elastic properties. I. Thin metal films,” *Physical Review B*, vol. 49, no. 15, pp. 10699–10706, 1994.
- [15] J. Diao, K. Gall, and M. L. Dunn, “Atomistic simulation of the structure and elastic properties of gold nanowires,” *Journal of the Mechanics and Physics of Solids*, vol. 52, no. 9, pp. 1935–1962, 2004.
- [16] V. Rosato, M. Guillope, and B. Legrand, “Thermodynamical and structural properties of f.c.c. transition metals using a simple tight-binding model,” *Philosophical Magazine A*, vol. 59, no. 2, pp. 321–336, 1989.
- [17] F. Cleri and V. Rosato, “Tight-binding potentials for transition metals and alloys,” *Physical Review B*, vol. 48, no. 1, pp. 22–33, 1993.
- [18] F. Delogu, E. Arca, G. Mulas, G. Manai, and I. Shvets, “Numerical investigation of the stability of Ag-Cu nanorods and nanowires,” *Physical Review B*, vol. 78, no. 2, Article ID 024103, 2008.
- [19] F. Delogu, “Numerical simulation of the compression behavior of nanometer-sized Ag particles,” *Journal of Nanoscience and Nanotechnology*, vol. 9, no. 5, pp. 2944–2949, 2009.
- [20] H. C. Andersen, “Molecular dynamics simulations at constant pressure and/or temperature,” *The Journal of Chemical Physics*, vol. 72, no. 4, pp. 2384–2393, 1980.
- [21] S. Nosé, “A unified formulation of the constant temperature molecular dynamics methods,” *The Journal of Chemical Physics*, vol. 81, no. 1, pp. 511–519, 1984.
- [22] M. Parrinello and A. Rahman, “Polymorphic transitions in single crystals: a new molecular dynamics method,” *Journal of Applied Physics*, vol. 52, no. 12, pp. 7182–7190, 1981.
- [23] M. P. Allen and D. Tildesley, *Computer Simulations of Liquids*, Clarendon Press, Oxford, UK, 1987.
- [24] J. Diao, K. Gall, and M. L. Dunn, “Surface-stress-induced phase transformation in metal nanowires,” *Nature Materials*, vol. 2, no. 10, pp. 656–660, 2003.
- [25] G. E. Tommei, F. Baletto, R. Ferrando, R. Spadacini, and A. Danani, “Energetics of fcc and decahedral nanowires of Ag, Cu, Ni, and C 60: a quenched molecular dynamics study,” *Physical Review B*, vol. 69, no. 11, Article ID 115426, 2004.
- [26] G. Mazzone, V. Rosato, M. Pintore, F. Delogu, P. Demontis, and G. B. Suffritti, “Molecular-dynamics calculations of thermodynamic properties of metastable alloys,” *Physical Review B*, vol. 55, no. 2, pp. 837–842, 1997.
- [27] H. P. Klug and L. E. Alexander, *X-ray Diffraction Procedures*, John Wiley & Sons, New York, NY, USA, 1974.
- [28] G. A. Adebayo and B. C. Anusionwu, “Dynamical properties of Ag-Cu binary alloy from molecular dynamics simulation,” *European Physical Journal B*, vol. 54, no. 4, pp. 423–427, 2006.